A reporter examines her own DNA *p. 1167*

Wishlist-worthy books for young readers *p. 1172*

Reducing youth violence via summer jobs *p. 1219*

Science

$10
5 DECEMBER 2014
sciencemag.org

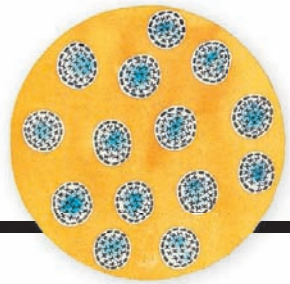
AAAS



A shocking predator

Electric eels remotely control muscles of their prey *p. 1231*

CONTENTS



1172 The kid's guide to microorganisms

5 DECEMBER 2014 • VOLUME 346 • ISSUE 6214

NEWS



IN BRIEF

1158 Roundup of the week's news

IN DEPTH

1161 **RESEARCHERS STRUGGLE TO GAUGE RISKS OF CHILDHOOD ANESTHESIA**
Neurological warning signals in animals drive push for new studies and public outreach *By K. Servick*

1162 **SATELLITES TRACK HERITAGE LOSS ACROSS SYRIA AND IRAQ**
Vandalism, looting, and collateral damage erase history *By A. Lawler*

1164 **THE OLD MAN AND THE DISEASE**
In Liberia's Ebola outbreak, star statistician Hans Rosling is facing the intellectual challenge of a lifetime *By K. Kupferschmidt*

1166 **BRAZILIAN SCIENTISTS PROTEST FUNDING BONANZA FOR BRAIN CAMPUS**
$100 million grant came as a surprise to many *By E. Underwood*

FEATURE

1167 **UNKNOWN SIGNIFICANCE**
Years of writing about genetic testing did not prepare me for my own foray into this rapidly changing world
By J. Couzin-Frankel

INSIGHTS

BOOKS *ET AL.*

1172 **MARS, MICROBES, AND MASTODONS... OH MY!**

1178 **FROM YOU TO THE UNIVERSE—AND EVERYTHING IN BETWEEN**

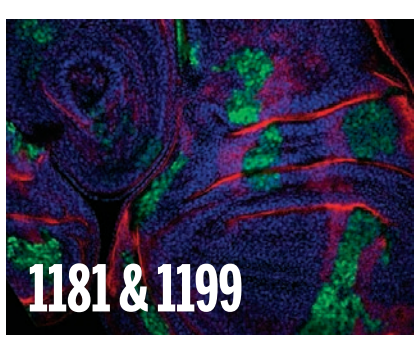
PERSPECTIVES

1180 **HOW ICE SHELVES MELT**
Warming of the water that flows under Antarctic ice shelves is key to their melting *By S. Gille*
▸ REPORT P. 1227

1181 **DEATH TO THE LOSERS**
Cell competition is linked to innate immunity mechanisms to eliminate unwanted cells and maintain healthy tissue *By G. Morata and L. Ballesteros-Arias*
▸ RESEARCH ARTICLE P. 1199

1183 **CALCULATING THE PRESSURE DEPENDENCE OF CHEMICAL REACTIONS**
A priori calculations can accurately predict rates of methane formation from radicals *By M. J. Pilling*
▸ REPORT P. 1212

1184 **DRIVING THE EARTH MACHINE?**
The region of the mantle directly below the tectonic plates plays a key role in mantle flow and volcanism
By D. L. Anderson and S. D. King



1186 **STABILITY AT THE SURFACE**
The structure beneath a surface is a key factor in its electronic and chemical function *By S. A. Chambers*
▸ REPORT P. 1215

1187 **SLEEPING DOGS OF THE GENOME**
Retrotransposable elements may be agents of somatic diversity, disease, and aging *By V. Gorbunova* et al.

1189 **USING AND IMPROVING THE SOCIAL COST OF CARBON**
Regular, institutionalized updating and review are essential
By W. Pizer et al.

***SCIENCE* PRIZE ESSAY**

1191 **SIZE DOES MATTER**
Lysosome-based signaling machine regulates cell growth *By L. Bar-Peled*

LETTERS

1193 **CONSERVING BRAZIL'S ATLANTIC FORESTS**
By R. Buckley and F. de Vasconcellos Pegas

1193 **RESPONSE**
By C. Banks-Leite et al.

1193 **ERRATA**

1194 **ONLINE BUZZ: HIGHER EDUCATION**

RESEARCH

IN BRIEF

1195 From *Science* and other journals

REVIEW

1198 **LUNAR GEOLOGY**
The lunar dynamo
B. P. Weiss and S. M. Tikoo
REVIEW SUMMARY; FOR FULL TEXT: dx.doi.org/10.1126/science.1246753

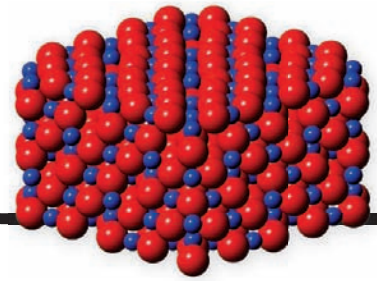
RESEARCH ARTICLES

1199 **CELL COMPETITION**
An ancient defense system eliminates unfit cells from developing tissues during cell competition *S. N. Meyer* et al.
RESEARCH ARTICLE SUMMARY; FOR FULL TEXT: dx.doi.org/10.1126/science.1258236
▸ PERSPECTIVE P. 1181

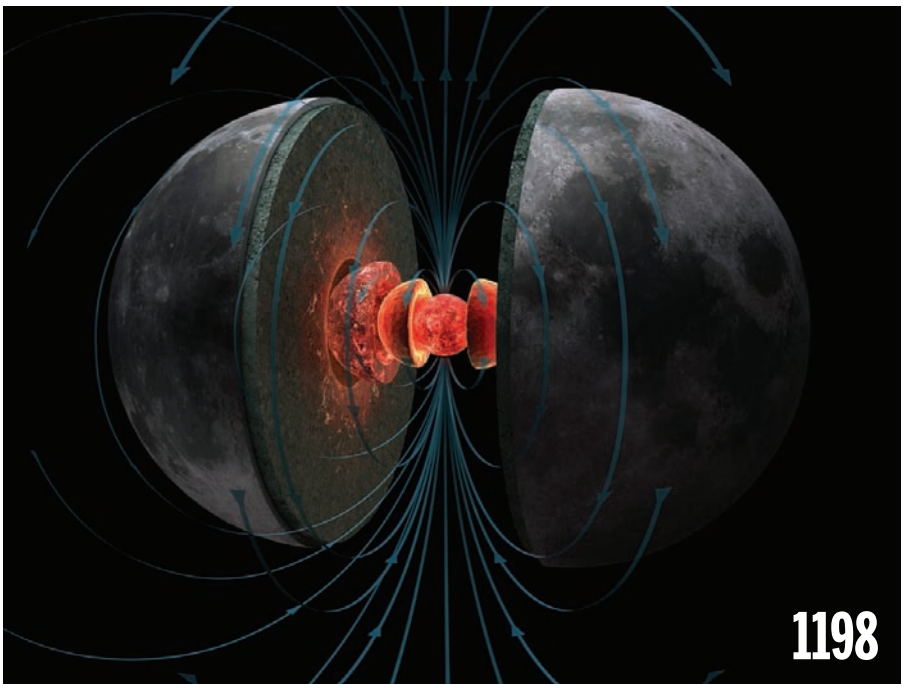
Published by AAAS

CONTENTS

5 DECEMBER 2014 • VOLUME 346 • ISSUE 6214



1186 & 1215
A close-up look at the surface of magnetite



1200 PLANT GENETICS
Dominance hierarchy arising from the evolution of a complex small RNA regulatory network *E. Durand* et al.

REPORTS

1205 VALLEYTRONICS
Ultrafast generation of pseudo-magnetic field for valley excitons in WSe_2 monolayers *J. Kim* et al.

1208 HEAVY FERMIONS
Two-dimensional Fermi surfaces in Kondo insulator SmB_6 *G. Li* et al.

1212 CHEMICAL KINETICS
Predictive a priori pressure-dependent kinetics *A. W. Jasper* et al.
▸ PERSPECTIVE P. 1183

1215 SURFACE STRUCTURE
Subsurface cation vacancy stabilization of the magnetite (001) surface *R. Bliem* et al.
▸ PERSPECTIVE P. 1186

1219 HUMAN CAPITAL
Summer jobs reduce violence among disadvantaged youth *S. B. Heller*

1223 PALEOCLIMATE
Coherent changes of southeastern equatorial and northern African rainfall during the last deglaciation *B. L. Otto-Bliesner* et al.

1227 OCEANOGRAPHY
Multidecadal warming of Antarctic waters *S. Schmidtko* et al.
▸ PERSPECTIVE P. 1180

1231 ANIMAL PHYSIOLOGY
The shocking predatory strike of the electric eel *K. Catania*
▸ PODCAST

1234 INFLAMMATION
Neutrophils scan for activated platelets to initiate inflammation *V. Sreeramkumar* et al.

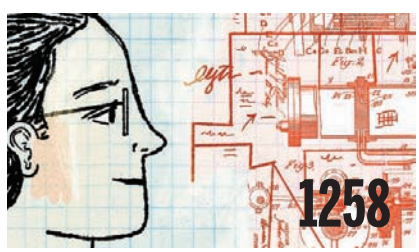
1238 TRANSCRIPTION
Chromatin decondensation is sufficient to alter nuclear organization in embryonic stem cells *P. Therizols* et al.

1242 STRUCTURAL BIOLOGY
Time-resolved serial crystallography captures high-resolution intermediates of photoactive yellow protein *J. Tenboer* et al.

DEPARTMENTS

1155 EDITORIAL
The measure of research merit
By Marcia McNutt

1258 WORKING LIFE
Finally free
By Vincent F. Scalfani



ON THE COVER



An electric eel (*Electrophorus electricus*) can generate up to 600 volts using modified muscles that act as batteries. This electrical weapon allows the eel to remotely activate the muscles in nearby prey to cause either involuntary movement or involuntary immobility, depending on the eel's needs. See page 1231 for details and links to movies that illustrate these findings.
Photo: © Kenneth Catania

Science Staff 1154
New Products 1247
Science Careers 1248

IMAGE: (TOP LEFT) HERNÁN CAÑELLAS

SCIENCE (ISSN 0036-8075) is published weekly on Friday, except the last week in December, by the American Association for the Advancement of Science, 1200 New York Avenue, NW, Washington, DC 20005. Periodicals mail postage (publication No. 484460) paid at Washington, DC, and additional mailing offices. Copyright © 2014 by the American Association for the Advancement of Science. The title SCIENCE is a registered trademark of the AAAS. Domestic individual membership and subscription (51 issues): $153 ($74 allocated to subscription). Domestic institutional subscription (51 issues): $1282; Foreign postage extra: Mexico, Caribbean (surface mail) $55; other countries (air assist delivery) $85. First class, airmail, student, and emeritus rates on request. Canadian rates with GST available upon request, GST #1254 88122. Publications Mail Agreement Number 1069624. **Printed in the U.S.A.**
Change of address: Allow 4 weeks, giving old and new addresses and 8-digit account number. **Postmaster:** Send change of address to AAAS, P.O. Box 96178, Washington, DC 20090–6178. **Single-copy sales:** $10.00 current issue, $15.00 back issue prepaid includes surface postage; bulk rates on request. **Authorization to photocopy** material for internal or personal use under circumstances not falling within the fair use provisions of the Copyright Act is granted by AAAS to libraries and other users registered with the Copyright Clearance Center (CCC) Transactional Reporting Service, provided that $30.00 per article is paid directly to CCC, 222 Rosewood Drive, Danvers, MA 01923. The identification code for *Science* is 0036-8075. *Science* is indexed in the *Reader's Guide to Periodical Literature* and in several specialized indexes.

Published by AAAS

Science
AAAS
1200 New York Avenue, NW, Washington, DC 20005
Bateman House, 82-88 Hills Road, Cambridge, UK CB2 1LQ

Editor-in-Chief Marcia McNutt
Executive Editor Monica M. Bradford **News Editor** Tim Appenzeller
Managing Editor, Research Journals Katrina L. Kelner
Deputy Editors Barbara R. Jasny, Andrew M. Sugden(UK), Valda J. Vinson, Jake S. Yeston

Research and Insights

SR. EDITORS Caroline Ash(UK), Gilbert J. Chin, Lisa D. Chong, Maria Cruz(UK), Julia Fahrenkamp-Uppenbrink(UK), Pamela J. Hines, Stella M. Hurtley(UK), Paula A. Kiberstis, Marc S. Lavine(Canada), Kristen L. Mueller, Ian S. Osborne(UK), Beverly A. Purnell, L. Bryan Ray, Guy Riddihough, H. Jesse Smith, Jelena Stajic, Peter Stern(UK), Phillip D. Szuromi, Brad Wible, Nicholas S. Wigginton, Laura M. Zahn **ASSOCIATE EDITORS** Brent Grocholski, Melissa R. McCartney, Margaret M. Moerchen, Sacha Vignieri **ASSOCIATE BOOK REVIEW EDITOR** Valerie B. Thompson **ASSOCIATE LETTERS EDITOR** Jennifer Sills **CHIEF CONTENT PRODUCTION EDITOR** Cara Tate **SR. CONTENT PRODUCTION EDITORS** Harry Jach, Trista Wagoner **CONTENT PRODUCTION EDITORS** Jeffrey E. Cook, Chris Filiatreau, Cynthia Howe, Lauren Kmec, Barbara P. Ordway **SR. EDITORIAL COORDINATORS** Carolyn Kyle, Beverly Shields **EDITORIAL COORDINATORS** Ramatoulaye Diop, Joi S. Granger, Lisa Johnson, Anita Wynn **PUBLICATIONS ASSISTANTS** Aneera Dobbins, Jeffrey Hearn, Dona Mathieu, Le-Toya Mayne Flood, Shannon McMahon, Scott Miller, Jerry Richardson, Rachel Roberts(UK), Alice Whaley(UK), Brian White **EXECUTIVE ASSISTANT** Anna Bashkirova **ADMINISTRATIVE SUPPORT** Janet Clements(UK), Michael Crabtree(UK, Intern), Lizanne Newton(UK), Maryrose Madrid, John Wood(UK)

News

NEWS MANAGING EDITOR John Travis **INTERNATIONAL EDITOR** Richard Stone **DEPUTY NEWS EDITORS** Daniel Clery(UK), Robert Coontz, Elizabeth Culotta, David Grimm, David Malakoff, Leslie Roberts **CONTRIBUING EDITORS** Martin Enserink(Europe), Mara Hvistendahl (Asia) **SR. CORRESPONDENTS** Jeffrey Mervis, Elizabeth Pennisi **NEWS WRITERS** Adrian Cho, Jon Cohen, Jennifer Couzin-Frankel, Carolyn Gramling, Eric Hand, Jocelyn Kaiser, Kelly Servick, Robert F. Service, Erik Stokstad, Emily Underwood **INTERNS** David Shultz, Jia You **CONTRIBUTING CORRESPONDENTS** Pallava Bagla(South Asia), Michael Balter(Paris), John Bohannon, Ann Gibbons, Sam Kean, Richard A. Kerr, Eli Kintisch, Kai Kupferschmidt(Berlin), Andrew Lawler, Christina Larson(Beijing), Mitch Leslie, Charles C. Mann, Eliot Marshall, Virginia Morell, Dennis Normile(Tokyo), Heather Pringle, Tania Rabesandratana(Brussels), Gretchen Vogel(Berlin), Lizzie Wade(Mexico City) **CAREERS** Jim Austin(Editor), Donisha Adams **COPY EDITORS** Kara Estelle, Nora Kelly, Jennifer Levin **ADMINISTRATIVE SUPPORT** Scherraine Mack

Executive Publisher Alan I. Leshner
Publisher Kent R. Anderson **Chief Digital Media Officer** Rob Covey

BUSINESS OPERATIONS AND ADMINISTRATION DIRECTOR Deborah Rivera-Wienhold **BUSINESS SYSTEMS AND FINANCIAL ANALYSIS DIRECTOR** Randy Yi **MANAGER OF FULFILLMENT SYSTEMS** Neal Hawkins **SYSTEMS ANALYST** Nicole Mehmedovich **ASSISTANT DIRECTOR, BUSINESS OPERATIONS** Eric Knott **MANAGER, BUSINESS OPERATIONS** Jessica Tierney **BUSINESS ANALYSTS** Cory Lipman, Cooper Tilton, Celeste Troxler **FINANCIAL ANALYST** Jeremy Clay **RIGHTS AND PERMISSIONS ASSISTANT DIRECTOR** Emilie David **PERMISSIONS ASSOCIATE** Elizabeth Sandler **RIGHTS, CONTRACTS, AND LICENSING ASSOCIATE** Lili Kiser

MARKETING DIRECTOR Ian King **MARKETING MANAGER** Julianne Wielga **MARKETING ASSOCIATE** Elizabeth Sattler **SR. MARKETING EXECUTIVE** Jennifer Reeves **SR. ART ASSOCIATE, PROJECT MANAGER** Tzeitel Sorrosa **ART ASSOCIATE** Seil Lee **ASSISTANT COMMERCIAL EDITOR** Selby Frame **MARKETING PROJECT MANAGER** Angelissa McArthur **SR. WRITER** Bill Zimmer **PROGRAM DIRECTOR, AAAS MEMBER CENTRAL** Peggy Mihelich **FULFILLMENT SYSTEMS AND OPERATIONS** membership@aaas.org **MANAGER, MEMBER SERVICES** Pat Butler **SPECIALISTS** LaToya Casteel, Javia Flemmings, Latasha Russell **MANAGER, DATA ENTRY** Mickie Napoleoni **DATA ENTRY SPECIALISTS** JJ Regan, Jaimee Wise, Fiona Giblin

DIRECTOR, SITE LICENSING Tom Ryan **DIRECTOR, CORPORATE RELATIONS** Eileen Bernadette Moran **SR. PUBLISHER RELATIONS SPECIALIST** Kiki Forsythe **PUBLISHER RELATIONS MANAGER** Catherine Holland **PUBLISHER RELATIONS, EASTERN REGION** Keith Layson **PUBLISHER RELATIONS, WESTERN REGION** Ryan Rexroth **MANAGER, SITE LICENSE OPERATIONS** Iquo Edim **FULFILLMENT ANALYST** Lana Guz **ASSOCIATE DIRECTOR, MARKETING** Christina Schlecht **MARKETING ASSOCIATES** Thomas Landreth, Minah Kim

DIRECTOR OF WEB TECHNOLOGIES Ahmed Khadr **SR. DEVELOPER** Chris Coleman **DEVELOPERS** Dan Berger, Jimmy Marks **SR. PROJECT MANAGER** Trista Smith **SYSTEMS ENGINEER** Luke Johnson **PRODUCT MANAGER** Walter Jones

CREATIVE DIRECTOR, MULTIMEDIA Martyn Green **DIRECTOR OF ANALYTICS** Enrique Gonzales **SR. WEB PRODUCER** Sarah Crespi **WEB PRODUCER** Alison Crawford **VIDEO PRODUCER** Nguyen Nguyen **SOCIAL MEDIA PRODUCER** Meghna Sachdev

DIRECTOR OF OPERATIONS PRINT AND ONLINE Lizabeth Harman **PRINT PRODUCTION DIRECTOR** Wendy K. Shank **PREFLIGHT MANAGER** Marcus Spiegler **ASSISTANT MANAGER ONLINE** Lisa Stanford **ASSISTANT MANAGER PRINT** Rebecca Doshi **SR SPECIALISTS** Steve Forrester, Jason Hillman, Antoinette Hodal, Tara Kelly, Anthony Rosen **SPECIALISTS** Jacob Hedrick, Nichele Johnston, Lori Murphy, Kimberley Oster

DESIGN DIRECTOR Beth Rakouskas **ASSOCIATE ART DIRECTOR** Laura Creveling **SR. ILLUSTRATORS** Chris Bickel, Katharine Sutliff **ILLUSTRATOR** Valerie Altounian **SR. ART ASSOCIATES** Holly Bishop, Preston Huey **ART ASSOCIATES** Kay Engman, Garvin Grullón, Chrystal Smith **SR. PHOTO EDITOR** William Douthitt **PHOTO EDITOR** Leslie Blizard

DIRECTOR, GLOBAL COLLABORATION, CUSTOM PUBLICATIONS, ADVERTISING Bill Moran **EDITOR, CUSTOM PUBLISHING** Sean Sanders: 202-326-6430 **ASSISTANT EDITOR, CUSTOM PUBLISHING** Tianna Hicklin: 202-326-6463 **ADVERTISING MARKETING MANAGER** Justin Sawyers: 202-326-7061 science_advertising@aaas.org **ADVERTISING MARKETING ASSOCIATE** Javia Flemmings **ADVERTISING SUPPORT MANAGER** Karen Foote: 202-326-6740 **ADVERTISING PRODUCTION OPERATIONS MANAGER** Deborah Tompkins **SR. PRODUCTION SPECIALIST/GRAPHIC DESIGNER** Amy Hardcastle **PRODUCTION SPECIALIST** Yuse Lajiminmuhip **SR. TRAFFIC ASSOCIATE** Christine Hall **SALES COORDINATOR** Shirley Young **ASSOCIATE DIRECTOR, COLLABORATION, CUSTOM PUBLICATIONS/CHINA/TAIWAN/KOREA/SINGAPORE** Ruolei Wu: +86-186 0822 9345, rwu@aaas.org **COLLABORATION/CUSTOM PUBLICATIONS/JAPAN** Adarsh Sandhu + 81532-81-5142 asandhu@aaas.org **EAST COAST/E. CANADA** Laurie Faraday: 508-747-9395, FAX 617-507-8189 **WEST COAST/W. CANADA** Lynne Stickrod: 415-931-9782, FAX 415-520-6940 **MIDWEST** Jeffrey Dembksi: 847-498-4520 x3005, Steven Loerch: 847-498-4520 x3006 **UK EUROPE/ASIA** Roger Goncalves: TEL/FAX +41 43 243 1358 **JAPAN** Katsuyoshi Fukamizu(Tokyo): +81-3-3219-5777 kfukamizu@aaas.org **CHINA/TAIWAN** Ruolei Wu: +186-0082-9345

WORLDWIDE ASSOCIATE DIRECTOR OF SCIENCE CAREERS Tracy Holmes: +44 (0) 1223 326525, FAX +44 (0) 1223 326532 tholmes@science-int.co.uk **CLASSIFIED** advertise@sciencecareers.org **U.S. SALES** Tina Burks: 202-326-6577, Nancy Toema: 202-326-6578 **SALES ADMINISTRATOR** Marci Gallun **EUROPE/ROW SALES** Axel Gesatzki, Sarah Lelarge **SALES ASSISTANT** Kelly Grace **JAPAN** Hiroyuki Mashiki(Kyoto): +81-75-823-1109 hmashiki@aaas.org **CHINA/TAIWAN** Ruolei Wu: +86-186 0082 9345 rwu@aaas.org **MARKETING MANAGER** Allison Pritchard **MARKETING ASSOCIATE** Aimee Aponte

AAAS BOARD OF DIRECTORS RETIRING PRESIDENT, CHAIR Phillip A. Sharp **PRESIDENT** Gerald R. Fink **PRESIDENT-ELECT** Geraldine (Geri) Richmond **TREASURER** David Evans Shaw **CHIEF EXECUTIVE OFFICER** Alan I. Leshner **BOARD** Bonnie L. Bassler, May R. Berenbaum, Carlos J. Bustamante, Claire M. Fraser, Laura H. Greene, Elizabeth Loftus, Raymond Orbach, Inder M. Verma

SUBSCRIPTION SERVICES For change of address, missing issues, new orders and renewals, and payment questions: 866-434-AAAS (2227) or 202-326-6417, FAX 202-842-1065. Mailing addresses: AAAS, P.O. Box 96178, Washington, DC 20090-6178 or AAAS Member Services, 1200 New York Avenue, NW, Washington, DC 20005

INSTITUTIONAL SITE LICENSES 202-326-6755 **REPRINTS:** Author Inquiries 800-635-7181 **COMMERCIAL INQUIRIES** 803-359-4578 **PERMISSIONS** 202-326-6765, permissions@aaas.org **AAAS Member Services** 202-326-6417 or http://membercentral.aaas.org/discounts

Science serves as a forum for discussion of important issues related to the advancement of science by publishing material on which a consensus has been reached as well as including the presentation of minority of conflicting points of view. Accordingly, all articles published in *Science*—including editorials, news and comment, and books reviews—are signed and reflect the individual views of the authors and not official points of view adopted by AAAS or the institutions with which the authors are affiliated.

INFORMATION FOR AUTHORS See pages 680 and 681 of the 7 February 2014 issue or access www.sciencemag.org/about/authors

SENIOR EDITORIAL BOARD
A. Paul Alivisatos, *Lawrence Berkeley Nat'l. Laboratory,* **Ernst Fehr,** *U. of Zürich*
Susan M. Rosenberg, *Baylor College of Medicine,* **Michael S. Turner,** *U. of Chicago*

BOARD OF REVIEWING EDITORS (Statistics board members indicated with **(S)**)
Adriano Aguzzi, *U. Hospital Zürich*
Takuzo Aida, *U. of Tokyo*
Leslie Aiello, *Wenner-Gren Foundation*
Judith Allen, *U. of Edinburgh*
Sonia Altizer, *U. of Georgia*
Virginia Armbrust, *U. of Washington*
Sebastian Amigorena, *Institut Curie*
Kathryn Anderson, *Memorial Sloan-Kettering Cancer Center*
Peter Andolfatto, *Princeton U.*
Meinrat O. Andreae, *Max-Planck Inst. Mainz*
Paola Arlotta, *Harvard U.*
Johan Auwerx, *EPFL*
David Awschalom, *U. of Chicago*
Jordi Bascompte, *Estación Biológica de Doñana CSIC*
Facundo Batista, *London Research Inst.*
Ray H. Baughman, *U. of Texas, Dallas*
David Baum, *U. of Wisconsin*
Kamran Behnia, *ESPCI-ParisTech*
Yasmine Belkaid, *NIAID, NIH*
Philip Benfey, *Duke U.*
Stephen J. Benkovic, *Penn State U.*
Carlo Beenakker, *Leiden U.*
Gabriele Bergers, *U. of California, San Francisco*
Christophe Bernard, *Aix-Marseille U.*
Bradley Bernstein, *Massachusettes General Hospital*
Peer Bork, *EMBL*
Bernard Bourdon, *Ecole Normale Supérieure de Lyon*
Chris Bowler, *École Normale Supérieure*
Ian Boyd, *U. of St. Andrews*
Emily Brodsky, *U. of California, Santa Cruz*
Ron Brookmeyer, *U. of California Los Angeles* **(S)**
Christian Büchel, *U. Hamburg-Eppendorf*
Joseph A. Burns, *Cornell U.*
Gyorgy Buzsaki, *New York U. School of Medicine*
Blanche Capel, *Duke U.*
Mats Carlsson, *U. of Oslo*
David Clapham, *Children's Hospital Boston*
David Clary, *U. of Oxford*
Joel Cohen, *Rockefeller U., Columbia U.*
Jonathan D. Cohen, *Princeton U.*
James Collins, *Boston U.*
Robert Cook-Deegan, *Duke U.*
Alan Cowman, *Walter & Eliza Hall Inst.*
Robert H. Crabtree, *Yale U.*
Roberta Croce, *Vrije Universiteit*
Janet Currie, *Princeton U.*
Jeff L. Dangl, *U. of North Carolina*
Tom Daniel, *U. of Washington*
Frans de Waal, *Emory U.*
Stanislas Dehaene, *Collège de France*
Robert Desimone, *MIT*
Claude Desplan, *New York U.*
Ap Dijksterhuis, *Radboud U. of Nijmegen*
Dennis Discher, *U. of Pennsylvania*
Gerald W. Dorn II, *Washington U. School of Medicine*
Jennifer A. Doudna, *U. of California, Berkeley*
Bruce Dunn, *U. of California, Los Angeles*
Christopher Dye, *WHO*
Todd Ehlers, *U. of Tuebingen*
David Ehrhardt, *Carnegie Inst. of Washington*
Tim Elston, *U. of North Carolina at Chapel Hill*
Gerhard Ertl, *Fritz-Haber-Institut, Berlin*
Barry Everitt, *U. of Cambridge*
Ernst Fehr, *U. of Zurich*
Anne C. Ferguson-Smith, *U. of Cambridge*
Michael Feuer, *The George Washington U.*
Kate Fitzgerald, *U. of Massachusetts*
Peter Fratzl, *Max-Planck Inst.*
Elaine Fuchs, *Rockefeller U.*
Daniel Geschwind, *UCLA*
Andrew Gewirth, *U. of Illinois*
Karl-Heinz Glassmeier, *TU Braunschweig*
Ramon Gonzalez, *Rice U.*
Julia R. Greer, *Caltech*
Elizabeth Grove, *U. of Chicago*
Kip Guy, *St. Jude's Children's Research Hospital*
Taekjip Ha, *U. of Illinois at Urbana-Champaign*
Christian Haass, *Ludwig Maximilians U.*
Steven Hahn, *Fred Hutchinson Cancer Research Center*
Michael Hasselmo, *Boston U.*
Martin Heimann, *Max-Planck Inst. Jena*
Yka Helariutta, *U. of Cambridge*
James A. Hendler, *Rensselaer Polytechnic Inst.*
Janet G. Hering, *Swiss Fed. Inst. of Aquatic Science & Technology*
Michael E. Himmel, *National Renewable Energy Lab.*
Kai-Uwe Hinrichs, *U. of Bremen*
Kei Hirose, *Tokyo Inst. of Technology*
David Hodell, *U. of Cambridge*
David Holden, *Imperial College*
Lora Hooper, *UT Southwestern Medical Ctr. at Dallas*
Raymond Huey, *U. of Washington*
Steven Jacobsen, *U. of California, Los Angeles*
Kai Johnsson, *EPFL Lausanne*
Peter Jonas, *Inst. of Science & Technology (IST) Austria*
Matt Kaeberlein, *U. of Washington*
William Kaelin Jr., *Dana-Farber Cancer Inst.*
Daniel Kahne, *Harvard U.*
Daniel Kammen, *U. of California, Berkeley*
Masashi Kawasaki, *U. of Tokyo*
Joel Kingsolver, *U. of North Carolina at Chapel Hill*
Robert Kingston, *Harvard Medical School*
Eitonne Koechlin, *Ecole Normale Suprieure*
Alexander Kolodkin, *Johns Hopkins U.*
Roberto Kolter, *Harvard Medical School*
Alberto R. Kornblihtt, *U. of Buenos Aires*
Leonid Kruglyak, *UCLA*
Thomas Langer, *U. of Cologne*
Mitchell A. Lazar, *U. of Pennsylvania*
David Lazer, *Harvard U.*
Thomas Lecuit, *IBDM*
Virginia Lee, *U. of Pennsylvania*
Stanley Lemon, *U. of North Carolina at Chapel Hill*
Ottoline Leyser, *Cambridge U.*
Marcia C. Linn, *U. of California, Berkeley*
Jianguo Liu, *Michigan State U.*
Luis Liz-Marzan, *CIC biomaGUNE*
Jonathan Losos, *Harvard U.*
Ke Lu, *Chinese Acad. of Sciences*
Christian Lüscher, *U. of Geneva*
Laura Machesky, *CRUK Beatson Inst. for Cancer Research*
Anne Magurran, *U. of St. Andrews*
Oscar Marin, *CSIC & U. Miguel Hernández*
Charles Marshall, *U. of California, Berkeley*
C. Robertson McClung, *Dartmouth College*
Graham Medley, *U. of Warwick*
Yasushi Miyashita, *U. of Tokyo*
Richard Morris, *U. of Edinburgh*
Alison Motsinger-Reif, *NC State U.* **(S)**
Sean Munro, *MRC Lab. of Molecular Biology*
Thomas Murray, *The Hastings Center*
James Nelson, *Stanford U. School of Med.*
Karen Nelson, *J. Craig Venter Institute*
Daniel Neumark, *U. of California, Berkeley*
Timothy W. Nilsen, *Case Western Reserve U.*
Pär Nordlund, *Karolinska Inst.*
Helga Nowotny, *European Research Advisory Board*
Ben Olken, *MIT*
Joe Orenstein, *U. of California Berkeley & Lawrence Berkeley National Lab*
Harry Orr, *U. of Minnesota*
Andrew Oswald, *U. of Warwick*
Steve Palumbi, *Stanford U.*
Jane Parker, *Max-Planck Inst. of Plant Breeding Research*
Giovanni Parmigiani, *Dana-Farber Cancer Inst.* **(S)**
Donald R. Paul, *U. of Texas, Austin*
John H. J. Petrini, *Memorial Sloan-Kettering Cancer Center*
Joshua Plotkin, *U. of Pennsylvania*
Albert Polman, *FOM Institute AMOLF*
Philippe Poulin, *CNRS*
David Randall, *Colorado State U.*
Colin Renfrew, *U. of Cambridge*
Felix Rey, *Institut Pasteur*
Trevor Robbins, *U. of Cambridge*
Jim Roberts, *Fred Hutchinson Cancer Research Ctr.*
Barbara A. Romanowicz, *U. of California, Berkeley*
Jens Rostrup-Nielsen, *Haldor Topsoe*
Mike Ryan, *U. of Texas, Austin*
Mitinori Saitou, *Kyoto U.*
Shimon Sakaguchi, *Kyoto U.*
Miquel Salmeron, *Lawrence Berkeley National Lab*
Jürgen Sandkühler, *Medical U. of Vienna*
Alexander Schier, *Harvard U.*
Randy Seeley, *U. of Cincinnati*
Vladimir Shalaev, *Purdue U.*
Robert Siliciano, *Johns Hopkins School of Medicine*
Joseph Silk, *Institut d'Astrophysique de Paris*
Denis Simon, *Arizona State U.*
Alison Smith, *John Innes Centre*
Richard Smith, *U. of North Carolina* **(S)**
John Speakman, *U. of Aberdeen*
Allan C. Spradling, *Carnegie Institution of Washington*
Jonathan Sprent, *Garvan Inst. of Medical Research*
Eric Steig, *U. of Washington*
Paula Stephan, *Georgia State U. and National Bureau of Economic Research*
Molly Stevens, *Imperial College London*
V. S. Subrahmanian, *U. of Maryland*
Ira Tabas, *Columbia U.*
Sarah Teichmann, *Cambridge U.*
John Thomas, *North Carolina State U.*
Shubha Tole, *Tata Institute of Fundamental Research*
Christopher Tyler-Smith, *The Wellcome Trust Sanger Inst.*
Herbert Virgin, *Washington U.*
Bert Vogelstein, *Johns Hopkins U.*
Cynthia Volkert, *U. of Göttingen*
Douglas Wallace, *Dalhousie U.*
David Wallach, *Weizmann Inst. of Science*
Ian Walmsley, *U. of Oxford*
David A. Wardle, *Swedish U. of Agric. Sciences*
David Waxman, *Fudan U.*
Jonathan Weissman, *U. of California, San Francisco*
Chris Wikle, *U. of Missouri* **(S)**
Ian A. Wilson, *The Scripps Res. Inst.* **(S)**
Timothy D. Wilson, *U. of Virginia*
Rosemary Wyse, *Johns Hopkins U.*
Jan Zaanen, *Leiden U.*
Kenneth Zaret, *U. of Pennsylvania School of Medicine*
Jonathan Zehr, *U. of California, Santa Cruz*
Len Zon, *Children's Hospital Boston*
Maria Zuber, *MIT*

BOOK REVIEW BOARD
David Bloom, *Harvard U.,* **Samuel Bowring,** *MIT,* **Angela Creager,** *Princeton U.,*
Richard Shweder, *U. of Chicago,* **Ed Wasserman,** *DuPont*

Published by AAAS

EDITORIAL

The measure of research merit

Each year, $1.4 trillion are invested in research by governments, foundations, and corporations. Hundreds if not thousands of high-profile prizes and medals are awarded to the best researchers, boosting their careers. Therefore, establishing a reliable predictor of future performance is a trillion-dollar matter. Last month, the Alexander von Humboldt Foundation convened an international assembly of leaders in academia, research management, and policy to discuss "Beyond Bibliometrics: Identifying the Best." Current assessment is largely based on counting publications, counting citations, taking note of the impact factor of the journals where researchers publish, and derivatives of these such as the h-index. These approaches were severely criticized for numerous reasons, with shortcomings particularly apparent when assessing young scientists for prestigious, interdisciplinary awards. It is time to develop more appropriate measures and to use the scientific method itself to help in this endeavor.



"It is time to remedy a flawed bibliometric-based assessment for young scientists."

The difficulty with assessing young scientists is well known. Their short career to date yields a brief publication record, making differences in the numbers of publications between candidates statistically questionable. Faced with the challenge of gauging the worth of limited publications, evaluators might turn to journal impact factors. Using this as a proxy for the importance of a paper is just plain wrong. As compared with a paper published in a higher-impact journal, there is no assurance that a paper published in a lower-impact journal is less important.

Citations are a better proxy for how much impact a paper is having, but for young scientists and interdisciplinary awards, this metric also has several limitations. For example, recent publications from young scientists have not yet accumulated citations. Altmetrics have been proposed as a possible solution: measuring downloads, page views, tweets, and other social media attention to published research. Analyses conducted by HighWire Press, the publisher of *Science* and many other academic journals, suggest that downloads of online papers poorly track eventual citations. This could indicate that some papers were found unworthy of being cited, or that some papers were influential, but just not cited because the author did not feel that the concept required a citation. Adding more context in referencing could reduce some ambiguity and encourage more appropriate referencing, but such proposals have not gained traction. Counting citations is also quantitatively inconsistent. If an author publishes a better method or an improved estimate for a physical parameter, other researchers who use those improvements are obligated to cite that paper. On the other hand, if a researcher publishes a novel idea, it can rapidly move from unknown to common knowledge such that its citation lifetime is exceptionally brief. Furthermore, citation counts scale with the publications in a field. The lowering of quality barriers by some open-access publishers has generated a citation explosion in some fields, boosting citation counts by publishing papers that otherwise might not have been published.

Consider a rather outrageous proposal. Perhaps there has been too much emphasis on bibliometric measures that either distort the process or minimally distinguish between qualified candidates. What if, instead, we assess young scientists according to their willingness to take risks, ability to work as part of a diverse team, creativity in complex problem-solving, and work ethic? There may be other attributes like these that separate the superstars from the merely successful. It could be quite insightful to commission a retrospective analysis of former awardees with some career track record since their awards, to improve our understanding of what constitutes good selection criteria. One could then ascertain whether those qualities were apparent in their backgrounds when they were candidates for their awards.

It is time to remedy a flawed bibliometric-based assessment for young scientists. After all, the future performance of a trillion-dollar enterprise is at stake.

– Marcia McNutt



Marcia McNutt
Editor-in-Chief
Science *Journals*

10.1126/science.aaa3796

IMAGES: (INSET) VERALUBIMOVA/ISTOCKPHOTO.COM; (RIGHT) STACEY PENTLAND PHOTOGRAPHY

Downloaded from www.sciencemag.org on December 5, 2014

Published by AAAS

NEWS

> "No one really wants to admit I exist."
>
> **James Watson**, who co-discovered the structure of DNA but has been criticized for making racist remarks, explaining why he is auctioning his Nobel medal.

IN BRIEF



This engraved shell was part of an assemblage of shells dated to 500,000 years ago.

Did *Homo erectus* engrave this shell?

Homo sapiens probably began engaging in a rudimentary form of symbolic behavior at least 100,000 years ago—much earlier than once suspected—etching abstract patterns onto pieces of ochre and animal bone. But in this week's issue of *Nature*, researchers report evidence that such behavior may go even farther back, to our predecessor species, *Homo erectus*. The scientists found a geometric zigzag pattern (inset) engraved on a freshwater mussel shell from the famous *Homo erectus* Trinil site on the Indonesian island of Java. The shell comes from an assemblage dated to at least 500,000 years ago. The team is cautious not to call this relatively simple engraving symbolic behavior, however, and some skeptics point out that the shell was dug up 120 years ago, leading them to question whether the pattern is the handiwork of "Java Man" or a modern human who came by hundreds of thousands of years later.



PHOTOS: WIM LUSTENHOUWER/VU UNIVERSITY AMSTERDAM (2)

AROUND THE WORLD

EC plan diverts research money

STRASBOURG, FRANCE | European Commission President Jean-Claude Juncker has sparked criticism with plans to raid the European Union's science budget to fodder a new "Investment Plan for Europe," aimed at boosting Europe's sluggish economy. Juncker, who presented the plan to the European Parliament in Strasbourg on 26 November, proposed diverting €2.7 billion from Horizon 2020, the bloc's €70 billion, 7-year research funding program, to contribute to a €21 billion investment pot. Juncker said this could multiply 15-fold to €315 billion over 3 years with contributions from industry and national governments and suggested this would eventually benefit research. But critics have expressed skepticism of this. "Let's stick with the Horizon 2020 budget, which we all welcomed in 2012," said Kurt Deketelaere, secretary-general of the League of European Research Universities, in a statement. http://scim.ag/JunckerHor2020

Merck in race for Ebola vaccine

WHITEHOUSE STATION, NEW JERSEY | Pharmaceutical giant Merck has jumped into the race to develop an Ebola vaccine. On 24 November, Merck of Whitehouse Station, New Jersey, announced a licensing agreement with NewLink Genetics of Ames, Iowa, to "research, develop, manufacture, and distribute" an Ebola vaccine. Now in small human trials, the vaccine—developed by the Public Health Agency of Canada and licensed to NewLink—contains a gene for the Ebola surface protein engineered into a crippled version of a livestock pathogen, vesicular stomatitis virus (VSV). The marriage puts the VSV Ebola vaccine on equal footing with another in phase I studies being developed by GlaxoSmithKline and the U.S. National Institute of Allergy and Infectious Diseases. Both vaccines could move into large-scale efficacy trials in West Africa in January, but their safety and efficacy won't be determined before April.

Downloaded from www.sciencemag.org on December 5, 2014

Published by AAAS

CSIRO to cut a fifth of its staff

SYDNEY, AUSTRALIA | The bad news just keeps coming for scientists at Australia's leading research organization. A new analysis of management documents by the union representing staff at the Commonwealth Scientific and Industrial Research Organisation (CSIRO) reveals that one in five employees will be out of a job by June 2015. This figure is higher than initially announced in May by management. In the previous financial year, CSIRO's workforce declined by 513 positions. The union forecasts that another 878 people will be let go, which combined with last year's job losses represents a 21.5% cut to the workforce. Broadly speaking, science and research positions will compose 57% of the 878 jobs set to be cut by June 2015, with the remaining losses coming from support or management roles. The cuts are a result of the government's decision in May to slash AU$115 million, or 16%, from the organization's budget over 4 years.

New U.S. rules to curb ozone

WASHINGTON, D.C. | The United States on 26 November proposed tightening the country's standard for smog-producing ozone from 75 parts per billion to between 65 and 70 parts per billion. The Environmental Protection Agency's (EPA's) science advisory board has endorsed lowering the threshold since the late 2000s, but 3 years ago the Obama administration shelved a draft proposal to impose a lower standard, suggesting that it would be too onerous during the country's recovery from a severe recession. The new proposal, announced by EPA, essentially renews much of that earlier proposal. States will be required to comply by 2020 to 2037, depending on the severity of their ozone problem. EPA will accept public comment on the proposal until the end of February 2015 and says it plans to finalize the new rules by 1 October 2015.
http://scim.ag/EPAozone

Science center on chopping block

ALTOS DE PIPE, VENEZUELA | On 18 November, scientists in Venezuela awoke to a surprise: The National Assembly's Commission on Science, Technology, and Innovation had introduced and approved a bill that would abolish the Venezuelan Institute for Scientific Research (IVIC), founded in 1959. IVIC would be replaced by a new institute devoted to "science that serves the people" rather than "science that wallows in itself," said Representative Guido Ochoa of the United Socialist Party of Venezuela, according to the newspaper *El Nacional*. The bill is "completely absurd," says Margarita Lampo, an IVIC ecologist. "If this law passes, 55 years of scientific work will be thrown in the trash." Lampo and other IVIC representatives met with the people's minister for higher education, science, and technology on 24 November in hopes of reforming the proposal. A date for the final vote has not been set.

U.K.'s bid for quantum tech lead

LONDON | The United Kingdom announced 26 November the creation of a £120 million network of four "quantum technology hubs"—involving 17 universities and 132 companies—to create commercially viable technologies based on quantum mechanics. Each hub, led by the universities of York, Glasgow, Oxford, and Birmingham, will focus on different applications of quantum technology: communications, sensing and imaging, computing and simulation, and sensing and metrology. Physicist Kai Bongs, who will lead Birmingham's effort, envisions a "U.K. quantum valley" where the industry will flourish and develop an ecosystem. "Companies are very hungry for atom devices," Bongs says. "We might see products coming out in the 5 years." The government announced the 5-year, £270 million National Quantum Technologies Programme last year.
http://scim.ag/UKquantum

Nature tries paper sharing

LONDON | Nature Publishing Group (NPG) has unveiled a new approach to freely sharing papers normally behind a paywall. The initiative, announced 1 December, is meant as an alternative to "dark sharing," in which scientists download PDFs of their own papers and e-mail them to nonsubscribers—problematic to publishers, who can't accurately gauge how often the

Crowdfunding boost for dancing spider study

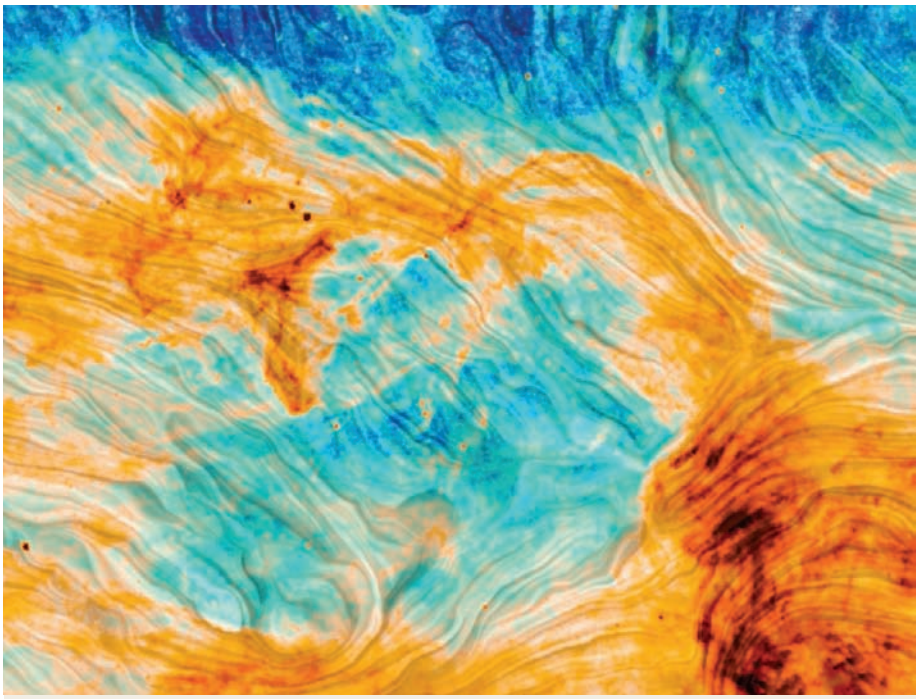
Like eight-legged birds of paradise, male jumping spiders flash red, blue, green, and orange patches as they circle, lunge, and wave their legs in a courtship dance. Taking advantage of the spiders' antics (and YouTube fame), researchers have raised more than $7000 from the public to study how well the spiders see color. Vision ecologist Daniel Zurek of the University of Pittsburgh in Pennsylvania and colleagues had found a red filter in the eyes of five *Habronattus* species of jumping spiders that greatly expands the diversity of color they see. To find out how widespread the red-filter adaptation is among the 100 *Habronattus* species, the team turned to Experiment.com, a crowdfunding website for scientists. Having reached their goal last week, the team plans to head to Arizona and southern California next spring to collect 12 to 25 species of the spiders; they'll test the spiders' eyes for color sensitivity and determine whether improved color vision coincides with flashier displays.



Some male jumping spiders are quite flamboyant.

PHOTO: © COLIN HUTTON

Published by AAAS



The Planck spacecraft has mapped the polarization of the CMB radiation across the sky.

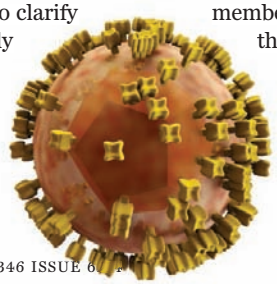
Another boost for cosmology's standard model

The latest study of cosmic microwave background (CMB) radiation—the afterglow of the big bang—confirms even more precisely the standard model of cosmology, researchers with Europe's Planck spacecraft reported at a press conference on 1 December in Ferrara, Italy. That victory for the theory leaves researchers with no puzzles to lead to a deeper understanding. "I was hoping to find an anomaly," says Nazzareno Mandolesi, a Planck team member with Italy's National Institute for Astrophysics in Bologna. But the results do not touch on the biggest controversy in cosmology. In March, researchers using the BICEP2 telescope at the South Pole reported swirls in the polarization of the CMB that could be proof that the infant universe underwent an exponential growth spurt called inflation. In September, Planck researchers showed that much of that signal likely comes from dust within our galaxy. The teams are now working on a joint analysis, but Planck researchers wouldn't say when it might be complete. **http://scim.ag/CMBconfirm**

articles are read. NPG's initiative, to last 1 year, will allow subscribers to share a link to a read-only version of the paper; the link will encode the identity of the sharer and of the paper and will lead to a full version of the paper that can be annotated but not downloaded or printed. **http://scim.ag/Naturesharing**

Move faster, NSABB tells U.S.

BETHESDA, MARYLAND | The U.S. government needs to move quickly to clarify and grant waivers to a recently announced moratorium on funding for potentially risky research involving three types of viruses—influenza, MERS, and SARS. Those are two main points in a 25 November statement from the National Science Advisory Board for Biosecurity (NSABB), which advises the government on problematic research. The pause, which was announced 17 October and has affected 18 projects at 14 institutions, has created confusion among researchers. It applies to so-called gain-of-function studies that could make a pathogen more dangerous, but researchers can apply for a waiver to continue studies that are deemed important for protecting public health. NSABB members, however, are concerned that the government has been slow to rule on waiver requests. **http://scim.ag/NSABBquick**



A moratorium on funding some research on the flu, MERS, and SARS viruses is confusing researchers.

BY THE NUMBERS

10%

Fraction of the estimated 100 billion galaxies in the universe in which complex life is possible. The rest are sterilized by gamma ray bursts. (*Physical Review Letters*)

75

Number of zoonotic pathogens (which can jump from animals to humans) out of 150 studied that show visible symptoms in animals. In the past 60 years, only 13 disease outbreaks were preceded by wildlife reports—suggesting many early warning signs were missed. (*EcoHealth*)

10 million

Years ago that a common ancestor of humans, chimps, and gorillas evolved a protein that could efficiently metabolize alcohol. (*Proceedings of the National Academy of Sciences*)

NEWSMAKERS

Surgeon under investigation

The Karolinska Institute in Stockholm is investigating misconduct allegations against surgeon **Paolo Macchiarini**, who led high-profile attempts to implant artificial tracheas in patients (*Science*, 19 April 2013, p. 266). Macchiarini operated on three patients at Karolinska University Hospital, replacing their damaged tracheas with an artificial scaffold seeded with stem cells. Two patients died; a third has been hospitalized since the operation 2 years ago. Four doctors involved in the patients' care have said that patients did not give proper consent and Macchiarini's papers left out serious complications. An external expert's report is expected in January. Meanwhile, Karolinska's ethics council is investigating questions raised by an outside surgeon about whether Macchiarini accurately described patient outcomes. Macchiarini says both sets of charges are baseless.

CREDITS: (TOP TO BOTTOM) ESA/PLANCK COLLABORATION; V. ALTOUNIAN/*SCIENCE*

Published by AAAS



IN DEPTH

Commonly used anesthetics in children have been associated with brain damage in animal studies.

BIOMEDICAL RESEARCH

Researchers struggle to gauge risks of childhood anesthesia

Neurological warning signals in animals drive push for new studies and public outreach

By **Kelly Servick**, *in Silver Spring, Maryland*

Anesthesiologists and surgeons who operate on children have been dogged by a growing fear—that being under anesthesia can permanently damage the developing brain. Although the few studies of children knocked out for surgeries have been inconclusive, evidence of impaired development in nematodes, zebrafish, rats, guinea pigs, pigs, and monkeys given common anesthetics has piled up in recent years. Now, the alarm is reaching a tipping point. "Anything that goes from [the roundworm] *C. elegans* to nonhuman primates, I've got to worry about," Maria Freire, co-chair of the U.S. Food and Drug Administration (FDA) science advisory board, told attendees at a meeting the agency convened here last month to discuss the issue.

The gathering came as anesthesia researchers and regulators consider several moves to address the concerns: a clinical trial of anesthetics in children, a consensus statement about their possible risks, and an FDA warning label on certain drugs. But each step stirs debate. Many involved in the issue are reluctant to make recommendations to parents and physicians based on animal data alone. At the same time, more direct studies of anesthesia's risks in children are plagued by confounding factors, lack of funding, and ethical issues.

"We have to generate—very quickly—an action item, because I don't think the status quo is acceptable," Freire said at the 19 November meeting. "Generating an action item without having the data is where things become very, very tricky."

Concerns first arose after a 1999 study, in which drugs that block *N*-methyl-D-aspartate (NMDA) receptors in the brain, including the common anesthetic ketamine, appeared to trigger the death of neurons in newborn rats. Similar results emerged for drugs that act on γ-aminobutyric acid (GABA) receptors, including sevoflurane, one of the most commonly used anesthetics in children. A 2011 FDA-led study also found that rhesus monkeys exposed to certain anesthetics in the first 6 days of life had permanent cognitive deficits, as measured by lab tests of learning and motivation.

Annual anesthesia use in the U.S.

6 million
Children under 15 years old

1.5 million
Infants under 12 months

Most surgeries performed in children under 3—when animal data suggest the developing brain is most vulnerable—are not optional, however. And there is no tried-and-true alternative to the drugs that have raised safety concerns. "Based on the current knowledge, we're kind of stuck," says David Warner, a pediatric anesthesiologist at the Mayo Clinic in Rochester, Minnesota, whose recent analyses of a database of local children point to increased risk of learning disabilities and lower test scores after multiple anesthesia exposures.

Further work has not been easy to fund. FDA can often compel companies to do safety studies of new drugs because they have massive investments at stake. But most current anesthetics have lost patent protection and are sold at low prices by generics manufacturers, says Russ Altman, a biomedical informatics specialist at Stanford University in Palo Alto, California, and the FDA science board's outgoing chair. Regulatory pressure on these companies "would just scare them away from creating these drugs."

To help fill the information gap, FDA in 2010 formed Strategies for Mitigating Anesthesia-Related neuroToxicity in Tots (SmartTots), a partnership with the International Anesthesia Research Society (IARS). The initiative has struggled to scrape together money from foundations, professional societies, and private donors. It has given out $600,000 to four ongoing projects that evaluate children previously given anesthesia.

But such studies can't separate the effects of anesthesia from other factors that might cause neurological damage, such as the stress of the surgery itself or the child's underlying medical condition. SmartTots is now shifting its focus to designing a large multicenter trial, which would randomize kids to receive different types of anesthesia, then follow up with cognitive testing over several years.

A task force assembled this spring proposed that the trial compare sevoflurane with a sedative called dexmedetomidine—an agent that in animal studies does not appear to be neurotoxic and that may even mitigate the damaging effects of other drugs. Anesthesiologist and task force member Dean Andropoulos of Baylor College of Medicine in

CREDITS: (IMAGE) JASON EDWARDS/NATIONAL GEOGRAPHIC SOCIETY/CORBIS; (DATA) NATIONAL HOSPITAL DISCHARGE SURVEY (2005) AND NATIONAL INPATIENT SAMPLE, U.S. AGENCY FOR HEALTHCARE RESEARCH AND QUALITY. VIA SUN, *BRITISH JOURNAL OF ANAESTHESIA*, 2010

Downloaded from www.sciencemag.org on December 5, 2014

Published by AAAS

Houston, Texas, estimates that the study will need to include about 700 children, at a cost of $5 million to $10 million—which the SmartTots leadership hopes will come from government sources in the United States and abroad.

Planning the trial and navigating ethical concerns "has been daunting, to say the least," says IARS Executive Director Thomas Cooper, who manages the SmartTots initiative. Despite the scientific appeal of a randomized study, investigators are obligated to not place children into a treatment group that may increase the risk of harm, he says, or give care that deviates from what is already accepted as safe and effective.

Because dexmedetomidine hasn't been widely used or studied in children, SmartTots collaborators are preparing a preliminary study in 50 kids to check that it's suitable for long surgeries; warning signs would include slowed heartbeat, low blood pressure, or a child who stirs too much while "under," Andropoulos says. He also anticipates a nonhuman primate study to scrutinize the drug's effects on the brain.

Warner, also an adviser on the project, notes that because the preliminary study would be on a tightly controlled population—children getting urological procedures is one favored option—any findings might not apply to kids getting anesthesia under other circumstances. "You would, in theory, need to do a different trial in every group of kids, which nobody's going to do."

With even this limited evidence years away, SmartTots is crafting a short "consensus statement," planned for December release, to convey current knowledge about risks of childhood anesthesia. A draft, unlike its 2012 predecessor, explicitly suggests delaying or postponing surgical procedures that require full anesthesia if possible.

That suggestion sparked lively discussion among the FDA science board. "Postponement is really bad medicine," argued pediatric orthopedic surgeon Laura Tosi of Children's National Health System in Washington, D.C. With surgeries for congenital defects, she said, any delay can lead to worse outcomes.

Several advisers supported the idea of a new FDA warning on the anesthetics that have been called into question. But others, including Tosi, vehemently opposed adding the most severe "black box" warning, which signifies a risk of serious adverse effects.

Some parents wary of cognitive damage are already resisting necessary procedures for their children, Tosi noted. "We have to be very careful about how we present that data," she said. "I think the fear of anesthesia in the public is already out there." ■

ARCHAEOLOGY

Satellites track heritage loss across Syria and Iraq

Vandalism, looting, and collateral damage erase history

By **Andrew Lawler**, *in San Diego, California*

More than 4000 years ago, the Bronze Age metropolis of Mari on the banks of the Euphrates River bustled with trade and boasted a half-dozen temples and a royal palace. But for millennia since then, its eroding walls and buried artifacts remained undisturbed until French archaeologists began excavating in the 1930s.

Today, this Syrian site just 10 kilometers from the Iraqi border is once again a busy place. A satellite image of Mari taken on 11 November shows alarming signs of massive, orchestrated looting, according to Scott Branting, an archaeologist at the Boston-based American Schools of Oriental Research (ASOR). Trucks and backhoes traverse the site, systematically uncovering artifacts while destroying the ancient structures. Looters have even built what may be a large storage depot for sorting and storing the valuable goods before they are exported for sale abroad.

> *"It is all seemingly never-ending and disheartening."*
> **Michael Danti**, Boston University

Such destruction is widespread across Syria and northern Iraq, Branting and other researchers lamented at ASOR's annual meeting here. Part of the ancient Fertile Crescent, the region holds archaeological riches spanning thousands of years. Since 2011, however, it has also been a battleground, fought over by the Syrian government and opposition groups, the radical Islamists of the Islamic State group, and their various opponents including Iraqi, Kurdish, and U.S. forces.

In an initiative funded by the U.S. State Department, ASOR is monitoring and assessing the damage. Recent satellite photos, as well as reports from observers on the ground, indicate that the artifacts and sites face multiple perils: Islamists who destroy ancient sites for religious reasons, systematic looters like those threatening Mari, and the collateral damage of war. "It is all seemingly never-ending and disheartening," says Michael Danti, a Boston University archaeologist who helps lead the ASOR project.

Shut out of a region plagued with competing armies, humanitarian crises, and hostile ideologies, archaeologists have largely been distant and anguished bystanders to the wave of ruin. But by tracking the damage, the ASOR researchers hope they can help raise a global outcry and lay the foundation for salvage and reconstruction when the wars end. "Even if what we are doing is largely ineffectual, it is better than sitting on our hands," Branting said at a special 23 November session on the crisis.

The Islamic State group has emerged as a particular threat, making concerted efforts to destroy the sacred sites of groups it views as heretical. The group has publicized its intentional destruction of dozens of sacred sites online or in its glossy magazine, *Dabiq*. "A soldier of the Islamic state clarifies to the people the obligation to demolish the tombs," states one caption in a recent issue that includes images of exploding shrines.

"It is all very choreographed," Danti says. He adds that the biggest spike in destruction took place in May, with nearly 20 sites demolished, followed by a half-dozen or so incidents each month thereafter. Almost half of the destroyed sites are associated with Shia Muslims, while the remainder are places sacred to Sufis, a mystical branch of Islam, as well as Christians and Yazidis, an ancient ethnic group centered in northern Iraq. More than 15% are statues and buildings predating Islam; images on the Internet, for example, show a yellow front loader toppling and pulverizing two massive black stone lions dating to the 9th century B.C.E. in the Islamic State provisional capital of Raqqa in northern Syria.

But researchers say that even more damage to archaeologically important sites stems from military action by all parties in the conflict, including the Syrian government and perhaps Iraqi and U.S. forces. "There is a lot of damage from military garrisoning," says Jesse Casana, an archaeologist at the University of Arkansas, Fayetteville, who is part of the ASOR team and has been closely examining dozens of Syrian sites. Tells, remnants of ancient settlements that dot the Syrian and Iraqi landscape, offer high ground for mili-

Downloaded from www.sciencemag.org on December 5, 2014

Published by AAAS



In a December 2012 satellite image of Apamea in Syria, holes dug by looters pepper the site of the ancient Roman city (*inset*).

tary units, which wreak havoc with heavy equipment as they fortify the sites. Archaeologists also fear that the warring forces are heavily mining strategic tells, creating a daunting threat for future excavators.

In October, Kurds captured Tell Shair, a site near the hotly contested Syrian town of Kobane. Images taken by the victors showed that the ousted Islamic State group fighters had dug trenches 2 to 3 meters deep on the mound, devastating the upper layers of the millennia-old settlement. The images also showed signs of bomb craters, possibly from U.S. raids—in the first half of October alone, the U.S. military reported conducting more than 135 airstrikes in the area. A Defense Department advisory group provides data to the U.S. military on important cultural heritage monuments so it can limit bomb damage. But whether such protection extends to smaller sites such as Tell Shair is unclear, several U.S. archaeologists say.

Casana is also using satellite photos to track another major source of damage: looting. At the important classical city of Apamea outside Hama in western Syria, for example, areas largely undisturbed in images from 2011 are pocked with large holes in 2012—holes big enough to suggest that they were dug by heavy machinery such as backhoes rather than shovels. Looting has since spread across the site in what looks like a "very organized fashion," Casana says. The Syrian government built a major military garrison, complete with bunkers and artillery emplacements, at the site of the former tourist restaurant at Apamea. "This strongly implicates the military as complicit or participating in looting," Casana adds. At another tell nearby, the looting holes are located within a few meters of military tents.

Classical sites like Apamea and Bosra, an ancient city in southern Syria that has also suffered significant damage, are more prone to looting than older sites because their artifacts are more sought-after on the international market. Archaeologists have observed a massive expansion in looting between August 2013 and April 2014 at Dura-Europos, a sprawling Roman-era city on the Euphrates in Syria. But Bronze Age cities like Ebla in the west—damaged by a Syrian government military garrison—and Mari, which is under the Islamic State group's control, are not immune. "There are rumors that armed groups are undertaking the work," ASOR's Branting says about Mari. Other reports suggest that the Islamic State group is profiting from the business, possibly by exacting a tax as well as by overseeing looting operations. But Danti adds that most looting appears to be the work of desperate Syrians attempting to survive in a devastated economy.

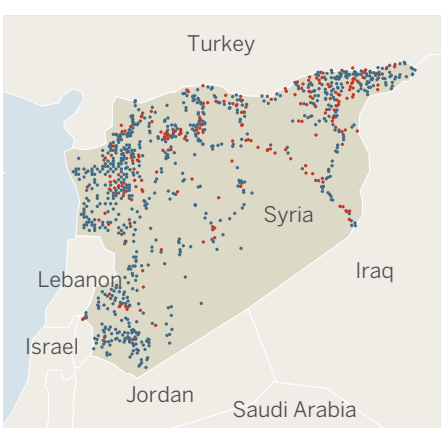
Massive looting, bomb craters, and damage by military garrisons can be spotted on satellite images, but smaller thefts, kidnapping, and violence against guards and inspectors at sites are difficult to confirm without on-the-ground intelligence. Sources told *Science* that Islamic State group forces kidnapped and tortured at least one antiquities inspector in northern Iraq before releasing him a few weeks ago. A 24 September circular from the group declared archaeology to be un-Islamic and closed the archaeology department at the University of Mosul, effective 18 October. And the Islamic State group's forces now occupy the Mosul Museum, which houses a collection of statues, friezes, and inscriptions from the Assyrian capital of Nimrud and Hatra, a classical site 110 kilometers southwest of Mosul. One source said the occupiers have emptied the museum and smashed objects too large to move. Many Iraqi archaeologists in Islamic State group–controlled areas are in hiding or have fled to Kurdistan.

Western colleagues hope that by gathering data on the situation, they will be ready to help rebuild cultural heritage sites and institutions once peace returns. And they hope that some of the region's heritage will survive the conflict. Archaeologists at the meeting were relieved to see a recent image of Hatra; Branting says it shows few signs of destruction or looting at the site, home to a large number of intact statues and buildings.

"It is incumbent on those of us who have built a research career in Syria to help," says Graham Philip of Durham University in the United Kingdom, who is organizing European archaeologists to analyze the situation and plan for the future. The human toll of the conflict is immense, but Abdal-Razzaq Moaz, a Syrian art historian at Indiana University, Bloomington, says the destruction of thousands of years of history inflicts its own pain. "We must consider cultural heritage as part of the humanitarian crisis." ■

Damage assessment

Many of Syria's ancient sites have sustained damage (red), as shown on a map based on satellite data. Sites in blue appear undamaged.



CREDITS: (PHOTO) JESSE CASANA, UNIVERSITY OF ARKANSAS; (MAP) ASOR SYRIAN HERITAGE INITIATIVE

Published by AAAS



Hans Rosling canceled his lectures and Christmas with his family to help fight Ebola in Liberia.

EPIDEMIOLOGY

The old man and the disease

In Liberia's Ebola outbreak, star statistician Hans Rosling is facing the intellectual challenge of a lifetime

By **Kai Kupferschmidt**, *in Monrovia*

Hans Rosling is a global health celebrity, a former head of the Division of Global Health at the Karolinska Institute in Stockholm whose riveting lectures have made him a star of TED talks, and a fixture of the World Economic Forum in Davos, Switzerland. But since 20 October, he has occupied room 319 of Liberia's Ministry of Health & Social Welfare, a large yellow building not far from the Atlantic Ocean. Working alongside the country's head of Ebola surveillance, Luke Bawo, he is helping the ministry make sense of the largest Ebola outbreak ever recorded.

Rosling has come without any affiliation, which he says helps him stay independent. "He just walked into the office and introduced himself," Bawo says.

He feels bad about not coming earlier. Ebola arrived in Liberia from Guinea in March, then spread south to Monrovia, where it exploded in August. Hospitals were closed and Ebola treatment units were overwhelmed. "I thought the Ebola outbreak could be stopped locally," Rosling says. "I just wasn't smart enough."

When he saw the epidemic curve go up in Sierra Leone and down in Liberia in October, he was skeptical, and he decided to find out firsthand what was happening. He canceled his lectures and contacted the Liberian government. "I'm not a virologist and I'm not a clinician, but I have considerable experience investigating messy epidemics in poor parts of Africa," he says.

A quarter-century ago, he faced a threat that seemed even more terrifying than Ebola. In August 1981, Rosling was working as a district medical officer in northern Mozambique when he faced a line of 30 women and children whose legs had become paralyzed over the past month. "I had this big neurology book, and their disease did not exist in that book," Rosling says. A South African submarine had been spotted in a nearby bay a few weeks earlier. "It was fully possible that it was biological warfare."

When he came home that evening, he told his wife to take their kids and drive them to a safer place a few hours away. He didn't sleep the next 48 hours. "When you face a disease that may be infectious, 98% of your intellectual capacity becomes blocked. You become so scared, thinking you will die, thinking you may be crippled, thinking about your children." It took 2 weeks before it became clear the affliction wasn't contagious. (Now called konzo, it's caused at least in part by toxic compounds in cassava roots.) A group of Italian nuns helped Rosling overcome his fears. "I don't think I could have done this without them," he says.

The experience left Rosling with a cool approach to health crises and a keen sense of what it takes to fight a disease in one of the poorest parts of the world. Soon after he arrived in Monrovia, he became convinced that the Liberian decline is real, driven in large part by changes in behavior that reduce the risk of infection. Liberia now reports only some 10 new cases a day. That's good news, but it also presents big new challenges. While Ebola was the main cause of death, safe burials were essential. Now that new infections are less common, people could in principle resume traditional funeral practices, which include contact with the body, for deaths not due to Ebola. But spreading that message could cause people to drop their guard with Ebola victims, too, leading to new infections. "Any decision will have many complicated consequences," Rosling says.

Rosling learned that lesson, too, in the konzo outbreak. Because he was initially unable to rule out an infectious disease, the Mozambican government set up a roadblock to stop the disease from spreading. A group of people took a boat along the coast to evade the blockade, and it sank. "I have stood there and seen the bodies of 18 women and children who drowned because of that roadblock," he says. "That stays with you. Eighteen bodies of people you killed."

After he arrived in Monrovia, Rosling started by doing simple things, such as proofreading the ministry's epidemiological reports, which he says nobody had time for. He changed an important detail in the updates: Rather than listing "0 cases" for counties that had not reported any numbers—which could be misleading—he left them blank. Next, he tackled the problem behind the missing data. Some health care workers couldn't afford to call in their reports, because they were paying the phone charges themselves; Rosling set up a small fund to pay for scratch cards that gave them airtime.

Now, he's focusing on how to get the number of new cases down to zero. That means finding every single case, tracing that patient's contacts, and isolating all of those who show symptoms—a huge challenge in a country where many villages are hours away from a road, Ebola symptoms like diarrhea and fever are common, and the fear of the deadly virus drives some con-

PHOTO: DANIEL VAN MOLL/LAIF

Downloaded from www.sciencemag.org on December 5, 2014

Published by AAAS

tacts to skip town and seek out a traditional healer. "We have to make a meticulously perfect system work in a country where such a system cannot exist," he says. "This is the biggest intellectual challenge I have participated in in my life."

On a whiteboard in his office, Rosling has drawn a complicated flow chart to show how the information about patients and their contacts moves through the system. Data are lost at several steps. Some people die on the way to the hospital; others give different ages or names at different points. Rosling's aim is to know how many of the newly discovered Ebola patients are already on one of the contact lists. But so far he has been struggling even to find out what county every patient is from.

Others on the front lines welcome Rosling's help. Kevin De Cock, who leads the U.S. Centers for Disease Control and Prevention (CDC) field team in Liberia, calls him "an eminent epidemiologist with immense African experience. He provides strong technical and intellectual input." Bawo says he admires Rosling's commitment but worries that he's overstretching himself. "He is welcome to stay, but I make it my business that he takes one day off a week," Bawo says. "Every Sunday I don't call him, he does not call me, and I do not want him to send me an e-mail."

Rosling says he's tired of the portrayal of Africa as a continent of incompetence, superstition, and rampant corruption. "I am astonished how good people are that I work with here, how dedicated, how serious," he says. When *The New York Times* reported that governmental infighting was hampering the Ebola response, Rosling tweeted: "Don McNeil misrepresents Liberia's EBOLA-response to win the MOST INCORRECT ARTICLE ABOUT EBOLA AWARD." His self-assurance and impatience with opinions he disagrees with can grate on others. "I find him quite irritating," says one Western colleague. "Mostly because he turns out to be right about most things."

Rosling is critical of Western nations' response to the crisis. Whereas experts from elsewhere in Africa have come as colleagues and stayed for long periods of time, for instance, agencies like CDC replace their staff every few weeks, which Rosling says hampers continuity. (CDC is like Cuba, Rosling says: "Amazing people, bad system.") The U.S. military won't transport patients or even blood samples in their helicopters, he adds: "Welcome to the continent of less superstition."

Rosling eventually wrote his Ph.D. thesis about the konzo outbreak, helped set up the Swedish chapter of Doctors Without Borders, and became a professor of global health at the Karolinska Institute, where he retired in 2012. His talks still garner "obscene fees," he says—some $600,000 annually—which he uses to finance the Gapminder Foundation, a nonprofit he set up to bring development statistics to a broad audience. His talks have been viewed by millions, 200,000 people follow him on Twitter, and he has rich and powerful fans. "Mark Zuckerberg called me yesterday," he says at one point, to ask how his money could help fight Ebola.

In his talks, which feature dazzling graphics, Rosling is fond of emphasizing that most people's view of the world is wrong. He often asks how many children get the standard childhood vaccinations—20%, 50%, or 80%? Most people answer 20%, but it's 80%. "The problem is that the education systems in North America and Europe and the media have not conveyed a fact-based view of the world."

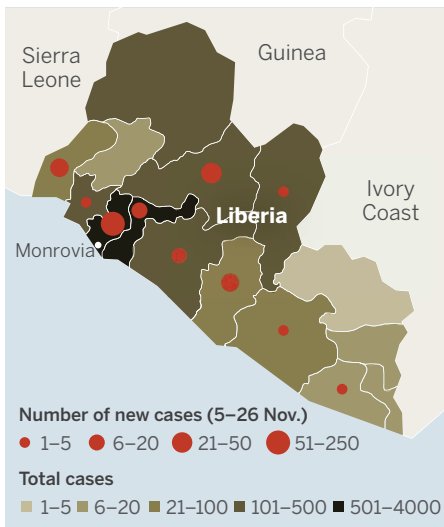
Similarly, many people lump everything from Turkey to Somalia together as the developing world, blurring the differences between middle-income countries and those dominated by extreme poverty. He likes to say that 1.5 billion people have a light bulb and a washing machine, 4 billion have only the light bulb, and about 1.5 billion have neither. The populations of Liberia, Guinea, and Sierra Leone mostly fall into the last category, he says. "And that is one reason we can have such a huge Ebola outbreak here."

Eradicating extreme poverty should be a top priority, says Rosling, who has been critical of programs that focus on a single disease, such as the multibillion-dollar initiative to eradicate polio. That has put him at odds with Bruce Aylward of the World Health Organization (WHO), who heads the campaign. Now, Aylward is also in charge of WHO's Ebola response, but in this case, there's no disagreement: "Ebola is different," Rosling says, adding that Aylward gave him important guidance. Aylward praises Rosling as "great added value."

Although he does not come into contact with Ebola patients, Rosling had one moment when his fear of infectious diseases returned. One night in his Monrovia hotel, he developed diarrhea. He skipped dinner and locked himself up in his room. "I had to plan. Should I tell my family? Should I not?" he says. He decided to take his temperature every 2 hours and watch for additional symptoms. "But I did finish my report before I went to bed." He felt fine the next morning, and he's not planning to return to Sweden soon. "I canceled Christmas with the family," he says. "But I hope to be home for Midsummer's Eve." ■

A declining epidemic

The number of reported new Ebola cases in Liberia has dropped to about 10 per day, which poses new challenges.





Rosling shares an office with Liberia's head of Ebola surveillance, Luke Bawo.

CREDITS: (DATA) WORLD HEALTH ORGANIZATION; (PHOTO) DANIEL VAN MOLL/LAIF

Published by AAAS

BRAZIL

Scientists protest funding bonanza for brain campus

$100 million grant came as a surprise to many

By **Emily Underwood**

Brazilian neuroscientist Miguel Nicolelis has won global attention for experiments with brain-controlled prostheses—and for masterminding a controversial World Cup kickoff by a paralyzed man in a robotic exoskeleton. But back home, controversy over the high-profile researcher's recent windfall has reached a boiling point. Last week, Brazil's largest scientific organization wrote a letter on behalf of more than 120 scientific societies questioning the federal government's decision to invest roughly U.S. $100 million in the Campus of the Brain, the neuroscience research and education initiative in rural northern Brazil spearheaded by Nicolelis.

According to Nicolelis, the funding provided by Brazil's Ministry of Education will cover operational costs over the next 4 years for the campus's health and education efforts and for its several dozen neuroscience research laboratories. The money is not being taken out of anyone else's pot, he stresses. "These funds do not come from annual federal research money—this is new money, a new appropriation."

Yet the Brazilian Society for the Advancement of Science (SBPC) argues that the nation's entire scientific community should have been given a chance to compete for the funding. "Allocating substantial resources for an ad-hoc initiative without, to our knowledge, the initiative having been vetted according to the scientific policies currently in effect represents a serious breach of protocol," the group writes.

Few knew about the large grant—it equals roughly half the value of the competitive grants being offered this year by Brazil's major research infrastructure funding agency ProInfra, SBPC writes in its letter—until months after it was awarded in July. The news broke on 4 November in the Brazilian paper, *Estadão*, says Paulo Saldiva, a pathologist who works for the science and technology ministry. Saldiva says that he and colleagues were so upset about the lack of discussion surrounding the grant that they are circulating a letter of complaint intended for ministry officials.



Miguel Nicolelis

Critics also argue that the neuroscience insitute that is part of the Campus of the Brain effort has failed to live up to expectations thus far. Launched in 2005 with a mishmash of private and federal funding—up to $50 million by some reports—the initiative has suffered from construction delays for its new buildings, as well as the exodus in 2011 of 10 principal investigators, who complained of "mismanagement" by Nicolelis and left for a separate neuroscience research center 25 km away in Natal (*Science*, 19 August 2011, p. 929). Frederico Graeff, a neuroscientist at the University of São Paulo, is among those unimpressed by the fledgling research institute's scientific productivity. "Any of us showing its record to a funding agency at the end of a grant would not get a single extra cent," he says.

Some Brazilian researchers attribute the new funding to Nicolelis's close contacts with powerful officials within the federal government. "Overall, the sense I get from my fellow Brazilian colleagues is the feeling that Miguel is benefiting from unfair access to the higher echelons of our federal government, when everyone else must go through the regular channels," says Suzana Herculano-Houzel, a neuroscientist at the Federal University of Rio de Janeiro.

Nicolelis says that the Campus of the Brain was awarded its grant through the same mechanism used to form other large scientific institutes throughout Brazil. Facilities such as the Brazilian Synchrotron Light Laboratory in Campinas and the National Institute for Pure and Applied Mathematics in Rio de Janeiro were created without extensive peer review, he says. He adds that the new grant is comparable in size to those awarded for other large science infrastructure projects. "These institutes receive similar contracts on the order of hundreds of millions of Reais," he says. "They are outstanding and when they were created I do not remember any protest at all. Why the protests now?"

Nicolelis pins some of the discontent on geographic rivalries. In 2011, more than 60% of the Brazilian National Research Council's budget went to the more developed south and southeastern regions, he notes. "Our project helps decentralize the scientific infrastructure of the country and this severe inequality," Nicolelis says. "Not surprisingly, most of our critics come from the southeast." Graeff counters that other projects have boosted science in Brazil's northeast and north "without spending huge amounts of money and making overstated advertisements."

Nicolelis says that such criticisms miss the broader social value of the Campus of the Brain, such as the prenatal care and schooling it is providing for roughly 1500 local children per year. "For any scientist worth his or her salt to complain about something like that is shameful," he says.

As *Science* went to press, Brazil's government had not yet responded to SBPC's letter. SBPC President Helena Nader, however, has requested a face-to-face meeting with the minister of education. ■



The near-complete building in Macaíba, Brazil, that will hold 30 neuroscience laboratories.

PHOTO: MIGUEL NICOLELIS; INSET: ABIO BERRIEL/LATINCONTENT/GETTY IMAGES

Downloaded from www.sciencemag.org on December 5, 2014

Published by AAAS



Downloaded from www.sciencemag.org on December 5, 2014

UNKNOWN SIGNIFICANCE

Years of writing about genetic testing did not prepare me for my own foray into this rapidly changing world

By **Jennifer Couzin-Frankel**

Rarely could I be described in a headline in *The New York Times*, which explains why I lingered over one earlier this fall. "Study of Jewish Women Shows Link to Cancer Without Family History," announced the 5 September story. Uneasily, I read on: "Women of Ashkenazi Jewish descent who tested positive for cancer-causing genetic mutations during random screenings have high rates of breast and ovarian cancer even when they have no family history of the disease, researchers reported Thursday."

Hmmm.

Science has been my professional home for the past 13 years, and in that time I've written extensively about genetic testing and spoken with dozens of experts at the field's cutting edge. I've chronicled the scientific advances, the ethical quandaries, the lives testing saves, the angst it ignites. I had never turned the lens on my own DNA.

Abruptly, there was no escaping it. My parents are both of Ashkenazi descent. To my knowledge, no one on either side of my family has ever had breast or ovarian cancer. But suddenly I saw how a mutation in the genes discussed in that article, *BRCA1* and *BRCA2*, might have slipped unnoticed through my father's small family, heavy on the Y chromosome—through him; his older

The author and her two children at play. She sought genetic testing, as many do, in part to protect her own health as they grow up.

PHOTO: © APRIL SAUL

Published by AAAS

brother; my three cousins, two of whom are male. I remembered that my paternal grandfather had suffered from prostate cancer, which eventually spread to his bones and killed him. My uncle had the disease, too. Along with their storied role in breast and ovarian cancers, *BRCA* mutations are associated with prostate cancer in men. I'd long known that Ashkenazi Jews are more likely to carry mutations in those genes. But that was as far as my knowledge went.

When I probed the numbers, they were not particularly reassuring. A quick Google search—why had I never done this before?—revealed that one in 40 Ashkenazis carry *BRCA* mutations, compared with as few as one in 800 in the general population. Like nearly all genes linked to cancer, *BRCA1* and *BRCA2* were first found in families riddled with the disease. But the September study, led by Ephrat Levy-Lahad, a medical geneticist at Shaare Zedek Medical Center in Jerusalem, argued that other families shared a similarly high risk if they carried the same mutations.

Several of the authors, among them Mary-Claire King of the University of Washington, Seattle, *BRCA1*'s discoverer, say all women regardless of family history should learn whether they carry dangerous mutations in *BRCA1* and *BRCA2*. Other experts are not yet convinced. Perhaps even more contentious is whom to screen for dozens of risk genes uncovered in the past decade, some only tenuously linked to cancer. I might have written a nuanced *Science* story laying out both sides of the debate. But when it came to my own health, 486 Israeli women with *BRCA* mutations, half without a family history but all highly vulnerable to cancer, was all I needed.

Time seemed of the essence. I am 38 years old; ovary removal in *BRCA* carriers is recommended by 40. I called the suburban Philadelphia hospital where my children, now 2 and 5 years old, were born and spoke with a genetic counselor. She took a family history and agreed that yes, *BRCA* testing was worthwhile, and yes, insurance would likely cover it in my case.

I booked an appointment. I was about to experience my own sliver of the brave new world of cancer genetic testing, which would take me beyond *BRCA* and into more uncertain terrain.

THE AUTOMATIC DOORS SWISH soundlessly open as I step into the hospital's cancer center. A genetic counselor with brown, curly hair and glasses approaches me, smiling, clipboard in hand. In her office, she pulls out a pedigree of my family sketched in pencil—squares for males, circles for females, diagonal slashes through anyone who has died with the cause of death jotted next to them. I thought I'd come prepared—after all, I'm here only for *BRCA* testing, and only because of my ancestry—but it turns out I haven't. Did my grandmother's hysterectomy include removal of her ovaries? (I hazard a guess and query family members after the fact; none knows whether I got it right.) Did my great-grandmother die of stomach or colon cancer? "She was in her 90s," I say. I still carry a dim memory of visiting her in the hospital, as a 3-year-old, shortly before she died. "Does it matter when someone is that old?"

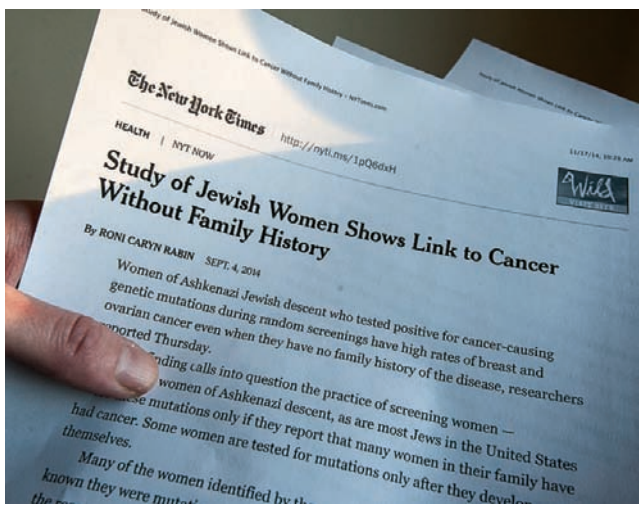
The counselor pulls out a sheet of paper and lays it on the table. It's a list of 21 genes associated with breast and ovarian cancer. Eleven are shaded pink and labeled "high-risk"; three are in the purple "moderate-risk" category; and seven others are turquoise and described, obliquely, as "newer genes." This is the Breast/Ovarian Cancer Panel from the company GeneDx in Gaithersburg, Maryland, but as is often the case in oncology, many of the genes contribute to other cancers, too. One confers a 40% to 83% risk of stomach cancer. Stomach removal is recommended if you test positive. Another, *TP53*, confers a nearly 100% chance of cancer in women and a 73% chance in men; *TP53* cancers include brain cancers and sarcomas.

When it comes to two of the genes on the panel, *BRCA1* and *BRCA2*, there's little doubt that in cancer-prone families, testing saves lives: Extensive study of *BRCA* carriers has found that those who have their ovaries removed are 80% less likely to die from ovarian cancer and 50% less likely to die from breast cancer. Prophylactic mastectomy appears to cut risk of breast cancer by at least 95%.

But many other genes for which testing was discouraged just a few years back because their impact on health was uncertain are "now being routinely offered," says Kenneth Offit, chief of the clinical genetics service at Memorial Sloan Kettering Cancer Center in New York City. "This is the paradox we've fallen into." Just as more cancer risk genes were being uncovered, the cost of sequencing them plunged. The result is a proliferation of panels designed to decipher DNA.

How much each of these genes raises risk in individuals, and at what age, is often fuzzy. "The clinical work got out ahead of us," says Fergus Couch, an authority on *BRCA* and other breast cancer genes at the Mayo Clinic in Rochester, Minnesota. "The [sequencing] technology changed so quickly" that "we did not have time" to develop answers to the questions patients and doctors are now asking.

In the summer of 2013, GeneDx launched its Breast/Ovarian Cancer Panel—spurred partly by the Supreme Court ruling against the Myriad Genetics patent claims on the *BRCA* genes. Other companies, including Myriad itself and Ambry Genetics, along with academic medical centers, have jumped in with panels of dozens of genes linked to an array of cancers. "We're really looking at things that will provide the physician with the ability to make a treatment plan," for example, by adding increased surveillance, says Sherri Bale, managing director of GeneDx. The genes on the company's panels are "a moving target," she says, with culprits added and sometimes deleted based on the available scientific evidence. Bale believes the panels, which cost in the neighborhood of two or three thousand dollars, are suitable for high-risk families but not yet for the general population.



The newspaper article that started it all, published in early September.

THE LIST OF 21 GENES sits between us, and I consider all I could learn by simply saying yes. The counselor isn't advocating I sign up for the full panel. But she draws my attention to one gene in the moderate-risk purple grouping, *CHEK2*. The list of cancers beside it is long: "Female Breast, Male Breast, Colon, Prostate, Thyroid, Renal, Endometrial (serous), Ovarian." I'm vaguely familiar with *CHEK2* as a breast cancer gene from my own reporting. "Is *CHEK2* more

PHOTO: © APRIL SAUL

Published by AAAS

common in Ashkenazis?" I ask, still stuck on heritage as my cancer driver and the reason I'm in this room to begin with.

"No," the counselor replies. But in addition to prostate, my paternal grandfather had colon cancer. "He was in his 70s!" I protest. Nonetheless, *CHEK2* testing for me is worth considering, the counselor says. A *CHEK2* mutation could roughly double my risk of breast cancer, to at least 20%. Annual breast MRIs and mammograms would likely be recommended.

I'm stymied. Adding another gene for testing had never occurred to me. And yet, if the test is positive, the course of action sounds relatively benign and potentially lifesaving.

"Let's do it," I say. We've been talking for about 40 minutes.

The counselor pulls out a consent form. "There's one more thing," she explains. A block of text is titled "Variant of uncertain significance (VUS)." It reads, in part: "I may learn that a VUS was identified by this test. This means that a genetic change (variant) was identified, but it is unknown whether the variant may cause cancer." A given cancer gene can have thousands of variants, some showing up in just a handful of families worldwide. Certain variants are a major contributor to disease, whereas others are benign changes in DNA that, practically speaking, mean nothing.

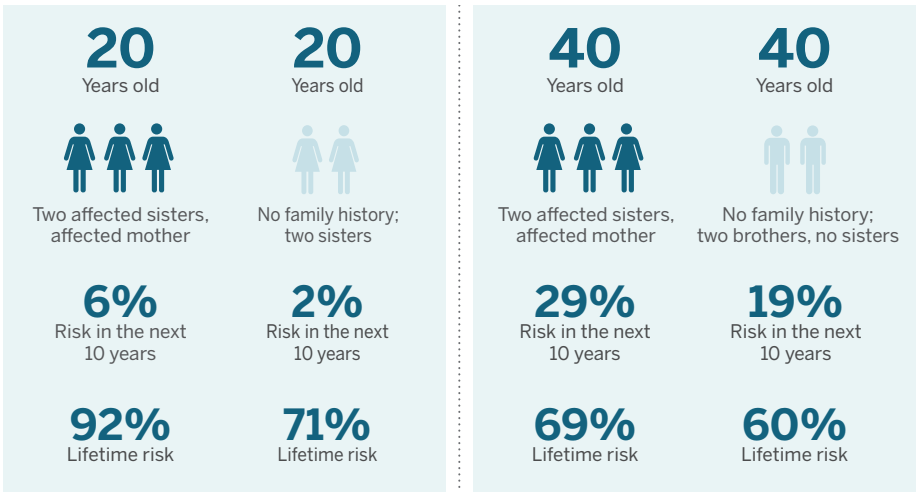
Again, my years of medical journalism have failed to prepare me. "How common are these in *BRCA* and *CHEK2*?" I demand. For *BRCA1* and *BRCA2*, the counselor explains, about 2% of people have a VUS. (I later learn that VUS rates fluctuate depending on the company offering the test.) She is not sure about *CHEK2* but is happy to find out. She stresses, too, that finding a VUS would not affect medical guidance and that the hospital will recontact me if a VUS is later reclassified as either harmless or pathogenic.

I push aside my hesitation, sign the forms, and am off to the lab for a blood draw.

Driving home, my intolerance for uncertainty rears its head. Do I really want to know if I have a VUS? What's the point? That afternoon, I send the counselor an e-mail. I tell her I'm worried that learning about VUSs "will cause me anxiety and there will be no benefit to having this information. I'm wondering whether it's possible not to receive information about any VUS that may turn up in testing. … Is this an option?"

The calculus of risk

How much a *BRCA1* mutation raises a woman's risk of breast cancer depends on her age, family history, and other variables, as the examples below illustrate.



Source: Courtesy of Antonis Antoniou/University of Cambridge/BOADICEA

> ***"People need to become more comfortable with uncertainty."***
>
> **Sharon Plon**, Baylor College of Medicine

She writes back quickly and kindly. She has checked with GeneDx and learned that, for regulatory reasons, they are obligated to share information if a VUS is found. She will ask her medical director whether the hospital can keep a VUS finding from me. But she wonders, too, whether "you will feel anxious not knowing whether or not you may be recontacted in the future regarding a reclassified VUS. … Chances are you will not have a VUS and then you may feel relief to know you do not have one."

Later, she writes to say that her medical director is comfortable withholding a VUS if no pathogenic variants turn up. And there's more good news: She has learned that the VUS rate for *CHEK2*, per GeneDx, is only 1.6%, far lower than she originally thought—although estimates vary depending on whom you ask. I shelve my inner dialogue over which information I want.

TWO DAYS LATER, while GeneDx is parsing my DNA**,** I'm on the phone with Susan Domchek, an oncologist studying breast cancer genes at the University of Pennsylvania. We are discussing cancer risk genes in people without a family history of disease. Unprompted, Domchek brings up *CHEK2* testing. "We don't know how to incorporate it into patient care," she complains, referring to women who test positive and their families. "What percentage of the time does it really add anything to the situation?" I don't mention that my own *CHEK2* test is in process. Instead, I inquire about the frequency of *CHEK2* mutations in the general population. Domchek's response that only about one in 200 people in the United States is a carrier helps me exhale.

Domchek is one of many researchers trying to illuminate the interplay between cancer genes and disease. Along with Offit, Couch, and others, she has developed an online registry called PROMPT that opened earlier this fall. It aims to register thousands of people who have had the panel testing offered by a host of companies, including GeneDx, Ambry, Myriad, Quest Diagnostics, and Pathway Genomics. Their goal is a database that will help them examine how specific gene variants affect health.

"We need to get the world's experience with all these panels," Couch says. He also points out an irony: Despite some uneasiness, scientists like him need panel testing to continue, because it's their best shot to gather enough data to tackle research questions. At the same time, "You don't want to do science … at the cost of the patient," he says. Couch is part of an international consortium called ENIGMA that's working to sequence breast cancer genes from 40,000 cancer patients and healthy people. The project will nail down the risk conferred by different mutations, and study the impact of VUSs on disease.

Published by AAAS

A menu of cancer genes

Multigene panels for cancer risk are proliferating and evolving, including this one of 21 genes associated with breast, ovarian, and other cancers, shared with the author prior to her own testing.

HIGH-RISK GENES

GENE	ASSOCIATED CANCERS AND RISKS
BRCA1	Female breast (57–84%), ovarian (24–54%), prostate (16–20%), male breast (4%), pancreatic (3%), melanoma, fallopian tube, primary peritoneal, endometrial (serous)
BRCA2	Female breast (41–84%), ovarian (11–27%), prostate (20–34%), pancreatic (5–7%), male breast (4–7%), melanoma, fallopian tube, primary peritoneal, endometrial (serous)
CDH1	Female breast (39–52%), diffuse gastric cancer (40–83%), colon
EPCAM *MLH1* *MSH2* *MSH6* *PMS2*	Ovarian (4–24%), colorectal (20–80%), endometrial (12–60%), stomach, pancreatic, biliary tract, urinary tract, small bowel, brain, sebaceous neoplasms
PTEN	Female breast (25–50%), thyroid (10%), endometrial (5–10%), colon, renal, melanoma
STK11	Female breast (32–54%), ovarian tumors (21%), colorectal (39%), pancreatic (11–36%), gastric (30%), lung (15%), small intestine (13%), cervical (10%), endometrial (10%), testicular tumors (9%)
TP53	Female breast, ovarian, soft tissue sarcoma, osteosarcoma, brain tumors, adrenocortical carcinoma; overall risk for cancer: nearly 100% in females, 73% in males

MODERATE-RISK GENES

ATM	Female breast, colon, pancreatic
CHEK2	Female breast, male breast, colon, prostate, thyroid, renal endometrial (serous), ovarian
PALB2	Female breast, male breast, pancreatic, ovarian

NEWER GENES

BARD1	Female breast, ovarian
BRIP1	Female breast, ovarian
FANCC	Female breast
NBN	Female breast, melanoma, non-Hodgkin lymphoma
RAD51C	Female breast, ovarian
RAD51D	Female breast, ovarian
XRCC2	Female breast, colon, pancreatic

Outside the United States, panels of cancer genes are largely restricted to research settings, and investigators often don't share information about mutations that carry a modest or unknown risk. There's much debate over what to tell volunteers. "We struggle with it," says Hans Ehrencrona, a clinical geneticist at Lund University Hospital in Sweden. "Where to draw that line, no one knows for sure."

Every woman in Sweden who receives *BRCA* testing is now also offered the chance to sign up for a study in which she's tested for 63 other cancer genes. Results from only seven of those are shared with the participants. Many moderate-risk genes are not on the list, says Ehrencrona, who's helping lead the effort. As an example, he points out, "*CHEK2* is quite common in Sweden. We do not return it."

ONE TUESDAY MORNING IN OCTOBER, minutes after a work conference call ends, my phone rings. "I have your results," the counselor announces. It's been 19 days since I met with her. "What do you want to know?"

Well, the pathogenic mutations, of course, I say.

There's great news, she tells me: No pathogenic mutations were detected in any of the three genes.

Relief rushes through me. "Do you want to know about any VUS?" she asks. I think about *CHEK2*, and the 1.6% VUS rate she quoted. What are the chances? "Sure," I say.

"There were no variants of unknown significance detected in *BRCA*, but a variant of unknown significance was detected in *CHEK2*," she tells me. Reading from the GeneDx report, she explains that my VUS is a deletion of 15 DNA nucleotides. The variant has been found in two men with prostate cancer, and in vitro analysis suggests it causes a partial loss of function of the gene.

I expected distress, a ringing in my ears, fear coiling in the pit of my stomach. Instead, I'm almost laughing. I think, "That's it? That's what's being shared with patients these days?" Two men with prostate cancer, cells in a petri dish, a loss of function that may or may not translate into pathogenicity: This does not merit my mental energy.

"People need to become more comfortable with uncertainty," Sharon Plon, a clinical geneticist at Baylor College of Medicine in Houston, Texas, tells me a few days later. But she stresses that acknowledging uncertainty "does not mean that we don't know anything." For many families with cancer, large panels provide constructive guidance.

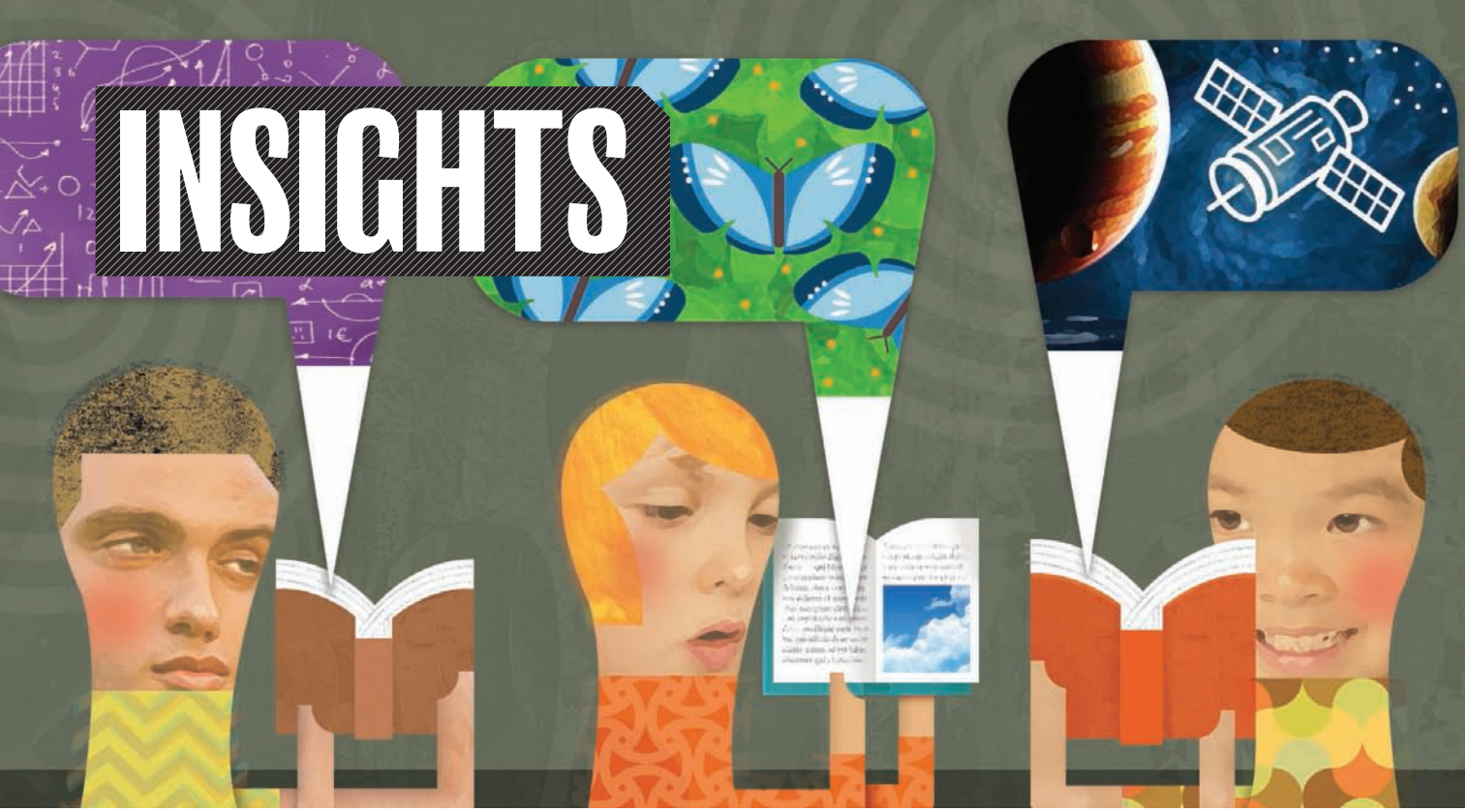
I write to my cousin in San Francisco to share my test results; she is the only close female relative on my father's side, where the cancer cases cluster. And she's more familiar than most with the panels: Her mother, my nonbiological aunt, is fighting ovarian cancer and signed up for a panel of 41 genes offered by the University of Washington, Seattle. She tested negative for all of them.

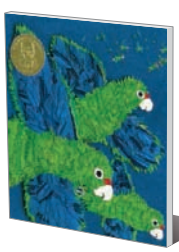
My cousin had urged me to consider the same panel, which has now expanded to 48 genes. In the end, I explain in my message to her, it wasn't something I wanted. "I know the panels are often discouraged," she writes back. It's a view she doesn't share. Even without a clear-cut action plan, she wants to know whatever message her DNA carries for her future. The only reason she's eschewed testing for herself is because insurance is unlikely to pay for it. "Knowledge is power," she writes. "I don't see any downside at all." ■

DATA: GENEDX ONCOLOGY PROGRAM

Published by AAAS

INSIGHTS

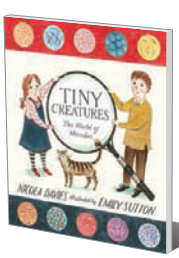




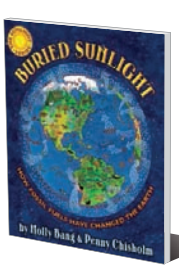
Parrots over Puerto Rico
Susan L. Roth and Cindy Trumbore, illustrated by Susan L. Roth
Lee & Low Books, 2013. 44 pp.



Have You Heard the Nesting Bird?
Rita Gray, illustrated by Kenard Pak
HMH Books for Young Readers, 2014. 32 pp.



Tiny Creatures: The World of Microbes
Nicola Davies, illustrated by Emily Sutton
Candlewick, 2014. 36 pp.



Buried Sunlight
Molly Bang and Penny Chisholm, illustrated by Molly Bang
The Blue Sky Press, 2014. 44 pp.

BOOKS *et al.*

SB&F PRIZES FOR EXCELLENCE IN SCIENCE BOOKS

Mars, microbes, and mastodons... oh my!

Do you know an aspiring astronaut or have a son or daughter who's fascinated with physics? Know a kid who can't stop talking about parrots or one who loves a good mystery? If so, then this year's finalists for the 2015 *Science Books and Films* Prizes for Excellence in Science Books will likely be of great interest. The prizes, sponsored by AAAS and Subaru, celebrate books that offer clear and engaging discussions of scientific topics for children and young adults. The finalists were chosen by a panel of librarians, scientists, and science literary experts from 175 submissions, all of which were published between September 2013 and September 2014. The winners for each category will be announced at the upcoming AAAS Annual Meeting in San Jose. We hope that you and your young readers will enjoy them as much as we did.

CHILDREN'S SCIENCE PICTURE BOOK

Parrots over Puerto Rico

Reviewed by **Yevgeniya Nusinovich, Solomon Nusinovich Ucko, Hadassah Nusinovich Ucko**

This is one of those rare books that are meant for young children but are interesting enough to be read by the whole family. In it, authors Susan Roth and Cindy Trumbore tell the true story of Puerto Rico's parrots, which almost vanished as a result of human development and habitat destruction and are now being brought back from the brink of extinction. The history of Puerto Rico is interwoven throughout the story, giving readers a glimpse into the political and cultural context that led to the parrots' predicament. The book is illustrated with beautiful collages by Susan Roth, a professional artist and author. The story is followed by

ILLUSTRATION: GORDON STUDER

Downloaded from www.sciencemag.org on December 5, 2014

Published by AAAS



ILLUSTRATION: EMILY SUTTON

an afterword, which contains photographs of the parrots and other species of birds that call Puerto Rico home, as well as the scientists and equipment involved in protecting the parrots and restoring their habitat. Although the primary audience for this book would be budding nature lovers, youngsters who are interested in history and culture will likely enjoy it as well. In addition, we recommend this book to families with children who are too young to read, because the exciting story and beautiful collages will entertain parents and their little ones.

Have You Heard the Nesting Bird?

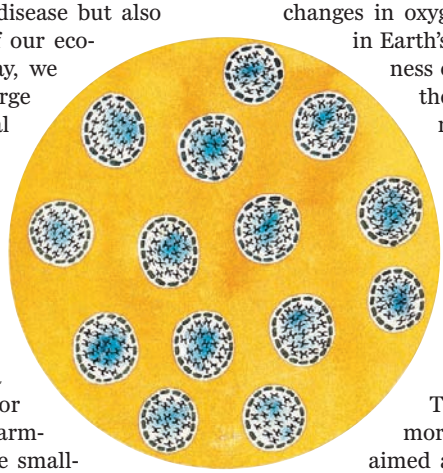
Reviewed by **Sacha Vignieri**

As children begin to engage with the world around them, often one of the things they are most attracted to are the birds that surround our homes and live in our parks. They point as they fly by or turn their heads at the interesting calls that sometimes seem to come from thin air. Author Rita Gray and illustrator Kenard Pak address these budding birders and naturalists with the simple prose and lovely illustrations in this book, which centers around one of the quietest birds in the yard, a nesting robin. The story showcases the chirps and trills of other common garden birds, giving young listeners their first exposure to the complexity of bird calls. By the end, readers and listeners learn why the robin has stayed so quiet throughout the story and gain some understanding of the diversity of birds and calls that surround us. The final pages feature an interview with the story's robin—"A Word with the Bird"—that provides more detailed information about nesting for the curious reader.

Tiny Creatures: The World of Microbes

Reviewed by **Trista Wagoner**

Since the late 19th century, scientists have been urging people to view microorganisms as not just agents of disease but also critical components of our ecosystem. Yet, even today, we continue to deploy a large arsenal of antimicrobial chemicals in a quest to become germ-free. Perhaps, then, we should try engaging children, who are often naturally drawn to things that adults avoid. In *Tiny Creatures*, author Nicola Davies and illustrator Emily Sutton offer a charming introduction to the smallest forms of life, engaging young primary-school children in topics ranging from microbial diversity (in size, shape, habitat, and energy source) to the parallels that exist between microbes and other forms of life. For example, we learn that the number of microbes in a teaspoon of soil is comparable to the number of people in India. Sutton's illustrations include pinwheel shapes and colorful squiggles, which make microbes vibrant and fun rather than frightening. Davies's text also reassures readers that microorganisms should not be feared, because most do not make us sick. In fact, "they are the invisible transformers of our world—the tiniest lives doing some of the biggest jobs." This book makes the invisible familiar and provides a foundation for a friendly, not adversarial, relationship between tiny people and tiny creatures.



Buried Sunlight

Reviewed by **Brent Grocholski**

Sunlight is the thread that ties together several concepts related to anthropogenic climate change in this children's book. The goal is to get children thinking about the potential consequences of burning hundreds of millions of years of fossil fuels, which authors Molly Bang and Penny Chisholm refer to as "buried sunlight." The book highlights the difference in time scale between how long it has taken to produce fossil fuels and the rate at which humans consume them. In the process, it does not shy away from introducing complex scientific concepts, including photosynthesis and the carbon cycle. The illustrations are thoughtful and necessary for a book that sets out to explain such a challenging set of ideas to a younger audience. To reinforce the theme of buried sunlight, dark pockets of fossil fuels are shown, laced with tiny golden suns. Large, wavy arrows illustrate changes in oxygen and carbon dioxide in Earth's atmosphere. The darkness of the illustrations gives the book a bit of an ominous tone as it hints at some of the negative consequences of climate change, but it closes on an optimistic note, encouraging us to work together to find alternative energy sources and reduce greenhouse gases. The final pages contain a more detailed notes section aimed at answering additional questions about the link between fossil fuel use and climate change.

Published by AAAS



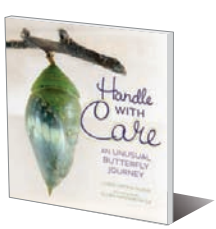
The Case of the Vanishing Honeybees: A Scientific Mystery
Sandra Markle
Milbrook Press, 2014. 48 pp.



Eyes Wide Open: Going Behind the Environmental Headlines
Paul Fleischman
Candlewick, 2014. 208 pp.



Plastic, Ahoy! Investigating the Great Pacific Garbage Patch
Patricia Newman, photography by Annie Crawley
Millbrook Press, 2014. 48 pp.



Handle with Care: An Unusual Butterfly Journey
Loree Griffin Burns, photography by Ellen Harasimowicz
Millbrook Press, 2014. 36 pp.



Mission: Mars
Pascal Lee, illustrated by Ryan Hobson
Scholastic, 2013. 48 pp.



The Kid's Guide to Exploring Nature
Brooklyn Botanic Garden Educators, illustrated by Laszlo Veres
Brooklyn Botanic Garden, 2014. 120 pp.



PHOTO: KATHY KEATLEY GARVEY

MIDDLE GRADES SCIENCE BOOK

The Case of the Vanishing Honeybees: A Scientific Mystery

Reviewed by **Beverly Purnell**

Honeybees have been disappearing at an astonishing rate since 2006. In this book, former elementary school science teacher Sandra Markle informs young (late elementary to early middle school) readers about this crisis, termed colony collapse disorder (CCD). In the beginning of the book, we learn that in recent years, as many as 30 to 50% of honeybees have vanished from hives, with few clues as to the cause. Because one-third of crops are pollinated by bees, this represents a serious problem. Cast as a mystery, the book includes informative explanations of plant and bee biology as well as a description of the "partnership between bees and plants" and the reliance of humans on this association. Throughout the book, Markle quotes scientists and beekeepers who theorize that CCD may be due to mites, a fungus, pesticides, altered farming and beekeeping practices, or a combination of assaults. Beautiful photographs and diagrams illustrate concepts as diverse as the bee life cycle, commercial beekeeping, and challenges in the bee habitat. A broad range of readers with interests in insects, agriculture, or the workings of science will likely find this book to be engaging and informative.

Eyes Wide Open: Going Behind the Environmental Headlines

Reviewed by **Julia Fahrenkamp-Uppenbrink**

Modern technology, from smart phones to air travel, is pervasive in today's society, making it inconceivable how humans could ever have lived without them. Yet, as children's writer Paul Fleischman explains in this book, the advances of the past 250 years have changed the world beyond recognition. Writing in an accessible and engaging style, he explains the environmental problems caused by climate change and the growing world population, including those that result from our consumption of goods and products, energy use, and food production. He highlights the vested interests and social mechanisms that prevent change and helps the reader to recognize environmental problems and their causes, both in their own cities and in the wider world. In the margins, numerous images, nuggets of information, and suggestions for further reading provide context. Aimed at teenagers, the book provides what the author calls the basic vocabulary for following the environmental debate—defining terms such as carbon capture, normalcy bias, and greenwashing. Its clarity and scope provide an excellent starting point for classroom discussion or independent reading.

Published by AAAS

Plastic, Ahoy! Investigating the Great Pacific Garbage Patch

Reviewed by **Marc Lavine**

When we think of large-scale waste disposal, we often think of giant, stinky landfill sites where garbage is buried. However, the largest collection of garbage isn't on land but rather in the Pacific Ocean. Known as both the Pacific trash vortex and the Great Pacific Garbage Patch, it is located in a part of the ocean called the North Pacific Central Gyre and spans waters from the west coast of North America to Japan. Here, the convergence of four currents creates a pocket of relatively calm water, which causes large quantities of small, primarily plastic, debris to accumulate. In this book, author Patricia Newman follows three young scientists—Miriam Goldstein, Chelsea Rochman, and Darcy Taniguchi—on an ocean voyage to explore the garbage patch as part of the Scripps Environmental Accumulation of Plastic Expedition (SEAPLEX). Despite its size, which both is hard to quantify and can vary through the year, the patch cannot be seen by satellites because most of the garbage is in the form of small particles and a large fraction may lie on the sea floor. Scientists hoping to study it must take to the open ocean, which also gives them the opportunity to study the impact of the patch on the local marine life and food chain. Newman narrates the book from the perspective of the researchers and crew and their daily activities, including anecdotes about the voyage itself, as well as the exploration of the garbage patch. She uses these adventures to show the reader what it means to be a scientist and to use scientific methods.

Handle with Care: An Unusual Butterfly Journey

Reviewed by **Michael D. Crabtree**

A mysterious package arrives at the Museum of Science in Boston from a farm in Costa Rica. What could it be? Bizarrely enough, it's butterfly larvae! Using stunning images and informative text, author Loree Griffin Burns and photographer Ellen Harasimowicz describe the life cycle and journey of these beautiful insects. The story begins at El Bosque Nuevo, a Costa Rican farm that "grows" butterflies for museums so that people around the world can learn more about them. Because El Bosque Nuevo is somewhat different from a normal farm, Burns describes some of the farmer's daily tasks, from preparing meals of crushed bananas and sugared water to wrapping the butterfly larvae in cotton and tissue paper for transport. According to Burns, the farmers work hard so that they can earn money to protect the forest around their property. The life cycle and metamorphosis of the blue morpho butterfly is wonderfully described, with superb photographs and useful diagrams. In the back of the book, readers will find an interesting comparison with other insects and their life cycles and a valuable glossary that explains some of the more technical words. This is an ideal book for an aspiring entomologist or those who are curious about the logistics behind museum exhibits.

Mission: Mars

Reviewed by **Maria Cruz**

This short but instructive and visually rich book is written as a training manual for budding Mars-bound astronauts. Aimed at children ages 9 to 12, it is packed full of information about the red planet, including what it would take to travel there and back. The author, Pascal Lee, is a planetary scientist who studies the history of water on Mars. As chairman of the Mars Institute, a nonprofit research organization whose mission is to further the scientific study, exploration, and public understanding of Mars, he has plenty of experience thinking about potential human missions to Mars, and he draws on this experience to engage the reader. Throughout the book, we see photographs of Lee testing a spacesuit in a simulated Martian dust storm and climbing down a steep Mars-like cliff on Devon Island in northern Canada. Lee expertly guides future Mars explorers through six phases of training, including basic facts about the planet, preparing for launch, navigating space, understanding what to expect aboard the spacecraft, landing on Mars and exploring its surface, and planning future steps in exploration. As in any training, there are a number of drills—short quizzes that test the reader's mastery of the topic—throughout the book. Those who successfully complete the final drill are invited to sign and date a certificate of achievement.

HANDS-ON SCIENCE BOOK

The Kid's Guide to Exploring Nature

Reviewed by **Marc Lavine**

Do you know a kid who is more interested in identifying wildflowers than in pulling them to make a bouquet? Are you out of your league when it comes to answering questions about why leaves change color or identifying rocks, leaves, birds, and insects? If so, help is available from the experts at the renowned Brooklyn Botanic Garden. Broken down by seasons, this book invites readers to explore the biodiversity around them in a wide range of locations, from the woods, to meadows and ponds, and even in the city. Packed with detailed, well-labeled illustrations, the book explores everything from "wonder weeds" and "awesome amphibians" to "rocks that will knock your socks off." Career profiles are woven throughout



the book and discuss a number of jobs that relate to exploring and preserving nature, including field biologist, nature educator, and botanical illustrator. The book also features a number of nature activity guides and scavenger hunts, as well as a detailed glossary of technical terms that are used throughout. Parents of young naturalists may especially appreciate the final pages of the book, which offer "tips for adult caregivers" that include ways to plan a successful outing and plants that are best avoided, complete with helpful photographs.

ILLUSTRATION: MANNY JOSE/COURTESY OF BROOKLYN BOTANIC GARDEN

Published by AAAS

Junk Drawer Physics

Reviewed by **Brent Grocholski**

The paper clips, batteries, rubber bands, straws, and other junk you can't bear to throw away are about to come in handy. In this book, high school physics teacher Bobby Mercer presents 50 fun projects that exploit principles of basic physics to fling objects, spin things, make noise, and amaze your friends. The experiments are broken down into topic sections of force, energy, sound, light, electricity, and fluids. Each project has a clear list of required objects and pictures to help the reader understand the setup instructions. A simple breakdown follows to explain the science behind how the experiment works. Although adult supervision is necessary for a few of the experiments, most of the projects can be tackled by older children (middle school and up) with ease. The book also has plenty to offer teenagers and adults, as many of the experiments double as cool party tricks and science fair inspiration. This book has something for everyone to enjoy, whether you want to build a pinhole camera, burn steel, make an air horn, construct a clothespin catapult, or impress your friends with a coin trick. These engaging experiments provide a fun way for everyone to learn a little bit of physics.

Plant a Pocket of Prairie

Reviewed by **Barbara Jasny**

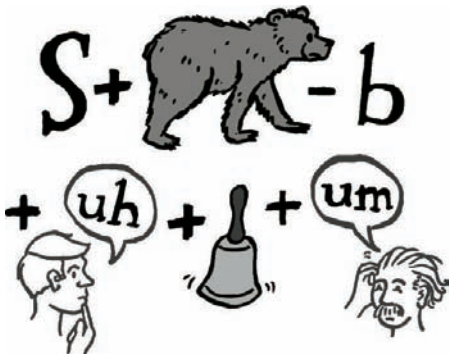
This is a book about the vanishing prairie and what children can do to preserve "pockets" of it. Although the message is delivered in a gentle manner with charming illustrations, the author, Phyllis Root, speaks to the disappearance of an entire ecosystem—the prairie that once covered 40% of the United States. Her recommendation is to begin small, by planting once-common species such as bluestem or butterfly weed or coneflowers and watching as they attract insects and small animals that have been looking for food and a home. From butterflies and chickadees to skinks and spadefoot toads, Root encourages children to dream big when it comes to restoring biodiversity, closing the story with a picture of bison, which could conceivably repopulate our landscape if our "prairie pockets" grow large enough. The final pages offer greater detail about the prairie, practical planting tips, and descriptions of animals and plants that are native prairie dwellers.

YOUNG ADULT SCIENCE BOOK

The Tale of the Dueling Neurosurgeons

Reviewed by **Valerie Thompson**

Macabre medical cases, including a deadly disease that evokes maniacal laughter in its victims and an addled alcoholic who lies compulsively, feature prominently in this book, which tells the story of the strange circumstances that have led to important breakthroughs in our understanding of the human brain. The cast of characters will be familiar to any brain enthusiast, including the infamous "H.M.," who never formed a new memory after undergoing an experimental surgical procedure, and the incredibly unlucky Phineas Gage, who wasn't the same after a railroad spike blasted through his frontal lobe. Each chapter begins with a built-in brain teaser that hints at the chapter's theme. The reader is also treated to some enjoyable trivia about some big names in early brain research. For example, in addition to shaping our understanding of the brain's anatomy, we learn that pathologist Santiago Ramón y Cajal was jailed at the age of 11 for building a cannon from an oil drum and using it to destroy a neighbor's gate and that Wilder Penfield, the neurosurgeon who meticulously mapped the brain, only became convinced of his calling after a German torpedo nearly claimed his life in 1916. The most compelling part of the narrative, however, is the way that it encourages the reader to internalize the information presented. What might it feel like to lose "memories of holidays and lovers and times we fell short," implores author Sam Kean, and in cases where questionable medical decisions led to great insights about the brain, does the end justify the means?



The Sixth Extinction: An Unnatural History

Reviewed by **Julia Fahrenkamp-Uppenbrink**

In this book, *New Yorker* staff writer Elizabeth Kolbert presents compelling evidence that we are in the midst of a human-caused mass extinction. According to Kolbert, this "sixth extinction" is of a similar magnitude to previous mass extinction events, including the Cretaceous event that famously spelled the end for the dinosaurs. The author is at her best when recounting her personal encounters with species or ecosystems in peril. Her account of the demise of North American bats from an introduced

ILLUSTRATIONS: (TOP TO BOTTOM) ANDREW J. BROZYNA; BETSY BOWEN



Published by AAAS

fungal disease, for example, is harrowing. She describes entering a cave that was covered with the remains of dead bats, making it impossible to avoid stepping on them. The next winter, she returns, and all that is left of the dead bats is a "carpet of delicate bones." She goes on to describe how bat species that counted in the millions less than 10 years ago are now officially listed as endangered. She also swims with researchers off the coast of a small Italian island to provide readers with a firsthand account of the effects of ocean acidification and travels to a Panamanian "frog hotel" devoted to saving frogs from a fungal disease that threatens to wipe out vast numbers of amphibian species. As Kolbert explains, mass extinction events are extremely rare because "life is extremely resilient but not infinitely so." She offers numerous examples to show how globalization and global warming are outpacing species' ability to adapt, with disastrous results for Earth's biodiversity.

Extreme Medicine: How Exploration Transformed Medicine in the Twentieth Century

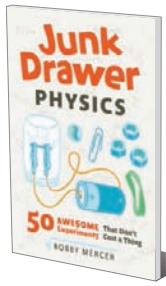
Reviewed by **Kristen L Mueller**

If you're trapped in a sinking vehicle, you're more likely to survive if it's daytime. This is because beyond a certain depth, you need sunlight to know which way is up. Kevin Fong weaves survival trivia throughout this book, which also features historical vignettes and personal accounts from his experiences as an anesthesiologist, intensive care specialist, and NASA researcher. The book is a gripping—although sometimes meandering—read, taking readers everywhere from Robert Falcon Scott's ill-fated expedition to the South Pole to the burn wards of a British hospital during World War II and, finally, to Mars (at least as a thought expedition). Fong uses these and other examples of extreme circumstances to argue that our species' urge to explore has driven critical advances in medicine. Our urge to explore, however, only accounts for some of these advances, as many of the examples described in the book fall far afield of an endeavor one might undertake in a recreational capacity. Among others, the breakthroughs that were precipitated by war, alone, included heart surgery, standardized trauma protocols, and the growing of skin grafts for burn victims. Fong's accounts of what happens to the body in zero gravity and what challenges this presents for getting humans to Mars, a topic he explores in great detail at the end of the book, is fascinating, although it remains to be seen whether this will have a significant effect on the practice of medicine. With its gripping accounts of human survival and compelling first-person anecdotes, *Extreme Medicine* will likely interest young adult readers (who may get more out of it if they've had some high school biology) and adults alike.

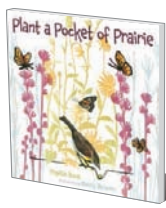
Shocked: Adventures in Bringing Back the Recently Dead

Reviewed by **Guy Riddihough**

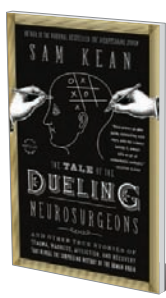
Anna, 29, loses control of her skis, crashes down a slope, falls through a sheet of ice, and is trapped underwater in a frigid, fast-flowing mountain stream for 80 min. When she is finally rescued and arrives at the hospital, she appears to be dead, but 5 hours later her heart is coaxed into beating, and 10 days later she wakes up with only minor nerve damage. Florence, 82, already chronically ill, suffers a heart attack in her retirement apartment, and within a very short time a team of paramedics arrives and restarts her heart. Unlike Anna, Florence never wakes up and, roughly 2 weeks later, dies. In this book, author David Casarett, himself a medical doctor, uses these and other near-death incidents to illustrate a lively, often humorous, and occasionally gruesome exploration of the science and history of resuscitation. He guides us through scientific successes and failures, explores the cutting edge of suspended animation research and the promise it holds for stabilizing patients until they can reach the hospital, and investigates how CPR likely really works (surprisingly, it may not be by restoring circulation). He illustrates the power that cheating death holds over us with discussions of coffins equipped with mechanisms to alert the outside world, should you revive from apparent death and find yourself entombed, and optimistic "cryonauts" who have their bodies frozen after death in the hope of future resurrection. Nor does he shy away from some of the moral issues raised by trying to save people, such as Florence, from death. For older teens (and adults), this book represents a fascinating window into the science of staying alive.



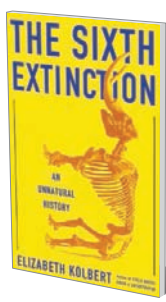
Junk Drawer Physics: 50 Awesome Experiments That Don't Cost a Thing
Bobby Mercer
Chicago Review Press, 2014. 203 pp.



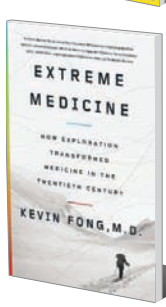
Plant a Pocket of Prairie
Phyllis Root, illustrated by Betsy Bowen
University of Minnesota Press, 2014. 40 pp.



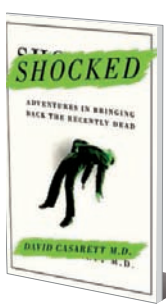
The Tale of the Dueling Neurosurgeons: The History of the Human Brain as Revealed by True Stories of Trauma, Madness, and Recovery
Sam Kean
Little, Brown, 2014. 416 pp.



The Sixth Extinction: An Unnatural History
Elizabeth Kolbert
Henry Holt, 2014. 330 pp.



Extreme Medicine: How Exploration Transformed Medicine in the Twentieth Century
Kevin Fong
Penguin Press, 2014. 304 pp.



Shocked: Adventures in Bringing Back the Recently Dead
David Casarett
Current, 2014. 270 pp.

Published by AAAS

ROYAL SOCIETY YOUNG PEOPLE'S BOOK PRIZE

From you to the universe—and everything in between

With the swipe of a screen or the click of a mouse, children now have access to more information than ever before. But when it comes to more advanced topics, the resulting information overload can leave a child with more questions than answers. Enter the six finalists for this year's Royal Society Young People's Book Prize, which break down complex concepts from fractals to personalized medicine into age-appropriate, kid-friendly servings. From a shortlist compiled by a jury of adult judges, young readers on judging panels throughout the United Kingdom ultimately chose Clive Gifford's *Eye Benders: The Science of Seeing and Believing* as the recipient of the top £10,000 prize. With engaging illustrations and smart, but playful, text, you won't go wrong with any of these fine books.



The Usborne Big Book of Stars and Planets

Reviewed by **Maria Cruz**

Stars and galaxies in all shapes and forms, as well as rockets, spacecraft, and telescopes, all feature prominently in this exquisitely illustrated book, which conveys the beauty and richness of the universe to young children. The illustrations of planets and stars are very detailed and true to the astronomical images on which they are based. Four-panel foldouts provide a sense of scale and offer readers insight into everything from the solar system to the rockets and spacecraft that help us study it. The foldout that showcases stars and galaxies is particularly breathtaking, featuring art based on images taken by the Hubble Space Telescope. The text is clear, concise, and up to date. Young readers will learn about the satellites that fly around Earth, the recently discovered icy dwarf planets that orbit beyond Pluto, and new tools for space study. But it is not all about what professional telescopes and space probes can see and do. The last two pages encourage young readers to discover the night sky for themselves.

How Animals Live

Reviewed by **Caroline Ash**

Life on Earth is ubiquitous, multidimensional, and complex, and what better medium to convey this than a pop-up book? This book devotes a full-page spread to six of the earth's biological regions, taking the reader from grassland savannahs to tangled rainforests, through chilly polar regions and dry deserts, and to fresh and saltwater environments. The book opens with some basic concepts and random facts about seasonality, biomes, and the evolution of the elephant's trunk. Opening the next page makes a rainforest spring up—complete with tapirs, macaws, and jaguars. The desert pages are covered with flaps that show that arid biomes are not as devoid of life as they may first appear (although why there is a jerboa in the dung beetle's burrow is not immediately clear). Subsequently, salmon leap out of a river against a backdrop of coniferous forests, and polar animals plunge off icebergs and bask in their blubber. There's even a colorful coral reef and its inhabitants. Here, flaps lift to reveal what animals can be found in the depths of the seas, and on other pages, the flaps show those that take over the habitats at night. The book is also peppered with intriguing facts: For example, the female ocean sunfish can lay 300 million eggs at a time, and the wingless midge can live without oxygen for as long as a month. The illustrations are free-form and quite impressionistic, but the overall effect is dynamic and should inspire a budding ecologist to ask questions.

What Makes You YOU?

Reviewed by **Michael D. Crabtree**

If you want to know what makes you *you*, at least at the biological level, then you have to start by looking at your DNA. However, as author and former biology teacher Gill Arbuthnott points out, "over 99.9 percent of your DNA is exactly the same as every other person on the planet." What's more, you also share the same, seemingly simple, four-letter code with all other life on earth. How can this be? Beginning with a brief overview of Charles Darwin and evolution, and a short introduction to DNA, Arbuthnott breaks down how, together, DNA and natural selection have led to the emergence of all of the different species of plants and animals on Earth today. She then explains how and why genes are manipulated for medical, agricultural, and scientific purposes, covering topics ranging from gene therapy to GMOs to tissue engineering. A wide range of other applications is also covered, including DNA fingerprinting, cloning, and stem cells. For budding scientists, an experiment to extract DNA from fruit is detailed at the end of the book. The cartoon illustrations help to explain some of the more complex points, making the informative and engaging text more accessible for younger children, although some of the topics may still be a bit advanced. This book would be a fantastic and enlightening read for anyone, child or adult, who desires to learn about the biological building blocks that make us who we are.

Lift-the-Flap Questions and Answers About Your Body

Reviewed by **Jennifer Sills**

How do cuts get better? What are freckles? Do we all dream at night? Lift the flaps on the pages of this colorfully illustrated book to find the answers to these questions and many more. Chapters are organized by type

ILLUSTRATION: USBORNE PUBLISHING LTD

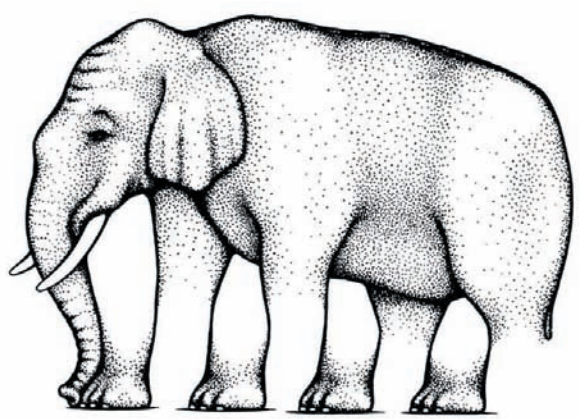
Downloaded from www.sciencemag.org on December 5, 2014

Published by AAAS

of question (e.g., Who? What? Where?), and each page covers a variety of topics, from breathing to blood to germs. Fun trivia is sprinkled throughout—"insect blood is yellow and lobster blood is blue," for example, and "children take more breaths a minute than adults." Author Katie Daynes exercises restraint in introducing vocabulary. She provides simple definitions for some terms, such as antibodies and ligaments, but refers to pores only as "tiny holes" and to bacteria as "germs." Children will learn about a healthy lifestyle through answers about balanced diets and teeth brushing, and they will undoubtedly want to share their new knowledge about nose picking, burps, and poop. The final page continues the interactive spirit of the book with questions for the child to answer—"What was your first word?" for example, and "How many teeth do you have at the moment?"

Eye Benders: The Science of Seeing and Believing

Reviewed by
Margaret Moerchen



Can't believe your eyes? It could be your brain that's lying to you. In this book, journalist Clive Gifford leads a tour of optical illusions that make you look twice and think one more time. Gifford begins by laying out the mechanics of how our eyes and nervous system collect and process information. Using colorful and clever images that elicit specific illusions, he goes on to explain the shortcuts the brain usually takes that lead it down the wrong path. We learn that optical illusions exploit everything from the brain's propensity to "fill in the gaps" when it receives inadequate sensory information, to its methods for estimating size and distance, to the curious way it recognizes edges. At times, the brain's strength at a given skill—such as facial recognition—is what brings about its momentary lapses. We see faces on Mars where only a broad mountain exists, for example, thanks to a phenomenon called pareidolia. On another page, two upside-down photos of human faces appear to be identical, but on upending the book, it's impossible not to see that the features in one photo have been right-side up all along, a phenomenon known as the Thatcherized illusion. The slim volume is aimed at 10- to 14-year-olds, but the delight that comes from putting one over on our own brains knows no age—all should find some fun surprises in this book.

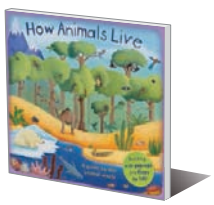
We've Got Your Number

Reviewed by **Marc Lavine**

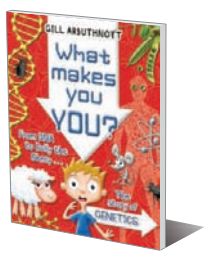
Before kids can read or recognize letters, they know their numbers. Don't believe me? Just offer a child any number of cookies, and I'm sure she'll ask for that number plus at least one more! Some numbers are quite familiar to young children—one nose, mouth, or bellybutton; two ears, eyes, hands, or feet; and 10 fingers or toes—but the significance of others may not be so obvious. If you string together a series of numbers, for example, a pattern may emerge, and if you think about how numbers connect to each other, you can start to develop relationships and theorems. Using numbers as his building blocks, Mukul Patel constructs his book around an exploration of how math intersects with the natural world, from the way we count and the reasons we count in different ways to the math that underlies many geometric objects and patterns. He also delves into the mathematical reasons behind the shapes and sizes of living objects, as well as the physics of sports and space travel. In addition to the basic concepts, the pages are packed with cartoons that illustrate the topics being discussed and activities to try at home. The careful reader will also notice that the pages are numbered in both decimal and hexadecimal. While you'll need to flip through the pages in the proper order if you wish to crack the number sequence puzzles that appear on the upper right-hand corner in each chapter, it is just as much fun to explore this book in a random, and perhaps unaccountable, way.



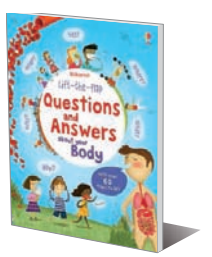
The Usborne Big Book of Stars and Planets
Emily Bone, illustrated by Fabiano Fiorin
Usborne, 2013. 28 pp.



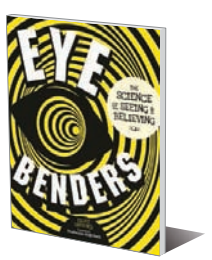
How Animals Live
Christiane Dorion, illustrated by Beverley Young
Templar, 2013. 18 pp.



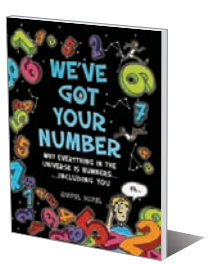
What Makes You YOU?
Gill Arbuthnott, illustrated by Marc Mones
A & C Black, 2013. 64 pp.



Lift-the-Flap Questions and Answers About Your Body
Katie Daynes, illustrated by Marie-Eve Tremblay
Usborne, 2013. 14 pp.



Eye Benders: The Science of Seeing and Believing
Clive Gifford
Ivy Press, 2013. 64 pp



We've Got Your Number
Mukul Patel, illustrated by Supriya Sahai
Kingfisher, 2013. 96 pp.

ILLUSTRATION: ROGER N. SHEPARD

Published by AAAS



Edge of Pine Island Glacier, Antarctica. The glacier is at top left, with sea ice and open water (blue) at bottom and right. [Photographed in the 2005/2006 summer season.]

OCEANOGRAPHY

How ice shelves melt

Warming of the water that flows under Antarctic ice shelves is key to their melting

By **Sarah Gille**

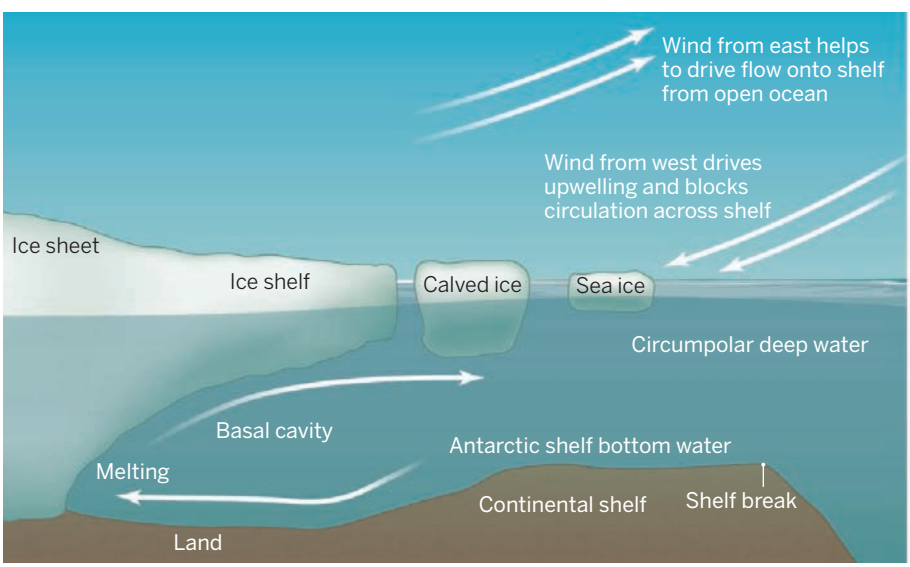
Nobody lives permanently in Antarctica. At first glance, studies of Antarctic climate might thus seem like a curiosity without obvious societal implications. Yet, if the entire West Antarctic Ice Sheet were to melt, global sea level would rise by 4.8 m, with major effects on coastal populations. Two studies published earlier this year offered convincing evidence that the West Antarctic Ice Sheet is indeed melting irrevocably (*1*, *2*). What are the processes behind this melting? On page 1227 of this issue, Schmidtko *et al.* (*3*) show that the water flowing under the ice shelves has warmed in recent decades and that upwelling winds at the continental shelf break may contribute to this process.

Because sea ice floats on water, melting or freezing of sea ice has no major effect on sea level. Ice sheets are a different story, however, because they sit on land and thus keep water frozen and out of the ocean. Ice shelves are the oceanic extensions of ice sheets (see the photo). Like sea ice, they float. However, they can be 200 to 1000 m thick (*4*) and can serve as buttresses, retaining the ice shelves on land (*5*, *6*).

Ice shelves may disintegrate by calving icebergs off the leading edge or by melting through warming from above or below. Warming from above is relatively ineffective because snow-covered ice reflects sunlight rather than absorbing it. Calving can reduce the size of ice shelves, but basal melting has by far the biggest effect on ice shelf melting (*5*, *7*). Ocean currents that circulate water into and out of the cavity under an ice shelf can carry a substantial amount of heat even if the ocean waters themselves are near freezing, and these currents are effective at melting ice from below. By analogy, if your Thanksgiving turkey is still frozen hours before you need to cook it, you can thaw it relatively rapidly by placing it under cold running water.

Water dense enough to circulate in basal cavities under the Antarctic ice shelves flows just above the sea floor on the Antarctic continental shelf (see the figure). This water, a combination of Circumpolar Deep Water and Winter Water, is referred to as Antarctic Continental Shelf Bottom Water. Circumpolar Deep Water, as its name suggests, comes from the Antarctic Circumpolar Current and is distributed all the way around Antarctica. Winter Water is cold water near the ocean surface that gains its properties as a result of wintertime convective cooling (*8*, *9*).

Glaciologists have long pointed to ocean circulation as a likely source of heat to



Melting from below. The Antarctic ice shelves are the ocean extensions of the Antarctic ice sheets. Ice shelves buttress the ice sheets onto the land. Comparatively warm water that circulates under the ice shelves can lead to basal melting of the underside of the ice shelves, ultimately breaking up the ice shelves. Schmidtko *et al.* (*3*) show that wind patterns at the continental-shelf break influence the properties of water on the continental shelf and in the basal cavity.

Scripps Institution of Oceanography, University of California San Diego, La Jolla, CA 92093-0230, USA. E-mail sgille@ucsd.edu

PHOTO CREDIT: DAVID VAUGHAN/SCIENCE PHOTO LIBRARY; ILLUSTRATION: P. HUEY/*SCIENCE*

Downloaded from www.sciencemag.org on December 5, 2014

Published by AAAS

drive basal melting (*2*, *5*–*7*, *10*). The details of circulation in the basal cavity remain elusive, however, because there is no easy way to drill through hundreds of meters of ice to deploy oceanographic instruments in the cavity. Schmitdko *et al.* avoid the challenges of in situ measurements in the basal cavity by instead evaluating the properties of the water that can be transported into the cavity. Their analysis of hydrographic ocean data collected since 1975 shows that over the past 40 years, Circumpolar Deep Water has warmed at all longitudes around Antarctica.

The authors also report that in some regions of the Antarctic continental shelf (for example, near the Amundsen and Bellingshausen Seas, adjacent to West Antarctica), changes in the Antarctic Continental Shelf Bottom Water appear to mirror changes in Circumpolar Deep Water. Other regions appear protected from the warming Circumpolar Deep Water. The critical difference is that in warming regions, Circumpolar Deep Water slopes upward to the shelf break, possibly as a response to strong winds from the west that are expected to induce upwelling (see the figure). In contrast, in regions without shelf warming, including the Ross and Weddell Seas, Circumpolar Deep Water slopes downward to the shelf break, consistent with winds from the east that limit onshore flow. An analysis of mooring data in the Amundsen Sea (*11*) also concluded that local winds play a key role in bringing water onto the Antarctic Shelf.

Schmidtko *et al.*'s results highlight the critical role of wind forcing. Winds north of the shelf break determine the properties of water that in turn influence basal melting of ice shelves. Both greenhouse warming and ozone depletion can intensify the Southern Hemisphere westerly winds and displace them southward (*12*). Although current wind conditions appear to shield the Ross and Weddell Seas from the melting effects associated with Circumpolar Deep Water, future changes in the winds could modify that and thus alter the ice-shelf buttresses, with further effects on global sea level rise. ■

REFERENCES

1. E. Rignot *et al.*, *Geophys. Res. Lett.* **41**, 3502 (2014).
2. I. Joughin, B. E. Smith, B. Medley, *Science* **344**, 735 (2014).
3. S. Schmidtko *et al.*, *Science* **346**, 1227 (2014).
4. J. A. Griggs, J. L. Bamber, *J. Glaciol.* **57**, 485 (2011).
5. S. S. Jacobs *et al.*, *Nat. Geosci.* **4**, 519 (2011).
6. H. D. Pritchard *et al.*, *Nature* **484**, 502 (2012).
7. M. A. Depoorter *et al.*, *Nature* **502**, 89 (2013).
8. A. P. S. Wong, N. L. Bindoff, A. Forbes, *Ocean, Ice, and Atmosphere: Interactions at the Antarctic Continental Margin Antarctic Research Series* **75**, 173 (1998).
9. Y.-H. Park *et al.*, *J. Mar. Syst.* **17**, 233 (1998).
10. E. Rignot, S. S. Jacobs, *Science* **296**, 2020 (2002).
11. A. K. Wåhlin *et al.*, *J. Phys. Oceanogr.* **43**, 2054 (2013).
12. S. Lee, S. B. Feldstein, *Science* **339**, 563 (2013).

10.1126/science.aaa0886

PHOTO: CORA BERGAÑITOS

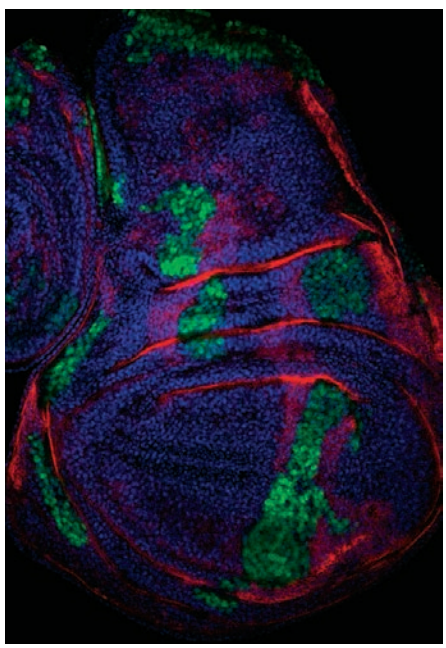
DEVELOPMENTAL BIOLOGY

Death to the losers

Cell competition is linked to innate immunity mechanisms to eliminate unwanted cells and maintain healthy tissue

By **Ginés Morata** *and* **Luna Ballesteros-Arias**

Insects use the innate immunity signaling pathways Toll and IMD to fight infections by foreign pathogens, bacteria, or fungi (*1*). These pathways induce the expression of powerful antimicrobial- antifungal peptides (AMPs) that are released from the fat body cells. On page 1199 of this issue, Meyer *et al.* (*2*) report that fruit flies make use of components of both pathways to build another pathway that removes its own cells that are abnormal and may impair tissue fitness or compromise the survival of the organism. In contrast to the antimicrobial operation, the killing signal does not come from outside the tissue; it originates from interactions of the doomed cell with neighboring cells through the process of cell competition.



Imaginal disc. An image of a wing imaginal disc (*Drosophilia melanogaster*) is shown, containing marked pairs of sibling cell clones generated by mitotic recombination. Cells expressing extra Myc protein (green) are competing against neighboring cells, including those in the sibling clones (red). Nuclei (blue) are stained with the DNA dye Hoechst.

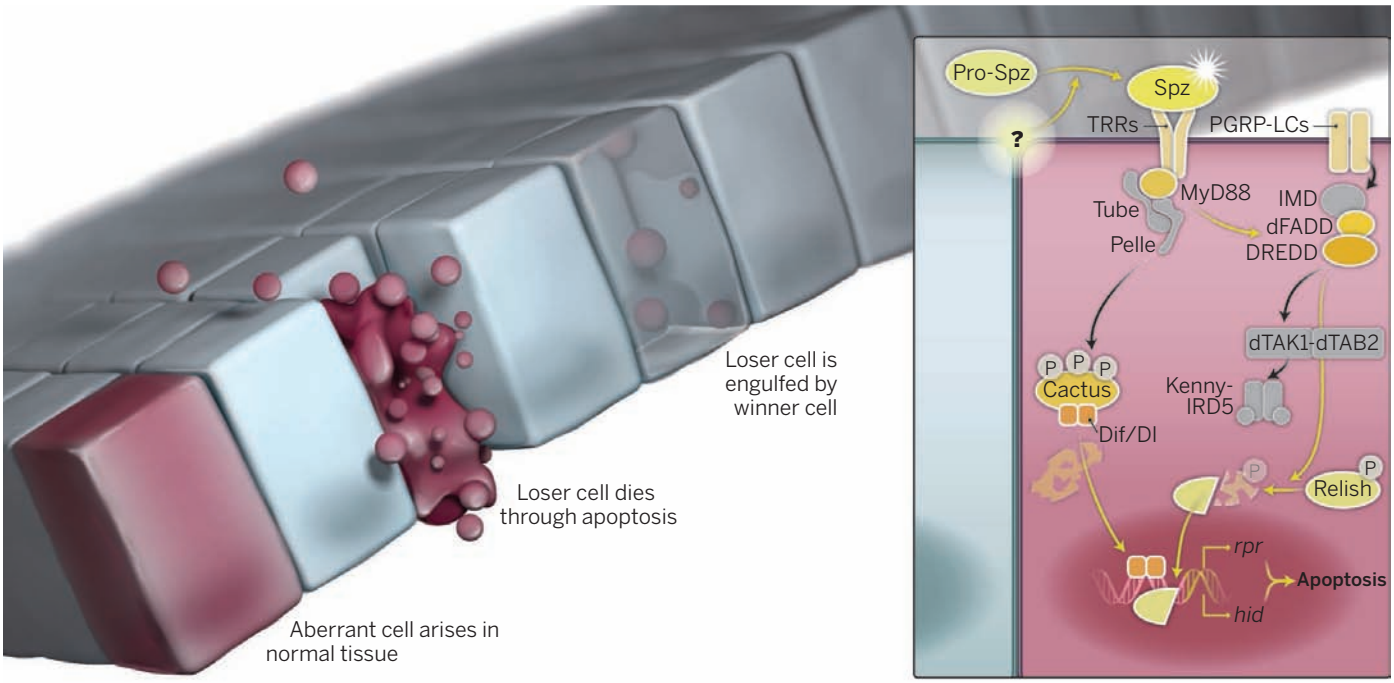
Cell competition is an interactive process originally reported in the imaginal discs (the precursors of the adult cuticle) (see the first figure) of *Drosophila melanogaster* (*3*, *4*), but more recent studies with mouse cells (*5*–*7*) indicate that it is a conserved mechanism in animal tissues. Cell competition is a general surveillance process that identifies and eliminates cells that are weaker than their neighbors, or are abnormal or not well adapted to their developmental context. Its function ensures genetic uniformity of cell populations and also contributes to the general fitness of developing tissues (*8*). As part of its surveillance function, cell competition exerts a therapeutic role by destroying oncogenic cells that may arise during development (*9*–*11*).

Cell competition is a context-dependent phenomenon. It describes interactions between two types of viable cells that lead to the death, by apoptosis (*12*), of one of the cell types. As reported in the classical experiments (*3*, *4*), slow-dividing cells ("losers") are perfectly viable on their own; they are eliminated only if residing in the same population as faster-dividing cells—the "winners." This is the characteristic feature of loser cells: They are viable but die under the influence of their neighbors. Another feature of interest is that it is a short-range phenomenon—the winners and losers lay very close to each other, possibly in physical contact.

A simple scenario for cell competition is a crosstalk between winner and loser cells that triggers apoptosis (*12*) in the losers and possibly activates engulfment genes in the winners; winners appear to consume (phagocytose) the losers (*13*). But what mechanisms underlie this interaction? What are the events leading to apoptosis in the loser cells? The study by Meyer *et al.* opens a new avenue of research into the molecular mechanism linking cell competition to innate immunity. They make the unexpected discovery that in the wing imaginal disc, loser cells are treated as foreign pathogens in their resident populations. The destruction of the loser cells is effected by the innate immune system, and presumably this activation is carried out by neighboring winner cells.

Centro de Biología Molecular CSIC-UAM, Universidad Autonoma de Madrid, 28049 Madrid, Spain. E-mail: gmorata@cbm.csic.es

Published by AAAS



Elimination. A proposal for how components of the innate immunity Toll and IMD signaling pathways are used in a different pathway (shown in yellow) to eliminate aberrant cells (purple) that have arisen within a normal tissue (in *Drosophila*). By a mechanism that is still unknown, aberrant cells are detected as different by their neighbors and are determined to be "losers." The end result is the activation of the proapoptotic genes *hid* and *rpr*, and death of the loser cells. They are subsequently engulfed by the neighboring "winner" cells, thereby restoring a healthy tissue. PGRP-LC, peptidoglycan recognition protein LC; IMD, immune deficiency; TAK1, transforming growth factor beta–activated kinase 1; DREDD, death-related ced-3/Nedd2-like caspase; FADD, FAS-associated death domain; TAB2, TAKI-associated binding protein 2; IRD5, immune-response deficient 5.

Meyer *et al.* assayed cell competition by looking at the cellular response to different amounts of Myc protein (a transcription factor that promotes cell proliferation) and/or the ribosomal protein RpL14. The rule is that viable cells with low amounts of either Myc or RpL14 become losers when surrounded by cells with higher amounts. The key finding of Meyer *et al.* is that loser cells are rescued from elimination when the wing imaginal disc is mutant for one of various components of the Toll and IMD signaling pathways. It is intriguing that some components of the Toll and IMD pathways are required but not others; this finding suggests that cell competition functions through a cascade of events different from the canonical Toll and IMD pathways (see the second figure). A key factor in the immune response is the cytokine Spätzle (Spz), a ligand of the Toll receptor; upon its absence, cell competition is suppressed. However, the loss of Toll still allows cell competition, which suggests that Spz functions through other Toll-related receptors (TRRs), of which there are several in *Drosophila*. The loss of some of them is very effective in suppressing cell competition. At the bottom of the cascade, the transcription factors Relish, Dorsal (Dl), and Dif are activated differentially, depending on the assay.

These transcription factors activate the expression of AMPs during the antimicrobial response, and Meyer *et al.* show that they also activate apoptosis in the loser cells. The proapoptotic genes called *head involution defective* (*hid*) and *reaper* (*rpr*) become activated by Relish and either Dl or Dif, although the requirements for *hid* and *rpr* appear to be different according to the cell competition assay used. The triggering of apoptosis by Toll and IMD factors is itself a new finding that may have general implications in the understanding of innate immunity and also of the regulation of programmed cell death.

The study of Meyer *et al.* poses some challenging questions about the mechanisms of cell competition. One concerns the activation of Spz in the loser cells in the wing disc. Normally Spz is expressed in several larval tissues, including hemocytes, the fat body (similar to the mammalian liver), and salivary glands but not in the imaginal discs. Because Spz is a secreted molecule, it could originate elsewhere and become accessible to wing cells, or it may be specifically produced and secreted by the winner cells. Moreover, its activation involves several proteolytic steps. How this process occurs autonomously in the loser cells is an intriguing problem.

Another question concerns the generality of the phenomenon. The two assays reported, the amounts of Myc or of the ribosomal protein RpL14, are based on the comparison of the metabolic activity of the interacting cells. It will be of interest to determine whether the innate immunity pathway also functions in other distinct cases of cell competition—for example, the elimination of cells with wrong identity (*14*) or the removal of oncogenic cells (*9*, *10*). The latter is especially appealing in view of recent evidence (*11*) that cell competition has an antitumor role also in the mouse thymus. Given the conservation of the innate immunity systems in *Drosophila* and mammals (*1*), it seems possible that innate immunity might have a similar antitumor role in mammals. ■

REFERENCES

1. L. A. O'Neill, D. Golenbock, A. G. Bowie, *Nat. Rev. Immunol.* **13**, 453 (2013).
2. S. N. Meyer *et al.*, *Science* **346**, 1258236 (2014).
3. G. Morata, P. Ripoll, *Dev. Biol.* **42**, 211 (1975).
4. P. Simpson, *Dev. Biol.* **69**, 182 (1979).
5. E. R. Oliver, T. L. Saunders, S. A. Tarlé, T. Glaser, *Development* **131**, 3907 (2004).
6. C. Clavería, G. Giovinazzo, R. Sierra, M. Torres, *Nature* **500**, 39 (2013).
7. M. Sancho *et al.*, *Dev. Cell* **26**, 19 (2013).
8. M. Amoyel, E. A. Bach, *Development* **141**, 988 (2014).
9. C. L. Chen, M. C. Schroeder, M. Kango-Singh, C. Tao, G. Halder, *Proc. Natl. Acad. Sci. U.S.A.* **109**, 484 (2012).
10. L. Ballesteros-Arias, V. Saavedra, G. Morata, *Oncogene* **33**, 4377 (2014).
11. V. C. Martins *et al.*, *Nature* **509**, 465 (2014).
12. E. Moreno, K. Basler, G. Morata, *Nature* **416**, 755 (2002).
13. W. Li, N. E. Baker, *Cell* **129**, 1215 (2007).
14. T. Adachi-Yamada, M. B. O'Connor, *Dev. Biol.* **251**, 74 (2002).

10.1126/science.aaa2345

Published by AAAS

CHEMICAL KINETICS

Calculating the pressure dependence of chemical reactions

A priori calculations can accurately predict rates of methane formation from radicals

By **Michael J Pilling**

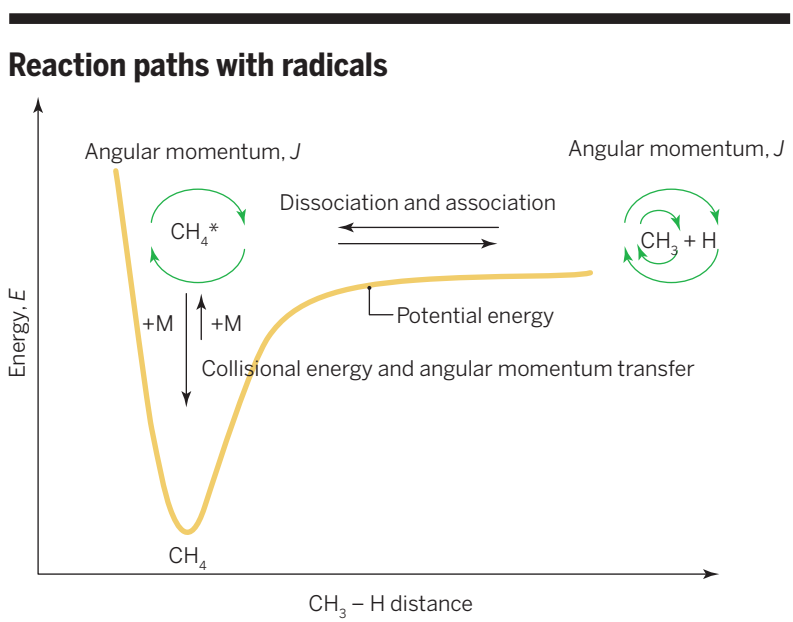
Complex chemical processes that occur during combustion and in the atmosphere involve a large number of elementary reactions. Models of these processes require knowing the rate of every relevant reaction, captured by the rate constant k, which traditionally has been determined experimentally. The vast number of reactions involved makes this approach daunting, but as theoretical methods have become increasingly accurate, they may provide a practical route for some reactions where k depends solely on temperature. For an important subset of reactions, k also depends on pressure; accurate a priori calculation of this dependence has proved elusive. On page 1212 of this issue, Jasper *et al.* (*1*) have developed a methodology that overcomes the difficulties and provides a general approach for the accurate prediction of rate constants for pressure-dependent reactions.

Many elementary reactions involve the transfer of an atom from one reactant to the other, e.g., $OH + H_2 \rightarrow H_2O + H$ (*2*). The reactants and products are separated by an energy barrier, caused by the reorganization of the electrons as one bond is broken and the other forms. This barrier locates the so-called transition state (TS) for the reaction, which acts as a bottleneck. Calculation of the rate constant with transition state theory requires an accurate determination of the energy of the TS and its properties (geometry and vibrational frequencies), which is demanding but feasible. Accurate results have been achieved for a number of important reactions involving relatively small numbers of atoms, including $OH + H_2$ (*2*).

Other reactions, such as those between two radicals, involve bond formation, e.g., $CH_3 + H \rightarrow CH_4$. There is no energy barrier to the reaction (see the figure), and the potential energy decreases as the new bond is formed. The reaction bottleneck is now more difficult to locate and depends on a combination of the decreasing potential energy and reductions in the freedom of movement of the reactants as they are constrained by the forming bond. The transition state is not fixed, but lies at smaller CH_3–H distances for more energetic reactants. The rate constant is very sensitive to the radial part of the calculated potential energy surface (the separation of CH_3 and H), and high-level, computer-intensive methods are needed. It also depends on the angular component of the potential energy, which describes the way in which the rotation of CH_3 becomes increasingly constrained as the reactants approach. Despite these difficulties, reliable methods have been developed for calculation of the rate constant which, arguably, are more accurate than experiment (*3*, *4*).

The total energy (kinetic + potential) of $CH_3 + H$ is conserved in isolation, and the newly formed CH_4 has sufficient energy to dissociate and will do so on a relatively short time scale (typically nanoseconds) unless at least some of this energy is removed. The main route for removing energy is by collision with another molecule, a third body, M. In both combustion systems and the atmosphere, M is nitrogen or oxygen, the majority species in the reaction environment. The collisions are said to be weak if only some of the energy of the newly formed methane, labeled CH_4^* in the figure, is removed in a single collision, and several collisions are needed to ensure formation of stable CH_4. As a result, the overall rate constant depends on pressure—collisions are more frequent at higher pressures, and the rate of stabilization increases.

The calculation of the rate constant now requires a model in which the competition between dissociation of CH_4^* and its collisional stabilization is recognized, which is achieved with a master equation that describes the evolution of the system in energy and time (*5*). The model requires the rate constants for reaction of CH_3 and H and for dissociation of CH_4^*, together with the rate constant for collisional stabilization. All are necessarily calculated at an energy-dependent level, because the evolution of the reaction depends on energy. Crucially, however, the values of k also depend on the angular momentum of methane, J. The J dependence arises because of a centrifugal barrier between the reactants that increases in magnitude as J increases. The master equation must recognize



Energy lost means products gained. As a methyl radical CH_3 and a proton H approach, the potential energy of interaction decreases as the C-H bond is formed. The newly formed, highly excited methane, CH_4^*, will dissociate back to the reactants unless some energy is lost in collisions with a third body, M. In modeling the overall reaction and calculating the pressure- and temperature-dependent rate constant for formation of CH_4 from $CH_3 + H$, Jasper *et al.* determined quantitatively how the energy and the angular momentum of CH_4 are changed in collisions with M.

School of Chemistry, University of Leeds, Leeds LS2 9JT, UK. E-mail: m.j.pilling@leeds.ac.uk

Downloaded from www.sciencemag.org on December 5, 2014

Published by AAAS

the evolution of both the total energy and the angular momentum as collisional stabilization takes place.

As discussed above, the calculation of the energy-dependent rate constants is computer intensive but proven. The theoretical description of collisional energy transfer has been more elusive. Two components are required: the collision frequency and the magnitude of the changes in E and J, ΔE and ΔJ, occurring upon collision. A theoretical framework has been available for some time—it is recognized that large values of ΔE and ΔJ are less likely than small values—but previous approaches have been empirical. Jasper *et al.* calculated the magnitude and probability distributions of ΔE and ΔJ using large numbers of trajectory calculations, in which methane molecules collide with a third body such as He. The results were used in the master equation calculations, and the final values of the temperature- and pressure-dependent rate constants for CH_3 + H were then compared with existing experimental data (*6*) and showed excellent accord. This is a substantial achievement, in that no fitting of the calculations to experiment was used—the calculations were entirely ab initio, and their work provides a means of accurately predicting rate parameters for pressure-dependent reactions.

There is still some way to go before predictions can be routinely made for all pressure-dependent reactions. Some such reactions involve multiple potential energy wells as the initial adduct isomerizes by intramolecular atom transfer. Dissociation from the isomers to several products is often possible, and the rate constants for the different product channels depend in different ways on the total energy and angular momentum. Such reactions are central components of, for example, models to increase the efficiency of automotive engines (*7*). The extension of the methodology described by Jasper *et al.* to such reactions places considerable demands on the quantitative description of the E- and J-dependent energy transfer processes and on the master equation modeling. Although extension to such reactions is challenging, their work shows that it is achievable. ■

REFERENCES

1. A. W. Jasper *et al.*, *Science* **346**, 1212 (2014).
2. T. L. Nguyen, J. F. Stanton, J. R. Barker, *J. Phys. Chem. A* **115**, 5118 (2011).
3. S. J. Klippenstein, L. B. Harding, *J. Phys. Chem. A* **103**, 9388 (1999).
4. S. J. Klippenstein, Y. Georgievskii, L. B. Harding, *Phys. Chem. Chem. Phys.* **8**, 1133 (2006).
5. J. A. Miller, S. J. Klippenstein, *J. Phys. Chem. A* **110**, 10528 (2006).
6. M. Brouard, M. T. Macpherson, M. J. Pilling, *J. Phys. Chem.* **93**, 4047 (1989).
7. J. Zador *et al.*, *Pror. Energy Combust. Sci.* **37**, 371 (2011).

10.1126/science.aaa1257

GEOLOGY

Driving the Earth machine?

The region of the mantle directly below the tectonic plates plays a key role in mantle flow and volcanism

By **Don L. Anderson**[1] *and* **Scott D. King**[2]

The asthenosphere—derived from the Greek asthenēs, meaning weak—is the uppermost part of Earth's mantle, right below the tectonic plates that make up the solid lithosphere. First proposed by Barrell 100 years ago (*1*), the asthenosphere has traditionally been viewed as a passive region that decouples the moving tectonic plates from the mantle and provides magmas to the global spreading ridge system. Recent studies suggest that the asthenosphere may play a more active role as the source of the heat and magma responsible for intraplate volcanoes. Furthermore, it may have a major impact on plate tectonics and the pattern of mantle flow.

Earth is a thermodynamic engine powered by its own finite internal reserves of fossil and radiogenic heat that are gradually brought to the surface and radiated to space. Mantle convection cannot be compared with a coffee percolator or a lava lamp, which are systems heated from below by outside energy sources. As Earth cools, the lithosphere cools and sinks (in the form of cold subducting slabs), displacing warmer material in the deeper mantle, which rises as broad passive updrafts. Recent convection simulations show that the region beneath the lithosphere is hotter than expected, and this has rekindled interest in the asthenosphere's role in Earth's engine.

Although comparatively thin, the asthenosphere has a remarkable impact on the mantle. Numerical simulations without an asthenosphere show a pattern of narrow plumes through which material wells up from the bottom of the mantle. When the simulations include a weak asthenosphere, this pattern changes to just two broad upwellings (*2*). These upwellings are consistent with large low–shear velocity provinces seen at the base of the mantle in global tomography models (see below) (*3*). Although some researchers have called these upwellings superplumes, we feel that this term is confusing, because fluid dynamicists describe plumes as features driven by their intrinsic buoyancy. Convection simulations with an asthenosphere show that these anomalies instead form in response to plates and subducting slabs (*2*, *4*, *5*). Indeed, the asthenosphere may be a necessary component of any self-consistent model of plate tectonics (*6*, *7*).

Caught between the mobile lithospheric plate above and the rest of the mantle below, the asthenosphere is a region of concentrated shear. Shearing and the resulting weak coupling between plates and the mantle have a profound influence on the composition of lavas. Near mid-ocean ridges, lavas tend to have homogeneous compositions, whereas lavas that erupt in the middle of tectonic plates are geochemically heterogeneous. The latter have been attributed to plumes that upwell from the deeper mantle, with the heterogeneity of the lavas thought to reflect heterogeneity in the mantle plume. However, Samuel and King (*8*) have shown that these differences may instead arise from differences in the degree of asthenosphere mixing. This mixing is very efficient near the ridge axis, but far from the ridge, the degree of mixing can drop by orders of magnitude. Geochemically heterogeneous lavas may be derived from these poorly mixed domains in the asthenosphere (*9*), and a plume may be unnecessary.

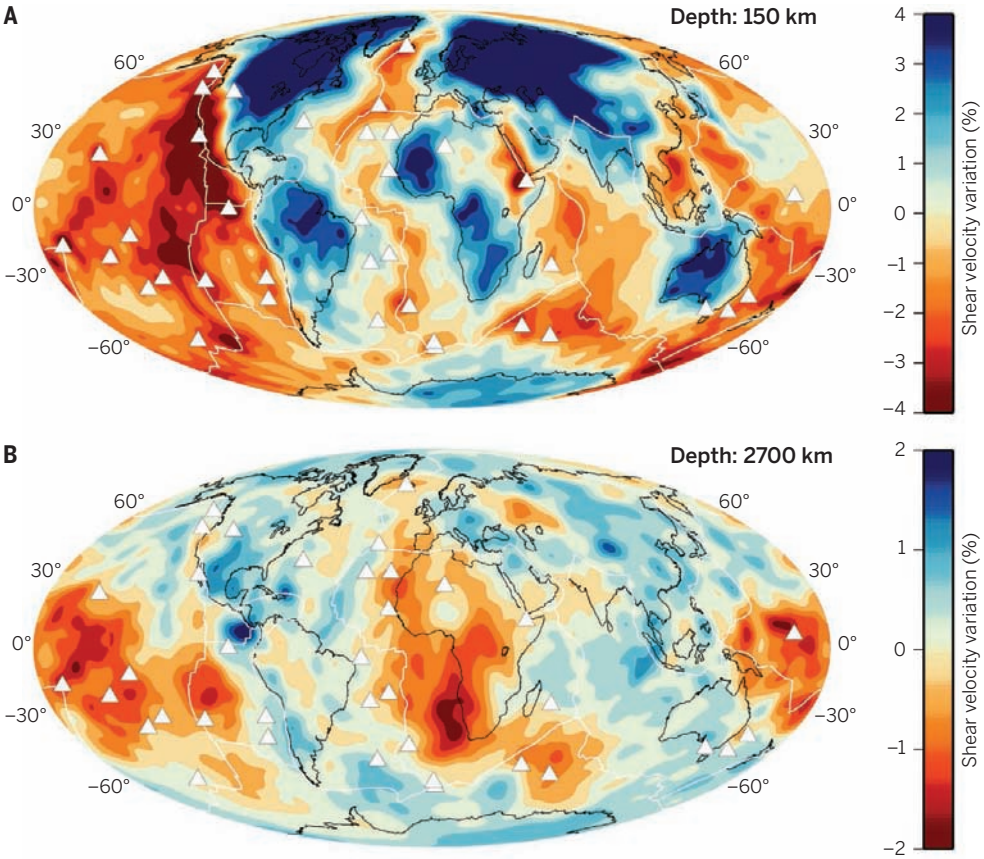
> ***"... the asthenosphere is by far the largest, most accessible, and most plausible source for hot spot magmas."***

Geophysical observations have long indicated the existence of a region of low material strength and low seismic velocities beneath the lithosphere, but the depth range of these properties (which define the asthenosphere) and a physical explanation for the seismic and mechanical properties have proven more elusive. These properties are consistent with the presence of partial melt (*10*). However, some melting experiments did not produce sufficient melt to explain the observations (*11*). In a remarkable series of experiments, Li and Weidner have shown that a solid with pockets of melt oriented by the shearing can produce the kind

[1]*Seismological Laboratory, California Institute of Technology, Pasadena, CA 91125, USA.* [2]*Department of Geosciences, Virginia Polytechnic Institute and State University, Blacksburg, VA 24060, USA. E-mail: sdk@vt.edu*

Downloaded from www.sciencemag.org on December 5, 2014

Published by AAAS



Top or bottom? Seismic anomalies in the asthenosphere (**A**) and at the base of the mantle, just above the core (**B**); the anomalies are relative to a one-dimensional reference model. The correlation between hot spots (triangles) and the edges of the slow (red) anomalies in the lower mantle has been used to argue that hot spots originate from plumes at these depths. However, hot spots correlate as well if not better with slow–wave speed anomalies in the asthenosphere, the region where the lavas originate.

of low–wave speed, low-viscosity anisotropic material that is consistent with the observed properties of the asthenosphere (*12*). Interaction of seismic waves with this material perturbs the material and further reduces the seismic wave speed (*12*). Density measurements of volatile-containing alkali basalts show that these melts are neutrally buoyant at the pressure and temperature conditions of the asthenosphere under continents (*10*), adding to the evidence that the asthenosphere is a zone of partial melt. Because both seismic and mechanical properties are used to describe the asthenosphere, the bottom boundary remains poorly defined.

There is also evidence that the asthenosphere is hotter than the mantle below it (*2*, *4*, *13*). Average temperature profiles from three-dimensional global mantle convection simulations show a local thermal maximum beneath the lithosphere because of the insulating properties of the tectonic plates (*4*, *13*). This increase in temperature can reduce the mechanical strength, lower the seismic wave speed, and eliminate the need to bring heat directly from Earth's core to the asthenosphere to explain volcanic activity at hot spots. The hottest regions in the asthenosphere may be as much as 200 C warmer than beneath mid-ocean ridges (*4*) and even hotter than the core-mantle boundary, when corrected for adiabatic cooling (the cooling that results from transporting material from high to low pressure). This is important because the asthenosphere is at or near its melting point, and a large temperature increase would thus produce a substantial amount of melt. Most researchers have assumed that the hottest material should be below ridges, leading them to invoke plumes to explain 200 C lateral temperature variations. Yet in the mantle, where a substantial fraction of the heat is generated by the decay of radiogenic elements, such lateral variations in temperature can arise without the need to deliver heat from the deep mantle via a plume (*4*).

Further information on mantle temperature comes from absolute seismic wave speeds, which can be coupled with a thermodynamic description of mantle minerals to estimate temperature. This approach confirms that the asthenosphere is anomalously hot, whereas the deep mantle is anomalously cold (*14*). Thus, the highest temperatures in the asthenosphere can be greater than those of the deep mantle, and magmas from beneath ridges can erupt at lower temperatures than magmas extracted from the asthenosphere beneath the middle of large plates.

Whereas Earth's interior has traditionally been viewed as a series of uniform layers, seismic tomography has enabled mapping of complex three-dimensional structures. French *et al.* (*3*) have resolved horizontally elongated, low–wave speed structures at depths of 200 to 350 km extending from the East Pacific Rise to the middle of the Pacific plate; they found similar features beneath other oceans. These low–wave speed structures occur below the average depth of the asthenosphere and represent the interaction of broad, passive upwellings with the base of the asthenosphere. Most hot spots occur above these low–wave speed regions (see the figure, panel A), and the correlation between hot spots and the edges of the low–shear velocity large structures at the core (see the figure, panel B)—a recent observation used to support the existence of deep mantle plumes—is no better than the correlation with the low–wave speed regions beneath the asthenosphere (*15*).

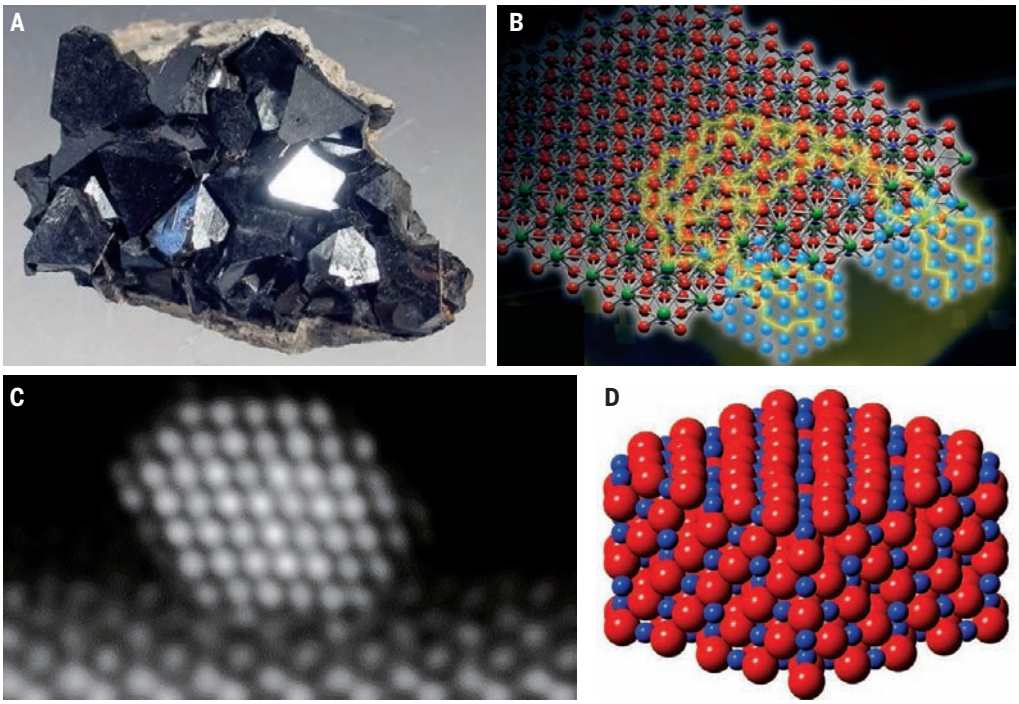
Plate tectonics and midplate volcanoes are the natural results of processes in the asthenosphere and lithosphere of the cooling Earth. Given that the hottest part of the mantle lies directly beneath the lithosphere (*2*, *4*, *13*), there is no need for heat from the core to be carried up in narrow plumes (*4*). As a result, the asthenosphere is by far the largest, most accessible, and most plausible source for hot spot magmas. Although many authors have ruled out this obvious source on the basis of geochemical assumptions, it is not ruled out by any data or theory. ■

REFERENCES

1. J. Barrell, *J. Geol.* **22**, 28 (1914).
2. N. Zhang *et al.*, *J. Geophys. Res.* **115**, B06401 (2010).
3. S. French *et al.*, *Science* **342**, 227 (2013).
4. D. L. Anderson, J. H. Natland, *Proc. Natl. Acad. Sci. U.S.A.* **111**, E4298 (2014).
5. B. H. Hager, R. J. O'Connell, *Tectonophysics* **50**, 111 (1978).
6. T. Hoink *et al.*, *Geophys. J. Int.* **191**, 30 (2012).
7. J. W. Crowley, R. J. O'Connell, *Geophys. J. Int.* **188**, 61 (2012).
8. H. Samuel, S. D. King, *Nat. Geosci.* **7**, 602 (2014).
9. D. L. Anderson, *J. Petrol.* **52**, 1547 (2011).
10. C. Crépisson *et al.*, *Earth Planet. Sci. Lett.* **393**, 105 (2014).
11. R. Dasgupta *et al.*, *Nature* **493**, 211 (2013).
12. L. Li, D. J. Weidner, *Phys. Earth Planet. Inter.* **222**, 1 (2013).
13. W. B. Moore, *J. Geophys. Res.* **113**, B11407 (2008).
14. J. Ritsema *et al.*, *Earth Planet. Sci. Lett.* **277**, 244 (2009).
15. B. R Julian *et al.*, paper to be presented at the American Geophysical Union fall meeting, 15 to 19 December 2014; see https://agu.confex.com/agu/fm14/webprogrampreliminary/Paper20489.html.

10.1126/science.1261831

Published by AAAS



On the surface. From minerals that react with molecules in the environment (**A**), to advanced electronic devices (**B**), to nanoscale heterogeneous catalysts (**C**), metal oxide surfaces with their sometimes unexpected structures (**D**) play a key role.

SURFACE SCIENCE

Stability at the surface

The structure beneath a surface is a key factor in its electronic and chemical function

By **Scott A. Chambers**

Metal oxides are ubiquitous as minerals in the terrestrial environment, as well as in a variety of technologically important structures such as electronic devices and heterogeneous catalysts. Within these various contexts, interfaces between oxides and gases, liquids, and solids drive many critically important phenomena ranging from the uptake of contaminants in groundwater by redox-active minerals to the switching of the millions of transistors found in every cell phone and computer. Function is tied to structure. Therefore, fundamental understanding of the structure of oxide surfaces and interfaces is crucial to the comprehension of a plethora of phenomena involving this broad class of materials (see the figure). On page 1215 of this issue, Bliem *et al.* (*1*) report a remarkable structural insight into the surface of the (001)-oriented crystal face of magnetite (Fe_3O_4), the first magnetic material discovered in antiquity.

Physical Sciences Division, Pacific Northwest National Laboratory, Richland, WA 99352, USA. E-mail: sa.chambers@pnnl.gov

It is most convenient to think of solid surfaces as simple truncations of the bulk crystal structure. However, by combining experimental and theoretical methods, Bliem *et al.* make a convincing case for the absence of Fe atoms at certain lattice sites in the third layer below the surface where they are expected, and the presence of Fe at certain interstitial sites in the second layer below the surface where they are not expected. The chemical composition within the first three atomic planes reported here ($Fe_{11}O_{16}$) is intermediate between that of bulk Fe_2O_3 and Fe_3O_4, and is driven by the oxidative environment in which the surface is prepared.

Bliem *et al.* used highly surface-sensitive electron diffraction and scanning probe microscopy, along with first-principles modeling, to establish the detailed atomic structure within the top ~0.4 nm. What they found was not at all expected based on the simple models of surface structure found throughout the literature. In conventional thinking, the surface is modeled as a termination of the bulk on some atomic plane, with lateral and/or transverse displacements within the top few layers. Such displacements generally have minimal impact on the electronic, magnetic, and chemical properties of the surface. As a result, limiting the descriptions of surfaces (and the interfaces these surfaces form when in contact with other materials) to such simple models has led to predictions of everything from chemical reactivity to electronic properties to magnetization that are often far from reality.

The study by Bliem *et al.* reminds us that nature does not always generate the simple, easily conceptualized structures that we like to envision. Rather, nature does what must be done to achieve equilibrium, which is that minimum-energy configurational space in which materials typically exist and function. In the case of oxides, the implications are far-reaching. For example, the optimized deposition of Cr metal onto semiconducting $SrTiO_3$(001) should lead to an atomically abrupt interface in which the Cr atoms crystallize into the body-centered cubic structure found in bulk Cr, but with a 45 rotation relative to the perovskite lattice of $SrTiO_3$ to minimize the interfacial energy. This electrical junction should be rectifying. However, even though the two lattices line up as expected, the junction is perfectly ohmic, and the contact resistance is as low as any measured for any metal on $SrTiO_3$ (*2*). The reason for this completely unexpected electrical behavior is an unanticipated interface structure in which a fraction of the first atomic layer of Cr atoms diffuses into the $SrTiO_3$, occupies interstitial sites in the lattice, transfers charge to the adjacent Ti ions, and metallizes the interface (*3*). To what extent does this process occur because of Sr metal vacancies present in the subsurface region of the $SrTiO_3$? We do not yet know.

Or consider the observation of conductivity at the interface of two oxide insulators, $SrTiO_3$ and $LaAlO_3$ (*4*), which has been the subject of more than 300 scientific journal articles and conference proceedings over the past decade. The original explanation, which still has many adherents, involves the assumption of an abrupt or nearly abrupt interface of two perfectly stoichiometric oxides. The nonzero charges on alternating layers of $(LaO)^+$ and $(AlO_2)^-$ are thought to generate a diverging electric

Downloaded from www.sciencemag.org on December 5, 2014

Published by AAAS

potential within the $LaAlO_3$, which triggers what is essentially dielectric breakdown and charge transfer to the $SrTiO_3$ at some critical thickness, thereby producing free carriers and conductivity. Yet, the expected potential drop across the $LaAlO_3$ film has not been detected by the most sensitive and direct techniques (*5*–*8*). Moreover, the interface has been shown to be chemically diffuse rather than atomically sharp (*9*, *10*), strikingly so at times (*6*), and certain cation rearrangements can eliminate the diverging potential that is thought to drive charge transfer and conductivity (*6*). To what extent does cation mixing depend on defects in the $SrTiO_3$? Again, we do not yet know. Additionally, recent experiments reveal that defects related to nonstoichiometry in the $LaAlO_3$ themselves play a crucial if not enabling role in activating conductivity, even though a comprehensive mechanistic understanding has not yet been developed (*11*, *12*).

The problem is that accurate detection and characterization of defects are hard work. Point defects, such as vacancies, are often detected indirectly by the structural perturbations they cause to surrounding atoms in the crystal lattice. If the defect structures do not exhibit long-range crystallographic order, as is often the case, their detection, and the theoretical treatment of their effect on structure and functional properties, is more difficult. However, with a combination of definitive experimental characterization and accurate theoretical modeling, like that presented by Bliem *et al.*, defects can be detected, understood, and eventually harnessed for scientific and technological advantage. In the case of metal oxides, defects are an important component of the associated equilibrium structures that are typically present. The sooner we acknowledge that surfaces and interfaces are not necessarily simple terminations and junctions of the bulk material, the sooner we can come to a realistic understanding of these important material structures and engineer metal oxides to the fullest possible extent. ■

REFERENCES

1. R. Bliem *et al.*, *Science* **346**, 1215 (2014).
2. C. Capan, G. Y. Sun, M. E. Bowden, S. A. Chambers, *Appl. Phys. Lett.* **100**, 052106 (2012).
3. S. A. Chambers *et al.*, *Adv. Mater.* **25**, 4001 (2013).
4. A. Ohtomo, H. Y. Hwang, *Nature* **427**, 423 (2004).
5. Y. Segal *et al.*, *Phys. Rev. B* **80**, 241107(R) (2009).
6. S. A. Chambers *et al.*, *Surf. Sci. Rep.* **65**, 317 (2010).
7. M. Takizawa, S. Tsuda, T. Susaki, H. Y. Hwang, A. Fujimori, *Phys. Rev. B* **84**, 245124 (2011).
8. E. Slooten *et al.*, *Phys. Rev. B* **87**, 085128 (2013).
9. P. R. Willmott *et al.*, *Phys. Rev. Lett.* **99**, 155502 (2007).
10. A. S. Kalabukhov *et al.*, *Phys. Rev. Lett.* **103**, 146101 (2009).
11. M. P. Warusawithana *et al.*, *Nat. Commun.* **4**, 2351 (2013).
12. E. Breckenfeld *et al.*, *Phys. Rev. Lett.* **110**, 196804 (2013).

10.1126/science.aaa1543

ILLUSTRATION: V. ALTOUNIAN/*SCIENCE*

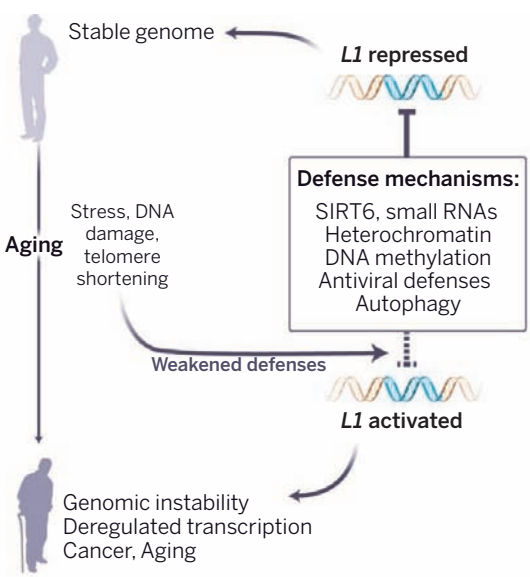
HUMAN GENOMICS

Sleeping dogs of the genome

Retrotransposable elements may be agents of somatic diversity, disease, and aging

By **Vera Gorbunova,[1] Jef D. Boeke,[2] Stephen L. Helfand,[3] John M. Sedivy[3]**

Retrotransposons have a way of staying under the radar. These mobile DNA elements are well-known agents of genome instability and evolution but are mostly thought of as oddities occasionally associated with an interesting phenotype or worse, because of their high copy number, confound the analysis of genome sequences. However, as much as two-thirds or more of the human genome is derived from repetitive sequences (*1*). Most of these are retrotransposon sequences that were active in the distant evolutionary past and are now present as fossils that litter our genomes. But this image belies the damage that can be wreaked by evolutionarily recent transposable elements.



Aging guards invite a jailbreak. With aging, increased stress, DNA damage, and telomere shortening weaken the multiple systems that keep retrotransposons in check. Aged cells lose repressive heterochromatin, SIRT6 relocalizes away from *L1* promoters, and autophagy becomes less efficient. Other defense pathways (see box) may also lose their effectiveness. The consequent unleashing of *L1* elements could lead to profound somatic damage, driving age-associated cell and tissue dysfunction.

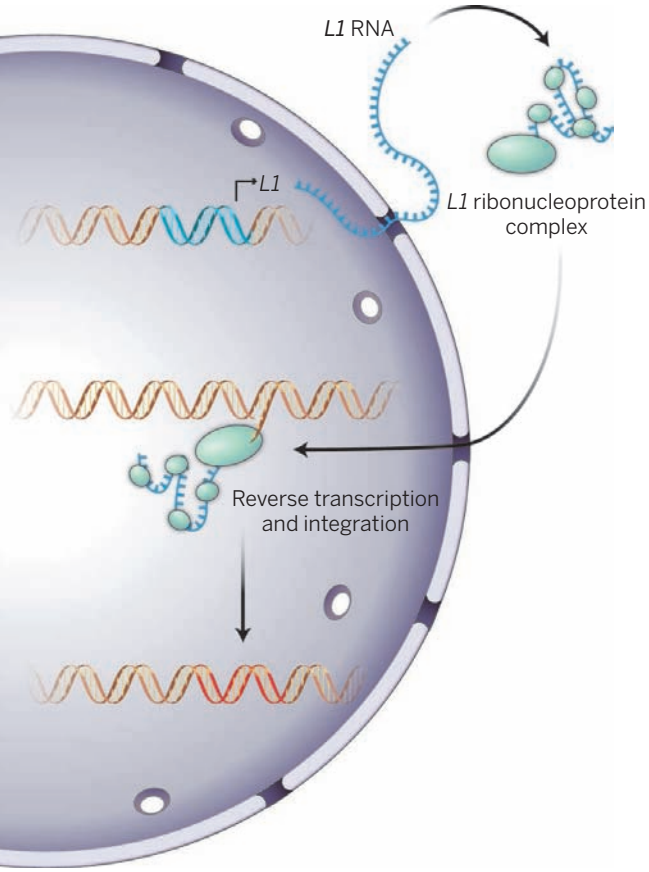
Retrotransposons can be copied into mRNA and then back to DNA that can integrate into the genome. The human genome harbors ~100 copies of an autonomously active retrotransposon called *long interspersed nuclear element–1* (*LINE-1*) *Homo sapiens* (*L1Hs*). The *L1Hs*-encoded proteins, including a reverse transcriptase, are essential for the retrotransposition process and form a ribonucleoprotein particle with the mRNA. A second abundant human retrotransposon, the *Alu* element, depends on *L1Hs* for its movement as it does not encode any proteins, and its transcripts are assembled with *L1Hs*-encoded proteins. Both *L1Hs* and *Alu* ribonucleoprotein particles then enter the nucleus and by a process called target primed reverse transcription, insert new DNA elements at quasi-random sites throughout the genome (see the second figure).

As the "selfish gene" theory predicts (*2*), for a transposable element to succeed in the evolutionary race, the critical battleground is the germ line. There are numerous examples of insertions that affect human health (*3*). Because of this constant threat of genetic mayhem, cells have an impressive armamentarium to combat mobile elements. Where does this battle stand today? On one hand, the human retrotransposon load has been reduced to perhaps as few as 100 active elements; yet, two-thirds of the human genome is scarred by the evidence of millions of years of warfare against mobile DNA elements, and new insertions occur at a frequency of 1 per 95 to 270 live births for *L1Hs*, and 1 in 20 for *Alu* (*3*).

What happens outside the germ line, in somatic tissues? Historically, little attention has been given to this question, because somatic retrotransposition is evolutionarily a dead-end process. However, rampant genomic instability and mutagenesis are deleterious to all cells, and somatic cells mount the same spectrum

[1]*Department of Biology, University of Rochester, Rochester, NY 14627, USA.* [2]*Institute for Systems Genetics, New York University Langone Medical Center, New York, NY 10016, USA.* [3]*Department of Molecular Biology, Cell Biology and Biochemistry, Brown University, Providence, RI 02912, USA. E-mail: john_sedivy@brown.edu*

Published by AAAS



Integration. *L1*-encoded RNA and proteins assemble into ribonucleoprotein particles. Reverse transcription of *L1* RNA is coupled to insertion into DNA at random sites throughout the genome.

of defenses as those of the germ line. These include epigenetic chromatin modification, interfering RNAs, repression systems based on specific DNA-binding proteins (with zinc finger motifs), and autophagy. But these surveillance mechanisms are not foolproof. Derepression of *L1* loci, *L1* transcription, L1 proteins, and de novo *L1* insertions have been detected in a variety of somatic contexts, including early embryos, adult brain, and certain stem cells (*4*). In the context of cancer, new *L1* insertions have been found in a variety of tumor types, including colorectal, prostate, and ovarian tumors (*5*). Intriguingly, the incidence of retrotransposition in tumors appears to increase with age (*6*).

Aging presents an especially complex situation. Retrotransposon surveillance needs to be high in reproductively active individuals. However, because natural selection drops in the postreproductive period of life, host defense mechanisms may begin to fail with age. Could this allow the activation of retrotransposons (see the first figure)? Indeed, derepression of retrotransposons was documented during replicative senescence of human cells (*7*) and aging in yeast (*8*). It was also observed in the fly nervous system (*9*) and several mouse tissues, including liver, muscle, and brain (*10*, *11*). In several contexts, derepression was associated with increased retrotransposon copy number and genome instability. Mutations in flies that derepress retrotransposons exacerbate age-dependent memory impairment and shorten life span (*9*). Calorie restriction delays age-related disorders and extends life span in most species, and also opposes the derepression of retrotransposons in mouse liver and skeletal muscle (*10*). A genetic intervention that increases surveillance by small interfering RNA reduces retrotransposon expression and extends life span in flies (*12*).

What could be the processes that fail and awaken these "sleeping dogs?" One prime candidate is the maintenance of repressive heterochromatin. Repetitive regions lose DNA methylation during aging, and widespread changes in chromatin modifications are increasingly being documented. Recently, a connection between aging, chromatin, and *L1* has been established through *SIRT6* (*11*). *SIRT6* is a prototypical longevity gene—mice without *Sirt6* age prematurely, and mice overexpressing *Sirt6* exhibit life-span extension (*13*). SIRT6 is a protein deacetylase and mono-ADP ribosyltransferase that promotes chromatin silencing and facilitates DNA repair. *SIRT6*-deficient cells show a marked derepression of *L1* transcription. SIRT6 silences *L1* by binding to its promoter and recruiting additional silencing factors. Interestingly, upon DNA damage, SIRT6 leaves *L1* promoters and relocalizes to the sites of DNA breaks. It is likely that a similar process plays out during aging: Chronic DNA damage and short telomeres accumulate, SIRT6 is redeployed, and the dormant retrotransposons are left unguarded.

Beyond generating new insertions, retrotransposons can result in aberrant expression of nearby genes through the promoters and cryptic splice sites that they harbor. Ribonucleoprotein particles that they form in the cytoplasm could trigger immune responses (antiviral defenses) or overwhelm the capacity of homeostatic mechanisms such as autophagy (*14*), and contribute to neurodegeneration or autoimmune disorders. Further, abortive retrotransposition can cause DNA damage and genotoxic stress.

Although aging is perhaps the most basic aspect of life, the mechanisms that explain it remain a puzzle. Retrotransposon activation brings in yet another dimension: We may be bogged down in a complex host–parasite-like struggle (with evolution acting on both parties), leaving open the possibility for profound collateral damage on our soma.

What can be done against this broad attack? Clearly, letting sleeping dogs lie by keeping them mired in heterochromatin is a compelling strategy. For this we need drugs targeted at chromatin regulators that could maintain distinct euchromatin and heterochromatin characteristics of the youthful state. Shoring up other processes that may decrease in effectiveness during aging, like small RNA pathways (*12*) or autophagy, should also help to rein in retrotransposons. In addition, reverse transcriptase inhibitors can prevent the spread of new elements throughout the genome. These drugs have been highly successful in treating HIV/AIDS but have side effects. However, experiments in mice are a feasible way to explore the merit of the overall strategy, and may warrant the development of new drugs highly specific to *L1Hs*.

Many questions remain. For example, the landscape of somatic retrotransposition across our tissues is unclear. It is also uncertain how the mechanisms that oppose retrotransposons change with age. Most importantly, investigating the impact of somatic retrotransposon activation on cellular physiology, disease, and aging should be a high research priority. Could controlling retrotransposons have beneficial therapeutic effects? ■

REFERENCES AND NOTES

1. A. P. de Koning, W. Gu, T. A. Castoe, M. A. Batzer, D. D. Pollock, *PLOS Genet.* **7**, e1002384 (2011).
2. R. Dawkins, *The Selfish Gene* (Oxford Univ. Press, New York, 1976).
3. S. Solyom, H. H. Kazazian Jr., *Genome Med.* **4**, 12 (2012).
4. G. J. Faulkner, *FEBS Lett.* **585**, 1589 (2011).
5. E. Lee *et al.*, *Science* **337**, 967 (2012).
6. S. Solyom *et al.*, *Genome Res.* **22**, 2328 (2012).
7. M. De Cecco *et al.*, *Aging Cell* **12**, 247 (2013).
8. P. H. Maxwell, W. C. Burhans, M. J. Curcio, *Proc. Natl. Acad. Sci. U.S.A.* **108**, 20376 (2011).
9. W. Li *et al.*, *Nat. Neurosci.* **16**, 529 (2013).
10. M. De Cecco *et al.*, *Aging* **5**, 867 (2013).
11. M. Van Meter *et al.*, *Nat. Commun.* **5**, 5011 (2014).
12. Y. A. Savva *et al.*, *Nat. Commun.* **4**, 2745 (2013).
13. S. Kugel, R. Mostoslavsky, *Trends Biochem. Sci.* **39**, 72 (2014).
14. H. Guo *et al.*, *Nat. Commun.* **5**, 5276 (2014).

ACKNOWLEDGMENTS: We gratefully acknowledge the National Institute on Aging program staff (M. Guo, R. Kohansky, F. Sierra) for organizing a workshop in August 2014 where many of these ideas were discussed and consolidated. We acknowledge the following funding sources: National Institutes of Health (NIH) grants R01AG027237 and P01AG047200 (V.G.); NIH grant P50GM107632 (J.D.B.); NIH grants R37AG016667 and R01AG024353 (S.L.H.); NIH grants R37AG016694, P30GM103410, and T32AG041688 and Samsung GRO program grant (J.M.S.); and Ellison Medical Foundation (V.G., S.L.H., J.M.S.), Life Extension Foundation (V.G.), Glenn Foundation for Medical Research (V.G., S.L.H., J.M.S.), and Glenn/American Federation for Aging Research BIG award (S.L.H. and J.M.S.).

10.1126/science.aaa3177

ILLUSTRATION: V. ALTOUNIAN/*SCIENCE*

Published by AAAS

ENVIRONMENTAL ECONOMICS

Using and improving the social cost of carbon

Regular, institutionalized updating and review are essential

By **William Pizer,[1,2]*† Matthew Adler,[1] Joseph Aldy,[2,3] David Anthoff,[4] Maureen Cropper,[2,5] Kenneth Gillingham,[6] Michael Greenstone,[7] Brian Murray,[1] Richard Newell,[1,2] Richard Richels,[8] Arden Rowell,[9] Stephanie Waldhoff,[10] Jonathan Wiener[1,2]**

The social cost of carbon (SCC) is a crucial tool for economic analysis of climate policies. The SCC estimates the dollar value of reduced climate change damages associated with a one-metric-ton reduction in carbon dioxide (CO_2) emissions. Although the conceptual basis, challenges, and merits of the SCC are well established, its use in government cost-benefit analysis (CBA) is relatively new. In light of challenges in constructing the SCC, its newness in government regulation, and the importance of updating, we propose an institutional process for regular SCC review and revision when used in government policy-making and suggest how scientists might contribute to improved SCC estimates.

POLICY

Although regulations issued by U.S. federal agencies have been subject to CBA for four decades, those analyses largely ignored economic benefits of carbon reduction until a federal court held in 2008 that carbon emission reductions have nonzero value. After a brief period during which different U.S. agencies used different SCC numbers, an interagency working group established a single set of government-wide values in 2009 and 2010, with an update in 2013 (*1*).

Such updates arise because the science, impact estimates, and socioeconomic models used to develop the SCC continue to evolve, as do expert opinions about how it should be synthesized. The results for CBA are consequential (see the graph). Using the most recent central value of interagency SCC estimates, a proposed U.S. rule on emissions from existing power plants would pass a CBA on climate benefits alone (*2*); using the central value SCC from a single agency in 2008 (*3*), it would not.

Estimating the SCC in a particular year, say 2015, involves four steps: (i) projecting a future path of global greenhouse gas (GHG) emissions; (ii) translating this emissions path, along with an alternative that adds 1 ton in 2015, into alternate scenarios of climate change; (iii) estimating physical impacts of these climate changes on humans and ecosystems; and (iv) monetizing these impacts and discounting future monetary damages back to 2015. The SCC is the difference in damage valuations with and without the extra ton of CO_2 in 2015.

Integrated assessment models [IAMs; e.g., DICE (*4*), FUND (*5*), and PAGE (*6*)], perform all four steps. Underlying step (i) are assumptions about future climate change policies and their effects on GHG emissions and about population, GDP growth, and technology. In step (ii), a simplified representation of the climate system translates emissions to metrics of climate change (e.g., change in global average temperature). Steps (iii) and (iv) require a damage function that relates climate change metrics to climate impacts and to valuations. Valuation of impacts often aggregates and/or extrapolates detailed climate impact studies and relies on population and economic assumptions from step (i) to project the level of human and economic activity exposed to these impacts in the future.

DIFFICULT CHOICES. Constructing an SCC for government CBA requires specific choices, beginning with the selection of which IAMs to include. Models vary in terms of breadth of use, degree of public access and available peer review, and incorporation of latest scientific results. New IAMs may emerge. How should a government select among models? Should selection evolve over time? Should models be weighted? If so, how?

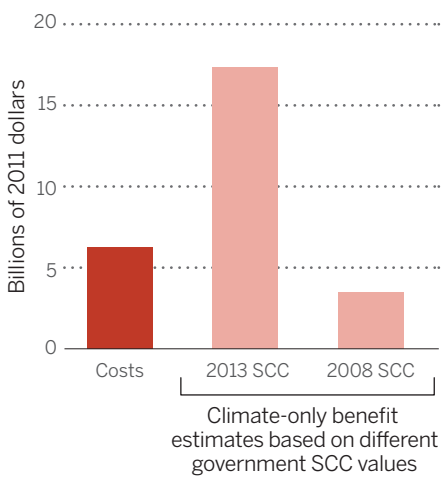
Next, one must choose what, if any, assumptions to harmonize across models. Such assumptions may be important for consistency between the SCC and other elements of a government CBA, to reflect important uncertainties, or to address possibly outdated assumptions.

This harmonization requires more tough choices. For example, the SCC will measure incremental policy benefits relative to a baseline or range of baselines, which must be explicitly selected. One must decide whether emissions are forecast on the basis of an ambitious climate policy (such as the scenario in which polluters are already forced to pay the estimated SCC), a scenario where only policies already on the books remain in place, or something in between.

There are also credible differences on analytic and ethical grounds regarding the appropriate discount rate. Previous government guidance for CBA suggested discount rates of 3 and 7% for most projects, with possibly lower rates for phenomena (like climate change) with important intergenerational effects (*7*). Such differences have enormous implications; federal SCC estimates tripled as the discount rate changes from 5 to 3% (*1*). For practical CBA, it is important to have distinct SCC estimates for different discount rates that can be paired with cost estimates based on a particular discount rate(s).

Each IAM will have its own internal discount rate determined by model parameters and socioeconomic forecasts. Low discount rates typically follow from low economic growth (*8*), and economic growth is tied to climate impacts. Given this connection, how problematic is it to impose a discount rate in the SCC that is different from the rate used within the IAM itself?

Costs and benefits of emissions reductions



Benefits of regulations vary. Estimated costs and climate change benefits of emission reductions in 2020 from proposed U.S. power plant regulations using 2008 (*3*) and 2013 (*2*) government SCC estimates. Estimates from table 18 in (*2*) using a 3% discount rate averaged over state and regional approaches. SCC estimate from table V-3 in (*3*), rising 2.4% per year to $8.67 in 2020, multiplied by avoided emissions estimates averaged over state and regional approaches from table 10 in (*2*), and inflation adjusted using the implicit GDP price index from the U.S. Bureau of Economic Analysis.

Downloaded from www.sciencemag.org on December 5, 2014

Published by AAAS

Should socioeconomic scenarios in the IAM be made consistent with the selected SCC discount rate, or vice-versa?

Finally, one must choose how much weight to give to climate change impacts outside the jurisdiction considering the SCC. In the United States, some have questioned the legality of using global SCC estimates (*9*). Unless a relevant statute clearly requires otherwise, the President and agencies have latitude to choose between domestic and global SCC values for regulatory analysis [including the authority to interpret silent or ambiguous statutes under the Chevron doctrine (*10*)]. Key U.S. statutes (e.g., Clean Air Act and National Environmental Policy Act) refer to global impacts in some sections and do not preclude a Presidential judgment that U.S. interests are best served via a global SCC.

Traditionally, regulatory CBA has used domestic impacts. However, unlike virtually all other regulated pollutants and risks, GHG emissions are overwhelmingly a problem of the global commons. A global SCC, used worldwide to determine policy, would maximize global net benefits. U.S. emissions cause the bulk of their damages beyond U.S. borders, and U.S. damages will largely depend on mitigation choices in other countries where emissions are larger and growing (*11*).

Beyond the moral, ethical, and security issues this raises, there is a strategic foreign relations question. The United States is engaged in international negotiations in which U.S. emission reductions are part of a deal for abatement by other countries. Benefits to each country are determined by the global effort. Even if the U.S. government cares only about domestic impacts, this potential to leverage foreign mitigation supports a domestic SCC estimate augmented by the expected foreign leverage. Our view is that these are compelling reasons to focus on a global SCC but, more important, to make a strategic choice and to conduct periodic review.

A PROCESS TO UPDATE THE SCC. Current U.S. government practice is vague regarding when and how a process of reviewing and updating the SCC might occur, which makes it difficult for stakeholders and researchers to anticipate future reviews and to plan for useful engagement in the process. A regularized and institutionalized process would allow both groups to align their activities more sensibly.

We see four components to an improved institutional process. First, revisions to the SCC should follow a regular schedule. A 5-year cycle would balance the need to respond to evolving research with the need for a thorough process.

Second, SCC revisions should continue to be an interagency process, led by an appropriate group within the Executive Office of the President. This emphasizes the need for consistent values across the whole of government and allows the process to draw on expertise from multiple agencies, as well as reflecting the strategic considerations noted above. The process should include public notice and comment.

"Current U.S. ... practice is vague regarding when and how ... reviewing and updating the SCC might occur."

Third, government SCC estimates should be regularly reviewed by the National Academy of Science's National Research Council (NRC). This would enhance the scientific credibility of the SCC and provide an avenue for experts to suggest changes for the next iteration. Such review could begin with the current estimates.

Finally, the entire process should be institutionalized through an executive order or an Office of Management and Budget (OMB) memorandum or circular. This would communicate the aforementioned components and achieve reasonably stable expectations about future practice. Moreover, a regular procedure with high-quality external review would help reduce any potential politicization of the SCC.

A regularized process for updating the SCC allows researchers to direct efforts toward policy-relevant issues. First, there is research on socioeconomic and emissions scenarios, climate science, and physical impacts, which are necessary inputs to IAMs and SCC estimates. Second, there is translation of physical impacts into human and ecosystem consequences, monetization of those consequences, and synthesis of this information into a consistent modeling framework to estimate the SCC. We believe there are especially appealing opportunities in the second area, which has not been as strongly supported as the physical science research.

Currently, estimates of human and ecosystem consequences of climate change, particularly in less-studied regions and impact categories, come from a small number of studies. Recent work suggests that temperature change may have different—and larger—impacts in poorer countries (*12*). Estimating damage from extreme climate change is a research area with particularly high value (*13*). Increased efforts to synthesize such studies for use in IAMs can facilitate their incorporation into SCC estimates.

SCC estimates could be improved by increasing opportunities for peer review of IAM development. This could be through model intercomparison projects focused specifically on the SCC, special journal issues to compare sector-by-sector impact valuations, and the NRC review process proposed earlier. This will require redirection of research time and funding, adjustments more easily planned in conjunction with a regularized updating schedule.

As the world makes progress in GHG mitigation, governments will need decision-making processes and information tools that reflect important trade-offs. That requires a regularized, transparent, and credible process that ensures that the SCC is reliable, well-supported, and up to date.

[1]Duke University, Durham, NC 27708, USA. [2]Resources for the Future, Washington, DC 20036, USA. [3]Harvard University, Cambridge, MA 02138, USA. [4]University of California Berkeley, Berkeley, CA 94720, USA. [5]University of Maryland, College Park, MD 20742, USA. [6]Yale University, New Haven, CT 06511, USA. [7]University of Chicago, Chicago, IL 60637, USA. [8]Electric Power Research Institute, Washington, DC 20036, USA. [9]University of Illinois, Champaign, IL 61801, USA. [10]Pacific Northwest National Laboratory, Richland, WA 99354, USA. *The views and opinions expressed in this paper are those of the authors alone. †E-mail: william.pizer@duke.edu.

REFERENCES AND NOTES

1. Interagency Working Group on Social Cost of Carbon, Technical support document: Social cost of carbon for regulatory impact analysis under Executive Order 12866 (White House, Washington, DC, 2013); http://1.usa.gov/18ftAsH.
2. Environmental Protection Agency, *Fed. Regist.* **79**(117), 34830 (2014).
3. National Highway Traffic and Safety Administration, *Fed. Regist.* **73**(86), 24352 (2008).
4. W. D. Nordhaus, *Proc. Natl. Acad. Sci. U.S.A.* **107**, 11721 (2010).
5. D. Anthoff, R. S. J. Tol, *Clim. Change* **117**, 515 (2013).
6. C. Hope, *Clim. Change* **117**, 531 (2013).
7. U.S. Office of Management and Budget, Circular A-4: Regulatory analysis (White House, Washington, DC, 2003); http://1.usa.gov/1yjoaVE.
8. K. Arrow *et al.*, *Science* **341**, 349 (2013).
9. T. Gayer, W. K. Viscusi, *Determining the Proper Scope of Climate Change Benefits* (Brookings Institution, Washington, DC, 2014): http://brook.gs/1HfJGRi.
10. Chevron *v.* Natural Resources Defense Council, 467 U.S. 837 (1984).
11. G. Blanford, J. Merrick, R. Richels, S. Rose, *Clim. Change* **123**, 527 (2014).
12. M. Dell, B. F. Jones, B. A. Olken, *Am. Econ. J. Macroecon* **4**, 66 (2012).10.1257/mac.4.3.66
13. S. C. Newbold, A. L. Marten, *J. Environ. Econ. Manage.* **68**, 111 (2014).

ACKNOWLEDGMENTS

The authors acknowledge Duke's Nicholas Institute for Environmental Policy Solutions and the Center for Law, Economics, and Public Policy for sponsoring the workshop where these ideas were developed and the Global Technology Strategy Program for supporting S.W. We appreciate many useful intellectual contributions from the workshop audience.

10.1126/science.1259774

Published by AAAS

ESSAY

SCIENCE & SCILIFELAB PRIZE ESSAY

Size does matter

Lysosome-based signaling machine regulates cell growth

By **Liron Bar-Peled**

From *Nanoarchaeum equitans*, a microbe barely measuring 400 nm across, to *Balaenoptera musculus*, the blue whale that often exceeds 30 m in length, one of the most distinguishing characteristics of an organism is its size. Animal size is determined by total cell number, which is achieved through cell proliferation. Proliferation in turn depends on cell growth, a process regulated by both genetic and environmental factors.

When nutrients are plentiful, cells engage key programs to increase their size and mass, whereas a dearth of nutrients triggers opposing programs that release much-needed cellular building blocks to maintain homeostasis. To couple nutrient availability to cell size regulation, eukaryotic organisms rely on signaling pathways that concomitantly sense environmental nutrient availability and control downstream processes required for growth.

In the past 20 years, the mechanistic target of the mechanistic target of rapamycin (mTOR) complex 1 (mTORC1) has emerged as the central signaling pathway that regulates cellular, organ, and organismal size (*1*). mTORC1 has major roles in controlling food intake, insulin sensitivity, and life span and, when deregulated, is implicated in the pathogenesis of common cancers and diabetes. mTORC1 responds to a wide variety of stimuli, including growth factors, oxygen availability, energy, and amino acid levels to control anabolic and catabolic processes (*2*). Although amino acids are absolutely essential for mTORC1 activation, surprisingly little is known about how they are sensed and activate mTORC1.

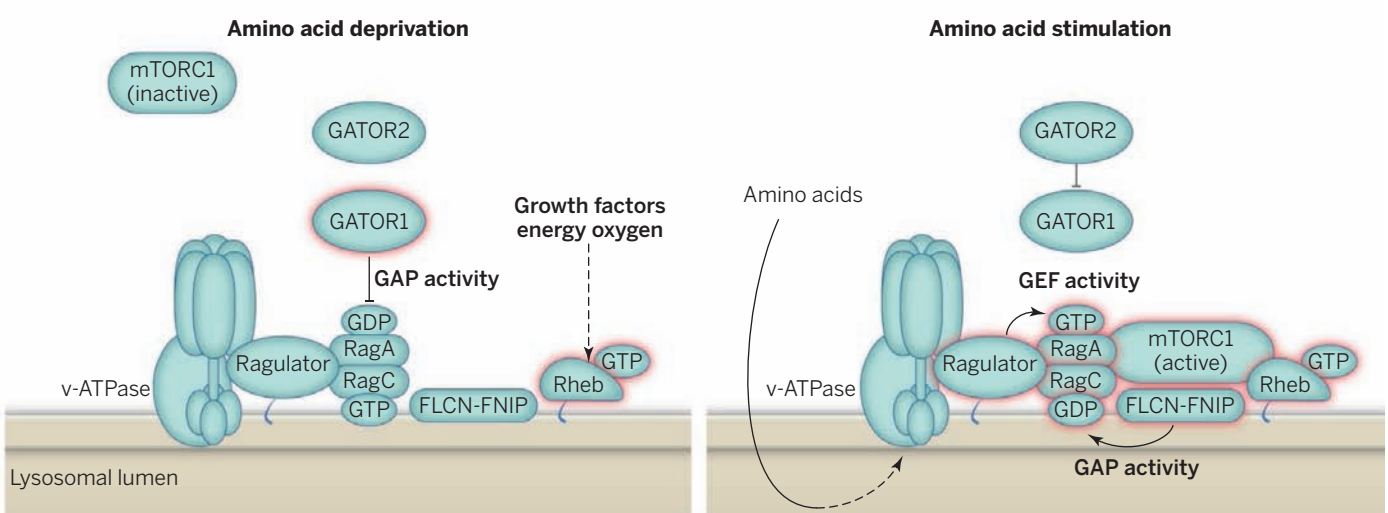


As a first-year graduate student in David Sabatini's laboratory at MIT, I contributed to finding the first pieces of the amino acid–sensing pathway. Amino acids promote mTORC1 translocation to the lysosomal surface, where it becomes activated. This translocation is mediated by Rags, a family of small guanosine triphosphatases (GTPases) (*3*, *4*) that are localized to the lysosomal surface by a mechanism that had not been elucidated. Unique among small GTPases, Rags are obligate heterodimers: the highly related RagA and RagB (RagA/B) bind to RagC or RagD (RagC/D), which are also very similar to each other. Amino acids regulate the binding of nucleotides to RagA/B, such that amino acid stimulation increases their guanosine triphosphate (GTP) loading, which leads to the recruitment and binding of mTORC1. Thus, a critical event in the amino acid–dependent regulation of mTORC1 is the conversion of RagA/B from a guanosine diphosphate (GDP)– to a GTP-bound state (*3*–*6*). My graduate thesis focused on identifying the protein factors that positively or negatively regulate the function of Rags by controlling their nucleotide state as well as their lysosomal localization.

I hypothesized that proteins that regulate Rags would do so through a direct interaction. By purifying Rags under several conditions, we identified five proteins that form a novel complex, which we named "Ragulator" (*5*, *6*). There is a mutation in humans that partially reduces the expression of one of the Ragulator components, and patients carrying this mutation are substantially smaller in size than their peers, a characteristic of mTORC1 pathway inhibition in model organisms (*1*, *2*, *7*).

Ragulator localizes to the lysosomal surface and specifically interacts with Rags. Through loss-of-function and mislocalization studies, we determined that Ragulator is both necessary and sufficient for Rag localization, and, as expected, mTORC1 could no longer localize to lysosomes and remains inactive in cells depleted of Ragulator proteins. Furthermore, the Rag-Ragulator interaction

The Scripps Research Institute, La Jolla, CA 92122, USA.
E-mail: lironbp@scripps.edu



The pathway of amino acid sensing by mTORC1. (**Left**) During amino acid deprivation, Ragulator is found as an inactive complex with the v-ATPase. GATOR1 GAP activity toward RagA keeps this GTPase in an inactive GDP-bound state that cannot recruit mTORC1. (**Right**) After amino acid stimulation, GATOR1 is inhibited by GATOR2, and Ragulator and the v-ATPase undergo a conformational change releasing the guanine nucleotide exchange factor (GEF) activity of Ragulator toward RagA. At the same time, the FLCN-FNIP complex activates RagC, by promoting its GTP hydrolysis. The now-active Rag heterodimer (RagA-GTP, RagC-GDP) recruits mTORC1 to the lysosomal surface, where it interacts with and is activated by the small GTPase Rheb, which is itself controlled by growth factor, energy, and oxygen levels (*1*).

Published by AAAS

Downloaded from www.sciencemag.org on December 5, 2014

is regulated by amino acids, which suggests that Ragulator might also control the nucleotide loading of the Rag GTPases (*6*). Rags pose a particular experimental challenge for identifying factors that regulate the nucleotide state of a single Rag, as they exist as obligate heterodimers, and so we developed several methods that allowed us to analyze the nucleotide binding state of one Rag at a time. This led to the discovery that Ragulator is a guanine nucleotide exchange factor for RagA/B that promotes GTP binding and activation (*6*). Although this exchange activity of Ragulator provides a mechanism by which amino acids activate the Rag GTPases, how amino acid deprivation inactivated Rags remained a mystery.

Negative regulators of small GTPases have short-lived interactions with their cognate GTPases (*8*). Thus, to identify negative regulators of Rags, we purified them in the presence of a chemical cross-linker that preserves transiently interacting proteins. This led to the identification of a complex of eight Rag-interacting proteins that we refer to as "GATOR" [GTPase-activating protein (GAP) activity toward Rags]. GATOR is defined by two distinct subcomplexes: GATOR1 and GATOR2. GATOR1 negatively regulates mTORC1, and its loss increases cell size, whereas GATOR2 positively regulates this pathway by inhibiting GATOR1. Subsequently, we discovered that GATOR1 directly interacts with the Rag GTPases and inhibits their function through its GAP activity for RagA/B, by stimulating GTP hydrolysis (*9*).

Upstream negative regulators of mTORC1 are commonly mutated in cancer and, indeed, inactivating mutations in GATOR1 genes are found in in a subset of glioblastoma and ovarian tumors. Moreover, the mTORC1 pathway is insensitive to amino acid starvation in cancer cell lines missing GATOR1 components and hypersensitive to treatment with a U.S. Food and Drug Administration–approved mTORC1 inhibitor, rapamycin (*9*). Thus, GATOR1 proteins may serve as useful biomarkers to help identify patients likely to respond to clinically approved pharmacological inhibitors of mTORC1. In addition to its role in cancer, the GATOR complex has also been implicated in epilepsy (*10*). Two recent studies uncovered that mutation of a GATOR1 component underlies familial focal epilepsy with multiple foci (*11*, *12*) and provides a molecular etiology for this disease.

After the identification of Ragulator and GATOR1 as the first positive and negative regulators of the Rag GTPases, respectively, additional studies highlighted the complexity of this signal transduction network with the identification of new members needed to integrate the amino acid signal with size regulation. These components include the lysosomal vacuolar adenosine triphosphatase (v-ATPase), which mediates the amino acid signal to Ragulator and is required for amino acid–dependent mTORC1 activation (*13*), as well as the folliculin–folliculin-interacting protein (FLCN-FNIP) tumor suppressor complex, which is responsible for activating RagC/D (*14*). These studies reveal the presence of a lysosome-based signaling machine that is required to sense nutrient availability for the spatiotemporal regulation of mTORC1 (see the figure), offering us a window into how the size of a cell is influenced by its environment. ■

2014 Grand Prize Winner



Cell and Developmental Biology: Liron Bar-Peled for his essay "Size does matter." Dr. Bar-Peled received his Bachelor of Science degree from the University of Georgia and his Ph.D. from the Massachusetts Institute of Technology, where he studied amino acid sensing in David Sabatini's lab. He received the 2014 Weintraub Award for Graduate Research, the 2013 Gary Bokoch memorial award from the American Society for Biochemistry and Molecular Biology, and the 2012 Abraham J. Siegel Fellowship Award from the Whitehead Institute for Biomedical Research. He is investigating how cells respond to oxidative stress in the laboratory of Benjamin Cravatt at the Scripps Research Institute in La Jolla. He is a Lallage Feazel Wall Fellow of the Damon Runyon Cancer Research Foundation.

Category Winners



Genomics and Proteomics: Dan Dominissini for his essay, "Roadmap to the epitranscriptome." Dr. Dominissini received his Bachelor of Medical Science degree from Tel-Aviv University, Israel, in 2007. He went on to study RNA posttranscriptional modifications for his Ph.D., focusing on adenosine deamination and methylation, with Gideon Rechavi at Tel-Aviv University. He is currently a Human Frontier Science Program postdoctoral fellow in the laboratory of Chuan He at the University of Chicago, where he develops novel chemistries for the study of nucleic acid modifications.



Translational Medicine: Simon C. Johnson for his essay, "A target for pharmacological intervention in an untreatable human disease." Dr. Johnson is an American Federation for Aging Research Fellow at the Albert Einstein College of Medicine in New York. He earned his Bachelor of Science degree at Oregon State University and received his Ph.D. from the University of Washington. He was a 2009 Howard Hughes Medical Institute EXROP scholar and was previously supported by the Nathan Shock Center Genetic Approaches to Aging predoctoral and Mechanisms of Cardiovascular Diseases postdoctoral competitive training grants. His work is centered on characterizing the role of genetic variation in insulin/IGF-1/mTOR signaling genes on human longevity.



Environment: Chelsea Wood for the essay, "Environmental change and the ecology of infectious disease." Dr. Wood received her Bachelor of Arts degree from Dartmouth College and her Ph.D. from Stanford University. She did postdoctoral research in Pieter Johnson's lab at the University of Colorado at Boulder, and is currently a Fellow in the Michigan Society of Fellows and an Assistant Professor in the Department of Ecology and Evolutionary Biology at the University of Michigan. She is interested in how parasites and pathogens respond to human impacts on the environment.

For the full text of all winning essays and further information, see http://scim.ag/SciLifeLab.

REFERENCES AND NOTES

1. L. Bar-Peled, D. M. Sabatini, *Trends Cell Biol.* **24**, 400 (2014).
2. M. Laplante, D. M. Sabatini, *Cell* **149**, 274 (2012).
3. Y. Sancak *et al.*, *Science* **320**, 1496 (2008).
4. E. Kim *et al.*, *Nat. Cell Biol.* **10**, 935 (2008).
5. Y. Sancak *et al.*, *Cell* **141**, 290 (2010).
6. L. Bar-Peled *et al.*, *Cell* **150**, 1196 (2012).
7. G. Bohn *et al.*, *Nat. Med.* **13**, 38 (2007).
8. J. L. Bos *et al.*, *Cell* **129**, 865 (2007).
9. L. Bar-Peled *et al.*, *Science* **340**, 1100 (2013).
10. R. J. Shaw, *Science* **340**, 1056 (2013).
11. L. M. Dibbens *et al.*, *Nat. Genet.* **45**, 546 (2013).
12. S. Ishida *et al.*, *Nat. Genet.* **45**, 552 (2013).
13. R. Zoncu *et al.*, *Science* **334**, 678 (2011).
14. Z. Y. Tsun *et al.*, *Mol. Cell* **52**, 495 (2013).

ACKNOWLEDGMENTS

I am grateful to my Ph.D. adviser D. M. Sabatini for his mentorship. I would also like to thank all the members of the Sabatini lab past and present and especially L. Chantranupong, Y. Sancak, L. Schweitzer, and R. Zoncu.

10.1126/science.aaa1808

PHOTO CREDITS: (TOP) SCRIPPS RESEARCH INSTITUTE; (SECOND AND LAST) PERSONAL PHOTOS; (THIRD) CITY HEADSHOTS

Published by AAAS

Conserving Brazil's Atlantic forests

IN THEIR REPORT "Using ecological thresholds to evaluate the costs and benefits of set-asides in a biodiversity hotspot" (29 August, p. 1041), C. Banks-Leite *et al.* calculate that Brazil could protect the most biodiverse 30% of its 143 million hectares of endangered Atlantic forests by reallocating 6.5% of its agricultural subsidies to pay landowners to set aside land for restoration. Reallocations are unlikely, however, because agrosubsidies serve different political constituencies than conservation incentives (*1*). Meanwhile, a successful and much cheaper stepwise program could be expanded.

The region is subdivided into small, scarcely viable, private farm holdings, which are partially forested and partially cleared. For rural properties in this biome, the current Brazilian Forest Code (*2*) requires 20% of the land to be set aside as protected Legal Reserves (Reservas Legais). These are managed for sustainable use, which includes selective logging. A voluntary land covenant program (*3*, *4*) allows an owner to establish a Private Natural Heritage Reserve (Reserva Particular do Patrimônio Natural) at the federal, state, or municipal level. Private Natural Heritage Reserves must be managed only for conservation, ecotourism, or education. Because the land is already required to be set aside as a Legal Reserve, opportunity costs for establishing the more conservation-friendly Private Natural Heritage Reserves are minimal. However, landholders are deterred by application and establishment costs. The state government pays conservation incentives to municipalities but not to landholders (*5*). A few Private Natural Heritage Reserve landholders meet costs through ecotourism, but as yet, only 4% nationally (*6*).

A partnership of local and international nongovernmental organizations (*7*, *8*) has provided strategic small grants known as editais to cover application and management costs for Private Natural Heritage Reserves. For one-third of Private Natural Heritage Reserves nationally, editais were critical in lifting landholders over this final hurdle for forest conservation. To date, this includes 57,000 ha in the Atlantic Forest biome, where the cost of this stepwise approach (*7*) is only 1 to 5% of the cost of outright land purchase. Expanding this approach may provide the best practical short-term prospect to conserve remaining biodiversity in Brazil's Atlantic forests.

Ralf Buckley* and Fernanda de Vasconcellos Pegas

Griffith University, Gold Coast, QLD 4222, Australia.

*Corresponding author. E-mail: r.buckley@griffith.edu.au

REFERENCES

1. D. Kleijn, W. J. Sutherland, *J. Appl. Ecol.* **40**, 947 (2003).
2. Government of Brazil, Código Florestal, Lei 12.651 (2012); www.planalto.gov.br/ccivil_03/_ato2011-2014/2012/lei/l12651.htm.
3. Government of Brazil, Lei 9.985 (2000); www.planalto.gov.br/ccivil_03/leis/l9985.htm.
4. ICMBio (www.icmbio.gov.br).
5. ICMS Ecológico, Repasses (www.icmsecologico.org.br).
6. F. Pegas, G. Castley, *J. Sust. Tour.* **24**, 604 (2014).
7. SOS Mata Atlântica (www.sosma.org.br).
8. Associação Mico Leão Dourado (www.micoleao.org.br).



Private Natural Heritage Reserve in Rio Grande do Sul, Brazil.

PHOTO: GUARAWOLF/WIKIMEDIA COMMONS

Response

BUCKLEY AND PEGAS claim that it would be politically difficult to reallocate agricultural subsidies to conservation. In our Report, we compare the economic costs of a strategy in which land is set aside for restoration to what is currently spent on agricultural subsidies. We do not suggest that agricultural subsidies be reallocated to conservation, but we also do not believe that such a strategy is improbable, as this has already been implemented in the United States (*1*, *2*) and is currently being discussed in Europe (*3*).

Buckley and Pegas then suggest that creating more Private Natural Heritage Reserves would be a more cost-effective strategy to protect the biodiverse regions of the Atlantic Forest. However, as we explained in our Report, preserving the Atlantic Forest is not enough; this biome needs to be restored to fully protect biodiversity. Private Natural Heritage Reserves are essentially a mechanism to preserve existing areas of pristine habitat inside private property and are only rarely used to set aside land to reforestation. The reserves are often managed to attract ecotourism, but it is unclear how degraded land undergoing restoration would serve such a purpose.

Private Natural Heritage Reserves would protect additional, pristine land, but the most biodiverse regions of the Atlantic Forest are already protected. One of our main conclusions is that 30% is the minimum amount of habitat needed to preserve biodiversity, and that restoration should be focused on landscapes that currently have between 20 and 30% forest cover. To this end, the protection of remaining Atlantic forest areas through private or public reserves has to be complemented with incentives for forest restoration.

Cristina Banks-Leite,[1,2]* Renata Pardini,[3] Leandro R. Tambosi,[2] William D. Pearse,[4] Adriana A. Bueno,[5] Roberta T. Bruscagin,[2] Thais H. Condez,[6] Marianna Dixo,[2] Alexandre T. Igari,[7] Alexandre C. Martensen,[8] Jean Paul Metzger[2]

[1]Grand Challenges in the Ecosystem and Environment, Department of Life Sciences, Imperial College London, Silwood Park Campus, Ascot SL5 7PY, UK. [2]Departamento de Ecologia, Instituto de Biociências, Universidade de São Paulo, 05508–090, São Paulo SP, Brazil. [3]Departamento de Zoologia, Instituto de Biociências, Universidade de São Paulo, 05508–090, São Paulo SP, Brazil. [4]Department of Ecology, Evolution, and Behavior, University of Minnesota, St. Paul, MN 55108, USA. [5]Fundação Florestal, 02377–000, São Paulo SP, Brazil. [6]Departamento de Zoologia, Instituto de Biociências, Universidade Estadual Paulista, 13506–900, Rio Claro SP, Brazil. [7]Curso de Gestão Ambiental, Escola de Artes, Ciências e Humanidades, Universidade de São Paulo, 03828–000, São Paulo SP, Brazil. [8]Department of Ecology and Evolutionary Biology, University of Toronto, Toronto, ON M5S 3B2, Canada.

*Corresponding author. E-mail: c.banks@imperial.ac.uk

REFERENCES

1. S. S. Batie, A. G. Sappington, *Am. J. Agricult. Econ.* **68**, 880 (1986).
2. R. A. Kramer, S. S. Batie, *Agricult. Hist.* **59**, 307 (1985).
3. H. van Zeijts *et al.*, *Greening the Common Agricultural Policy: Impacts on Farmland Biodiversity on an EU Scale* (PBL Netherlands Environmental Assessment Agency, 2011).

ERRATA

Erratum for the Report: "Washing away your sins: Threatened morality and physical cleansing" by C.-B. Zhong and K. Liljenquist, *Science* **346**, aaa2510 (2014). Published online 21 November 2014; 10.1126/science.aaa2510

Downloaded from www.sciencemag.org on December 5, 2014

Published by AAAS

ONLINE BUZZ: HIGHER EDUCATION

China's balancing act

In his Editorial "China's private universities" (24 October, p. 401), H. Jin expresses hope that the Chinese government will soon treat public and private universities equally, giving private institutions the funding and opportunities they need to flourish. Readers analyzed the trade-offs involved in such a decision in the online comments section. Excerpts from their comments are below. Read the full comments, and add your own, at http://comments.sciencemag.org/content/10.1126/science.1262035.

A selection of your thoughts:

…[I]f you…receive any funds from government, then it is impossible to get [around] its constraints. [W]hy are there no investors interested in the private universities? What's more, nearly all the talented students in China are enrolled in the best public universities…. Thus, it seems unwise to distribute the education funds to the private universities rather than the public ones for the government, as the money is always insufficient. ***Tong Ruif***

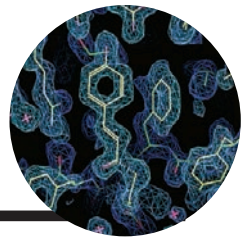
…From the private university's perspective…, it's hardly possible to get any funding from the government, which results in extremely high tuition…; from China's common families' perspective, the bad environment of study is [not worth the] expense, [so] the public school will be the priority; from the government's perspective, lots of private universities are supported or funded by commercial companies or groups (e.g., [Jin] is the president of Sanlian Group), and how to…manage such connections [and potential resulting conflicts of interest] remains to be considered. ***Eniac Gui***

…While students and faculty are both eager to embrace an U.S. private university model, in which philanthropists often seed the initial development, such a high-profile, high-impact private university hasn't flourished…. I believe the private universities need to rely on innovative educational models and show their national stature in attracting bright faculty and students first. Without doing so, [moving] money from any public sources to private [institutions] would be hard to justify for Chinese taxpayers. ***Jake Chen***

RESEARCH

X-ray free electron lasers reveal protein dynamics

Tenboer et al., *p. 1242*



IN *SCIENCE* JOURNALS

Edited by **Stella Hurtley**

OCEANOGRAPHY

Bringing up the problem of ice shelf melting

Warm water intruding from below is heating up the ocean that covers the continental shelf of Antarctica. Schmidtko *et al*. report that Circumpolar Deep Water has been warming and moving further up onto the shelf around Antarctica for the past 40 years, causing higher rates of ice sheet melting (see the Perspective by Gille). These observations need to be taken into account when considering the potential for irreversible retreat of parts of the West Antarctic Ice Sheet. — HJS

Science, this issue p. 1227; see also p. 1180



Ice shelf melting in the Antarctic

ANIMAL PHYSIOLOGY

Eels shock their prey into risky behavior

Electric eels can deliver a shock powerful enough to immobilize a horse, but their true targets are smaller fish and invertebrate prey. Now, Catania suggests that electric eels "remotely control" their prey's movements. The electrical discharge causes whole-body contraction and twitch in the prey by affecting motor neurons rather than muscles directly. This first stimulates prey to move and reveal itself and then to freeze, allowing its capture. — SNV

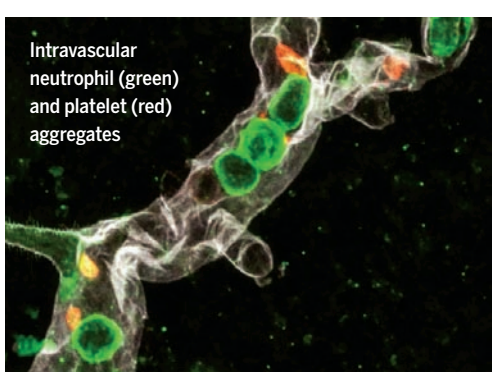
Science, this issue p. 1231

INFLAMMATION

A two-cell collaboration for inflammation

Immune cells called neutrophils are first responders to infection. Neutrophils move within and through blood vessels to get to sites of infection quickly. Sreeramkumar *et al*. found that mouse neutrophils rely on platelets to help find such sites. Neutrophils extended protrusions into blood vessels. When these protrusions came into contact with platelets, the neutrophils migrated into the surrounding tissue to carry out their inflammatory functions. Preventing these neutrophil-platelet interactions alleviated collateral inflammatory damage to tissues in several injury models in mice. — KLM

Science, this issue p. 1234



Intravascular neutrophil (green) and platelet (red) aggregates

CHEMICAL KINETICS

Theoretical chemistry can withstand the pressure

Theoretical methods can predict the chemical consequences of a discrete molecular collision in exquisite detail. However, practical chemistry, whether in a flame, in Earth's atmosphere, or in an industrial reactor, involves billions of trillions of such collisions. Predicting the aggregate reaction rate requires an accurate means of treating the pressure dependence. Jasper *et al*. present such a method, which shows strong agreement with experimental measurements (see the Perspective by Pilling). Unlike past approaches that require parameters derived from empirical fits to data, the new technique relies strictly on simulations. — JSY

Science, this issue p. 1212; see also p. 1183

HERPES SIMPLEX VIRUS

Epigenetic control during herpes virus infection

Epigenetic modifications are a sort of genetic metadata—they alter gene expression without changing the underlying DNA. Hill *et al*. hypothesized that epigenetic modification could be exploited for treating herpes virus infection. Herpes virus infection and reactivation from latency depends on the histone demethylases LSD1 and JMJD2, which are responsible for making epigenetic marks on chromosomes. Epigenetic modifications inhibited viral infection in animal models that represent three different stages of herpes simplex virus infection: suppression of primary infection, a block

Downloaded from www.sciencemag.org on December 5, 2014

PHOTOS: (TOP TO BOTTOM) TENBOER *ET AL.*; © WORLD TRAVEL COLLECTION/ALAMY; SREERAMKUMAR *ET AL.*

Published by AAAS

to subclinical shedding, and reduction in recurrent lesions. — ACC

Sci. Transl. Med. **6**, 265ra169 (2014).

HUMAN CAPITAL

An ounce of prevention is better than violence

Children and adolescents spend a large fraction of their lives in schools. Many discussions about improving adult behavior focus on improving cognitive skills. Nevertheless, retrospective analyses also highlight the importance of noncognitive skills. Heller reports on the positive effects of a Chicago program that offered disadvantaged youths 25 hours per week of summer employment. Youths enrolled in this program committed fewer violent crimes for at least a year after the summer job ended. — GJC

Science, this issue p. 1219

VALLEYTRONICS

Using light to manipulate atomic valleys

The electronic structure of atomic layers of transition-metal dichalcogenides, such as WSe_2, has two distinct valleys with equal energies. Knowing which valley an electron comes from can make it a carrier of information. Kim *et al.* used optical methods to distinguish between the valleys. They shone circularly polarized light on a sample of WSe_2, which caused the energy needed to create an exciton—a bound state of an electron and a hole—to shift in one valley but not the other. The method may enable the manipulation of the valley degree of freedom for use in quantum information processing. — JS

Science, this issue p. 1205

TRANSCRIPTION

Unpacking for travel to the nuclear interior

The position of a gene within the cell nucleus is correlated with its activity. Those near the nuclear periphery are generally repressed, whereas those in the center are (or will be) active. It is not clear whether this relocalization is a cause or a consequence of gene regulation. Therizols *et al*. found that transcriptional activation or simply chromatin decondensation both drove the relocation of genes to the interior of the nucleus. The nuclear position was maintained in daughter cells, suggesting that the cell has an epigenetic memory of the gene's position within the nucleus. — GR

Science, this issue p. 1238

PLANT GENETICS

Dominance cascades in self-incompatibility

Plants often cannot use their own pollen to set seed. This is known as self-incompatibility. Although some of the underlying genetics and mechanisms of self-incompatibility are understood, the evolution and maintenance of the system have remained mysterious. Durand *et al.* identified a collection of small RNAs and their respective matching targets within a self-incompatibility locus in *Arabidopsis halleri*. A subset of these alleles functioned in a dominant manner, which helps to explain how self-incompatibility is maintained. — LMZ

Science, this issue p. 1200

BIOCHEMISTRY

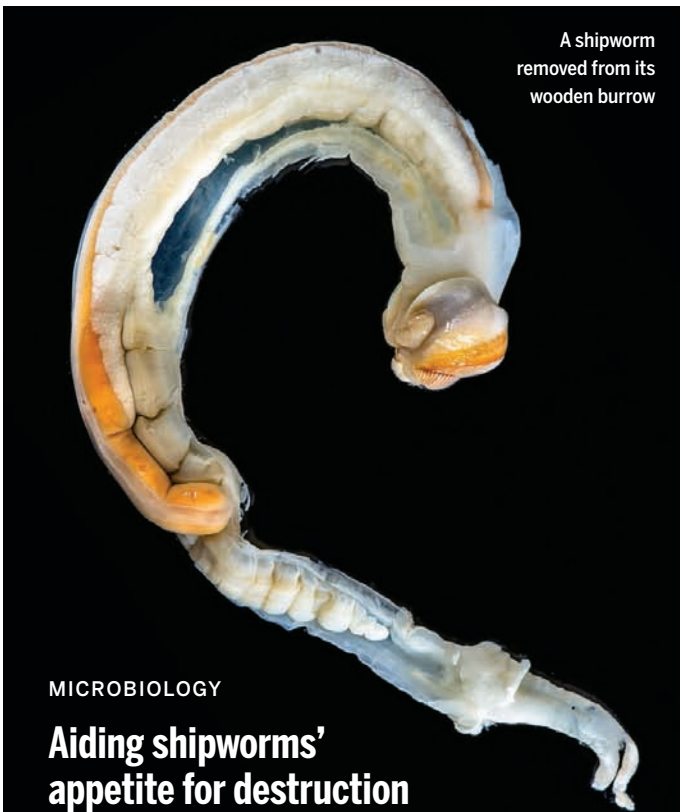
Cancer by activating a binding partner

Some cancers are associated with mutations that increase the activity of members of the EGFR family of tyrosine receptor kinases, such as HER1. Although HER3 has little kinase activity, it can contain cancer-associated mutations. HER3 binds to other EGFR family members that do have kinase activity. Littlefield *et al.* crystallized the kinase domain of HER1 bound to the kinase domain of normal HER3 or HER3 with cancer-associated mutations. Cancer-associated mutations in HER3 increased its binding to and allosteric activation of HER1. — NRG

Sci. Signal. **7**, ra114 (2014)

IN OTHER JOURNALS

Edited by **Kristen Mueller** *and* **Jesse Smith**



A shipworm removed from its wooden burrow

MICROBIOLOGY

Aiding shipworms' appetite for destruction

Shipworms are in fact mollusks that consume wood. They can cause devastation to wooden ships but they also clean up wreckage. Mollusks cannot eat wood unaided (the lack the right enzymes) so O'Connor *et al.* puzzled over the absence of symbiotic wood-digesting organisms in the gut of shipworms. To their surprise, they discovered that the gills of a shipworm called *Bankia setacea* harbored *Teredinibacter turnerae* bacteria, which produce several wood-digesting enzymes. It seems the shipworm's tissues not only tolerate but also selectively transfer these foreign enzymes into their guts for digesting its formidable meals. –CA

Proc. Natl. Acad. Sci. U.S.A. 10.1073/pnas.1413110111 (2014).

STEM CELLS

An inhibitor to expand mouse stem cells

Among their many side effects, treatments such as chemotherapy and radiation deplete stem cells. Therapies to boost their numbers may positively affect patient outcomes. One possible therapeutic target is the protein phosphatase SHIP1. Hematopoietic stem cells expand in mice lacking SHIP1; however, they also develop inflammatory disease. To boost stem cells numbers while hopefully avoiding inflammation, Brooks *et al.* developed a SHIP1 inhibitor. Adult hematopoietic and mesenchymal stem cell numbers increased in normal mice treated transiently with the inhibitor. The inhibitor also helped mice recover their hematopoietic-lineage cells after radiation treatment. — BAP

Stem Cells 10.1002/stem.1902 (2014).

PHOTO: R. M. O'CONNOR *ET AL., PNAS* 111, **47** (25 NOVEMBER 2014) © 2014 NATIONAL ACADEMY OF SCIENCES

Published by AAAS

SUPERCONDUCTIVITY

Beefing up thin-film superconductivity

Conventional superconductors, such as lead, owe their exotic properties to the interaction of electrons and lattice vibrations. In contrast, in the more recently discovered iron-based superconductors (IBSs), magnetic interactions are thought to play a major role. Lee *et al.* show that in thin films of the IBS FeSe deposited on $SrTiO_3$, a combination of the two mechanisms may be at play. Using angle-resolved photoemission spectroscopy, they discovered a vibrational mode of the $SrTiO_3$ substrate that interacts with the electrons in FeSe. The interaction roughly doubles the temperature at which the film becomes superconducting, when compared with bulk IBSs with similar electronic structures. — JS

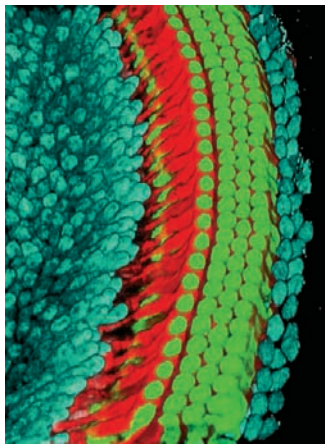
Nature **515**, 245 (2014).

MARINE BIOLOGY

Gray seals: the North Sea's great whites?

Harbor porpoises with missing bellies first appeared on Dutch beaches in 2006; soon, dozens of mutilated porpoises began mysteriously and gruesomely washing ashore each year. Now, Leopold *et al.* have cracked the murderers' identity: gray seals. Photographs and autopsy results of more than 1000 stranded porpoises from 2003 to 2013 revealed torn blubber, scratch marks, and canine teeth marks—all pointing to seals. Finding the smoking gun—seal saliva DNA in the wounds—seemed impossible, as seawater should wash it away. But the team did find seal DNA at the bottom of deep narrow bite marks on three porpoises. Humans may be to blame for the change in seal hunting targets: With rising gas prices, fishermen switched from trawling to cheaper nets anchored to the seabed, which can also trap porpoises. The seals may have stumbled onto them and then gone on to hunt this larger, fattier prey. —JY

Proc. R. Soc. London ser. B, 10.1098/rspb.2014.2429(2014).



Hair cells (green) and supporting cells (cyan) in a neonatal mouse cochlea

HEARING LOSS

Supporting cells take on a starring role

"Supporting cells" in the inner ear have more to offer than their uninspiring name suggests. Studies of deafness often emphasize the role of hair cells, the sensory cells that transmit sound signals to the brain. Loss of hair cells causes permanent deafness, because these cells cannot regenerate. Loss of supporting cells also causes deafness, but a new study suggests that there may be hope. Mellado Lagarde *et al.* found that supporting cells can regenerate during a brief time period after birth. When they selectively eliminated supporting cells in newborn mice, nearby cells rapidly replaced them, thereby preserving hearing. The next step is to find a drug that induces regeneration. — PAK

Proc. Natl. Acad. Sci. U.S.A. 10.1073/pnas.1408064111 (2014).

NANOMATERIALS

Ionic charge manages transformation

One way to create nanoparticles that otherwise are difficult to synthesize de novo is to swap out the cations of existing nanoparticles. De Trizio *et al.* show that the transformation of colloidal copper selenide ($Cu_{2-x}Se$) nanoparticles with tin (Sn) ions leads to vastly different products for Sn^{2+} versus Sn^{4+}. The smaller Sn^{4+} ions move readily through the $Cu_{2-x}Se$ lattice. The homogeneous transformation stops at Cu_2SnSe_3 and retains a cubic lattice. The larger Sn^{2+} cations are blocked, and regions of SnS form at the surface; the stress created at the interface of this heterogeneous nanoparticle drives the distortion of Se anion lattice that allows orthorhombic SnS to form. — PDS

J. Am. Chem. Soc. 10.1021/ja508161c (2014).

TROPICAL PALEOECOLOGY

Revealing the forests of an ancient landmass

The biogeographical history of Southeast Asia is complex. During the Pleistocene glacial cycles, sea levels repeatedly fell, exposing large areas of land and linking islands to the Asian mainland. Especially notable was Sundaland, which united Borneo, Sumatra, and the Malay Peninsula. But what kind of vegetation—forest or savannah—dominated this now-submerged landscape? To find out, Raes *et al.* combined geographical distribution models for species of the dominant dipterocarp tree family with models of past climates. They found that continuous rainforest was the most likely vegetation of much of Sundaland during the Pleistocene glacial cycles. — AMS

Proc. Natl. Acad. Sci. U.S.A. 10.1073/pnas.1403053111 (2014).



Cleaning up after the 2014 Napa, California, earthquake

NATURAL HAZARDS

Getting a bigger jump on earthquakes

Developing better earthquake early warning (EEW) systems, which could help lessen earthquake damage, requires operational testing. Grapenthin *et al.* present a performance analysis of ShakeAlert, an EEW demonstration system along the western coast of the United States, during the 2014 magnitude 6.0 Napa earthquake. The system uses a real-time GPS network to pick up very early shaking and quickly estimate earthquake size and location. ShakeAlert successfully provided a slip model of the earthquake after only half a minute of shaking. The Napa quake shows that ShakeAlert works well and provides vital information on how EEW systems can be improved. — BG

Geophys. Res. Lett. 10.1002/2014GL061923 (2014).

PHOTOS: (TOP TO BOTTOM) GUOQIANG WAN; LIU YILIN XINHUA NEWS AGENCY/NEWSCOM

Published by AAAS

ALSO IN *SCIENCE* JOURNALS

Edited by **Stella Hurtley**

LUNAR GEOLOGY

Lunar magnetism persisted via dynamo

Today the Moon has no magnetic field, but this was not always the case. Remnant magnetization in lunar rock and crust samples indicates that substantial fields existed billions of years ago. Weiss and Tikoo review how modern magnetic studies have established that these fields were powered by a magnetic dynamo that lasted from 4.2 to 3.56 billion years ago. However, the possible mechanics behind the dynamo, such as mantle precession or core crystallization, remain under investigation. To find out how and when the dynamo came and went now requires improvements in magnetohydrodynamic models and more accurate paleointensity measurements, possibly even those that show the field direction. — MMM

Science, this issue p. 1198

CELL COMPETITION

Cell competition and immunity

Even in what appears to be homogeneous tissue, cell variability exists. The presence of mutant cells can compromise the functional integrity of a tissue and ultimately the organism's health. Cell competition is an internal cell surveillance mechanism that monitors cell fitness to eliminate compromised cells and prevent them from contributing to the tissue. However, how cells recognize fitness differences has remained elusive. Meyer *et al.* report that this recognition uses signaling pathways from the innate immune response system. Cell-cell differences in fitness activate distinct NF-κB/Rel factors in the weaker population that lead to activation of distinct pro-apoptotic genes, leading to cell death in the losing cells. — BAP

Science, this issue p. 1199

HEAVY FERMIONS

Teasing out the topological character

When theoretical physicists proposed the existence of an exciting class of materials called topological insulators (TIs), they had in mind a material that is electrically insulating in the bulk but conducts electricity on its surface. Experimentally discovered TIs, however, still have considerable bulk conductivity. Theoreticians then noticed that the material SmB_6, which has long been known as an insulator with peculiar conduction properties, may be a TI. However, confirming that SmB_6 is a TI has been an arduous process. Li *et al.* traced the electronic structure of SmB_6 in high magnetic fields and found that it does indeed have two-dimensional surface states. —JS

Science, this issue p. 1208

SURFACE STRUCTURE

Stabilization of the surfaces of magnetite

Accurate structures of iron oxide surfaces are important for understanding their role in catalysis, and, for oxides such as magnetite, applications in magnetism and spin physics. The accepted low-energy electron diffraction (LEED) structure for the surface of magnetite, in which the bulk surface termination undergoes an undulating distortion, has a relatively poor agreement with experiment. Bliem *et al.* show that the LEED structure is much more accurately described by a structure that includes subsurface cation vacancies and occupation of interstitial sites (see the Perspective by Chambers). Such cation redistribution occurs in many metal oxides and may play a role in their surface structures. — PDS

Science, this issue p. 1215; see also p. 1186

PALEOCLIMATE

Greenhouse gases drove African rainfall

Much of equatorial Africa suddenly became much wetter ~14,700 years ago, ushering in an "African Humid Period" that continued well into the Holocene. Why? Otto-Bliesner *et al.* use a climate model to show that a reduction in the Atlantic Meridional Overturning Circulation (AMOC) at the beginning of the last deglaciation caused a reduction in precipitation in northern and southeastern equatorial Africa. When the AMOC became stronger again, wetter conditions developed in response to a combination of increasing greenhouse gas concentrations and strong summer sun. As atmospheric greenhouse gas concentrations continue to increase, these results may have implications for the future of African hydroclimate, water resources, and agriculture. — HJS

Science, this issue p. 1223

STRUCTURAL BIOLOGY

Watching a protein molecule in motion

X-ray crystallography has yielded beautiful high-resolution images that give insight into how proteins function. However, these represent static snapshots of what are often dynamic processes. For photosensitive molecules, time-resolved crystallography at a traditional synchrotron source provides a method to follow structural changes with a time resolution of about 100 ps. X-ray free electron lasers (XFELs) open the possibility of performing time-resolved experiments on time scales as short as femtoseconds. Tenboer *et al.* used XFELs to study the light-triggered dynamics of photoactive yellow protein. Electron density maps of high quality were obtained 10 ns and 1 μs after initiating the reaction. At 1 μs, two intermediates revealed previously unidentified structural changes. — VV

Science, this issue p. 1242

GEOLOGY

What drives Earth's thermodynamic engine?

The asthenosphere lies right below Earth's tectonic plates. The asthenosphere is a thin layer of partially molten rock that has long been thought to play a minor role in Earth's thermodynamic engine. In a Perspective, Anderson and King highlight recent studies that point to a much more active role for the asthenosphere. They argue that this layer is hotter than the mantle below. It may thus be a source of hotspot volcanoes that have been widely attributed to plumes rising up from the lower mantle. Furthermore, model studies suggest that the asthenosphere has a strong effect on patterns of mantle flow. — JFU

Science, this issue p. 1184

Published by AAAS

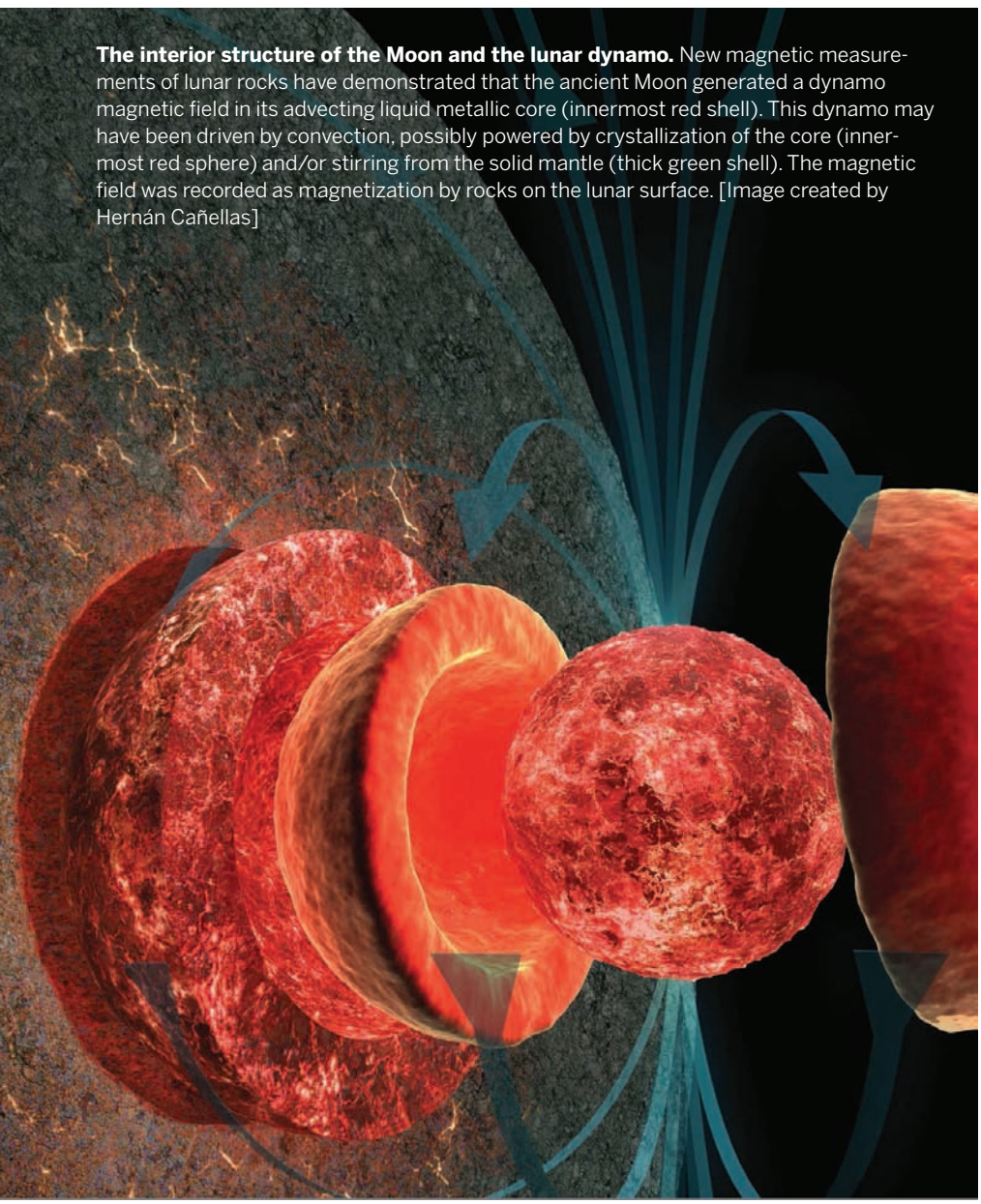
REVIEW SUMMARY

LUNAR GEOLOGY

The lunar dynamo

Benjamin P. Weiss[1*] and **Sonia M. Tikoo**[2,3]

BACKGROUND: It is unknown whether the Moon has a fully differentiated and melted structure with a metallic core or retains a partially primordial, unmelted interior. The differentiation history of the Moon is manifested by its record of past magnetism (paleomagnetism). Although the Moon today does not have a global magnetic field, the discovery of remanent magnetization in lunar rocks and in the lunar crust demonstrated that there was a substantial lunar surface field billions of years ago. However, the origin, intensity, and lifetime of this field have been uncertain. As a result, it has been unclear whether this magnetization was produced by a dynamo in the Moon's advecting metallic core or by fields generated externally to the Moon. Establishing whether the Moon formed a core dynamo would have major implications for understanding its interior structure, thermal history, and mechanism of formation, as well for our understanding of the physics of planetary magnetic field generation.



The interior structure of the Moon and the lunar dynamo. New magnetic measurements of lunar rocks have demonstrated that the ancient Moon generated a dynamo magnetic field in its advecting liquid metallic core (innermost red shell). This dynamo may have been driven by convection, possibly powered by crystallization of the core (innermost red sphere) and/or stirring from the solid mantle (thick green shell). The magnetic field was recorded as magnetization by rocks on the lunar surface. [Image created by Hernán Cañellas]

ADVANCES: A new generation of laboratory magnetic studies of lunar rocks and spacecraft measurements of lunar crustal magnetic fields have produced major advances in our understanding of the evolution of ancient magnetic fields on the Moon. It has now been established that a dynamo magnetic field likely existed on the Moon from at least 4.5 billion to 3.56 billion years ago, with an intensity similar to that at the surface of Earth today. The field then declined by at least an order of magnitude by 3.3 billion years ago. The early epoch of high field intensities may require an exceptionally energetic power source such as mechanical stirring from mantle precession. The extended history of the lunar dynamo appears to demand long-lived power sources such as mantle precession and core crystallization.

ON OUR WEB SITE

Read the full article at http://dx.doi.org/10.1126/science.1246753

OUTLOOK: Measurements of the intensity of the ancient lunar dynamo have shown that it was surprisingly intense and long-lived. The next phase of lunar magnetic exploration will be to obtain more accurate measurements of field paleointensities and to determine when the dynamo initiated and finally disappeared. This will be coupled with the continued development of magnetohydrodynamic models for characterizing mechanical and other unusual dynamo mechanisms and further investigations into the thermal, structural, and geodynamical history of the lunar core and mantle. The eventual availability of absolutely oriented samples and in situ spacecraft measurements of bedrock should enable the first measurements of the paleo-orientation of lunar magnetic fields. Such directional data could determine the lunar field's geometry and reversal frequency, as well as constrain ancient local and global-scale tectonic events. ■

[1]Department of Earth, Atmospheric, and Planetary Sciences, Massachusetts Institute of Technology, 77 Massachusetts Avenue, Cambridge, MA 02139, USA. [2]Department of Earth and Planetary Science, University of California, Berkeley, CA 94720, USA. [3]Berkeley Geochronology Center, 2455 Ridge Road, Berkeley, CA 94709, USA.
***Corresponding author. E-mail: bpweiss@mit.edu**
Cite this article as B. P. Weiss, S. M. Tikoo, *Science* 346, 1246753 (2014); DOI: 10.1126/science.1246753

Published by AAAS

Downloaded from www.sciencemag.org on December 5, 2014

REVIEW

LUNAR GEOLOGY

The lunar dynamo

Benjamin P. Weiss[1]* and Sonia M. Tikoo[2,3]

The inductive generation of magnetic fields in fluid planetary interiors is known as the dynamo process. Although the Moon today has no global magnetic field, it has been known since the Apollo era that the lunar rocks and crust are magnetized. Until recently, it was unclear whether this magnetization was the product of a core dynamo or fields generated externally to the Moon. New laboratory and spacecraft measurements strongly indicate that much of this magnetization is the product of an ancient core dynamo. The dynamo field persisted from at least 4.25 to 3.56 billion years ago (Ga), with an intensity reaching that of the present Earth. The field then declined by at least an order of magnitude by ~3.3 Ga. The mechanisms for sustaining such an intense and long-lived dynamo are uncertain but may include mechanical stirring by the mantle and core crystallization.

One of the most important events in planetary history is early global differentiation, the large-scale melting and sequestration of compositionally distinct materials into a radially layered structure with a central metallic core and silicate mantle. The terrestrial planets inevitably differentiated during the first ~10 million to 100 million years (My) of their history due to their large sizes (radii > 2400 km), which led to the release of large quantities of gravitational energy during their accretion (*1*). By comparison, the gravitational energy of formation of even the largest asteroids (radii < 500 km) is only sufficient to have globally heated these bodies by up to few tens of degrees Celsius.

The fate of the Moon, which has an intermediate radius (1737 km), is less certain: Formation by gradual accretion of small planetesimals would not heat the body above the solidus (melting temperature) unless most energy was retained during accretion. In contrast, formation by the impact of a Mars- or larger-sized planetesimal on the early Earth would likely produce a Moon at or above the solidus (*2*). The latter giant impact scenario might naturally lead to the formation of an early molten core and dynamo magnetic field (*3*).

The Moon today does not have a global magnetic field, but the Apollo-era discoveries of remanent magnetization in the lunar crust and returned samples demonstrated that there were substantial lunar surface fields billions of years ago (*4*). However, it has long been unclear whether this magnetization was produced by a core dynamo and/or by magnetic fields generated externally to the Moon. Establishing whether the Moon formed a metallic core and dynamo would have major implications for the Moon's origin, igneous and thermal history, and large-scale interior structure. Furthermore, the Moon's small size makes it a unique natural laboratory for studying the physics of dynamo generation in a parameter regime not represented by other known planetary bodies. In particular, the apparent persistence and intensity of lunar magnetic fields are a powerful and potentially illuminating challenge to dynamo theory.

Over the past decade, a burst of experimental and theoretical advances has greatly improved our understanding of the lunar paleomagnetic record, global geophysical properties, and dynamo theory. Here, we review how these coupled discoveries have confirmed the existence of an ancient lunar dynamo, defined its temporal evolution and lifetime, and stimulated a new view of planetary magnetic field generation.

Scientific understanding of the Moon by the end of the Apollo era

Before the Apollo missions, there were two disparate views of the nature of the lunar interior. Urey (*5*) conceived of the Moon as largely a primordial, undifferentiated relic from the early solar system, whereas Kuiper (*6*) and others conceived of the Moon as a differentiated body with endogenic volcanism and a metallic core. Early magnetometry measurements by the Luna 1 and 2 spacecraft appeared consistent with Urey's view, finding no evidence of an intrinsic lunar field (*7*); we now know that the lunar dipole moment is $\leq 8 \times 10^{-9}$ that of the Earth [using recent Lunar Prospector spacecraft measurements and the sequential model of (*8*)]. Furthermore, early measurements of the Moon's gravity and physical libration (i.e., three-dimensional temporally varying rotation) observed that its normalized polar moment of inertia appeared indistinguishable from that of a uniform sphere

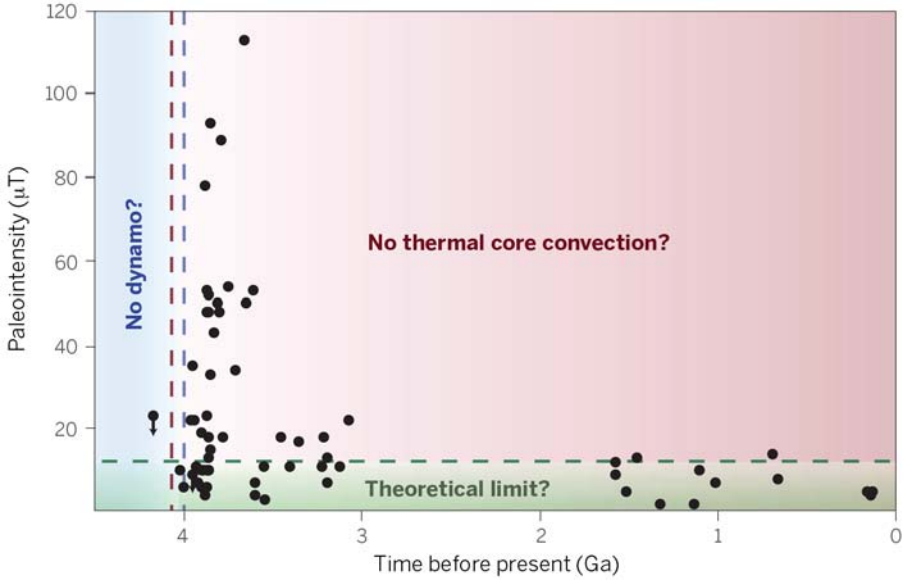


Fig. 1. Apollo-era paleointensity measurements of the lunar magnetic field and their perceived difficulties. Each point represents the inferred field intensity for a single lunar rock. Points with arrows represent upper limits. Both the intensity values and their ages are uncertain. The apparent rapid rise in paleointensities between 4.0 and 3.9 Ga has been taken as evidence that the origin of the lunar dynamo, and perhaps of the core itself, were delayed by 500 My (*3*) (blue), apparently at odds with a giant impact origin of the Moon. Energy flux scaling (Eq. 2) predicts maximum paleointensities of only less than ~12 μT (green), apparently well below many measured values. Early thermal evolution models (*25*, *27*) predicted that a core dynamo powered by purely thermal convection is unlikely to have persisted beyond ~4.1 Ga, before virtually all measured paleointensities (red). The weakest surface fields today are <0.2 nT (*29*). Paleointensities are obtained from the IRM normalization method as compiled by (*4*, *17*).

[1]Department of Earth, Atmospheric, and Planetary Sciences, Massachusetts Institute of Technology, 77 Massachusetts Avenue, Cambridge, MA 02139, USA. [2]Department of Earth and Planetary Science, University of California, Berkeley, CA 94720, USA. [3]Berkeley Geochronology Center, 2455 Ridge Road, Berkeley, CA 94709, USA.
*Corresponding author. E-mail: bpweiss@mit.edu

(for which C/MR^2 = 0.4, where C is the polar moment of inertia and M and R are the lunar mass and radius). However, the subsequent discovery that the mare plains are basaltic by Surveyor 5 (*9*) and that the lunar highlands are anorthositic by Apollo 11 (*10*) confirmed that, beginning with an early post-accretional large-scale magma ocean, the Moon repeatedly experienced igneous processing over >2 billion years. Furthermore, improved spacecraft tracking in the mid-1970s established that C/MR^2 ~ 0.392 ± 0.003 (*11*), consistent with (although not requiring) the existence of a small metallic core (1 to 4% of the lunar mass) (*12*, *13*). Finally, the discovery of natural remanent magnetization (NRM) in the lunar crust and Apollo samples from spacecraft and laboratory measurements hinted at the possibility of an ancient but now extinct lunar dynamo.

Paleomagnetic measurement methodology

NRM is a vector quantity that reflects the macroscopic, semipermanent alignment of electron spins within ferromagnetic minerals. The major ferromagnetic minerals in unbrecciated lunar rocks are the metals kamacite (α-$Fe_{1-x}Ni_x$ for x < ~0.05) and martensite (α_2-$Fe_{1-x}Ni_x$ for ~0.05 < x < ~0.25) (*4*, *14*, *15*). Igneous rocks become magnetized when they cool in the presence of an ambient magnetic field below their Curie temperature (780°C for kamacite), a form of NRM known as thermoremanent magnetization (TRM). For weak planetary fields, the TRM intensity, M, is given by

$$M = \chi_{TRM} B_{paleo} \quad (1)$$

where B_{paleo} is the ancient magnetizing field and χ_{TRM} is the TRM susceptibility, a sample-dependent constant that quantifies the abundance and magnetization efficiency of the ferromagnetic grains. Other forms of NRM, such as crystallization remanent magnetization (CRM) (acquired when ferromagnetic minerals crystallize) or shock remanent magnetization (SRM) (acquired when rocks experience transient high pressures), are presently more difficult to relate quantitatively to ancient field intensities. NRM in typical planetary materials can persist for longer than the age of the solar system, well after any ancient field has decayed away.

Because essentially all returned lunar rocks are regolith samples, their original orientations are largely unknown (*16*). Therefore, laboratory measurements of Apollo samples have usually sought to obtain the paleointensity, and not paleodirection, of past lunar fields. To obtain B_{paleo}, the first step is to measure the quantity on the left side of Eq. 1, M_{NRM} [after removing any partial magnetization overprints using alternating field (AF) or thermal demagnetization]. Then, because χ_{TRM} is difficult to measure, the sample is remagnetized in a known laboratory field, B_{lab}, and the resulting magnetization, M_{lab}, is measured. If χ_{TRM} is unchanged by this process, then the two resulting equations can be divided to obtain $M_{NRM}/M_{lab} = B_{paleo}/B_{lab}$ and then solved for B_{paleo}. In principle, the most accurate paleointensity estimates for igneous rocks could be obtained if M_{lab} were produced as a TRM, because this would resemble the form of the NRM. Doing so is the basis of Thellier-Thellier paleointensity experiments. However, heating-induced chemical alteration, combined with magnetostatic interactions between ferromagnetic grains, can change χ_{TRM} in a way that is difficult to quantify, leading to experimental failure (*4*). Such problems have frustrated Thellier-Thellier experiments of lunar rocks for decades, such that essentially none have been able to meet the standards of success typical for Earth rocks (*17*, *18*). As a result, most paleointensities have been inferred using nonheating methods to produce M_{lab}. In particular, either a saturating field [to produce an isothermal remanent magnetization (IRM)] or weak field superposed on a strong AF [to produce an anhysteretic remanent magnetization (ARM)] is applied to the samples as a proxy for TRM. Using these methods, B_{paleo} can usually be estimated with a factor of ~5 uncertainty (2 SD) (tables S2 to S4).

Apollo-era measurements

By the end of the Apollo era (the early 1980s), analyses of hundreds of samples seemed to indicate the existence of ancient magnetic fields with intensities ranging from 0.1 to 120 μT over the period <200 million years ago (Ma) up to 4.0 billion years ago (Ga) (*4*) (Fig. 1). This huge range of intensities far exceeds the expected surface variations for a constant, selenocentric (i.e., Moon-centered) dipole moment, suggesting that the Moon's magnetic field may have experienced dramatic temporal variations (*19*).

Despite the wealth of data, there was no consensus on the origin or meaning of lunar magnetization. One reason is that many samples were complex breccias that experienced multiple shock and brecciation events (Fig. 2). Not only is it uncertain when such rocks became magnetized, but it is often not clear that the NRM being measured is actually a TRM (*17*, *18*). For some samples, it was apparent that the NRM was contaminated during sample handling by the astronauts and/or after return to Earth (*14*, *20*, *21*). Furthermore, even apparently unshocked materials (i.e., those that never experienced peak pressures exceeding the 5-GPa threshold at which petrographic effects become evident), which include most mare basalts, yielded uncertain results because their constituent ferromagnetic minerals are usually in the form of multidomain crystals that have poor magnetic recording properties. As a result of these problems, both the age of the NRMs and the associated paleointensities were uncertain for the majority of analyzed samples.

Attempting to account for the nominal paleointensity record from a theoretical perspective is also very challenging. Perhaps most surprising is that the inferred paleointensities for many lunar samples are up to 1 to 2 orders of magnitude greater than the maximum surface fields predicted by dynamo scaling laws. For example, analysis of a diversity of numerical simulations of Earth-like dynamos powered by convection suggests that the mean dipole magnetic field intensity at the Moon's surface may be estimated as

$$B \approx d\left(\frac{R_c}{R}\right)^3 (2\mu_0 cf\rho)^{1/2}\left(\frac{\alpha G}{3C_P}\right)^{1/3}(4\pi R_c^2 q_a)^{1/3} \quad (2)$$

where d is the ratio of the dipolar field to the total field at the core-mantle boundary, R_c is the core radius, R is the planetary radius, μ_0 is the magnetic permeability of free space, f is the ratio of ohmic dissipation to total dissipation, ρ is the core density, α is the volumetric coefficient of thermal expansion for the core, G is the gravitational constant, C_P is the heat capacity at constant pressure for the core, $q_a = q_d - q_t$ is the power flux available to power the dynamo, q_d is the power flux dissipated at the core mantle boundary, q_t is the threshold power flux for dynamo generation, and c is a constant of proportionality (*22*, *23*). The major difficulty is that the tiny radius of the lunar core, R_c [estimated to be only ~0.2 R (*24*)], means that core dipole fields are highly attenuated at the planetary surface, given their $(R_c/R)^3$ dependence. Using R_c = 250 to 450 km (see below) and otherwise assuming approximately Earth-like values scaled to lunar core pressures for the remaining parameters, B is predicted to be below 12 μT, and most likely no more than ~3 μT, for essentially all estimated power sources (see table S5). This is well below many of the paleointensity values inferred from the Apollo-era data for the period ~3.6 to 3.9 Ga (Fig. 1).

Furthermore, the data seemed to suggest that lunar paleointensities increased rapidly during the period ~4.0 to 3.9 Ga, such that the field perhaps did not originate until more than ~400 My after lunar formation. It has been argued that the apparent lack of an early dynamo conflicts with the giant impact hypothesis for the origin of the Moon, which would have likely produced a hot, rapidly cooling lunar interior just after formation (*3*). Moreover, until very recently, essentially all lunar evolution models were unable to explain why the dynamo was apparently able to persist well beyond ~4.1 Ga (*25*–*27*).

Another unresolved issue was when the dynamo declined. Fuller (*28*) argued that the dynamo ceased abruptly sometime between 3.6 and 3.7 Ga, implying that younger paleointensity values are within error of zero field, while Runcorn (*3*) proposed that the dynamo declined in intensity to ~1 to 20 μT but persisted until at least ~3.2 Ga and possibly much longer. Particularly problematic for the latter viewpoint are the youngest paleointensity values, which are derived from impact melt samples that formed from 1.5 Ga to as little as <200 Ma. If these are accurate, the lack of a field today [<0.2 nT at many surface locations (*29*)] would seem to suggest that we are observers in a special time window occurring just after the decay of the dynamo.

These issues collectively led to a suspicion that the lunar paleointensity data may not in fact be

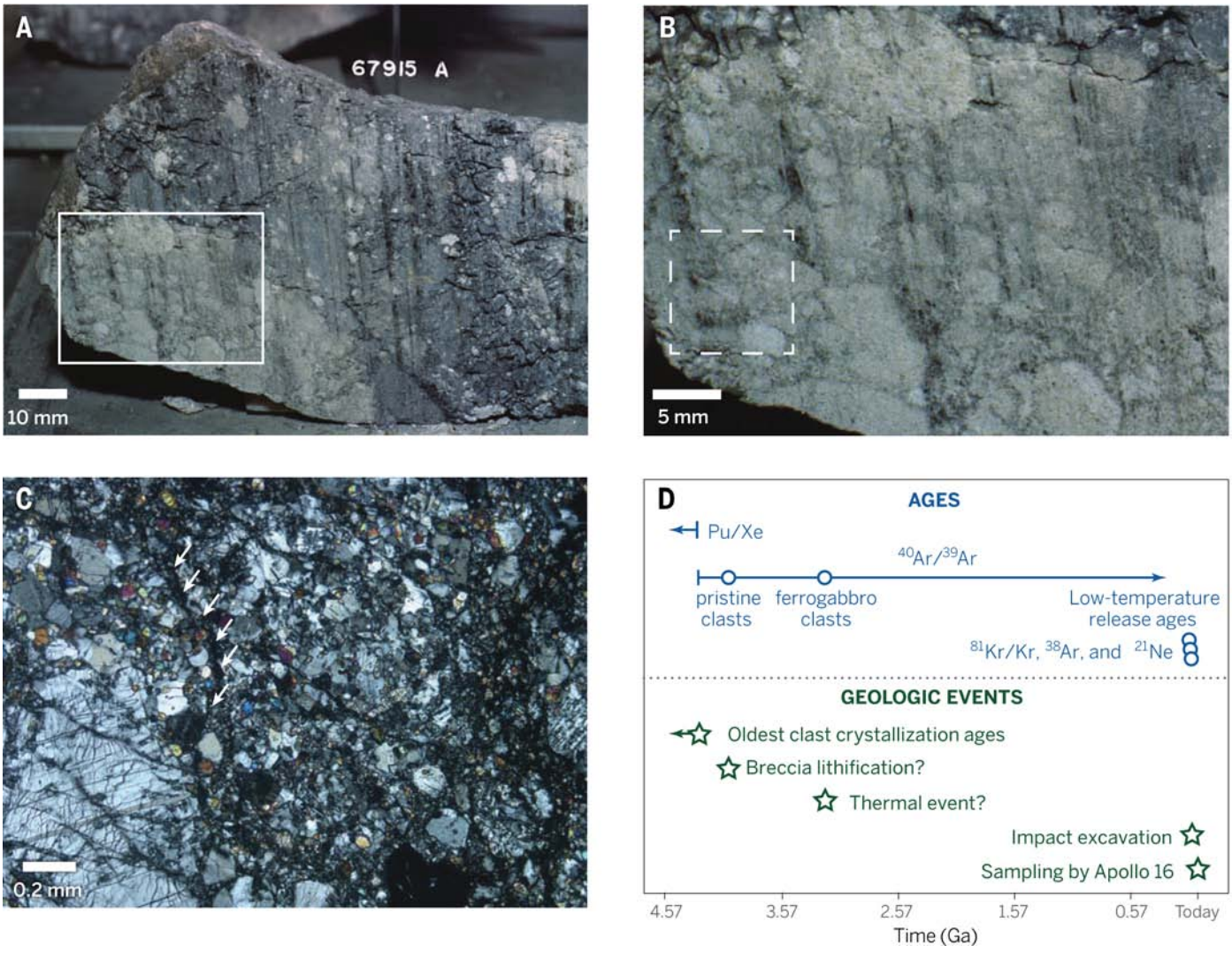


Fig. 2. Petrography and geologic history of Apollo 16 feldspathic polymict breccia 67915. Apollo-era paleomagnetic measurements of this rock, which inferred near-null (<3 μT) paleointensities at ~4.0 Ga, were interpreted as evidence that the initiation of the lunar dynamo was delayed by 500 My after the Moon's formation. However, the magnitude and age of this paleointensity constraint are highly uncertain, given the protracted and complex history experienced by the rock and its constituents. (**A**) Photograph of slab cut at NASA Johnson Space Center in 1972 (NASA photo S72-52255). Numerous diverse clasts are visible, including large (50 by 20 cm) white clast at lower left. Close-up of boxed region is shown in (B). (**B**) Close-up image of large white clast in (A). The large clast is actually itself a polymict breccia composed of numerous rounded white clasts. The thin section shown in (C) was subsampled from below the approximate location shown by the dashed box. (**C**) Photomicrograph in transmitted light with crossed polars of thin section 67915,76 taken from a single rounded white clast at the location shown in (B) (JSC photo 02973-x2). The rounded clast is revealed to be itself a breccia composed of shocked fragments of plagioclase (gray) and pyroxene and olivine (brown, green, and purple grains). The rock is also crosscut by fine-scale (<0.1 mm thick) young, glassy melt veins (dark, sinuous, branching channels) that postdate assembly of the breccia (one example identified with white arrows). (**D**) Summary of radiometric and exposure ages (top) and inferred geologic events (bottom) for 67915. The Pu/Xe and oldest $^{40}Ar/^{39}Ar$ ages indicate that the oldest materials crystallized at ≥4.3 Ga. $^{40}Ar/^{39}Ar$ age spectra from a diversity of clasts—including granulitic breccias, pristine troctolites, and sodic ferrogabbros—exhibit a range of apparent ages from 4.3 to <0.26 Ga, thought to correspond to multiple thermal events recorded by clasts with different Ar diffusivities. $^{81}Kr/Kr$, ^{38}Ar, and ^{21}Ne cosmic ray exposure ages are thought to date the impact that formed Cone Crater and excavated 67915. Ages and paleomagnetic data are presented in table S7.

a record of an ancient dynamo. The young paleointensity values, all of which are associated with impactites, motivated an alternative hypothesis that some or perhaps even all lunar paleofields were the products of plasmas transiently generated by meteoroid impacts on the lunar surface (*30*, *31*). Theoretical models have suggested that such fields might reach tens or even hundreds of μT but would be short-lived, lasting up to a day for the largest, basin-forming impacts and less than seconds for most smaller impacts. Although impact fields would only be capable of imparting a full TRM on samples that cool from the Curie temperature to surface temperatures more quickly than these time scales (*32*), an SRM could be readily acquired by virtually any rock shocked in the presence of such fields, given the near instantaneous pressure changes associated with shock waves (*33*). If correct, the impact plasma fields hypothesis would have profound implications for all of extraterrestrial paleomagnetism, because it implies that NRM may not be a record of internal geophysical processes on planetary bodies.

The impact plasma fields proposal appeared to be critically bolstered by Apollo subsatellite magnetometry, which mapped the lunar field between latitudes of 35°N and 35°S and identified numerous crustal magnetic anomalies (*34*). These anomalies can be interpreted as either localized crustal regions with anomalously high χ_{TRM} (resulting, for example, from high metal abundances) and/or regions exposed to locally

intense magnetizing fields. The origin of the anomalies was enigmatic because they did not appear to have clear associations with geological features. A major exception was the most spatially extensive and intense anomalies, which are located on the southern lunar farside in a region that is approximately antipodal to the four youngest large (>600 km in diameter) lunar basins: Imbrium, Serenitatis, Crisium, and Orientale (Fig. 3). This association led some investigators to interpret this association as the result of magnetic field amplification (i.e., locally high B_{paleo}) by impact-generated plasmas in these regions (*34*). Regardless of the formation mechanism, the southern farside and other strong anomalies indicate that large volumes of the crust must have extremely high mean NRM: Assuming a 1-km-thick source layer, the NRM is ~1 to 10 A m^{-1}, which is ~1 to 3 orders of magnitude larger than the NRM of most Apollo mare basalts and breccias and 3 to 5 orders of magnitude larger than the NRM of pristine feldspathic rocks, which are thought to make up the majority of the lunar crust (*35*).

By the end of the Apollo era, it was certain that there were magnetic fields on the ancient Moon, but the intensity, timing, and, most important, physical origin of these fields were unclear. Whether the magnetization in lunar materials was the product of a core dynamo

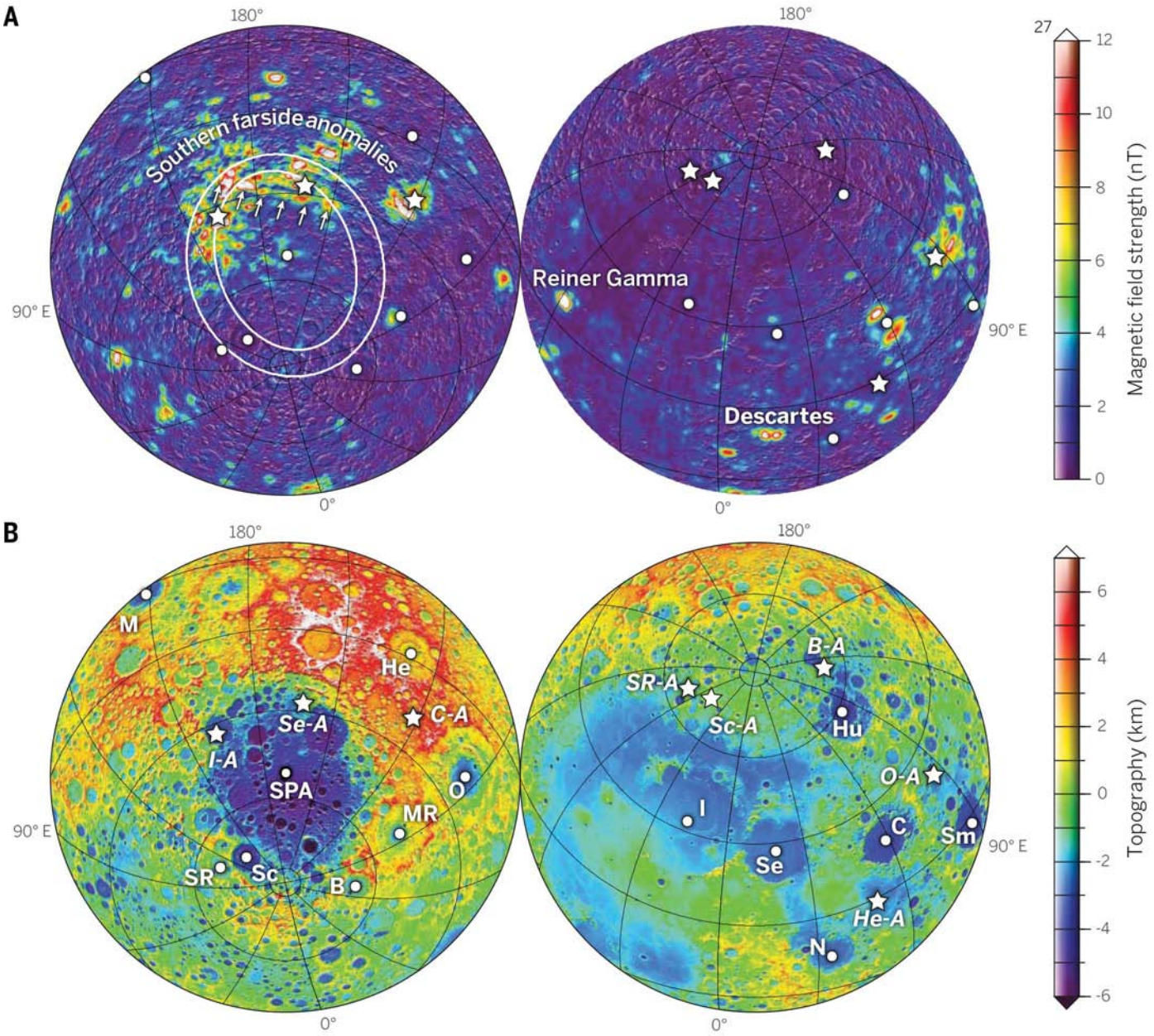


Fig. 3. Lunar crustal magnetic anomalies and their geologic relationships. (**A**) Lunar Prospector total magnetic field map at 30-km altitude from the sequential model of (*8*). Prominent magnetic anomalies (southern farside, Reiner Gamma, and Descartes) are identified. Nested ellipses denote the inner basin floor and outer structural rim of the SPA basin (*82*). Arrows denote a possible linear dike, as identified by (*71*). Circles and stars represent impact basin centers and impact basin antipodes identified in (B). (**B**) Topography from the Lunar Orbiter Laser Altimeter (*83*), showing centers of selected major impact basins (circles) and the antipodes of the eight youngest impact basins (stars). Basin centers are identified by the following: B, Bailly; C, Crisium; M, Moscoviense; MR, Mendel-Rydberg; He, Hertzsprung; Hu, Humboldtianum; I, Imbrium; O, Orientale; N, Nectaris; Sc, Schrödinger; Se, Serenitatis; Sm, Smythii; SPA, South Pole-Aitken; and SR, Sikorsky-Rittenhouse. Basin antipodes are identified with the previous abbreviations appended by "–A". [Modified from (*72*)]

or impact-generated plasmas remained unresolved. A key difficulty was that criteria for distinguishing between these two field sources from measurements of NRM had not been firmly established.

Modern developments

Since the end of the Apollo era, there have been major improvements in analytical techniques in geochronology, petrology, and paleomagnetism and a deepening understanding of rock magnetism and global lunar geophysics. Beginning about 6 years ago, a new generation of paleomagnetic analyses, thermal evolution models, and dynamo simulations have applied these advances toward resolving the origin of lunar magnetism. The broad goal of these efforts has been to answer the following questions: Did the Moon form a dynamo? If so, how strong was the dynamo? When did it form? When did it decline? And what were the physical field-generating mechanisms and power sources? We begin by discussing recent theoretical advances in our understanding of the lunar dynamo and then compare their predictions to new magnetic measurements of Apollo samples and the lunar crust.

Lunar dynamo mechanisms

A dynamo requires organized advection of conducting fluid, which generates magnetic fields by the process of electromagnetic induction (*36*). For the terrestrial planets, this is thought to occur in their liquid metallic cores. Therefore, if the Moon once had an internally generated, global magnetic field, this implies the existence of an ancient advecting lunar metallic core. The case for the existence of such a core has been greatly strengthened over the past two decades. Lunar Prospector estimates of the lunar moment of inertia (*37*) and induced dipole moment (*38*, *39*) are consistent with a core of radius ~220 to 450 km. Lunar rotational dissipation inferred from four decades of laser ranging further suggests that the core is at least partially in a fluid state (*40*). Recent reprocessing of Apollo seismic data suggests the presence of a ~250- to 420-km radius liquid Fe outer core possibly surrounding a ~200- to 240-km radius solid inner core (*24*, *41*).

Fluid motions in all known dynamos in the solar system today are generally thought to be powered by convection. The buoyancy flux in Earth's core is provided by secular heat flow, as well as by latent heat release and compositional differences arising from crystallization of the core (*42*). The field's intensity (*22*) and longevity (*36*) are thought to depend on the heat flux at the core-mantle boundary (Fig. 4). The heat flux out of the core is in turn strongly controlled by the thermal evolution of the overlying mantle. Purely thermal convection in the core (i.e., occurring in the absence of core crystallization) requires that the core-mantle boundary heat flux exceed that which can be conducted along a core adiabat. Estimates for the lunar core adiabatic heat flux range widely (between ~2 and 10 mW m^{-2}) (*43*).

For a dry lunar interior, thermal evolution models assuming a monotonically cooling core-mantle boundary typically find that a pure thermal convection dynamo can persist at most until sometime between ~4.3 and 4.1 Ga (*25*, *26*, *44*). Enrichment of the lower lunar mantle by 40 parts per million (ppm) H_2O [below that recently inferred from mare basalts (*45*)] may lower the mantle viscosity by ~2 orders of magnitude, thereby enabling a thermal convection dynamo to persist until perhaps ~3.4 Ga (*46*). Additionally, it is possible that at the end of magma ocean crystallization, the core was surrounded by a radiogenic element-rich cumulate layer. Thermal models (*26*) have estimated that radioactive heating from such a layer could delay initiation of a thermal convection dynamo (*47*) until sometime between 4.2 and 4.0 Ga and postpone the dynamo cessation until perhaps ~3.5 Ga. The generally short lifetime predicted for a purely thermal convection dynamo has motivated alternative hypotheses that the lunar dynamo was powered either by thermochemical convection from core crystallization or mechanical stirring by differential rotation between the mantle and core.

Mechanical dynamos have yet to be definitively identified to operate in any planetary body today. At least two forms of these exotic mechanisms have been described for the Moon. The first proposes that large meteoroid impacts, by driving transient large-amplitude mantle librations or even temporarily unlocking the mantle from synchronous rotation, powered dynamos lasting for up to several thousand years after each impact event (*48*, *49*). However, because this mechanism requires highly energetic impact

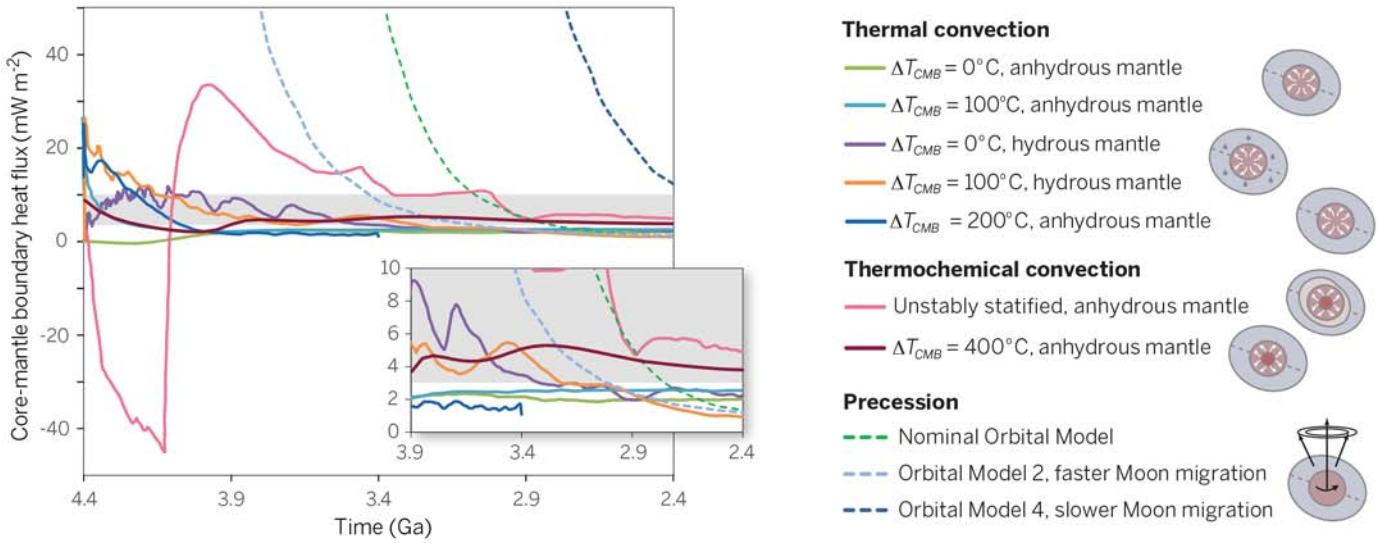


Fig. 4. Estimated longevity of various lunar dynamo mechanisms versus time. Shown is the estimated core-mantle boundary energy flux supplied by purely thermal core convection, thermochemical convection driven by core crystallization, and precession. Solid curves depict a variety of end-member convective dynamo power models demonstrating the effects of: (i) an initially stably stratified (all curves except light red curve) or unstably stratified (light red curve) mantle; (ii) a completely anhydrous (all curves except purple and orange) or hydrous (40 ppm H_2O) (purple and orange curves) mantle; (iii) an initial temperature difference between the core and mantle (ΔT_{CMB}) of either 0°C (green and purple curves), 100°C (light blue and orange curves) [models D07, D09, D37, and D39, respectively, of (*46*)], 200°C (dark blue curves) [model TB-0 of (*26*)], or 400°C (dark red curve); and (iv) inner core crystallization (light red and dark red curves) [model H50E100V5e19 of (*54*) and ΔT_{CMB} = 400 K, 4 wt % S model of (*56*), respectively]. Dashed curves depict estimated power from mantle precession for the three orbital models considered by (*23*): Nominal (green), Model 2 (light blue), and Model 4 (dark blue). Gray boxes indicate the estimated range of critical core heat flux values required for field generation in thermal convection dynamos (3 to 10 mW m^{-2}). Dynamos driven by precession and compositional convection may operate subadiabatically. (Inset) Magnified model results for the time spanning 3.9 to 2.4 Ga. Because the models shown here assumed modestly differing properties of the lunar interior (e.g., core radius and sulfur abundance), their results should only be compared qualitatively.

events, it seems only likely to have occurred before the final basin-forming impact that formed the crater Orientale at 3.72 Ga (*50*).

A mechanical dynamo could also be powered by mantle precession (*40*, *51*). Although initially locked, the lunar core and mantle began to precess around different axes when the Moon's orbit migrated to beyond >26 to 29 Earth radii (*52*). The power associated with this differential motion should have been extremely large compared to that driving thermal convection (Fig. 4) but declined over time as the angle between the core and mantle spin axes decreased. The lifetime of the precession dynamo is highly uncertain because it could operate subadiabatically and because the lunar orbital evolution is poorly constrained. Nevertheless, for a typical choice of lunar physical parameters (*23*), it is estimated that such a dynamo could be sustained until the Earth-Moon distance reached ~43 to 48 Earth radii (i.e., until ~3.4 to 2.0 Ga, depending on which lunar orbital evolution model is assumed). Considering a broader range of acceptable lunar parameters, it is conceivable that a precession dynamo could even last until as late as ~0.6 Ga (*14*). Not only is a precession dynamo potentially very long-lived, but very recent magnetohydrodynamic (MHD) simulations (*53*) also have found that it might have produced surface fields up to the ~100 μT intensities suggested by the Apollo-era paleointensity record for the period before ~3.6 Ga (Fig. 1). Interestingly, this MHD model also finds that the dynamo would terminate at about the same time that the Apollo-era paleomagnetic data suggest a decline in paleointensities (i.e., after ~3.6 Ga).

None of the above mechanisms currently appear capable of powering a dynamo beyond ~0.6 to 2 Ga. However, they do not take into account the main power source for Earth's dynamo, core crystallization. Thermal evolution models predict that a solid core should have formed within the Moon for core sulfur contents of less than ~12 weight percent (wt %) (*44*, *54*). Given possible seismic evidence for a solid inner core (*24*) and recent modeling of lunar mantle siderophile element depletions suggesting a bulk core sulfur abundance of ~6 wt % (*55*), core crystallization could have played an important role in sustaining a late lunar dynamo.

Two lunar thermal evolution models (*54*, *56*) have recently emerged that consider the effects of core crystallization on the dynamo (Fig. 4). However, only one of these models (*56*) considered the central advantages of core crystallization for prolonging the dynamo: the ability to drive convection even for subadiabatic heat core–mantle boundary heat fluxes and the high efficiency by which these heat fluxes are transmitted into buoyancy fluxes by compositional convection. Given the uncertainties on the core sulfur content, it was found that a dynamo could be powered for billions of years and perhaps even until the present day.

However, core crystallization again appears only able to generate surface fields of just a few μT or less and is therefore apparently unable to explain the high paleointensities from the period before 3.56 Ga. Furthermore, the longevity

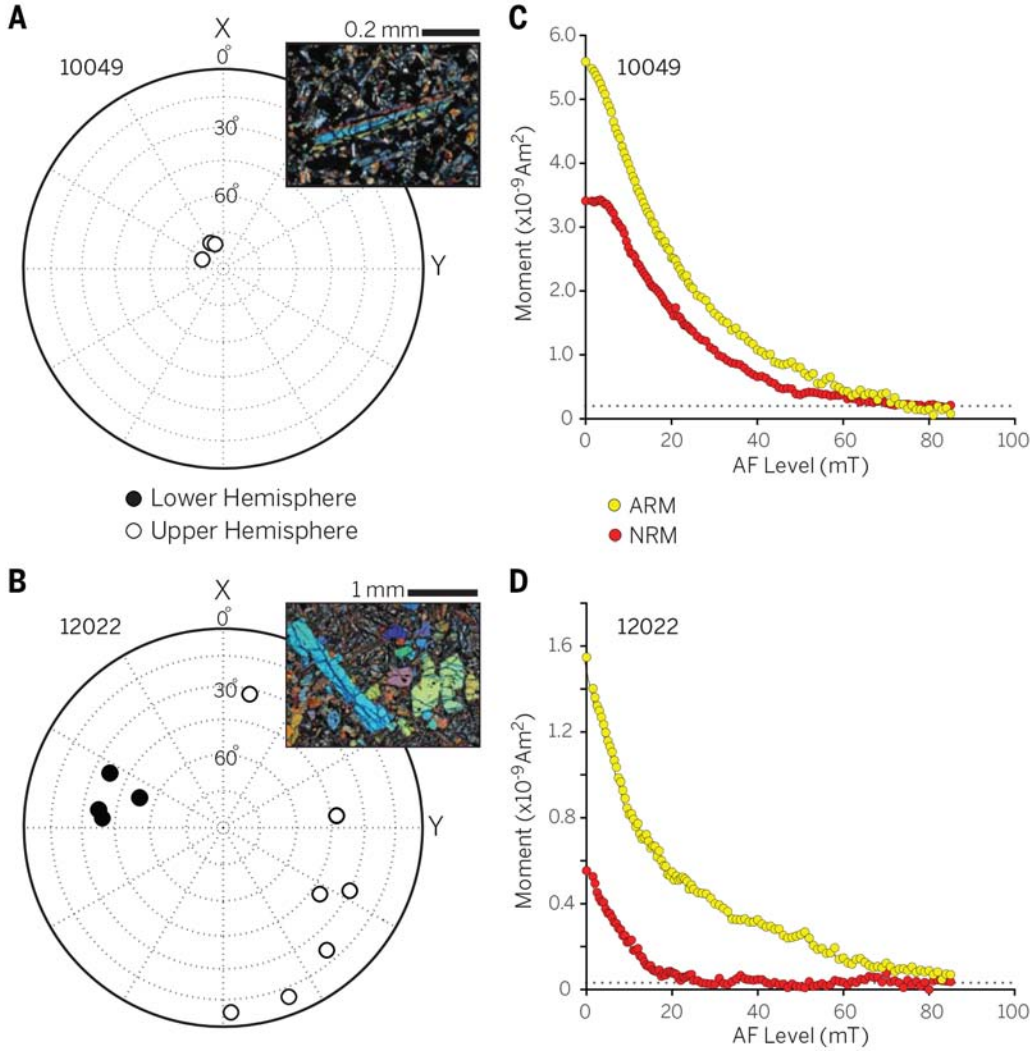


Fig. 5. NRM of two mare basalts that formed during and after the high-field epoch. (**A** and **B**) Equal-area stereographic projection showing the most stable magnetization component directions observed for mutually oriented subsamples of 10049 (A) and 12022 (B). Insets contain transmitted light, crossed polars photomicrographs of thin sections of each rock (10049,40 and 12022,110), showing their unshocked and unbrecciated textures (JSC photos 04194-x3 and 04491-x2, respectively). Visible are plagioclase (gray), pyroxene and olivine (brown, green, and purple grains), and oxides (opaque grains). The sizes of these plagioclase grains indicate that these rocks cooled slowly relative to putative impact-generated magnetic fields (**C** and **D**) AF demagnetization of 10049 subsample 102-1 (C) and 12022 subsample 310a (D). Shown is the NRM intensity during AF demagnetization compared with that of a laboratory ARM, a TRM proxy. Horizontal dashed lines indicate the magnetic moment at which the sample was effectively completely demagnetized (as indicated by instability of the magnetization direction). For 10049, the unidirectional NRM (A) and its persistence to similar AF levels as reached by the ARM (C) are consistent with a primary TRM origin (Box 1). For 12022, the nonunidirectional orientation of the NRM (B) and its complete removal at AF levels lower than that for ARM (D) are inconsistent with a primary TRM origin. Rather, the stable magnetization in 12022 is interpreted to be an overprint from saw-cutting and long-term exposure to Earth's field. [Data from (*14*, *50*)]

of power from core crystallization may open a new problem of explaining why there is apparently no lunar dynamo today. A possible solution is that the core crystallization models discussed here assumed that the lunar core began by crystallizing from the bottom up like the Earth's core. In fact, early lunar core conditions were likely close to the threshold that could permit bottom-up or top-down (Fe snow) crystallization (which depends critically on the poorly known sulfur content of the liquid core and thermal expansion of iron-sulfur liquids) (*57*, *58*). Given that the Moon presently lacks a detectable dynamo field, it was proposed that as the liquid core became progressively enriched in sulfur, a shift from bottom-up to top-down crystallization occurred that induced dynamo shutoff. However, the expected timing for such a transition remains unknown (*56*).

In summary, it is possible that a lunar dynamo powered by core crystallization could have persisted for far longer than permitted by any other mechanism and for as long as the Apollo-era data seem to require. However, only precession dynamos currently appear capable of accounting for the high apparent paleointensities measured during the Apollo era for the period before ~3.6 Ga. We now reassess the fidelity of this paleointensity record in the light of modern laboratory and spacecraft magnetometry measurements.

New paleomagnetic measurements

Modern paleomagnetic studies have taken advantage of new, highly sensitive and automated magnetometry technology and four decades of continued geochemical and petrologic studies of the Apollo samples. A particularly important contribution has been the development of several criteria for identifying high-fidelity dynamo paleointensity records (Box 1). Critically, rocks have been studied that are unbrecciated and unshocked and with cooling time scales from the kamacite Curie point to ambient surface temperatures far longer than any putative impact plasma-generated fields, requiring that any primary TRM be the product of a long-lived field like a core dynamo (Fig. 5).

Such studies have now provided strong evidence for the existence of a lunar core dynamo. Analyses have found that the lunar troctolite 76535 recorded a dynamo field with intensity a few tens of μT at 4.25 Ga (*32*, *59*). This is the earliest record of the lunar magnetic field and demonstrates that a dynamo existed as far back in history as we have records (Fig. 6). This early period is exactly the time when thermal evolution models predict that a purely thermal convection dynamo could have been active. Furthermore, this result marginally excludes the thermal blanket convection dynamo models (*26*, *54*), which predict that dynamo initiation would be delayed until ~4.2 to 3.9 Ga and would perhaps coincide with the onset of major mare volcanism (~4.0 Ga).

Subsequent studies of mare basalt 10020 identified evidence for a core dynamo field with an intensity of ~66 μT at 3.72 Ga (*60*). Additional evidence for a similarly substantial field at 3.7 to 3.8 Ga was also provided by a study of three Apollo 17 mare basalts (*61*). The existence of a dynamo at 3.8 to 3.7 Ga likely excludes a purely thermal convection dynamo (*25*), unless the lunar mantle is H_2O-rich (*46*) (Fig. 6).

The lifetime of the dynamo was then found to persist until at least 3.56 Ga, with similarly strong intensities (~71 to ~77 μT) from analyses of mare basalts 10017 and 10049 (Fig. 5, A and C) (*50*). Given that these samples are 160 My younger than the last basin-forming impact, they likely exclude an impact-driven mechanical dynamo at this time in lunar history in favor of a precession, core crystallization, and/or thermal convection dynamo in an H_2O-rich lunar interior (Fig. 6).

After these studies, the question remained as to when the dynamo declined and ultimately ceased. A key recent step toward addressing this has been the realization that the poor magnetic recording properties of most mare basalts preclude retrieval of TRM acquired in fields less than ~20 μT using typical AF demagnetization methods, which introduce spurious magnetization that can obscure the underlying NRM (*62*). This limit is barely within the range of the Apollo-era paleointensity values after 3.5 Ga, strongly suggesting that most of those values are simply upper limits and are consistent with a weak to null field. Therefore, establishing the history of the late lunar dynamo requires measurements of samples with unusually high magnetic recording fidelity. Recent analyses of two such samples, mare basalts 15597 and 12022, demonstrated that the dynamo field had declined to below ~7 μT by ~3.3 Ga and below ~4 μT, and possibly even vanished altogether, by 3.19 Ga (Fig. 5, B and D, and Fig. 6) (*14*). These values are broadly consistent with a possible 5-μT upper limit obtained for Thellier-Thellier measurements of <3.46 Ga anorthositic breccia 60015 (*14*, *18*) (Fig. 6). Finally, a recent paleomagnetic study of a <7-Ma impact melt glass demonstrated that lunar surface fields likely remained below ~7 μT into the recent past (*62*, *63*) (Fig. 6).

The ~4-μT upper limit inferred for the Moon at 3.19 Ga is nevertheless at the upper end of the range predicted by the energy flux scaling (Eq. 2). In particular, for typically assumed lunar parameters, essentially all published thermal and evolution models of the lunar dynamo (*23*, *26*, *44*, *47*, *48*, *56*) predict surface fields >0.1 μT for more than ~90% of the time period in which the dynamo is active in the models. Such a minimum field is comparable to estimates of the strongest lunar crustal surface fields (*64*) and below even the weakest known dynamo surface field in the solar system today (*65*). Therefore, the current paleointensity constraints do not at all exclude a lunar dynamo after 3.56 Ga. Determining when the dynamo truly ceased requires a sample with extraordinary magnetic recording capabilities. Tikoo *et al.* (*66*) very recently suggested that the melt-glass matrix of regolith breccia 15498 (which contains a population of high-fidelity single-domain ferromagnetic grains) was magnetized in a ~2-μT core dynamo field. The age of the TRM is uncertain but must be less than the 3.3 Ga age of basalt clasts in the breccia, whereas trapped Ar data suggest a lithification age of perhaps only ~1.3 Ga (*67*). If confirmed, this result would extend the lifetime of the lunar dynamo by at least 0.2 to 2 billion years, suggesting that the dynamo operated in two different intensity regimes: a pre-3.3-Ga high-field epoch and a post-3.3-Ga weak-field epoch. Depending on the age of the NRM in 15498, precession and core crystallization are the only mechanisms currently thought

Box 1. Sample criteria for lunar dynamo studies.

Lunar dynamo paleointensity studies should target samples containing a high-fidelity TRM acquired in a temporally stable field at a well-constrained time in lunar history. This motivates the following selection criteria:

1. TRM origin. Current experimental procedures are most accurate for inferring paleointensity estimates from samples containing TRM. Samples containing total TRM (i) are igneous in origin and/or were at least heated above the Curie temperature during the last remagnetization event and (ii) show no petrographic evidence for shock (pressures <5 GPa) or brecciation after the last major remagnetization event. To help ensure that their NRM has high stability and can be cleaned of overprinting magnetization, samples should also (iii) contain the finest ferromagnetic grains (ideally pseudosingle domain or smaller). Other key characteristics of total TRM are (iv) unidirectionality within the samples, (v) high stability against laboratory demagnetization, and (vi) demagnetization in the laboratory like a laboratory-produced TRM.

2. Core dynamo field. To ensure that any observed TRM was acquired from a long-lived field like a dynamo, samples should have cooled from 780° to ~0°C more slowly than the estimated lifetimes of impact-generated fields [~1 day for the largest impacts (*30*) and at most a few seconds for the smaller impacts after 3.7 Ga (*14*)]. A lack of major shock effects (criterion ii in 1) will also help to exclude an impact-generated field source.

3. Known age. To enable the assignment of accurate ages to paleointensity estimates, samples should have geochronologically constrained thermal histories. Identification of a TRM origin (criteria i to vi in 1) is important for assigning radiometric ages to the NRM.

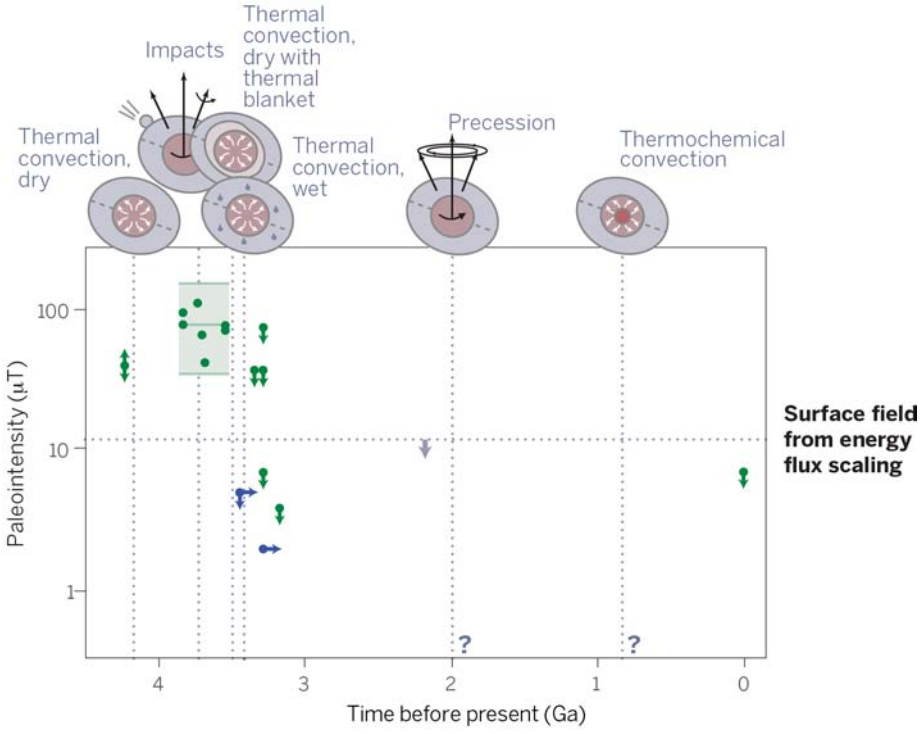


Fig. 6. Paleointensity measurements of the lunar magnetic field using modern methods and estimated lifetimes of various lunar dynamos. Each point represents measurements of a single Apollo sample. Circles represent actual paleointensities, downward arrows represent upper limits on paleointensity, and right arrows represent upper limits on age. Green and blue points were measured using the IRM and Thellier-Thellier methods, respectively, and the upper limits were derived from the ARM method. Note the datum at <7 Ma at the extreme right of the figure. The shaded green box encompasses the mean paleointensity value for the period 3.56 to 4.25 Ga (central green line) and its estimated 2 SD uncertainty (upper and lower lines) (see table S6). The paleointensity value for 76535 (leftmost green point) is currently not well constrained due to spurious demagnetization effects. Vertical dashed lines show estimated maximum lifetimes of various proposed lunar dynamo mechanisms: purely thermal convection in a dry mantle (with and without an early thermal blanket surrounding the core); impact-driven mantle rotational changes, purely thermal convection in a wet mantle; precession; and thermochemical core convection driven by core crystallization. The horizontal line shows the maximum lunar surface field as estimated from Eq. 2. The lifetimes of the precession and thermochemical dynamos are highly uncertain. Paleointensity data set is from (*14*, *18*, *50*, *59*–*61*, *63*, *66*) and is also listed in table S6.

to be able to power a dynamo this late in history (Figs. 4 and 6).

These results confirm some Apollo-era conclusions and refute others. Modern paleomagnetic measurements have now demonstrated that a core dynamo likely existed on the Moon at least as far back in time as 4.25 Ga, in contradiction to the hypothesis of a late origin (i.e., after 4.0 Ga). On the other hand, modern measurements have confirmed the existence of a high-field (mean of ~77 μT from six samples) epoch lasting from at least 3.85 to 3.56 Ga, as originally recognized during the Apollo era. However, we now see that the dynamo subsequently declined precipitously to <~4 μT by 3.2 Ga. In particular, modern analyses of samples 3.3 Ga or younger suggest that most or all of the Apollo-era paleointensity analyses from this late epoch, which ranged up to apparent values of 20 μT, are only upper limits on the lunar field and therefore do not require a dynamo at this time. Finally, a recent analysis of a potentially very young lunar sample (*66*) hints that the dynamo may have nevertheless persisted in a weakened state (surface field of ~2 μT) until sometime after 3.3 Ga.

The global context of crustal magnetism

Coincident with these new paleointensity experiments, there have also been important recent investigations of the lunar crustal magnetic anomalies. As discussed above, a key finding from the Apollo-era measurements was the discovery of several intense magnetic anomalies, including those on the southern farside, that apparently require crustal materials with NRM larger than that of nearly all known Apollo samples (*35*). Global magnetic field maps from the Lunar Prospector spacecraft, which only became available 6 years ago (*8*, *29*, *68*), have now confirmed the unique size and intensity of the southern farside anomalies and their spatial correlation with antipodes of four, or perhaps even five (*69*), of the eight youngest basins. However, the acquisition of the first high-resolution global topography data in 1993 by the Clementine laser altimeter (*70*) led to the identification of another geologic association with the southern farside anomalies: They lie on the northern edge of the vast South Pole-Aitken (SPA) basin, the largest known impact crater on the Moon.

This discovery has led to two explanations for these anomalies as alternatives to the impact-plasma fields hypothesis. Both propose that rather than reflecting locally high B_{paleo}, they are a manifestation of materials with locally high χ_{TRM} that were magnetized in a dynamo field. The first of these proposals (*71*) identifies the anomalies with the inferred locations of <4.0 Ga basaltic dikes located within the SPA (Fig. 3). The assumed great vertical thickness (30 km) of these dikes enables them to produce the strong SPA anomalies despite the weak NRM of typical mare basalts.

The second proposal (*72*) emphasizes that the anomalies are in the expected locations of ejecta and impact melt derived from the SPA impactor (Fig. 3). The key advantage of this proposal is that typical chondritic impactors, which are far more Fe-rich, have χ_{TRM} ~100 and 10^4 times that of mare basalts and pristine feldspathic rocks, respectively. Therefore, deposition of relatively thin layers (perhaps just tens to thousands of meters thick) of such material should have fundamentally enhanced the magnetic properties on the surface. SPA ejecta, as well as that from more recent impacts, could also account for most of the other isolated crustal anomalies. However, thus far no evidence has yet been identified indicating that at least the surface layer (top ~30 cm) of the southern farside anomaly region is anomalously iron metal-rich (*73*).

Both of these new proposals require only dynamo fields rather than plasma fields to explain the magnetic anomalies. Yet more evidence for a dynamo comes from the recent identification of many anomalies within the interiors of most Nectarian (i.e., ~3.85 to 3.92 Ga) basins and some pre-Nectarian (i.e., more than ~3.92 Ga) basins (Fig. 3) (*74*–*76*). These impacts likely demagnetized any existing NRM, producing impact melt sheets that should have cooled from the kamacite Curie point to ambient lunar surface temperatures far more slowly (given their >1 km thicknesses, over a period of $>10^4$ years) than any impact-generated field. Therefore, these central basin anomalies likely require a steady field like that expected from a core dynamo during the Nectarian and pre-Nectarian periods. However, once again, the inferred TRM intensities (~1 A m^{-1}) exceed what is achievable with known endogenous lunar materials and may reflect the addition of Fe-rich impactor materials.

It has been suggested (*29*) that the apparent lack of anomalies in the centers of Imbrian basins (<1 nT at the surface, suggesting that the central impact melt layer has an NRM less than ~10^{-3} A m^{-1}) may indicate that the dynamo was no longer active by the time of their formation (i.e., after ~3.85 Ga). However, this proposal is not consistent with the strong evidence for a core dynamo from paleomagnetic analyses of 3.56 to 3.85 Ga (Imbrian-aged) Apollo 11 and 17 basalts (see above). In fact, the sample and orbital data sets are consistent if the composition

of the impact melt in these locations is similar to that of pristine feldspathic rocks or if the dynamo reversed during the cooling time of the impact melt (perhaps several My, assuming a 10-km thickness). Therefore, the lack of central basin anomalies does not exclude the existence of a dynamo during the Imbrian epoch. The strong anomalies observed in the older Nectarian basins (see above) could still be explained by impact melts with higher χ_{TRM} (although it is unclear why these would only occur in the older basins) or perhaps a longer reversal period during this earlier time.

Key unknowns about the lunar field

The new data make it clear that a dynamo once existed on the Moon. A central remaining mystery is now the nature of the physical mechanism(s) that powered it. The challenge is to find a dynamo-generation mechanism that can account for several outstanding features of the lunar paleointensity record. Foremost is the extremely high paleointensities (average of 77 μT) inferred for the period 3.56 to 3.85 Ga (table S6). Even though we estimate that these individual paleointensities each likely has a 2-SD uncertainty of a factor ~5 (tables S2 to S4), the mean value should only have a 2-SD uncertainty of factor ~2.2 if the samples formed in a field of constant intensity (table S6). Therefore, we consider that any successful dynamo model must predict a minimum paleointensity of ~35 μT for the high-field epoch, at least three times the maximum value estimated by the energy flux scaling (Fig. 6).

One possibility is that the lunar dynamo field strengths are underestimated by Eq. 2. This is conceivable given that this relationship was inferred from convective dynamo models only and, moreover, that these models operate in a highly viscous regime not found in planetary cores (*77*, *78*). Given the possible recent prediction by a precession MHD model of paleointensities up to 100 μT (*53*), this seems to be likely for at least some mechanical dynamos. Another less likely possibility is that Eq. 2 is applicable to the lunar dynamo, but one or more of the assumed parameter values are inaccurate. Although the values of many of these parameters are indeed uncertain, the form of Eq. 2 shows that B is only strongly dependent on R_c/R (and to a lesser extent, on d). For example, even simultaneously lowering the adiabatic power threshold to its minimal value of 0 W m^{-2} while increasing the dipolarity d to its maximal value of 1 would be insufficient to explain the paleointensities during the high-field epoch. Increasing the core size to an Earth-like value of about half the lunar radius could account for the high paleointensities, but this appears to be incompatible with the moment of inertia and bulk density data (*12*, *13*).

A related problem is presented by the order of magnitude decline in paleointensities during the period 3.56 to ~3.3 Ga. This is because no single lunar dynamo model has yet been able to account for such a rapid decline while simultaneously enabling the dynamo to persist in a weakened state (if we accept the evidence for a ~2-μT dynamo persisting until sometime between 3.3 and 1.3 Ga from sample 15498). If we assume that this rapid paleointensity decrease was a manifestation of a declining power source, then the energy flux scaling law (Eq. 2) predicts a rapid relative drop in paleointensities only when q_a approaches 0 (i.e., when q_d approaches q_t). Thus, unless the absolute magnitude of the time derivative of q_d rapidly dropped after 3.56 Ga, a given power source is likely to become insufficient to power dynamo action (i.e., to maintain $q_d > q_t$) for another 0.2 to 2 billion years after the paleointensities declined. A possible solution is to postulate at least two distinct dynamo mechanisms, one during the high-field epoch [perhaps with field intensities described by a relationship distinct from Eq. 2, as may be the case for the precession dynamo (*53*)], and a different dynamo mechanism afterwards. This is appealing because the apparent ~2-μT paleointensities during the later history of the dynamo are well predicted by scaling relationships for the core crystallization dynamo scenarios in late lunar history (*56*) (Fig. 6). A second speculative explanation is that only a single dynamo mechanism acted over the entire period from 4.2 to 1.3 Ga but that this dynamo was bistable, transitioning from a strong, dipole-dominated geometry to a weaker, multipolar state between 3.56 and 3.3 Ga. Bistable dynamos have been observed in dynamo models when the local Rossby number, which quantifies the ratio of inertial to Coriolis forces, is less than ~0.1 (*79*, *80*). Although the nature of the physical events that would have caused the Moon to transition from the strong to weak branch is uncertain, such transitions have been observed to occur spontaneously after reversals (*81*). Paleomagnetic records constraining the geometry of the lunar paleofield and its evolution in time would be an important test of this mechanism.

A final problem is the persistence of the lunar dynamo. The new evidence for a dynamo lasting until at least 3.3 Ga, and perhaps as late as 1.3 Ga, makes extreme demands on the longevity of the power source. At present, only thermochemical convection driven by core crystallization can supply such long-lived power, but that may open a new problem of explaining how the dynamo subsequently turned off.

Outlook

A diversity of geophysical and geochemical evidence now indicates that the Moon formed a ~1 to 4 wt % metallic core. This core was once advecting and generated a dynamo magnetic field. As far back in time as we have paleomagnetic records (4.25 Ga), it appears that the Moon had a dynamo, consistent with an early, partially molten body like that expected after a giant impact origin. The Moon is therefore a highly differentiated object like the terrestrial planets.

The surface field intensity was in the range of several tens of μT from at least 4.25 to 3.56 Ga but then declined precipitously (by at least an order of magnitude) between 3.56 and 3.19 Ga. The only mechanism that has yet been proposed to be capable of generating such high intensities in the early period is precession. The next major steps in the magnetic exploration of the Moon should be to obtain better constraints on global geophysical parameters (particularly the adiabatic heat flux and sulfur content of the core and a better understanding of the thermal evolution of the mantle) and accurate measurements of the field intensity in time. Furthermore, a determination of the time when the dynamo finally ceased would have major implications for constraining the power mechanism for the late dynamo. Eventual measurements of the absolute orientation of the lunar magnetic field from laboratory measurements of oriented samples and in situ measurements of lunar bedrock should provide transformative constraints on the geometry of the field, its time variability (reversal frequency and secular variation), and local and global-scale tectonics like crustal deformation and true polar wander.

REFERENCES AND NOTES

1. F. Hoyle, On the condensation of the planets. *Mon. Not. R. Astron. Soc.* **106**, 406–422 (1946). doi: 10.1093/mnras/106.5.406
2. M. E. Pritchard, D. J. Stevenson, in *Origin of the Earth and Moon*, R. M. Canup, K. Righter, Eds. (Univ. of Arizona Press, Tucson, AZ, 2000), pp. 179–196.
3. S. K. Runcorn, The formation of the lunar core. *Geochim. Cosmochim. Acta* **60**, 1205–1208 (1996). doi: 10.1016/0016-7037(96)00024-5
4. M. Fuller, S. M. Cisowski, Lunar paleomagnetism, in *Geomagnetism*, J. A. Jacobs, Ed. (Academic Press, Orlando, FL, 1987), vol. 2, pp. 307–455.
5. H. C. Urey, The origin and significance of the moon's surface. *Vistas Astron.* **2**, 1667–1680 (1956). doi: 10.1016/0083-6656(56)90091-5
6. G. P. Kuiper, On the origin of the lunar surface features. *Proc. Natl. Acad. Sci. U.S.A.* **40**, 1096–1112 (1954). doi: 10.1073/pnas.40.12.1096; pmid: 16589596
7. S. S. Dolginov, Y. G. Yeroshenko, L. N. Zhuzgov, N. V. Pushkov, Investigation of the magnetic field of the Moon. *Geomagn. Aeron.* **1**, 18 (1961).
8. M. E. Purucker, J. B. Nicholas, Global spherical harmonic models of the internal magnetic field of the Moon based on sequential and coestimation approaches. *J. Geophys. Res.* **115** (E12), E12007 (2010). doi: 10.1029/2010JE003650
9. A. L. Turkevich, E. J. Franzgrote, J. H. Patterson, Chemical analysis of the Moon at the Surveyor V landing site. *Science* **158**, 635–637 (1967). doi: 10.1126/science.158.3801.635; pmid: 17732956
10. J. A. Wood, J. S. Dickey, U. B. Marvin, B. N. Powell, Lunar anorthosites and a geophysical model of the moon. *Proc. Apollo 11 Lunar Sci. Conf.*, 965 (1970).
11. J. P. Gapcynski, W. T. Blackshear, R. H. Tolson, H. R. Compton, A determination of the lunar moment of inertia. *Geophys. Res. Lett.* **2**, 353–356 (1975). doi: 10.1029/GL002i008p00353
12. L. L. Hood, J. H. Jones, Geophysical constraints on lunar bulk composition and structure: A reassessment. *J. Geophys. Res.* **92**, E396–E410 (1987). doi: 10.1029/JB092iB04p0E396
13. S. Mueller, G. J. Taylor, R. J. Phillips, Lunar composition: A geophysical and petrological synthesis. *J. Geophys. Res.* **93** (B6), 6338 (1988). doi: 10.1029/JB093iB06p06338
14. S. M. Tikoo *et al.*, Decline of the lunar core dynamo. *Earth Planet. Sci. Lett.* (2014). doi: 10.1016/j.epsl.2014.07.010
15. Pristine lunar highlands rocks and lunar breccias contaminated with meteoritic debris can also contain minor quantities of the ferromagnetic minerals taenite (γ-$Fe_{1-x}Ni_x$ with x >~0.05), schreibersite [$(Fe,Ni)_3P$], and cohenite [$(Fe,Ni)_3C$]. To our knowledge, tetrataenite (γ"-$Fe_{0.5}Ni_{0.5}$) has never been identified in lunar rocks, likely because its formation is inhibited by their typically fast cooling rates (>1000°C My^{-1}).
16. There have been a number of attempts to recover the absolute paleodirections of lunar fields from Apollo samples using analyses of magnetic anisotropy fabrics and from the lunar crust using spacecraft field maps (table S1). However, the paleohorizontal indicators in the Apollo samples are indirect and analysis of the spacecraft data are limited by the fundamental nonuniqueness of inferring magnetization from

magnetic field measurements, the likelihood of multiple magnetization components, and the lack of radiometric age constraints. This may explain why the inferred positions of the lunar geomagnetic pole are scattered. Nevertheless, the clustering of some poles hints at the possibility of a dipolar field and even apparent polar wander.
17. M. A. Wieczorek *et al*., The constitution and structure of the lunar interior. *Rev. Mineral. Geochem.* **60**, 221–364 (2006). doi: 10.2138/rmg.2006.60.3
18. K. Lawrence, C. Johnson, L. Tauxe, J. S. Gee, Lunar paleointensity measurements: Implications for lunar magnetic evolution. *Phys. Earth Planet. Inter.* **168**, 71–87 (2008). doi: 10.1016/j.pepi.2008.05.007
19. For a selenocentric axial dipole, the surface field intensity varies with latitude λ as: $B \propto (1+3\sin^2\lambda)^{1/2}$. For the latitudes of the Apollo landing sites, which ranged from 0.7° (Apollo 11) up to 26.1° (Apollo 15), the surface field is therefore only expected to vary by 26% if the dipole moment was constant.
20. G. W. Pearce, W. A. Gose, D. W. Strangway, Magnetic studies on Apollo 15 and 16 lunar samples. *Proc. Lunar Sci. Conf. 4th* **3**, 3045 (1973).
21. N. Sugiura, D. W. Strangway, Comparisons of magnetic paleointensity methods using a lunar sample. *Proc. Lunar Planet. Sci. Conf. 11th*, 1801 (1980).
22. U. R. Christensen, Dynamo scaling laws and applications to the planets. *Space Sci. Rev.* **152**, 565–590 (2010). doi: 10.1007/s11214-009-9553-2
23. C. A. Dwyer, D. J. Stevenson, F. Nimmo, A long-lived lunar dynamo driven by continuous mechanical stirring. *Nature* **479**, 212–214 (2011). doi: 10.1038/nature10564
24. R. C. Weber, P.-Y. Lin, E. J. Garnero, Q. Williams, P. Lognonné, Seismic detection of the lunar core. *Science* **331**, 309–312 (2011). doi: 10.1126/science.1199375; pmid: 21212323
25. W. Konrad, T. Spohn, Thermal history of the Moon: Implications for an early core dynamo and post-accretional magmatism. *Adv. Space Res.* **19**, 1511–1521 (1997). doi: 10.1016/S0273-1177(97)00364-5
26. D. R. Stegman, A. M. Jellinek, S. A. Zatman, J. R. Baumgardner, M. A. Richards, An early lunar core dynamo driven by thermochemical mantle convection. *Nature* **421**, 143–146 (2003). doi: 10.1038/nature01267; pmid: 12520295
27. S. K. Runcorn, The ancient lunar core dynamo. *Science* **199**, 771–773 (1978). doi: 10.1126/science.199.4330.771; pmid: 17836293
28. M. Fuller, Lunar magnetism: A retrospective view of the Apollo sample magnetic studies. *Phys. Chem. Earth* **23**, 725–735 (1998). doi: 10.1016/S0079-1946(98)00083-4
29. D. S. Mitchell *et al*., Global mapping of lunar crustal magnetic fields by Lunar Prospector. *Icarus* **194**, 401–409 (2008). doi: 10.1016/j.icarus.2007.10.027
30. L. L. Hood, N. A. Artemieva, Antipodal effects of lunar basin-forming impacts: Initial 3D simulations and comparisons with observations. *Icarus* **193**, 485–502 (2008). doi: 10.1016/j.icarus.2007.08.023
31. D. A. Crawford, P. H. Schultz, Electromagnetic properties of impact-generated plasma, vapor and debris. *Int. J. Impact Eng.* **23**, 169–180 (1999). doi: 10.1016/S0734-743X(99)00070-6
32. I. Garrick-Bethell, B. P. Weiss, D. L. Shuster, J. Buz, Early lunar magnetism. *Science* **323**, 356–359 (2009). doi: 10.1126/science.1166804; pmid: 19150839
33. J. Gattacceca *et al*., Can the lunar crust be magnetized by shock: Experimental groundtruth. *Earth Planet. Sci. Lett.* **299**, 42–53 (2010). doi: 10.1016/j.epsl.2010.08.011
34. R. P. Lin, K. A. Anderson, L. L. Hood, Lunar surface magnetic field concentrations antipodal to young large impact basins. *Icarus* **74**, 529–541 (1988). doi: 10.1016/0019-1035(88)90119-4
35. L. L. Hood, P. J. Coleman JrC. T. Russell, D. E. Wilhems, Lunar magnetic anomalies detected by the Apollo substatellite magnetometers. *Phys. Earth Planet. Inter.* **20**, 291–311 (1979). doi: 10.1016/0031-9201(79)90052-9
36. D. J. Stevenson, Planetary magnetic fields: Achievements and prospects. *Space Sci. Rev.* **152**, 651–664 (2010). doi: 10.1007/s11214-009-9572-z
37. A. S. Konopliv *et al*., Improved gravity field of the moon from lunar prospector. *Science* **281**, 1476–1480 (1998). doi: 10.1126/science.281.5382.1476; pmid: 9727968
38. L. L. Hood, D. L. Mitchell, R. P. Lin, M. H. Acuna, A. B. Binder, Initial measurements of the lunar induced magnetic dipole moment using Lunar Prospector magnetometer data. *Geophys. Res. Lett.* **26**, 2327–2330 (1999). doi: 10.1029/1999GL900487
39. H. Shimizu, M. Matsushima, F. Takahashi, H. Shibuya, H. Tsunakawa, Constraint on the lunar core size from electromagnetic sounding based on magnetic field observations by an orbiting satellite. *Icarus* **222**, 32–43 (2013). doi: 10.1016/j.icarus.2012.10.029
40. J. G. Williams, D. H. Boggs, C. F. Yoder, J. T. Ratcliff, J. O. Dickey, Lunar rotational dissipation in solid body and molten core. *J. Geophys. Res.* **106** (E11), 27933 (2001). doi: 10.1029/2000JE001396
41. R. F. Garcia, J. Gagnepain-Beyneix, S. Chevrot, P. Lognonné, Very preliminary reference Moon model. *Phys. Earth Planet. Inter.* **188**, 96–113 (2011). doi: 10.1016/j.pepi.2011.06.015
42. F. Nimmo, Thermal and compositional evolution of the core. *Treatise on Geophysics* **9**, 217–241 (2007). doi: 10.1016/B978-044452748-6/00147-4
43. Throughout this paper, we assume that the lunar core has an adiabatic threshold of 5 mW m^{-2} for the purposes of comparing the predicted relative lifetimes for various thermal convection dynamo models. Choice of a different threshold may change the absolute dynamo lifetimes.
44. M. Laneuville, M. A. Wieczorek, D. Breuer, N. Tosi, Asymmetric thermal evolution of the Moon. *J. Geophys. Res.* **118**, 1435–1452 (2013). doi: 10.1002/jgre.20103
45. E. H. Hauri, T. Weinreich, A. E. Saal, M. C. Rutherford, J. A. Van Orman, High pre-eruptive water contents preserved in lunar melt inclusions. *Science* **333**, 213–215 (2011). doi: 10.1126/science.1204626; pmid: 21617039
46. A. J. Evans, M. T. Zuber, B. P. Weiss, S. M. Tikoo, A wet, heterogeneous lunar interior: Lower mantle and core dynamo evolution. *J. Geophys. Res.* **119**, 1061–1077 (2014). doi: 10.1002/2013JE004494
47. F. Takahashi, H. Tsunakawa, Thermal core-mantle coupling in an early lunar dynamo: Implications for a global magnetic field and magnetosphere of the early Moon. *Geophys. Res. Lett.* **36**, L24202 (2009). doi: 10.1029/2009GL041221
48. M. Le Bars, M. A. Wieczorek, O. Karatekin, D. Cébron, M. Laneuville, An impact-driven dynamo for the early Moon. *Nature* **479**, 215–218 (2011). doi: 10.1038/nature10565; pmid: 22071767
49. D. Cébron, R. Hollerbach, Tidally driven dynamos in a rotating sphere. *Astrophys. J.* **789**, L25 (2014). doi: 10.1088/2041-8205/789/1/L25
50. C. Suavet *et al*., Persistence and origin of the lunar core dynamo. *Proc. Natl. Acad. Sci. U.S.A.* **110**, 8453–8458 (2013). doi: 10.1073/pnas.1300341110; pmid: 23650386
51. R. Smoluchowski, Magnetism of the moon. *Moon* **7**, 127–131 (1973). doi: 10.1007/BF00578811
52. J. Meyer, J. Wisdom, Precession of the lunar core. *Icarus* **211**, 921–924 (2011). doi: 10.1016/j.icarus.2010.09.016
53. B. Y. Tian, S. Stanley, S. M. Tikoo, B. P. Weiss, *AGU Fall Meeting*, abstract GP54A-04 (2014).
54. N. Zhang, E. M. Parmentier, Y. Liang, A 3-D numerical study of the thermal evolution of the Moon after cumulate mantle overturn: The importance of rheology and core solidification. *J. Geophys. Res.* **118**, 1789 (2013). doi: 10.1002/jgrd.50279
55. N. Rai, W. van Westrenen, Lunar core formation: New constraints from metal–silicate partitioning of siderophile elements. *Earth Planet. Sci. Lett.* **388**, 343–352 (2014). doi: 10.1016/j.epsl.2013.12.001
56. M. Laneuville *et al*., A long-lived lunar dynamo powered by core crystallization. *Earth Planet. Sci. Lett.* **401**, 251–260 (2014). doi: 10.1016/j.epsl.2014.05.057
57. Q. Williams, Bottom-up versus top-down solidification of the cores of small solar system bodies: Constraints on paradoxical cores. *Earth Planet. Sci. Lett.* **284**, 564–569 (2009). doi: 10.1016/j.epsl.2009.05.019
58. Z. Jing *et al*., Sound velocity of Fe–S liquids at high pressure: Implications for the Moon's molten outer core. *Earth Planet. Sci. Lett.* **396**, 78–87 (2014). doi: 10.1016/j.epsl.2014.04.015
59. I. Garrick-Bethell, B. P. Weiss, Lunar Science Forum abstract, https://lunarscience.nasa.gov/lsf2013/content/ian-garrick-bethell-new-lunar-magnetic-field-paleointensity-estimate-troctolite-76535 (2013).
60. E. K. Shea *et al*., A long-lived lunar core dynamo. *Science* **335**, 453–456 (2012). doi: 10.1126/science.1215359; pmid: 22282809
61. C. Cournède, J. Gattacceca, P. Rochette, Magnetic study of large Apollo samples: Possible evidence for an ancient centered dipolar field on the Moon. *Earth Planet. Sci. Lett.* **331-332**, 31–42 (2012). doi: 10.1016/j.epsl.2012.03.004
62. S. M. Tikoo *et al*., Magnetic fidelity of lunar samples and implications for an ancient core dynamo. *Earth Planet. Sci. Lett.* **337-338**, 93–103 (2012). doi: 10.1016/j.epsl.2012.05.024
63. J. Buz, Recent lunar magnetism, thesis, Massachusetts Institute of Technology, Cambridge, MA; http://dspace.mit.edu/handle/1721.1/69470 (2011).
64. D. Hemingway, I. Garrick-Bethell, Magnetic field direction and lunar swirl morphology: Insights from Airy and Reiner Gamma. *J. Geophys. Res.* **117** (E10), E10012 (2012). doi: 10.1029/2012JE004165
65. B. J. Anderson *et al*., The magnetic field of Mercury. *Space Sci. Rev.* **152**, 307–339 (2010). doi: 10.1007/s11214-009-9544-3
66. S. M. Tikoo, B. P. Weiss, D. L. Shuster, M. D. Fuller, *Lunar Planet Sci. Conf. XLV*, abstract no. 1972 (2014).
67. A. L. Fagan, K. H. Joy, D. D. Bogard, D. A. Kring, Ages of globally distributed lunar paleoregoliths and soils from 3.9 Ga to the present. *Earth Moon Planets* **112**, 59–71 (2014). doi: 10.1007/s11038-014-9437-7
68. N. C. Richmond, L. L. Hood, A preliminary global map of the vector lunar crustal magnetic field based on Lunar Prospector magnetometer data. *J. Geophys. Res.* **113** (E2), E02010 (2008). doi: 10.1029/2007JE002933
69. L. L. Hood, N. C. Richmond, P. D. Spudis, Origin of strong lunar magnetic anomalies: Further mapping and examinations of LROC imagery in regions antipodal to young large impact basins. *J. Geophys. Res.* **118**, 1265–1284 (2013). doi: 10.1002/jgre.20078
70. M. T. Zuber, D. E. Smith, F. G. Lemoine, G. A. Neumann, The shape and internal structure of the moon from the Clementine mission. *Science* **266**, 1839–1843 (1994). doi: 10.1126/science.266.5192.1839; pmid: 17737077
71. M. E. Purucker, J. W. Head III, L. Wilson, Magnetic signature of the lunar South Pole-Aitken basin: Character, origin, and age. *J. Geophys. Res.* **117** (E5), E05001 (2012). doi: 10.1029/2011JE003922
72. M. A. Wieczorek, B. P. Weiss, S. T. Stewart, An impactor origin for lunar magnetic anomalies. *Science* **335**, 1212–1215 (2012). doi: 10.1126/science.1214773; pmid: 22403388
73. J. T. S. Cahill, D. J. Lawrence, J. J. Hagerty, R. L. Klima, D. T. Blewett, *Lunar Planet Sci. Conf. XLV*, abstract no. 2253 (2014).
74. L. L. Hood, Central magnetic anomalies of Nectarian-aged lunar impact basins: Probable evidence for an early core dynamo. *Icarus* **211**, 1109–1128 (2011). doi: 10.1016/j.icarus.2010.08.012
75. J. S. Halekas, R. P. Lin, D. L. Mitchell, Magnetic fields of lunar multi-ring impact basins. *Meteorit. Planet. Sci.* **38**, 565–578 (2003). doi: 10.1111/j.1945-5100.2003.tb00027.x
76. L. L. Hood, H. Tsunakawa, P. D. Spudis, *Lunar Planet Sci. Conf. XLV*, abstract no. 1482 (2014).
77. L. Oruba, E. Dormy, Predictive scaling laws for spherical rotating dynamos. *Geophys. J. Int.* **198**, 828–847 (2014). doi: 10.1093/gji/ggu159
78. E. M. King, B. A. Buffett, Flow speeds and length scales in geodynamo models: The role of viscosity. *Earth Planet. Sci. Lett.* **371-372**, 156–162 (2013). doi: 10.1016/j.epsl.2013.04.001
79. T. Gastine, L. Duarte, J. Wicht, Dipolar versus multipolar dynamos: The influence of the background density stratification. *Astron. Astrophys.* **546**, A19 (2012). doi: 10.1051/0004-6361/201219799
80. R. D. Simitev, F. H. Busse, Bistable attractors in a model of convection-driven spherical dynamos.. *Phys. Scr.* **86**, 018409 (2012). doi: 10.1088/0031-8949/86/01/018409
81. G. Glatzmaier, R. S. Coe, L. Hongre, P. H. Roberts, The role of the Earth's mantle in controlling the frequency of geomagnetic reversals. *Nature* **401**, 885–890 (1999). doi: 10.1038/44776
82. I. Garrick-Bethell, M. T. Zuber, Elliptical structure of the lunar South Pole-Aitken basin. *Icarus* **204**, 399–408 (2009). doi: 10.1016/j.icarus.2009.05.032
83. D. E. Smith *et al*., Initial observations from the Lunar Orbiter Laser Altimeter (LOLA). *Geophys. Res. Lett.* **37**, L18204 (2010). doi: 10.1029/2010GL043751

ACKNOWLEDGMENTS

We thank the NASA Lunar Advanced Science and Exploration Program, the NASA Solar System Exploration Research Virtual Institute, the Massachusetts Institute of Technology International Science and Technology Initiatives Global Seed Fund, and the Miller Institute for Basic Research in Science for support. We thank M. Fuller, M. Laneuville, M. Wieczorek, I. Garrick-Bethell, A. Scheinberg, J. Buz, S. Stanley, and B. Tian for sharing their unpublished manuscripts and thoughts with us. We also thank L. Hood, R. Harrison, and an anonymous referee for thoughtful reviews; J. Gattacceca, C. Suavet, B. Buffett, and M. Purucker for helpful discussions; and B. Carbone for administrative help.

SUPPLEMENTARY MATERIALS

www.sciencemag.org/content/346/6214/1246753/suppl/DC1
Tables S1 to S7

10.1126/science.1246753

RESEARCH ARTICLE SUMMARY

CELL COMPETITION

An ancient defense system eliminates unfit cells from developing tissues during cell competition

S. N. Meyer,[1*] M. Amoyel,[2*†] C. Bergantiños,[2*] C. de la Cova,[2] C. Schertel,[1] K. Basler,[1‡] L. A. Johnston[2‡]

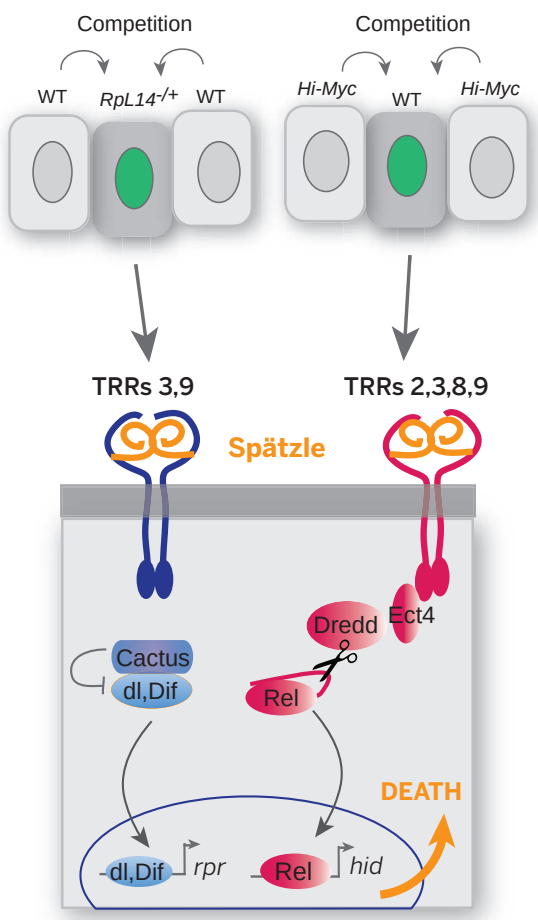
INTRODUCTION: The function of a tissue and, therefore, the health of an organism can be compromised by the presence of mutant or unfit cells. Cell competition is a mechanism that has evolved to prevent such cells from contributing to tissues. Two widely studied models of cell competition are *Myc*-induced supercompetition, whereby cells with increased levels of Myc outcompete and actively kill neighboring wild-type cells, and competition in which wild-type cells eliminate cells carrying a *Minute* mutation, a class of mutants in *Drosophila* affecting ribosomal protein genes. *Minute* cells are viable, but when surrounded by wild-type cells they are eliminated by apoptosis. Relative cell vigor or fitness is believed to be a critical feature assessed in cell competition, but the mechanisms that underlie the recognition and elimination of the less-fit "loser" cell remain mysterious.

RATIONALE: The recognition and elimination of unfit or mutant cells in cell competition is reminiscent of the detection of pathogens by the innate immune system. In *Drosophila*, the Toll and immune deficiency (IMD) signaling pathways govern the innate immune response to a broad range of pathogens and activate the NFκB transcription factor homologs Relish (Rel), Dorsal (dl), or Dorsal-related immunity factor (Dif). The conceptual similarities between innate immunity and cell competition led us to investigate whether the Toll and IMD pathways were required for cell competition in *Drosophila* wing discs.

RESULTS: Analysis of both *Myc*-induced and *Minute*-induced cell competition revealed requirements for two related but distinct cohorts of components from the IMD and Toll pathways. Both signaling cohorts required the extracellular ligand Spätzle and noncanonical Toll-related receptors (TRRs) and led to elimination of the less-fit loser cells by inducing NFκB-dependent activation of proapoptotic genes. However, our analysis uncovered interesting differences between the signaling module deployed in each competitive context. In *Myc*-induced competition, elimination of wild-type loser cells required four of the nine TRRs encoded in the *Drosophila* genome (*Toll-2*, *Toll-3*, *Toll-8*, and *Toll-9*) in nonredundant roles. By contrast, elimination of *RpL14–/+* cells in *Minute*-induced competition required only *Toll-3* and *Toll-9*. Furthermore, the NFκB factor activated downstream of the TRRs was also context-dependent. Signal transduction within wild-type loser cells led to selective activation of Relish, whereas the death of *RpL14–/+* loser cells in *Minute*-induced competition required Dorsal and Dif. These results suggest that signaling from the different TRR subsets influenced which NFκB factor was activated. Finally, although in each competitive context apoptosis of the relatively less-fit cells was induced, the specific death-inducing gene expressed was determined by the specifically activated NFκB factor.

ON OUR WEB SITE

Read the full article at http://dx.doi.org/10.1126/science.1258236



TRR/NFκB modules mediate the elimination of loser cells in two distinct contexts of cell competition. (**Top**) The relatively less-fit cells in mosaic tissues (green) are eliminated via cell competition. (**Bottom**) The competitive context influences the TRR/NFκB signaling module that is triggered in the loser cells. This module then selectively activates a proapoptotic inducer that kills the loser cells.

CONCLUSION: In two genetically distinct contexts of cell competition, the ancient innate immune defense response system is activated and drives the elimination of the cells perceived as relatively less fit. In each competition paradigm, different signaling modules are employed, suggesting that the genetic identity of the competing cell populations influences the pathway that is activated. Our results thus provide evidence for evolutionary adaptation of TRR-NFκB signaling modules in an organismal surveillance system that measures internal tissue fitness rather than external pathogenic stimuli. ■

RELATED ITEMS IN *SCIENCE*

G. Morata, L. Ballesteros-Arias, Death to the losers. *Science* **346**, 1181–1182 (2014).

[1]Institute of Molecular Life Sciences, University of Zurich, Zurich, Switzerland. [2]Department of Genetics and Development, Columbia University, New York, NY 10032, USA.
*These authors contributed equally to this work.
†Present address: Department of Biochemistry and Molecular Pharmacology, New York University School of Medicine, New York, NY 10016, USA.
‡Corresponding author. E-mail: konrad.basler@imls.uzh.ch (K.B.); lj180@columbia.edu (L.A.J.)
Cite this article as S. N. Meyer *et al.* *Science* **346**, 1258236 (2014). DOI: 10.1126/science.1258236

Downloaded from www.sciencemag.org on December 5, 2014

Published by AAAS

RESEARCH ARTICLE

CELL COMPETITION

An ancient defense system eliminates unfit cells from developing tissues during cell competition

S. N. Meyer,[1]* M. Amoyel,[2]*† C. Bergantiños,[2]* C. de la Cova,[2] C. Schertel,[1] K. Basler,[1]‡ L. A. Johnston[2]‡

Developing tissues that contain mutant or compromised cells present risks to animal health. Accordingly, the appearance of a population of suboptimal cells in a tissue elicits cellular interactions that prevent their contribution to the adult. Here we report that this quality control process, cell competition, uses specific components of the evolutionarily ancient and conserved innate immune system to eliminate *Drosophila* cells perceived as unfit. We find that Toll-related receptors (TRRs) and the cytokine Spätzle (Spz) lead to NFκB-dependent apoptosis. Diverse "loser" cells require different TRRs and NFκB factors and activate distinct pro-death genes, implying that the particular response is stipulated by the competitive context. Our findings demonstrate a functional repurposing of components of TRRs and NFκB signaling modules in the surveillance of cell fitness during development.

Successful development of multicellular animals requires cooperative cell-cell interactions that ensure tissue integrity. Mechanisms exist to enforce this behavior (*1*–*4*). One such mechanism monitors genetic identity so that potentially noncooperating mutant cells are prevented from contributing to the tissue (*5*, *6*). How genetic disparities are recognized is unknown, but evidence points to cell vigor or fitness as a critical component. For instance, mutation of genes encoding ribosomal proteins (Rp), known in *Drosophila* as *Minute* mutants, or of the Myc transcriptional regulator, which controls numerous genes involved in metabolism and growth, can occur without inherently compromising cell viability. However, when surrounded by wild-type (WT) cells, the mutant cells are recognized and actively eliminated (*7*–*10*). This cell selection process, known in *Drosophila* and in mammals as cell competition, promotes tissue fitness by recognizing and eliminating genetically different or suboptimal somatic cells. Supercompetition, a variation of cell competition, occurs when cells with activated oncogenes like Myc compete with neighboring WT cells (*11*–*18*). Short-range signaling between Myc supercompetitor cells and WT cells instructs the latter to die, whereas the supercompetitors "win" and colonize the tissue. Cell competition can therefore be homeostatic (WT versus unfit cells) or potentially pathologic (supercompetitors versus WT cells, which may promote cancer). Myc-regulated cell competition has been documented in *Drosophila* wing imaginal discs and among mouse epiblast cells, where fluctuations in Myc expression precede the transition of cells to a more limited developmental potential and correlate with survival (*9*, *11*, *14*, *19*).

The Toll signaling pathway was first identified as a developmental regulatory module that patterns the embryonic dorsoventral axis in *Drosophila* but was subsequently recognized to also function in host defense against infection. Toll-like receptors and NFκB transcription factors are key signaling and transcriptional mediators of the ancient and broadly conserved innate immune recognition system activated in response to nonself (e.g., microbial infection) or altered-self cells (e.g., viruses, cancer) (*20*–*24*). The early appearance of these factors in metazoan evolution and their conserved use in altered-self recognition in a process akin to cell competition led us to probe whether they mediate the response to mutant or otherwise compromised cells in developing tissues. We report here that components of the innate immune system function to eliminate cells recognized as unfit during cell competition.

Mutations in the Toll and IMD pathways prevent Myc-induced cell competition

To test for involvement of innate immune factors in cell competition, we used a simple genetic assay in wing discs for Myc-induced competition, wherein cells constitutively express a Myc transgenic FRT cassette (>*Myc*>), increasing the expression of Myc ~1.5-fold above the endogenous level (*11*, *13*). Removal of this cassette via Flp/FRT-mediated recombination generates clones of WT cells and concomitantly allows expression of the Gal4 transcriptional activator and the Gal4-regulated upstream activating sequence–green fluorescent protein (UAS-GFP) (Fig. 1A). Cells in these clones are WT for Myc expression but because they are surrounded by cells that retain the Myc cassette, they become "losers" and are competitively eliminated via apoptosis. Within 24 hours of clone induction, cell death increased within the loser clones (fig. S1, A and B). Over time, this led to a significant reduction in clone size relative to control clones generated in a noncompetitive environment (Fig. 1B, green versus gray bars, respectively) (*11*, *12*, *25*). Genetic studies have shown that in the absence of the proapoptotic factor, Hid, WT loser clones grow to the same size as controls, implicating Hid as a critical mediator of loser cell elimination (*11*, *12*, *25*).

In *Drosophila*, two signaling pathways and three NFκB family members govern the innate immune response. Infection by Gram-negative bacteria induces the immune deficiency (IMD) pathway (*26*, *27*), which activates the NFκB homolog Relish (Rel) (*28*), whereas the Toll pathway is activated upon infection by Gram-positive bacteria and fungi and leads to activation of the other NFκB homologs Dorsal (dl) and Dorsal-related immunity factor (Dif) (Fig. 1D) (*29*, *30*). We induced loser clones in genetic backgrounds mutant for genes in the IMD or Toll pathways and measured their size after a defined period of time. Loss of the receptor PGRP-LC, the adaptor BG4/FADD, Dredd, the apical caspase implicated in Rel cleavage and activation, and Rel itself suppressed the loss of loser cells and increased the size of the clones (Fig. 1B), indicating that their competitive elimination was blocked (*11*, *12*, *25*). However, mutations in *key* (*kenny*, encoding IKK-γ), *ird5* (*immune response deficient-5*, encoding IKK-β), and *dTak1*, all necessary for infection-induced Rel activation, did not prevent elimination of loser cells (Fig. 1B). Because dTak1 is a homolog of transforming growth factor–β activated kinase and is an activator of Jun N-terminal kinase (JNK) signaling (*31*), this result is consistent with the previous demonstration that, although activated, JNK is not essential for Myc-induced competition (*11*). Loss of *imd*, encoding a protein that links FADD and Dredd to PGRP-LC, also did not prevent loser cell elimination (Fig. 1B). From the Toll pathway, Myc-induced competition was not suppressed in genetic backgrounds that lacked the NFκB factors Dorsal or Dif, the kinase Pelle, or the Toll/interleukin-1 receptor (TIR)–domain containing adaptor MyD88 (Fig. 1B). By contrast, mutation of *Ect4*, which encodes the TIR-domain protein dSarm, completely suppressed loser cell elimination without affecting the growth of control clones (Fig. 1C). *tube* encodes an IRAK-4 homolog in the Toll pathway (*32*), and heterozygotes displayed dominant genetic interactions with *Rel* that were specific to the competitive context (table S1), suggesting that Tube also functions during cell competition.

Activation of innate immune pathways in cell competition involves noncanonical receptors and the ligand Spz

Loser cells were also not eliminated in Spätzle (*spz*) mutant backgrounds (Fig. 1B and table S1). Spz is a secreted cytokine and a ligand for the

[1]Institute of Molecular Life Sciences, University of Zurich, Zurich, Switzerland. [2]Department of Genetics and Development, Columbia University, New York, NY 10032, USA.
*These authors contributed equally to this work. †Present address: Department of Biochemistry and Molecular Pharmacology, New York University School of Medicine, New York, NY 10016, USA.
‡Corresponding author. E-mail: konrad.basler@imls.uzh.ch (K.B.); lj180@columbia.edu (L.A.J.)

Toll receptor in innate immunity and in embryonic dorsoventral patterning (*30*, *33*–*35*). However, RNA interference (RNAi)–mediated knockdown of *Toll* itself (*Toll-1*) had little effect on competition (fig. S2C). The *Drosophila* genome encodes nine Toll-related receptors (TRRs), but most are poorly characterized. Notably, loss of *Toll-2 (18wheeler)*, *Toll-3 (Mst-Prox)*, *Toll-8* (*tollo*), and *Toll-9* blocked elimination of the loser cells and significantly increased clone size (Fig. 1, E and F, and fig. S2A) but did not affect growth of control clones (Fig. 1E and fig. S2A). RNAi-mediated knockdown specifically in the loser population indicated that the receptors were required within the loser cells (fig. S2A). By contrast, RNAi directed against Toll-4, -5, and -7 had little effect on competition (fig. S2C).

These observations suggest that a cohort of components of the IMD pathway—PGRP-LC, Fadd, Dredd, and Rel—could be united in a functional circuit with four noncanonical TRRs, the Toll ligand Spz, the Tube adaptor, and the TIR domain protein dSarm to eliminate WT loser cells in response to Myc-induced competition. *Toll-8 (tollo)* mutants were especially efficient at suppressing the loser fate (Figs. 1, E and F, and 2, A and B). Consistent with this, Toll-8ΔLRR, an activating truncation of Toll fused to Toll-8 transmembrane and intracellular domains (*36*), enhanced competition when expressed in loser cells, without altering control clones (fig. S2B). This outcome suggests that Toll-8 activity is specific to the competitive context and implies that factors not present under noncompetitive conditions are also required. It is possible that if, as our data suggest, a Toll-8–dependent signaling pathway leads to death of loser cells, it requires heterotypic interactions with Toll-2, Toll-3, or Toll-9. Notably, expression of Toll-2, Toll-8, and Toll-9 mRNA was down-regulated in Myc-expressing S2 cells (fig. S2D), which could bias signaling to the loser cells.

Transcriptional up-regulation of *hid* via the nuclear mediator Rel

Based on the TRR signaling components required for the elimination of WT loser cells, we postulated that Rel could be the nuclear mediator of their death. Consistent with this idea, loser clones generated in a *Rel* mutant background contained many fewer dying cells than

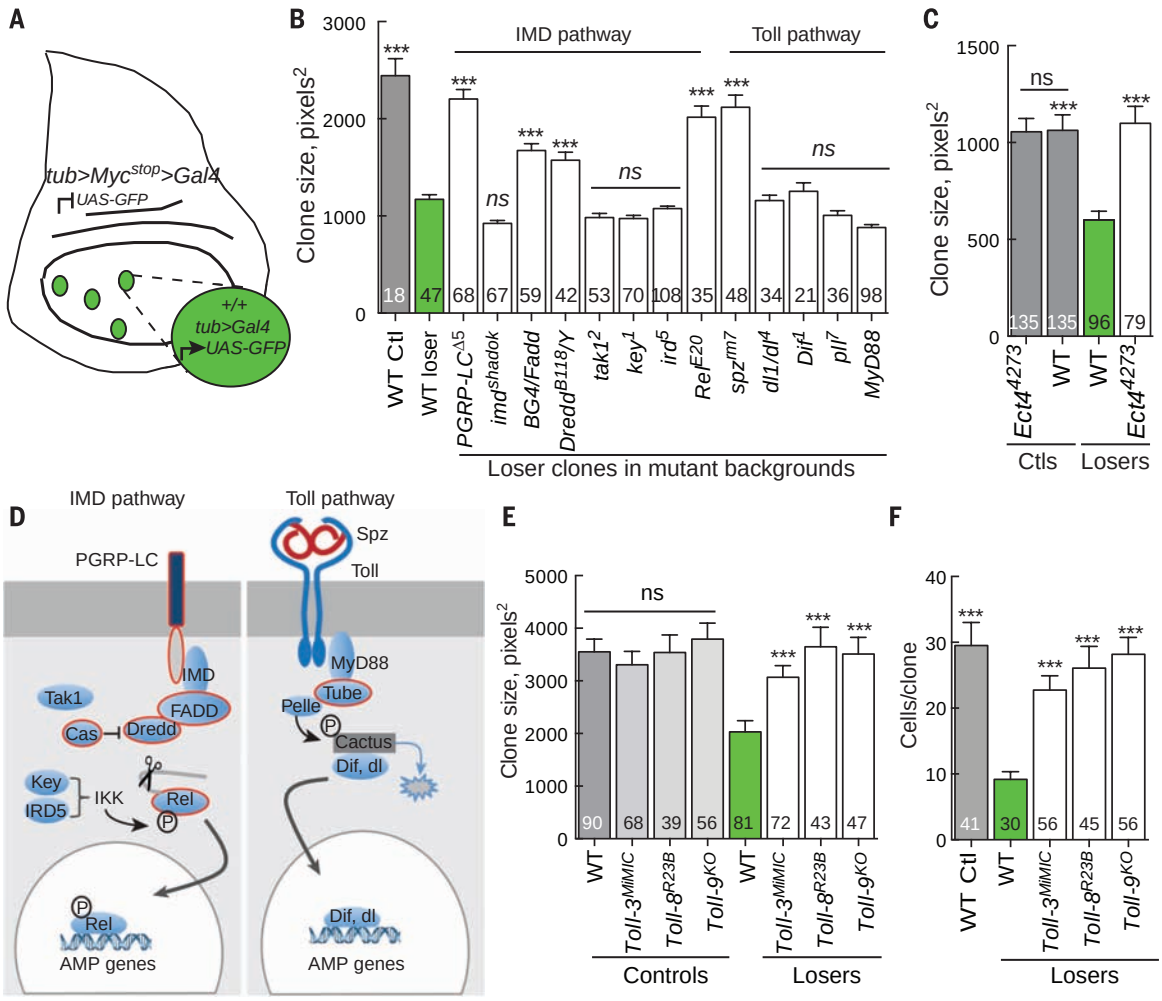


Fig. 1. Select components of the IMD and Toll pathways are required to eliminate WT loser cells in Myc-induced cell competition. (**A**) Schematic of the assay for Myc-induced cell competition. See the materials and methods section for details. (**B**) Mean clone size in wing discs of the indicated genotype. In all figures, gray bars show the mean size of control clones (generated in the absence of cell competition), green bars show the mean size of loser clones in WT wing discs, and white bars show the mean size of loser clones in wing discs of the indicated genotype. The number of clones scored for each genotype is indicated in each graph. Mutations in *PGRP-LC*, *BG4/FADD*, *Dredd*, and *Rel* of the IMD pathway and mutations in the Toll pathway gene *spz* suppress elimination of the loser cells, resulting in a significant increase in clone growth. Mutations in most genes in the Toll pathway (including *dl*, *Dif*, and *MyD88*) encoding a TIR-domain protein do not alter the outcome of WT loser cells. (**C**) The TIR-domain protein Ect4/dSarm is required to eliminate WT loser cells in wing discs. The *Ect4*^{4273} mutant does not affect control wing disc clones but completely suppresses elimination of loser cells. (**D**) Simplified schematic of the *Drosophila* innate immune pathways. In the IMD pathway, signaling from the transmembrane protein PGRP-LC, IMD/RIP, FADD, and DREDD/Caspase-8 causes endo-proteolytic cleavage of Relish (Rel), removing an autoinhibitory domain and allowing the Rel-homology domain (RHD/Rel-68) to translocate to the nucleus and activate AMP genes. In the Toll pathway, binding of Spz to the Toll receptor recruits a complex consisting of Myd88, Tube/IRAK-4, and Pelle/IRAK-1, which phosphorylates Cactus/IκB and targets it for degradation. This releases Dorsal or Dif for activation of distinct AMP genes in the nucleus. Components outlined in red denote those also required for Myc-induced cell competition. P, phosphorylation. (**E** and **F**). Null mutations in *Toll-3*, *Toll-8*, or *Toll-9* suppress elimination of loser cells, increasing loser clone size (E) and cell number per clone (F), but do not alter control clones. Error bars in this figure are SEM. All *P* values are relative to WT loser clones except in (E) at left—they are relative to WT control clones. ***$P < 0.001$. ns, not significant (Mann-Whitney test).

WT loser clones (Fig. 2, A and B). To determine whether Rel functioned within the loser cells, we expressed *Rel*-RNAi (or *Rel*-RNAi and Dicer-2 to increase RNAi efficiency) specifically in that population. Indeed, *Rel*-RNAi suppressed the loss of loser cells, consistent with a role as a regulator of their fate (Fig. 2C). Moreover, Rel's effect on the cells was specific to the competitive condition, because neither a *Rel* mutant nor *Rel*-RNAi altered growth of control clones (Fig. 2C and fig. S3A). Rel undergoes proteolytic cleavage by the caspase Dredd after pathogenic infection, which releases an active, N-terminal Rel68 fragment and allows its nuclear translocation (*37*). Null alleles of *Dredd* suppressed the elimination of loser cells (Fig. 2D), as did overexpression of the Dredd inhibitor Caspar (Casp) (*38*) in loser cells, whereas mutants of *casp* enhanced their loss (fig. S3, B and C). Again, these treatments did not affect cells in a noncompetitive environment and thus were specific to the competitive context. In addition, dominant genetic interactions between *Dredd* and *Rel* compound heterozygotes blocked elimination of loser cells as effectively as complete loss of *Dredd* (Fig. 2D). Thus, loser cells have heightened Dredd activity, which could lead to Rel activation during cell competition. *Dredd* overexpression in *Drosophila* S2 cells leads to cleavage of Rel (*39*), and expression of UAS-*Dredd* in cell clones in WT wing discs induced cell death and reduced clone size (Fig. 2E and fig. S3, D to F), phenocopying cell competition. Dredd's effect on clone size required Rel, as it was prevented by concomitant expression of *Rel*-RNAi (Fig. 2E). These results suggest that TRR activation increases Dredd activity and leads to activation of Rel, which results in the elimination of loser cells.

To determine whether cell competition led to nuclear translocation of Rel and activation of antimicrobial target genes, as occurs during innate immunity, we used a cell-based competition assay (*12*). Conditioned medium (CM) from cocultures of competing WT and Myc-expressing *Drosophila* S2 cells contains diffusible factors that confer the outcomes of the competitive interactions, including Hid-dependent cell death, on naïve S2 cells (*12*, *25*). Consistent with our genetic results in vivo, double-stranded RNA (dsRNA)–mediated knockdown of *Rel* prevented the death of naïve S2 loser cells (Fig. 3A). To examine the subcellular localization of Rel, we transfected S2 cells with GFP-tagged Relish (GFP::Rel). In control experiments, treatment of the transfected cells with bacterial peptidoglycan (PGN) increased the fraction of cells with nuclear GFP::Rel (Fig. 3B) and also induced expression of several AMP genes (fig. S4A). Treatment of the transfected S2 cells with competitive CM (cCM) also increased nuclear translocation of GFP::Rel, but cCM was unable to activate expression of AMP genes, in contrast to PGN challenge (fig. S4A). Likewise, AMP gene expression was not activated in wing disc cells or in any larval tissue in animals in which cell competition was induced in vivo (fig. S4F). Disc cells may lack factors necessary to activate an immune response, because although infection of larvae with *Erwinia carotovora* induced expression of several AMP genes (fig. S4, B and C) and reporter transgenes in larval immune tissues (fig. S4, D and E), they were not expressed in wing disc cells. IKKβ phosphorylation of Rel is required for induction of AMP gene expression during the immune response (*39*); thus, the lack of AMP induction may reflect Rel-dependent transcriptional programs that are accessed by diverse signaling pathways: IKK-dependent for immune response activation of AMPs and IKK-independent for cell competition. The absence of requirements for *ird5*/IKK-β and *key*/IKK-γ in cell competition (Fig. 1B) is consistent with this notion.

In considering relevant transcriptional targets of Rel during cell competition, we examined *hid*, given its role in elimination of WT loser cells (*11*, *12*, *25*). Bioinformatic analysis identified consensus NFκB binding sites in the *Wrinkled* (*W*) locus, which encodes Hid (fig. S5). Expression of *Rel68* (the active form of Rel) in wing disc cells activated $hid^{P\text{-}lacZ}$, a transcriptional reporter inserted in the *W* locus (Fig. 3, C and D). *Rel68*-expressing cell clones were small and underrepresented in the disc, as expected because Hid expression leads to cell death (Fig. 3, E and F). Notably, the presence of the $hid^{P\text{-}lacZ}$ insertion, not only a transcriptional reporter but also a mutant allele, allowed clones to grow as well as GFP-expressing control clones (Fig. 3, E to G). Expression of *Rel68* in wing discs upregulated *hid* mRNA approximately threefold above the WT level (Fig. 3H) but did not induce expression of *reaper (rpr)*, a proapoptotic gene in the same chromosomal region, indicating that Rel induces death of wing disc cells by the selective activation of Hid. Both Rel and Hid are required in the loser cells for their elimination; thus, we infer that Rel activation during competition triggers loser cell death via its induction of Hid expression (*11*, *12*, *25*).

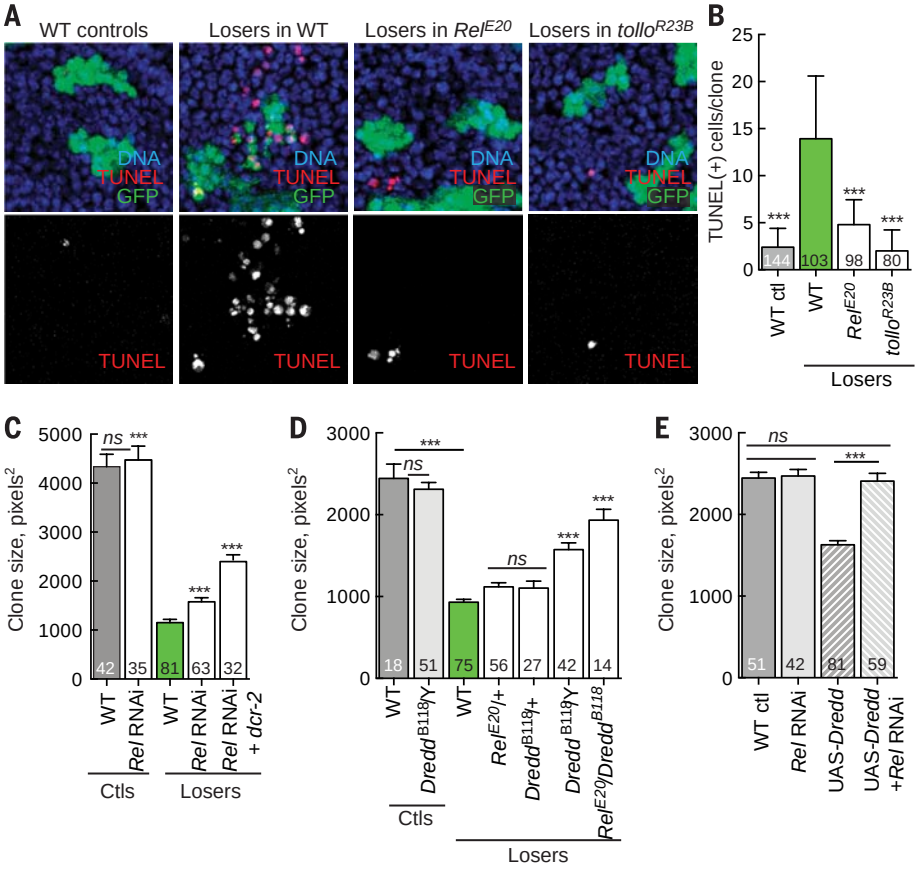


Fig. 2. Dredd-mediated Rel activation eliminates loser cells. (**A**) Rel and Tollo are required for death of loser cells. TUNEL assays showing cell death in control clones, WT loser clones, and loser clones in Rel^{E20} and $tollo^{R23B}$ mutant backgrounds 24 hours after clone induction. Many WT loser cells are TUNEL-positive, but their death is suppressed in the mutant backgrounds. (**B**) Quantification of data from (A). (**C**) Expression of *Rel*-RNAi (or *Rel*-RNAi and Dicer to enhance RNAi efficiency) within loser cells suppresses their loss but does not affect control clones. (**D**) Dredd and Rel are critical for elimination of WT loser cells. Loss of *Dredd* suppresses the loss of loser clones but does not affect the growth of control clones. Whereas $Dredd^{B118-/+}$ has little effect on loser death, in combination with $Rel^{E20-/+}$ it strongly suppresses death. (**E**) Expression of *Dredd* in the absence of competition reduces clone size, but this is blocked by coexpression of *Rel* RNAi. The number of clones scored for each genotype is indicated. All *P* values are relative to WT loser clone size except in (C): ***$P < 0.001$. ns, not significant (Mann-Whitney test).

Elimination of *Minute* loser cells requires a partially overlapping signaling module

A defining feature of cell competition is its context dependence, so that cells perceive themselves as more or less fit as a direct result of interactions with their neighbors (*5*, *6*). To determine whether the TRR-NFκB signaling module that we identified was specific to competition induced by Myc or was a more general mechanism, we examined the *Minute* competition paradigm. We used larvae in which all cells carried one mutant copy of the *RpL14* gene ($M^{RpL14-/+}$cells) but were rescued to WT by expression of a genomic RpL14 transgene (*gRpL14*) (Fig. 4A). In this background, we generated GFP-marked wing disc clones of $M^{RpL14-/+}$ cells through Flp-FRT-mediated removal of the *gRpL14* transgene. These clones were competitively eliminated at high frequency, as scored by counting how many GFP-positive $M^{RpL14-/+}$ clones persisted in larvae (Fig. 4, A and B). Using this assay, we targeted individual genes in the Toll and IMD pathways with RNAi to determine if their loss prevented the competitive elimination of the GFP-$M^{RpL14-/+}$ loser cells (Table 1 and fig. S6A). We identified a group of innate immune genes that prevented loss of $M^{RpL14-/+}$ loser cells that were also required for Myc-induced competition [including *spz*, *Toll-3*, *Toll-9*, and *Rel* (Table 1)], indicating that this signaling mechanism was not restricted to Myc-induced competition or due to oncogenic effects of Myc supercompetitor cells. However, the assay also revealed an interesting difference between the two competitive contexts: RNAi targeted against *dl* or *Dif* or expression of their inhibitor, *cact*, strongly suppressed $M^{RpL14-/+}$ clone loss. Likewise, compound heterozygotes carrying the dl^1 allele and a deficiency that removed both *dl* and *dif* suppressed their elimination, whereas RNAi against *cact* enhanced it (Table 1 and Fig. 4B). Thus, although in each competitive context the outcome for the loser population was elimination, the signaling module required for this to occur was only partially overlapping.

Competitive context determines selection of NFκB factor and apoptotic inducer

Because the loser cells were WT in one of our competitive paradigms and in the other they were $M^{RpL14-/+}$, we considered the possibility that the specific signaling module activated within the loser cells was influenced by the identity of the competing populations, similar to the response of innate immune signaling to diverse pathogens. In particular, the NFκB factor required for the elimination of the loser population in the two contexts appeared to be different. To investigate this further we measured clone size and cell number in GFP-$M^{RpL14-/+}$clones in wing discs and found that *Rel* RNAi only mildly suppressed competition against $M^{RpL14-/+}$ cells. Loss of both Dif and Dorsal activity (achieved by *cact* overexpression) strongly blocked elimination of $M^{RpL14-/+}$losers, and coexpression of *Rel* RNAi with *cactus* enhanced this effect (fig. S7, A and B). Dif and Dorsal therefore appear to be the predominant NFκB mediators of $M^{RpL14-/+}$ loser elimination, in contrast to the exclusive requirement for Rel in triggering death of WT loser cells (Figs. 1B and 2, A to C). Elimination of the $M^{RpL14-/+}$cells depended upon apoptosis and was suppressed by expression of *cact* (Fig. 4, C and D), as well as a chromosomal deficiency called *H99* that removes *hid*, *rpr*, and other pro-death genes or expression of the

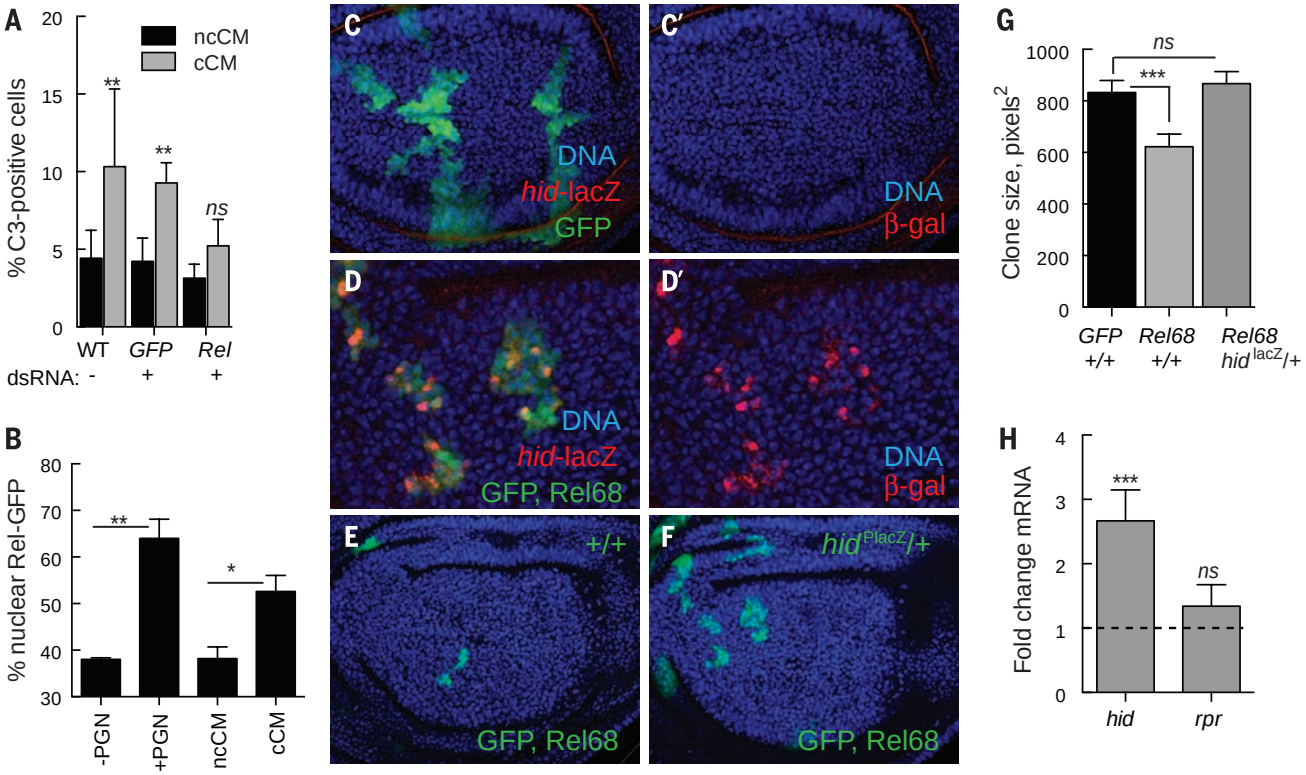


Fig. 3. Rel triggers death of WT loser cells by inducing the proapoptotic factor Hid. (**A**) *Rel* is required to kill naïve S2 cells. cCM from control cocultures or those treated with dsRNA against GFP increased death of naïve cells, as measured by activated caspase-3 staining. Cell death was prevented by dsRNA against *Rel*. Both cocultures and naïve cells in these assays were treated with the indicated dsRNA. Error bars denote SD. (**B**) Cell competition increases nuclear translocation of Rel. Nuclear localization of Rel-GFP in transfected WT-S2 cells treated ± PGN, noncompetitive (nc) CM, or competitive (c) CM for 4 hours is shown. Error bars indicate SD. (**C** and **D**) Wing disc with control, GFP-expressing cell clones (C) and cell clones expressing UAS-*Rel68* (activated Rel) and UAS-GFP (D) from animals carrying a *lacZ* reporter insertion in the *hid* locus (*hid-lacZ*, red). DNA is stained with Hoechst (blue). *hid-lacZ* is not induced in control clones (C and **C′**). *Rel68*-expressing clones activate expression of *hid-lacZ* (D and **D′**), grow poorly, and are small compared with controls (**E** and **G**) but are rescued by the mutation caused by the hid^{PlacZ} insertion (**F** and G). Clones in (D) are shown at higher magnification to facilitate resolution of *hid-lacZ* expression. (G) Average clone size of control clones (GFP), *Rel68*-expressing clones in a +/+ background, and *Rel68*-expressing clones in the hid^{PlacZ}/+ mutant background. Error bars denote SEM. (**H**) Expression of UAS-*Rel68* in WT wing discs induces *hid* mRNA but not *rpr* mRNA in quantitative RT-PCR experiments on RNA isolated from wing discs. Error bars indicate SD. ***$P < 0.001$, **$P < 0.01$, *$P < 0.05$. ns, not significant (Mann-Whitney test).

caspase inhibitor p35 (Fig. 4E). However, whereas expression of RNAi targeted specifically against *rpr* prevented loss of $M^{RpL14-/+}$ loser cells, RNAi against *hid* did not (Fig. 4E). This suggested that distinct apoptotic regulators were induced by the selective activation of a NFκB factor within each loser population. Like *Rel*, *dl* expression reduced clone size in wing discs (Fig. 4F) and induced pro-death gene expression, except that *dl* (and *Dif*) led to preferential expression of *rpr* rather than *hid* (Fig. 4G). In contrast, Hid is required for Rel68-mediated elimination of WT cells (Fig. 3, G and H) and WT loser cells in Myc-induced competition (*11*, *12*, *25*). Thus, in two genetically distinct competitive contexts, partially overlapping signaling components activate different NFκB factors and prompt expression of distinct proapoptotic target genes yet trigger the same outcome: the death and elimination of the loser cells.

Conclusions

Altogether, our results demonstrate that the conceptual resemblance between cell competition and innate immunity is matched with genetic and mechanistic similarities. Thus, cells within developing tissues that are recognized as mutant or compromised are competitively eliminated via a TRR- and NFκB-dependent signaling mechanism. Although similar core signaling components are activated in both processes, cell

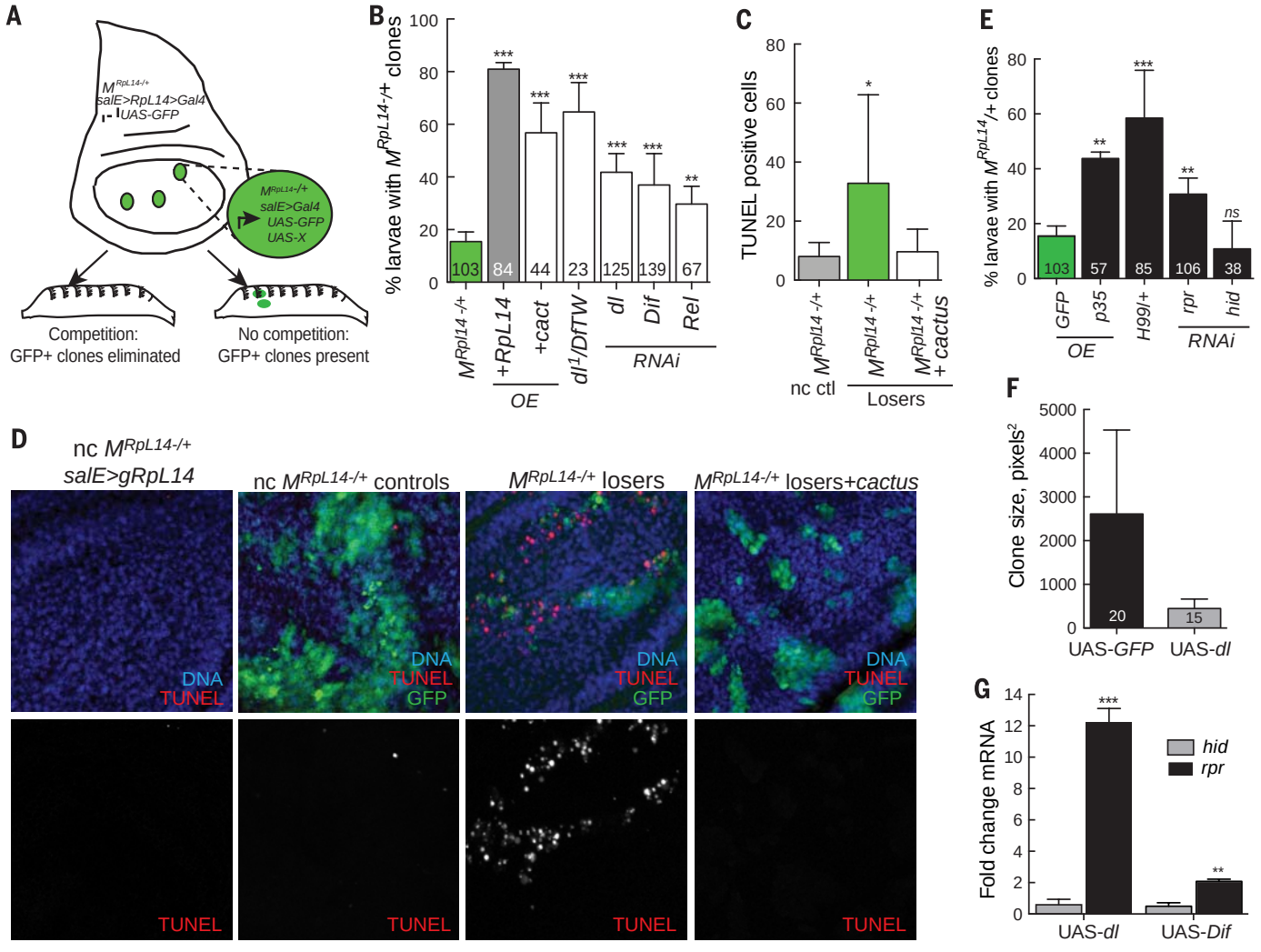


Fig. 4. Competitive context influences selection of the TRR-NFκB signaling module and proapoptotic inducer. (**A**) Scheme for larval screening of innate immune pathway components in competition between WT and $M^{RpL14-/+}$ cells. GFP-positive wing disc clones ($M^{RpL14-/+}$ loser cells) are generated in a background of essentially WT cells ($M^{RpL14-/+}$ rescued with *gRpL14*); see materials and methods for details. The GFP-$M^{RpL14-/+}$ loser clones are competitively eliminated and thus not present in larvae. If competition is suppressed by overexpression or RNAi, the GFP-positive wing disc clones persist in the larvae. (**B**) Competitive elimination of $M^{RpL14-/+}$ loser cells is predominantly triggered by Dorsal and Dif. Overexpression of Cactus, RNAi against *dl* or *Dif*, or dl^1/Df(2L)TW119, a deficiency that removes both *dl* and *Dif*, each suppress loss of $M^{RpL14-/+}$ loser cells. Overexpression of UAS-*RpL14* was used as a control for clone survival. See fig. S6 for the full data set. (**C** and **D**) Cell death mediates $M^{RpL14-/+}$ cell competition. (C) Apoptosis, marked by TUNEL staining, is high in $M^{RpL14-/+}$ loser cells but is reduced when Dorsal and Dif activity are blocked by UAS-*cactus* expression. (D). TUNEL staining of wing discs with UAS-*GFP*–expressing clones, quantified in (C). Left to right: control noncompetitive (nc) $M^{RpL14-/+}$ wing disc rescued by *gRpL14* expression; control nc *act>Gal4*, *UAS-GFP* clones generated in unrescued $M^{RpL14-/+}$wing disc; $M^{RpL14-/+}$ loser clone generated in $M^{RpL14-/+}$ *salE*>gRpL14 disc; and $M^{RpL14-/+}$ loser clone expressing UAS-*cactus* generated in $M^{RpL14-/+}$ *salE*>gRpL14 disc. (**E**) Competitive elimination of $M^{RpL14-/+}$ loser cells requires cell death induced by Reaper (Rpr). Elimination of $M^{RpL14-/+}$ loser clones is prevented by expression of the apoptosis inhibitor p35; by one copy of the *H99* deficiency that removes *hid*, *rpr*, and other proapoptotic genes; and by RNAi against *rpr*, but not RNAi against *hid*. Number of larvae scored per genotype is indicated. (**F**) *dorsal*-expressing clones are smaller than WT sibling clones. Mitotic recombination generated GFP-positive clones that express UAS-*dorsal* and WT GFP-negative sibling clones. The graph shows the mean clone size of the indicated number of clones. (**G**) Expression of UAS-*dorsal* and UAS-*Dif* induces expression of *rpr*, but not *hid*, in quantitative RT-PCR experiments on RNA isolated from wing discs. Error bars in (B) and (E) to (G) denote SD; error bars in (C) indicate SEM. ***P < 0.001, **P < 0.01, *P < 0.05 (Student's t test).

competition culminates in local expression of proapoptotic genes rather than systemic induction of antimicrobial genes. Because cell competition is initiated by the emergence of cells of different fitness than their neighbors in a tissue, we surmise that the initiating signal is common to many competitive contexts. Our genetic data lead us to propose a model for how this signal is detected and transduced. Our results point to a role for Spz in signal detection, as it is a secreted protein that is required for the killing activity of cCM (fig. S8A), is a known ligand for the Toll receptor, and is produced by several tissues in the larva (fig. S8B). Thus, we speculate that Spz functions as a ligand for one or more TRR in cell competition. Because Spz must be activated through a series of proteolytic steps, the relevant proteases may respond directly to the initiating signal in cell competition. We propose that the genetic identity or context of the competing populations influences activation of different TRR signaling modules and that the precise configuration of TRRs on loser cells dictates which of the three *Drosophila* NFκB proteins is activated (Fig. 5). How signaling to the NFκBs is restricted to the loser cells is not known, but higher expression of *Toll-2*, *Toll-8*, and *Toll-9* in loser cells (fig. S2D) could bias signal transduction. PGRP-LC, a receptor known to bind only bacterial products, also plays a role in Myc-induced competition. As commensal gut microflora is known to influence larval growth (*40*–*42*), this raises the possibility that it also contributes to the competitive phenotype.

Throughout evolution, signaling modules have adapted to fulfill different functions even within the same species. Here we have provided evidence for adaptation of TRR-NFκB signaling modules in an organismal surveillance system that measures internal tissue fitness rather than external stimuli. It is noteworthy that the killing of WT cells by supercompetitor cells is a potentially pathological form of cell competition that could propel expansion of premalignant tumor cells. If so, activated TRR-NFκB signaling modules in nonimmune tissues could be diagnostic markers, and their competitive functions could serve as therapeutic targets for cancer prevention.

Materials and methods

Bacterial infection

To elicit an immune response as a control for AMP gene induction, we orally infected larvae with *E. carotovora carotovora15* as in (*43*). 200 μl of bacterial pellet was added to 400 μl of crushed banana into a 2-ml microfuge tube. Thirty third instar larvae were placed inside the tube and fed the banana-bacteria mixture for 30 min at room temperature. The larvae and bacteria-banana were then transferred to standard molasses food and allowed to feed overnight at 29°C. At 24 hours after infection, larval tissues were examined for AMP gene expression by quantitative real-time polymerase chain reaction (qRT-PCR) or reporter activity. Similar results were obtained with septic infections of larvae with *Escherichia coli*.

Bioinformatics

Rel binding sites were identified in the *hid/W* locus using the Web-based program Genome Surveyor (*44*).

Cell culture and generation of conditioned medium

Drosophila S2 cells were maintained at 25°C in Schneider's *Drosophila* Medium supplemented with 10% fetal bovine serum, 0.5% yeast extract, and penicillin and streptomycin (50 IU/ml each). cCM and noncompetitive cCM (ncCM) were generated as described in (*12*). Briefly, direct cocultures of either WT S2 cells with pMT-HA-Myc S2 cells or WT S2 cells with WT-S2 cells were plated at a density of 4×10^5 per ml per cell type for a total density of 8×10^5 cells per ml, as described (*12*). Conditioned medium was collected after

Table 1. Suppression of $M^{RpL14-/+}$ loser clone elimination by Toll and IMD pathway genes. *P* values are compared with that of $M^{RpL14-/+}$ (*t* test).

Genotype	% larva with GFP$^+$ clones	SD	*P* value
$M^{RpL14-/+}$	15.5	3.7	
	$M^{RpL14-/+}$ + *overexpression*		
UAS-*RpL14*	80.5	2.5	4.30×10^{-5}
UAS-*p35*	43.8	2.3	4.40×10^{-7}
UAS-*cact*	49.2	1.4	0.03
	$M^{RpL14-/+}$ + *RNAi*		
UAS-*cact*	6.6	4.7	0.03
UAS-*dl*	41.8	7.1	0.00
UAS-*Dif*	37.0	11.9	0.03
UAS-*pelle*	24.3	1.4	0.01
UAS–*Toll-3*	39.3	13.3	0.03
UAS–*Toll-9*	30.1	8.0	0.03
UAS-*spz*	28.8	8.2	0.04
UAS-*imd*	27.0	4.2	0.01
UAS-*Rel*	29.6	6.8	0.02

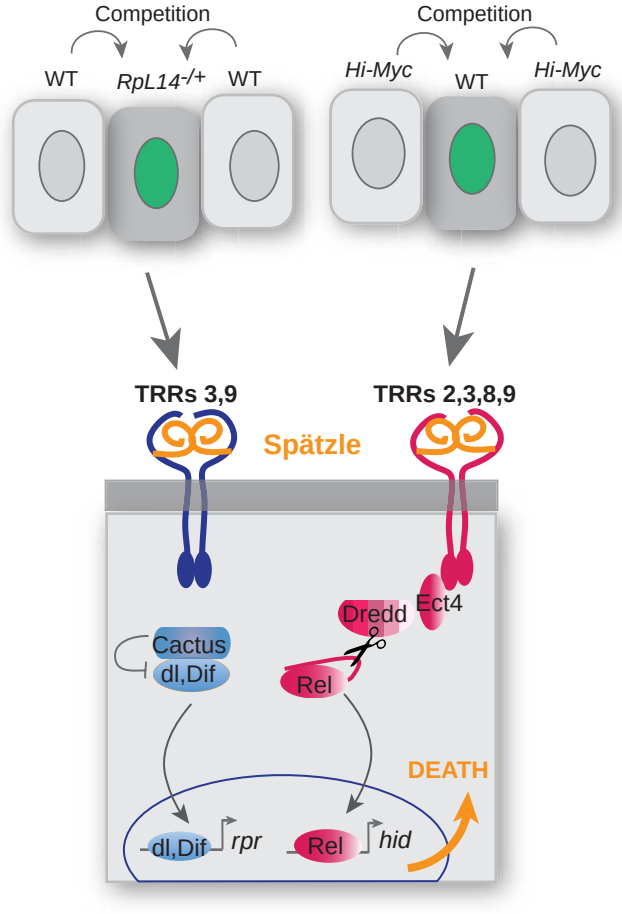


Fig. 5. A model of the role of TRR-NFκB modules in cell competition. A model for TRR-NFκB function in cell competition, incorporating data from both competitive contexts. See text for full description. We propose that in both *Minute*- and Myc-induced competitive contexts, loser cells are eliminated through a signaling pathway mediated by Spz, TRRs, and NFκB function. Context- and/or genetic-dependent interactions that cause Rel activation trigger expression of Hid, whereas those activating Dif and Dorsal trigger expression of Rpr. Apoptosis is the ultimate fate of both loser populations. Red denotes genes required for Myc-induced competition, blue indicates those required for competition in *M/+* mosaics, and orange denotes shared requirements.

24 hours ± 125 μM $CuSO_4$ treatment and centrifuged at 1200 revolutions per minute for 3 min. 125 μM $CuSO_4$ was added to the conditioned medium without $CuSO_4$ to control for inducer effects (*12*). The CM was then used for treatments in experiments. Activity of the CM was verified by C3 activity measurements as described (*12*). For Rel-GFP assays, S2 cells were transfected with a pMT-Rel-GFP transgene (gift from E. Foley) as follows: WT S2 cells were seeded in a 12-well plate with one coverslip per well at 8×10^5 cells per ml and cultured at 25°C overnight. Transfection was done using Cellfectin II Reagent as directed (Invitrogen). Subcellular location of pMT-Rel-GFP in WT-S2 cells or Myc-S2 cells was scored after treatment ± 50 μg/ml LPS as a source of PGN (Sigma) + 125 μM $CuSO_4$, cCM, or ncCM. At least 200 cells per condition were scored per experiment. The ratio of cells positive for nuclear localization of GFP-Relish to total GFP-positive cells was calculated.

Drosophila *stocks and care*

The following mutant strains were used in this study: Rel^{E20} (gift from D. Hultmark); imd^{shadok} and imd^{1} (gifts from D. Ferrandon); key^{1}, $tak1^{1}$, $tak1^{2}$, and Dif^{1}, (gifts from B. Lemaitre); $FADD^{f06954}$ (*BG4*), $Dredd^{B118}$, $ird5^{KG08072}$, pll^{2}, pll^{7}, $tube^{2}$, spz^{2}, dl^{4}, dl^{1}, *Df(2L) TW119*, *Df(2L)J4*, $cact^{1}$, $cact^{4}$, $hid^{W05014\ (Plac-Z)}$, $Ect4^{4273}$, and Rel^{E38} (from Bloomington Drosophila Stock Center, http://flystocks.bio.indiana.edu); $casp^{P1}$ (gift from J. Chung); $Tollo^{14.5}$ (gift of J. Kim); $Tollo^{R23B}$ and $Tollo^{R5A}$ (gifts from P. Simpson); $PGRP\text{-}LC^{TotemΔ5}$ and $PGRP\text{-}LC^{E12}$ (gifts from B. Matthey-Prevot); and spz^{rm7} (gift from C. Hashimoto). For Myc competition, control or loser clones were generated in wild type, mutants, or with UAS-transgenes using these strains: *yw hsflp;;act>y>Gal4,* UAS-*GFP* (controls), *ywhsflp;;tub>Myc>Gal4,* UAS-*GFP, ywhsflp;*UAS-*GFP tub>Myc>Gal4* (*11*), and *ywhsflp;;*UAS-*Myc* (*7*). *ywhsflp;;FRT82B ubi-GFP*, *ywhsflp;;FRT82B* Rel^{E20}/TM6B was used for fig. S3. *FRT82B* Rel^{E20} was generated by recombination and screened for presence of the mutation by PCR using primers from (*45*). For $M^{RpL14-/+}$ competition, UAS-transgenes were driven in a *ywhsflp* UAS-*GFP::CD8;;* $M^{RpL14(w+)-/+}$*salE>gRpL14(w+)>Gal4/TM6B* strain. UAS-*RNAi* lines were from the Vienna Drosophila Resource Center (http://stockcenter.vdrc.at) or the Transgenic RNAi Project (TRiP) collection (BDSC) and are listed in table S3. Other strains include UAS-*Toll-8ΔLRR* (gift from J.-L. Imler), UAS-*dicer2* (BDSC), *yw;;*UAS-*cactus-HA/TM3* and *yw;;*UAS-*cactus, yw* UAS-*GFP hsFLP; tub-Gal80 FRT40, Ubi-GFP FRT40; tub-Gal4,* UAS-*dorsal*, *w* $P(w^{+}$, *Dros-LacZ)*, *yw* $P(w^{+}$,*Dipt-LacZ),* and UAS-*Dredd* (gifts from B. Lemaitre), *yw;;CecA-lacZ* (gift from S. Stöven), UAS-*Rel68* (gift from N. Silverman), and UAS-*caspar* (gift from J. Chung). Null mutants were used when possible. A complete list of mutant strains is included in table S1. Flies were raised at 25°C on cornmeal-molasses food supplemented with penicillin and streptomycin, as indicated below.

dsRNA treatment of S2 cells

The sequences for dsRNA against Relish and Spz were obtained from the Drosophila RNAi Screening Center (DRSC 37194 for Relish and DRSC 17065 for Spz). The dsRNA was synthesized in vitro with T7 RNA polymerase as directed (Roche). Single cultures of WT or pMT-HA-Myc S2 cells were seeded at 8×10^5 cell per ml in 12-well plates. Sixteen hours later dsRNA was transfected using Cellfectin II Reagent (Invitrogen), as described (*12*). Three days after the dsRNA transfection, WT S2 cells with pMT-HA-Myc S2 cells (cCM) or WT S2 cells with WT-S2 (ncCM) were seeded at a density $(4 + 4) \times 10^5$ cell per ml, and CM was obtained as described above. Naïve WT S2 cells were also transfected with dsRNA 72 hours before the treatment with CM. Efficiency of the dsRNA treatment was assayed by RT-PCR.

Heat shock induction of loser clones

In the Myc competition assays, eggs from appropriate crosses were collected on yeasted grape-agar plates for 2 to 4 hours. After hatching, larvae were transferred to standard molasses food vials (≤50 per vial) supplemented with Pen and Strep and fresh yeast and raised at 25ºC. The *tub>myc>Gal4* transgene was used to generate random UAS-*GFP*-marked *tub>Gal4* clones via FLPase-mediated recombination, as described (*11*). *tub>Gal4* clones were induced by heat shock (HS) of larvae at 37°C for 10 to 15 min at 48 hours after egg-laying (AEL), and progeny were allowed to grow at 25°C for either 48 or 96 hours. The *act>y>Gal4* transgene was used to generate random UAS-*GFP*– or UAS-*Rel68*–expressing *act>Gal4* clones in WT wing discs. *act>Gal4* clones were induced by larval HS at 37°C for 6 min at 48 hours AEL and larvae were treated as above. These heat shock times were optimized to generate only a few clones per disc, to avoid merged clones. Clone area (in square pixels) was scored for clones in the central area of the wing disc (wing pouch and proximal hinge). For some genotypes, cell number per clone was also counted. The MARCM (mosaic analysis with a repressible cell marker) technique (*46*) was used to generate mitotic clones that expressed UAS-*GFP* as a lineage marker ± UAS-*dorsal*. Expression of *hs-CD2* was used to mark the sibling clones (*11*). Nonparametric Mann-Whitney tests were performed for statistical significance.

In the $M^{RpL14-/+}$ competition assays, the driver strain carried a *Minute* mutation in the gene *RpL14* ($M^{RpL14-/+}$), the *salE>gRpL14(w+)>Gal4* flip-out transgene (*salE* is a wing pouch–specific enhancer), and *UAS-GFP*::*CD8* (CD8 targets GFP for membrane localization). In $M^{RpL14-/+}$ clones, Gal4 is expressed instead of the RpL14 genomic rescue construct, and GFP expression is activated. The driver strain was crossed to RNAi or overexpression transgene strains, and flies were allowed to lay eggs for 12 to 16 hours. Parental flies were removed, and larval progeny were heat-shocked 24 hours later for 15 min at 37°C and analyzed using a fluorescence binocular or confocal microscope 76 to 80 hours later (for larval clone assays) or 48 to 52 hours later (for clone measurements and cell counting assays). The UAS-*GFP*–marked $M^{RpL14-/+}$ clones are generally eliminated from larvae within 80 hours, resulting in the absence of GFP in late third instar wing discs. In cases where the induced transgene rescues the clones, GFP is readily visible through the larval cuticle. Each transgene was tested in biological triplicate, and the average number of larvae with surviving clones was compared to the WT control. *yw, yw;;*UAS-*RpL14(w+)/TM6B, and yw;Sp/CyO;*UAS-*P35 (w+)* strains were used as controls. Nonparametric *t* tests were used to test for statistical significance.

Imaging, image analysis, and quantifications

Cell clones were imaged in larvae with a Zeiss MZFLIII and in fixed wing discs with a Zeiss Axiophot, Leica SP5, or Leica LSM710 confocal microscope. Clone area was measured (in square pixels) using ImageJ or Photoshop software. Cells per clone were counted in the GFP and/or DNA channels. Only clones in the wing pouch and proximal hinge area were measured; in the $M^{RpL14-/+}$ assays, this corresponded to the *salE* expression domain. Significance was determined using Student's *t* and Mann-Whitney tests.

Immunohistochemistry

Wing disc cells were fixed in 4% paraformaldehyde/phosphate-buffered saline (PBS) for 20 min at room temperature and washed with PBS 0.01% Tween-20. Hoechst 33258 or 4′,6-diamidino-2-phenylindole was used to stain DNA. The primary antibodies used include mouse anti-Relish (DHSB), rabbit anti-β-galactosidase (Cappel), and rabbit anticleaved Caspase-3 (Cell Signaling Technology). Secondary antibodies were Alexa-conjugated anti-mouse and anti-rat and Cy3-conjugated anti-rabbit (Molecular Probes). For cell culture, cells seeded on glass coverslips were fixed in 4% paraformaldehyde/PBS for 30 min. Coverslips were washed with PBS once, permeabilized in 0.5% TX-100/PBS for 5 min, then blocked for 30 min in 3% BSA, 0.1% Tween-20/PBS. After blocking, each coverslip was flipped onto 50 μl of primary antibody in blocking buffer for 1 hour at room temperature. Coverslips were washed 3× with PBS, and primary antibodies were incubated in AlexaFluor 546 goat anti-rabbit or goat anti-rat immunoglobulin G (Molecular Probes) for 45 min at room temperature. Coverslips were washed 3× for 5 min each with PBS, counterstained for DNA with Hoechst 33258 for 4 min, washed 3× for 5 min each, then mounted on slides. TUNEL (terminal deoxynucleotidyl transferase–mediated deoxyuridine triphosphate nick end labeling) assays were carried out on fixed discs using either TUNEL TMR (Roche Diagnostics) or ApopTag Red (Chemicon).

RNA isolation and qRT-PCR

Total RNA was isolated from wing disc using the Nucleo SpinII RNA isolation kit (Machery Nagel) or Trizol (Invitrogen). RNA quantity was measured using a NanoDrop ND-1000 UV-Vis Spectrophotometer (NanoDrop Technologies, Wilmington, DE). For qRT-PCR of Rel-expressing cells, *yw;; tub>CD2>Gal4* flies were crossed either with *yw;;* UAS-*GFP* or *yw;;*UAS-*Rel68* and heat-shocked for 30 min at 37°C. At 24 hours after clone induction,

the wing discs were dissected, and total RNA was isolated. qRT-PCR was performed using Applied Biosystems 7900HT Real-Time PCR Systems (Applied Biosystems, Foster City, CA). Primer sets were obtained from either Microsynth (Microsynth AG, Balgach, Switzerland) or MWG (Huntsville, AL). For qRT-PCR, total RNA was treated with RNAse-free DNaseI, and cDNA was synthesized by using oligo-dT primers and Superscript RT-III (Invitrogen). Samples were then used for qRT-PCR with the ABI SYBR green system. Measurements of transcript level were normalized to *actin5c* and/or *tubulinα1*. The following primers were used for qRT-PCR: *hid,* F: TCTACGAGTGGGTCAGGATGT, R: GCGGATACTGGAAGATTTGC; *reaper,* F: GAGCAGAAGGAGCAGCAGAT, R: GGACTTTCTTCCGGTCTTCG; *diptericin,* F: GTTCACCATTGCCGTCGCCTTAC, R: CCCAAGTGCTGTCCATATCCTCC; *drosomycin*, F: TTGTTCGCCCTCTTCGCTGTCCT, R: GCATCCTTCGCACCAGCACTTCA; *attacin*, F: GTGGTGGGTCAGGTTTTCGC, R: TGTCCGTTGATGTGGGAGTA; *Toll,* F: GGTCTTTTGGCCGGTTTCAC, R: CTCCACATCTCCGATGTCCG; *Toll-2*, F: GAGGCTATAGGCTGCCCTTG, R: ATGTTGCGGCACACAAACTC; *Toll-3*, F: CCTTCCAGCGAAACTGGACT, R: ACTTATGAGGACAGGGGGCT; *Toll-8*, F: CTCCCATGCTGGAAATGGGT, R: GCGAAGATCGGGATCGAGTT; *Toll-9*, F: CTTTTGCCCATCTGGGGGAT, R: AAACATGGCGGGAGTGAGAG; *act5c,* F: TGTGACGAAGAAGTTGCTGCT, R: AGGTCTCGAACATGATCTGG; *tubα1*, F: GCCAGATGCCGTCTGACAA, R: AGTCTCGCTGAAGAAGGTGTTGA.

The following primers were used for dsRNA knockdown in S2 cells: *Relish,* F: GCATGGAACACATGGATCGC, R: CTGATGGGAATGTGGGCTGT; *Spätzle*, F: CTCTCGCTGTCGTGTGTTCT, R: TTCCTTTGCACGTTTGCGAG.

REFERENCES AND NOTES

1. L. W. Buss, *The Evolution of Individuality* (Princeton Univ. Press, Princeton, NJ, 1987).
2. N. King, The unicellular ancestry of animal development. *Dev. Cell* **7**, 313–325 (2004). doi: 10.1016/j.devcel.2004.08.010; pmid: 15363407
3. K. J. Niklas, S. A. Newman, The origins of multicellular organisms. *Evol. Dev.* **15**, 41–52 (2013). doi: 10.1111/ede.12013; pmid: 23331916
4. M. Dejosez, H. Ura, V. L. Brandt, T. P. Zwaka, Safeguards for cell cooperation in mouse embryogenesis shown by genome-wide cheater screen. *Science* **341**, 1511–1514 (2013). doi: 10.1126/science.1241628; pmid: 24030493
5. L. A. Johnston, Competitive interactions between cells: Death, growth, and geography. *Science* **324**, 1679–1682 (2009). doi: 10.1126/science.1163862; pmid: 19556501
6. N. E. Baker, Cell competition. *Curr. Biol.* **21**, R11–R15 (2011). doi: 10.1016/j.cub.2010.11.030
7. L. A. Johnston, D. A. Prober, B. A. Edgar, R. N. Eisenman, P. Gallant, *Drosophila myc* regulates cellular growth during development. *Cell* **98**, 779–790 (1999). doi: 10.1016/S0092-8674(00)81512-3; pmid: 10499795
8. G. Morata, P. Ripoll, Minutes: Mutants of *Drosophila* autonomously affecting cell division rate. *Dev. Biol.* **42**, 211–221 (1975). doi: 10.1016/0012-1606(75)90330-9; pmid: 1116643
9. C. Clavería, G. Giovinazzo, R. Sierra, M. Torres, Myc-driven endogenous cell competition in the early mammalian embryo. *Nature* **500**, 39–44 (2013). doi: 10.1038/nature12389; pmid: 23842495
10. E. R. Oliver, T. L. Saunders, S. A. Tarlé, T. Glaser, Ribosomal protein L24 defect in belly spot and tail (*Bst*), a mouse *Minute*. *Development* **131**, 3907–3920 (2004). doi: 10.1242/dev.01268; pmid: 15289434
11. C. de la Cova, M. Abril, P. Bellosta, P. Gallant, L. A. Johnston, *Drosophila* myc regulates organ size by inducing cell competition. *Cell* **117**, 107–116 (2004). doi: 10.1016/S0092-8674(04)00214-4; pmid: 15066286
12. N. Senoo-Matsuda, L. A. Johnston, Soluble factors mediate competitive and cooperative interactions between cells expressing different levels of *Drosophila* Myc. *Proc. Natl. Acad. Sci. U.S.A.* **104**, 18543–18548 (2007). doi: 10.1073/pnas.0709021104; pmid: 18000039
13. D. C. Wu, L. A. Johnston, Control of wing size and proportions by *Drosophila* myc. *Genetics* **184**, 199–211 (2010). doi: 10.1534/genetics.109.110379; pmid: 19897747
14. E. Moreno, K. Basler, dMyc transforms cells into super-competitors. *Cell* **117**, 117–129 (2004). doi: 10.1016/S0092-8674(04)00262-4; pmid: 15066287
15. R. M. Neto-Silva, S. de Beco, L. A. Johnston, Evidence for a growth-stabilizing regulatory feedback mechanism between Myc and Yorkie, the *Drosophila* homolog of Yap. *Dev. Cell* **19**, 507–520 (2010). doi: 10.1016/j.devcel.2010.09.009; pmid: 20951343
16. M. Ziosi *et al*., dMyc functions downstream of Yorkie to promote the supercompetitive behavior of hippo pathway mutant cells. *PLOS Genet.* **6**, e1001140 (2010). doi: 10.1371/journal.pgen.1001140; pmid: 20885789
17. A. B. Rodrigues *et al*., Activated STAT regulates growth and induces competitive interactions independently of Myc, Yorkie, Wingless and ribosome biogenesis. *Development* **139**, 4051–4061 (2012). doi: 10.1242/dev.076760; pmid: 22992954
18. J. P. Vincent, G. Kolahgar, M. Gagliardi, E. Piddini, Steep differences in wingless signaling trigger Myc-independent competitive cell interactions. *Dev. Cell* **21**, 366–374 (2011). doi: 10.1016/j.devcel.2011.06.021; pmid: 21839923
19. M. Sancho *et al*., Competitive interactions eliminate unfit embryonic stem cells at the onset of differentiation. *Dev. Cell* **26**, 19–30 (2013). doi: 10.1016/j.devcel.2013.06.012; pmid: 23867226
20. E. B. Kopp, R. Medzhitov, The Toll-receptor family and control of innate immunity. *Curr. Opin. Immunol.* **11**, 13–18 (1999). doi: 10.1016/S0952-7915(99)80003-X; pmid: 10047546
21. S. M. Kanzok *et al*., Origin of Toll-like receptor-mediated innate immunity. *J. Mol. Evol.* **58**, 442–448 (2004). doi: 10.1007/s00239-003-2565-8; pmid: 15114422
22. X. Song, P. Jin, S. Qin, L. Chen, F. Ma, The evolution and origin of animal Toll-like receptor signaling pathway revealed by network-level molecular evolutionary analyses. *PLOS ONE* **7**, e51657 (2012). doi: 10.1371/journal.pone.0051657; pmid: 23236523
23. M. E. Gauthier, L. Du Pasquier, B. M. Degnan, The genome of the sponge *Amphimedon queenslandica* provides new perspectives into the origin of Toll-like and interleukin 1 receptor pathways. *Evol. Dev.* **12**, 519–533 (2010). doi: 10.1111/j.1525-142X.2010.00436.x; pmid: 20883219
24. J. M. Roach, L. Racioppi, C. D. Jones, A. M. Masci, Phylogeny of Toll-like receptor signaling: Adapting the innate response. *PLOS ONE* **8**, e54156 (2013). doi: 10.1371/journal.pone.0054156; pmid: 23326591
25. C. de la Cova *et al*., Supercompetitor status of *Drosophila* Myc cells requires p53 as a fitness sensor to reprogram metabolism and promote viability. *Cell Metab.* **19**, 470–483 (2014). doi: 10.1016/j.cmet.2014.01.012; pmid: 24561262
26. T. Tanji, X. Hu, A. N. Weber, Y. T. Ip, Toll and IMD pathways synergistically activate an innate immune response in *Drosophila melanogaster*. *Mol. Cell. Biol.* **27**, 4578–4588 (2007). doi: 10.1128/MCB.01814-06; pmid: 17438142
27. R. S. Khush, F. Leulier, B. Lemaitre, *Drosophila* immunity: Two paths to NF-κB. *Trends Immunol.* **22**, 260–264 (2001). doi: 10.1016/S1471-4906(01)01887-7; pmid: 11323284
28. M. S. Dushay, B. Asling, D. Hultmark, Origins of immunity: Relish, a compound Rel-like gene in the antibacterial defense of *Drosophila*. *Proc. Natl. Acad. Sci. U.S.A.* **93**, 10343–10347 (1996). doi: 10.1073/pnas.93.19.10343; pmid: 8816802
29. R. Steward, Dorsal, an embryonic polarity gene in *Drosophila*, is homologous to the vertebrate proto-oncogene, c-rel. *Science* **238**, 692–694 (1987). doi: 10.1126/science.3118464; pmid: 3118464
30. Y. T. Ip *et al*., Dif, a dorsal-related gene that mediates an immune response in *Drosophila*. *Cell* **75**, 753–763 (1993). doi: 10.1016/0092-8674(93)90495-C; pmid: 8242747
31. N. Silverman *et al*., Immune activation of NF-κB and JNK requires *Drosophila* TAK1. *J. Biol. Chem.* **278**, 48928–48934 (2003). doi: 10.1074/jbc.M304802200; pmid: 14519762
32. P. Towb, H. Sun, S. A. Wasserman, Tube Is an IRAK-4 homolog in a Toll pathway adapted for development and immunity. *J. Innate Immun.* **1**, 309–321 (2009). doi: 10.1159/000200773; pmid: 19498957
33. X. Meng, B. S. Khanuja, Y. T. Ip, Toll receptor-mediated *Drosophila* immune response requires Dif, an NF-κB factor. *Genes Dev.* **13**, 792–797 (1999). doi: 10.1101/gad.13.7.792; pmid: 10197979
34. D. Morisato, K. V. Anderson, The spätzle gene encodes a component of the extracellular signaling pathway establishing the dorsal-ventral pattern of the *Drosophila* embryo. *Cell* **76**, 677–688 (1994). doi: 10.1016/0092-8674(94)90507-X; pmid: 8124709
35. D. Stein, J. S. Goltz, J. Jurcsak, L. Stevens, The Dorsal-related immunity factor (Dif) can define the dorsal-ventral axis of polarity in the Drosophila embryo. *Development* **125**, 2159–2169 (1998).pmid: 9570779
36. S. Tauszig, E. Jouanguy, J. A. Hoffmann, J. L. Imler, Toll-related receptors and the control of antimicrobial peptide expression in *Drosophila*. *Proc. Natl. Acad. Sci. U.S.A.* **97**, 10520–10525 (2000). doi: 10.1073/pnas.180130797; pmid: 10973475
37. S. Stoven *et al*., Caspase-mediated processing of the *Drosophila* NF-κB factor Relish. *Proc. Natl. Acad. Sci. U.S.A.* **100**, 5991–5996 (2003). doi: 10.1073/pnas.1035902100; pmid: 12732719
38. M. Kim, J. H. Lee, S. Y. Lee, E. Kim, J. Chung, Caspar, a suppressor of antibacterial immunity in *Drosophila*. *Proc. Natl. Acad. Sci. U.S.A.* **103**, 16358–16363 (2006). doi: 10.1073/pnas.0603238103; pmid: 17050695
39. D. Ertürk-Hasdemir *et al*., Two roles for the *Drosophila* IKK complex in the activation of Relish and the induction of antimicrobial peptide genes. *Proc. Natl. Acad. Sci. U.S.A.* **106**, 9779–9784 (2009). doi: 10.1073/pnas.0812022106; pmid: 19497884
40. G. Storelli *et al*., *Lactobacillus plantarum* promotes *Drosophila* systemic growth by modulating hormonal signals through TOR-dependent nutrient sensing. *Cell Metab.* **14**, 403–414 (2011). doi: 10.1016/j.cmet.2011.07.012; pmid: 21907145
41. N. A. Broderick, N. Buchon, B. Lemaitre, Microbiota-induced changes in *Drosophila melanogaster* host gene expression and gut morphology. *mBio* **5**, e01117-14 (2014). doi: 10.1128/mBio.01117-14; pmid: 24865556
42. S. C. Shin *et al*., *Drosophila* microbiome modulates host developmental and metabolic homeostasis via insulin signaling. *Science* **334**, 670–674 (2011). doi: 10.1126/science.1212782; pmid: 22053049
43. A. Basset *et al*., The phytopathogenic bacteria *Erwinia carotovora* infects *Drosophila* and activates an immune response. *Proc. Natl. Acad. Sci. U.S.A.* **97**, 3376–3381 (2000). doi: 10.1073/pnas.97.7.3376; pmid: 10725405
44. M. Kazemian, M. H. Brodsky, S. Sinha, Genome Surveyor 2.0: *cis*-regulatory analysis in *Drosophila*. *Nucleic Acids Res.* **39** (suppl.), W79-W85 (2011). doi: 10.1093/nar/gkr291; pmid: 21593125
45. M. Hedengren *et al*., Relish, a central factor in the control of humoral but not cellular immunity in *Drosophila*. *Mol. Cell* **4**, 827–837 (1999). doi: 10.1016/S1097-2765(00)80392-5; pmid: 10619029
46. T. Lee, L. Luo, Mosaic analysis with a repressible cell marker (MARCM) for *Drosophila* neural development. *Trends Neurosci.* **24**, 251–254 (2001). doi: 10.1016/S0166-2236(00)01791-4; pmid: 11311363

ACKNOWLEDGMENTS

We thank numerous colleagues for providing fly strains and reagents; L. Alpar, J. D'Arcangelo, S. Park, E. Bates, and F. Mayer for discussions and assistance with some experiments; J.-M. Reichhart, T. Ip, N. Silverman, and P. Meier for helpful discussions early in the project; and D. Littman, S. Reiner, and members of the Johnston and Basler labs for advice. Stocks obtained from the Bloomington *Drosophila* Stock Center (NIH P40OD018537) and the Harvard TRiP collection (National Institute of General Medical Sciences R01-GM084947) were used in this study. This work was supported by a European Molecular Biology Organization Long-Term Postdoctoral Fellowship (M.A.), the Leukemia and Lymphoma Society (C.B.), the European Research Council (K.B.), the Swiss National Science Foundation (K.B. and S.N.M.), and the NIH (L.A.J.). The S2 cells used in the cell-based competition assays in this study are available under a materials transfer agreement from Columbia University.

SUPPLEMENTARY MATERIALS

www.sciencemag.org/content/346/6214/1258236/suppl/DC1
Figs. S1 to S8
Tables S1 and S2

2 July 2014; accepted 31 October 2014
10.1126/science.1258236

RESEARCH ARTICLE

PLANT GENETICS

Dominance hierarchy arising from the evolution of a complex small RNA regulatory network

Eléonore Durand,[1]* Raphaël Méheust,[1]* Marion Soucaze,[1] Pauline M. Goubet,[1]† Sophie Gallina,[1] Céline Poux,[1] Isabelle Fobis-Loisy,[2] Eline Guillon,[2] Thierry Gaude,[2] Alexis Sarazin,[3] Martin Figeac,[4] Elisa Prat,[5] William Marande,[5] Hélène Bergès,[5] Xavier Vekemans,[1] Sylvain Billiard,[1] Vincent Castric[1]‡

The prevention of fertilization through self-pollination (or pollination by a close relative) in the Brassicaceae plant family is determined by the genotype of the plant at the self-incompatibility locus (*S* locus). The many alleles at this locus exhibit a dominance hierarchy that determines which of the two allelic specificities of a heterozygous genotype is expressed at the phenotypic level. Here, we uncover the evolution of how at least 17 small RNA (sRNA)–producing loci and their multiple target sites collectively control the dominance hierarchy among alleles within the gene controlling the pollen *S*-locus phenotype in a self-incompatible *Arabidopsis* species. Selection has created a dynamic repertoire of sRNA-target interactions by jointly acting on sRNA genes and their target sites, which has resulted in a complex system of regulation among alleles.

Sporophytic self-incompatibility (SI) is a genetic system that evolved in hermaphroditic plants to enforce outcrossing (by preventing self-fertilization) and involves a polymorphism in which multiple alleles are maintained and display dominance-recessivity relations. In the genus *Arabidopsis*, SI is controlled by a single genomic region "the *S* locus," which contains two tightly linked genes that encode the pollen *S*-locus cysteine-rich (SCR) and stigma *S*-locus receptor kinase (SRK) recognition proteins, whose ligand-receptor molecular docking leads to self-pollen rejection (*1*–*4*). The pollen recognition phenotype is controlled by the diploid paternal parent's genotype, but even though most plants are heterozygous at this locus (*5*), the pollen recognition phenotype is typically determined by one of the two alleles only, according to the alleles' relative positions in a hierarchy or network of dominance-recessivity interactions between *S* alleles (*6*). Selection is expected to favor genetic elements ("dominance modifiers"), which establish dominance-recessivity interaction rather than codominance, because individuals with a codominant genotype can produce pollen rejected by more potential mates than would occur in a dominant-recessive system (*7*, *8*). On the basis of modeling (*8*), the large nonrecombining region composing the *S* locus (*9*–*11*) is a strong candidate region for hosting such genetic elements.

Until recently, the dominance modifiers assumed in models (*7*, *8*) remained hypothetical. A particular small RNA (sRNA) has been identified (*12*) within the *S* locus of dominant alleles in Brassica (called *Smi*). This sRNA acts as a trans-modifier of the gene controlling pollen specificity via de novo methylation of the promoter of recessive alleles, which leads to transcriptional silencing of recessive alleles by dominant alleles (*13*, *14*). However, the mechanism in the more complex dominance-recessivity networks in species that have many levels in the dominance hierarchy (*15*, *16*) is unknown. Indeed, balancing selection typically leads to the maintenance of a large number of *S* alleles in self-incompatible

[1]Laboratoire Génétique et Evolution des Populations Végétales, CNRS UMR 8198, Université Lille 1, F-59655 Villeneuve d'Ascq cedex, France. [2]Reproduction et Développement des Plantes, Institut Fédératif de Recherche 128, Centre National de la Recherche Scientifique, Institut National de la Recherche Agronomique, Université Claude Bernard Lyon I, Ecole Normale Supérieure de Lyon, F-69364 Lyon, Cedex 07, France. [3]Department of Biology, Swiss Federal Institute of Technology Zurich, CH-8093 Zurich, Switzerland. [4]UDSL Université Lille 2 Droit et Santé, and Plate-forme de génomique fonctionnelle et structurale IFR-114, F-59000 Lille, France. [5]Centre National des Ressources Génomiques Végétales, INRA UPR 1258, Castanet-Tolosan, France.
*These authors contributed equally to this work. †Deceased.
‡Corresponding author. E-mail: vincent.castric@univ-lille1.fr

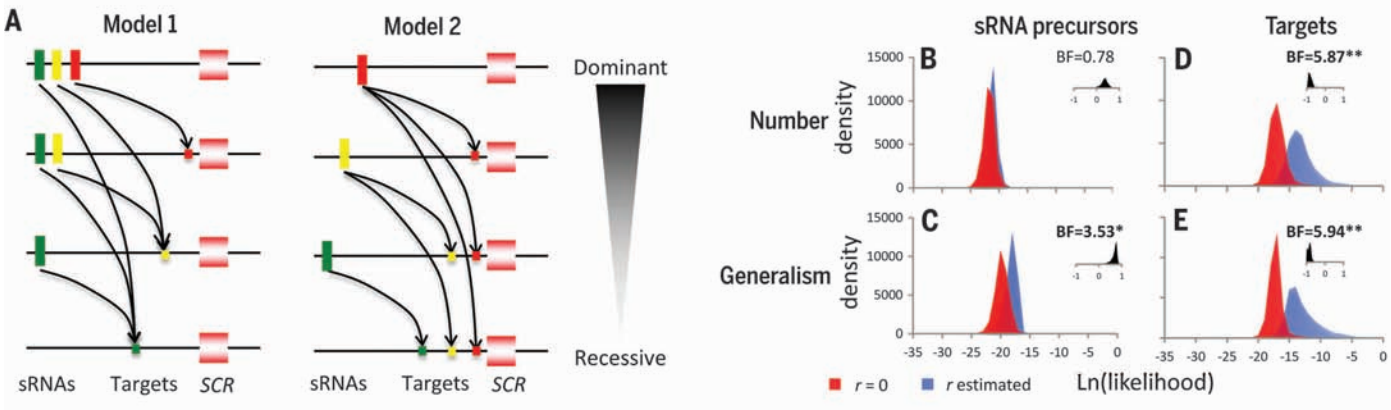


Fig. 1. Models for the control of dominance-recessivity by sRNA-target interactions in a multiallelic system. (**A**) Two models were tested to explain how a simple mechanistic model (*12*) can be generalized to a multiallelic system. Under model 1, dominant *S* alleles carry a larger set of sRNA precursor genes, whereas, under model 2, the same linear hierarchy is achieved by a larger set of sRNA targets carried by recessive *S* alleles. Under model 1, sRNA targets of recessive alleles are also more "generalist" than those of dominant alleles, whereas, under model 2, it is the sRNA precursors of the dominant alleles that are more generalist. (**B** to **E**) Likelihood distributions of Bayesian models if one assumes no correlation or allows for some level of correlated evolution between: (B) dominance and the number of sRNAs precursors expressed; (C) dominance and sRNA generalism, defined as the average number of targets used per sRNA precursor; (D) dominance and the number of target sites; and (E) dominance and target sites generalism, defined as the average number of distinct sRNA precursors using each target. The Bayes factor (BF) comparing both models is given on each panel as asterisks, as well as the distribution of correlation coefficients. *BF > 2: evidence for the dependent model, **BF > 5: strong evidence, and ***BF > 10: very strong evidence (*38*).

Downloaded from www.sciencemag.org on December 5, 2014

species, and the >50 *S* alleles observed in outcrossing *Arabidopsis* species (*17*) are predicted to form up to 1225 distinct heterozygous genotypes. In Brassica, class II alleles similarly show a linear dominance hierarchy that cannot be explained by the action of *Smi* alone (*12*, *18*). Under the mechanistic model involving sRNAs and their targets within the *SCR* gene, two hypotheses could explain an allelic series of *n* distinct *S* alleles in a linear dominance hierarchy. First, the most-dominant allele might produce *n* – 1 distinct sRNAs, each specifically targeting a given more-recessive *S* allele, whereas the next-most-dominant allele might produce sRNAs targeting all *S* alleles more recessive than itself, and so on (with the bottom recessive producing no sRNAs but having targets for all more-dominant alleles). This model predicts that the top dominant allele produces the largest number of sRNAs and that the bottom recessive allele carries the fewest but is targeted by the largest number of sequences; we refer to this as model 1 (Fig. 1A). Alternatively, the most dominant allele might produce a single sRNA, as in Brassica (*12*), and all subsequent more-recessive *S* alleles might carry a specific target that interacts with the most-dominant allele in a manner that results in nonexpression (Fig. 1A); the next allele in the hierarchy (that is recessive to the top dominant, but dominant to other classes) might produce a different sRNA, whose target sequence is present in all alleles recessive to itself, and so on. This model (model 2 in Fig. 1A) predicts that only a single sRNA is produced in all but the most-recessive allele, where the most-recessive allele carries the largest number of target sequences (each targeted by a different dominant allele).

Results

Phenotypic characterization of the dominance network

To determine the mechanisms of *S*-allele dominance in the self-incompatible plant *Arabidopsis halleri*, we first phenotypically characterized the dominance network between six *S* alleles, by crossing each of the 15 heterozygous genotypic combinations to both of its respective "tester" lines (i.e., lines that express a single *S* allele) (*19*). Overall, combining these results with those from previous studies (*16*), we determined all possible pairwise relations and observed dominance in 14 cases (93.3%) and codominance for a single case (Fig. 2A). The resulting network is fully transitive and takes the form of a simple linear hierarchy with two alleles at the top of the hierarchy (Ah13 and Ah20) (Fig. 2B).

S locus–specific sRNA precursor genes

We then examined the highly differentiated nonrecombining region within the *S* locus (*9*) (Fig. 3A) and deep-sequenced sRNA populations of floral buds (*19*) from 11 individuals carrying the six *S* alleles in various heterozygous combinations. Applying a set of criteria for annotating plant micro-RNA (miRNA) genes (*19*, *20*), we identified a total of 17 sRNA precursor sequences among the six tested alleles (Fig. 3B and fig. S2), with an average of about 2.8 sRNA precursors per allele (Fig. 3B). Given the large number of *S* alleles segregating in natural populations of *A. halleri* (*17*), this is fewer than expected if dominant alleles targeted each individual recessive allele by a distinct sRNA gene (as predicted from model 1).

The 17 expressed motifs (Fig. 3B) can be classified into eight distinct families on the basis of sequence divergence (fig. S3). Three of these families (*mir1887*, *mir4239*, and *mir867*) have clear homology to miRNA genes annotated in the *A. thaliana* genome and are present in the miRBase database (*21*), although it is unclear whether they should be considered bona fide miRNA genes, especially because it has been suggested that *Smi* might achieve silencing through a different—largely uncharacterized—sRNA pathway (*22*). In *A. thaliana*, these miRNA genes were all in the region flanked by *At4g21350* and *At4g21380*, which contains the relics of the degenerate *S* locus (*23*). Although their function has not been assessed so far, our results suggest that these motifs may have served as modifiers of *S*-allele dominance, consistent with the fact that the *A. thaliana S* locus has only recently undergone degeneration (*24*). The five other families we identified have no homology to any sequence in miRBase.

Identification and functional validation of sRNA-target interactions

The model proposed in *Brassica* was from observations of specific targeting of the promoter region of recessive *SCR* alleles involving sequences in recessive alleles showing similarity with the 24–nucleotide (nt) sRNA produced by dominant ones (*12*). We therefore searched for similarities between sRNA sequences produced by the 17 sRNA precursors identified above and sequences within 1 kilobase (kb) on either side of the six *SCR* alleles, where the majority of regulatory elements and, thus, potential target sites of the sRNAs are most likely to be found (*25*–*27*). In total, with stringent alignment criteria (*28*) (alignment threshold = 18), we identified potentially strong signals for 21 pairwise sRNA-*SCR* interactions (Fig. 3B and fig. S4), greater than expected on the basis of randomized sequences with nucleotide composition identical to that of real *SCR* sequences (fig. S5). Thus, *SCR* sequences appear to be highly enriched in sRNA target sites.

We focused on one specific sRNA-target interaction to validate in planta the regulatory effect of the sRNA gene on its target. The SI system can be transferred in *A. thaliana*, a self-fertile species, by transformation with the *SRK-SCR* genes from self-incompatible Brassicaceae (*29*), and the SI response is particularly robust and stable on stage 13 stigmas from the C24 ecotype (*30*, *31*). We thus transformed C24 *A. thaliana* plants with either *AhSRK01* or *AhSCR01*, i.e., the female and male determinants, respectively, of the most recessive *S* allele, Ah01 (*19*). Pollen from the hemizygous *AhSCR01*-transformed line was rejected on stage 13 stigmas from the *AhSRK01*-transformed line but was functional on wild-type (WT) stigmas, which demonstrated a reconstructed SI response (Fig. 4A and table S1) (*19*). We then tested the effect of the *mirS3* sRNA precursor gene produced by Ah20 (*Ah20mirS3*), which we

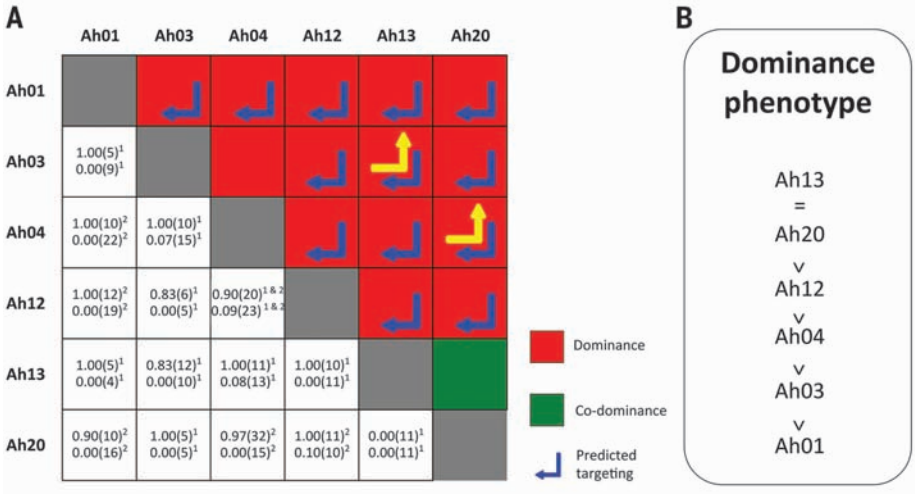


Fig. 2. Phenotypic network of dominance-recessivity interactions between alleles. (**A**) Dominance network obtained by controlled crosses and comparison with the molecular model. Below the diagonal, the proportion of compatible crosses on female tester lines of the column allele is given first for each heterozygote combination, followed by the proportion of compatible crosses on female tester lines of the row allele. Numbers in parentheses indicate the number of replicate crosses to determine the proportion in each type of crosses. Superscripts indicate the source of the data: 1, present study; 2, (*16*). Above the diagonal, pairwise dominance interactions, as inferred from the crosses, are represented in red and codominance in green. Blue arrows indicate that the column allele is producing a sRNA that is predicted to target the row allele. Yellow arrows indicate that the row allele is producing a sRNA that is predicted to target the column allele (Smith and Waterman stringency threshold = 18). (**B**) Controlled crosses (detailed in Fig. 2) can be represented as a linear dominance hierarchy among the six *S* alleles.

predicted to be the genetic element causing dominance of Ah20 over Ah01 (Figs. 2A and 3B). We generated *Ah20mirS3 A. thaliana* transgenic lines, which we crossed with the *AhSCR01* line to obtain hybrid plants containing the two transgenes in hemizygous state (i.e., as biologically relevant for *S* alleles) (table S1) (*19*). Pollen from these hybrid plants could germinate on *AhSRK01* stigmas, which showed that the presence of *Ah20mirS3* was sufficient to abolish the SI response conferred by *AhSCR01* alone (Mood's median test *P* value = 2.2×10^{-4} and 3.2×10^{-5} on two replicate *Ah20mirS3* insertion lines) (Fig. 4A). Finally, we produced a mutated *AhSCR01* line (*AhSCR01**) in which we introduced a set of four point mutations specifically in the *Ah20mirS3* predicted target (located in the intron of *AhSCR01*) (Figs. 3B and 4B), which we crossed with lines containing *Ah20mirS3*. As expected, pollen from the *AhSCR01* Ah20mirS3* hybrid plants was insensitive to the effect of *Ah20mirS3* and was rejected on *AhSRK01* stigmas. Hence, our data demonstrate that our predicted target site for *AhSCR01* was necessary for the regulatory effect of *Ah20mirS3* (Fig. 4B). Note that sRNA target sites within introns of genes have already been observed and validated experimentally, in a different context (*32*). Overall, our validation procedure provides direct experimental support to identify sRNA genes and their target sites, although a complete experiment involving all 21 predicted sRNA-target interactions would arguably be required to fully validate the proposed regulatory mechanism between the six *S* alleles.

Power and accuracy of the molecular model

We evaluated power and accuracy of our model of dominance-recessivity interactions by comparing molecular predictions with the phenotypic observations from controlled crosses. With two exceptions, most (93.1%) of the predictions connect a sRNA produced by a dominant allele to a target present in a more-recessive allele above the proportion expected by chance alone (about 63 to 79%, obtained by 100,000 random permutations) (fig. S6), which suggests that our molecular prediction of target sites is reliable, with a low false-positive rate. Overall, 13 of the 14 dominance-recessivity relations observed in our tests (93%) were predicted by at least one sRNA targeting prediction (Fig. 2A), which suggests that sRNAs can explain the majority of the interactions we observe at the phenotypic level. Thus, a simple molecular model explaining the control of dominance through factors closely linked to the *S* locus can predict observed dominance phenotypes.

A single interaction (Ah04>Ah03) remains unexplained by this simple mechanism. We thus enlarged our search to sRNA reads in the *S* locus that are not derived from hairpins. Because of the high transposable element (TE) content of the *S* locus (*9*), such small interfering RNAs (siRNAs) are particularly abundant in the region. Collectively, siRNAs seem to target dominant alleles about as frequently as recessive alleles (fig. S6) and are very close to random expectations, which suggests that, even though some of them may indeed regulate dominance, most of them are probably derived from the TE control machinery with no specific role in controlling dominance-recessivity interactions. In the case of the unexplained Ah04>Ah03 interaction, none of the siRNAs produced by Ah04 is predicted to target *AhSCR03* (fig. S7). It is possible that another sRNA, whose low abundance may remain undetected, is controlling dominance of Ah04 over Ah03.

Dominance and recessivity—More sRNAs or more targets?

Given the diversity of both sRNA precursors and their targets, we asked whether the position of *S* alleles along the dominance hierarchy is explained by models 1 or 2 (Fig. 1A), i.e., by number or by "generalism" (the ability of their resulting

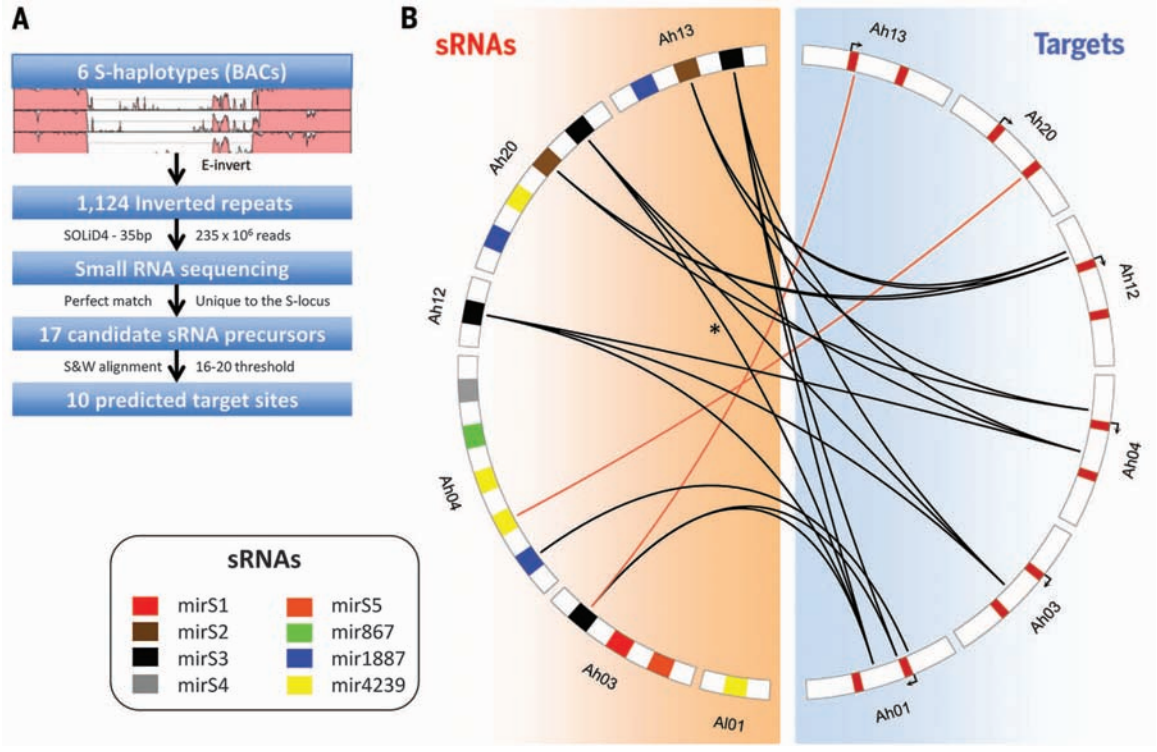


Fig. 3. Regulatory network determined from sRNAs and their predicted targets in *A. halleri*. (**A**) Flowchart of the annotation procedure of sRNA precursors. (**B**) Repertoire of sRNAs precursors and their predicted targets. sRNA precursors carried by each *S* allele are represented on the left. Precursor families are color-coded, and the correspondence between colors and precursor families is given in the box on the bottom left. sRNA targets on the *SCR* gene (±1 kb) are represented on the right. *S* alleles are displayed according to their position along the dominance hierarchy represented on Fig. 2B (dominant alleles on top, recessive alleles at the bottom). Red boxes on the target side correspond to the two exons on *SCR*, with arrows giving the direction of transcription. For clarity, length variation of the *SCR* intron is not represented. A line joins a precursor with a target whenever the precursor produces a sRNA that is predicted to use that target (based on an alignment threshold of 18). Black and red lines represent targeting relations that are and are not consistent with the phenotypic network, respectively. The star symbol indicates the sRNA-target interaction that we functionally validate in Fig. 4 (*Ah20mirS3* on *AhSCR01*).

sRNAs to target a broader spectrum of *S* alleles) of the sRNA precursors and the targets they carry. Taking the phylogeny of the *S* alleles into account, we compared with Bayes factors (BFs) if the sRNA precursors or their inferred targets evolve in a correlated manner with dominance or if they are independent. We detected an asymmetry between the functional evolution of sRNAs and that of their targets. Overall, we confirmed that sRNA precursors in dominant *S* alleles are predicted to target more *S* alleles than those of recessive alleles [BF = 21.7***, correlation coefficient (r) = 0.99] (fig. S8) [for the explanation of asterisk indications, see the legend to (Fig. 1)]. However, dominant *S* alleles do not do this by increased total numbers of sRNA precursors [BF = 0.78 (not significant), r = 0.33] (Fig. 1B) but rather by greater sRNA precursor generalism (BF = 3.53*, r = 0.64) (Fig. 1C). In contrast, the observed increased degree to which recessive alleles are targeted by sRNAs (BF = 21.7***, r = −0.99) (fig. S8) appears to have involved both increased total numbers of targets (BF = 5.87**, r = −0.81) (Fig. 1D) and increased generality of each target (BF = 5.94**, r = −0.84) (Fig. 1E). Overall, our results support model 2, with the addition that several sRNA precursors cooperate to provide the full targeting spectrum of dominant alleles. However, targets carried by recessive alleles have wider spectra than those of more-dominant alleles, a feature of model 1.

Evolution by gain and loss

To infer the evolutionary changes in the regulatory network in a broader phylogenetic context, we inspected the repertoire of sRNA precursors and their targets on a set of 14 additional *S* alleles from bacterial artificial chromosome (BAC) sequences for the *S* locus [(*9*, *10*, *33*) and this study]. sRNA precursor genes were inferred from sequence similarity with the 17 sRNA genes examined, plus the *Smi* sRNA precursor of *Brassica* (*12*). Overall, the 20 *S* alleles yielded 86 putative sRNA genes with sequence similarity to either *Smi* or one of the eight sRNA families (Fig. 5 and fig. S3). From the six *S* alleles for which small RNA–sequencing (sRNA-seq) data were available, 23 sequence motifs were detected from this homology search. Hence, six motifs were present in addition to the 17 sRNA precursors in Fig. 3B but not supported by sRNA reads, which suggested that some of these elements may be expressed at levels too low to detect by sRNA-seq. Notably, although significant hits of *Smi* motifs were identified in seven different *A. halleri S* alleles, none of them was expressed at a detectable level. In some *S* alleles, several of these "silent" motifs have as many predicted targets as expressed motifs from the same family (fig. S9), but on average, these motifs tend to have fewer predicted targets than those that are expressed (fig. S9). This finding suggests that these sRNA genes may have undergone functional degeneration with decreased targeting ability, which may suggest a turnover of active sRNA genes on the *S* alleles.

The presence or absence of the 86 putative sRNA genes was consistent with the phylogeny of the different alleles from the *SRK* gene, which suggested that interallelic recombination at the *S* locus in SI lineages is infrequent (*9*–*11*). Accordingly, ancestral states reconstruction inferred the most likely scenario of gains and losses of the different precursors in a Bayesian framework (Fig. 5 and fig. S10) (*19*). This reconstruction indicates that some sRNA precursor families (*mirS2*, *mirS3*, and *mir4239*) are ancient and can be traced back to the most recent common ancestor of all extant *S* alleles. In contrast, several precursor families seem to have evolved more recently, during the diversification of this species' *S* alleles (*mirS1*, *mir867*, *mirS4*, and *mirS5*) and are found only in the two lineages of more-recessive alleles [classes II and III, according to (*15*)] (Fig. 5). For the two remaining families (*mirSmi* and *mir1887*) ancestral reconstruction indicates multiple independent origins on different alleles, although horizontal transfer by occasional recombination between *S* alleles may also potentially explain this pattern. Repertoires of precursors on the different *S* alleles were also modified in the course of evolution by repeated deletions, and we infer at least eight independent deletion events. Finally, some precursor families seem to have been expanded by duplication, as several *S* haplotypes have multiple paralogs of a given sRNA precursor family (up to four *mir4239* precursors on allele Al13) (Fig. 5).

Reconstruction of ancestral states is more challenging for the sRNA targets, because of their more-variable phylogenetic distribution. From our analyses, we observed that evolution of the newly arisen *mir867* precursor—from the common ancestor of Ah04, Ah10, and Al16—and acquisition of the *mirS4* precursor by Ah04 are both associated with the acquisition of their cognate targets on the respective branch from the same ancestral node, which indicated that allelic diversification was closely followed by the emergence of sRNA-target interactions. At least one target is also inferred to be ancient (that of *mirS3* in the intron of *SCR*), which suggested that there may be functional constraint over evolutionary times. No putative target could be identified for *mirS1* and *mirS5*, which may control dominance over currently unidentified alleles known to exist in the species (*17*, *34*).

Evolutionary conservation of the sRNA genes

To evaluate functional constraints of the sRNA motifs, we compared sequence divergence between functional orthologs of the *S*-locus region

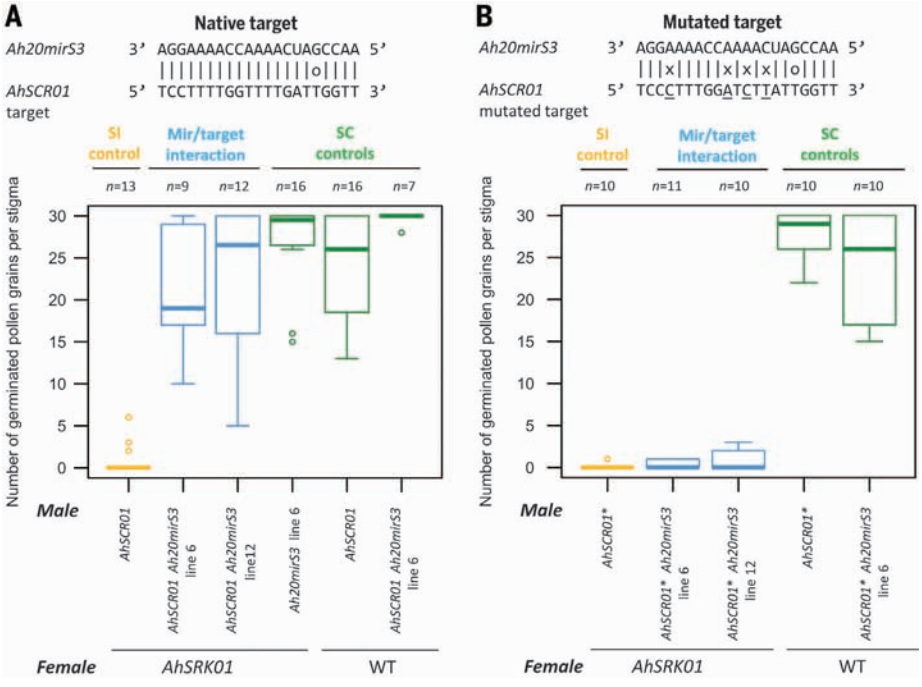


Fig. 4. *In planta* functional validation that Ah20 controls phenotypic expression of *SCR01* through specific targeting by *mirS3*. (**A**) *Ah20mirS3* is sufficient to abolish the SI response of *AhSCR01*. (**B**) The mutated target makes *AhSCR01** insensitive to the effect of *Ah20mirS3*. Pollen compatibility was estimated by the number of germinated pollen grains per stigma. Incompatible crosses (SI) are colored in yellow-orange, compatible controls (SC) in green, and tests of the mir-target interactions in blue (see table S1). Mir-target interactions were tested on hybrids produced from two *Ah20mirS3*-independent insertion lines, named lines 6 and 12. Thick bars represent the median, boxes the interquartile range, whiskers extend out 1.5 times the interquartile range, and individual points are outliers. The number of replicates (n) is indicated above each cross. (A) (Top) The most abundant targeting sRNA produced by the *Ah20mirS3* precursor is aligned with the *SCR01* predicted target; in (B), it is aligned with the mutated target. Mismatches are represented by "x," and G:U wobbles by "o." Mutated bases are underlined.

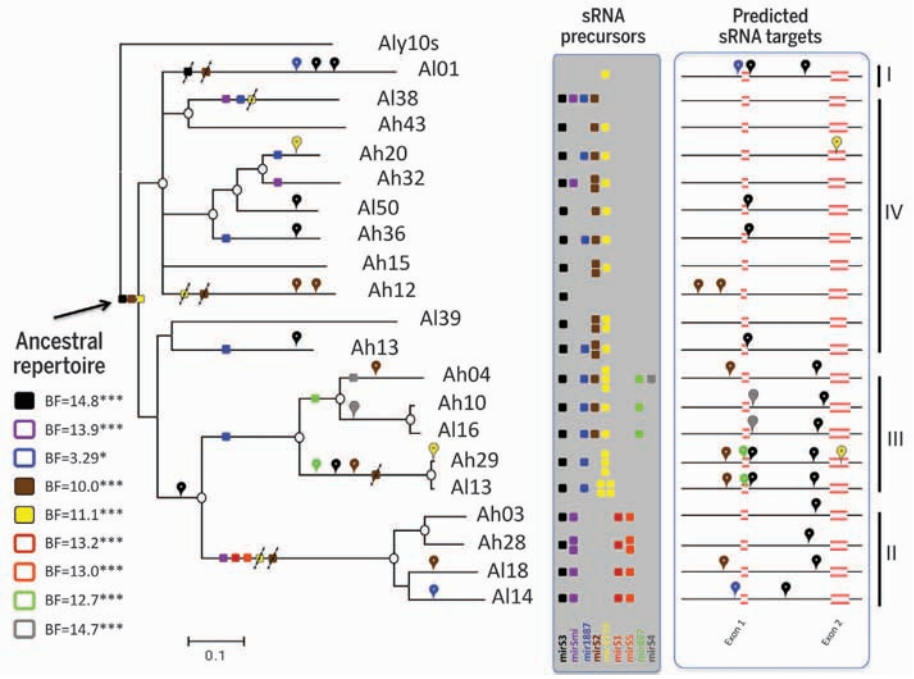


Fig. 5. Repertoire of sRNA genes and their targets along the phylogeny of *S* alleles. The Bayesian phylogeny is based on full *A. halleri* and *A. lyrata SRK* amino acid sequences. Node support was assessed by posterior probabilities (PP), and nodes with PP > 0.95 are represented by white circles. Phylogenetic classes are reported (I, II, III, and IV) (*15*). The scenario of gain and loss for sRNA precursors and their targets is represented on the branch where each event is inferred. Solid and open squares indicate precursors that are inferred to have been present and absent from the ancestral repertoire, respectively. For each precursor, asterisks for BFs indicate the level of confidence on the presence or absence from the ancestral repertoire. *BF > 2: some evidence, **BF > 5: strong evidence, and ***BF > 10: very strong evidence (*38*).

in *A. halleri*, *A. lyrata*, and *A. thaliana* (*17*). As a whole, this nonrecombining region includes large amounts of noncoding and repetitive sequences and displays extremely high levels of sequence divergence (*9*) (fig. S11). However, the two protein-coding genes in the region, *SCR* and *SRK*, as well as the set of sRNA precursors, form islands of sequence conservation, even in the comparison with *A. thaliana*, over at least 10 million years, which suggests that substantial functional constraints exist on these motifs, at least comparable to that acting upon the protein-coding genes controlling SI specificity.

Conclusions

The molecular mechanisms of genetic dominance (and its flip side, recessivity), integral to Mendel's discoveries, have been strongly debated. For deleterious mutations, this debate was largely resolved by the understanding that physiological properties of metabolic pathways rather than dominance modifiers (i.e., genetic elements controlling the dominance of genes) explain many, if not all, dominance-recessivity interactions in genomes (*35*). For balanced polymorphisms, however, dominance modifiers could evolve under natural selection in theoretical models (*36*, *37*), and our analysis now provides a molecular basis for most of the control of dominance levels for SI. Although regulatory networks have typically been viewed as arising between genes in a genome, we present a surprisingly complex example of a regulatory network among alleles at a single genetic locus. Moreover, as predicted theoretically, the sRNA genes that we identified as involved in the control of dominance are found within the *S*-locus region.

An interesting question is how natural selection has shaped the genetic elements controlling this network. Although our empirical results support the theoretical predictions cited above, there is a major difference between the single dominance modifiers assumed by the models and the system of interacting sequences that produce the actual *SCR* dominance relations in *A. halleri*; the system of sRNAs and their targets entails a coevolutionary process between the two interacting partners, which is not found in previous models (*7*, *8*). Such a coevolutionary process could potentially correspond either to an evolutionary arms race (with dominant *S* alleles accumulating sRNA genes, whereas recessive ones escape silencing by mutations in their targets) or to a mutualistic system. One can argue that the latter is more likely because the models show that natural selection on this type of SI system mostly acts against codominance and that dominance and recessivity are both equally advantageous (*7*, *8*). When such data will be extended to more alleles, it will be interesting to compare the results with further theoretical expectations based on evolutionary arms race or mutualistic interactions models.

REFERENCES AND NOTES

1. C. R. Schopfer, M. E. Nasrallah, J. B. Nasrallah, *Science* **286**, 1697–1700 (1999).
2. S. Takayama *et al.*, *Proc. Natl. Acad. Sci. U.S.A.* **97**, 1920–1925 (2000).
3. J. C. Stein, B. Howlett, D. C. Boyes, M. E. Nasrallah, J. B. Nasrallah, *Proc. Natl. Acad. Sci. U.S.A.* **88**, 8816–8820 (1991).
4. T. Takasaki *et al.*, *Nature* **403**, 913–916 (2000).
5. D. De Nettancourt, *Incompatibility and Incongruity in Wild and Cultivated Plants* (Springer-Verlag, Berlin, 2001).
6. A. J. Bateman, *Heredity* **9**, 53–68 (1955).
7. V. Llaurens, S. Billiard, V. Castric, X. Vekemans, *Evolution* **63**, 2427–2437 (2009).
8. D. J. Schoen, J. W. Busch, *Evolution* **63**, 2099–2113 (2009).
9. P. M. Goubet *et al.*, *PLOS Genet.* **8**, e1002495 (2012).
10. Y. L. Guo, X. Zhao, C. Lanz, D. Weigel, *Plant Physiol.* **157**, 937–946 (2011).
11. G. Suzuki *et al.*, *Genetics* **153**, 391–400 (1999).
12. Y. Tarutani *et al.*, *Nature* **466**, 983–986 (2010).
13. H. Shiba *et al.*, *Plant Cell* **14**, 491–504 (2002).
14. H. Shiba *et al.*, *Nat. Genet.* **38**, 297–299 (2006).
15. N. L. Prigoda, A. Nassuth, B. K. Mable, *Mol. Biol. Evol.* **22**, 1609–1620 (2005).
16. V. Llaurens *et al.*, *Evolution* **62**, 2545–2557 (2008).
17. V. Castric, J. Bechsgaard, M. H. Schierup, X. Vekemans, *PLOS Genet.* **4**, e1000168 (2008).
18. H. Shiba, S. Takayama, *Dev. Growth Differ.* **54**, 120–128 (2012).
19. Materials and methods are available as supplementary materials on *Science* Online.
20. B. C. Meyers *et al.*, *Plant Cell* **20**, 3186–3190 (2008).
21. A. Kozomara, S. Griffiths-Jones, *Nucleic Acids Res.* **39** (Database), D152–D157 (2011).
22. E. J. Finnegan, D. Liang, M. B. Wang, *Trends Plant Sci.* **16**, 238–241 (2011).
23. X. Vekemans, C. Poux, P. M. Goubet, V. Castric, *J. Evol. Biol.* **27**, 1372–1385 (2014).
24. J. S. Bechsgaard, V. Castric, D. Charlesworth, X. Vekemans, M. H. Schierup, *Mol. Biol. Evol.* **23**, 1741–1750 (2006).
25. T. R. O'Connor, C. Dyreson, J. J. Wyrick, *Bioinformatics* **21**, 4411–4413 (2005).
26. G. Zeller *et al.*, *Genome Res.* **18**, 918–929 (2008).
27. W. Zhang, T. Zhang, Y. Wu, J. Jiang, *Plant Cell* **24**, 2719–2731 (2012).
28. T. F. Smith, M. S. Waterman, *J. Mol. Biol.* **147**, 195–197 (1981).
29. M. E. Nasrallah, P. Liu, J. B. Nasrallah, *Science* **297**, 247–249 (2002).
30. M. E. Nasrallah, P. Liu, S. Sherman-Broyles, N. A. Boggs, J. B. Nasrallah, *Proc. Natl. Acad. Sci. U.S.A.* **101**, 16070–16074 (2004).
31. N. A. Boggs, J. B. Nasrallah, M. E. Nasrallah, *PLOS Genet.* **5**, e1000426 (2009).
32. Y. Meng, C. Shao, X. Ma, H. Wang, *Rice* **6**, 8 (2013).
33. T. T. Hu *et al.*, *Nat. Genet.* **43**, 476–481 (2011).
34. B. K. Mable, M. H. Schierup, D. Charlesworth, *Heredity* **90**, 422–431 (2003).
35. H. C. Bagheri, *J. Exp. Zoolog. B Mol. Dev. Evol.* **306B**, 329–359 (2006).
36. S. P. Otto, D. Bourguet, *Am. Nat.* **153**, 561–574 (1999).
37. S. Billiard, V. Castric, *Trends Genet.* **27**, 441–445 (2011).
38. M. Pagel, A. Meade, *Am. Nat.* **167**, 808–825 (2006).

ACKNOWLEDGMENTS

We thank D. Charlesworth, T. Tsuchimatsu, M. Boccara, D. J. Schoen, and M. Mirouze for advice and comments on the manuscript and J. Kitt, A. C. Holl, E. Schmitt, B. Huss, G. Neutelings, A. Achard, G. Laroche, and D. Achour for technical assistance. We acknowledge financial support from Agence Nationale de la Recherche Jeunes Chercheurs BRASSIDOM (ANR 11 JSV7-008-01), *Bonus Qualité Recherche* Université Lille 1 and Région Nord Pas de Calais (program "projets

émergents" MICRO2). R.M. was supported by an apprentice grant from CNRS. R.M. and E.D. contributed equally to this work. E.D. contributed to the crossing design and the phenotypic analysis. R.M., E.D., M.S., P.M.G., and S.G. contributed to the bioinformatics analysis. E.D., I.F.-L., E.G., and T.G. performed the functional validation experiment. C.P. performed the phylogenetic analysis. M.F. performed the sRNA-seq experiments. E.P., W.M., and H.B. constructed the BAC libraries and performed the screening and BAC sequencing. V.C., S.B., X.V., I.F.-L., and T.G. designed the experiments. All authors discussed the results. E.D., R.M., I.F.-L., X.V., S.B., and V.C. wrote the paper. V.C. and S.B. coordinated the project. *S*-locus sequences have been deposited on the European Molecular Biology Organization public database, sRNA sequences on the GEO public database (see table S2 for accession numbers), and data matrices and phylogenetic trees on the TreeBASE database (http://purl.org/phylo/treebase/phylows/study/TB2:S16394). BAC clones produced in this project will be distributed through http://cnrgv.toulouse.inra.fr/Library/Arabidopsis upon signature of a material transfer agreement for in-house academic research.

SUPPLEMENTARY MATERIALS

www.sciencemag.org/content/346/6214/1200/suppl/DC1
Materials and Methods
Figs. S1 to S12
Tables S1 and S2
References (*39*–*57*)

31 July 2014; accepted 17 October 2014
10.1126/science.1259442

REPORTS

VALLEYTRONICS

Ultrafast generation of pseudo-magnetic field for valley excitons in WSe_2 monolayers

Jonghwan Kim,[1]* Xiaoping Hong,[1]* Chenhao Jin,[1] Su-Fei Shi,[1,2] Chih-Yuan S. Chang,[3] Ming-Hui Chiu,[4] Lain-Jong Li,[3,4] Feng Wang[1,2,5]†

The valley pseudospin is a degree of freedom that emerges in atomically thin two-dimensional transition metal dichalcogenides (MX_2). The capability to manipulate it, in analogy to the control of spin in spintronics, can open up exciting opportunities. Here, we demonstrate that an ultrafast and ultrahigh valley pseudo-magnetic field can be generated by using circularly polarized femtosecond pulses to selectively control the valley degree of freedom in monolayer MX_2. Using ultrafast pump-probe spectroscopy, we observed a pure and valley-selective optical Stark effect in WSe_2 monolayers from the nonresonant pump, resulting in an energy splitting of more than 10 milli–electron volts between the K and K′ valley exciton transitions. Our study opens up the possibility to coherently manipulate the valley polarization for quantum information applications.

Atomically thin layers of transition metal dichalcogenides (MX_2) have emerged as an exciting two-dimensional semiconductor platform for nanoelectronics and optoelectronics (*1*, *2*). In particular, a pair of degenerate bands are present at the K and K′ valleys in the momentum space of hexagonal MX_2 monolayers, giving rise to a valley degree of freedom that is analogous to electron spin (*3*). Recent polarization-resolved photoluminescence (PL) studies show that the valley pseudospin in MX_2 can couple directly to the helicity of excitation photons (*4*–*7*) and that the pseudospin polarization between two valleys exhibits coherent behavior (*7*). It raises the intriguing prospect of valleytronics, which exploits the valley degree of freedom to carry information (*1*, *3*–*9*).

Just as spin manipulation is essential in spintronics, the capability to control the valley pseudospin is essential for valleytronics based on MX_2 materials. In spintronics, the electron spin can be manipulated through any external perturbation that breaks the energy degeneracy of two orthogonal spin polarizations. This can be achieved either through an external magnetic field (*10*, *11*) or through a pseudo-magnetic field generated by other stimuli. For example, circularly polarized light can produce a pseudo-magnetic field that can be used to manipulate electron spins in semiconductor quantum wells and quantum dots (*12*, *13*) through the optical Stark effect. (The optical Stark effect, a well-established phenomenon in atomic physics and quantum optics, describes the energy shift in a two-level system induced by a nonresonant laser field.) It is highly desirable to realize similar control of valley excitons in MX_2 by using light-induced pseudo-magnetic field for valleytronics.

[1]Department of Physics, University of California at Berkeley, Berkeley, CA 94720, USA. [2]Material Science Division, Lawrence Berkeley National Laboratory, Berkeley, CA 94720, USA. [3]Institute of Atomic and Molecular Sciences, Academia Sinica, Taipei 10617, Taiwan. [4]Physical Sciences and Engineering, King Abdullah University of Science and Technology, Thuwal, Saudi Arabia. [5]Kavli Energy NanoSciences Institute, University of California Berkeley and Lawrence Berkeley National Laboratory, Berkeley, CA 94720, USA.
*These authors contributed equally to this work, **†Corresponding author. E-mail: fengwang76@berkeley.edu**

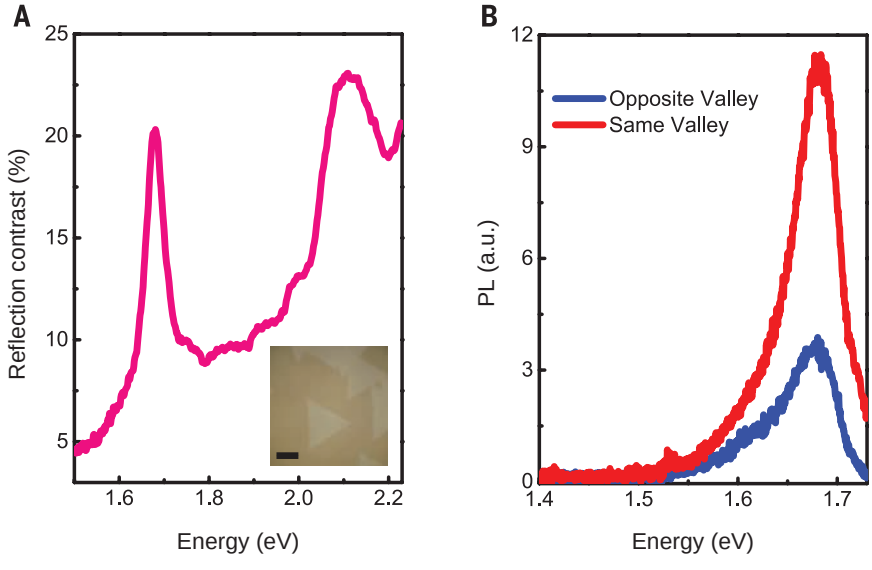


Fig. 1. Valley exciton transitions in monolayer WSe_2. (**A**) The optical reflection spectrum of a WSe_2 monolayer on a sapphire substrate at 77 K. It shows strong A- and B-exciton resonances at 1.68 and 2.1 eV, respectively. (Inset) Optical microscopy image of the sample. Scale bar, 25 μm. (**B**) Polarization-resolved PL spectra of a WSe_2 monolayer at 77K. For a 1.8-eV excitation laser with left circular polarization, the PL spectra show a prominent emission peak at the A-exciton resonance (1.68 eV), and the PL intensity with left circular polarization (red curve) is about four times stronger than that with right circular polarization (blue curve). It demonstrates that valley-polarized A-exciton population can be created by circularly polarized resonant excitation and it can be detected with polarization-resolved PL spectroscopy.

Here, we demonstrate a valley-selective optical Stark effect in monolayer WSe_2 to generate an ultrafast and ultrahigh pseudo-magnetic field for valley excitons. Previously, resonant pump-probe spectroscopy has been used to probe ultrafast carrier dynamics after the pump photons are absorbed by exciton transitions in MX_2 monolayers (*14*–*17*). We used nonresonant circularly polarized laser pumping with photon energies below the bandgap, which induces a coherent and dissipationless valley-selective optical Stark effect for pseudospin manipulation.

We used triangular monolayers of WSe_2 grown by means of chemical vapor deposition on sapphire substrates (Fig. 1A, inset) (*18*). The optical reflection spectrum of monolayer WSe_2 at 77 K exhibits two prominent resonances at 1.68 and 2.1 eV (Fig. 1A), which correspond, respectively, to the A- and B-excitons split by the spin-orbital coupling (*19*, *20*). In this study, we focused on the lowest-energy A-exciton transition. This A-exciton is well separated from other excited states in energy thanks to strong electron-hole interactions in monolayer WSe_2. As a result, we can approximate the ground state and the A-exciton as a two-level system and neglect the effect from other excited states. In monolayer WSe_2, the A-exciton states at K and K′ valleys are time-reversal pairs and have degenerate energy levels. However, they have distinct optical selection rules and couple to photons of opposite helicity (*3*, *4*). The dipole transition matrix element of the K valley A-exciton is characterized by $P_K^{\sigma\pm} = \langle K|\hat{p}_x \pm i\hat{p}_y|0\rangle$, where $|K\rangle$ and $|0\rangle$ correspond to the K valley A-exciton and ground state, respectively; $\hat{p}_x$, $\hat{p}_y$ are momentum operators; and σ_+/σ_- corresponds to left/right circular light. In MX_2 monolayers, $P_K^{\sigma+}$ has a finite value, but $P_K^{\sigma-}$ is approximately zero. Consequently, the A-exciton at the K valley couples exclusively to left-circularly polarized light. The A-exciton at the K′ valley, on the other hand, couples only to the right-circularly polarized light. This dipole selection rule for valley

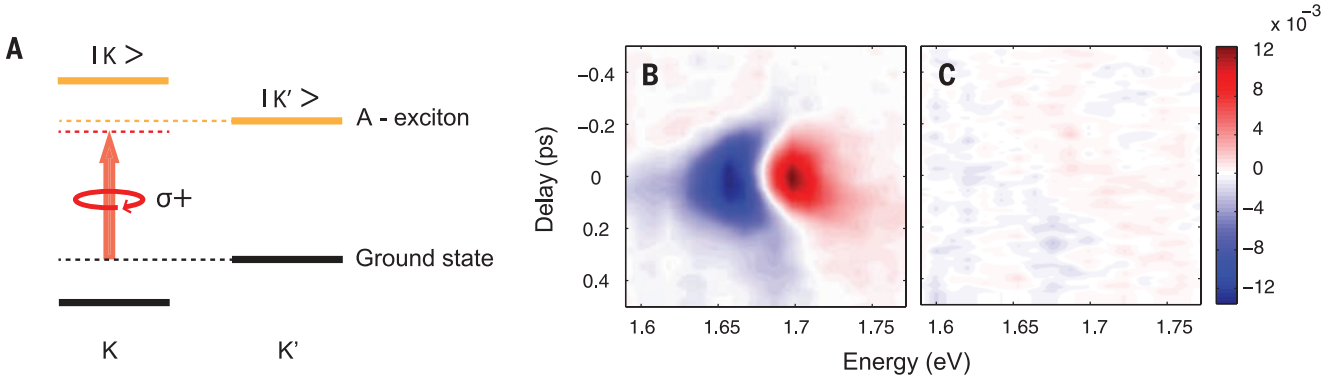


Fig. 2. Valley-dependent optical Stark effect with nonresonant circularly polarized pump. (**A**) Schematic of the optical Stark effect for valley transitions with nonresonant, left circularly polarized σ_+ pump. The dashed black and yellow lines denote the unperturbed ground and exciton states, respectively, and the pump photon energy is lower than the exciton resonance energy (red arrow). In the dressed atom picture, the dressed ground state (with N σ_+ photons) and the K valley A-exciton (with N-1 σ_+ photons) are coupled by dipole transition, which results in energy-level repulsion (left, solid black and yellow lines) and an increased exciton transition energy. On the other hand, σ_+ pump does not affect K′ valley A-exciton resonance because of the optical selection rule (right). (**B** and **C**) Transient reflection spectra of A-exciton resonance at 77 K. The color scale, horizontal axis, and vertical axis represent the relative reflectivity change $\Delta R/R$, the probe photon energy, and the pump-probe time delay, respectively. For atomically thin WSe_2 on sapphire substrate, $\Delta R/R$ is proportional to absorption change. Nonresonant σ_+ pump of photon energy at 1.53 eV leads to (B) a strong transient absorption signal for probes with the same polarization σ_+, but (C) produces no transient response for probes with the opposite polarization σ_-.

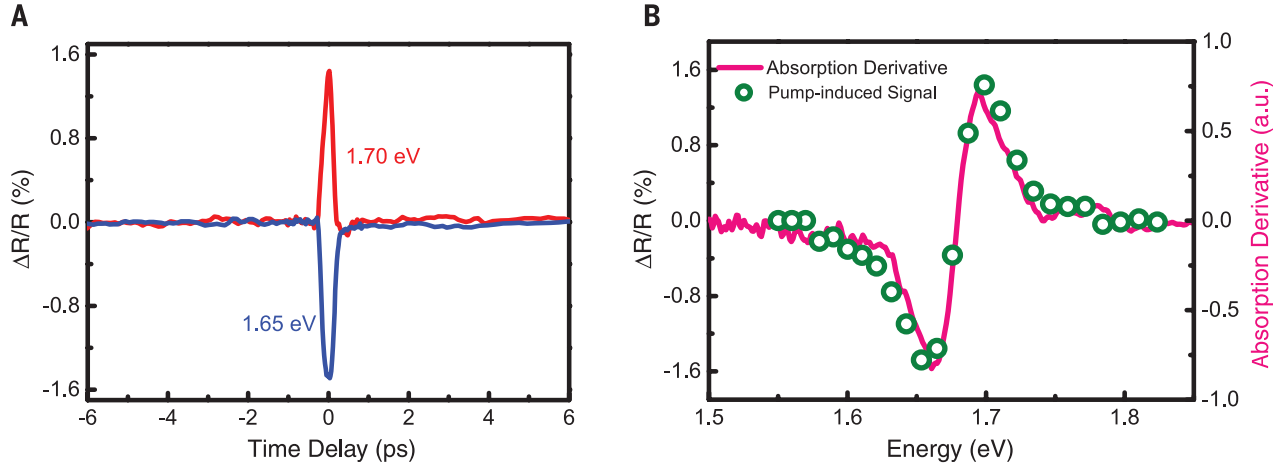


Fig. 3. Time evolution and spectral lineshape of the valley-dependent transient reflection spectra for σ_+ pump and σ_+ probe configuration. (**A**) Time evolution of the pump-induced transient reflectivity $\Delta R/R$ at probe energies of 1.65 eV (blue line) and 1.7 eV (red line). Both signals reach the maximum magnitude at the pump-probe delay $\tau = 0$ with symmetric rise and decay dynamics (limited by our pulse width ~250 fs), which is characteristic of an instantaneous optical response. The transient reflectivity has opposite signs for 1.65 and 1.7 eV probes. (**B**) The transient reflection spectrum at $\tau = 0$ (green circles). The transient reflectivity signal changes sign at the A-exciton resonance energy E_A = 1.68 eV, and it shows a dispersive line shape. This transient reflection spectrum matches well with the derivative of linear absorption spectrum in monolayer WSe_2 and can be fully accounted for by a 4-meV blueshift of the K valley A-exciton resonance (magenta line).

transitions in monolayer WSe_2 governs both resonant and nonresonant excitations, which can have different manifestations in valley physics.

The valley-dependent resonant excitation enables both the generation of a valley-polarized exciton population through the absorption of circularly polarized light and the detection of valley-polarized excitons through polarization-resolved photoluminescence (PL) (*4*–*6*). Displayed in Fig. 1B are polarization-resolved PL spectra of our WSe_2 samples upon laser excitation at 1.8 eV with σ_+ circular polarization, in which the PL intensity with helicity matching the excitation light (σ_+; Fig. 1B, red curve) is about four times stronger than that for the opposite helicity (σ_-; Fig. 1B, blue curve). This behavior is similar to that reported in previous studies (*4*–*7*) and verifies the valley-selective excitation and emission in our WSe_2 monolayers. The nonzero σ_- polarized PL is presumably caused by a finite intervalley scattering because the excitation energy is ~120 meV higher than the A-exciton resonance.

To manipulate the valley polarization, however, nonresonant coupling based on the optical Stark effect is more advantageous because it avoids the dissipation and dephasing naturally accompanying real excitations. The optical Stark effect is widely used in quantum optics to control a rich variety of quantum systems, ranging from the manipulation of cold atoms (*21*) and individual trapped ions (*22*) to coherent control of superconducting qubits (*23*) and electron spins (*24*). In a two-level system, the optical Stark effect can be readily understood by using the dressed-atom picture (*25*). Consider the two-level system composed of the ground state and A-exciton state at the K (or K′) valley in a monolayer WSe_2. Illustrated in Fig. 2A is the effect of a left circularly polarized (σ_+) pump with photon energies below the exciton resonance (Fig. 2A, red arrow). In the dressed-atom picture, the dressed-ground state (with N σ_+ photons), and the K valley A-exciton (with N-1 σ_+ photons) are coupled by the dipole transition, which leads to wave function hybridization and energy-level repulsion. It effectively shifts down the ground-state energy and shifts up the K valley exciton energy. The A-exciton at the K′ valley, on the other hand, cannot couple to the ground state with an extra σ_+ photon because of the optical selection rule, and the related states are not shifted by σ_+ polarized light. As a result, the energy degeneracy between K and K′ valley states is lifted by the valley-selective optical Stark effect, which can be characterized by a valley pseudo-magnetic field.

We measured the valley-selective optical Stark shift in WSe_2 monolayers with nonresonant circularly polarized excitation using pump-probe spectroscopy. Femtosecond pump pulses with tunable photon energies below the A-exciton resonance were generated with an optical parametric amplifier. Optical Stark shifts of the WSe_2 exciton transitions induced by the pump pulses was then probed in transient reflection spectra over the spectral range of 1.59 to 1.77 eV by using a laser-generated supercontinuum light. Displayed in Fig. 2, B and C, are two-dimensional plots of transient reflection spectra in a monolayer WSe_2 with σ_+ and σ_- polarized probe light, respectively, upon σ_+ polarized pump excitation. Here, the nonresonant pump photons are at 1.53 eV, which is 150 meV below the exciton resonance and do not excite any real transitions. The color scale in Fig. 2, B and C, represents the pump-induced change of the probe beam reflectivity $\Delta R/R$, the horizontal axis shows the probe photon energy, and the vertical axis shows the pump-probe time delay. For atomically thin WSe_2 layers on a transparent sapphire substrate, the reflection change $\Delta R/R$ is directly proportional to the change in the absorption coefficient (*26*, *27*). It is apparent that strong changes in the exciton absorption are present only for σ_+ probe pulses (Fig. 2B), and no pump-induced signals can be detected above the noise level for σ_- probe pulses (Fig. 2C). This indicates that the nonresonant σ_+ pump substantially modifies the A-exciton transition at the K valley, but not at the K′ valley.

To better examine the time evolution and spectral lineshape of the photo-induced transient reflection spectra in WSe_2 monolayers, we plot in Fig. 3 vertical and horizontal linecuts of the two-dimensional plot for the σ_+ pump and σ_+ probe configuration (Fig. 2B). Displayed in Fig. 3A are the transient reflection signals at the probe photon energy below (1.65 eV; Fig. 3A, blue line) and above (1.7 eV; Fig. 3A, red line) the exciton resonance at different pump-probe delay τ (Fig. 2B, vertical linecuts). Both signals have the largest magnitude at $\tau = 0$ and show a symmetric rise and decay dynamics. This is characteristic of an instantaneous response, with the rise/decay time limited by the laser pulse width of ~250 fs. It shows that the exciton absorption is modulated only when the pump radiation is present. In addition, the transient reflectivity has opposite signs for probe energies at 1.65 and 1.7 eV. Detailed transient reflection spectrum $\Delta R/R$, which is proportional to the transient absorption change (*26*, *27*), is shown in Fig. 3B (green circles) for $\tau = 0$ through a horizontal linecut in Fig. 2B. We observed that the transient absorption signal changes sign exactly at the A-exciton resonance energy (E_A) = 1.68 eV. The pump laser leads to reduced absorption below E_A and increased absorption above E_A, which matches well the linear derivative of the WSe_2 monolayer absorption spectrum (Fig. 3B, magenta line). Quantitatively, the photo-induced absorption change can be perfectly described by a simple blueshift of ~4 meV of the K valley exciton resonance. The blueshift in transition energy, instantaneous time response, and valley selectivity demonstrate unambiguously the optical Stark effect in monolayer WSe_2 upon nonresonant pump excitation. The photo-induced signal becomes nondetectable immediately after the pump pulses, indicating negligible dissipative processes associated with real exciton absorption. We also performed the pump-probe spectroscopy using linearly polarized pump and probe pulses (fig. S1). Here, photo-induced absorption changes are of similar magnitude, independent of the pump and probe polarizations. This is because the linear-polarized pump has both σ_+ and σ_- components, which lead to optical Stark shifts for both K and K′ valley exciton transitions.

Next, we examined how the valley-selective optical Stark shift varies with the pump laser intensity and detuning. The pump detuning $\hbar\Omega$ is defined as the difference between the exciton resonance energy ($\hbar\omega_0$) and the pump photon energy ($\hbar\omega_p$). Shown in Fig. 4 is the transient reflection data (Fig. 4, left axis) and the corresponding energy shift of the A-exciton energy (Fig. 4, right axis, and supplementary text) at the K valley for σ_+ pump and σ_+ probe configuration with different pump detuning (Fig. 4A, green dots) and pump intensities (Fig. 4B, green dots). We observed that the optical Stark shift is inversely proportional to the pump detuning (Fig. 4A, magenta dashed line) and scales linearly with the laser intensity (Fig. 4B, magenta dashed

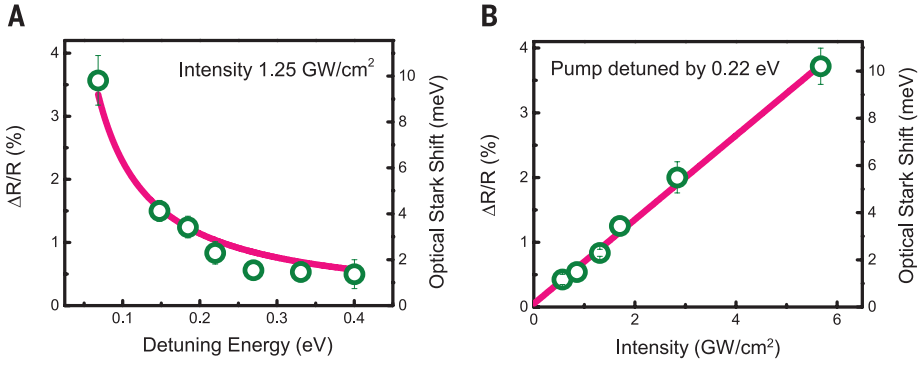


Fig. 4. Pump detuning and pump intensity dependence of the valley-selective optical Stark shift. (**A**) The transient reflection signal at 1.7 eV (left axis) and the corresponding optical Stark shift (right axis) as a function of the pump detuning energy (green dots). The dependence can be nicely described by an inverse proportional relationship (magenta line). (**B**) The transient reflection signal at 1.7 eV (left axis) and the corresponding optical Stark shift (right axis) as a function of the pump laser intensity (green dots), which shows a linear scaling behavior (magenta line). The optical Stark shift can selectively shift the K valley exciton transition by as much as 10 meV, which corresponds to a valley pseudo-magnetic field of ~60 T.

line). Such scaling matches well with the theoretical prediction of optical Stark shift $\delta(\hbar\omega_0) = 2S{\cdot}E_p^2/\hbar\Omega$, where S is the optical Stark shift constant related to the transition dipole moment and E_p is the electric field of the pump pulse (*25*, *28*). From the experimental data, we can determine an optical Stark shift constant $S \sim 45\ D^2$ for A-exciton in monolayer WSe_2, which is of similar magnitude to that for exciton transition in semiconductor quantum wells (*29*).

The valley-selective optical Stark shift breaks the degeneracy of valley exciton transitions in monolayer WSe_2 and defines an effective valley pseudo-magnetic field. In our experiment, the photo-induced energy splitting between K and K′ exciton transitions can be as large as 10 meV (Fig. 4 and supplementary text). The corresponding pseudo-magnetic field B_{eff} for valley excitons can be

estimated with $B_{eff} = \frac{\Delta E}{2g_{ex}\mu_B}$, where μ_B is the

Bohr magneton and g_{ex} is the effective g-factor for valley exciton transitions in WSe_2. The effective exciton g-factor g_{ex} combines contributions from both electrons and holes and has a theoretically predicted value of ~1.5 for WSe_2 (supplementary text). Using this g-factor, we estimate a pseudo-magnetic field B_{eff} as high as 60 T for a 10-meV splitting of valley exciton transitions. A real magnetic field of this magnitude is difficult to achieve even with superconducting magnets, but such a pseudo-magnetic field for MX_2 valley excitons can be produced conveniently and with femtosecond temporal control by using light pulses.

It has been reported recently that excitons in different valleys in monolayer WSe_2, resonantly excited by linear polarization light, can maintain their phase coherence over extended time (*7*). The valley-dependent optical Stark effect offers a convenient and ultrafast way to lift the valley degeneracy and introduce a controlled phase difference between the two valley states, therefore enabling coherent rotation of resonantly excited valley polarizations with high fidelity (fig. S2). In analogy with spintronics, such coherent manipulation of valley polarization can open up fascinating opportunities for valleytronics.

REFERENCES AND NOTES

1. X. Xu, W. Yao, D. Xiao, T. F. Heinz, *Nat. Phys.* **10**, 343–350 (2014).
2. Q. H. Wang, K. Kalantar-Zadeh, A. Kis, J. N. Coleman, M. S. Strano, *Nat. Nanotechnol.* **7**, 699–712 (2012).
3. D. Xiao, G. B. Liu, W. Feng, X. Xu, W. Yao, *Phys. Rev. Lett.* **108**, 196802 (2012).
4. T. Cao *et al.*, *Nat. Commun.* **3**, 887 (2012).
5. K. F. Mak, K. He, J. Shan, T. F. Heinz, *Nat. Nanotechnol.* **7**, 494–498 (2012).
6. H. Zeng, J. Dai, W. Yao, D. Xiao, X. Cui, *Nat. Nanotechnol.* **7**, 490–493 (2012).
7. A. M. Jones *et al.*, *Nat. Nanotechnol.* **8**, 634–638 (2013).
8. Y. J. Zhang, T. Oka, R. Suzuki, J. T. Ye, Y. Iwasa, *Science* **344**, 725–728 (2014).
9. K. F. Mak, K. L. McGill, J. Park, P. L. McEuen, *Science* **344**, 1489–1492 (2014).
10. C. P. Poole, *Electron Spin Resonance* (Wiley, New York, ed. 2, 1983)
11. F. H. L. Koppens *et al.*, *Nature* **442**, 766–771 (2006).
12. J. A. Gupta, R. Knobel, N. Samarth, D. D. Awschalom, *Science* **292**, 2458–2461 (2001).
13. D. Press, T. D. Ladd, B. Zhang, Y. Yamamoto, *Nature* **456**, 218–221 (2008).
14. H. Shi *et al.*, *ACS Nano* **7**, 1072–1080 (2013).
15. Q. Wang *et al.*, *ACS Nano* **7**, 11087–11093 (2013).
16. E. J. Sie, Y.-H. Lee, A. J. Frenzel, J. Kong, N. Gedik, Biexciton formation in monolayer MoS2 observed by transient absorption spectroscopy, http://arxiv.org/abs/1312.2918 (2013).
17. C. Mai *et al.*, *Nano Lett.* **14**, 202–206 (2014).
18. J.-K. Huang *et al.*, *ACS Nano* **8**, 923–930 (2014).
19. A. Splendiani *et al.*, *Nano Lett.* **10**, 1271–1275 (2010).
20. K. F. Mak, C. Lee, J. Hone, J. Shan, T. F. Heinz, *Phys. Rev. Lett.* **105**, 136805 (2010).
21. P. Jessen, I. Deutsch, *Adv. At. Mol. Opt. Phys.* **37**, 95–138 (1996).
22. C. Cohen-Tannoudji, *Phys. Scr.* **T76**, 33 (1998).
23. D. I. Schuster *et al.*, *Phys. Rev. Lett.* **94**, 123602 (2005).
24. J. Berezovsky, M. H. Mikkelsen, N. G. Stoltz, L. A. Coldren, D. D. Awschalom, *Science* **320**, 349–352 (2008).
25. C. Cohen-Tannoudji, S. Reynaud, *J. Phys. At. Mol. Opt. Phys.* **10**, 345–363 (1977).
26. F. Wang *et al.*, *Science* **320**, 206–209 (2008).
27. K. F. Mak *et al.*, *Phys. Rev. Lett.* **101**, 196405 (2008).
28. Y.-R. Shen, *The Principles of Nonlinear Optics* (Wiley-Interscience, New York, 1984).
29. A. Von Lehmen, D. S. Chemla, J. E. Zucker, J. P. Heritage, *Opt. Lett.* **11**, 609–611 (1986).

ACKNOWLEDGMENTS

This work was supported by Office of Basic Energy Science, U.S. Department of Energy under contract DE-SC0003949 (Early Career Award) and DE-AC02-05CH11231 (Materials Science Division). L.J.L. thanks the support from Academia Sinica and National Science Council Taiwan (NSC-102-2119-M-001-005-MY3). F.W. also acknowledges the support from a David and Lucile Packard fellowship. All data described in the paper are presented in this report and supplementary materials.

SUPPLEMENTARY MATERIALS

www.sciencemag.org/content/346/6214/1205/suppl/DC1
Materials and Methods
Supplementary Text
Figs. S1 and S2
References (*30*–*34*)

30 June 2014; accepted 5 November 2014
10.1126/science.1258122

HEAVY FERMIONS

Two-dimensional Fermi surfaces in Kondo insulator SmB_6

G. Li,[1] Z. Xiang,[1,2] F. Yu,[1] T. Asaba,[1] B. Lawson,[1] P. Cai,[1,3] C. Tinsman,[1] A. Berkley,[1] S. Wolgast,[1] Y. S. Eo,[1] Dae-Jeong Kim,[4] C. Kurdak,[1] J. W. Allen,[1] K. Sun,[1] X. H. Chen,[2] Y. Y. Wang,[3] Z. Fisk,[4] Lu Li[1]*

In the Kondo insulator samarium hexaboride (SmB_6), strong correlation and band hybridization lead to an insulating gap and a diverging resistance at low temperature. The resistance divergence ends at about 3 kelvin, a behavior that may arise from surface conductance. We used torque magnetometry to resolve the Fermi surface topology in this material. The observed oscillation patterns reveal two Fermi surfaces on the (100) surface plane and one Fermi surface on the (101) surface plane. The measured Fermi surface cross sections scale as the inverse cosine function of the magnetic field tilt angles, which demonstrates the two-dimensional nature of the conducting electronic states of SmB_6.

The recent development of topological insulators is a triumph of single electron band theory (*1*–*8*). Kondo insulators can be used to explore whether similar exotic states of matter can arise in the presence of strong electronic interactions. In these strongly correlated heavy-fermion systems (*9*), the hybridization between itinerant electrons and localized orbitals opens a gap and makes the material insulating. Once the sample temperature is cold enough, the electronic structure can be mapped to a state that resembles a normal topological insulator (TI) (*10*), with a bulk insulating state and a conductive surface state. In samarium hexaboride (SmB_6), the existence of the surface state has been suggested by recent experimental observations of the surface conductance as well as a mapping of the hybridization gap (*11*–*13*). We report the observation of quantum oscillations in Kondo insulator SmB_6 using torque magnetometry via the de Haas–van Alphen (dHvA) effect. The observed Fermi surfaces are shown to be two-dimensional (2D) and arise from the crystalline (101) and (100) surfaces.

One major difference between SmB_6 and the conventional topological insulators is the crystal structure, which for SmB_6 is simple cubic (Fig. 1A). SmB_6 single crystals were grown by conventional flux methods. Each sample was etched with acid to remove the leftover flux. Figure 1B shows a photo of a piece of SmB_6 single crystal. Beside a flat (001) surface, there are four (101) planes.

We use torque magnetometry to resolve the Landau Level quantization and the resulting

[1]Department of Physics, University of Michigan, Ann Arbor, MI 48109, USA. [2]Hefei National Laboratory for Physical Science at Microscale and Department of Physics, University of Science and Technology of China, Hefei Anhui 230026, China. [3]Department of Physics, Tsinghua University, Beijing, China. [4]Department of Physics and Astronomy, University of California at Irvine, Irvine, CA 92697, USA.
***Corresponding author. E-mail: luli@umich.edu**

quantum oscillations in magnetization. Electronic transport measurements have been used to detect quantum oscillations in conventional topological materials (*14*–*22*). In contrast, magnetization is simply the derivative of the magnetic free energy G with respect to magnetic field H. Therefore, torque magnetometry probes the oscillations in the free energy and is sensitive to Fermi surface (FS) topology of both 3D and 2D electronic systems (*23*–*27*). Torque magnetometry measures directly the anisotropy of the magnetic susceptibility of a sample (*25*). With the tilted magnetic field $\vec{H}$ confined to the $\hat{a}$ - $\hat{c}$ plane, the torque τ of a paramagnet is shown as follows:

$$\tau = \mu_0\chi_a H_a H_c - \mu_0\chi_c H_c H_a = \mu_0\Delta\chi H^2 \sin\phi\cos\phi \quad (1)$$

where μ_0 is the vacuum permeability, ϕ is the tilt angle of $\vec{H}$ away from the crystalline $\hat{a}$ - $\hat{c}$ axis, and $\Delta\chi = \chi_a - \chi_c$ is the magnetic susceptibility anisotropy. Therefore, any change of the FS topology caused by the Landau Level quantization is revealed by torque magnetometry.

In our experimental setup, an SmB_6 single crystal is glued to the tip of a thin brass cantilever (Fig. 1C, inset). The magnetic torque τ is measured by tracking the capacitance change between the cantilever and a gold film underneath. An example torque τ versus magnetic field $\mu_0 H$ curve (Fig. 1C), taken at temperature T = 0.3 K and $\phi \sim 44°$, is quadratic overall, reflecting the linear H dependence of the sample magnetization and the paramagnetic nature of SmB_6. Large oscillations and small wiggles start to appear as the magnetic field goes beyond 5 T; for $\mu_0 H > 10$ T, the fast oscillation patterns dominate.

The first question that arises is whether it is possible for the thin atomic layer of the surface state to be responsible for the observed magnitude of the magnetic torque and magnetization. The magnitude of the observed magnetic torque was recorded by the relative capacitance change, then converted to absolute values using the calibrated spring constant of the cantilevers (see supplementary materials). Figure 1D shows the field dependence of the effective magnetic moment $M \equiv \frac{\tau}{\mu_0 H}$ in a magnetic field H as high as 45 T. The maximum oscillatory M is around 3×10^{-12} A·m^2. Using the total area of all the surfaces of the SmB_6 sample, including the dominating top and bottom (100) surfaces and other small edge surfaces, we can estimate that there are 7.5×10^{11} unit cells on the sample surfaces. By normalizing the magnetic moment M to the number of surface unit cells, we find the maximum change of oscillatory M is around $\Delta M \sim 0.4\ \mu_B$ per surface unit cell, where μ_B is the Bohr magneton. The gray scale bar in Fig. 1D marks $0.5\ \mu_B$ per surface unit cell for comparison.

Our measured oscillatory M is consistent with the surface carrier density measured by the Fermi pocket size. As we will demonstrate later, the measured pocket size (300 T ~ 400 T) leads to a total carrier density of ~1×10^{14}/cm^2, which is ~0.17 electrons per unit cell. The theoretical value of the oscillatory M is 2 μ_B per electron in 2D electronic systems, confirmed experimentally in (*26*). The carrier density implies a magnetization oscillation of 0.34 μ_B per surface unit cell. Our observed maximum $\Delta M \sim 0.4\ \mu_B$ per surface unit cell is consistent with this simple estimate.

Figure 2 presents the oscillation pattern of the magnetic torque. The oscillatory torque τ_{OSC} is defined by subtracting a quadratic background from the torque τ. τ_{OSC} is periodic in $1/\mu_0 H$ (Fig. 2A), reflecting the quantization of the Landau Levels. The magnetic torque is measured in H up to 45 T. For metals, the oscillation frequency F is determined by the cross section area A of the Fermi surface (*23*):

$$F = \frac{\hbar}{2\pi e} A \quad (2)$$

where $\hbar$ is the reduced Planck constant, and e is the electrical charge. The fast Fourier transformation (FFT) of the oscillatory τ_{OSC}, measured at 0.3 K and $\phi \sim 32°$ (Fig. 2B) shows a number of peaks, including a small pocket α at $F^\alpha \sim 35$ T, a larger pocket β at $F^\beta \sim 300$ T, and the largest pocket γ at $F^\gamma \sim 450$ T. In the higher-frequency range, we observed a series of new features: the second harmonic of the β pocket at $2\beta \sim 600$ T and the third harmonic of the β pocket at $3\beta \sim 900$ T. Most notably, the other peak (marked as β') appears at ~520 T and arises from the oscillation due to the β pocket in a neighboring (101) surface plane. This determination is based on the angular dependence of the oscillation frequencies, as discussed in detail below and in Fig. 3.

The electronic properties of these three Fermi surfaces are revealed by tracking the temperature and field dependence of the oscillatory torque τ_{osc} (Fig. 2C). Even though an insulating gap is observed in the temperature dependence of the conductivity of SmB_6 (*11*–*13*), the temperature dependence of τ_{osc} is very much like that of a normal metal. In metals, the oscillating magnetic torque is well described by the Lifshitz-Kosevich (LK) formula (*23*). The temperature and magnetic field dependences of the oscillation amplitude are determined by the product of the thermal damping factor

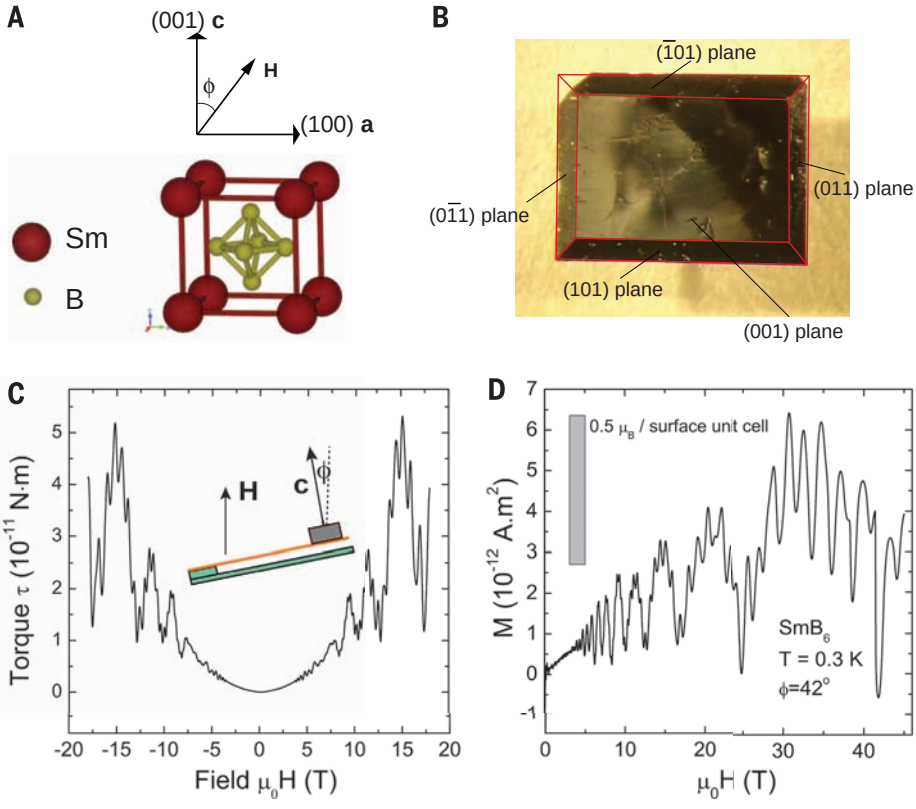


Fig. 1. Experimental setup. (**A**) The crystal structure of Kondo insulator SmB_6. The B_6 cluster and rare earth element Sm form a simple cubic structure. (**B**) Photograph of an SmB_6 single crystal. Guide lines are drawn to label the crystalline plane of each surface. (**C**) The field dependence of the magnetic torque τ in SmB_6. The data were taken at temperature T = 300 mK. Inset: sketch of the measurement setup. The sample stage is rotated to tilt magnetic field $\vec{H}$ in the crystalline $\hat{a}$ - $\hat{c}$ plane. The magnetic field was applied to the sample with a tilt angle ϕ ~44° relative to the crystalline ĉ axis. The spring constant of the cantilever was determined using the sample weight. (**D**) The field dependence of the magnetic moment M, taken at 0.3 K and under a magnetic field as high as 45 T. The low-field linear M–H dependence reflects the paramagnetism in SmB_6. The vertical gray scale bar shows the M value corresponding to 0.5 μ_B per surface unit cell.

R_T and the Dingle damping factor R_D, defined as

$$R_T = \alpha T m^*/B \sinh(\alpha T m^*/B)$$
$$R_D = \exp(-\alpha T_D m^*/B) \quad (3)$$

where the effective mass $m = m^* m_e$ and the Dingle temperature $T_D = \hbar/2\pi k_B \tau_S$. τ_S is the scattering rate, k_B is the Boltzmann Constant, m_e is the bare electron mass, $B = \mu_0 H$ is the magnetic flux density, and $\alpha = 2\pi^2 k_B m_e/e\hbar$ ~14.69 T/K (*23*).

Fitting the temperature dependence of the normalized oscillation amplitudes to the thermal damping factor R_T (Fig. 2C) yields m = $0.119m_e$ for Fermi surface α, m = $0.129m_e$ for Fermi surface β, and m = $0.192m_e$ for Fermi surface γ. Figure 2D displays the field dependence of the oscillation amplitude, normalized by the thermal damping factor R_T. Fitting the curves to R_D yields T_D ~15.9 K for Fermi surface α, T_D ~18.6 K for Fermi surface β, and T_D ~ 29.5 K for Fermi surface γ. Based on the extracted oscillation frequencies, effective masses, and Dingle temperatures, we are able to characterize the observed Fermi surfaces in SmB_6 (Table 1).

The long mean free path l measured for all three pockets (Table 1) supports the idea of intrinsic metallic surface states. The mean free path is two orders of magnitude larger than the crystal lattice constant of ~0.4 nm. Such a long mean free path is incompatible with the surface/bulk conductance arising from hopping between impurities.

The low effective mass that we measured (Table 1) is quite surprising, because most of the theoretical work on the topological Kondo insulator predicts a heavy mass of the surface states (*28*). The observed mass in SmB_6 is also much smaller than that of the divalent hexaboride compounds such as La-doped CaB_6 and EuB_6 (*29*, *30*). Pockets with heavier masses may still exist but could not be observed in our experimental conditions because of the thermal and Dingle dampings. Measurements in higher magnetic field and in colder temperatures would help resolve such extra Fermi pockets.

The most important feature of the observed quantum oscillations is the two-dimensionality (2D). For a 2D planar metallic system, the magnetic field projected to the normal axis of the plane determines the Landau Level quantizations. Thus, the oscillation frequency versus tilt angle curve generally follows the inverse of a sinusoidal function (*15*–*17*). We rotate the whole cantilever setup to track how the oscillation frequency F changes as a function of the tilt angle ϕ in a broad range of more than 180°. Using the complete FFT plots (figs. S3 to S5), we obtain the angular dependences of the oscillation frequencies of all the Fermi pockets on the (100) and (101) family surfaces, as displayed in Fig. 3, A to C.

For the dominating oscillatory pattern from pocket β, the oscillation frequency F^β not only displays a large angular dispersion but also closely tracks the 2D angular dependence from the (101) surface families. There are four branches of the $F^\beta - \phi$ patterns, as a result of the fourfold crystalline symmetry of the SmB_6 cubic structure. At each ϕ, there are two appearances of the β family. For example, at ϕ ~ 30°, there is one F^β from the (101) plane and another one from the neighboring $(\bar{1}01)$ plane (the latter contribution is marked as β′ in Fig. 2B). Most notably, all the F^β points track the solid lines of the function $F_0^\beta/\cos(\phi + 45^\circ), F_0^\beta/\cos(\phi - 45^\circ), F_0^\beta/\cos(\phi - 135^\circ)$, and $F_0^\beta/\cos(\phi - 225^\circ)$. We observe F^β at frequencies as high as 900 T—a more than 200% increase from the minimum value of 286 T. Such large divergence and the close tracking of the inverse cosine dependence strongly support the 2D nature of the observed β pocket on the (101) surface plane families.

In contrast, the angular dependence of the oscillation frequency of the α pocket F^α follows a different pattern. In Fig. 3A, the F^α values are plotted against the tilt angle ϕ of two SmB_6 single crystals. The uncertainty of F^α is determined by the half width at half-height of the F^α peak in the FFT plot. Similar to F^β, the F^α pattern has a fourfold symmetry, but the minima are located at ϕ = 0°, 90°, and 180°, that is, along the (100) crystalline axes. Fitting the data to the 2D form for this family, $F_0^\alpha/\cos(\phi - 0^\circ)$, $F_0^\alpha/\cos(\phi - 90^\circ)$, and $F_0^\alpha/\cos(\phi - 180^\circ)$, with F_0^α = 30.5 T (solid lines in Fig. 3A) results in reasonable agreement. This suggests that the observed α pocket arises from a surface state on the (100) plane families. Similarly, Fig. 3C shows that the angular dependence of the γ pocket F^γ follows the functional form of $F_0^\gamma/\cos(\phi - 0^\circ)$, $F_0^\gamma/\cos(\phi - 90^\circ)$, and $F_0^\gamma/\cos(\phi - 180^\circ)$ with F_0^γ ~385 T, suggesting the two-dimensionality of the γ pocket on the (100) surface plane.

Further, given the small value and large uncertainly of F^α, there is still a chance that an extremely elongated 3D ellipsoidal Fermi surface may fit the F^α versus ϕ dependence. Experiments with cleaner SmB_6 crystals may resolve the issue.

The angular dependence of the oscillation frequency suggests that the Fermi surface β is two-dimensional and likely arises from the crystalline (101) plane. In contrast, most of the theoretical modeling focuses on the surface states in the

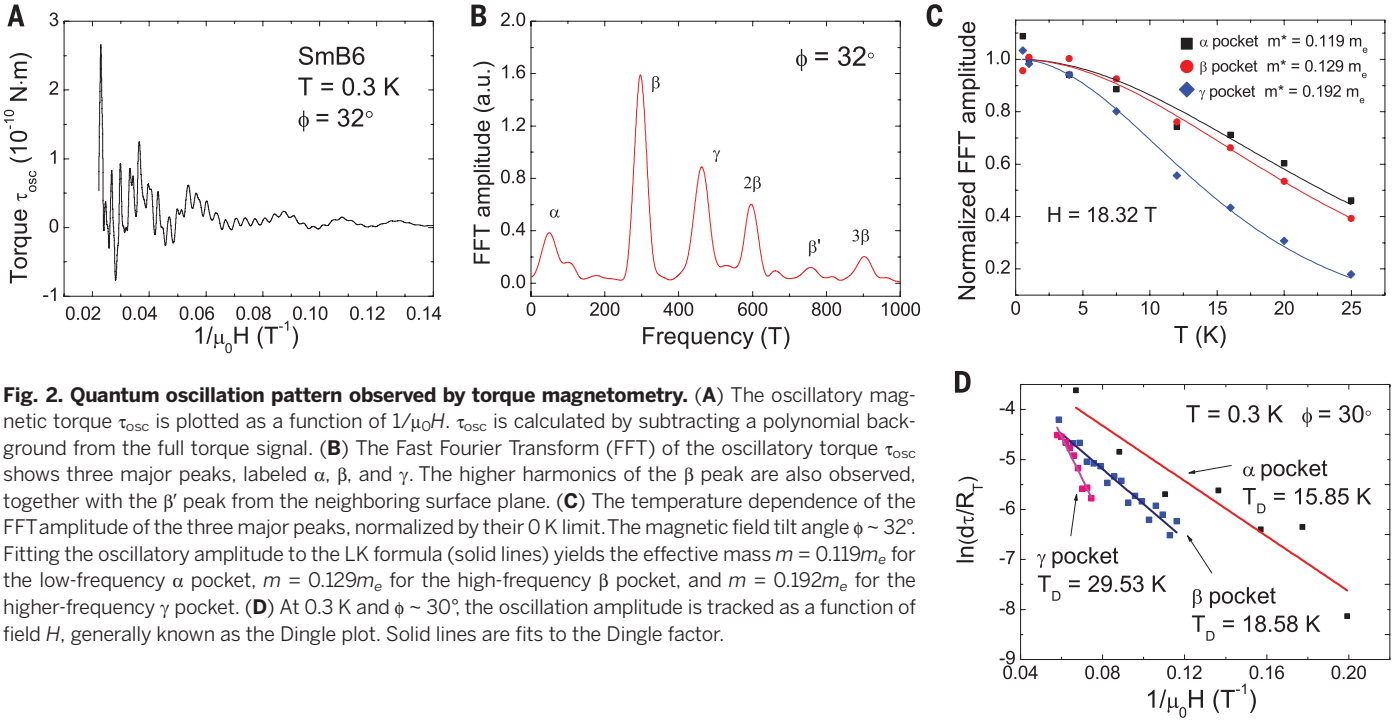


Fig. 2. Quantum oscillation pattern observed by torque magnetometry. (**A**) The oscillatory magnetic torque τ_{osc} is plotted as a function of $1/\mu_0 H$. τ_{osc} is calculated by subtracting a polynomial background from the full torque signal. (**B**) The Fast Fourier Transform (FFT) of the oscillatory torque τ_{osc} shows three major peaks, labeled α, β, and γ. The higher harmonics of the β peak are also observed, together with the β′ peak from the neighboring surface plane. (**C**) The temperature dependence of the FFT amplitude of the three major peaks, normalized by their 0 K limit. The magnetic field tilt angle ϕ ~ 32°. Fitting the oscillatory amplitude to the LK formula (solid lines) yields the effective mass $m = 0.119m_e$ for the low-frequency α pocket, $m = 0.129m_e$ for the high-frequency β pocket, and $m = 0.192m_e$ for the higher-frequency γ pocket. (**D**) At 0.3 K and ϕ ~ 30°, the oscillation amplitude is tracked as a function of field H, generally known as the Dingle plot. Solid lines are fits to the Dingle factor.

(100) planes (*31*), in which the mapping of the band inversion *X*-point gives two Fermi pocket cross sections on the (100) surface plane. Our observed α and γ pockets may be the two predicted pockets. Recent angle resolved photoemission spectroscopy (ARPES) measurements on SmB_6 revealed two Fermi pocket areas on the (100) surface Brillouin zone (*32*–*36*). Our measured Fermi surface area and the mass of pocket γ are comparable to those of a small Fermi surface centered at the Γ point and measured by ARPES. For a detailed comparison of our dHvA result and the ARPES results, see (*37*).

Questions remain as to the origin of the observed Fermi surface in the (101) plane. In the (101) plane, there are four high symmetry points [(0, 0), (0, π/a), ($\pi/\sqrt{2}a$, 0), and ($\pi/\sqrt{2}a$, π/a)]. For example (Fig. 3D), projecting the bulk band X points to the (101) plane leads to a pocket at (0, π/a) and a pair of pockets at ($\pi/\sqrt{2}a$,0) and ($-\pi/\sqrt{2}a$,0). Based on the time-reversal symmetry, only (0, π/a) has a Dirac point, which is consistent with the experimental observation. However, the topological theory does not prohibit pairs of Dirac points at low symmetry points (*37*), which offers another possible origin for the observed pockets.

The other important question is whether the 2D electronic state on the surface follows the Dirac dispersion. A general test is to track the Landau Level index plots to find out the infinite field limit, i.e., the geometric Berry phase factor. Using 45 T, the quantum limit is reached for pocket α, which, in the infinite magnetic field limit, points to −0.45 ± 0.07, very close to −1/2, the geometric Berry phase contribution, similar to other 2D Dirac electronic systems such as graphene (*18*, *19*). As the oscillation frequencies of Fermi pocket β and γ are quite close, filtering is needed to isolate the *H* dependence of the oscillation patterns for each Fermi pocket. This filtering may cause additional uncertainty of the oscillation phase, and the Zeeman effect and correlations may lead to some nonlinear effect of the Landau level index plots (*37*).

Because Al flux is used in the sample growth, the observed effective masses, oscillation frequencies, and angular dependence bear some similarity to those of pure aluminum (Al) (*38*). However, the oscillation periods of all the observed Fermi surfaces are symmetric about crystalline symmetry axes in the rotation plane. The observed fourfold symmetry and the behavior $F^{\alpha} \sim 1/\cos\phi$, $F^{\beta} \sim 1/\cos(\phi - 45^{\circ})$ and $F^{\gamma} \sim 1/\cos\phi$ cannot be explained by a residual Al impurity [for more details, see (*37*)]. Therefore, the observed quantum oscillation pattern is an intrinsic property of single-crystalline SmB_6.

We note also that our observed quantum oscillation feature is quite robust against oxidization, as the samples were always in atmosphere for storage. The ordinary surface states known to occur for vacuum clean surfaces of metal hexaborides such as LaB_6 disappear under even modest oxygen exposure (*37*, *39*).

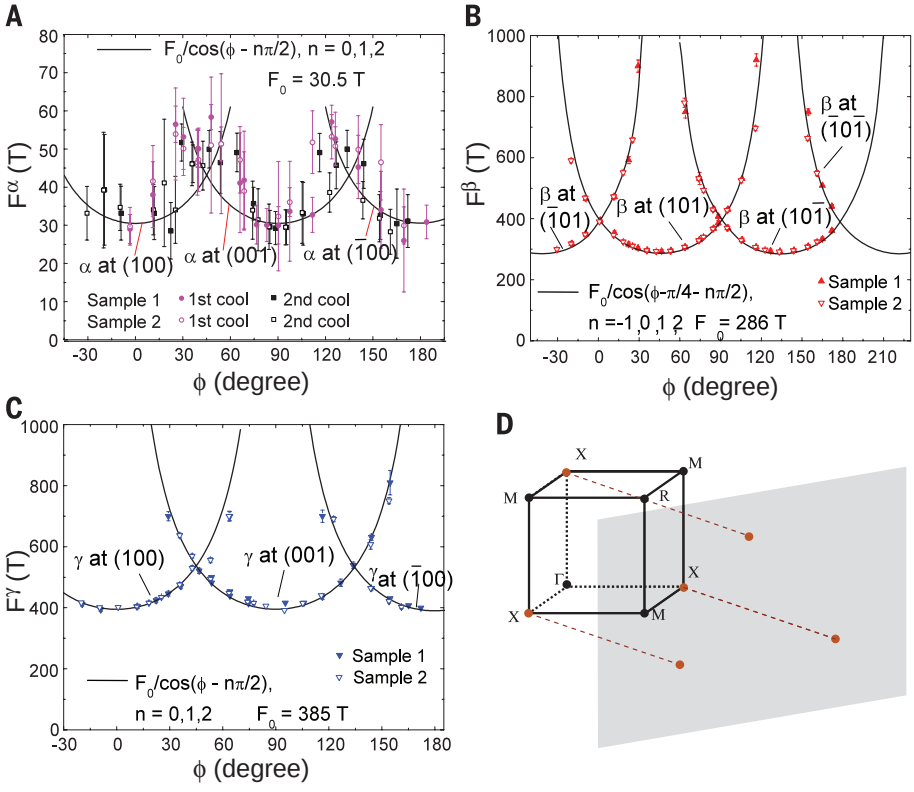


Fig. 3. Angular dependence of the oscillating frequencies in SmB_6. (**A**) Oscillation frequency F^{α} of the observed Fermi surfaces α is shown as a function of ϕ. The error bar of F^{α} is defined as the half-width at half-height of the peak in the FFT plot. To improve the statistics, two SmB_6 samples were cooled down twice. All the oscillation frequencies are inferred from the FFT spectra at many tilt angles ϕ from −30° to 180° (figs. S3 to S5) (*37*). The data are in agreement with a fit to the solid lines (described by $F_0/\cos(\phi - \phi_0)$, where ϕ_0 = 0°, 90°, and 180°). The lines correspond to 2D Fermi surfaces on the surface planes (100), (001), and (−1 0 0). (**B**) Oscillation frequency F^{β} of the observed Fermi surfaces β measured in two SmB_6 samples. F^{β} is consistent with the expected 2D Fermi surface sitting at the four surface planes of the (101) surface family. The solid line is the fitting curve $F_0/\cos(\phi - \phi_0)$, where ϕ_0 = −45°, 45°, 135°, and 225°. (**C**) The angular dependence of the oscillation frequency F^{γ} of the pocket γ. Solid lines are fits to $F_0/\cos(\phi - \phi_0)$ with ϕ_0 = 0°, 90°, and 180°. (**D**) Sketch of the Brillouin zone of SmB_6. Band inversion occurs at the *X* points. The projection of these *X* points to the (101) plane shows a possible location of the Fermi surfaces in the (101) surface state.

Table 1. Parameters in the three Fermi pockets in SmB_6. The oscillation frequency *F* and Fermi wavevector k_F are obtained from the dHvA period. The effective mass *m*, Fermi velocity v_F, mean free path *l*, and the mobility μ are inferred from the *T* and *H* dependences of the oscillation amplitude. The Landau level index plot yields the infinite field limit δ.

	α	β	γ
F (T)	29.3 ± 4	286 ± 5	385 ± 5
Crystalline surface Origin	(1 0 0)	(1 0 1)	(1 0 0)
k_F (nm^{-1})	0.30 ± 0.02	0.941 ± 0.008	1.080 ± 0.011
m/m_e	0.119 ± 0.007	0.129 ± 0.004	0.192 ± 0.005
v_F ($10^5 ms^{-1}$)	2.90 ± 0.39	8.45 ± 0.33	6.50 ± 0.21
l (nm)	22 ± 8	52 ± 6	25 ± 4
μ (×10^3 $cm^2/V{\cdot}s$)	1.1 ± 0.5	0.84 ± 0.10	0.36 ± 0.05
$k_F l$	6.6 ± 2.9	49 ± 6	27 ± 4
δ	−0.45 ± 0.07	−0.44 ±0.06	−0.32 ± 0.07

REFERENCES AND NOTES

1. L. Fu, C. L. Kane, E. J. Mele, *Phys. Rev. Lett.* **98**, 106803 (2007).
2. X.-L. Qi, T. L. Hughes, S.-C. Zhang, *Phys. Rev. B* **78**, 195424 (2008).
3. J. E. Moore, L. Balents, *Phys. Rev. B* **75**, 121306 (2007).
4. D. Hsieh *et al.*, *Nature* **452**, 970–974 (2008).
5. Y. L. Chen *et al.*, *Science* **325**, 178–181 (2009).
6. M. König *et al.*, *Science* **318**, 766–770 (2007).
7. M. Z. Hasan, C. L. Kane, *Rev. Mod. Phys.* **82**, 3045–3067 (2010).
8. X.-L. Qi, S. C. Zhang, *Rev. Mod. Phys.* **83**, 1057–1110 (2011).

9. A. Menth, E. Buehler, T. H. Geballe, . *Phys. Rev. Lett.* **22**, 295–297 (1969).
10. M. Dzero, K. Sun, V. Galitski, P. Coleman, *Phys. Rev. Lett.* **104**, 106408 (2010).
11. S. Wolgast *et al.*, *Phys. Rev. B* **88**, 180405 (2013).
12. D. J. Kim *et al.*, *Sci. Rep.* **3**, 3150 (2013).
13. X. Zhang *et al.*, *Phys. Rev. X* **3**, 011011 (2013).
14. J. G. Checkelsky *et al.*, *Phys. Rev. Lett.* **103**, 246601 (2009).
15. K. Eto, Z. Ren, A. A. Taskin, K. Segawa, Y. Ando, *Phys. Rev. B* **81**, 195309 (2010).
16. J. Analytis *et al.*, *Nat. Phys.* **6**, 960–964 (2010).
17. D. X. Qu, Y. S. Hor, J. Xiong, R. J. Cava, N. P. Ong, *Science* **329**, 821–824 (2010).
18. K. S. Novoselov *et al.*, *Nature* **438**, 197–200 (2005).
19. Y. Zhang, Y. W. Tan, H. L. Stormer, P. Kim, *Nature* **438**, 201–204 (2005).
20. B. Sacépé *et al.*, *Nat. Commun.* **2**, 575 (2011).
21. J. Xiong *et al.*, *Phys. Rev. B* **86**, 045314 (2012).
22. K. Behnia, L. Balicas, Y. Kopelevich, *Science* **317**, 1729–1731 (2007).
23. D. Shoenberg, Magnetic Oscillations in Metals. (Cambridge Univ. Press, Cambridge, UK, 1984).
24. S. E. Sebastian *et al.*, *Nature* **454**, 200–203 (2008).
25. L. Li *et al.*, *Science* **321**, 547–550 (2008).
26. J. P. Eisenstein *et al.*, *Phys. Rev. Lett.* **55**, 875–878 (1985).
27. S. A. J. Wiegers *et al.*, *Phys. Rev. Lett.* **79**, 3238–3241 (1997).
28. V. Alexandrov, M. Dzero, P. Coleman, *Phys. Rev. Lett.* **111**, 226403 (2013).
29. M. C. Aronson, J. Sarrao, Z. Fisk, M. Whitton, B. Brandt, *Phys. Rev. B* **59**, 4720–4724 (1999).
30. D. Hall *et al.*, *Phys. Rev. B* **64**, 233105 (2001).
31. F. Lu, J. Zhao, H. Weng, Z. Fang, X. Dai, *Phys. Rev. Lett.* **110**, 096401 (2013).
32. N. Xu *et al.*, *Phys. Rev. B* **88**, 121102 (2013).
33. M. Neupane *et al.*, *Nat. Commun.* **4**, 2991 (2013).
34. J. Jiang *et al.*, *Nat. Commun.* **4**, 3010 (2013).
35. E. Frantzeskakis *et al.*, *Phys. Rev. X* **3**, 041024 (2013).
36. J. D. Denlinger *et al.*, Temperature dependence of linked gap and surface state evolution in the mixed valent topological insulator SmB6. http://arxiv.org/abs/1312.6637 (2013).
37. Additional information may be found in the supplementary materials on *Science* Online.
38. C. O. Larson, W. L. Gordon, *Phys. Rev.* **156**, 703–715 (1967).
39. See, for example, B. Nishitani, *et al., Surface Science* **95**, 341 (1980).

ACKNOWLEDGMENTS

This study is based on work supported by the U. S. Department of Energy (DOE) under Award no. DE-SC0008110 (high-field torque magnetometry), by the startup fund and the Mcubed project at the University of Michigan (low-field magnetization characterization), and by the NSF DMR-0801253 and Univ. of California–Irvine CORCL grant MIIG-2011- 12-8 (Z. F. group, sample growth). Part of the work performed at the University of Michigan was supported by NSF grant DMR-1006500 (C.K. group, device fabrication) and by NSF grant ECCS-1307744 (L.L. group, device transport characterization). Z.X. and X.H.C. thank the China Scholarship Council for support and the National Basic Research Program of China (973 Program, grant no. 2012CB922002). B.L. thanks the NSF graduate research fellowship (F031543) for support. T.A. thanks the Nakajima Foundation Scholarship for support. The Corbino samples were fabricated at the Lurie Nanofabrication Facility (LNF), a member of the National Nanotechnology Infrastructure Network, which is supported by the NSF. The high-field experiments were performed at the National High Magnetic Field Laboratory, which is supported by NSF Cooperative Agreement no. DMR-084173, by the State of Florida, and by the DOE.

SUPPLEMENTARY MATERIALS

www.sciencemag.org/content/346/6214/1208/suppl/DC1
Materials and Methods
Supplementary Text
Figures S1 to S14
Table S1
Equation S1
References (*40*–*50*)

2 January 2014; accepted 5 November 2014
10.1126/science.1250366

CHEMICAL KINETICS

Predictive a priori pressure-dependent kinetics

Ahren W. Jasper,[1] Kenley M. Pelzer,[2] James A. Miller,[2] Eugene Kamarchik,[1] Lawrence B. Harding,[2] Stephen J. Klippenstein[2]*

The ability to predict the pressure dependence of chemical reaction rates would be a great boon to kinetic modeling of processes such as combustion and atmospheric chemistry. This pressure dependence is intimately related to the rate of collision-induced transitions in energy *E* and angular momentum *J*. We present a scheme for predicting this pressure dependence based on coupling trajectory-based determinations of moments of the *E*,*J*-resolved collisional transfer rates with the two-dimensional master equation. This completely a priori procedure provides a means for proceeding beyond the empiricism of prior work. The requisite microcanonical dissociation rates are obtained from ab initio transition state theory. Predictions for the $CH_4 = CH_3 + H$ and $C_2H_3 = C_2H_2 + H$ reaction systems are in excellent agreement with experiment.

Pressure-dependent reactions are ubiquitous in applications of gas-phase chemical kinetics to practical problems, such as combustion (<100 bar), atmospheric chemistry (≤1 bar), and chemical vapor deposition (<<1 bar). These reactions can take various forms involving chemical or thermal activation, single or multiple unimolecular potential wells, and single or multiple sets of bimolecular products. Such reactions are enormously complicated problems to treat theoretically, even for a single-channel, single-well dissociation, which is the case we focus on here. The accurate first-principles prediction of pressure-dependent rate coefficients would dramatically improve the utility of theoretical kinetics as a tool for global chemical modeling.

There are two constants of motion in an isolated dissociating molecule: the total internal (vibrational-rotational) energy, *E*, and the total angular momentum, *J*. A physically correct description of the kinetics requires a quantitative understanding of the rate of collision-induced transitions in these two variables, $k_c(E,J;E',J')$, and the corresponding *E*- and *J*-resolved dissociation/isomerization rate constant, $k(E,J)$. The master equation treats the time dependence of the state-resolved species populations arising from collisions and dissociation. This time dependence can be directly related to pressure-dependent thermal dissociation rate constants $k(T,p)$ (*1*–*4*).

Although many of the foundational formulations of reaction rate theory considered pressure dependence, subsequent theoretical developments have almost exclusively focused on pressure-independent reactions. Such pressure-independent rate coefficients are generally obtained from a thermal average of $k(E,J)$ and are independent of the collisional transition process. Many classes of pressure-independent reactions can now be treated with very high accuracy. For example, quantitative first-principles kinetics calculations for pressure-independent bimolecular reactions of three- and four-atom (*5*–*7*) and larger systems (*8*) have been highlighted as milestones in the development of reaction rate theory. For larger systems, ab initio transition state theory provides high-accuracy predictions for the high-pressure addition rates as illustrated, for example, in our recent studies of $O(^3P)$ + alkenes (*9*), of $^1CH_2$ + alkenes (*10*), and of alkyl radical + alkyl radical reactions (*11*), where a priori theory and experiment agreed to within 20%. In contrast, accurate first-principles methods for predicting pressure-dependent reaction rates have not been similarly developed.

In the low-pressure limit, $k(T,p)$ is independent of $k(E,J)$ and is instead determined by the details of the collision-induced transitions in *E* and *J* (*12*). At intermediate pressures, both the collision-induced transition rates and the decomposition rates play an important role in the kinetics. Prior theoretical kinetics work has employed simple empirical models for the collisional transition rates, with parameters adjusted to reproduce available experimental data (*13*, *14*). This empiricism severely limits the utility of theoretical kinetics as a mechanism development tool. Empirical theories are effectively limited to interpolations and extrapolations of the pressure and temperature ranges for reactions that have already been studied experimentally. Correlation of the energy transfer parameters with physical properties (e.g., molecular size, collision bath gas, reaction temperature) provides some predictive ability, but currently such correlations are not well determined and introduce additional uncertainties in the rate estimates of at least a factor of 2. For example, information regarding the temperature dependence of the energy transfer parameters is very limited, especially for temperatures that deviate strongly from 300 K. Furthermore, for complex multiple-well, multiple-product reactions, the effects of the uncertainties in such correlations are greatly

[1]Combustion Research Facility, Sandia National Laboratories, MS 9055, Livermore, CA 94551-0969, USA. [2]Chemical Sciences and Engineering Division, Argonne National Laboratory, Argonne, IL 60439, USA.
***Corresponding author. E-mail: sjk@anl.gov**

Downloaded from www.sciencemag.org on December 5, 2014

amplified, particularly for higher-energy channels and well-skipping reactions that involve dynamical passage over intermediate wells with only partial stabilization (*15*).

The most commonly used model (*1*, *3*) for the energy transfer process neglects the dependence of the kinetics on the total angular momentum J and employs a so-called "exponential down" form for the probability of a collision-induced transition from E' to E (*16*):

$$P(E;E') \propto \exp\left(-\frac{\Delta E}{\alpha}\right);\ E < E' \qquad (1)$$

In Eq. 1, $\Delta E = E - E'$, and α is a fitting parameter, which represents the average downwards energy transferred, $\langle \Delta E_d \rangle$, in a single deactivating collision. The energy transfer rate $k_c(E;E')$ is then generally represented as the product of a Lennard-Jones collision rate, Z_{LJ}, with $P(E;E')$. Within this one-dimensional master equation (1DME) model, $k(T,p)$ may be obtained via empirical estimates for the parameter α.

An obvious shortcoming of this simple approach is its neglect of J. Explicitly including J requires the solution of the two-dimensional (in E and J) master equation (2DME) and some characterization of the four-dimensional function $k_c(E,J;E',J')$, which we also write as the product of a total collision rate, Z, and a normalized probability, $P(E,J;E',J')$, of a collision producing the state (E,J) from an initial state (E',J'). The 2DME reduces to a 1DME if one assumes the distributions in E and J are separable and then makes a microcanonical strong collider in J assumption (i.e., the final rotational state is assumed to be independent of the initial rotational state with its probability determined by the J dependence of the microcanonical density of states) (*17*, *18*). In this "2D/φ" model, we write $P(E,J;E',J')$ as $P(E;E')\,\varphi(E,J)$, where $\varphi(E,J) = \rho(E,J)/\rho(E)$, with $\rho(E,J)$ and $\rho(E)$ as the E,J- and E-resolved density of states for the molecular complex, respectively.

A priori kinetic predictions were recently obtained within this 2D/φ model for CH_4 dissociation via classical trajectory calculations of the parameter $\alpha = \langle \Delta E_d \rangle$ (*19*). However, detailed comparisons with experimental data indicate that such predictions are not highly accurate, being about a factor of 2 too high, at least once anharmonic effects on the vibrational state densities are accounted for (*19*).

The assumption in the 2D/φ model that single collisions produce microcanonical statistical distributions of J is clearly not valid; kinetically relevant distributions of J typically are much wider than the average J-transferred in a single collision (*12*) (e.g., by a factor of 5 or more; compare fig. S2, a and b). One might also question the use of classical mechanics in the estimation of the energy transfer rates. However, the Ehrenfest theorem states that averaged quantum mechanical variables increasingly obey classical laws as the classical (high-E) limit is approached. The sensitivity of kinetic predictions to collisional transfer rates only at energies near the dissociation threshold then suggests that quantum effects on these rates should be negligible (*20*).

Furthermore, as thermal energies are generally much larger than relevant rotational energy-level spacings, quantization of J is also not expected to be important. Thus, the key question is, how much does the deviation from the microcanonical strong collider in J assumption affect the kinetic predictions (*12*)?

As a first exploration of this question, we approximated the four-dimensional collision kernel as a product of independent energy, $P(E;E')$, and angular momentum, $P(J;J')$, kernels. Further approximating each of these kernels with exponential down functions [Eq. 1 and $P(J;J') = \exp(-\Delta J/\gamma)$] provides a simple model for exploring the role of weak collisions in J. The plots in Fig. 1 illustrate the effect of varying the parameter γ on the predicted rate constant for CH_3 + H (+ He) recombination at 600 K. The predictions for $\gamma \le 2$ are in excellent agreement with the experimental data. Meanwhile, the predictions for higher γ values converge to the 2D/φ model, which lies about a factor of 2 higher than experiment. However, trajectory calculations predict $\gamma = 5$. This discrepancy demonstrates the need for detailed nonseparable models of the collision kernel, as considered next.

Here we use a direct coupling of classical trajectory-based explorations of the full collision kernel $k_c(E,J;E',J')$ with solutions to the 2DME to obtain completely a priori predictions of pressure-dependent kinetics. A full characterization of the four-dimensional collisional kernel k_c requires a large number of trajectory simulations (e.g., 10^6) because of its high-probability elastic peak and low-probability long tails. However, the rate constants are expected to depend most sensitively on the low-order moments of ΔE and ΔJ (*21*, *22*). Thus, we avoid here a detailed characterization of k_c and instead develop a practical model for k_c that reproduces its low-order moments.

The low-order moments of P for the changes in E and J are defined as

$$\langle \Delta E^m \Delta J^n \rangle (E', J') = \int_0^\infty dJ \int_{-E_0}^\infty dE\, P(E,J;E',J') \Delta E^m \Delta J^n \qquad (2)$$

Although these moments are dependent on the initial energy, E', and initial angular momentum, J', a detailed characterization of the initial state dependence of $\langle \Delta E^m \Delta J^n \rangle$ is not pursued here. Instead, we define and evaluate double moments,

$$\langle\langle \Delta E^m \Delta J^n \rangle\rangle = \int_0^\infty dJ'\, h(J') \langle \Delta E^m \Delta J^n \rangle (E'_0, J') \qquad (3)$$

where $h(J')$ are reference (e.g., thermal) J' distributions, and E'_0 is the rotationless threshold

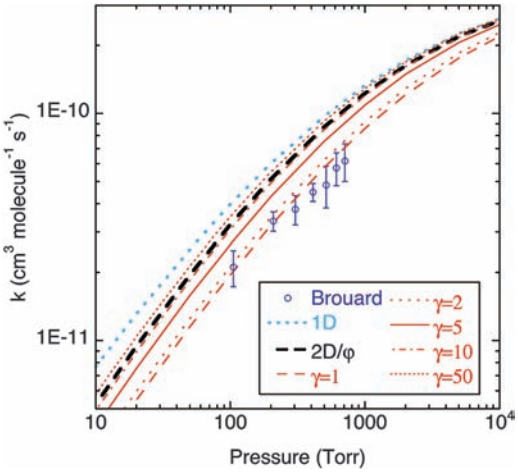


Fig. 1. Plot of the pressure-dependent rate constant for CH_3 + H (+He) → CH_4 (+He) at 600 K for various approximate models: the simple separable two-parameter 2DME model as a function of the ΔJ range parameter γ, the one-parameter 2D/φ model, and the one-parameter 1DME model. Symbols denote experimental results and error bars from Brouard *et al*. (*29*).

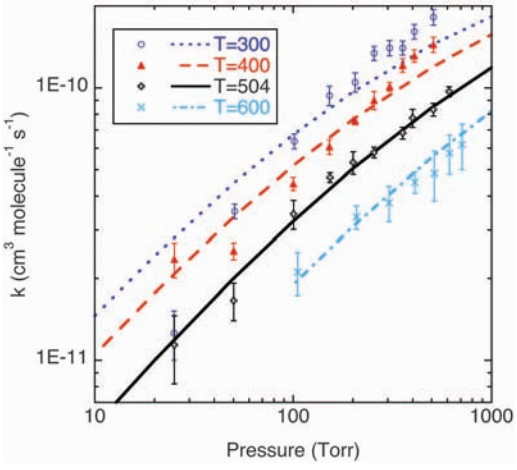


Fig. 2. Plot of the full 2DME a priori predictions (lines) for the pressure-dependent rate constant for CH_3 + H → CH_4 for a variety of temperatures, all with He as a bath gas. Symbols denote experimental results and error bars from Brouard *et al*. (*29*).

energy for dissociation. We have explicitly neglected to characterize the E' dependence in P because the solution to the 2DME depends only on E' values near the dissociation threshold, where the dependence of P on E' is very weak. These low-order moments may be readily evaluated with a limited number of trajectories (e.g., 10^3), which facilitates routine implementation of the approach and even suggests the feasibility of performing direct trajectory evaluations.

To solve the master equation, we use an ad hoc analytic representation of the energy transfer function that is simple, yet flexible enough to reproduce the low-order double moments defined in Eq. 3. Details are given in the supplementary material. Briefly, the functional form allows for the modeling of weak collisions in J, the nonseparability of ΔE and ΔJ, long tail (nonexponential) collisions in both ΔE and ΔJ, and an explicit dependence on J'. The analytic functional form has nine parameters that are determined such that the analytic representation reproduces 135 low-order double moments of the energy transfer function (Eq. 3) calculated using classical trajectories.

Barker and Weston have recently explored the mapping of the four-dimensional collision-induced transition kernel with trajectory simulations in a study of the energy deactivation process for excited pyrazine and ethane (*23*). These and earlier trajectory studies cited therein elucidated important details of P, but these details have not found their way into kinetics calculations. Some prior master equation studies have implemented the full 2DME (*24*–*26*), but these studies used empirical separable models owing to the absence of data for the collision kernel.

The details of the present theoretical calculations are provided in the supplementary material, where the (i) implementation of the 2DME, (ii) ab initio transition state theory calculations, (iii) representation and fitting of the collisional energy transfer kernel, and (iv) classical trajectory simulations are each discussed at length. These descriptions include an illustration of the quality of the present moment-fitting procedure in fig. S2 and in table S2.

As a demonstration of our approach, we obtained a priori predictions for three representative classes of reaction, focusing on specific reactions for which the experimental record appears fairly definitive. In particular, we studied CH_3 + H radical-radical recombination, H + C_2H_2 radical-molecule recombination, and C_2H_3 radical decomposition. Each of these reactions has also been the subject of previous theoretical studies by our team where the pressure dependence was treated empirically via adjustments of α to reproduce the experimental $k(T,p)$ using the 2D/φ model (*18*, *27*, *28*). Although the present comparisons serve as a useful test of the approach, its true power will be in making predictions of rate coefficients for cases where there are little or no experimental data. In this regard, it is important to emphasize that the present approach is readily applicable to essentially arbitrary reactions and bath gases.

The pressure dependence of the CH_3 + H recombination rate coefficient was considered at four temperatures ranging from 300 to 600 K. The predicted rate coefficients (Fig. 2) are seen to be in excellent agreement with the experimental data of Brouard *et al.* (*29*), generally within the error bars. Although there are a few discordant points at the lowest pressures for the two lowest temperatures, there are some apparent irregularities in the experimental data in that range. For example, the value near p = 25 Torr for 300 K is below that for 400 K, which is difficult to rationalize theoretically. Aside from that irregularity, theory and experiment generally agree to within 20%.

The pressure dependence of the room temperature rate coefficient for the H + C_2H_2 radical-molecule recombination to form C_2H_3 has been studied experimentally over an exceptionally broad range of pressures (from 1 to 1000 Torr) by Keil *et al.* (*30*) and by Payne and Stief (*31*). Meanwhile, the related reverse dissociation of vinyl was studied by Knyazev and Slagle (*32*) for a range of pressures at temperatures near 1000 K. Taken together, the two sets of data provide a stringent test for the present a priori approach. As shown in Figs. 3 and 4, the predictions for both the low-temperature recombination rate constants and the high-temperature dissociation rate constants are in very good agreement with the experimental data, with maximum deviations of about 20%.

In summary, the present pressure-dependent kinetic analysis solves the two-dimensional master equation for the representation of the collisional E,J transition kernel specified by eqs. S1 to S5, with the parameters in the representation obtained from fits to trajectory-based determinations of its low-order moments (Eq. 2). The requisite (E,J)-resolved dissociation rate constants are obtained from ab initio transition state theory calculations. The excellent performance of this fully a priori J-resolved pressure-dependent kinetic analysis for these three test cases strongly suggests that the present representation of the collision kernel (eq. S3) is accurate enough for obtaining kinetic estimates and that the trajectory-based prediction of the underlying parameters is also quantitatively accurate. Thus, this method should prove highly effective for predicting the pressure dependence of experimentally unstudied reactions and will serve as a great boon to the development of chemical models for complex gas phase environments. It should also allow for the quantitative prediction of the bath gas dependence of the rate

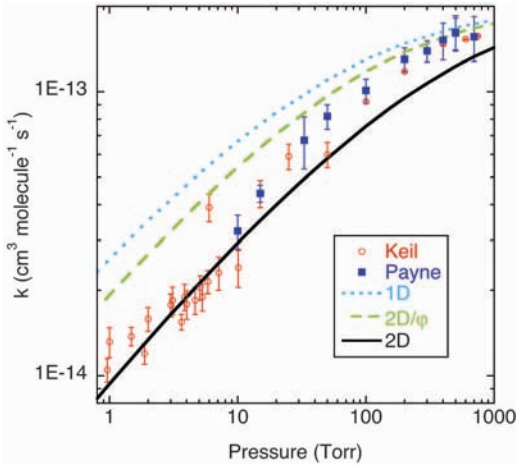


Fig. 3. Plot of the 1DME, 2D/ϕ, and full 2DME predictions for the pressure-dependent rate constant for H + C_2H_2 → C_2H_3 at room temperature with He as a bath gas. Symbols denote experimental results and error bars from Keil *et al.* (*30*) and Payne and Stief (*31*).

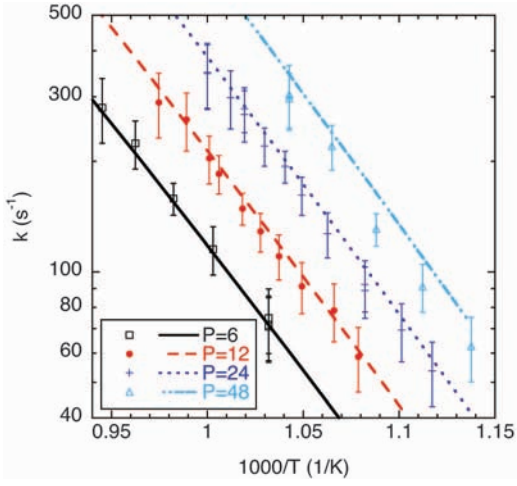


Fig. 4. Plot of the 2DME a priori predictions for the temperature-dependent rate constant for C_2H_3 → H + C_2H_2 at a range of densities that correlate with pressures of ~ 6, 12, 24, and 48 Torr, all with He as a bath gas. Symbols denote experimental results and error bars from Knyazev and Slagle (*32*).

coefficients, a topic of considerable current interest in combustion kinetics, for example.

For more complex reactions, involving multiple product channels and/or multiple wells, the competition between channels is strongly dependent on the details of the energy transfer process. It is likely that prior empirical master equation-based calculations for such reactions have largely yielded poor representations of the kinetics, at least for the higher-energy channels. The quantitative prediction of such rate coefficients may require the development of more complete representations of the collision kernel. For example, the competition between two channels with widely disparate rotational constants may require an improved representation of the J' dependence of the kernel, which could perhaps be achieved through quadratic rather than linear expansions of the parameters in eq. S5. Meanwhile, the quantitative modeling of the competition between two channels with quite different thresholds requires an accurate description of the ΔE dependence of the kernel over a broad range of E. Although the stretched exponentials allow some flexibility in this regard, it may also prove necessary to employ a more general representation incorporating, for example, a sum of terms of the form of eq. S3. Such double exponentials have proven useful in studying the effect of high-energy tails (supercollisions) (*33*) in prior 1DME studies (*3*, *18*, *34*). The present single-well single-product case study provides a roadmap for such multiple-product multiple-well analyses.

REFERENCES AND NOTES

1. B. Widom, *Science* **148**, 1555–1560 (1965).
2. K. A. Holbrook, M. J. Pilling, S. H. Robertson, *Unimolecular Reactions* (Wiley, West Sussex, 1996).
3. R. G. Gilbert, S. C. Smith, *Theory of Unimolecular and Recombination Reactions* (Blackwell Scientific, Oxford, UK, 1990).
4. J. A. Miller, S. J. Klippenstein, *J. Phys. Chem. A* **110**, 10528–10544 (2006).
5. D. C. Clary, *Science* **279**, 1879–1882 (1998).
6. D. H. Zhang, M. A. Collins, S.-Y. Lee, *Science* **290**, 961–963 (2000).
7. S. L. Mielke *et al.*, *Phys. Rev. Lett.* **91**, 063201 (2003).
8. T. Wu, H.-J. Werner, U. Manthe, *Science* **306**, 2227–2229 (2004).
9. H. Sabbah *et al.*, *Science* **317**, 102–105 (2007).
10. D. Polino, S. J. Klippenstein, L. B. Harding, Y. Georgievskii, *J. Phys. Chem. A* **117**, 12677–12692 (2013).
11. S. J. Klippenstein, Y. Georgievskii, L. B. Harding, *Phys. Chem. Chem. Phys.* **8**, 1133–1147 (2006).
12. A. W. Jasper, J. A. Miller, S. J. Klippenstein, *J. Phys. Chem. A* **117**, 12243–12255 (2013).
13. V. D. Knyazev, *J. Phys. Chem.* **99**, 14738–14741 (1995).
14. R. Sivaramakrishnan *et al.*, *J. Phys. Chem. A* **115**, 3366–3379 (2011).
15. C. F. Goldsmith, A. S. Tomlin, S. J. Klippenstein, *Proc. Combust. Inst.* **34**, 177–185 (2013).
16. In many works, the total internal energy E is replaced with the active energy ε, which represents the vibrational energy of the molecule.
17. S. C. Smith, R. G. Gilbert, *Int. J. Chem. Kinet.* **20**, 307–329 (1988).
18. J. A. Miller, S. J. Klippenstein, C. Raffy, *J. Phys. Chem. A* **106**, 4904–4913 (2002).
19. A. W. Jasper, J. A. Miller, *J. Phys. Chem. A* **115**, 6438–6455 (2011).
20. G. C. Schatz, G. Lendvay, *J. Chem. Phys.* **106**, 3548–3557 (1997).
21. J. Keck, G. Carrier, *J. Chem. Phys.* **43**, 2284–2298 (1965).
22. J. Troe, *J. Chem. Phys.* **66**, 4745–4757 (1977).
23. J. R. Barker, R. E. Weston Jr., *J. Phys. Chem. A* **114**, 10619–10633 (2010).
24. S. J. Jeffrey, K. E. Gates, S. C. Smith, *J. Phys. Chem.* **100**, 7090–7096 (1996).
25. S. H. Roberston, M. J. Pilling, K. E. Gates, S. C. Smith, *J. Comput. Chem.* **18**, 1004–1010 (1997).
26. P. K. Venkatesh, A. M. Dean, M. H. Cohen, R. W. Carr, *J. Chem. Phys.* **111**, 8313–8329 (1999).
27. S. J. Klippenstein, Y. Georgievskii, L. B. Harding, *Proc. Combust. Inst.* **29**, 1229–1236 (2002).
28. J. A. Miller, S. J. Klippenstein, *Phys. Chem. Chem. Phys.* **6**, 1192–1202 (2004).
29. M. Brouard, M. T. Macpherson, M. J. Pilling, *J. Phys. Chem.* **93**, 4047–4059 (1989).
30. D. G. Keil, K. P. Lynch, J. A. Cowfer, J. V. Michael, *Int. J. Chem. Kinet.* **8**, 825–857 (1976).
31. W. A. Payne, L. J. Stief, *J. Chem. Phys.* **64**, 1150–1155 (1976).
32. V. D. Knyazev, I. R. Slagle, *J. Phys. Chem.* **100**, 16899–16911 (1996).
33. N. J. Brown, J. A. Miller, *J. Chem. Phys.* **80**, 5568–5580 (1984).
34. V. Bernshtein, I. Oref, *J. Phys. Chem.* **97**, 12811–12818 (1993).

ACKNOWLEDGMENTS

This work is supported by the Division of Chemical Sciences, Geosciences, and Biosciences, Office of Basic Energy Sciences, U.S. Department of Energy (DOE-BES). The work at Argonne was supported under Contract no. DE-AC02-06CH11357 as part of the Argonne-Sandia Consortium on High-Pressure Combustion Chemistry (FWP no. 59044). Sandia is a multiprogram laboratory operated by Sandia Corporation, a Lockheed Martin Company, for the U.S. DOE under Contract no. DE-AC04-94-AL85000. Software development was supported by the AITSTME project as part of the Predictive Theory and Modeling component of the Materials Genome Initiative of DOE-BES. K. Pelzer acknowledges the support of the DOE Computational Science Graduate Fellowship under grant no. DE-FG02-97ER25308.

SUPPLEMENTARY MATERIALS

www.sciencemag.org/content/346/6214/1212/suppl/DC1
Materials and Methods
Figs. S1 and S2
Tables S1 and S2
References (*35*–*45*)

5 September 2014; accepted 28 October 2014
10.1126/science.1260856

SURFACE STRUCTURE

Subsurface cation vacancy stabilization of the magnetite (001) surface

R. Bliem,[1] E. McDermott,[2] P. Ferstl,[3] M. Setvin,[1] O. Gamba,[1] J. Pavelec,[1] M. A. Schneider,[3] M. Schmid,[1] U. Diebold,[1] P. Blaha,[2] L. Hammer,[3] G. S. Parkinson[1]*

Iron oxides play an increasingly prominent role in heterogeneous catalysis, hydrogen production, spintronics, and drug delivery. The surface or material interface can be performance-limiting in these applications, so it is vital to determine accurate atomic-scale structures for iron oxides and understand why they form. Using a combination of quantitative low-energy electron diffraction, scanning tunneling microscopy, and density functional theory calculations, we show that an ordered array of subsurface iron vacancies and interstitials underlies the well-known $(\sqrt{2}\times\sqrt{2})$R45° reconstruction of Fe_3O_4(001). This hitherto unobserved stabilization mechanism occurs because the iron oxides prefer to redistribute cations in the lattice in response to oxidizing or reducing environments. Many other metal oxides also achieve stoichiometry variation in this way, so such surface structures are likely commonplace.

The properties of metal oxide surfaces are inextricably linked to their atomic-scale structure, which makes obtaining a precise structural model a vital prerequisite to understanding and modeling surface processes. The typical starting point to guess the structure of a metal oxide surface is the Tasker surface polarity criteria (*1*). These simple and convenient rules have proven remarkably successful for predicting the stable terminations of model systems such as TiO_2, MgO, and ZnO (*2*, *3*). A second guiding principle to emerge from 20 years of metal oxide surface science is the vital role played by oxygen vacancies (V_Os).

[1]Institute of Applied Physics, Wiedner Hauptstrasse 8-10, Vienna University of Technology, 1040 Vienna, Austria. [2]Institute of Materials Chemistry, Getreidemarkt 9, Vienna University of Technology, 1060 Vienna, Austria. [3]Chair of Solid State Physics, University of Erlangen-Nürnberg, Staudtstrasse 7, 91058 Erlangen, Germany.
***Corresponding author. E-mail: parkinson@iap.tuwien.ac.at**

The surface V_O concentration is usually in equilibrium with the bulk, where such defects form when the oxide is reduced. At the surface, V_Os strongly affect the electronic structure, are active sites for chemical reactions (*4*, *5*), and play a central role in surface reconstructions. There exists another class of metal oxides, however, in which stoichiometric variation is accommodated primarily via the cations; the iron oxides are the prototypes. Wüstite (FeO), magnetite (Fe_3O_4), and hematite (α-Fe_2O_3) are all based on a close-packed O^{2-} anion lattice and differ primarily in the number, oxidation state, and distribution of the cations among octahedral and tetrahedral interstitial sites, Fe_{oct} and Fe_{tet} (*6*). Near the phase boundaries, FeO can incorporate up to 17% of Fe_{oct} vacancies, whereas the metastable phase maghemite (γ-Fe_2O_3) is essentially Fe_3O_4 with 1/6 of the Fe_{oct} removed. We now show that an ordered array of subsurface cation vacancies and interstitials underlies

the well-known $(\sqrt{2} \times \sqrt{2})$R45° reconstruction of Fe_3O_4(001). This stabilization is driven by the material adopting a stoichiometry compatible with its environment. The oxides of Co, Mn, and Ni exhibit similar cation redistributions in reducing and oxidizing environments, so such reconstructions may be a common occurrence.

In the (001) direction, Fe_3O_4 consists of alternating planes of Fe_{tet} and $(Fe_{oct})_2O_4$ and thus appears to be a classic Tasker type 3 polar surface (*1*, *3*). Indeed, early studies of the $(\sqrt{2} \times \sqrt{2})$R45° reconstruction considered only structures compatible with polarity compensation (*7*–*9*). However, Fe_3O_4 is metallic, so it is not clear why the polar catastrophe should occur at all. In fact, the current model for the Fe_3O_4(001) surface is based on a nominally polar bulk truncation at the Fe_{oct}-O plane. For this termination (Fig. 1A), density functional theory–based calculations (DFT+U) (*10*–*12*) find pairs of surface Fe_{oct} relaxed in opposite directions perpendicular to the row. This structure produces the requisite $(\sqrt{2} \times \sqrt{2})$R45° periodicity and is in qualitative agreement with undulating rows of Fe_{oct} atoms observed in scanning tunneling microscopy (STM) images (*7*, *8*). The emergence of orbital order among the Fe_{oct} cations in subsurface layers has been likened to the "Verwey" phase of Fe_3O_4 (*11*), which forms below a transition temperature of 125 K. This structure has been widely accepted, largely on the basis of low-energy electron diffraction (LEED *IV*) (*12*) and surface x-ray diffraction (SXRD) (*10*) measurements, which purport to confirm the structure. However, the quantitative measure of agreement between experimental and theoretical LEED *IV* curves, the Pendry *R*-factor (R_P) (*13*), was poor (R_P = 0.34) in comparison with what is achieved for metal and elemental semiconductor surfaces (R_P < 0.2). This classic study, and several others (*14*–*16*), suggest that the achievable R_P is limited for metal oxide surfaces, either because the scattering calculations fail to account for ionic bonding (*14*–*16*) or because oxides contain many defects (*12*).

Perspective (Fig. 1B) and top (Fig. 1C) views of the subsurface cation vacancy (SCV) structure of Fe_3O_4(001), as determined with DFT+U calculations, show that the $(\sqrt{2} \times \sqrt{2})$R45° periodicity arises from replacing two Fe_{oct} from the third layer by an interstitial Fe_{int} with tetrahedral coordination in the second layer—a net removal of one cation per $(\sqrt{2} \times \sqrt{2})$R45° unit cell. The subsurface reorganization distorts the surface layer, and the resulting undulations in the Fe_{oct} rows are more pronounced than in the bulk truncation model (Fig. 1, A and B). All cations in the four outermost layers possess a magnetic moment of 3.85 to 4.01 μB. This is indicative of an Fe^{3+}-like character that is also observed in x-ray photoelectron spectroscopy (XPS) (*9*); angle-resolved XPS spectra are provided in fig. S1 (*17*). The Fe_{oct} and Fe_{tet} sublattices remain antiferromagnetically coupled as in the bulk, yielding a reduced net magnetic moment in the SCV reconstruction. The absence of Fe^{2+} suggests that the contribution of the orbital moment should be small. The magnetic moments of all atoms in the surface region are contained in table S1 (*17*) together with their optimized DFT+U coordinates. The energetic preference for the SCV structure is borne out by atomistic thermodynamics calculations (Fig. 1E) (*18*). The distorted bulk truncation is only favored below an oxygen chemical potential of –3 eV, corresponding to an O_2 partial pressure of $<10^{-20}$ mbar at 900 K. Under such reducing conditions, however, Fe-rich surface phases occur (*19*). Although α-Fe_2O_3 is predicted to take over as the thermodynamically stable phase above ≈10^{-9} mbar, the $(\sqrt{2} \times \sqrt{2})$R45° reconstruction persists up to 10^{-5} mbar. It has been shown that α-Fe_2O_3 inclusions grow slowly at 10^{-6} mbar O_2 (*20*), whereas conversion of the surface to γ-Fe_2O_3(001) requires extremely oxidizing conditions (*9*).

A key success of the SCV structure is that it explains the extraordinary thermal stability of Au, Ag, and Pd adatoms at the Fe_3O_4(001) surface, which resist agglomeration into clusters up to

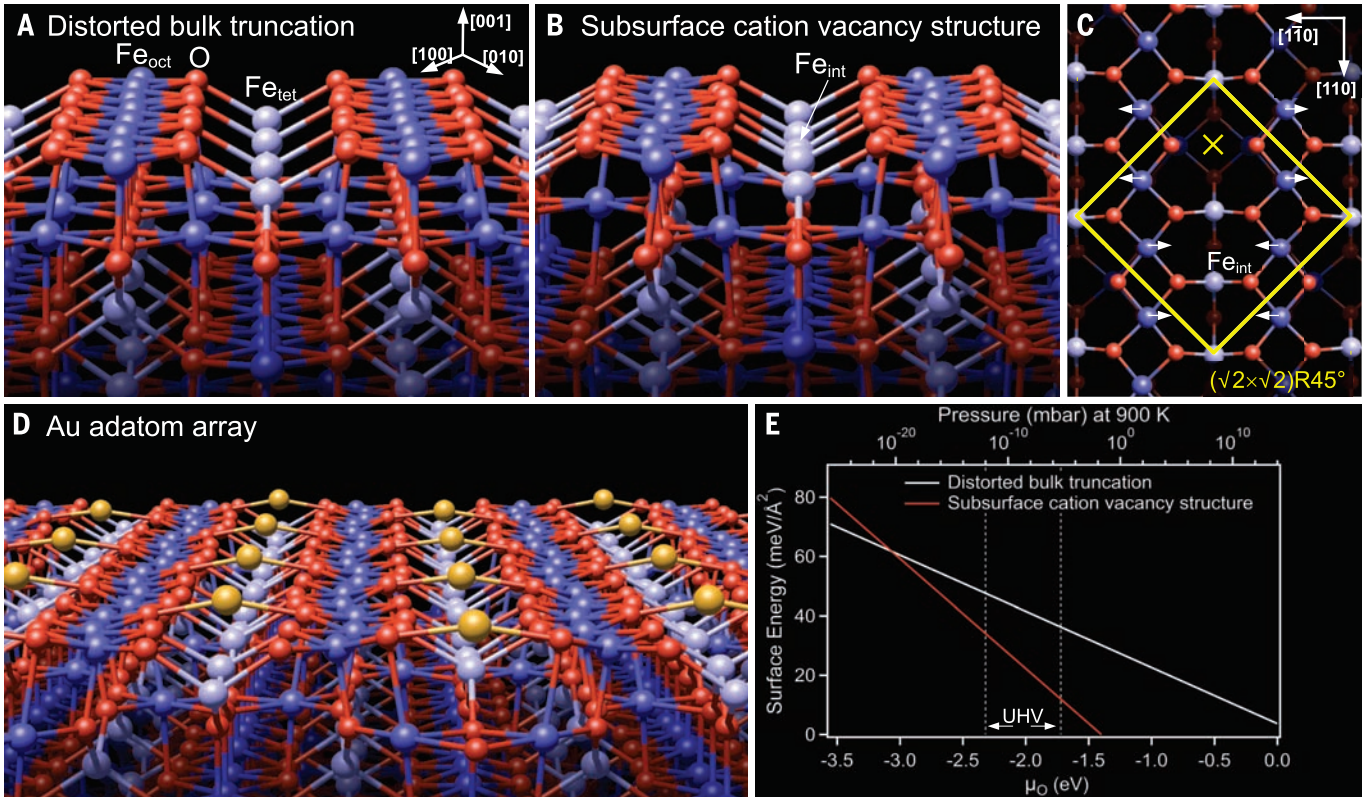


Fig. 1. DFT+U calculations show that an ordered array of cation vacancies underlies the $(\sqrt{2} \times \sqrt{2})$R45° reconstruction of the Fe_3O_4(001) surface. (**A**) Minimum-energy structure of the distorted bulk truncation model (*10*, *12*). (**B** and **C**) Perspective and plan views of the subsurface cation vacancy structure. A pair of Fe_{oct} cations from the third layer is replaced by an interstitial Fe_{tet} (labeled Fe_{int}) in the second layer. (**D**) Au adatoms bind strongly (2.03 eV) to surface O at positions without second-layer Fe_{tet} atoms. These sites, marked with an "×" in (C), result in a nearest-neighbor Au distance of 8.4 Å (*21*). (**E**) Surface energy as a function of oxygen chemical potential, μ_O, for both structures. The μ_O is converted to an O_2 pressure for a nominal annealing temperature of 900 K. The cation vacancy structure is stable in all experimentally accessible conditions.

700 K (*19*, *21*–*23*). Adatoms exclusively occupy just one of the two available bulk continuation sites per $(\sqrt{2} \times \sqrt{2})$R45° unit cell. This finding is difficult to reconcile with the distorted bulk truncation model because the two sites are identical save for the subtle relaxations and the subsurface orbital ordering. Unsurprisingly, DFT+U calculations for Au adatom adsorption on the bulk-truncated surface reveal no clear preference for one specific site. On the SCV structure, the interstitial Fe_{int} blocks the adsorption of an adatom in the bulk continuation site directly above. For Au, a

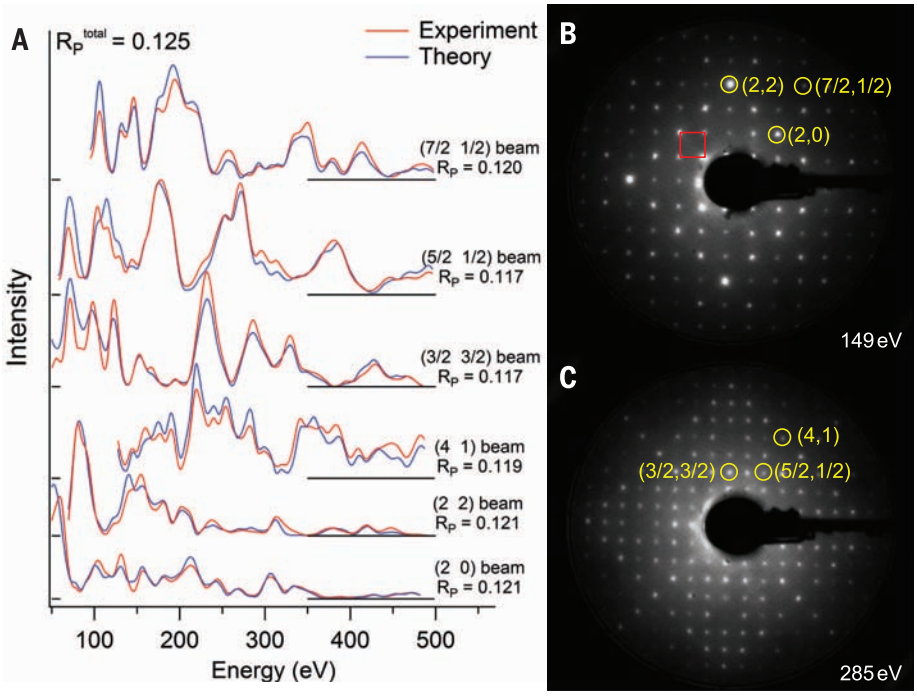


Fig. 2. Quantitative low-energy electron diffraction measurements unambiguously confirm the subsurface cation vacancy termination of Fe_3O_4(001). (**A**) Comparison of selected experimental LEED *IV* spectra and theoretical curves for the optimized subsurface vacancy structure. The final R_P for the best-fit structure is 0.125; the selected beams have an individual R_P close to this average. (**B** and **C**) Experimental LEED patterns for electron energies of 149 and 285 eV, respectively. Diffraction spots highlighted with yellow circles correspond to the curves in (A). The red square indicates the $(\sqrt{2} \times \sqrt{2})$R45° unit cell.

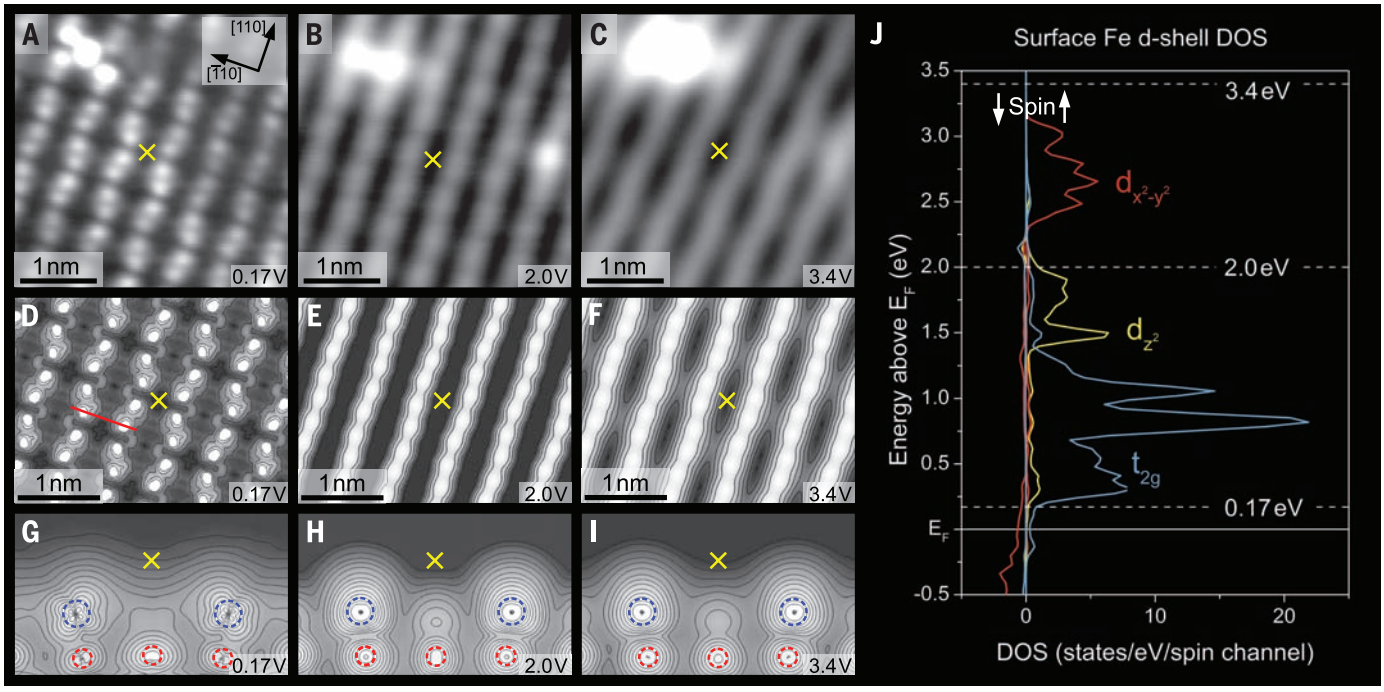


Fig. 3. STM images of the Fe_3O_4(001) surface are dominated by electronic effects. (**A** to **C**) Empty-state STM images obtained on the same sample area in (A) constant-height and constant-current mode with (B) tunneling current (I_t) = 0.15 nA and (C) I_t = 0.15 nA. The bias voltages are given in each panel. An Fe adatom defect in the top left of each image defines a constant position (equivalent to the position of the yellow "×"). As the STM bias is increased, the apparent undulations in the Fe_{oct} rows reverse phase. (**D** to **F**) Simulated STM images at scanning conditions corresponding to (A) to (C). (**G** to **I**) Electronic charge density contour plots in cross section at the position indicated by the red line in (D). The t_{2g} orbitals of the surface Fe_{oct} atoms (blue dashed circles) are distorted, resulting in a density that is asymmetric about the atom core position. (**J**) Electronic density of states above E_F for the surface Fe_{oct} atoms. As the tunneling bias is increased, different Fe *d* orbitals contribute to the STM images. At 0.17 V, only part of the t_{2g} orbital is accessed, followed by more spherically symmetric d_z^2 and $d_{x^2-y^2}$ e_g orbitals at higher bias. The higher bias gives a more realistic indication of the atomic core positions.

stable binding configuration (2.03 eV) is found only in the twofold coordinated site located above the "bulk-like" subsurface region (Fig. 1D), which results in nearest neighbors 8.4 Å apart (*19*, *21*–*23*).

To independently confirm the SCV structure of Fe_3O_4(001), we conducted LEED *IV* experiments. Selected experimental spectra are shown in Fig. 2A, together with best-fit curves resulting from optimized structural parameters. [The supplementary materials contain the full set of curves (fig. S3), the optimized coordinates (table S2), their associated error estimates, and a structure file that can be opened by most visualization software programs (*17*).] The best-fit structure achieved R_P = 0.125, a vast improvement over the 0.34 obtained previously for the distorted bulk truncation model (*12*). Moreover, the agreement between the LEED *IV* parameters and the DFT+U optimized structure is excellent (table S3) (*17*). In the surface layer, all atoms relax toward the nearest interstitial Fe_{int} atom in the second layer (Fig. 1, B and C). The largest relaxation (0.28 Å in the surface plane) occurs for the O furthest from Fe_{int}. In DFT+U calculations, this atom has a large magnetic moment (0.35 μ_B) and is close to a –1 charge state. The lateral relaxations of the surface Fe_{oct} atoms (0.11 Å) produce a peak-to-peak undulation of 0.22 Å in the Fe_{oct} rows. Whereas the Fe_{int} atom resides 0.08 Å below the bulk-like Fe_{tet} atoms, a slight rumpling in the neighboring Fe_{oct}-O layers preserves the Fe-O bond lengths within 2% (1.889 Å).

Because STM is the method of choice for monitoring dispersed adsorbates, it is important to establish the appearance of adsorption sites in the SCV structure. Three empty-state STM images taken at the same area with different tunneling voltages are shown in Fig. 3, A to C. An Fe adatom [a typical defect after sputter/anneal cycles (*24*)] in the upper left corner served as a marker. Fe occupies the same adsorption site as Au, Ag, and Pd adatoms (*19*, *21*–*23*), the bulk continuation site marked with the yellow "×" in Fig. 1C. At low sample bias, the undulations in the Fe_{oct} row appeared pronounced, and the × is located where the Fe rows apparently come closest together. [In our previous work (*19*, *21*–*23*), we called this position the "narrow site."] When the bias was increased to 2.0 V, the Fe_{oct} rows appeared almost straight, and it was difficult to discern the $(\sqrt{2} \times \sqrt{2})$R45° periodicity. At 3.4 V, the undulations returned, but the × was located in the opposite phase of the reconstruction, where the Fe_{oct} rows were furthest apart.

This trend was borne out in STM simulations (Fig. 3, D to F) and can be understood by examining the density of states (DOS) of the surface Fe_{oct} atoms (Fig. 3J) and the corresponding charge density contour plots (Fig. 3, G to I). At positive sample bias, electrons tunnel from the tip into empty states above the Fermi level (E_F). The *d* states are split by the crystal field, and the t_{2g} orbitals straddle E_F. At 0.17 V, electrons can tunnel only into a t_{2g} orbital, which is tilted off-axis because of an antibonding interaction with the underlying O-atom (Fig. 3G). Thus, the imaged electron density is not symmetric about the atom cores. At 3.4 V, when tunneling is dominated by the symmetric d_{z^2} and $d_{x^2-y^2}$ e_g orbitals, the STM images are more in line with the true relaxations as determined with DFT+U and LEED *IV*.

The SCV structure described here could not have been predicted by using polarity compensation rules (*3*). The driving force of the reconstruction is the oxygen chemical potential, which is consistent with previous reports of reduced terminations on the Fe_3O_4(111) (*25*, *26*) and Fe_2O_3(0001) (*27*) surfaces. Although the bulk is restricted to the FeO (rocksalt), Fe_3O_4 (spinel), and Fe_2O_3 (corundum) structures, the lack of three-dimensional periodicity at the surface permits the formation of the SCV structure, a distinct phase with an intermediate $Fe_{11}O_{16}$ stoichiometry. In this light, the $(\sqrt{2} \times \sqrt{2})$R45° reconstruction must be seen as the first stage in the oxidation of Fe_3O_4. With all cations in a bulk-like environment, it is a highly stable configuration. It is unlikely that the structure penetrates deeper because there the interstitial Fe_{int} would prevent the occupation of a bulk Fe_{tet} site in the next layer above. The same effect is at work in the surface layer (Fig. 1D), where the Fe_{int} blocks Au adsorption in one of the bulk continuation Fe_{tet} sites.

The R_P of 0.125 achieved in our LEED *IV* experiments strongly supports the SCV structure and also shows that there is no inherent problem in the LEED *IV* methodology that limits the obtainable agreement for complex metal oxide surfaces. Although it is of course important to ensure that the surface under investigation is of the highest quality (ideally cross-checked with in situ imaging), and to minimize damage by the LEED electron beam, using the correct trial structure in the calculations is essential. To reinforce this point, we also analyzed the experimental data set acquired in a previous LEED *IV* study of this surface (*12*). Despite the crystals, vacuum system, measurement temperature, and preparation conditions differing between the measurements, a similar R_P of 0.124 was obtained.

Understanding the true structure of the Fe_3O_4(001)-$(\sqrt{2} \times \sqrt{2})$R45° surface is vital to correctly interpret experimental results acquired for this surface. For example, the observation of a surface band gap was taken as evidence for a "surface Verwey transition" (*11*). Our results show that the modified electronic structure is in fact due to an entirely different iron oxide phase being present at the surface and is not related to charge/orbital ordering. The SCV reconstruction also likely explains why spin-polarized photoemission does not yield the 100% spin polarization predicted for the bulk (*28*). This surface-sensitive technique mainly probes the $Fe_{11}O_{16}$ phase, which has little DOS at E_F, no pronounced spin polarization (Fig. 3J), and a reduced net magnetization. Such a "magnetic dead layer" has been blamed for the poor performance of Fe_3O_4-based spintronics devices (*29*, *30*). Perhaps the most exciting consequence of the SCV structure is that it supports isolated metal adatoms that remain stable against agglomeration until the reconstruction is lifted at 700 K (*23*, *31*). This distinctive property, which represents the ultimate limit of the adsorption template phenomenon, provides a well-defined initial state for fundamental studies of cluster nucleation and growth (*22*, *23*) and offers an ideal model system with which to uncover the mechanisms of single-atom catalysis (*32*).

Given that the oxides of Co, Mn, and Ni exhibit a similar tendency to rearrange the cation lattice as the iron oxides, and even traverse the same oxidation pathway (from rocksalt structures through spinel to corundum), cation vacancy reconstructions are likely commonplace.

REFERENCES AND NOTES

1. P. W. Tasker, *J. Phys. C Solid State* **12**, 4977–4984 (1979).
2. C. Wöll, *Prog. Surf. Sci.* **82**, 55–120 (2007).
3. C. Noguera, *J. Phys. Condens. Matter* **12**, R367–R410 (2000).
4. Z. Dohnálek, I. Lyubinetsky, R. Rousseau, *Prog. Surf. Sci.* **85**, 161–205 (2010).
5. G. Pacchioni, H. Freund, *Chem. Rev.* **113**, 4035–4072 (2013).
6. R. M. Cornell, U. Schwertmann, *The Iron Oxides: Structure, Properties, Reactions, Occurrences and Uses* (Wiley-VCH, New York, 2003).
7. R. Wiesendanger *et al*., *Science* **255**, 583–586 (1992).
8. B. Stanka, W. Hebenstreit, U. Diebold, S. A. Chambers, *Surf. Sci.* **448**, 49–63 (2000).
9. S. A. Chambers, S. A. Joyce, *Surf. Sci.* **420**, 111–122 (1999).
10. R. Pentcheva *et al*., *Phys. Rev. Lett.* **94**, 126101 (2005).
11. Z. Łodziana, *Phys. Rev. Lett.* **99**, 206402 (2007).
12. R. Pentcheva *et al*., *Surf. Sci.* **602**, 1299–1305 (2008).
13. J. B. Pendry, *J. Phys. C Solid State Phys.* **13**, 937–944 (1980).
14. R. Lindsay *et al*., *Phys. Rev. Lett.* **94**, 246102 (2005).
15. V. B. Nascimento *et al*., *Phys. Rev. B* **75**, 035408 (2007).
16. K. Pussi *et al*., *Surf. Sci.* **606**, 1–6 (2012).
17. Materials and methods are available as supplementary materials on *Science* Online.
18. K. Reuter, M. Scheffler, *Phys. Rev. B* **65**, 035406 (2001).
19. Z. Novotny *et al*., *Phys. Rev. B* **87**, 195410 (2013).
20. S. Nie *et al*., *J. Am. Chem. Soc.* **135**, 10091–10098 (2013).
21. Z. Novotný *et al*., *Phys. Rev. Lett.* **108**, 216103 (2012).
22. G. S. Parkinson *et al*., *Nat. Mater.* **12**, 724–728 (2013).
23. R. Bliem *et al*., *ACS Nano* **8**, 7531–7537 (2014).
24. G. S. Parkinson, Z. Novotny, P. Jacobson, M. Schmid, U. Diebold, *Surf. Sci. Lett.* **605**, L42–L45 (2011).
25. N. G. Condon *et al*., *Phys. Rev. B* **55**, 15885–15894 (1997).
26. S. K. Shaikhutdinov, M. Ritter, X. G. Wang, H. Over, W. Weiss, *Phys. Rev. B* **60**, 11062–11069 (1999).
27. C. H. Lanier, A. N. Chiaramonti, L. D. Marks, K. R. Poeppelmeier, *Surf. Sci.* **603**, 2574–2579 (2009).
28. J. G. Tobin *et al*., *J. Phys. Condens. Matter* **19**, 315218 (2007).
29. W. Kim, K. Kawaguchi, N. Koshizaki, M. Sohma, T. Matsumoto, *J. Appl. Phys.* **93**, 8032 (2003).
30. X. W. Li, A. Gupta, G. Xiao, W. Qian, V. P. Dravid, *Appl. Phys. Lett.* **73**, 3282 (1998).
31. N. C. Bartelt *et al*., *Phys. Rev. B* **88**, 235436 (2013).
32. X.-F. Yang *et al*., *Acc. Chem. Res.* **46**, 1740–1748 (2013).

ACKNOWLEDGMENTS

G.S.P. and O.G. acknowledge support from the Austrian Science Fund project number P24925-N20. R.B. and E.M. acknowledge a stipend from the Vienna University of Technology and Austrian Science Fund doctoral college SOLIDS4FUN, project number W1243. U.D. and J.P. acknowledge support by the European Research Council advanced grant "OxideSurfaces." P.B. was supported by the Austrian Science Fund project SFB-F41 ViCoM. The computational results were achieved (in part) using the Vienna Scientific Cluster (VSC). All authors acknowledge Z. Mao and T. J. Liu (Tulane University) for the synthetic sample used in this work. We thank W. Moritz for sharing experimental LEED *IV* spectra.

SUPPLEMENTARY MATERIALS

www.sciencemag.org/content/346/6214/1215/suppl/DC1
Materials and Methods
Figs. S1 to S3
Tables S1 to S3
References (*33*–*35*)
Database S1

28 August 2014; accepted 17 October 2014
10.1126/science.1260556

HUMAN CAPITAL

Summer jobs reduce violence among disadvantaged youth

Sara B. Heller[1,2]*

Every day, acts of violence injure more than 6000 people in the United States. Despite decades of social science arguing that joblessness among disadvantaged youth is a key cause of violent offending, programs to remedy youth unemployment do not consistently reduce delinquency. This study tests whether summer jobs, which shift focus from remediation to prevention, can reduce crime. In a randomized controlled trial among 1634 disadvantaged high school youth in Chicago, assignment to a summer jobs program decreases violence by 43% over 16 months (3.95 fewer violent-crime arrests per 100 youth). The decline occurs largely after the 8-week intervention ends. The results suggest the promise of using low-cost, well-targeted programs to generate meaningful behavioral change, even with a problem as complex as youth violence.

Every day in the United States, acts of violence kill almost 150 people and injure over 6000 more (*1*, *2*). This "public health crisis" (*3*) disproportionately involves youth, who are twice as likely as adults to be both victims and perpetrators of violence (*4*). The problem is most concentrated among disadvantaged minority youth; violent-crime arrest rates for African-American juveniles are five times as high as that of their white counterparts (*5*).

Poverty scholar W. J. Wilson identifies one major cause of these racial violence disparities among young people: joblessness (*6*). His argument adds to decades of social science investigating how poor job prospects cause crime, from weakening social bonds to generating psychic strain to reducing the perceived cost of punishment (*7*–*10*). Policy discussions often conclude that public employment and training programs are a solution to youth violence on the grounds that "nothing stops a bullet like a job" (*11*).

The empirical literature on youth employment programs, however, suggests that the practical applications of this idea are limited (*12*). Several major employment programs fail to reduce delinquency among youth (*13*, *14*). The two experimentally evaluated interventions that do lower crime, at least during the program, involve such intensity and expense that their benefits fail to outweigh their costs (*15*, *16*). Attempts to provide shorter, more scalable employment services have, if anything, increased adolescents' criminal behavior (*17*). The theoretical promise of using employment interventions to fight youth violence does not appear to translate easily into empirical reality; only very high levels of investment seem able to reduce crime (supplementary materials, section 2.1) (*18*).

But, one widespread type of youth employment program has not yet been rigorously evaluated: summer jobs (*19*, *20*). Despite some promising observational studies (*21*), there is little convincing causal evidence on the effects of these short-term, low-cost programs and, to my knowledge, no experimental evidence on whether summer jobs can reduce crime (supplementary materials, section 2.1).

This paper presents the results of a large-scale randomized controlled trial that tests a public summer jobs program in Chicago called One Summer Plus (OSP). OSP offers 8 weeks of part-time summer employment at Illinois' minimum wage ($8.25/hour). Local community organizations place youth in nonprofit and government jobs (for example, summer camp counselors, workers in a community garden, or office assistants for an alderman). Youth are assigned job mentors—adults who help them learn to be successful employees and to navigate barriers to employment—at a ratio of about 10 to 1. Half the treatment group also receives social-emotional learning (SEL) based on cognitive behavioral therapy principles, aimed at teaching youth to understand and manage the aspects of their thoughts, emotions, and behavior that might interfere with employment (supplementary materials, section 2.2).

The study randomly assigns 1634 8th- to 12th-grade applicants enrolled in 13 high-violence Chicago schools to program (jobs-only or jobs + SEL) or control conditions (*22*). Youth in the jobs-only group are offered 25 hours per week of paid employment; youth in the jobs + SEL group are paid for 15 hours of work and 10 hours of SEL weekly. Control youth are excluded from the program but free to pursue other opportunities.

The existing employment literature might suggest that this kind of low-dosage jobs program is unlikely to change criminal behavior. But, there is an important difference between summer jobs for in-school youth and the previous literature: The well-studied youth employment programs generally act as tertiary prevention, targeting youth already out of school and struggling in the labor market. Research in domains such as education and health, however, suggests that for many negative outcomes caused at least in part by prior behavior (for example, poor school performance and dropout, or certain types of cancer), primary and secondary prevention—intervening before onset rather than managing or trying to reverse a problem once it occurs—can improve outcomes more effectively, with less intensive treatment (*23*–*25*)

If this well-established idea that prevention can be more effective than remediation also applies to the employment domain, teaching adolescents how to be successful employees, facilitating connections to employer networks, and providing work experience before they drop out of school might reduce crime with less intensive intervention than is required for already disconnected youth. Offering summer employment at this key point in the life course could make crime a relatively less attractive option, strengthen social bonds, and develop "soft" skills such as self-efficacy and impulse control (*7*, *26*–*28*). Waiting until after dropout to intervene may make it more difficult to reduce violence in particular, given the apparently causal relationship between school dropout and criminal behavior, especially murder and assault (*29*). Limiting the intervention to summer avoids direct conflicts between work and school. Summer jobs also provide wages and structured activity during a high-crime season when youth might otherwise be idle, both of which may affect crime (*30*, *31*).

However, the theory on summer jobs is not entirely clear-cut. Additional income could be spent on crime-inducing goods such as drugs and alcohol, and time spent traveling to and from work might increase exposure to criminal opportunities. Even the attempt to keep youth busy (the "incapacitation effect") may be poorly targeted because most jobs are during business hours, whereas most crime occurs during evenings and weekends. More broadly, a short-term subsidized job might not be enough to generate behavior changes beyond the summer itself. The effects of summer jobs are therefore an empirical question.

Data come from matching study youth to administrative data sources (supplementary materials, materials and methods). Program participation is from provider-tracked attendance records. Student-level administrative records from the Chicago Public Schools capture pre- and post-program academic outcomes from the 2011–2012 and 2012–2013 academic years, respectively. Demographic information on applicants' neighborhoods comes from matching the Census tract of youths' home addresses to the 2010 American Community Survey. The main outcome measures are from individual-level Chicago Police Department arrest records covering both juveniles and adults (*32*). The study uses data through 25 September 2013, which is 16 months after randomization (13 months after the end of the program).

The analysis categorizes arrests by offense type (violent, property, drug, and other). It is common for social interventions to have differential impacts on these different types of crime (*31*, *33*, *34*), likely because some of the underlying causes differ. Violent crime stems from conflicts between people, so problematic cognitive and emotional responses to social interactions—including hostile attribution bias, uncontrolled anger, and "hot" decision-making—are thought to be proximal causes of youth violence in particular (*35*, *36*). Nonviolent crimes, which involve property or

[1]Department of Criminology, University of Pennsylvania, Philadelphia, PA, USA. [2]University of Chicago Crime Lab, Chicago, IL, USA.
*Corresponding author. E-mail: hellersa@sas.upenn.edu

Downloaded from www.sciencemag.org on December 5, 2014

drugs more often than interpersonal conflict, may be relatively more responsive to situational and economic factors (*37*, *38*). Because OSP could affect how youth perceive and respond to social interactions differently from how it affects their economic situations, opportunities for crime, or drug use, the study estimates program effects separately by crime type.

Average applicant characteristics on a variety of preprogram measures are shown in Table 1. None of the differences across the columns is statistically significant, nor are they jointly significant ($F_{31,1517}$ = 0.37, P = 0.9995), confirming the success of randomization.

Applicants are on average just over age 16 years (minimum, 14 years; maximum, 21 years), and almost all are African-American. Over 90% are eligible for free or reduced price lunches (a proxy for family poverty), with average grade point averages (GPAs) around a C in the prior fall semester. Study youth missed 18% of the preprogram school year, or around 6 weeks. About 20% had been arrested at baseline, and just over 20% had been victimized. Applicants live in highly disadvantaged neighborhoods: Unemployment averages over 19%; a third of households are under the poverty line; and violent crime rates are extremely high (more than 2100 incidents per 100,000 people).

The main text presents intent-to-treat (ITT) estimates, which measure the average difference between those randomly assigned to treatment and control groups. Three quarters of treatment youth actually participate (supplementary materials, section 2.3, and table S1). Because not all youth who are offered the program enroll, the ITT understates the effect of the program on those who choose to participate. This treatment-on-the-treated effect is discussed and estimated in the materials and methods section and section 2.4 of the supplementary materials. Program impacts are shown both for the treatment group as a whole and each treatment arm.

During the 16-month follow-up period, ~17% of the control group (n = 155 youth) is arrested for any crime, with an average of 0.30 arrests per youth. The main ITT results are presented in Fig. 1. Violent-crime arrests among the treatment group decrease by 43% relative to the control group (0.0395 fewer arrests, or almost 4 fewer per 100 youth; P = 0.022). There are no significant changes in other types of arrests (*39*). The results are robust to accounting for the number of hypothesis tests conducted, allowing youth outcomes to be correlated within schools and using a nonlinear specification for count data (supplementary materials, section 2.5). Although the study was not powered to detect heterogeneous treatment effects across subgroups, there is suggestive evidence that arrests fall more among youth at higher risk of violence (supplementary materials, section 2.7).

An important question concerns what mechanisms drive this considerable behavioral change. One hypothesis for why prior youth employment programs require high intensity to succeed is that disadvantaged adolescents may lack the "soft skills"

Table 1. Mean preprogram characteristics for treatment and control groups. To test baseline equivalence, each characteristic was regressed on treatment indicator and blocking variables using heteroskedasticity-robust standard errors; the P value column reports statistical significance of treatment indicator's coefficient. Demographic and schooling data are from Chicago Public Schools' administrative records on pre-program year (2011–2012 school year). Free/reduced price lunch is proxy for family poverty. Days absent are reported as a percentage of days enrolled (average missed, 29 days). Arrest and victimization data are from Chicago Police Department administrative records. Neighborhood characteristics are from 2010 American Community Survey and Chicago Police Department's community-area crime rates. "Percent unemployed" is percent of civilian labor force over age 16 years looking for work but without a job. Table uses nonmissing data only (5 youth missing school attendance data, 60 missing fall GPA, 1 missing neighborhood violent-crime rate). Gender is not included in the table because it is captured by the blocking variables; 38% of the sample is male.

	Control mean	Treatment mean	*P* value
	(n = 904)	(n = 730)	
Demographics			
Age	16.79	16.78	0.46
Grade	10.15	10.12	0.55
Percent Black	96%	94%	0.84
Percent Hispanic	2.9%	3.8%	0.74
Percent free/reduced price lunch	92%	92%	0.98
Schooling			
Percent days absent	18%	18%	0.99
GPA in fall 2011 (4 point scale)	2.37	2.32	0.93
Percent enrolled in summer school 2011	8.8%	9.0%	1.00
Crime and victimization			
Percent ever arrested	19%	22%	0.37
No. of violent-crime arrests	0.13	0.18	0.20
No. of property-crime arrests	0.09	0.09	0.71
No. of drug arrests	0.05	0.08	0.55
No. of other arrests	0.15	0.19	0.55
Percent ever victimized	21%	24%	0.36
No. of victimizations	0.29	0.33	0.30
Neighborhood characteristics			
Percent unemployed	19%	19%	0.94
Percent below poverty line	33%	35%	0.71
Median household income (US$)	35,665	34,321	0.58
Violent crime rate (per 100,000)	2,128	2,136	0.95

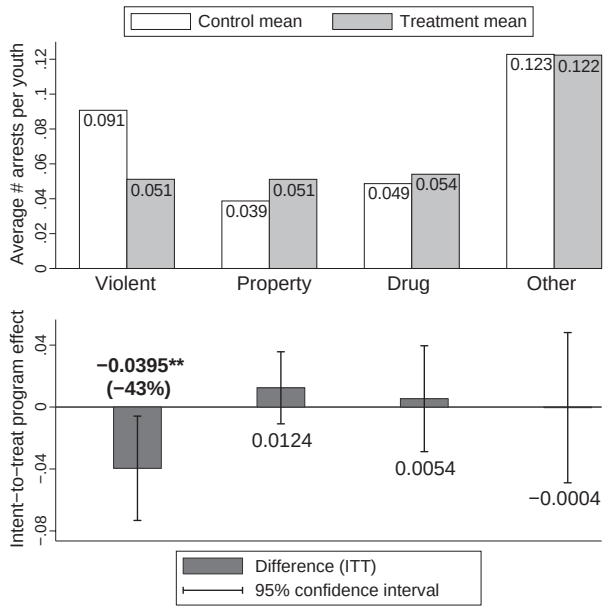


Fig. 1. ITT program effect on crime by arrest type. Shown are the control group mean, regression-adjusted treatment mean, difference between the two (ITT), and 95% confidence interval for the difference by arrest type. Data are from Chicago Police Department administrative arrest records through 16 months after randomization. ITT was calculated by using ordinary least squares regression with heteroskedasticity-robust SEs, controlling for baseline covariates and blocking variables. Percent change is relative to the control mean. ***P < 0.01, **P < 0.05, *P < 0.10

to engage with less intensive pro-social programming (*40*). If so, OSP's SEL curriculum—which focuses on emotion and conflict management, social information processing, and goal setting—could be a key driver of the violence decrease. Because SEL was randomly assigned, the study can separately identify any additional role of SEL.

ITT violence effects by treatment group are shown in Table 2. Not only is the difference between groups statistically insignificant, but the magnitude is also tiny (1% of the control mean). The nearly identical point estimates suggest that the statistical similarity across groups is not just the result of limited power to detect subgroup differences. Instead, it appears that both groups of youth experienced very similar drops in violence. The same is true for other crime types (supplementary materials, section 2.6, and table S4).

Although the experimental design can only directly isolate the role of SEL, another potentially important mechanism is testable indirectly: whether the decrease in violence is a mechanical result of youth having less time to engage in crime while working over the summer (an "incapacitation" effect). If so, and youth returned to their prior behavioral patterns immediately after the program ended, one would expect to see a large violence drop during the program period, after which there would be no treatment-control difference. This is not the case. The ITT violence decrease during the 3 months between random assignment and the end of the program is proportionally large but statistically insignificant (–0.005 violent-crime arrests, $P = 0.39$, control mean = 0.01). During the following 13 months (excluding the program period), treatment reduces the number of violent-crime arrests by –0.035 ($P = 0.03$, control mean = 0.08).

Table 2. ITT effect on violent-crime arrests by treatment group. Results are from regression of number of violent-crime arrests on separate treatment group indicators, baseline covariates, and block fixed effects. Bottom row shows the magnitude and SE of the difference in effect across treatment arms. Heteroskedasticity-robust standard errors are in parentheses. ***$P < 0.01$, **$P < 0.05$, *$P < 0.10$

Jobs-only	–0.0391* (0.0205)
Jobs + SEL	–0.0399** (0.0203)
Difference between groups	0.0008 (0.0220)

The time path of the violence decrease is shown in Fig. 2 in greater detail. It graphs the cumulative treatment effect over time, with each point adding an additional month of data to the prior effect. The drop in arrests becomes statistically different from zero around month 6, 3 months after the end of the program, and continues to grow through month 11, after which it flattens out. The downward slope of the effect makes it clear that the bulk of the drop in violence accrues between months 5 and 11, well after the end of the program at month 3.

One way the program might have changed behavior during these later months is by increasing time spent in school, either by developing pro-social attitudes or providing information on how the labor market values education. However, schooling data suggest that this is unlikely to be the key mechanism. There is no treatment effect on days present (or other academic outcomes) during the following school year, with confidence intervals small enough to make changes in attendance an implausible cause of the drop in violence (supplementary materials, section 2.10, and table S7).

Prior research on youth employment suggests that only costly and intensive employment programs can reduce crime. The current study demonstrates that when offered to youth still in school, an intervention need not be lengthy to change behavior; an 8-week summer jobs program reduces violence among an adolescent population living in some of the most violent neighborhoods in the country.

The results are consistent with the idea that employment programs can have a larger impact at lower cost when offered to disadvantaged youth before school exit. There are, however, other possible reasons why this study finds larger effects than previous work. For example, OSP involved an adult job mentor making regular visits to the workplace, whereas most of the evaluated U.S. youth programs do not. The measurement of crime may also matter. If reaching youth before school exit is the key difference, one might expect multiple-year interventions for high school youth that aim to improve both education and employment outcomes to generate even larger impacts than seen here. In fact, they generally find no effects on crime (*41*, *42*). But, the evaluations of those two programs use self-reported overall crime rates, separating only drug and alcohol use. Given that effects are heterogeneous by crime type, it is possible that these programs also reduced violence, but that the studies aggregated crime outcomes to a level that masked the effect.

The estimates in this paper rely on administrative arrest records, which only capture offenses known to the police. Nationally, about half of violent incidents are reported to police, about half of which result in an arrest (*43*, *44*). As such, the estimates here may considerably understate the number of violent crimes prevented (supplementary materials, section 2.9).

The fact that both the jobs-only and jobs + SEL versions of the program were equally effective means that SEL cannot be the only operative mechanism. A similar SEL program has reduced violence on its own (*45*), but the jobs-related programming was enough to generate the steep drop in violence independently. Because replacing 2 hours of work with an SEL curriculum neither improved nor reduced the intervention's impact, the relevant mechanism is likely to be something common across the two types of programming.

One possibility is that the substance of the SEL curriculum—teaching youth to process social information, manage thoughts and emotions, and set and achieve goals more successfully—was taught equally well on the job. Youth could have learned these skills from interactions with the job mentors, who were part of both treatment arms. Reports from the program providers suggest that the mentors play a large part in helping youth learn to manage conflict in the workplace, in addition to teaching basic job skills. The process of working itself might also be enough to improve self-control, develop self-efficacy, and reduce frustration (all potential determinants of how youth perceive and respond to conflict). One study, which randomly assigned adults to an earnings subsidy program to increase employment, found that treated individuals report a greater sense of control over their lives and less anger about their lack of opportunities (*46*).

Another possibility is that the relevant mechanism was something else that both groups received: income, a caring adult, job skills, and/or employer connections. The experimental design cannot tease out which program element or elements generate the decrease in violence. Nonetheless, because schooling outcomes show little movement, it is unlikely that changes in

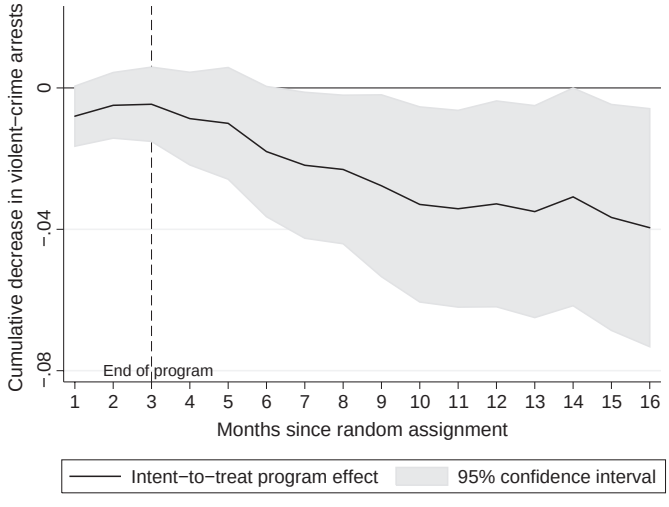


Fig. 2. Time path of violence decrease. Shown is the regression-adjusted cumulative difference in the number of violent-crime arrests between treatment and control youth by month. Random assignment lottery occurred at month 0; program ended at month 3. Regressions include baseline covariates and blocking variables. Confidence intervals were calculated by using heteroskedasticity-robust SEs.

perceptions about the value of schooling, or simply the amount of time in school, are the main drivers of the violence drop. The program provides a relatively large income shock, averaging $1400 in neighborhoods where one third of households are below the poverty line and median income is about $35,000. Additional income could change criminal behavior directly or increase parental supervision by reducing how much parents need to work away from home. It is also possible that improved post-program employment plays a role, although the direction of that effect is theoretically ambiguous. Working more could reduce all types of crime through incapacitation or by making it more costly to be incarcerated. But, the increased income could also have mixed effects, for example by reducing economically motivated crimes such as theft while increasing the ability to purchase drugs.

The fact that OSP only reduces violent crime is perhaps most consistent with a role for improvements in self-control, social information processing, and decision-making, which as discussed above are more central to violent behavior than to other types of crime. Other interventions that target these skills through either explicit curricula or mentorship have also reduced youth delinquency with very few contact hours (*47*, *48*).

One key insight from the data is that incapacitation alone—the mechanical reduction in free time during the summer—cannot explain the program's success. Violence reductions are large and statistically significant during the 13 months after the program is over, and the point estimate is 7 times larger at the end of the follow-up period than at the end of the summer. This pattern is not consistent with the idea that behavior only changed during the initial 8 weeks of the program; something about youths' summer experiences also changed their future behavior.

As in any social experiment, external validity is not guaranteed. The study sample is fairly representative of low-income, African-American youth living in urban neighborhoods who are still enrolled in school. Many other cities have successfully implemented summer jobs programs, suggesting that the basic approach is one that may not be difficult to scale (although displacement effects that reduce the number of jobs available to nonprogram youth become a bigger concern in larger-scale programs). A better understanding of how broadly these results will generalize requires replications in other cities with different service environments and youth populations. Policymakers should proceed with caution until future studies can establish exactly what works for whom, how long effects persist, and whether the program's benefits outweigh its costs (supplementary materials, section 2.11).

In the meantime, this study provides causal evidence on the effects of a widespread but understudied intervention. The results echo a common conclusion in education and health research: that public programs might do more with less by shifting from remediation to prevention. The findings make clear that such programs need not be hugely costly to improve outcomes for disadvantaged youth; well-targeted, low-cost employment policies can make a substantial difference, even for a problem as destructive and complex as youth violence.

REFERENCES AND NOTES

1. Center for Disease Control and Prevention, Web-based Injury Statistics Query and Reporting System (WISQARS) (2014).
2. Numbers are daily averages from the 5 most recent years of violence- related fatalities (from death certificates) and nonfatal injuries (from emergency room reports).
3. Center for Disease Control and Prevention, STRYVE to Prevent Youth Violence Website, 2014; available at www.cdc.gov/features/youthviolence/index.html.
4. Authors' calculations for ages 10 to 24 years versus over 24 are from 2012 Federal Bureau of Investigation (FBI) Uniform Crime Reports, Census data, and (*1*).
5. Office of Juvenile Justice and Delinquency Prevention, OJJDP Statistical Briefing Book, U.S. Department of Justice, Washington DC, 2014; available at www.ojjdp.gov/ojstatbb/crime/JAR_Display.asp?ID=qa05261.
6. W. J. Wilson, *When Work Disappears: The World of the Urban Poor* (Alfred Knopf, New York, 1996).
7. G. S. Becker, *J. Polit. Econ.* **76**, 169–217 (1968).
8. T. P. Thornberry, R. L. Christenson, *Am. Sociol. Rev.* **49**, 398–411 (1984).
9. R. J. Sampson, J. H. Laub, *Am. Sociol. Rev.* **55**, 609–627 (1990).
10. R. K. Merton, *Am. Sociol. Rev.* **3**, 672–682 (1938).
11. P. J. Cook, J. Ludwig, in *Controlling Crime: Strategies and Tradeoffs*, P. J. Cook, J. Ludwig, J. McCrary, Eds. (University of Chicago Press, Chicago, 2011), pp. 1–39.
12. The focus here is on youth programs because disadvantaged youth are at such disproportionate risk of violent offending. There have been many public efforts to provide vocational or on-the-job training, job search assistance, and remedial education to adults as well. Those programs' crime effects are also mixed (*49*), perhaps in part because the largest employment impacts tend to be among adult women—a group with very low levels of criminal involvement (supplementary materials, section 2.1).
13. M. Millenky, D. Bloom, S. Muller-Ravett, J. Broadus, *Staying on Course: Three-Year Results of the National Guard Youth ChalleNGe Evaluation* [Manpower Demonstration Research Corportation (MDRC), New York, 2011].
14. C. Uggen, *Am. Sociol. Rev.* **65**, 529–546 (2000).
15. P. Z. Schochet, J. Burghardt, S. McConnell, *Am. Econ. Rev.* **98**, 1864–1886 (2008).
16. G. Cave, H. Bos, F. Doolittle, C. Toussaint, *JOBSTART. Final Report on a Program for School Dropouts* (MDRC, New York, 1993).
17. H. S. Bloom *et al*., *J. Hum. Resour.* **32**, 549–576 (1997).
18. Although there is a consensus that generating measurable changes in youth outcomes requires comprehensive and expensive intervention, conclusions about how much investment is desirable differ by author (*19*, *40*, *49*, *50*).
19. R. J. LaLonde, in *Means-Tested Transfer Programs in the United States*, R. A. Moffitt, Ed. (Univ. Chicago Press, Chicago, IL, 2003), pp. 517–586.
20. A. L. Fernandes-Alcantara, *Vulnerable Youth: Federal Funding for Summer Job Training and Employment* (Congressional Research Service, Washington, DC, 2011).
21. A. E. Schwartz, J. Leos-Urbel, *Expanding Summer Employment Opportunities for Low-Income Youth* (Brookings Institution, The Hamilton Project, Washington, DC, 2014).
22. Youth were individually randomized within a blocked design, in which blocks were defined by school and gender. All analyses control for the blocking variable. Materials and methods are available as supplementary materials on *Science* Online.
23. E. I. Knudsen, J. J. Heckman, J. L. Cameron, J. P. Shonkoff, *Proc. Natl. Acad. Sci. U.S.A.* **103**, 10155–10162 (2006).
24. D. M. Cutler, *J. Econ. Perspect.* **22**, 3–26 (2008).
25. The emphasis on those already exhibiting symptoms of the underlying problem is true of most major programs focused on youth employment. The youth elements of the National Supported Work Demonstration, JOBSTART, the National Guard ChalleNGe, and the Job Training Partnership Act all focus on high school dropouts (*13*, *16*, *17*, *51*). Job Corps requires applicants to need additional education, training, or vocational skills—all signs that they are already experiencing difficulties in the labor force (*15*). Year Up serves youth no longer in school (*52*). There are well-evaluated programs for high school youth that integrate employment programming with long-term educational interventions [such as (*41*, *42*)]. However, because they are also lengthy and intensive—and aim to improve educational attainment directly, which may have an independent impact on crime (*29*)—they do not provide a test of the hypothesis proposed here: that low-dose, low-cost employment interventions could have a larger effect than suggested by the existing employment literature when used as primary and secondary prevention.
26. R. J. Sampson, J. H. Laub, *Crime in the Making: Pathways and Turning Points Through Life* (Harvard Univ. Press, Cambridge, MA, 1995).
27. R. Agnew, *Criminology* **30**, 47–88 (1992).
28. P. Moss, C. Tilly, *Work Occup.* **23**, 252–276 (1996).
29. L. Lochner, E. Moretti, *Am. Econ. Rev.* **94**, 155–189 (2004).
30. J. Grogger, *J. Labor Econ.* **16**, 756–791 (1998).
31. B. A. Jacob, L. Lefgren, *Am. Econ. Rev.* **93**, 1560–1577 (2003).
32. Additional results on violent victimizations are provided in supplementary materials, section 2.7.
33. D. Deming, *Q. J. Econ.* **126**, 2063–2115 (2011).
34. J. R. Kling, J. Ludwig, L. F. Katz, *Q. J. Econ.* **120**, 87–130 (2005).
35. K. A. Dodge, D. Schwartz, in *Handbook of Antisocial Behavior*, D. M. Stoff, J. Breiling, J. D. Maser, Eds. (John Wiley & Sons, Hoboken, NJ, 1997), pp. 171–180.
36. J. Ludwig, A. Shah, "Think Before You Act: A New Approach to Preventing Youth Violence and Dropout," Discussion Paper 2014-02 (The Hamilton Project, Brookings Institution, Washington, DC, 2014).
37. A. M. Piehl, in *The Handbook of Crime and Punishment*, M. Tonry, Ed. (Oxford Univ. Press, Oxford, 1998), pp. 302–319.
38. S. Raphael, R. Winter-Ebmer, *J. Law Econ.* **44**, 259–283 (2001).
39. The reliance on official arrest data means that violent crime is a better-measured outcome; nationally, violent crimes are 2.5 times more likely to result in an arrest than are property crimes (*43*). Differential arrest probabilities also help explain why the control means for property and drug arrests are around half as large as for violent-crime arrests, despite the fact that nonviolent crimes are more common (*43*). The supplementary materials, section 2.9, discusses how underreporting might affect the results.
40. C. J. Heinrich, H. J. Holzer, *Ann. Am. Acad. Pol. Soc. Sci.* **635**, 163–191 (2011).
41. J. J. Kemple, C. J. Willner, *Career Academies: Long-Term Impacts on Labor Market Outcomes, Educational Attainment, and Transitions to Adulthood* (MDRC, New York, 2008).
42. A. Schirm, E. Stuart, A. McKie, *The Quantum Opportunity Program Demonstration: Final Impacts* (Mathematica Policy Research, Washington, DC, 2006).
43. Federal Bureau of Investigation, "Crime in the United States 2012," Uniform Crime Report (U.S. Department of Justice, Washington DC, 2012).
44. L. Langton, M. Berzofsky, C. Krebs, H. Smiley-McDonald, "Victimizations Not Reported to the Police, 2006–2010" (Bureau of Justice Statistics, U.S. Department of Justice, Washington, DC, 2012).
45. S. Heller, H. A. Pollack, R. Ander, J. Ludwig, "Preventing Youth Violence and Dropout: A Randomized Field Experiment," NBER Working Paper no. 19014 (National Bureau of Economic Research, Cambridge, MA, 2013).
46. P. Gottschalk, *J. Policy Anal. Manage.* **24**, 485–498 (2005).
47. J. B. Grossman, J. P. Tierney, *Eval. Rev.* **22**, 403–426 (1998).
48. R. Barnoski, S. Aos, "Outcome evaluation of Washington State's research-based programs for juvenile offenders" (Washington State Institute for Public Policy, Olympia, WA, 2004).
49. S. Raphael, in *Controlling Crime: Strategies and Tradeoffs*, P. J. Cook, J. Ludwig, J. McCrary, Eds. (Univ. Chicago Press, Chicago, 2011), pp. 521–565.
50. J. J. Heckman, A. B. Krueger, *Inequality in America: What Role for Human Capital Policies?* (MIT press, Cambridge, MA, 2003).
51. Manpower Demonstration Research Corporation, *Summary and Findings of the National Supported Work Demonstration* (Ballinger Publishing Company, Cambridge, MA, 1980).
52. A. Roder, M. Elliott, *A Promising Start: Year Up's Initial Impacts on Low-Income Young Adults' Careers* (Economic Mobility Corporation, New York, 2011).

ACKNOWLEDGMENTS

This project was supported by award B139634411 from the U.S. Department of Labor and grant 2012-MU-FX-0002 from the Office of Juvenile Justice and Delinquency Prevention, Office of Justice Programs, U.S. Department of Justice. The study received approval from the University of Chicago's IRB (protocol 12-1112) with secondary approval from the University of Pennsylvania's IRB (protocol 818707). I gratefully acknowledge the City of Chicago and Mayor R. Emanuel, the work of the Chicago Department of Family Support Services, especially E. Diaz, J. Axelrod, A. Fernandez, and J. Welch, and the organizations that implemented the program: Phalanx Family Services, Sinai Community Institute, Saint Sabina Employment Resource Center, SGA Youth and Family Services, and Youth Guidance. I thank Chicago Public Schools partners J. Foreman, K. Klein, J. Loudon, and S. Norris; Chief R. Tracy, T. Lavery, and the Chicago Police Department; R. Goerge and Chapin Hall; R. Ander, S. Coussens, J. Davis, G. Cusick, M. Egan, H. Pollack (Chicago PI), R. Harris, N. Hess, A. Métivier, and J. Rountree for project support; and K. Charles, J. Guryan, C. Loeffler, J. Ludwig, J. MacDonald, E. Owens, S. Raudenbush, S. Sotelo, and D. Tannenbaum for helpful comments. Replication data are posted at the University of Michigan's ICPSR data depository (http://doi.org/10.3886/E18627V1); see supplementary materials section 1.5 for details. All content is the responsibility of the author and does not represent the official position or policies of the Chicago Police Department, Chicago Public Schools, Chicago Department of Family and Support Services, U.S. Department of Justice, or U.S. Department of Labor.

SUPPLEMENTARY MATERIALS

www.sciencemag.org/content/346/6214/1219/suppl/DC1
Materials and Methods
Supplementary Text
Tables S1 to S8
References (*53*–*96*)

23 June 2014; accepted 7 November 2014
10.1126/science.1257809

PALEOCLIMATE

Coherent changes of southeastern equatorial and northern African rainfall during the last deglaciation

Bette L. Otto-Bliesner,[1]* James M. Russell,[2] Peter U. Clark,[3] Zhengyu Liu,[4,5] Jonathan T. Overpeck,[6] Bronwen Konecky,[3,7] Peter deMenocal,[8] Sharon E. Nicholson,[9] Feng He,[4] Zhengyao Lu[5]

During the last deglaciation, wetter conditions developed abruptly ~14,700 years ago in southeastern equatorial and northern Africa and continued into the Holocene. Explaining the abrupt onset and hemispheric coherence of this early African Humid Period is challenging due to opposing seasonal insolation patterns. In this work, we use a transient simulation with a climate model that provides a mechanistic understanding of deglacial tropical African precipitation changes. Our results show that meltwater-induced reduction in the Atlantic meridional overturning circulation (AMOC) during the early deglaciation suppressed precipitation in both regions. Once the AMOC reestablished, wetter conditions developed north of the equator in response to high summer insolation and increasing greenhouse gas (GHG) concentrations, whereas wetter conditions south of the equator were a response primarily to the GHG increase.

The future response of African rainfall to increasing greenhouse gas (GHG) concentrations is a critical socio-economic issue, with implications for water resources, agriculture, and potential conflict (*1*), but uncertainties among model projections remain (*2*–*4*). African hydroclimate changed substantially during the last deglaciation, the most recent time period during which natural global warming was associated with increases in GHG concentrations. Numerous proxy records from Africa indicate that dry conditions during the Last Glacial Maximum (LGM) (~21,000 years ago, or 21 ka) were rapidly replaced by a much wetter interval, referred to as the African Humid Period (AHP), starting ~14.7 ka over much of Africa. Over North Africa (NA), the start of the AHP has been widely recorded in lake-level records (*5*, *6*) and proxies of aeolian and fluvial processes preserved in marine sediments from the eastern Atlantic Ocean (*7*–*10*). At the same time, a near-contemporaneous precipitation increase is also recorded in southeastern equatorial Africa (SEA) (to 9°S) by lake-level records (*11*–*14*), as well as in pollen and geochemical records from lake sediments (*14*–*16*).

Models and data establish that the initial increase of NA summer monsoonal rainfall occurred in response to increasing local insolation associated with orbital variations (*17*), amplified through feedbacks with the ocean and possibly vegetation (*18*–*20*), but the cause of the abrupt start of the AHP remains unclear. Proposed triggers include a nonlinear threshold response to gradually changing summer insolation (*8*) and/or the recovery of deep convection in the North Atlantic following cessation of a Northern Hemisphere meltwater event (*21*). Similarly, the cause for the synchronous onset of the AHP in the SEA region has remained enigmatic, as models and theory suggest that orbital forcing of local summer insolation at these latitudes should have reduced precipitation (*22*).

Here, we analyze transient simulations of the climate evolution from the LGM to the early Holocene (11 ka) with a global coupled atmosphere–ocean–sea ice–land general circulation model (CCSM3) to assess possible mechanisms for the abrupt, synchronous onset of the AHP in NA and SEA. The model has a latitude-longitude resolution of ~3.75° in the atmosphere and ~3° in the ocean and includes a dynamic global vegetation module (supplementary text). The model successfully captures the large-scale observed modern features of African climate, including seasonal shifts of winds, the intertropical convergence zone (ITCZ), and precipitation to the summer hemispheres (figs. S2 and S3). To characterize the regional precipitation responses during the deglaciation, we examine model changes in the NA region defined by 11.1° to 18.6°N and 5.6° to 20.6°E and in the SEA region defined by 0° to 7.4°S and 24.4° to 43.1°E (see supplementary text and fig. S7 for sensitivity of model results to the definitions of the regions).

The prescribed forcings and boundary conditions for the full-forcing simulation (TraCE) include orbitally forced insolation changes, increasing atmospheric concentrations of the long-lived GHGs, and retreating ice sheets and associated meltwater release to the oceans (*23*, *24*) (fig. S1). We also explore the individual contributions of orbital forcing and GHGs during the deglaciation with two sensitivity experiments: (i) TraCE orbital-only, where only the orbital forcing is allowed to vary, with all other forcings kept at their values for 17 ka, and (ii) TraCE GHG-only, where only the concentrations of the GHGs change, increasing from low concentrations at 17 ka to close to their pre-industrial concentrations by 10 ka. In both sensitivity experiments, the ice sheets and meltwater release are held constant at 17-ka conditions, and this meltwater maintains a strongly reduced Atlantic meridional overturning circulation (AMOC) afterward.

The temporal evolution of the simulated deglacial precipitation shows good agreement with individual proxy records. TraCE and a proxy record of humidity (*9*) both show dry conditions in the central Sahel at the LGM, a decrease in precipitation at ~17 ka, an abrupt increase at the onset of the Bølling-Allerød warm interval, an episode of drying during the Younger Dryas (YD) (12.9 to 11.7 ka), and an increase during the early Holocene (Fig. 1B). The total leaf-area index of simulated vegetation over the Sahel

[1]Climate and Global Dynamics Division, National Center for Atmospheric Research, Boulder, CO 80307-3000, USA. [2]Department of Earth, Environmental, and Planetary Sciences, Brown University, Providence, RI 02912, USA. [3]College of Earth, Ocean, and Atmospheric Sciences, Oregon State University, Corvallis, OR 97331, USA. [4]Center for Climatic Research and Department of Atmospheric and Oceanic Sciences, University of Wisconsin-Madison, Madison, WI 53706, USA. [5]Laboratory for Climate, Ocean and Atmosphere Studies, School of Physics, Peking University, Beijing 100871, P. R. China. [6]Department of Geosciences and Institute of the Environment, University of Arizona, Tucson, AZ 85721, USA. [7]Cooperative Institute for Research in Environmental Sciences, University of Colorado Boulder, Boulder, CO 80309, USA. [8]Department of Earth and Environmental Sciences, Columbia University, New York, NY 10027, USA. [9]Department of Earth, Ocean, and Atmospheric Science, Florida State University, Tallahassee, FL 32306, USA.
*Corresponding author. E-mail: ottobli@ucar.edu

closely parallels changes in precipitation, starting from low values signifying primarily bare ground followed by increasing values starting at ~16 ka (Fig. 1C). To the extent that precipitation and vegetation cover influence availability of sediment for aeolian transport, the temporal evolution of these simulated properties can be used to explain a record of terrigenous dust flux sourced from subtropical NA (*8*) (Fig. 1C).

Simulated deglacial changes in SEA hydrology are similar to those simulated for NA, including a near-synchronous start and subsequent persistence of the AHP. After peak dry conditions at ~17 ka, TraCE simulates a gradual increase in precipitation starting at ~16.5 ka and a large, abrupt increase at ~14.7 ka associated with the start of the AHP (Fig. 1D). These changes are observed in two SEA proxy records from Lakes Tanganyika (*16*) and Challa (*14*) (Fig. 1D), which show an abrupt onset of the AHP synchronous within a few hundred years of the precipitation increase simulated by the model. Rainfall changes in the Congo basin of western equatorial Africa, which integrate precipitation changes north and south of the equator, indicate drying from LGM to 17 ka and then increasing precipitation in both TraCE and proxy data (*25*) (Fig. 1E).

We use empirical orthogonal functions (EOFs) and their associated principal components (PCs) to extract the dominant modes of precipitation variability from the TraCE simulation and moisture balance from proxy data (table S1). The first EOF mode (EOF1) (48.0% of total variance) of the proxy data shows an in-phase relation over most of Africa that extends southward to the latitude of Lake Malawi (9° to 14°S, 34° to 35°E), whereas the associated PC1 indicates increasing moisture from the LGM to early Holocene (Fig. 2A). EOF1 of model precipitation (39.2% of total variance) and its associated PC1 (Fig. 2B) reproduce the overall spatial and temporal behavior seen in the data, except in southeastern Africa. A record of the Zambezi River discharge from this part of Africa (*26*) that is not included in the EOF analysis because of its shorter length (<17 ka) shows an out-of-phase relation with the north, consistent with the TraCE simulation.

Because seasonal insolation trends are antiphased between the two hemispheres, the in-phase relation over most of Africa shown by the data and model suggests that some other forcing must be driving precipitation change during the deglaciation. A primary role for GHG forcing of this spatially coherent hydroclimatic change is evident from the similarity of the EOF1 fields for the TraCE GHG-only (fig. S4B) and TraCE experiments (Fig. 2B). Although EOF1 for the TraCE orbital-only experiment indicates that local insolation played an important role in explaining increasingly humid conditions over NA, it has negligible loadings over the SEA region (fig. S4A), in contradiction with both proxy data and the TraCE simulation (Fig. 2).

The second EOF modes of the data and TraCE (16.4 and 17.2% of total variance, respectively) both indicate an in-phase relation of much of NA and SEA (Fig. 2, C and D). The character of the data PC2 is similar to that simulated by the model, particularly when the model PC2 is sampled at the same resolution as the data to account for potential aliasing artifacts (Fig. 2, C and D), although the model has a more muted recovery from the YD. There is a clear relation between the model PC2 (Fig. 2D) and the simulated AMOC (Fig. 1A), supporting arguments for a strong millennial modulation of African precipitation by changes in the AMOC (*21*, *27*, *28*).

We next assess the model responses to deglacial forcings that caused the AHP. In NA, our TraCE model results suggest that the AHP is largely associated with increased precipitation during the boreal summer (fig. S5A). From 17 to 11 ka, the summer monsoon over NA intensifies and shifts northward due to the combined effects of orbital and GHG forcing, though, as for all comparable climate models (*18*), not as far northward as the data suggest, highlighting a shortcoming of the models in simulating the AHP climate of this northerly region. Sea-level pressure decreases over NA, and attendant increased southwesterly flow brings moisture from the Atlantic into NA and enhances precipitation in a broad east-west band over the Sahel and southern Sahara to ~22°N (Fig. 3A). For the other seasons, simulated precipitation remains

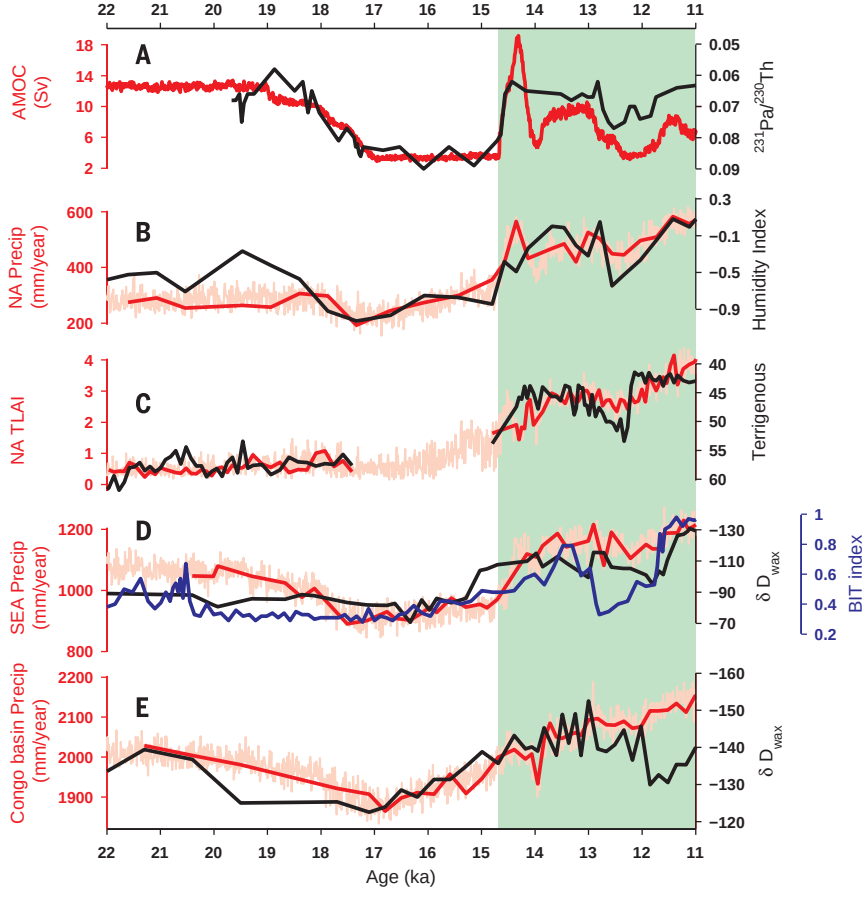


Fig. 1. TraCE simulation with all deglacial forcings (fig. S1) in comparison to proxy data. Model variables are plotted as decadal means (light red) and as sampled at temporal resolution of data (darker red). See Fig. 3 for definition of model NA and SEA regions. (**A**) ^{231}Pa/^{230}Th ratio at Bermuda rise (GGC5 core, 33°42′N, 57°35′W) as a proxy for AMOC export (black) (*32*) and model maximum AMOC (Sv). (**B**) GeoB7920-2 (20°45′N, 18°35′W) continental humidity index (black) (*9*) and model NA precipitation (millimeters per year). (**C**) Ocean Drilling Program site 658C (20°45′N, 18°35′W) terrigenous percentage (black) (*8*) and model NA total leaf area index (TLAI) (square meters per square meters). (**D**) Lake Tanganyika (6°42′S, 29°50′E) hydrogen isotopic composition of leaf waxes (δD_{wax}) (per mil versus Vienna standard mean ocean water, black) (*16*), Lake Challa (3°19′S, 37°42′E) branched and isoprenoid tetraether (BIT) index (blue) (*14*), and model SEA precipitation (millimeters per year). (**E**) GeoB6518 (5°35′S, 11°13′E) δD_{wax} (black) (*25*) and Congo Basin (7.4°N to 11.1°S, 13.1°E to 28.1°E) model precipitation (millimeters per year). Green shading delineates AHP.

low throughout the entire simulation from the LGM to the early Holocene (fig. S5A).

Results from our single forcing experiments indicate that GHG and orbital forcings each contributed to the enhanced summer monsoon and precipitation increase across NA from 17 to 11 ka seen in the TraCE results. TraCE GHG-only shows an increase in precipitation in the southern Sahel but little broadening of the tropical rainbelt (Fig. 3B). TraCE orbital-only similarly shows enhanced precipitation in the Sahel while additionally expanding the monsoon precipitation northward (Fig. 3C). In the central Sahel, orbital forcing explains ~60% of the precipitation increase from 17 to 11 ka and GHG forcing explains the remaining ~40% (fig. S6).

The simulated AHP in SEA is associated with increased precipitation from the austral spring through fall, whereas simulated precipitation remains low during the austral winter [June-July-August (JJA)] throughout the deglacial period (fig. S5B). TraCE suggests a different seasonal nature of SEA precipitation at LGM than during the AHP, with austral summer [December-January-February (DJF)] precipitation explaining proportionately more of the annual precipitation (fig. S5B). In general, DJF precipitation increases from 17 to 11 ka throughout the southern tropics, extending from the Atlantic Ocean, across Africa, and into the Indian Ocean (Fig. 3D). The single forcing experiments indicate that most of this response (90%) is from the increase in GHGs (fig. S6), which caused DJF precipitation over the SEA region to increase from 17 to 11 ka (Fig. 3E). In the TraCE orbital-only experiment, on the other hand, decreased DJF insolation cools the land relative to the ocean, slightly weakening convection and precipitation over SEA near Lake Tanganyika while enhancing convection and precipitation over the Indian Ocean from 17 to 11 ka (Fig. 3F).

Proxy records and TraCE also exhibit consistent patterns and amplitude of changes in sea surface temperature (SST) around Africa from 17 to 11 ka (Fig. 4A and table S2). The differential warming in the northern Atlantic Ocean relative to the south, and in the western Indian Ocean relative to the east, is important in driving the increased precipitation in NA and SEA, respectively. The single forcing experiments indicate that increases in GHGs are primarily responsible for the overall SST increases and their regional patterns (Fig. 4B). Orbital forcing further reduces the meridional SST gradient in the North Atlantic, with warming north of the equator and slight cooling at and south of the equator (Fig. 4C).

Although our single forcing experiments demonstrate that GHG forcing played an important role in the moistening trends over NA (and particularly SEA), linking precipitation changes between the hemispheres, our TraCE simulation shows that millennial-scale changes in the AMOC are critical in synchronizing the onset of the AHP in these regions (Figs. 1 and 2). Our simulation agrees with other modeling studies (*27*–*29*) in finding that freshwater added to North Atlantic sites of deepwater formation reduces the AMOC, with an attendant shift in the ITCZ southward over the Atlantic Ocean in response to higher SSTs south of the equator and cooling north of the equator and a reduction of precipitation over NA. The bipolar Atlantic SST response and southward shift in the ITCZ also explain the opposite loadings of model EOF2 between North Africa and western equatorial Africa (Fig. 2D).

Cooling over the North Atlantic is also rapidly transmitted eastward into Europe and Asia through the atmosphere (*30*), enhancing the boreal winter Mediterranean-Arabian anticyclone. This results in northerly wind anomalies advecting cool and dry air over East Africa and the western Indian Ocean. This in turn results in cooler western Indian Ocean SSTs both north and south of the equator and a reduction of SEA precipitation (supplementary text and fig. S8). At ~14.7 ka, the cessation of meltwater forcing, the rapid resumption of AMOC, and the associated SST changes triggered abrupt and synchronous increases in precipitation in NA and SEA associated with the start of the AHP.

The spatial pattern of precipitation in EOF1 (Fig. 2B) is markedly similar to the historical patterns (*31*), as well as CMIP5 ensemble projection for precipitation changes over tropical Africa by the end

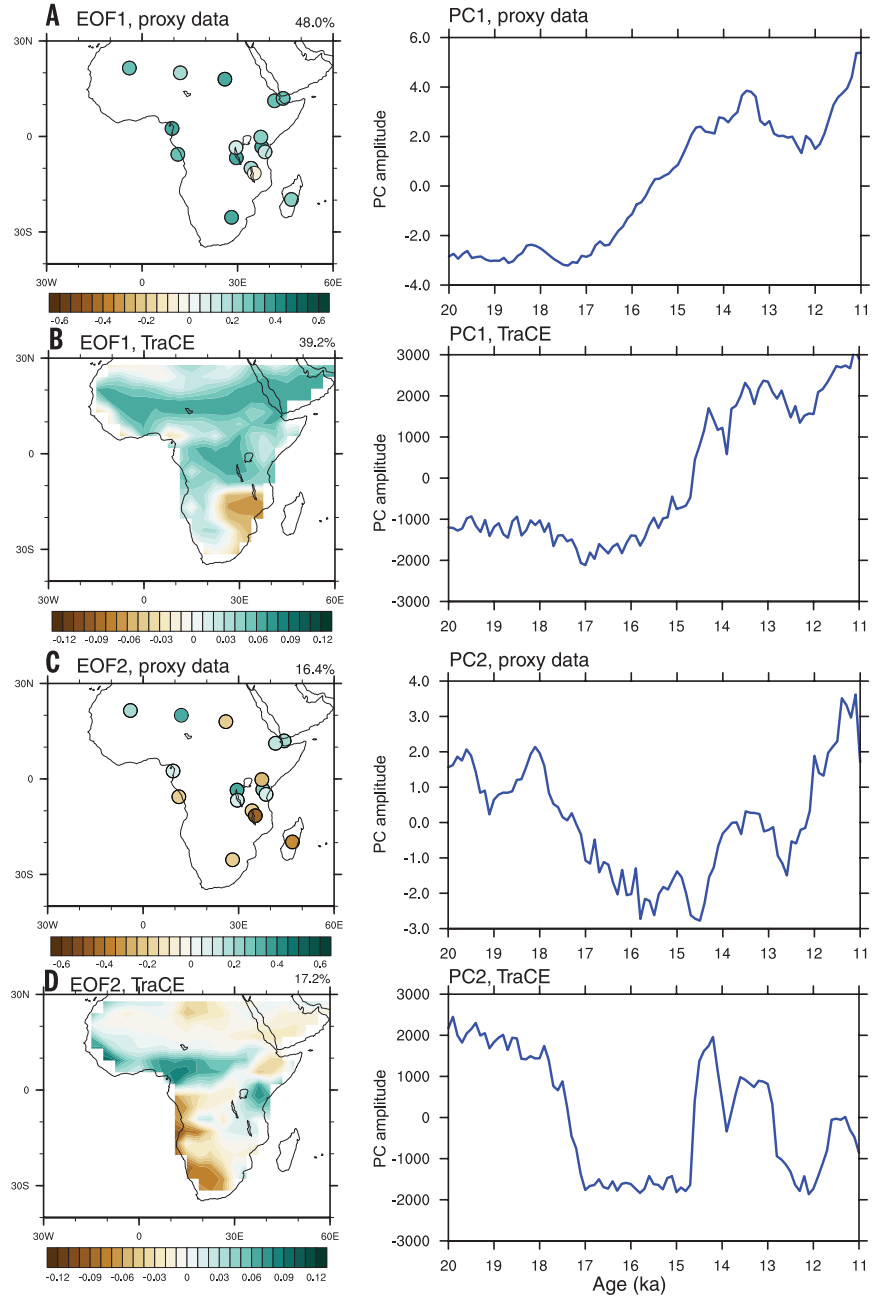


Fig. 2. EOFs and associated PCs for the deglacial period 20 to 11 ka. EOF1 and PC1 of (**A**) proxy data for moisture availability and (**B**) TraCE annual precipitation (millimeters per year). (**C** and **D**) Same as (A) and (B) except for EOF2 and PC2. Model results and proxy records (table S1) are interpolated to the same 100-year resolution.

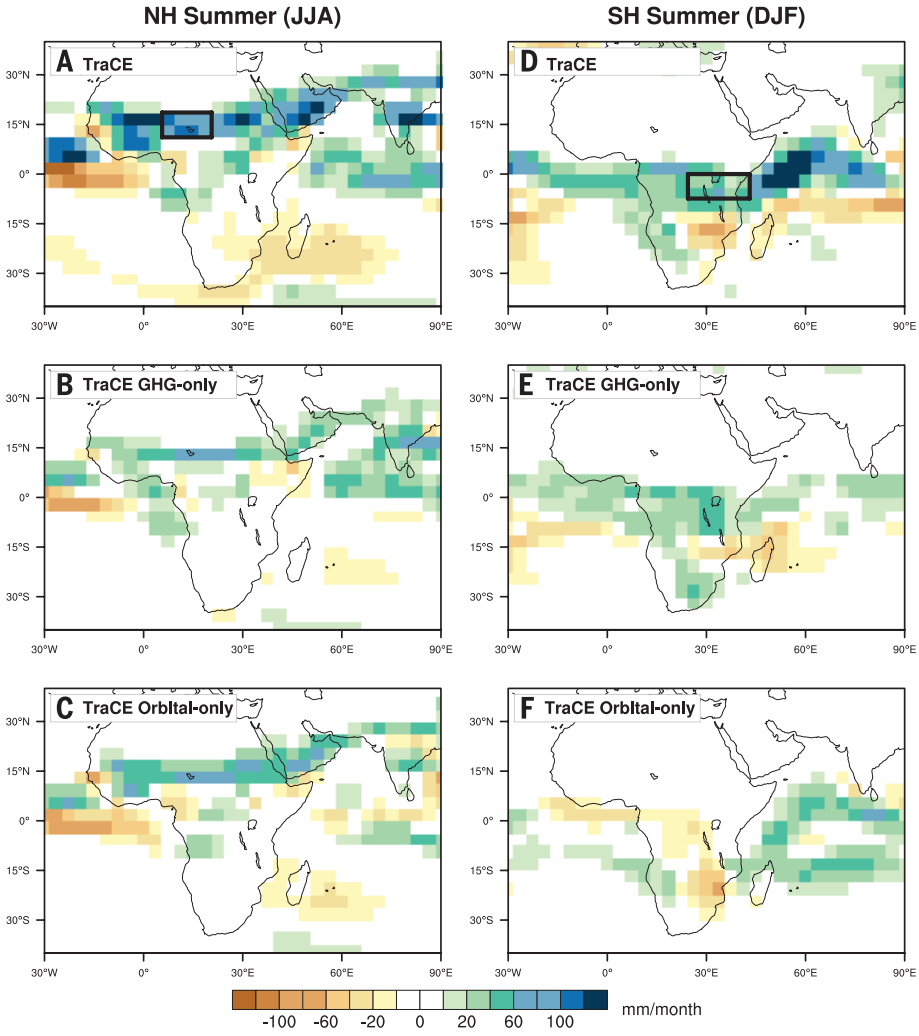


Fig. 3. Deglacial precipitation change (millimeters per month), 11 ka minus 17 ka, as simulated by the model. (**A** and **D**) TraCE, (**B** and **E**) TraCE GHG-only, and (**C** and **F**) TraCE orbital-only. The box in (A) represents the NA region used to characterize model results (11.1° to 18.6°N, 5.6° to 20.6°E); the box in (D) represents the SEA region (0° to 7.4°S, 24.4° to 43.1°E). NH, Northern Hemisphere; SH, Southern Hemisphere. JJA, June-July-August; DJF, December-January-February.

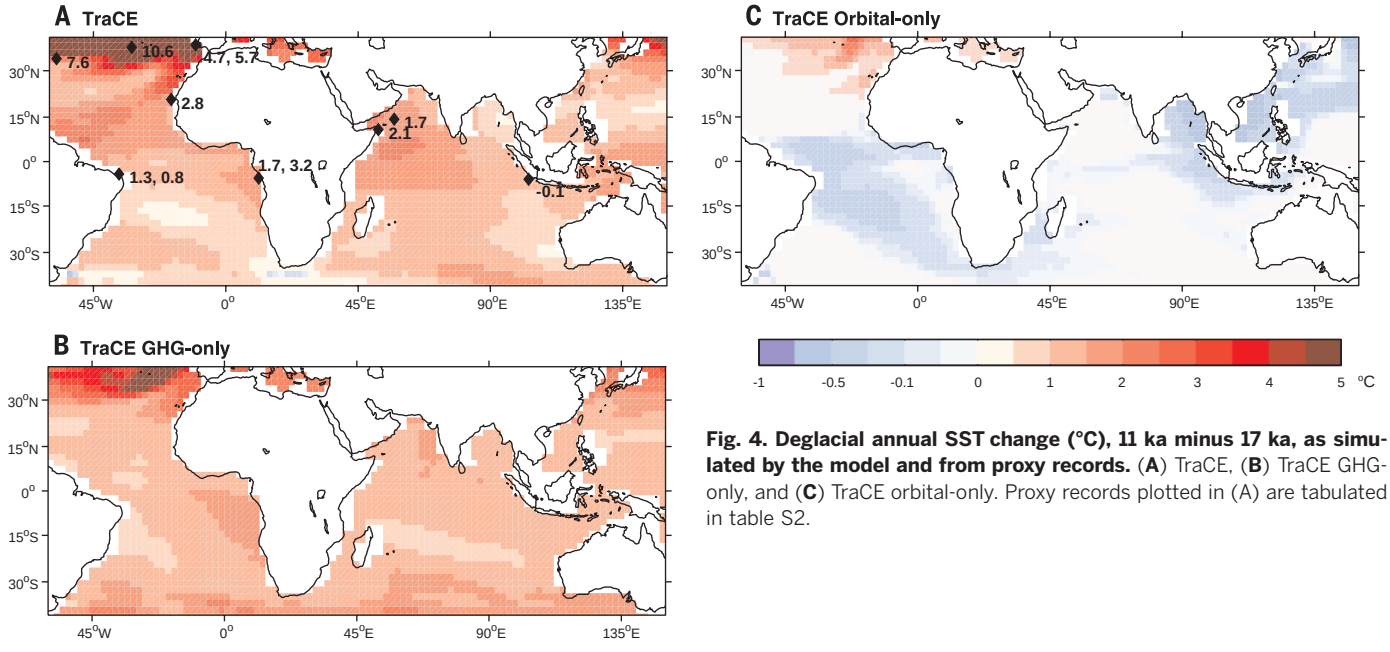


Fig. 4. Deglacial annual SST change (°C), 11 ka minus 17 ka, as simulated by the model and from proxy records. (**A**) TraCE, (**B**) TraCE GHG-only, and (**C**) TraCE orbital-only. Proxy records plotted in (A) are tabulated in table S2.

of this century (*3*). Although multiple forcings influenced African climate during the deglaciation, the agreement between proxy records and our simulated evolution of rainfall indicates that the processes and sensitivity of GHG-driven rainfall change are well simulated in our fully coupled global climate model. This lends confidence to the CMIP5 climate model ensemble projections of future precipitation change over tropical Africa at the continental scale.

REFERENCES AND NOTES

1. I. Niang *et al.*, "Africa," in *Climate Change 2014: Impacts, Adaptation, and Vulnerability. Part B: Regional Aspects. Contribution of Working Group II to the Fifth Assessment Report of the Intergovernmental Panel on Climate Change*, V. R. Barros *et al.*, Eds. (Cambridge Univ. Press, New York, 2014), pp. 1199–1265.
2. A. Giannini, M. Biasutti, I. M. Held, A. H. Sobel, *Clim. Change* **90**, 359–383 (2008).
3. M. Collins *et al.*, "Long-term climate change: Projections, commitments and irreversibility," in *Climate Change 2013: The Physical Science Basis. Contribution of Working Group I to the Fifth Assessment Report of the Intergovernmental Panel on Climate Change*, T. F. Stocker *et al.* Eds. (Cambridge Univ. Press, New York, 2013), pp. 1029–1136.
4. J. H. Christensen *et al.*, "Climate phenomena and their relevance for future regional climate change," in *Climate Change 2013: The Physical Science Basis. Contribution of Working Group I to the Fifth Assessment Report of the Intergovernmental Panel on Climate Change*, T. F. Stocker *et al.*, Eds. (Cambridge Univ. Press, New York, 2013), pp. 1217–1308.
5. T. M. Shanahan *et al.*, *Palaeogeogr. Palaeoclimatol. Palaeoecol.* **242**, 287–302 (2006).
6. F. A. Street, A. T. Grove, *Quat. Res.* **12**, 83–118 (1979).
7. J. M. Cole, S. L. Goldstein, P. N. deMenocal, S. R. Hemming, F. E. Grousset, *Earth Planet. Sci. Lett.* **278**, 257–266 (2009).
8. P. deMenocal *et al.*, *Quat. Sci. Rev.* **19**, 347–361 (2000).
9. R. Tjallingii *et al.*, *Nat. Geosci.* **1**, 670–675 (2008).
10. S. Weldeab, D. W. Lea, R. R. Schneider, N. Andersen, *Science* **316**, 1303–1307 (2007).
11. F. Gasse, F. Chalie, A. Vincens, M. A. J. Williams, D. Williamson, *Quat. Sci. Rev.* **27**, 2316–2340 (2008).
12. T. C. Johnson *et al.*, *Science* **273**, 1091–1093 (1996).
13. M. M. McGlue *et al.*, *J. Paleolimnol.* **40**, 635–653 (2008).
14. D. Verschuren *et al.*, *Nature* **462**, 637–641 (2009).
15. R. Bonnefille, F. Chalie, *Global Planet. Change* **26**, 25–50 (2000).
16. J. E. Tierney *et al.*, *Science* **322**, 252–255 (2008).
17. J. E. Kutzbach, B. L. Otto-Bliesner, *J. Atmos. Sci.* **39**, 1177–1188 (1982).
18. P. Braconnot *et al.*, *Nat. Clim. Change* **2**, 417–424 (2012).
19. J. E. Kutzbach, Z. Liu, *Science* **278**, 440–443 (1997).
20. O. Timm, P. Kohler, A. Timmermann, L. Menviel, *J. Clim.* **23**, 2612–2633 (2010).
21. F. A. Street-Perrott, R. A. Perrott, *Nature* **343**, 607–612 (1990).
22. Z. Liu, B. Otto-Bliesner, J. Kutzbach, L. Li, C. Shields, *J. Clim.* **16**, 2472–2490 (2003).
23. Z. Liu *et al.*, *Science* **325**, 310–314 (2009).
24. Z. Liu *et al.*, *Proc. Natl. Acad. Sci. U.S.A.* **109**, 11101–11104 (2012).
25. J. W. H. Weijers, E. Schefuß, S. Schouten, J. S. Sinninghe Damsté, *Science* **315**, 1701–1704 (2007).
26. E. Schefuß, H. Kuhlmann, G. Mollenhauer, M. Prange, J. Pätzold, *Nature* **480**, 509–512 (2011).
27. M. Kageyama *et al.*, *Clim. Past* **9**, 935–953 (2013).
28. R. J. Stouffer *et al.*, *J. Clim.* **19**, 1365–1387 (2006).
29. S. Mulitza *et al.*, *Paleoceanography* **23**, PA4206 (2008).
30. B.-W. Dong, R. T. Sutton, *Geophys. Res. Lett.* **29**, 18-1–18-4 (2002).
31. S. E. Nicholson, *Holocene* 10.1177/0959683614551230 (2014).
32. J. F. McManus, R. Francois, J.-M. Gherardi, L. D. Keigwin, S. Brown-Leger, *Nature* **428**, 834–837 (2004).

ACKNOWLEDGMENTS

We thank the reviewers for comments that improved the manuscript. The National Center for Atmospheric Research (NCAR) is sponsored by the NSF. This research was also supported by the Office of Science (Biological and Environmental Research), U.S. Department of Energy (DOE), the NSF Paleo Perspectives on Climate Change (P2C2) program, and NSF grant AGS 1160750. This research used resources of the Oak Ridge Leadership Computing Facility, located in the National Center for Computational Sciences at Oak Ridge National Laboratory, which is supported by the DOE Office of Science. The observed data are downloadable from the National Oceanic and Atmospheric Administration Paleoclimatology (www.ncdc.noaa.gov/data-access/paleoclimatology-data) and/or Pangaea (www.pangaea.de/). The model data are downloadable from the Earth System Gateway at NCAR (www.earthsystemgrid.org/home.htm).

SUPPLEMENTARY MATERIALS

www.sciencemag.org/content/346/6214/1223/suppl/DC1
Supplementary Text
Fig. S1 to S8
Tables S1 and S2
References (*33*–*72*)

4 August 2014; accepted 6 November 2014
10.1126/science.1259531

OCEANOGRAPHY

Multidecadal warming of Antarctic waters

Sunke Schmidtko,[1,2]* Karen J. Heywood,[1] Andrew F. Thompson,[3] Shigeru Aoki[4]

Decadal trends in the properties of seawater adjacent to Antarctica are poorly known, and the mechanisms responsible for such changes are uncertain. Antarctic ice sheet mass loss is largely driven by ice shelf basal melt, which is influenced by ocean-ice interactions and has been correlated with Antarctic Continental Shelf Bottom Water (ASBW) temperature. We document the spatial distribution of long-term large-scale trends in temperature, salinity, and core depth over the Antarctic continental shelf and slope. Warming at the seabed in the Bellingshausen and Amundsen seas is linked to increased heat content and to a shoaling of the mid-depth temperature maximum over the continental slope, allowing warmer, saltier water greater access to the shelf in recent years. Regions of ASBW warming are those exhibiting increased ice shelf melt.

The Antarctic ice sheet is the largest reservoir of terrestrial ice and is a significant contributor to sea level rise in a warming climate (*1*). Massive ice shelf disintegration and rapid acceleration of glacial flow have occurred in recent decades (*2*) or are potentially looming (*3*). These events are generally linked to enhanced basal melt (*4*, *5*), which reduces buttressing and accelerates glacier flow. An increase in basal melt may be linked to stronger sub–ice shelf circulation of Circumpolar Deep Water (CDW). It is not known whether changes in the delivery of warm water to the underside of the ice shelf are caused by increased heat content, increased volume flux responding to changes in wind and buoyancy forcing, or some combination of the two (*6*, *7*). Here, we focus on documenting long-term temperature and salinity changes in ocean properties over the continental shelf and slopes.

We refer to the water occupying the sea floor on the Antarctic continental shelf as Antarctic Continental Shelf Bottom Water (ASBW) and the temperature minimum layer, representing the remnant of the winter mixed layer, as Winter Water (WW). Atmospheric processes, adjacent water masses, ice shelf and continental freshwater fluxes, and bathymetry-dependent cross-shelf water exchange at the shelf break determine the hydrographic properties of ASBW. Hence, ASBW is a mixture of CDW, WW, and waters originating from continental runoff, ice shelf melting, or sea ice formation. Temporal changes in ASBW may represent changes either in formation processes or in properties of source waters. ASBW has freshened in the Ross Sea (*8*) and northwest Weddell Sea (*9*), with the former generally linked to enhanced upstream ice shelf melt. Recent research has identified large-scale warming of both CDW north of 60°S (*10*) and Antarctic Bottom Water (AABW) (*11*). However, statistically significant long-term warming of ASBW has been observed only in localized regions (*12*), and trends in CDW properties over the Antarctic continental slope have not previously been described in detail.

Using a comprehensive compilation of observational data sets (table S1) [(*13*) and supplementary materials], we found that temporal trends in ASBW temperature and salinity have a distinct regional pattern (Fig. 1). The Bellingshausen Sea and Amundsen Sea shelves show significant warming (0.1° to 0.3°C decade^{-1}; Fig. 1, C and E) and salinification (0.01 to 0.04 g kg^{-1} decade^{-1}; Fig. 1, D and F) since the 1990s, when sufficient observations became available (fig. S2). The Ross Sea is freshening (−0.027 ± 0.012 g kg^{-1} decade^{-1}), and the western Weddell Sea reveals a slight cooling (−0.05° ± 0.04°C decade^{-1}) and freshening (−0.01 ± 0.007 g kg^{-1} decade^{-1}); older measurements allow these trends to be calculated from the 1970s. The Cosmonaut Sea is

[1]Centre for Ocean and Atmospheric Sciences, School of Environmental Sciences, University of East Anglia, Norwich NR4 7TJ, UK. [2]GEOMAR Helmholtz Centre for Ocean Research Kiel, Düsternbrooker Weg 24, 24105 Kiel, Germany. [3]Environmental Science and Engineering, California Institute of Technology, Pasadena, CA 91125, USA. [4]Institute of Low Temperature Science, Hokkaido University, Sapporo 060-0819, Japan.
*Corresponding author. E-mail: sschmidtko@geomar.de

freshening (−0.05 ± 0.03 g kg^{-1} decade^{-1}). These trends agree with the available but limited regional observations (*12*). The previously documented regional Ross Sea freshening (*8*) (−0.03 g kg^{-1} decade^{-1}) is within the range of the locally mapped values obtained here (−0.01 to −0.05 g kg^{-1} decade^{-1}; Fig. 1D). Focusing only on data since the mid-1980s (Fig. 1F) produces a more pronounced average Ross Sea freshening (−0.05 ± 0.02 g kg^{-1} decade^{-1}). The freshening trend in the western Weddell Sea shelf changes sign when only data from the 1990s are used (Fig. 1E and fig. S10). Freshening is observed in the northwestern Weddell Sea (Fig. 1D), although the trend doubles and is similar to reported values when only data from the late 1980s to the mid-2000s are considered (*9*).

Temperature trends are typically uniform across the width of the shelf up to the shelf break. In contrast, salinity trends show a cross-shelf gradient with freshening generally intensified close to the coast (Fig. 1D); this is particularly pronounced over the Ross Sea and Weddell Sea continental shelves. A cross-shelf salinity trend gradient points to physical processes that induce a larger change in salinity than in temperature near the continent. For example, changes in surface meltwater runoff and changes in sea ice melting or freezing would be seen primarily in salinity, whereas changes in ocean-induced ice shelf basal melting would be seen in both temperature and salinity; atmospheric cooling would be seen in temperature but not salinity, unless sea ice is formed. Although changes in meltwater runoff and sea ice formation are consistent with the observed temperature and salinity trends, our analysis cannot distinguish between these mechanisms. Lateral variations of the trend vary according to the time period analyzed. The shoreward intensification of the freshening is significantly stronger when all data are used than when only data since 1990 are used (Fig. 1D and fig. S10). This difference may originate in poor data coverage from recent decades (figs. S1 and S2) or may indicate multiannual variability in any combination of processes described above (Fig. 1, E and F).

We next assessed the origins of ASBW property trends (Fig. 1, C and D) by analyzing changes in the properties and the depth of source water masses: the temperature maximum layer approaching the continental shelf break (CDW core; Fig. 2) and the temperature minimum layer (WW; Fig. 3). CDW shows significant warming and shoaling in most regions around Antarctica (Fig. 2, D and F), with trends on the order of 0.1°C decade^{-1} and −30 m decade^{-1}, respectively. These values are similar to those of isopycnal heave found farther north (*10*) and at depth (*14*). There are few significant changes in CDW salinity close to Antarctica; the most pronounced freshening is observed in the Antarctic Circumpolar Current (ACC) in the Indian Ocean sector, likely owing to variations in front location in regions of large meridional gradients (Fig. 2, B and E).

In addition to regional changes in water mass properties, changes in the depth of the CDW core also show spatial variability. Deepening of the CDW core only occurs along the northern limb of the Weddell Gyre and in the Cosmonaut Sea (Fig. 2F). Areas where the CDW core deepens tend to be correlated with cooling. The strongest shoaling of CDW is found in the Bellingshausen and Amundsen seas, where temporal shoaling rates locally exceed −50 ± 18 m decade^{-1}. Around the Antarctic margins, the core of CDW typically deepens approaching the continental shelf, as in the Weddell and Ross gyres (Fig. 2C and Fig. 4B). However, in the Bellingshausen and Amundsen seas, the core of CDW slopes upward approaching the shelf (Fig. 4A).

The other water mass present over the shelf and slope is WW (Fig. 3). WW is freshening along the southwestern limb of the Ross Gyre and in the western Indian Ocean sector, while WW is becoming saltier in the northwestern Weddell

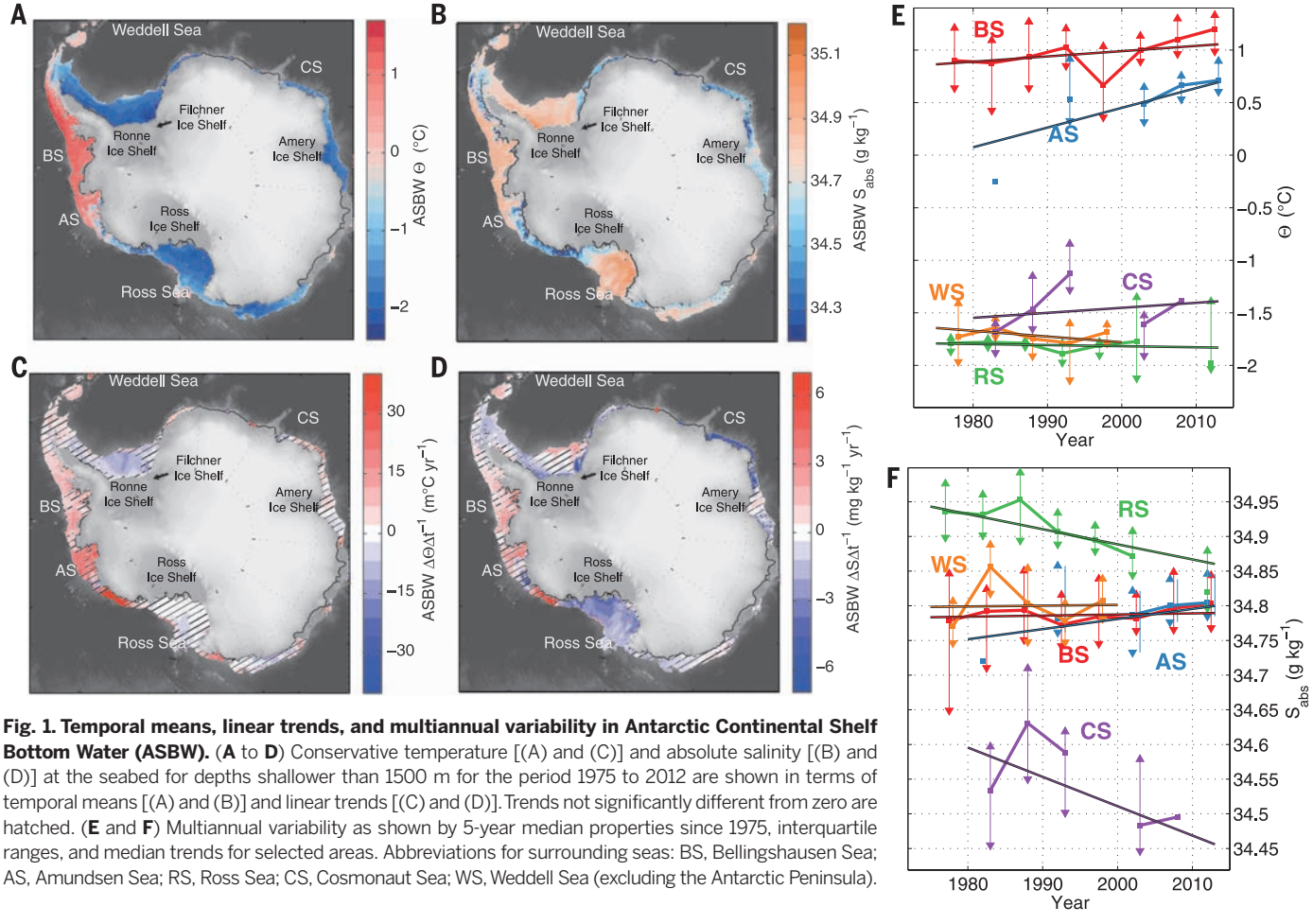


Fig. 1. Temporal means, linear trends, and multiannual variability in Antarctic Continental Shelf Bottom Water (ASBW). (**A** to **D**) Conservative temperature [(A) and (C)] and absolute salinity [(B) and (D)] at the seabed for depths shallower than 1500 m for the period 1975 to 2012 are shown in terms of temporal means [(A) and (B)] and linear trends [(C) and (D)]. Trends not significantly different from zero are hatched. (**E** and **F**) Multiannual variability as shown by 5-year median properties since 1975, interquartile ranges, and median trends for selected areas. Abbreviations for surrounding seas: BS, Bellingshausen Sea; AS, Amundsen Sea; RS, Ross Sea; CS, Cosmonaut Sea; WS, Weddell Sea (excluding the Antarctic Peninsula).

Sea (Fig. 3E). Significant shoaling of WW is present in the eastern Indian Ocean sector and Amundsen Sea (Fig. 3F). Origins of the salinity changes in WW are likely to differ among regions, including changes to sea ice concentration caused by ice motion trends (*15*) and changes to sea ice concentration caused by increased accumulation of ice shelf meltwater (*16*).

The trends in Figs. 1 and 2 show a link between changes in the properties of ASBW and those of CDW over the continental slope. The CDW thermal structure may be broadly categorized into two regimes, shown schematically in Fig. 4: CDW (i) sloping upward or (ii) sloping downward toward the shelf break. The Weddell and Ross gyres are subject to a large-scale cyclonic wind stress, leading to strong easterly winds over the shelf break that depresses isotherms (Fig. 4B). Cyclonic wind patterns are also found over the Amundsen and Bellingshausen seas, but the center of the low-pressure systems is found over the continental shelf. Thus, in these regions, weaker easterly or even westerly winds are found at the shelf break, causing upward-tilting

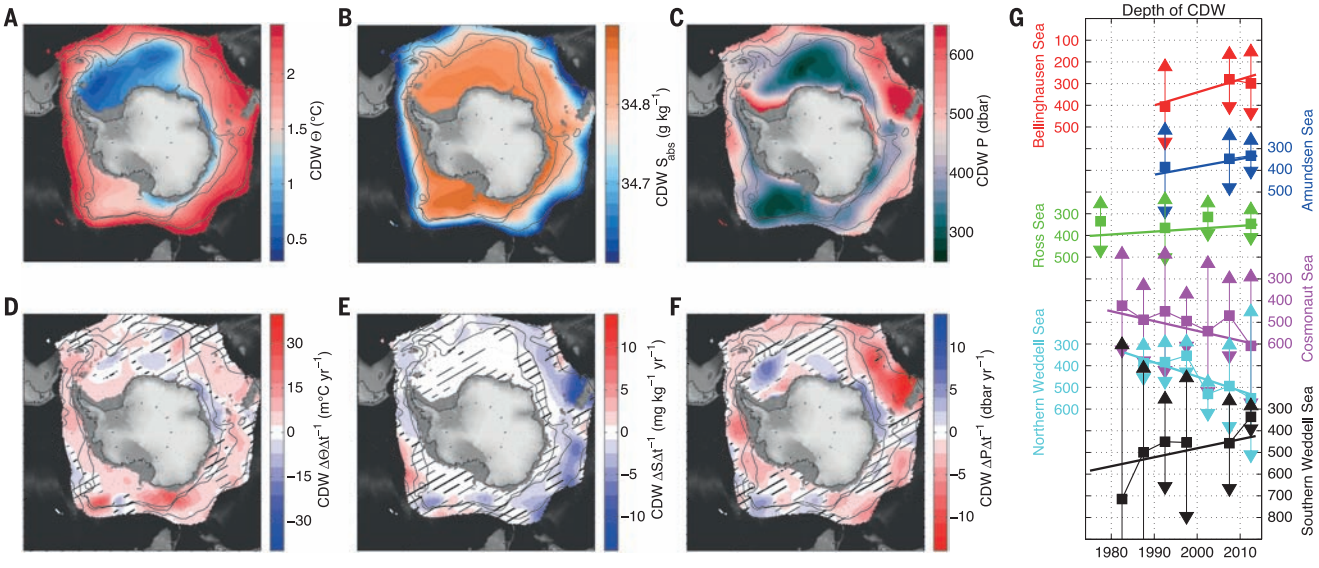


Fig. 2. Temporal means and linear trends in Circumpolar Deep Water (CDW). (**A** to **F**) Conservative temperature [(A) and (D)], absolute salinity [(B) and (E)], and core depth [(C) and (F)] of CDW between 1975 and 2012 are shown in terms of temporal means [(A) to (C)] and linear trends [(D) to (F)]. Trends not significantly different from zero are hatched. Fronts (*28*) related to the ACC are shown as black lines. Only regions where the ocean depth exceeds 1500 m and the underlying CDW is cooler than 2.8°C are shown. (**G**) Trends and data for selected locations.

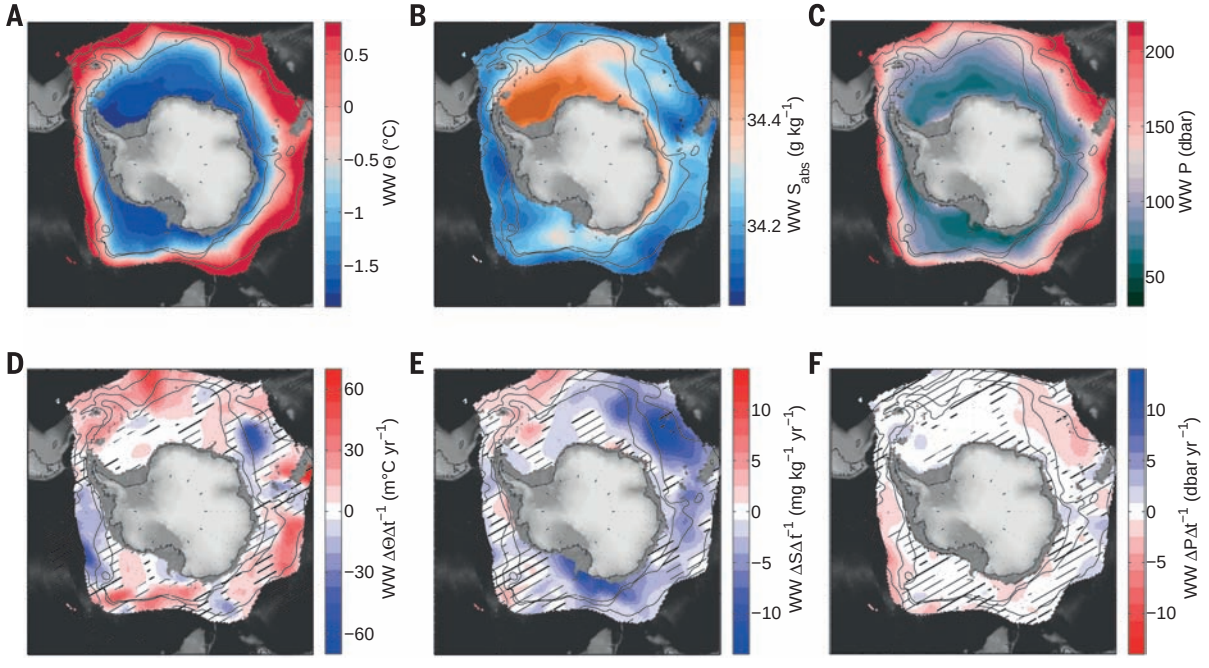


Fig. 3. Temporal means and linear trends in Winter Water (WW). (**A** to **F**) Conservative temperature [(A) and (D)], absolute salinity [(B) and (E)], and core depth [(C) and (F)] of WW between 1975 and 2012 are shown in terms of temporal means [(A) to (C)] and linear trends [(D) to (F)]. Trends not significantly different from zero are hatched. Fronts (*28*) related to the ACC are shown as black lines. Only regions where the ocean depth exceeds 1500 m and the underlying CDW is cooler than 2.8°C are shown.

CDW and enhanced onshore intrusions (*17*, *18*) (Fig. 4A). Furthermore, the Bellingshausen and Amundsen seas do not export a significant volume of AABW, and a bottom-intensified alongslope Antarctic Slope Current does not form (Fig. 4A).

Although warming and shoaling of CDW is present around Antarctica, the regions that have experienced the most intense warming and shoaling are associated with areas where CDW has greater access to the shelf break (Fig. 4A). Additionally, in all regions where CDW both slopes upward toward the shelf break and is shoaling over time, ASBW temperatures are rising. This link suggests that changes occurring to CDW offshore in the Bellingshausen and Amundsen seas (Fig. 2, D and F) are more likely to be transmitted onto the shelf and to be reflected in regional ASBW properties. By contrast, in regions where CDW slopes downward toward the shelf break, offshore trends in CDW properties show no correlation to bottom water masses on the continental shelves (e.g., near the Ross, Amery, Filchner, and Ronne ice shelves) (Fig. 4B). Thus, the segments of continental shelf in the Weddell and Ross seas are in effect shielded from offshore changes in CDW. The one possible exception, though, is the intense shoaling of CDW in the southern Weddell Sea, which raises questions about the future stability of ASBW temperatures in front of the Filchner and Ronne ice shelves (*19*) (Fig. 2, F and G).

Recent dynamical studies have highlighted the importance of surface forcing on links between offshore and onshore properties. In Ross and Weddell gyre idealized model configurations, surface forcing by the polar easterlies controls onshore transport of WW and CDW as well as the characteristic slope of mid-depth density surfaces toward the shelf break (*17*). In the Amundsen Sea, offshore atmospheric anomalies modify the thermal gradient across the continental shelf and under the ice shelf (*18*). Buoyancy forcing may also be critical to long-term trends. A simple balance model (*6*) suggests that regional properties are largely set by atmospheric patterns of heating and cooling, but changes in ASBW may depend on the penetration depth of convection. Finally, over the continental slope, mesoscale variability plays a critical role in setting temperature distributions and is sensitive to changes in wind forcing (*20*). It is critical to note that these dynamical processes occur at scales that are necessarily smoothed by our analysis. However, the large-scale trends point to key regions that require more intense analysis through high-resolution modeling with improved bathymetric data to determine the mechanistic cause of these changes.

Because ice shelf melting and ice sheet collapse depend on the delivery of warm water by ocean currents, ice sheet predictability requires accurate estimates of oceanic heat transport. Shoaling CDW has the potential to significantly increase this heat transport and must be represented in climate models for future ice shelf predictions. Current climate models still have limitations in Southern Ocean mixed layer processes (*21*) and are thus unlikely to represent WW and the underlying CDW shoaling correctly. In addition to onshore transport, capturing changes in exported AABW properties is also critical for modeling the global circulation. The changes in ASBW salinity taking place in AABW formation regions such as the Weddell and Ross seas (Fig. 1D) resemble the observed freshwater changes in AABW around Antarctica (*14*, *22*). AABW has freshened in the Indian (*22*) and Pacific sectors and to a lesser extent in the Atlantic sector (*14*). Temperature changes seen in AABW (*11*, *23*) are not apparent in ASBW (Fig. 1C).

The observed trends in water mass properties have a number of implications. Changes in ASBW may influence Southern Ocean ecosystems through the distribution of salps and krill (*24*), although the impact of warming oceans on Antarctic krill is still debated (*25*) because of their spatially diverse life cycles. We expect that megafaunal communities (*26*) on the shelf—in particular, in the Bellingshausen Sea and Amundsen Sea sectors—have experienced warmer and more frequent warm-water intrusions of CDW. Further shoaling of CDW will increase both the number of ice shelves and the area of each ice shelf that are influenced by offshore warming. This has the potential to increase the spatial extent of enhanced basal melt and to lead to irreversible retreat of a portion of the West Antarctic Ice Sheet, which will have an impact on global sea level (*3*, *27*).

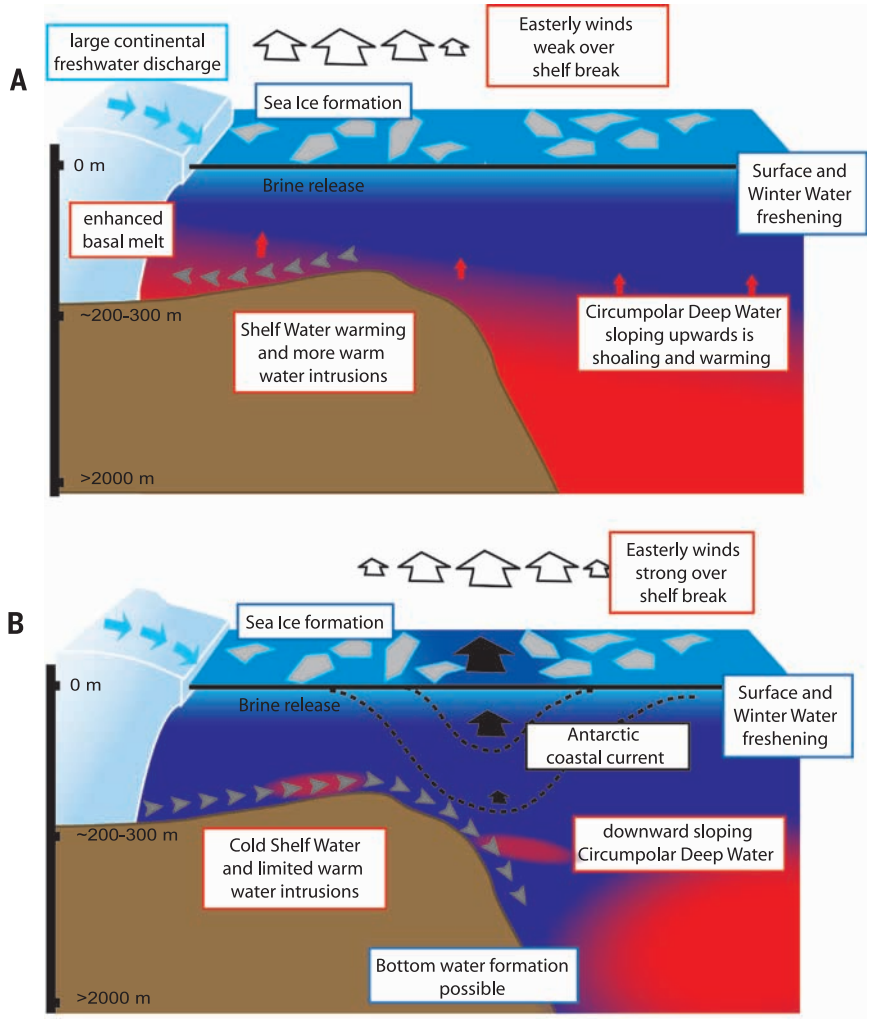


Fig. 4. Schematic differences of shelf water masses. (**A**) Schematic of the Amundsen and Bellingshausen seas with warm water at the bottom of the water column on the shelf. (**B**) Schematic of the shelf in the Ross and Weddell seas, with a strong Antarctic Slope Current.

REFERENCES AND NOTES

1. A. Shepherd *et al.*, *Science* **338**, 1183–1189 (2012).
2. H. De Angelis, P. Skvarca, *Science* **299**, 1560–1562 (2003).
3. I. Joughin, B. E. Smith, B. Medley, *Science* **344**, 735–738 (2014).
4. E. Rignot, S. S. Jacobs, *Science* **296**, 2020–2023 (2002).
5. H. D. Pritchard *et al.*, *Nature* **484**, 502–505 (2012).
6. A. A. Petty, D. L. Feltham, P. R. Holland, *J. Phys. Oceanogr.* **43**, 920–940 (2013).
7. P. Spence *et al.*, *Geophys. Res. Lett.* **41**, 2014GL060613 (2014).
8. S. S. Jacobs, C. F. Giulivi, *J. Clim.* **23**, 4508–4524 (2010).
9. H. H. Hellmer, O. Huhn, D. Gomis, R. Timmermann, *Ocean Sci.* **7**, 305–316 (2011).
10. S. T. Gille, *J. Clim.* **21**, 4749–4765 (2008).
11. S. G. Purkey, G. C. Johnson, *J. Clim.* **23**, 6336–6351 (2010).
12. M. Azaneu, R. Kerr, M. M. Mata, C. A. E. Garcia, *J. Geophys. Res. Oceans* **118**, 4213–4227 (2013).

13. S. Schmidtko, G. C. Johnson, J. M. Lyman, *J. Geophys. Res. Oceans* **118**, 1658–1672 (2013).
14. S. G. Purkey, G. C. Johnson, *J. Clim.* **26**, 6105–6122 (2013).
15. P. R. Holland, R. Kwok, *Nat. Geosci.* **5**, 872–875 (2012).
16. R. Bintanja, G. J. van Oldenborgh, S. S. Drijfhout, B. Wouters, C. A. Katsman, *Nat. Geosci.* **6**, 376–379 (2013).
17. A. L. Stewart, A. F. Thompson, *Geophys. Res. Lett.* **39**, L18604 (2012).
18. P. Dutrieux *et al.*, *Science* **343**, 174–178 (2014).
19. H. H. Hellmer, F. Kauker, R. Timmermann, J. Determann, J. Rae, *Nature* **485**, 225–228 (2012).
20. M. S. Dinniman, J. M. Klinck, E. E. Hofmann, *J. Clim.* **25**, 4799–4816 (2012).
21. C. Heuzé, K. J. Heywood, D. P. Stevens, J. K. Ridley, *Geophys. Res. Lett.* **40**, 1409–1414 (2013).
22. S. R. Rintoul, *Geophys. Res. Lett.* **34**, L06606 (2007).
23. W. Zenk, E. Morozov, *Geophys. Res. Lett.* **34**, L14607 (2007).
24. A. Atkinson, V. Siegel, E. Pakhomov, P. Rothery, *Nature* **432**, 100–103 (2004).
25. A. Atkinson *et al.*, *Mar. Ecol. Prog. Ser.* **362**, 1–23 (2008).
26. L. J. Grange, C. R. Smith, *PLOS ONE* **8**, e77917 (2013).
27. E. Rignot, J. Mouginot, M. Morlighem, H. Seroussi, B. Scheuchl, *Geophys. Res. Lett.* **41**, 3502–3509 (2014).
28. A. H. Orsi, T. Whitworth III, W. D. Nowlin Jr., *Deep Sea Res. I* **42**, 641–673 (1995).

ACKNOWLEDGMENTS

All data used in this manuscript are publicly available; data sources are detailed in the supplementary materials. We thank all officers, crews, and scientists involved in collecting and calibrating the data in the often harsh Southern Ocean environment, as well as everyone involved in making the data publicly available. We thank three anonymous reviewers for helpful discussions and feedback. Supported by the German Federal Ministry for Education and Research (BMBF) project MiKlip (S.S.); NERC Antarctic Funding Initiative research grant GENTOO NE/H01439X/1 (S.S. and K.J.H.); a Grant-in-Aid for Scientific Research of the Ministry of Education, Culture, Sports, Science and Technology, Japan, and a Daiwa Foundation Small Grant (S.A.); and NSF award OPP-1246460 (A.F.T.).

SUPPLEMENTARY MATERIALS

www.sciencemag.org/content/346/6214/1227/suppl/DC1
Materials and Methods
Figs. S1 to S11
Table S1
References (*29*, *30*)

15 May 2014; accepted 27 October 2014
10.1126/science.1256117

ANIMAL PHYSIOLOGY

The shocking predatory strike of the electric eel

Kenneth Catania

Electric eels can incapacitate prey with an electric discharge, but the mechanism of the eel's attack is unknown. Through a series of experiments, I show that eel high-voltage discharges can activate prey motor neurons, and hence muscles, allowing eels to remotely control their target. Eels prevent escape in free-swimming prey using high-frequency volleys to induce immobilizing whole-body muscle contraction (tetanus). Further, when prey are hidden, eels can emit periodic volleys of two or three discharges that cause massive involuntary twitch, revealing the prey's location and eliciting the full, tetanus-inducing volley. The temporal patterns of eel electrical discharges resemble motor neuron activity that induces fast muscle contraction, suggesting that eel high-voltage volleys have been selected to most efficiently induce involuntary muscle contraction in nearby animals.

The electric eel (*Electrophorus electricus*) is one of just a few species that uses electrical discharges to capture prey and defend against predators. It is the most powerful electrogenic fish, with most of its body composed of electrocytes (muscle-derived biological batteries), providing a combined discharge of up to 600 V (*1*). Early attempts to understand electricity made use of electric eels (*2*), and more recently, eels were important for identifying acetylcholine receptors (*3*) and for providing insights into the evolution of electric organs (*4*), but little is known about how the eel's electrical discharge affects prey. In this study, I designed a set of experiments to explore the impacts of the electric eel discharges on potential prey and the mechanism that operates during such attacks.

Electric eels emit three distinct types of electric organ discharges: (i) low-voltage pulses for sensing their environment, (ii) pairs and triplets of high-voltage pulses given off periodically while hunting in complex environments, and (iii) high-frequency volleys of high-voltage pulses during prey capture or defense (movie S1) (*5*–*9*). Under most conditions, eels attack free-swimming prey with the latter strategy, using high-voltage volleys combined with a suction-feeding strike. To explore this more common behavior, I simultaneously recorded eel behavior and electric organ discharges in a naturalistic experimental environment (*10*). Eels began their attack with a high-frequency (~400 Hz) volley of high-voltage pulses 10 to 15 ms before their predatory strike. In response to these volleys, prey voluntary movement was completely arrested 3 to 4 ms after the first strong discharge (Fig. 1 and movie S2). Fish that were not successfully captured during this period of immobility were often able to

Department of Biological Sciences, Vanderbilt University, VU Station B, Box 35-1634, Nashville, TN 37235, USA.
E-mail: ken.catania@vanderbilt.edu

Downloaded from www.sciencemag.org on December 5, 2014

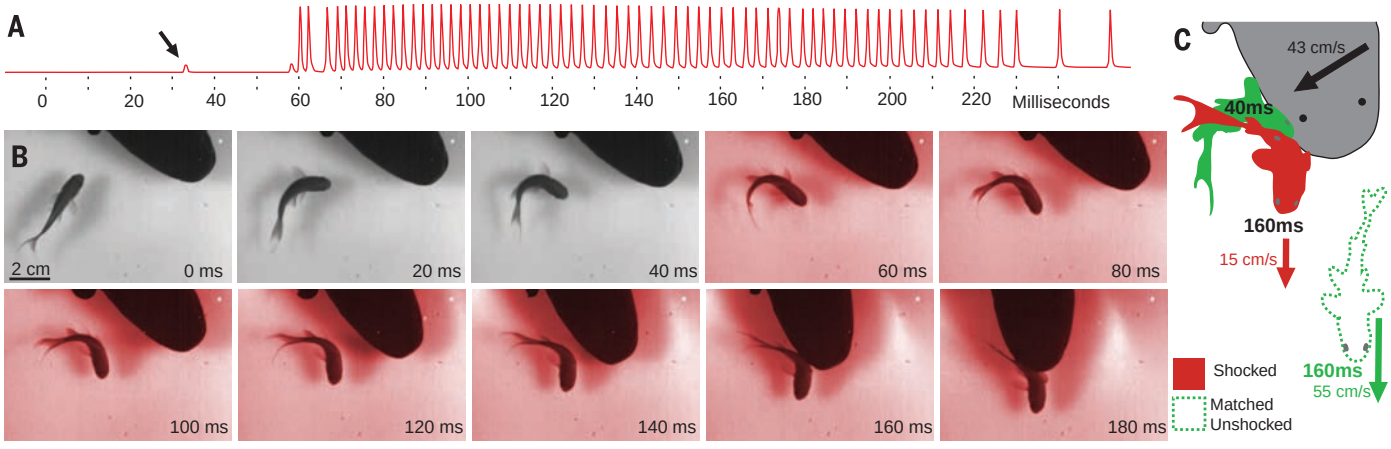


Fig. 1. Eel's discharge and strike. (**A**) Electric organ discharge corresponding to plates below. Arrow indicates low-amplitude discharge. (**B**) Video frames showing that fish movement is arrested by discharge. Red frames indicate electric organ discharge (movie S1). (**C**) The utility of the discharge illustrated. Shown are the prey fish at 40 ms (green) and later, the position and velocity of the eel and fish at 160 ms (red fish). Green dotted fish outline shows velocity and location of uninterrupted escaping fish matched in time, size, and position from 40 ms, suggesting that the eel would have missed without the discharge.

return to previous movement patterns and escape (movie S2).

To characterize the mechanism by which high-voltage volleys cause this remote immobilization of prey (*10*), anesthetized fish were pithed (to destroy the brain), the hole was sealed with cyanoacrylate, and the fish was attached to a force transducer. An eel in the aquarium was separated from the fish by an electrically permeable agar barrier (Fig. 2A) (*11*) and fed earthworms, which it attacked with volleys of its high-voltage discharge. The discharge directed at the earthworms induced strong muscular contractions in the fish preparation, precisely correlated in time with the volley (no tension developed during the weak discharge). A steep rise in fish tension occurred with a mean latency of 3.4 ms (n = 20 trials) after the first strong pulse (Fig. 2B), which is similar to the 2.9-ms mean immobilization latency (n = 20 trials) observed in free-swimming fish. Tension induced by the eel in the fish preparation was similar to the maximum that could be induced experimentally (fig. S1) (*10*). This result indicates that fish are immobilized by massive, involuntary muscle contraction.

To further investigate the fidelity of prey muscle contractions relative to the electric organ

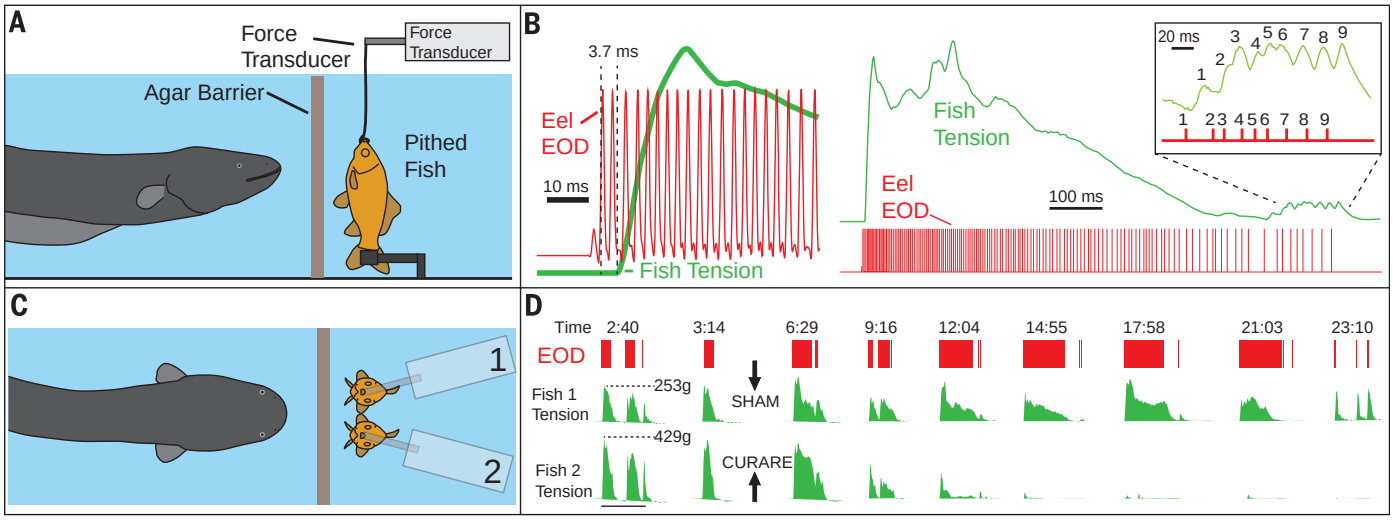


Fig. 2. Paradigm for investigating strong electric organ discharge. (**A**) An agar barrier separated eels from pithed fish. Eels shocked earthworms while fish tension was recorded. (**B**) All eels induced whole-body tension, occurring 2 to 4 ms after strong discharge onset. No tension was developed from weak discharge. At low frequencies, individual twitches emerged for each discharge (top right) (fig. S2). (**C**) Two pithed fish (fish 1, 19 g; fish 2, 21 g) preparation. (**D**) Effect of curare. Red trace indicates strong electric organ discharge matched in time to unnormalized fish tension (green). Arrows indicate time of injections (fig. S3). Bar in (D) = 500 ms.

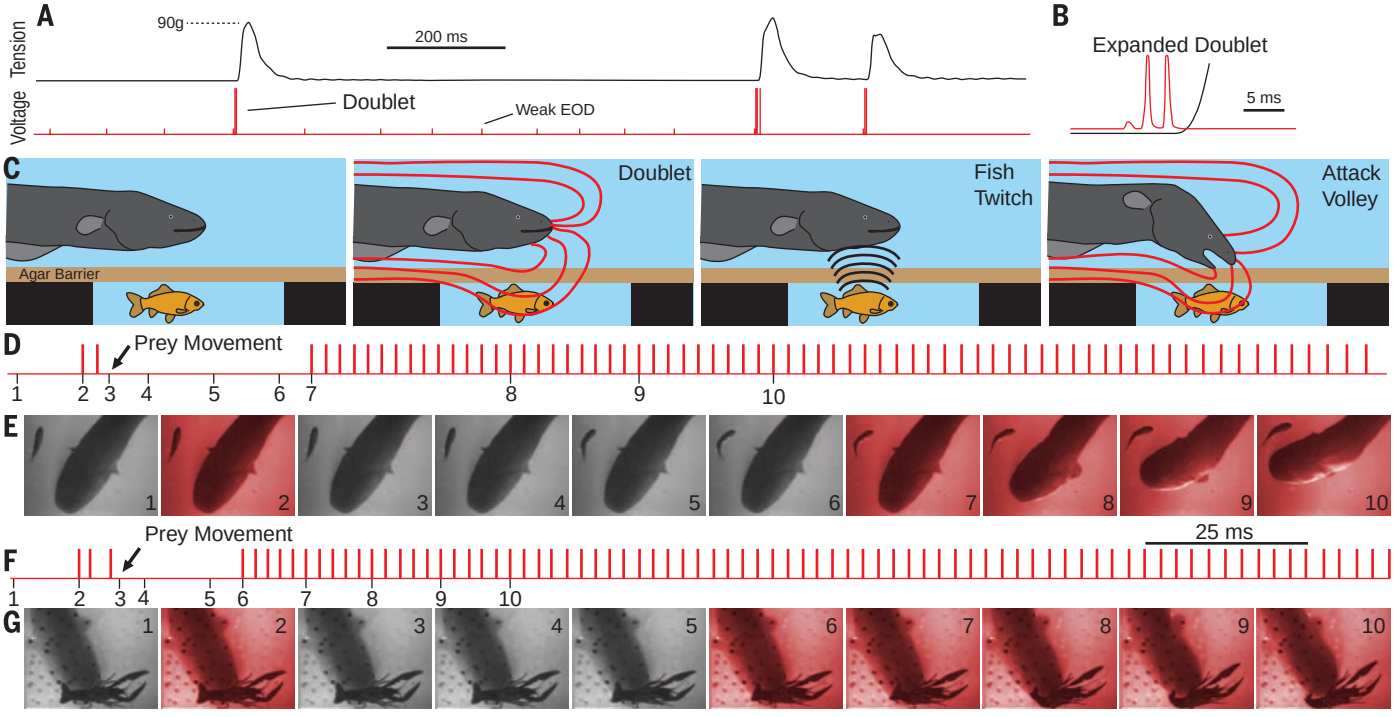


Fig. 3. Doublets during hunting. (**A**) Examples of doublets and corresponding tension responses. (**B**) Expansion of the first doublet and corresponding tension trace (off-scale peaks were estimated). (**C**) Schematic of attack sequence. (**D**) Example of high-voltage electric organ discharge for an attack preceded by a doublet. (**E**) Video frames from volley shown in (D). Numbers correspond to numbers in (D). (**F**) Timing of the high-voltage discharge for attack preceded by a triplet. (**G**) Video frames for volley shown in (F).

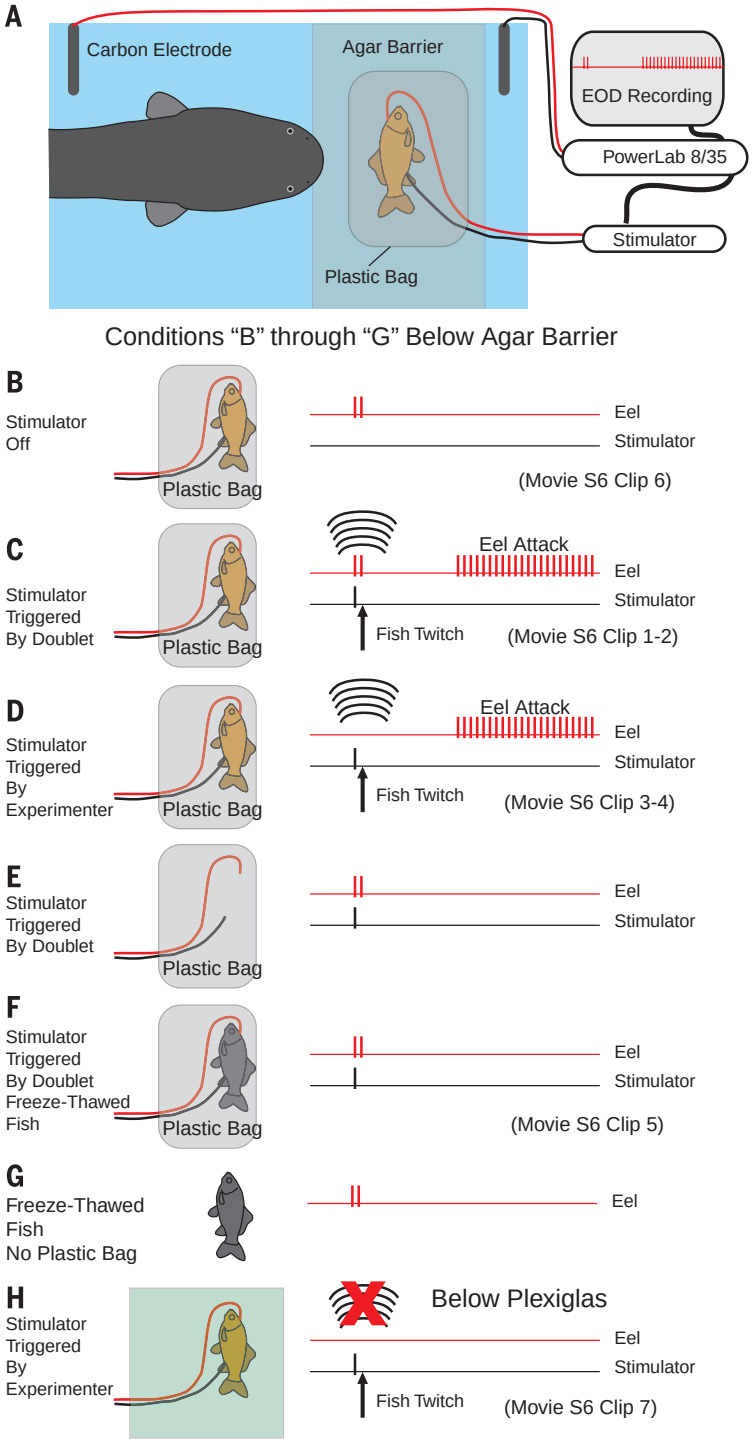


Fig. 4. Paradigm and controls showing eels attack doublet-generated movements. (**A**) Movement in electrically isolated pithed fish (below agar) was generated through stimulator. (**B**) Without fish twitch, eels did not follow doublets with attack (10 trials each for two eels). (**C**) When stimulator triggered fish twitch after doublets, eels attacked (10 trials each for two eels). (**D**) Without doublets, fish twitches also elicited attack volleys (10 trials each of two eels). (**E**) Doublets that triggered stimulator leads in bag did not elicit attack (10 trials for each of two eels). (**F**) Likewise, no attack volleys were elicited after stimulation of a freeze-thawed fish (10 trials each of two eels). (**G**) Doublets directed at a freeze-thawed fish under agar without the plastic bag or stimulator did not elicit eel attack volleys or strikes (10 trials each of two eels). These latter conditions, along with (**H**) trials with Plexiglas barrier, show that visual cues did not generate eel attacks. Examples are provided in movie S6 and (*10*).

discharge, and the mechanism of the contractions' induction, two pithed-fish preparations were stationed side by side (Fig. 2C). The high-voltage discharge reliably created muscle tension with similar form and time course in both fish (fig. S2). As the discharge frequency decreased, individual fish twitches often emerged on the tension trace, each corresponding to a single discharge (Fig. 2B and fig. S2). To determine whether the discharge induced muscle contractions by initiating action potentials directly in prey muscles or through activation of some portion of fish motor neurons, one of two similarly sized fish was injected with curare (an acetylcholine antagonist) so as to block the acetylcholine gated ion channels at the neuromuscular junction, whereas the other fish was sham-injected (Fig. 2D). In each of four cases, tension responses in the curarized fish dropped to near zero, whereas the sham-injected fish continued to respond (fig. S3). These findings indicate that fish motor neuron activation is required to induce tetanus in prey. To determine whether this activation of prey motor neurons was the result of central nervous system (spinal) activity or activity in efferent branches of motor neurons, the dual tension experiment was repeated twice with extensively double-pithed fish (in which both the brain and spinal cord were destroyed, but the branches of motor efferents were left intact within the fish body) and compared with a brain-pithed fish. No diminution in contractile response, or difference in contractile response latency, was observed for the double-pithed fish relative to the brain-pithed fish (fig. S2). These experiments suggest that the electric eel's strong electric organ discharge remotely activates motor neuron efferents of its prey, although this activation could occur anywhere between the spinal cord and the presynaptic side of the neuromuscular junction. Given that the eel's strong electric organ discharge remotely activates prey motor neurons, it was useful to consider the form of this pulse train in the context of prey muscle activation. Analysis of the first 11 impulses from strong discharge volleys from each of four eels showed that each begins with a doublet—two pulses with a shorter interpulse interval (fig. S4). Doublets at the onset of motor neuron trains have been shown to induce high rates of muscle tension (*12*–*15*). Moreover, the overall distribution of pulses in the eel's strong discharge resembles motor neuron trains found to be near optimal for muscle tension development (*16*, *17*). These observations raise the possibility that eel volleys have been selected to efficiently induce rapid muscle tension.

As described above, hunting eels often pause and give off isolated high-voltage doublets (*9*), particularly in complex environments, when seeking hidden prey or when exploring conductors (movie S3). In the course of the present study, eels stationed behind the agar barrier in the fish tension experiments occasionally emitted such isolated doublets or triplets and then attempted to break through the barrier to reach the fish preparation (movie S4). This suggested that eels were able to detect fish movements through the thin agar barrier, which was not designed to mask

mechanosensory cues. To identify the function of this additional behavior, eels were presented with prey hidden below a thin agar barrier (Fig. 3C). In some cases, eels detected prey through the barrier and attacked directly, but in other cases, the eel investigated the agar surface with a low-amplitude electric organ discharge and then produced a high-voltage doublet. The doublet invariably caused prey movement. Stimulated prey movement was closely followed (in 20 to 40 ms) by a full predatory strike consisting of a strong electric discharge volley and directed attack (Fig. 3 and movie S5), as characterized in the first experiments. The distinct form of the discharge trace in these trials consisted of a doublet (or triplet) followed by a 20- to 40-ms pause (during which prey moved) and then a full discharge volley (Fig. 3, D and F).

The results of the doublet experiment suggest that the eels may use doublet and triplet discharges to detect cryptic prey by inducing movement. To test this hypothesis, a pithed fish was placed in a thin plastic bag to isolate it from the eel's discharge. The electrically isolated fish was positioned below an agar barrier, with electrical leads embedded in the head and tail region (*10*) that allowed production of artificial fish twitch by the experimenter. Artificial fish twitch was triggered remotely through a stimulator (Fig. 4A), allowing control over its timing and occurrence. When the stimulating electrodes were inactive, eel doublets caused no response in the pithed fish and eels did not attack the preparation (Fig. 4B and movie S6). However, when the stimulator was configured to trigger fish twitch when the eel produced a doublet, the eel's full "doublet attack" behavior was replicated (Fig. 4C and movie S6). The attack pattern consisted of a doublet, followed by a short pause, during which the prey moved (resulting from the triggered stimulator), followed by a high-voltage volley and strike. This key experiment showed that eels never (10 of 10 trials for each of two eels) followed a doublet with an attack volley without a "mechanosensory echo" from the prey, but attacked in response to the stimulator-generated fish twitch (10 of 10 trials for each of two eels; $P < 0.0001$, binomial test). Experimenter-triggered twitches, in the absence of eel hunting doublets, also generated attacks (movie S6) with the time course observed above (Fig. 4D and supplementary materials). Thus, prey movement, whether doublet-generated or independently generated, elicited short latency (20 to 40 ms) attacks. Eels also appeared to use either active or passive electrolocation to detect live prey under agar and often attacked without a preceding doublet. But in no case did an attack volley follow a doublet in the absence of prey response. Thus, the doublet appears to answer the question, "Are you living prey?" when information is limited. Preliminary observations suggest that "doublet hunting" is most common in complex environments (movie S7). A range of controls confirmed that eels were responding to twitch-generated mechanosensory cues in this paradigm (Fig. 4 and movie S6).

Together, the results of these experiments show that high-voltage discharges of electric eels remotely activate motor neuron efferents in nearby animals. Prey that have been detected can be immobilized and captured. Hidden prey can be induced to twitch, revealing their location. The latter strategy, which often triggers an escape response, depends on the eel's short reaction time. An eel can discharge its high-voltage train 20 ms after a mechanosensory stimulus, allowing it to cancel the very escape response it has generated. Overall, this study reveals that the electric eel has evolved a precise remote control mechanism for prey capture, one that takes advantage of an organisms' own nervous system.

REFERENCES AND NOTES

1. H. Grundfest, *Prog. Biophys. Biop. Chem.* **1957**, 1–85 (1956).
2. S. Finger, M. Piccolino, *The Shocking History of Electric Fishes: From Ancient Epochs to the Birth of Modern Neurophysiology* (Oxford Univ. Press, Oxford, 2011), p. 5.
3. J. Keesey, *J. Hist. Neurosci.* **14**, 149–164 (2005).
4. J. R. Gallant *et al.*, *Science* **344**, 1522–1525 (2014).
5. R. Bauer, *Behav. Ecol. Sociobiol.* **4**, 311–319 (1979).
6. C. W. Coates, R. T. Cox, W. A. Rosemblith, M. B. Brown, *Zoologica* **25**, 249 (1940).
7. S. Hagiwara, T. Szabo, P. S. Enger, *J. Neurophysiol.* **28**, 775–783 (1965).
8. T. H. Bullock, *Brain Behav. Evol.* **2**, 85–101 (1969).
9. G. M. Westby, *Behav. Ecol. Sociobiol.* **22**, 341–354 (1988).
10. Materials and methods are available as supplementary materials on *Science* Online.
11. A. J. Kalmijn, *J. Exp. Biol.* **55**, 371–383 (1971).
12. R. Hennig, T. Lømo, *Nature* **314**, 164–166 (1985).
13. K. K. Pedersen, O. B. Nielsen, K. Overgaard, *Physiol. Rep.* **1**, e00026 (2013).
14. A. J. Cheng, N. Place, J. D. Bruton, H. C. Holmberg, H. Westerblad, *J. Physiol.* **591**, 3739–3748 (2013).
15. J. Celichowski, K. Grottel, *Acta Neurobiol. Exp. (Warsz.)* **58**, 47–53 (1998).
16. F. E. Zajac, J. L. Young, *J. Neurophysiol.* **43**, 1206–1220 (1980).
17. F. E. Zajac, J. L. Young, *J. Neurophysiol.* **43**, 1221–1235 (1980).

ACKNOWLEDGMENTS

I thank E. Catania for suggesting experimental designs and manuscript comments. This work was supported by a Pradel Award from the National Academy of Sciences, a Guggenheim Fellowship, and NSF grant 0844743. Raw data are available in the supplementary materials.

SUPPLEMENTARY MATERIALS

www.sciencemag.org/content/346/6214/1231/suppl/DC1
Materials and Methods
Supplementary Text
Figs. S1 to S4
Movies S1 to S7

4 September 2014; accepted 13 November 2014
10.1126/science.1260807

INFLAMMATION

Neutrophils scan for activated platelets to initiate inflammation

Vinatha Sreeramkumar,[1] José M. Adrover,[1] Ivan Ballesteros,[2] Maria Isabel Cuartero,[2] Jan Rossaint,[3] Izaskun Bilbao,[1,4] Maria Nácher,[1,5] Christophe Pitaval,[1] Irena Radovanovic,[1] Yoshinori Fukui,[6] Rodger P. McEver,[7] Marie-Dominique Filippi,[8] Ignacio Lizasoain,[2] Jesús Ruiz-Cabello,[1,4] Alexander Zarbock,[3] María A. Moro,[2] Andrés Hidalgo[1,9]*

Immune and inflammatory responses require leukocytes to migrate within and through the vasculature, a process that is facilitated by their capacity to switch to a polarized morphology with an asymmetric distribution of receptors. We report that neutrophil polarization within activated venules served to organize a protruding domain that engaged activated platelets present in the bloodstream. The selectin ligand PSGL-1 transduced signals emanating from these interactions, resulting in the redistribution of receptors that drive neutrophil migration. Consequently, neutrophils unable to polarize or to transduce signals through PSGL-1 displayed aberrant crawling, and blockade of this domain protected mice against thromboinflammatory injury. These results reveal that recruited neutrophils scan for activated platelets, and they suggest that the neutrophils' bipolarity allows the integration of signals present at both the endothelium and the circulation before inflammation proceeds.

Neutrophils are primary effectors of the immune response against invading pathogens but are also central mediators of inflammatory injury (*1*). Both functions rely on their remarkable ability to migrate within and through blood vessels. The migration of neutrophils is initiated by tethering and rolling on inflamed venules, a process mediated by endothelial selectins (*2*). Selectin- and chemokine-triggered activation of integrins then allows firm adhesion, after which leukocytes actively crawl on the endothelium before they extravasate or return to the circulation (*3*). A distinct feature of leukocytes recruited to inflamed vessels is the rapid shift from a symmetric morphology into a polarized form, in which intracellular proteins and receptors rapidly segregate (*4*). In this way, neutrophils generate a moving front or leading edge where the constant formation of lamellipodia (actin projections) guides movement, and a uropod or trailing edge where highly glycosylated receptors accumulate (*5*, *6*). We deemed it unlikely that this dramatic reorganization served to exclusively generate a front-to-back axis for directional movement, and we explored the possibility that neutrophil polarization functions as an additional checkpoint during inflammation.

We performed intravital microscopy (IVM) imaging of venules in cremaster muscles of mice treated with the cytokine tumor necrosis factor–α (TNF-α), an inflammatory model in which the vast majority of recruited leukocytes are neutrophils (fig. S1). Within seconds after arresting, leukocytes formed a lamellipodia-rich domain, or leading edge, and a CD62L-enriched uropod, which we could identify by its localization opposite to the leading edge and the direction of cell movement (movie S1 and Fig. 1A) (*6*–*8*). Confirming previous reports, we observed numerous interactions of platelets with the leading edge of adherent neutrophils [Fig. 1A and fig. S2A (*8*–*10*)]. During these experiments, we noticed that the uropod underwent continuous collisions with circulating platelets, a fraction of which established measurable interactions that were usually transient (Fig. 1B and movie S2). Because platelets captured by the uropod represented a substantial fraction of all interactions (31%), we searched for the receptor(s) mediating these contacts. We reasoned that PSGL-1, a glycoprotein ligand for P-selectin (*11*) that segregates to the uropod of polarized neutrophils (*12*), could be responsible for these interactions. Analysis of mice deficient in PSGL-1 (*Selplg*$^{-/-}$ mice) revealed marked reductions in platelet interactions with the uropod, whereas those at the leading edge remained unaffected (Fig. 1B). In contrast, deficiency in the β2 integrin Mac-1 (*Itgam*$^{-/-}$) resulted in reductions at both the uropod and leading edge (Fig. 1B). In vivo labeling of Mac-1 and PSGL-1 confirmed these functional data, with Mac-1 localized throughout the cell body and PSGL-1 exclusively at the uropod (Fig. 1C). Specifically, PSGL-1 clustered in a small region of the uropod, whereas CD62L was widely distributed in this domain (Fig. 1C). Analyses of mice expressing a functional Dock2-GFP protein (GFP, green fluorescent protein), a guanine nucleotide exchange factor of Rac GTPases (*13*), revealed colocalization of Dock2 with PSGL-1 clusters on crawling neutrophils (fig. S3 and movie S3), suggesting active structural dynamics within this region. This observation together with the high frequency of platelet collisions with the PSGL-1 clusters suggested that this domain might be actively protruding into the vessel lumen. Using high-speed spinning-disk IVM, we could obtain three-dimensional (3D) reconstructions of polarized neutrophils within inflamed venules of Dock2-GFP mice (Fig. 1D), demonstrating that the PSGL-1 clusters indeed projected toward the vessel lumen in about 40% of adherent neutrophils, whereas in the remaining 60% of the cells, it extended laterally, parallel to the endothelial surface (Fig. 1, D and E, and movie S4). As a consequence, the luminal space of inflamed venules was populated by multiple PSGL-1–bearing clusters suitably positioned to interact with circulating cells (Fig. 1F and movie S5).

The observation that only a small fraction of circulating platelets engaged in interactions with the uropod prompted us to search for subsets of platelets prone to this behavior. In vivo labeling for P-selectin or for active β3 integrins revealed that virtually all platelets interacting with the uropod were activated (P-selectin^{+} or with active β3 integrins), whereas a fraction of those engaging the leading edge were not (Fig. 1G and figs. S2B and S4). These findings further suggested that P-selectin present on the surface of activated platelets might be mediating the interactions with the PSGL-1 clusters. Analyses of mice deficient in P-selectin (*Selp*$^{-/-}$ mice) indeed demonstrated patterns of platelet interactions with the two leukocyte subdomains that were similar to those found in mice lacking PSGL-1 (Fig. 1B). These results indicated that neutrophils recruited to inflamed vessels extend a PSGL-1–bearing microdomain into the vessel lumen that scans for activated platelets present in the bloodstream through P-selectin.

During the course of our IVM experiments, we also noticed alterations in the intravascular behavior of adherent neutrophils in the different mutant mice. Deficiency in Mac-1 severely compromised neutrophil crawling on the inflamed vasculature (Fig. 2, A and B), a process previously reported to be mediated by this integrin (*3*). Surprisingly, although PSGL-1 was excluded from the area of contact with the endothelium (Fig. 1, D and E), neutrophils deficient in this glycoprotein also displayed reductions in crawling displacement and velocity (Fig. 2, A and B),

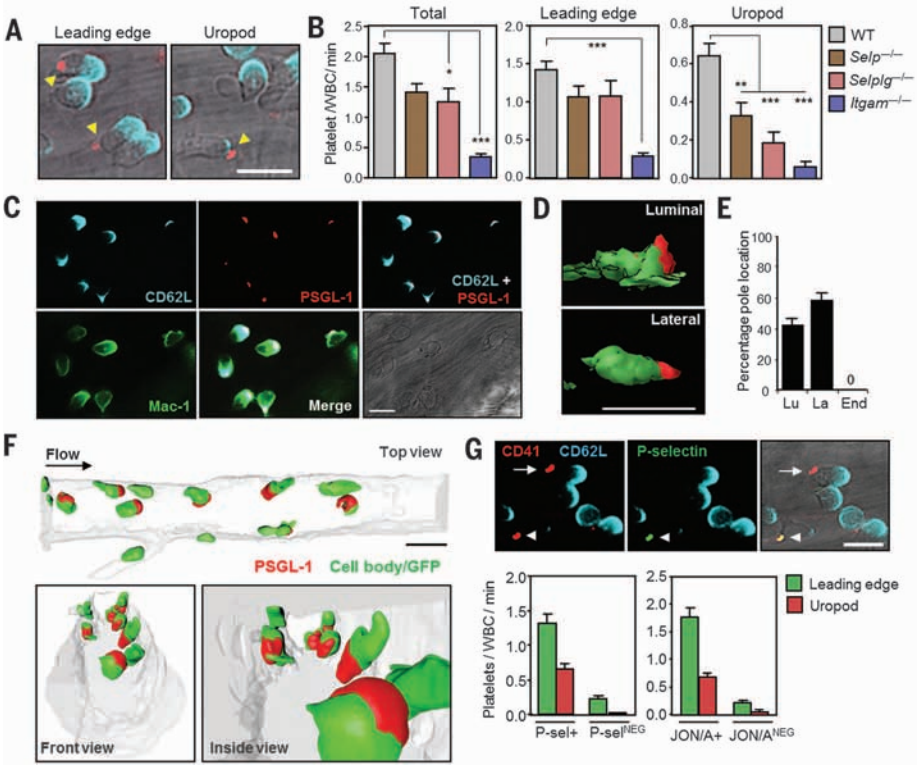


Fig. 1. Neutrophils recruited to inflamed venules interact with activated platelets via protruding PSGL-1 clusters. (**A**) Micrographs of polarized neutrophils interacting with platelets (red; yellow arrowheads) through the leading edge or the CD62L-labeled uropod (blue). (**B**) Quantification of total or domain-specific platelet interactions in wild-type mice or mice deficient in P-selectin (*Selp*$^{-/-}$), PSGL-1 (*Selplg*$^{-/-}$), or Mac-1 (*Itgam*$^{-/-}$); n = 5 to 8 mice, 38 to 133 interactions. (**C**) In vivo receptor distribution on polarized wild-type neutrophils. (**D**) Examples of luminal and lateral projections from 3D reconstructions of polarized Dock2-GFP neutrophils (see also movie S4). (**E**) Frequency of neutrophils extending PSGL-1 clusters into the lumen (Lu), laterally (La) or between the cell body and the endothelium (En). n = 6 mice, 251 cells. (**F**) 3D reconstructions of an inflamed vessel showing the distribution of PSGL-1 clusters (movie S5). (**G**) Representative micrographs of neutrophils interacting with nonactivated (arrow) or activated P-selectin^{+} platelets (arrowhead), and quantification of interactions of each domain with P-selectin^{+} or JON/A^{+} platelets. n = 3 to 4 mice, 66 to 116 interactions. Scale bars, 10 μm. Bars show mean ± SEM. *P < 0.05; ***P < 0.001, one-way analysis of variance (ANOVA) with Tukey's post-hoc test.

[1]Department of Atherothrombosis, Imaging and Epidemiology, Centro Nacional de Investigaciones Cardiovasculares (CNIC), Madrid, Spain. [2]Unidad de Investigación Neurovascular, Department of Pharmacology, Faculty of Medicine, Universidad Complutense and Instituto de Investigación Hospital 12 de Octubre (i+12), Madrid, Spain. [3]Department of Anesthesiology and Critical Care Medicine, University of Münster and Max Planck Institute Münster, Münster, Germany. [4]Ciber de Enfermedades Respiratorias (CIBERES), Madrid, Spain. [5]Faculty of Science, Medicine and Health, University of Wollongong, New South Wales, Australia. [6]Division of Immunogenetics, Department of Immunobiology and Neuroscience, Kyushu University, Japan. [7]Cardiovascular Biology Research Program, Oklahoma Medical Research Foundation, Oklahoma City, OK, USA. [8]Division of Experimental Hematology and Cancer Biology, Cincinnati Children's Research Foundation, University of Cincinnati College of Medicine, Cincinnati, OH, USA. [9]Institute for Cardiovascular Prevention, Ludwig-Maximilians-University, Munich, Germany.
***Corresponding author. E-mail: ahidalgo@cnic.es**

and these defects were cell-intrinsic (fig. S5 and movie S6). To exclude potential defects originating from PSGL-1 contributions in the early steps of leukocyte recruitment by binding endothelial P-selectin (*14*), we prevented PSGL-1 binding to P-selectin using a blocking antibody injected after neutrophils had adhered. Inhibition at this stage did not affect leukocyte adhesion to inflamed venules but specifically decreased interactions with the uropod (fig. S6) and caused reductions in crawling kinetics (Fig. 2, A and B). We thus speculated that the engagement of PSGL-1 at the uropod might promote crawling of polarized neutrophils. To test this hypothesis, we first induced transient depletion of platelets, a treatment that resulted in virtual suppression of crawling (Fig. 2, A and B, and fig. S7A). We next analyzed two models in which neutrophil polarization or signaling through PSGL-1 was impaired. In the first model, we induced hematopoietic-specific deletion of the gene encoding Cdc42 (fig. S8A), a small Rho-GTPase required for neutrophil polarization (*15*). Confirming previous in vitro observations, Cdc42-deficient neutrophils were unable to form a leading edge–to–uropod axis and instead formed multiple protrusions, lacked a distinguishable uropod, and failed to form PSGL-1 clusters in vivo (fig. S8B). Impaired polarization in these mutants compromised interactions between neutrophils and circulating platelets (fig. S8C), and neutrophils in these mice displayed severely impaired crawling kinetics (Fig. 2, C and D). In the second model, we analyzed mice in which PSGL-1 is normally distributed at the cell surface and can interact with P-selectin but cannot propagate outside-in signals because of the absence of the cytoplasmic domain [PSGL-1$^{\Delta Cyt}$ mice (*16*)]. Although neutrophil adhesion to TNF-α–stimulated vessels was partially compromised in PSGL-1$^{\Delta Cyt}$ mice because of reductions in the surface levels of PSGL-1, those cells that adhered polarized normally (fig. S9A) and displayed marked reductions in crawling kinetics (Fig. 2, C and D) despite elevated levels of Mac-1 on the surface (fig. S9B). Thus, polarization of a signaling-competent PSGL-1 drives the intravascular migration of neutrophils.

To search for possible mechanisms by which PSGL-1–derived signals promoted crawling, we analyzed the in vivo distribution of Mac-1 and the chemokine receptor CXCR2, two receptors required for the intravascular migration of neutrophils (*3*, *17*). In wild-type cells, Mac-1 was homogeneously distributed throughout the cell body, whereas CXCR2 preferentially localized at the leading edge (Fig. 2E and movie S7). Neutrophils deficient in PSGL-1 exhibited a mislocalization of both receptors (Fig. 2E, fig. S10, and movie S8). These alterations were even more dramatic in wild-type mice upon platelet depletion (figs. S7B and S10 and movie S9), which agreed with the suppression of crawling in these mice (Fig. 2A). The absence or inhibition of PSGL-1 in Mac-1–deficient mice did not lead to further reductions in platelet interactions or crawling kinetics (fig. S11), indicating that these receptors function along the same pathway and

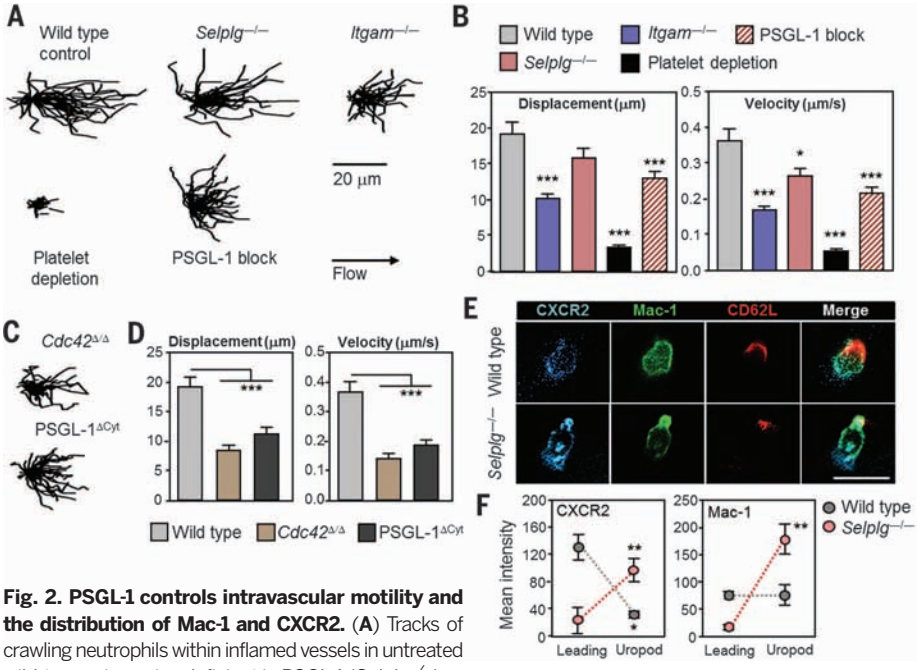


Fig. 2. PSGL-1 controls intravascular motility and the distribution of Mac-1 and CXCR2. (**A**) Tracks of crawling neutrophils within inflamed vessels in untreated wild-type mice, mice deficient in PSGL-1 (*Selplg*$^{-/-}$) or Mac-1 (*Itgam*$^{-/-}$), and mice depleted of platelets by antiplatelet serum or treated with a PSGL-1–blocking antibody. (**B**) Quantification of the crawling displacements and instantaneous velocities of neutrophils in the same groups as (A); n = 50 to 56 cells, 4 to 9 mice. (**C**) Tracks of neutrophils with conditional deletion of *Cdc42* or expressing a mutant form of PSGL-1 that lacks the cytoplasmic tail (PSGL-1$^{\Delta Cyt}$) and (**D**) quantification of the displacement per minute and instantaneous velocities of adhered neutrophils. n = 50 to 55 cells, 3 to 5 mice. (**E**) Representative micrographs and quantification (**F**) of the in vivo distribution of CXCR2 and Mac-1 in polarized neutrophils from wild-type and PSGL-1–deficient mice; n = 17 to 19 cells, 3 mice. Scale bar, 10 μm. Data show mean ± SEM. *P < 0.05; ** P < 0.01; ***P < 0.001; ANOVA with Tukey's multigroup test (B) or unpaired t test (F).

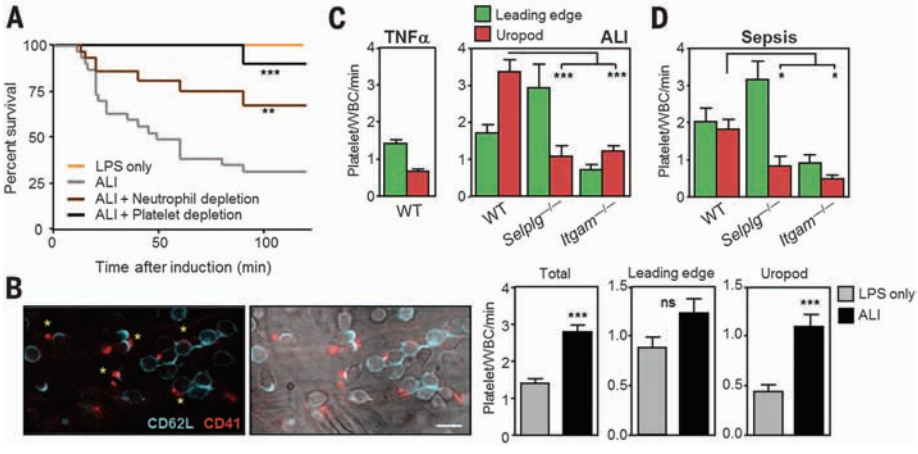


Fig. 3. PSGL-1 at the uropod becomes a preferred docking site for platelets during pathological inflammation. (**A**) Survival curves of Balb/c mice treated with lipopolysaccharide (LPS) alone or LPS plus anti–MHC-I (MHC, major histocompatibility complex) to induce ALI. Neutrophils were depleted using anti-Ly6G, and platelets using antiplatelet serum before the induction of ALI; n = 5 to 20 mice. (**B**) (Left) Representative micrographs of inflamed venules during ALI. The asterisks indicate platelets interacting with the uropod of neutrophils. (Right) Quantification of platelet interactions with the leading edge or uropod in control (LPS only) and ALI-induced mice. Scale bar, 10 μm. n = 3 to 4 mice, 32 to 73 interactions. (**C**) Frequency of interactions with the leading edge or uropod in TNF-α–treated or ALI-induced mice, and distribution of interactions in wild-type mice and mice deficient in PSGL-1 (*Selplg*$^{-/-}$) or Mac-1 (*Itgam*$^{-/-}$); n = 3 to 5 mice, 23 to 137 interactions. (**D**) Frequency of interactions with the leading edge or uropod during sepsis in wild-type mice and mice deficient in PSGL-1 or Mac-1. n = 3 to 4 mice, 32 to 56 interactions. Bars show mean ± SEM. *P < 0.05; ***P < 0.001 as determined by ANOVA with Tukey's multigroup test.

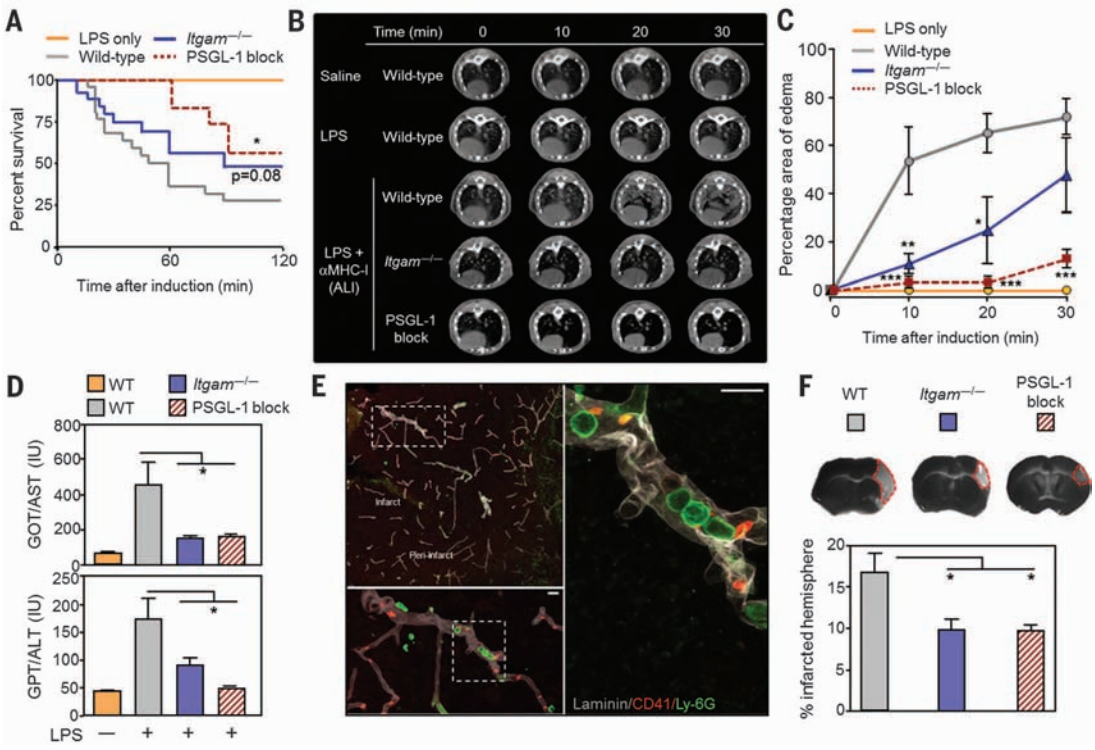


Fig. 4. PSGL-1–mediated interactions trigger vascular injury. (**A**) Survival curves of Balb/c mice treated with LPS alone or LPS plus anti–MHC-I to induce ALI. The absence of Mac-1 or inhibition of PSGL-1 protects from death; $n = 5$ to 19 mice. (**B**) Representative axial slices of the thorax of Balb/c mice at different times after induction of ALI. The white signal in the pulmonary space identifies edema, which is quantified in (**C**); $n = 7$ to 8 mice per group. (**D**) Quantification of hepatic injury as levels of AST and ALT transaminases in plasma of the indicated group of mice 24 hours after treatment with LPS; $n = 7$ to 11 mice. (**E**) Representative brain sections of wild-type mice 24 hours after inducing ischemia, showing vessels at increasing magnifications and intravascular neutrophil (Ly6G, green)–platelet (CD41, red) aggregates. Scale bars, 10 μm. (**F**) Percentages of infarcted hemispheres 24 hours after arterial occlusion in control wild-type mice, mice deficient in Mac-1 ($Itgam^{-/-}$), and wild-type mice after blocking PSGL-1. Images are representative brain sections stained with TTC, showing the extent of ischemia as white areas with a red outline; $n = 5$ to 8 mice. Bars show mean ± SEM. *$P < 0.05$; **$P < 0.01$; ***$P < 0.001$, ANOVA with Tukey's multigroup test.

that additional platelet-derived mediators and unknown neutrophil receptors that mediate platelet interactions can regulate crawling. Thus, intact distribution of and signaling through PSGL-1 at the uropod regulates neutrophil crawling, at least in part by orchestrating the appropriate distribution of adhesive and chemotactic receptors.

We next explored how this phenomenon might contribute to pathogenic inflammation. We used a model of acute lung injury (ALI) in Balb/c mice that closely simulates transfusion-related ALI (*18*). In this model, the transient elimination of neutrophils or platelets protects from death [Fig. 3A and (*19*)], indicating that this might be an appropriate model to study the functional partnership between these cells. Intravital analyses of the cremaster microvessels in ALI-induced mice confirmed the findings in crawling kinetics, receptor distribution, and luminal or lateral projections made using TNF-α (fig. S12 and movie S10) and further revealed that during ALI, the uropod becomes the predominant domain for platelet interactions, which contrasted with the preferred use of the leading edge in the nonpathogenic TNF-α–induced model (Fig. 3, B and C). Interactions at the uropod during ALI were mediated by PSGL-1, whereas Mac-1 mediated interactions with both domains (Fig. 3C and fig. S13). We obtained similar responses in a model of endotoxemia (Fig. 3D), indicating that during pathological inflammation, the uropod becomes the dominant interacting domain for circulating platelets.

To test whether the engagement of PSGL-1 at the uropod was causally related to neutrophil-mediated vascular inflammation, we explored its contribution in the model of ALI. Intravital imaging of the pulmonary microcirculation revealed a rapid increase in platelets captured by recruited neutrophils that were strongly inhibited by blocking PSGL-1 (fig. S14). In addition, deficiency in PSGL-1 or Mac-1, or inhibition of PSGL-1, resulted in moderate protection from ALI-induced death (Fig. 4A and fig. S15A). The use of computed tomography to track pulmonary edema over time revealed partial protection from ALI in mice deficient in Mac-1 and almost complete protection when PSGL-1 interactions were blocked (Fig. 4, B and C). This protection correlated with reduced neutrophil infiltrates in the lung (fig. S16) and suggested that interactions at the uropod critically contribute to vascular injury. Deficiency in either receptor or inhibition of PSGL-1 also prevented hepatic damage during endotoxemia (Fig. 4D and fig. S15B). Consistent with previous reports (*20*, *21*), we detected elevations in the plasma levels of neutrophil-derived extracellular traps (NETs) during ALI and sepsis. These elevations were completely blunted when platelets were depleted, by blocking PSGL-1, or in the absence of Mac-1 (fig. S17), suggesting that other forms of neutrophil activation can be triggered upon platelet interactions through PSGL-1.

Finally, we examined whether PSGL-1–mediated interactions also underlie ischemic injury, a prevalent form of vascular disease (*22*). We used a model of stroke triggered by permanent occlusion of the middle cerebral artery, in which neutrophil depletion significantly reduces tissue death as measured by the percentage of infarcted hemisphere [fig. S18 and (*23*))] Interactions between neutrophils and platelets within the microvasculature of infarcted brains were inhibited by blocking PSGL-1 (Fig. 4E and fig. S19), and this correlated with significant reductions in infarct volumes when PSGL-1 was inhibited or in the absence of Mac-1 (Fig. 4F).

We have uncovered a critical checkpoint during the early stages of inflammation: Neutrophils recruited to injured vessels extend a domain into the lumen, where PSGL-1 clusters scan for the presence of activated platelets. Only when productive interactions occur do neutrophils organize additional receptors needed for intravascular migration or generate NETs, and inflammation ensues (fig. S20 and movie S11). Our findings reveal that the dynamic reorganization of neutrophil domains and receptors allows simultaneous interactions with both the vascular wall and activated platelets in the circulation to provide a rapid and efficient regulatory mechanism early during inflammation.

REFERENCES AND NOTES

1. M. Phillipson, P. Kubes, *Nat. Med.* **17**, 1381–1390 (2011).
2. K. Ley, C. Laudanna, M. I. Cybulsky, S. Nourshargh, *Nat. Rev. Immunol.* **7**, 678–689 (2007).
3. M. Phillipson *et al.*, *J. Exp. Med.* **203**, 2569–2575 (2006).

4. K. F. Swaney, C. H. Huang, P. N. Devreotes, *Annu. Rev. Biophys.* **39**, 265–289 (2010).
5. A. J. Ridley *et al.*, *Science* **302**, 1704–1709 (2003).
6. F. Sánchez-Madrid, J. M. Serrador, *Nat. Rev. Mol. Cell Biol.* **10**, 353–359 (2009).
7. For more details on this and other procedures, please refer to the Materials and Methods section in the Supplemental Materials.
8. A. Hidalgo *et al.*, *Nat. Med.* **15**, 384–391 (2009).
9. J. W. Semple, J. E. Italiano Jr., J. Freedman, *Nat. Rev. Immunol.* **11**, 264–274 (2011).
10. M. L. von Brühl *et al.*, *J. Exp. Med.* **209**, 819–835 (2012).
11. K. L. Moore *et al.*, *J. Cell Biol.* **128**, 661–671 (1995).
12. E. Y. Chiang, A. Hidalgo, J. Chang, P. S. Frenette, *Nat. Methods* **4**, 219–222 (2007).
13. Y. Kunisaki *et al.*, *J. Cell Biol.* **174**, 647–652 (2006).
14. A. Zarbock, K. Ley, R. P. McEver, A. Hidalgo, *Blood* **118**, 6743–6751 (2011).
15. K. Szczur, Y. Zheng, M. D. Filippi, *Blood* **114**, 4527–4537 (2009).
16. J. J. Miner *et al.*, *Blood* **112**, 2035–2045 (2008).
17. B. McDonald *et al.*, *Science* **330**, 362–366 (2010).
18. M. R. Looney, B. M. Gilliss, M. A. Matthay, *Curr. Opin. Hematol.* **17**, 418–423 (2010).
19. M. R. Looney *et al.*, *J. Clin. Invest.* **119**, 3450–3461 (2009).
20. A. Caudrillier *et al.*, *J. Clin. Invest.* **122**, 2661–2671 (2012).
21. S. R. Clark *et al.*, *Nat. Med.* **13**, 463–469 (2007).
22. G. A. Donnan, M. Fisher, M. Macleod, S. M. Davis, *Lancet* **371**, 1612–1623 (2008).
23. M. I. Cuartero *et al.*, *Stroke* **44**, 3498–3508 (2013).

ACKNOWLEDGMENTS

We thank G. Crainiciuc, J. A. Quintana, I. Ortega, and A. Santos for technical support and D. Sancho and S. González for insightful comments. The data presented in this manuscript can be found in the main paper and supplementary materials. This study was supported by NIH grants HL03463, HL085607 (R.P.M.), and HL090676 (M.-D.F.); German Research Foundation grants ZA428/8-1, ZA428/6-1, and SFB 1009-TP A05 (A.Z.); FP7 Marie Curie (ITN-264864; π-net) and S2010/BMD-2326 from Comunidad de Madrid (J.R-C.); Grants-in-Aid for Scientific Research from the Japan Society for the Promotion of Science (Y.F.); CSD2010-00045 and SAF2012-33216 from Ministerio de Economia y Competitividad (MINECO) and S2010/BMD-2336 from Comunidad de Madrid (M.A.M.); and a Ramón y Cajal Fellowship (RYC-2007-00697), SAF2009-11037 and 2012-31142 from MINECO, S2010/BMD-2314 from Comunidad de Madrid, and 246655 from FP7-People-IRG Program (A.H.). The CNIC is supported by the MINECO and the Pro-CNIC Foundation. R.P.M. is cofounder of Selexys Pharmaceuticals, which is developing monoclonal antibodies to PSGL-1 and P-selectin to treat inflammatory and thrombotic diseases. A patent application for the blockade of PSGL-1 in thromboinflammation has been filed by V.S. and A.H. (EP14382425.8). The authors declare no other conflicts of interest.

SUPPLEMENTARY MATERIALS

www.sciencemag.org/content/346/6214/1234/suppl/DC1
Materials and Methods
Figs. S1 to S20
Tables S1 and S2
References (*24*–*29*)
Movies S1 to S11

27 May 2014; accepted 7 November 2014
10.1126/science.1256478

TRANSCRIPTION

Chromatin decondensation is sufficient to alter nuclear organization in embryonic stem cells

Pierre Therizols, Robert S. Illingworth, Celine Courilleau, Shelagh Boyle, Andrew J. Wood, Wendy A. Bickmore*

During differentiation, thousands of genes are repositioned toward or away from the nuclear envelope. These movements correlate with changes in transcription and replication timing. Using synthetic (TALE) transcription factors, we found that transcriptional activation of endogenous genes by a viral trans-activator is sufficient to induce gene repositioning toward the nuclear interior in embryonic stem cells. However, gene relocation was also induced by recruitment of an acidic peptide that decondenses chromatin without affecting transcription, indicating that nuclear reorganization is driven by chromatin remodeling rather than transcription. We identified an epigenetic inheritance of chromatin decondensation that maintained central nuclear positioning through mitosis even after the TALE transcription factor was lost. Our results also demonstrate that transcriptional activation, but not chromatin decondensation, is sufficient to change replication timing.

Radial nuclear organization of the genome is conserved in eukaryotes (*1*), with an accumulation of heterochromatin, gene-poor and late-replicating chromatin domains found near the nuclear envelope (*2*). Lamin-associated domains (LADs) are gene-poor, show low levels of transcription, and are depleted for active histone marks (*3*). Artificial tethering to the nuclear envelope has demonstrated that a peripheral nuclear environment is sufficient to induce transcriptional down-regulation of both reporter genes and some endogenous genes in somatic cells (*4*, *5*), and during differentiation many genes change their association with components of the nuclear lamina—often correlated with altered gene expression (*6*). However, these correlations do not determine whether relocalization relative to the nuclear periphery is a cause or a consequence of gene regulation during differentiation.

Two-thirds of the genes that lose lamin B1 association during differentiation of embryonic stem cells (ESCs) to neural precursor cells (NPCs) are transcriptionally up-regulated. The others are more likely to be strongly activated later in differentiation (*6*). *Ptn*, *Sox6*, and *Nrp1* are three genes that are up-regulated during ESC differentiation (*7*); they exhibit some of the largest losses of lamin B1 association during ESC-to-NPC differentiation (*6*) and, concomitantly, *Ptn* loses its peripheral nuclear position (*8*). The expression of *Ptn* and *Nrp1* begins to increase as ESCs differentiate into epiblast stem cells (EpiSCs) (Fig. 1B). Although there are no data on LADs in EpiSCs, fluorescence in situ hybridization (FISH) showed that *Ptn*, *Sox6*, and *Nrp1* loci relocate away from the nuclear periphery and toward more central nuclear positions, correlated to their expression changes, during the differentiation of ESCs to EpiSCs or to NPCs ($P < 0.01$; Fig. 2B and fig. S1).

To directly address the role of transcription in nuclear reorganization, we ectopically activated *Ptn*, *Sox6*, or *Nrp1* in ESCs by means of synthetic transcription factors composed of TALE (transcription activator–like effector) DNA binding domains with specificity for the respective gene promoters (*9*) fused to VP64, a tetramer of the VP16 acidic transcriptional activator (*10*, *11*) (Fig. 1A). When transfected into ESCs, tPtn-VP64 induced expression of its target by a factor of >30 to 90 (Fig. 1, B and C). Other than *Ptn*, only two additional genes (*Il33* and *Nnmt*) were significantly up-regulated, and genes involved in ESC pluripotency or differentiation were not significantly changed. This suggests that *Ptn* up-regulation is not just an indirect consequence of differentiation triggered by transfection or the nonspecific expression of an acidic activator (Fig. 1C and fig. S2). Specific activation of *Nrp1* or *Sox6* in cells transfected by tNrp1-VP64 or tSox6-VP64, respectively, also showed no expression signature of differentiation (Fig. 1B). Control plasmids lacking the VP64 domain (tPtn-Δ, tSox6-Δ, and tNrp1-Δ) had almost no effect (Fig. 1, B and C). Moreover, we did not detect any changes in the expression of genes neighboring those targeted by the TALEs (Fig. 1C and fig. S3).

As well as activating *Ptn*, *Nrp1*, or *Sox6*, FISH showed that tPtn-VP64, tNrp1-VP64, and tSox6-VP64 caused specific relocalization of the targeted loci toward the center of ESC nuclei, relative to control [enhanced green fluorescent protein (eGFP)] transfection (tPtn-VP64, $P = 4.6 \times 10^{-9}$; tNrp1-VP64, $P = 5.3 \times 10^{-14}$; tSox6-VP64, $P = 6.4 \times 10^{-12}$) or to constructs lacking the activation domain (tPtn-Δ, $P = 3 \times 10^{-6}$; tNrp1-Δ, $P = 8.1 \times 10^{-10}$; tSox6-Δ, $P = 8 \times 10^{-12}$) (Fig. 2, A and B). The extent of this relocalization was similar to that seen upon normal

MRC Human Genetics Unit, Institute of Genetics and Molecular Medicine, University of Edinburgh, Crewe Road, Edinburgh EH4 2XU, UK.
*Corresponding author. E-mail: wendy.bickmore@igmm.ed.ac.uk

differentiation of ESCs to EpiSCs or NPCs (Fig. 2B and fig. S1). tPtn-VP64 and tNrp1-VP64 did not significantly affect radial positioning of *Sox6* (tPtn-VP64, $P = 0.56$; tNrp1-VP64, $P = 0.06$), and tSox6-VP64 did not affect *Nrp1* positioning ($P = 0.08$) (fig. S4, A to C). This reinforces the idea that TALE transfection does not simply induce differentiation. We conclude that forced *Ptn*, *Nrp1*, or *Sox6* expression induces relocalization of the targeted loci toward the center of the nucleus, independent of differentiation. This is consistent with a report

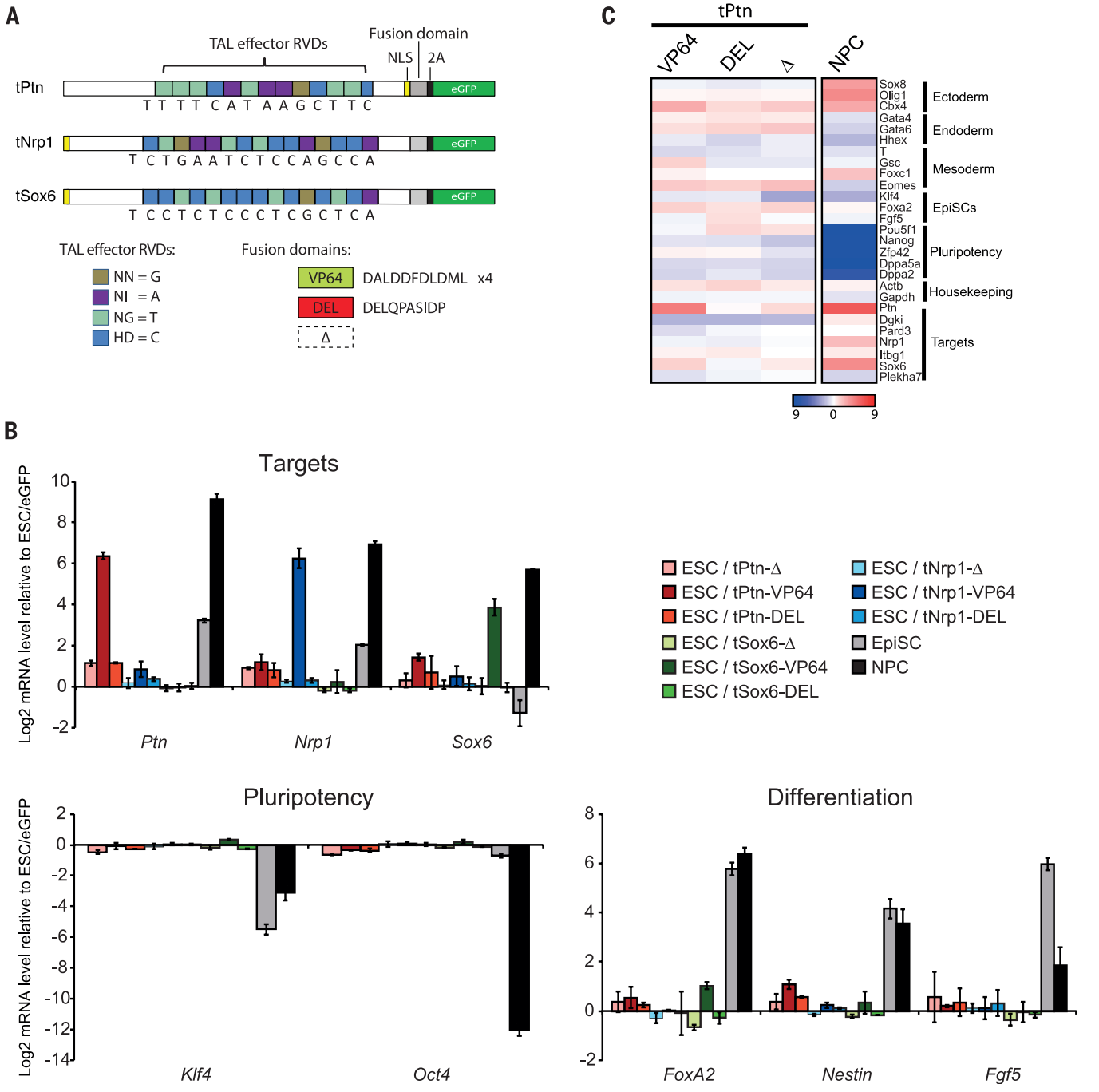


Fig. 1. TAL effector (TALE) transcription factor induces transcriptional activation in mouse ESCs. (**A**) Schematics of TALE constructs specific for *Ptn*, *Nrp1*, and *Sox6*. DNA binding domains were fused to either four repeats of VP16 (VP64) or DELQPASIDP peptide (*13*). Constructs (Δ) with the VP64 domain removed served as a negative control. Expression of eGFP from the same construct via a self-cleaving (2A) peptide allows for isolation of cells expressing the construct by fluorescence-activated cell sorting (FACS). Amino acid abbreviations: A, Ala; D, Asp; E, Glu; F, Phe; I, Ile; L, Leu; M, Met; P, Pro; Q, Gln; S, Ser. RVD, repeat variable diresidue. (**B**) Mean (± SEM) $\log_2$ mRNA level, established by quantitative reverse transcription polymerase chain reaction (RT-PCR), for TALE target genes (*Ptn*, *Nrp1*, *Sox6*), genes involved in pluripotency (*Klf4*, *Oct4*), or genes involved in differentiation (*FoxA2*, *Nestin*, *Fgf5*) in ESCs transfected with the different TALE vectors. Expression is shown relative to eGFP transfection. Expression changes are also shown for the differentiation of ESCs to EpiSCs or NPCs ($n = 3$ biological replicates). (**C**) Heat map showing 27 genes from the expression microarray selected to represent different differentiation states, as well as genes surrounding the regions targeted by the TALEs. Log_2 transformed mRNA ratios for ESCs transfected by the different tPtn constructs relative to eGFP transfection, or for cells differentiated into NPCs relative to levels in ESCs, are displayed using the color code shown.

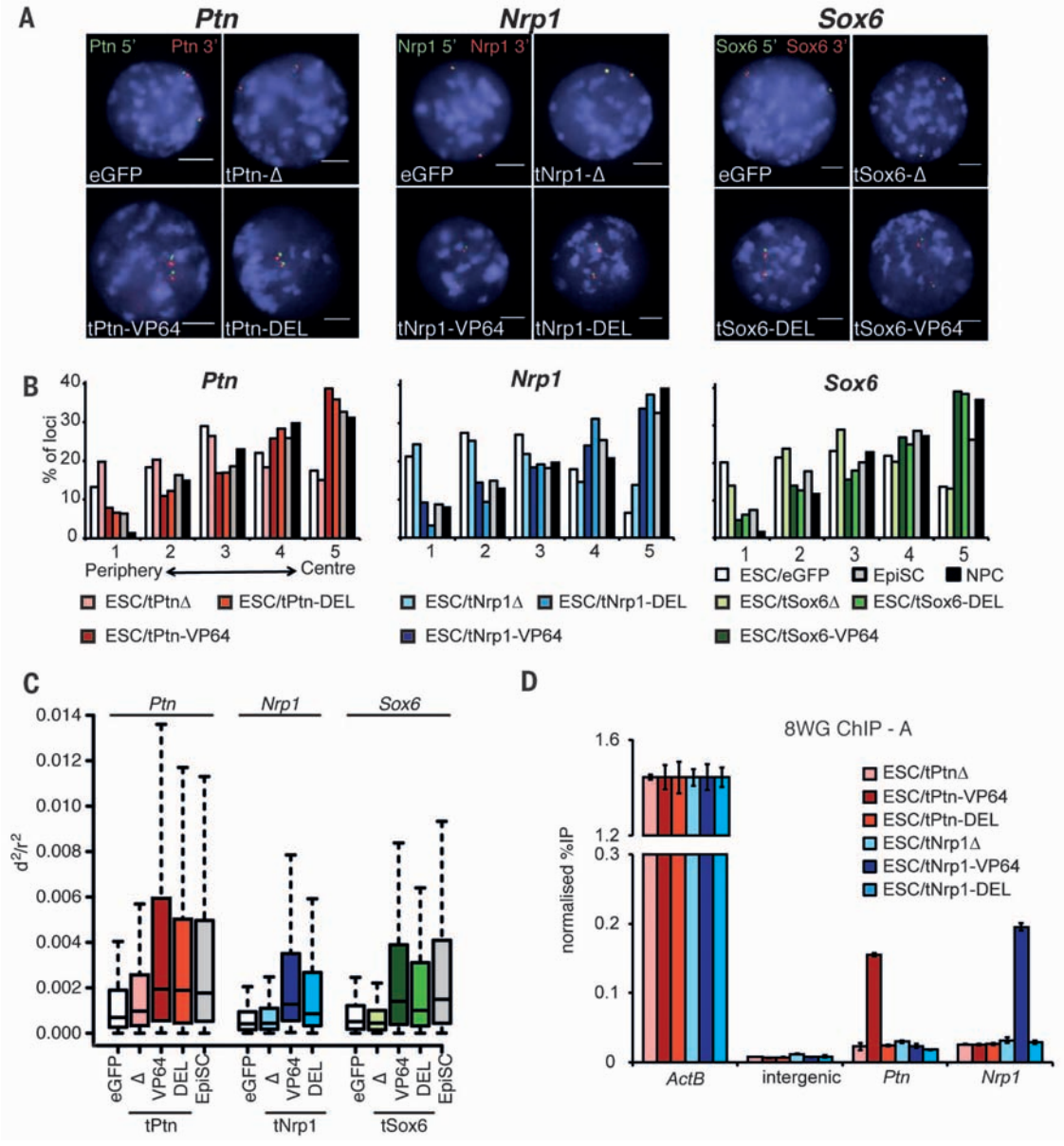


Fig. 2. Synthetic chromatin decondensation causes gene relocalization. (**A**) FISH with probes flanking *Ptn* (left), *Nrp1* (center), and *Sox6* (right) in nuclei of ESCs transfected by eGFP or the -Δ, -VP64, and -DEL TALEs targeting *Ptn*, *Nrp1*, and *Sox6*. Nuclei were counterstained with 4′,6-diamidino-2-phenylindole (DAPI; blue). Scale bars, 5 μm. (**B**) Distribution of *Ptn*, *Nrp1*, and *Sox6* hybridization signals across five concentric shells eroded from the periphery (shell 1) through to the center (shell 5) of the nucleus (fig. S1A) in ESCs transfected by eGFP or the different TALE constructs, or for ESCs differentiated to EpiSCs and NPCs (n = 100 to 150 nuclei for at least two biological replicates). (**C**) Box plots showing the distribution of normalized squared interprobe distances (d^2/r^2) at *Ptn* (left), *Nrp1* (center), and *Sox6* (right) in ESCs transfected by eGFP (open bars) or the corresponding TALEs. Untransfected EpiSCs differentiated from ESCs are shown for comparison (dark gray). Shaded boxes show the median and interquartile range of the data (n = 100 to 150 nuclei). See table S1 for statistical analysis. (**D**) ChIP for RNAPII (8WG antibody) at *Actb*, *Ptn*, and *Nrp1* promoters and at an intergenic negative control, in ESCs transfected by tPtn-Δ, tPtn-VP64, tPtn-DEL, tNrp1-Δ, tNrp1-VP64, or tNrp1-DEL. Enrichment is shown as mean percentage input bound ± SD over three technical replicates of biological replicate A (replicate B is shown in fig. S5).

showing that targeting of VP16 to lamin B1–associated sequences disrupts chromatin at the nuclear periphery in somatic cells, although in that case, this could not be linked to specific effects on transcription (*12*).

To dissect which step of gene activation is required for gene repositioning, we replaced the VP64 domain of the TALE transcription factors with an acidic peptide, DELQPASIDP, which is known to decondense chromatin when targeted to an artificial transgene array in somatic cells but without activating transcription; this yielded the constructs tPtn-DEL, tNrp1-DEL, and tSox6-DEL (Fig. 1, B and C) (*13*). We confirmed the absence of significant gene expression changes in cells transfected with t-DEL constructs (Fig. 1, B and C, and fig. S2). Analysis of normalized mean squared interprobe distances (d^2/r^2) (*14*) between FISH probes flanking *Ptn*, *Nrp1*, and *Sox6* revealed that DEL peptide recruitment caused significant chromatin decondensation across the targeted loci relative to the eGFP control (tPtn-DEL, $P = 2.4 \times 10^{-6}$; tNrp1-DEL, $P = 6.1 \times 10^{-10}$; tSox6-DEL, $P = 3.6 \times 10^{-6}$; Fig. 2C and table S1). In contrast, constructs lacking a trans-activation domain had no effect. The effect of the DEL peptide on chromatin decondensation was similar to that observed with VP64 and to that seen at *Ptn* and *Sox6* upon differentiation of ESCs to EpiSCs (Fig. 2C and table S1). Chromatin decondensation at *Ptn*, *Nrp1*, or *Sox6* induced by their respective t-DELs was accompanied by relocation of the respective loci toward the nuclear center (tPtn-DEL, $P = 6.22 \times 10^{-6}$; tNrp1-DEL, $P = 3.4 \times 10^{-23}$; tSox6-DEL, $P = 1.8 \times 10^{-8}$; Fig. 2B). The nuclear repositioning induced by DEL peptide was similar to that induced by VP64 (tPtn-VP64, $P = 0.93$; tNrp1-VP64, $P = 0.03$; tSox6-VP64, $P = 0.9$). Neither tPtn nor tNrp1 affected *Sox6* condensation, and *Nrp1* condensation was not affected by TALEs targeting *Sox6* (fig. S4D and table S1). We also did not observe any off-target effects for TALE-DEL proteins on radial positioning (fig. S4, A to C). Using chromatin immunoprecipitation (ChIP) for RNA polymerase II (RNAPII) (*9*), we confirmed that the effect of the DEL peptide was independent of the transcription

machinery. We observed RNAPII recruitment at *Ptn* and *Nrp1* promoters in cells transfected by tPtn-VP64 and tNrp1-VP64, respectively; no significant enrichment was observed with tPtn-DEL or tNrp1-DEL (Fig. 2D and fig. S5).

Mitosis is followed by stochastic repositioning of LADs and late-replicating domains to the nuclear periphery (*12*, *15*, *16*). However, it is not clear to what extent this reestablishment of nuclear organization depends on the persistence of transcriptional states or chromatin structure. We therefore examined nuclear repositioning of *Ptn* after loss of the original stimulus. TALE plasmid transfections of ESCs were transient; hence, GFP expression from the

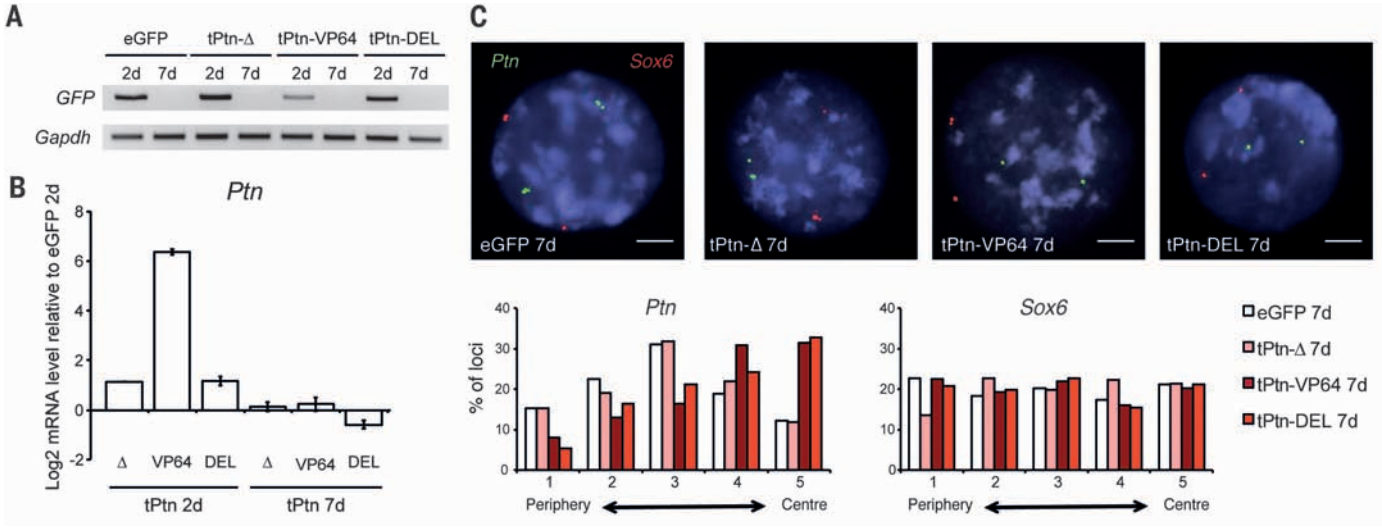


Fig. 3. Central nuclear positioning is maintained after loss of gene induction. (**A**) RT-PCR of *Gfp* mRNA in ESC, 2 or 7 days after transfection with tPtn-Δ, tPtn-VP64, or tPtn-DEL. *Gapdh* serves as a constitutively expressed control. (**B**) Mean (± SEM) $\log_2$ mRNA level for *Ptn* in ESCs 2 days (left) or 7 days (right) after transfection with tPtn-Δ, tPtn-VP64, or tPtn-DEL. Expression is shown relative to eGFP transfection (n = 3; one technical and two biological replicates). (**C**) FISH at *Ptn* (green) and *Sox6* (red) in ESCs 7 days after transfection by eGFP, tPtn-Δ, tPtn-VP64, or tPtn-DEL. Scale bars, 5 μm. Histograms below quantify the nuclear distribution of *Ptn* and *Sox6* signals (as in Fig. 2B) for ESCs 7 days after transfection by eGFP, tPtn-Δ, tPtn-VP64, and tPtn-DEL (n = 100 to 150 nuclei for each condition for each of at least two biological replicates).

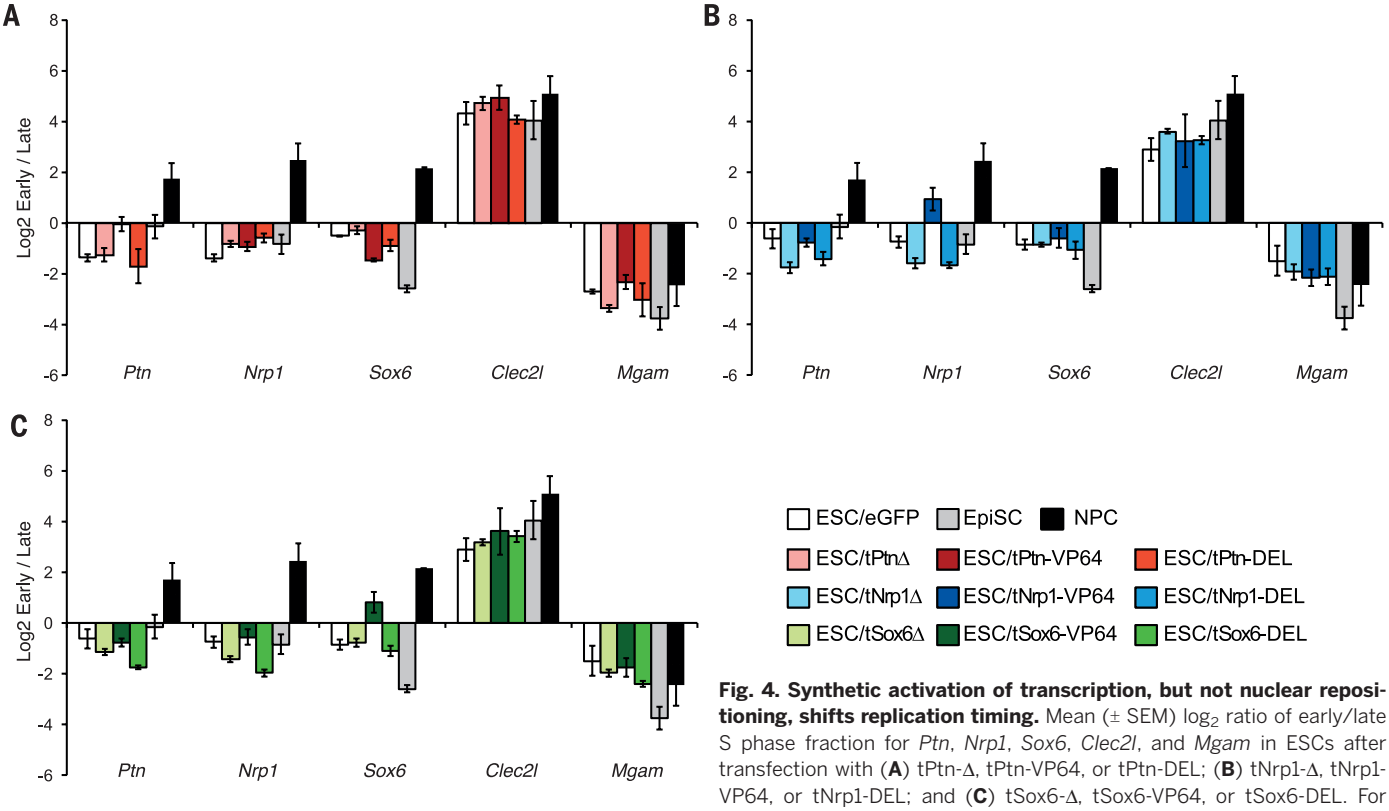


Fig. 4. Synthetic activation of transcription, but not nuclear repositioning, shifts replication timing. Mean (± SEM) $\log_2$ ratio of early/late S phase fraction for *Ptn*, *Nrp1*, *Sox6*, *Clec2l*, and *Mgam* in ESCs after transfection with (**A**) tPtn-Δ, tPtn-VP64, or tPtn-DEL; (**B**) tNrp1-Δ, tNrp1-VP64, or tNrp1-DEL; and (**C**) tSox6-Δ, tSox6-VP64, or tSox6-DEL. For comparison, changes in replication timing during differentiation of ESCs to EpiSCs or NPCs are included in all panels. Transfection with eGFP is also shown at left of each group in all panels.

constructs was no longer detected after 7 days in culture (Fig. 3A). Concomitant with overall loss of the tPtn-VP64 plasmid, 7 days after transfection *Ptn* expression had returned close to its level in ESCs, although we cannot exclude some cell-to-cell heterogeneity (Fig. 3B). However, *Ptn* remained in a more central nuclear position at this time point after both tPtn-VP64 and tPtn-DEL transfections ($P = 6.5 \times 10^{-9}$ and 4.73×10^{-8} relative to eGFP; Fig. 3C). This suggests that there might be epigenetic inheritance of an altered radial nuclear position, at least for the tested *Ptn* locus.

Late-replicating DNA is concentrated around the nuclear periphery; transcriptional activation and gene relocation away from the nuclear envelope often correlate with a shift to an earlier replication time during S phase (*8*, *17*, *18*). Indeed, replication timing of *Ptn*, *Nrp1*, and *Sox6* shifts from late to early S phase during ESC-to-NPC differentiation (*18*). We confirmed the late replication timing of *Ptn* in undifferentiated ESCs and its progressive shift to earlier time points during differentiation (Fig. 4). *Nrp1* and *Sox6* remained late-replicating in EpiSCs but became early-replicating in NPCs. *Clec2l* and *Mgam* regions served as early- and late-replicating controls, respectively, and their replication timing remained unchanged during ESC differentiation.

To dissect the relationships among transcription, chromatin decondensation, nuclear positioning, and replication timing, we measured the effect of the different TALE constructs on the replication timings of *Ptn*, *Nrp1*, and *Sox6* in ESCs (*9*). TALEs lacking an activation domain (Δ) had no effect, but TALE-VP64–mediated activation was sufficient to advance the replication timing of the targeted locus (Fig. 4), with no detectable off-target effects on the other tested loci. In contrast, the DEL peptide, which decondensed chromatin (Fig. 2C) and relocated (Fig. 2B) the targeted locus without inducing expression (Fig. 1, B and C) or recruiting RNAPII (Fig. 2D), had no effect on replication timing (Fig. 4). This demonstrates that neither chromatin decondensation nor nuclear relocalization are sufficient to shift replication time, and suggests that the switch to early replication requires the activation of gene expression. This conclusion is reinforced by the analysis of replication timing 7 days after tPtn-VP64 transient transfection, by which time *Ptn* activation was lost. At this time point, *Ptn* had returned to a late-replicating state (fig. S6), even though it retained a central radial nuclear position (Fig. 3C). We therefore conclude that altered replication timing is likely to be a direct consequence of transcription.

Our data suggest that the global nuclear reorganization observed during early embryogenesis could be the consequence of chromatin regulation. This could happen concomitantly with transcription changes, as for *Ptn* or *Nrp1* that are both repositioned (Fig. 2B and fig. S1) and up-regulated (Fig. 1B) in EpiSCs, or it could occur independently, as for *Sox6*, which we found to decondense and relocate in EpiSCs without any detectable transcriptional changes. A full dissection of chromatin events mediated by the DEL peptide, and those present at targeted genes after loss of the original TALE transcription factor, would give further insight into the mechanisms involved.

REFERENCES AND NOTES

1. P. Meister, A. Taddei, *Curr. Opin. Genet. Dev.* **23**, 96–103 (2013).
2. A. Akhtar, S. M. Gasser, *Nat. Rev. Genet.* **8**, 507–517 (2007).
3. L. Guelen *et al.*, *Nature* **453**, 948–951 (2008).
4. L. E. Finlan *et al.*, *PLOS Genet.* **4**, e1000039 (2008).
5. K. L. Reddy, J. M. Zullo, E. Bertolino, H. Singh, *Nature* **452**, 243–247 (2008).
6. D. Peric-Hupkes *et al.*, *Mol. Cell* **38**, 603–613 (2010).
7. T. S. Mikkelsen *et al.*, *Nature* **448**, 553–560 (2007).
8. I. Hiratani *et al.*, *PLOS Biol.* **6**, e245 (2008).
9. See supplementary materials on *Science* Online.
10. F. Zhang *et al.*, *Nat. Biotechnol.* **29**, 149–153 (2011).
11. Q. Ding *et al.*, *Cell Stem Cell* **12**, 238–251 (2013).
12. J. Kind *et al.*, *Cell* **153**, 178–192 (2013).
13. A. E. Carpenter, S. Memedula, M. J. Plutz, A. S. Belmont, *Mol. Cell. Biol.* **25**, 958–968 (2005).
14. R. Eskeland *et al.*, *Mol. Cell* **38**, 452–464 (2010).
15. D. S. Dimitrova, D. M. Gilbert, *Mol. Cell* **4**, 983–993 (1999).
16. I. Thomson, S. Gilchrist, W. A. Bickmore, J. R. Chubb, *Curr. Biol.* **14**, 166–172 (2004). 10.1016/j.cub.2003.12.024
17. R. R. Williams *et al.*, *J. Cell Sci.* **119**, 132–140 (2006).
18. I. Hiratani *et al.*, *Genome Res.* **20**, 155–169 (2010).

ACKNOWLEDGMENTS

We thank E. Freyer for FACS analysis, A. Tsakiridis and A. Lavigni for cell culture assistance, P. Perry for help with image analysis, and P. Madapura-Marulasiddappa and N. Gilbert for their insightful comments. Supported by a Marie Curie Intra European Fellowship (P.T.), Sir Henry Wellcome and Sir Henry Dale Fellowships from the Wellcome Trust (A.J.W.), the UK Medical Research Council, and European Research Council advanced grant 249956. The Gene Expression Omnibus accession number for microarray expression data is GSE62379.

SUPPLEMENTARY MATERIALS

www.sciencemag.org/content/346/6214/1238/suppl/DC1
Materials and Methods
Figs. S1 to S6
Tables S1 to S3
References (*19*–*25*)

4 August 2014; accepted 29 October 2014
10.1126/science.1259587

STRUCTURAL BIOLOGY

Time-resolved serial crystallography captures high-resolution intermediates of photoactive yellow protein

Jason Tenboer,[1] Shibom Basu,[2] Nadia Zatsepin,[3] Kanupriya Pande,[1] Despina Milathianaki,[4] Matthias Frank,[5] Mark Hunter,[5]* Sébastien Boutet,[4] Garth J. Williams,[4] Jason E. Koglin,[4] Dominik Oberthuer,[6] Michael Heymann,[7] Christopher Kupitz,[2]† Chelsie Conrad,[2] Jesse Coe,[2] Shatabdi Roy-Chowdhury,[2] Uwe Weierstall,[3] Daniel James,[3] Dingjie Wang,[3] Thomas Grant,[8] Anton Barty,[7] Oleksandr Yefanov,[7] Jennifer Scales,[1] Cornelius Gati,[6,7] Carolin Seuring,[6] Vukica Srajer,[9] Robert Henning,[9] Peter Schwander,[1] Raimund Fromme,[2] Abbas Ourmazd,[1] Keith Moffat,[9,10] Jasper J. Van Thor,[11] John C. H. Spence,[3] Petra Fromme,[2] Henry N. Chapman,[6,7] Marius Schmidt[1]‡

Serial femtosecond crystallography using ultrashort pulses from x-ray free electron lasers (XFELs) enables studies of the light-triggered dynamics of biomolecules. We used microcrystals of photoactive yellow protein (a bacterial blue light photoreceptor) as a model system and obtained high-resolution, time-resolved difference electron density maps of excellent quality with strong features; these allowed the determination of structures of reaction intermediates to a resolution of 1.6 angstroms. Our results open the way to the study of reversible and nonreversible biological reactions on time scales as short as femtoseconds under conditions that maximize the extent of reaction initiation throughout the crystal.

X-ray structure analysis has successfully determined high-resolution structures of more than 100,000 proteins and nucleic acids. But these structures represent static pictures of the biomolecules, which during their reactions engage in rapid dynamic motion. Time-resolved macromolecular crystallography (TRX) (*1*) unifies structure determination with protein kinetics, as both can be determined from the same set of data (*2*, *3*). TRX is traditionally performed using pump-probe experiments and the Laue method at a synchrotron source, in which light-sensitive molecules within a crystal at near-physiological temperature are illuminated by a laser pump pulse to initiate their reaction, followed by a polychromatic probe x-ray pulse. These experiments rely on the exceptional stability of synchrotron sources to measure small, time-dependent differences between diffraction patterns with and without the pump laser pulse. Synchrotron-based Laue diffraction experiments are currently restricted by the x-ray beam brilliance to strongly scattering, relatively large (typically 6×10^5 μm^3) crystals, whose optical density

Downloaded from www.sciencemag.org on December 5, 2014

makes high (>25%), uniform reaction initiation difficult. Further, the time resolution is limited to ~100 ps by the duration of the probe x-ray pulse. However, difference electron density (DED) maps from synchrotron-based TRX experiments have revealed that large structural changes occur in times shorter than 100 ps (*4*–*7*). Important structural changes associated with key chemical processes such as isomerization evidently occur in the range of femtoseconds to tens of picoseconds, inaccessible to synchrotron experiments. The advent of free electron lasers such as the Linac Coherent Light Source (LCLS) and the SPring-8 Angstrom Compact Free-Electron Laser (SACLA) has opened a new avenue for ultrafast time-resolved structural studies. These lasers emit femtosecond pulses of hard x-rays whose peak brilliance is higher than that available at the most advanced synchrotrons by a factor of 10^9.

The method of serial femtosecond crystallography (SFX) (*8*) has opened new opportunities for time-resolved structural studies (*9*, *10*). In SFX, a stream of micro- or nanocrystals in their mother liquor at near-physiological temperature is delivered by a liquid jet injector (*11*) to the x-ray interaction region, where the diffraction pattern of a single tiny crystal is recorded by illuminating the jet with an individual x-ray pulse from the x-ray free electron laser (XFEL). Diffraction patterns are obtained rapidly (e.g., at 120 Hz) at the LCLS. Although enormous x-ray doses, up to 1000 times the room-temperature synchrotron "safe dose" (*12*), are deposited in the crystal by the femtosecond x-ray pulse, the processes that lead to destruction are sufficiently slow that the crystals diffract before they are destroyed (*8*, *13*, *14*). Structures are solved using thousands of diffraction patterns of individual crystals; these patterns extend to near-atomic resolution (*15*, *16*). To conduct a time-resolved SFX (TR-SFX) experiment at the XFEL with femtosecond time resolution, a reaction must be initiated in a light-sensitive crystal by a femtosecond laser pump pulse, then probed after a time delay Δt by a femtosecond x-ray probe pulse (*9*, *17*).

TR-SFX is challenging because of the very different properties of the x-ray pulses emitted by synchrotrons and by XFELs (*10*, *18*). Time-resolved synchrotron studies take advantage of an x-ray beam with exceptional stability, where ideally a data set is collected on one large single crystal at essentially constant beam energy, bandwidth, photon flux, and volume of the crystal exposed to the x-rays. The resulting data consist of sets of consecutive light and dark images collected at the same orientation from the large single crystal. This consistency of data acquisition is important, as structure factor changes between the light and dark states are often very small. By contrast, several inherent pulse-to-pulse variations make TR-SFX at atomic resolution challenging: (i) The XFEL photon flux per pulse can vary by up to an order of magnitude; (ii) the peak energy and spectral content of the x-ray beam changes from pulse to pulse; and (iii) the crystal size is variable, and even if it were constant, the volume of the crystal interacting with the beam can change. These factors give rise to large fluctuations in the diffracted intensities. However, the resulting total error is inversely proportional to the square root of the number of diffraction patterns (*18*), and by collecting diffraction patterns from a large number of tiny crystals, high-quality x-ray data can be obtained (*15*, *16*, *19*).

Despite these challenges, TR-SFX offers several advantages over time-resolved Laue crystallography at a synchrotron: (i) Time resolution, largely set by the duration of the x-ray pulse in the femtosecond time range, is substantially higher; (ii) the diffraction-before-destruction principle overcomes the x-ray damage problem; (iii) each crystal diffracts only once and crystals are rapidly exchanged, which provides an easy way to address irreversible processes; (iv) the quasi-monochromatic FEL x-ray beam allows investigation of crystals with large unit cells; (v) diffraction patterns are less sensitive to crystal mosaicity than in the Laue method; and (vi) the small size of the crystals (often <10 μm) allows more uniform laser initiation of the reaction of the molecules in the crystal. These advantages were exploited in the first TR-SFX studies of the large protein complexes, the photosystem I–ferredoxin complex and photosystem II, as model systems (*20*, *21*). Structural changes were recently discovered in a pump-probe TR-SFX study of the water-splitting complex in photosystem II at 5.5 Å resolution (*22*), but their interpretation remains provisional, in part because of the limited resolution.

We demonstrate that high-resolution, interpretable DED maps can be determined by applying TR-SFX to a well-studied model system: the bacterial blue light photoreceptor PYP (photoactive yellow protein). Upon absorption of a blue photon, PYP enters a photocycle in which numerous intermediates are occupied on time scales from femtoseconds to seconds (Fig. 1A) (*23*–*25*). Structural changes on time scales longer than 100 ps have been investigated to high resolution by time-resolved crystallography using the Laue method at synchrotrons (*4*, *5*, *26*). Even barriers of activation have now been determined solely from temperature-dependent time-resolved x-ray data (*3*). The photocycle examined by time-resolved crystallography contains six intermediates denoted I_T, I_{CT}, pR_1, pR_2, pB_1, and pB_2. The strongest features appear in the DED maps when pR_1 and pR_2 are substantially populated, because the sulfur of Cys^{69} to which the chromophore is covalently attached is considerably displaced in both these intermediates. This occurs between ~200 ns and 100 μs (Fig. 1B). For our TR-SFX experiments, we selected a delay time of 1 μs in order to clearly reveal these features. A second data set was collected at a delay of 10 ns, where three distinct intermediates are substantially populated whose interpretation requires high-quality data. The DED maps were calculated from x-ray data analyzed by Monte Carlo integration over a large number of diffraction patterns, each of which is subject to all the stochastic fluctuations outlined above (*18*). Comparison with synchrotron Laue data established that the DED maps determined by the two methods are very similar. These findings open the way to high-resolution TR-SFX studies of light-driven processes and, by extension, to reversible and nonreversible reactions that may be initiated by other methods.

We collected TR-SFX data for the dark and excited states in an interleaved mode by using two 20-Hz nanosecond lasers to initiate the reaction. Every third x-ray pulse probed a laser-

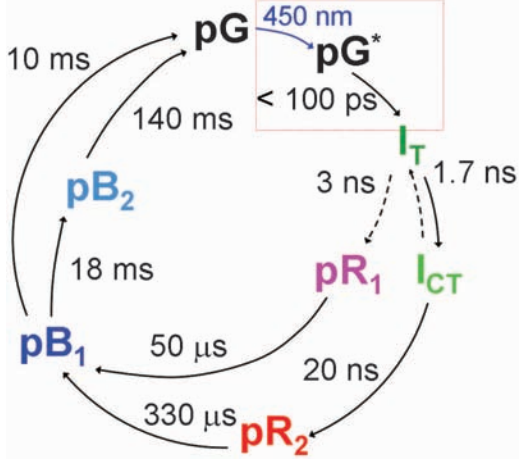


Fig. 1. Simplified PYP photocycle. The cycle is shown from the perspective of a time-resolved crystallographer (*3*, *4*, *26*). The dark state pG is activated by absorption of a blue photon (450 nm) to pG* that begins the photocycle. The crystal structures of longer-lived intermediate states I_T, I_{CT}, pR_1 (pR_{E46Q}), pR_2 (pR_{cw}), pB_1, and pB_2 are known.

[1]Physics Department, University of Wisconsin, Milwaukee, WI 53211, USA. [2]Department of Chemistry and Biochemistry, Arizona State University, Tempe, AZ 85287, USA. [3]Department of Physics, Arizona State University, Tempe, AZ 85287, USA. [4]Linac Coherent Light Source, SLAC National Accelerator Laboratory, Sand Hill Road, Menlo Park, CA 94025, USA. [5]Lawrence Livermore National Laboratory, Livermore, CA 94550, USA. [6]Centre for Ultrafast Imaging, University of Hamburg, 22761 Hamburg, Germany. [7]Center for Free Electron Laser Science, Deutsches Elektronen Synchrotron DESY, Notkestrasse 85, 22607 Hamburg, Germany. [8]Hauptman-Woodward Institute, State University of New York at Buffalo, 700 Ellicott Street, Buffalo, NY 14203, USA. [9]Center for Advanced Radiation Sources, University of Chicago, Chicago, IL 60637, USA. [10]Department of Biochemistry and Molecular Biology and Institute for Biophysical Dynamics, University of Chicago, Chicago, IL 60637, USA. [11]Faculty of Natural Sciences, Life Sciences, Imperial College, London SW7 2AZ, UK. *Present address: Linac Coherent Light Source, SLAC National Accelerator Laboratory, Sand Hill Road, Menlo Park, CA 94025, USA. †Present address: Physics Department, University of Wisconsin, Milwaukee, WI 53211, USA. **‡Corresponding author. E-mail: m-schmidt@uwm.edu**

excited crystal, resulting in a light-dark-dark scheme (fig. S1). The time-resolved data sets were obtained for pump-probe delay times of 10 ns and 1 μs, at a laser pulse energy of 15 μJ focused to a 150-μm beam diameter at the sample (~800 μJ/mm^2). The microcrystal hit rate varied between 1% and 18%, and 60% of the resulting diffraction patterns were successfully indexed (table S1). Data quality, as judged by the R-split values, progressively improved with the number of indexed patterns (table S2 and fig. S4). R-split values for the dark data approached the overall value of 6.5% for 65,000 indexed patterns, remained below 10% to ~2 Å resolution, and was still acceptable (22.4%) at the highest resolution of 1.6 Å. Because the data collection scheme generated twice as many dark patterns as light patterns, the light data showed a somewhat larger value of R-split (9.2% for 32,000 indexed patterns). DED maps were calculated from weighted difference structure factor amplitudes (*2*) with phases derived from a structural model of PYP refined against the x-ray FEL dark data (see supplementary materials). The initial model was obtained from Protein Data Bank (*27*) entry 2PHY.

The results are shown in Figs. 2 and 3. Monte Carlo integration robustly determines intensities for the strongly diffracting PYP crystals. Synchrotron-quality DED maps with positive and negative peaks around 10 standard deviations σ (*3*) are obtained with only 4000 indexed light patterns (see supplementary materials). Because the unit cell of PYP crystals is relatively small and the crystals are a few micrometers in size, intensity fringes between Bragg reflections caused by the shape transform of the crystals (*28*) are absent. In addition, the mosaicity of PYP crystals is extremely small, so that many reflections may be collected almost as full reflections. As a result, sufficiently accurate intensities are obtained from fewer diffraction patterns. Strong DED features can already be observed at very large R-split values (table S2) corresponding to higher experimental noise in the structure amplitudes. If the noise in the amplitudes is too high, DED features deteriorate (*29*, *30*). To extract faint DED features associated with small structural changes of PYP, diffraction patterns should preferably be collected with a laser-on, laser-off sequence to accumulate an equal number of light and dark patterns, aiming for redundancies on the order of 1500 in the highest-resolution shell.

Figure 2 shows an overview of the 1-μs light-minus-dark DED map superimposed on the refined PYP dark structure. The largest DED peak is located on the sulfur of the chromophore (Fig. 2A) and has a highly significant negative value of –22σ (where σ is the root mean squared value of the DED across the asymmetric unit). The largest positive DED peak (18σ) is close to the same sulfur. These features reveal substantial displacement of the sulfur 1 μs after laser excitation, associated with a change in chromophore configuration from trans to cis. Chromophore isomerization triggers further protein conformational changes

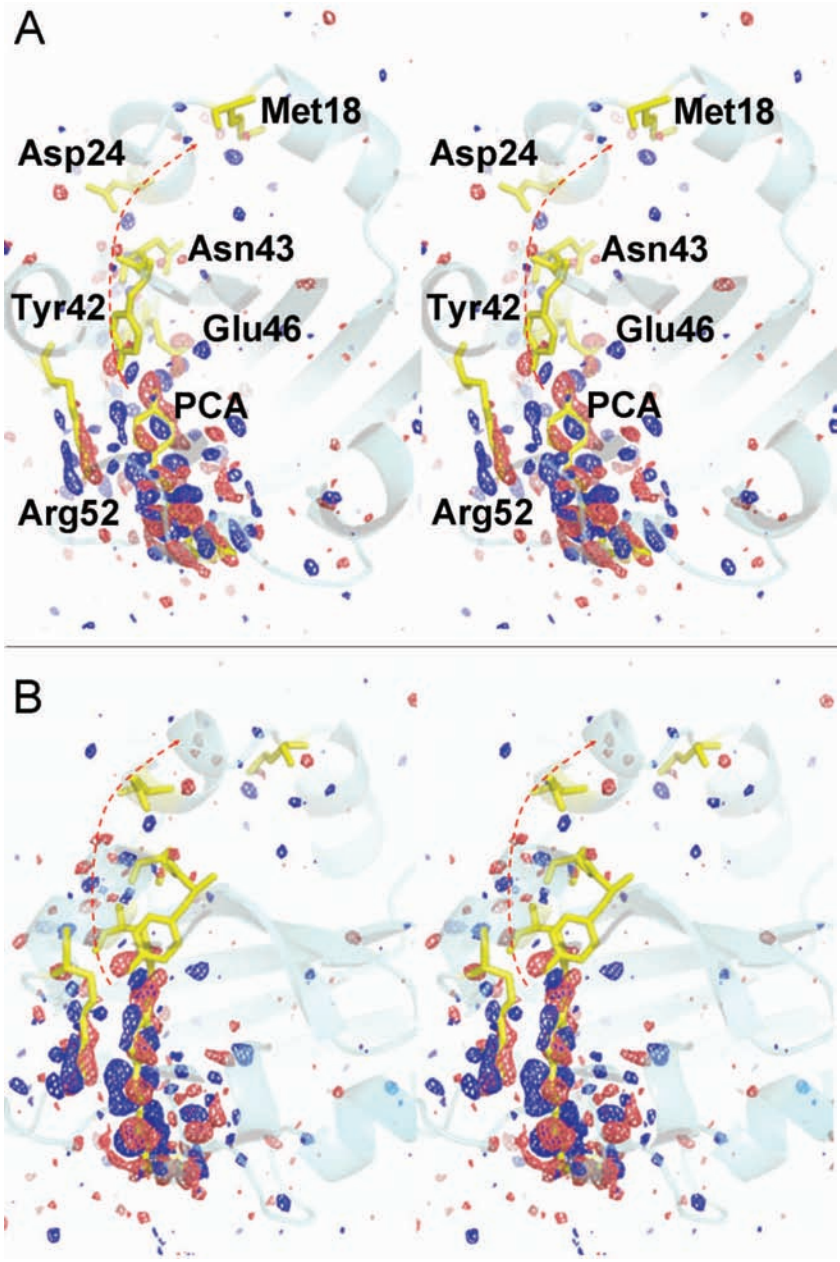


Fig. 2. Stereo view of the light-dark 1.6 Å difference electron density map at 1-μs time delay, superimposed on the dark PYP structure (cyan). Contour levels: red/blue –3σ/+3σ. Chromophore and some important chromophore pocket residues are shown in yellow and marked in (A). (**A**) Red arrow: Plume of structural displacements extends to Met[18], close to the N-terminal helix, which may be strongly displaced at longer times (*26*, *34*). (**B**) View rotated by ~90°. A large part of the molecule does not display sizable DED features and remains structurally unaltered.

extending to the periphery of the protein (red arrow). The positive (blue) and negative (red) DED peaks are contiguous and can be interpreted in terms of atomic models (Fig. 3, B and C). When the resolution is reduced below 3 Å, the difference signal disappears (fig. S7) and clear interpretation of structural changes in PYP becomes impossible. We note, however, that the minimum resolution needed to observe structural changes is likely system-dependent, and an extension to other systems must await further work.

In Fig. 3, A and D, the electron densities of the dark PYP structure derived from SFX are compared with those from the Laue method. The maps are of comparable quality and can be interpreted by the same reference structure (yellow). Shown in Fig. 3, B and C, are DED maps obtained at time delays of 10 ns and 1 μs from TR-SFX data. The DED maps are initially interpretable with intermediate structures derived from our earlier Laue experiments at BioCARS beamline 14-ID at the Advanced Photon Source

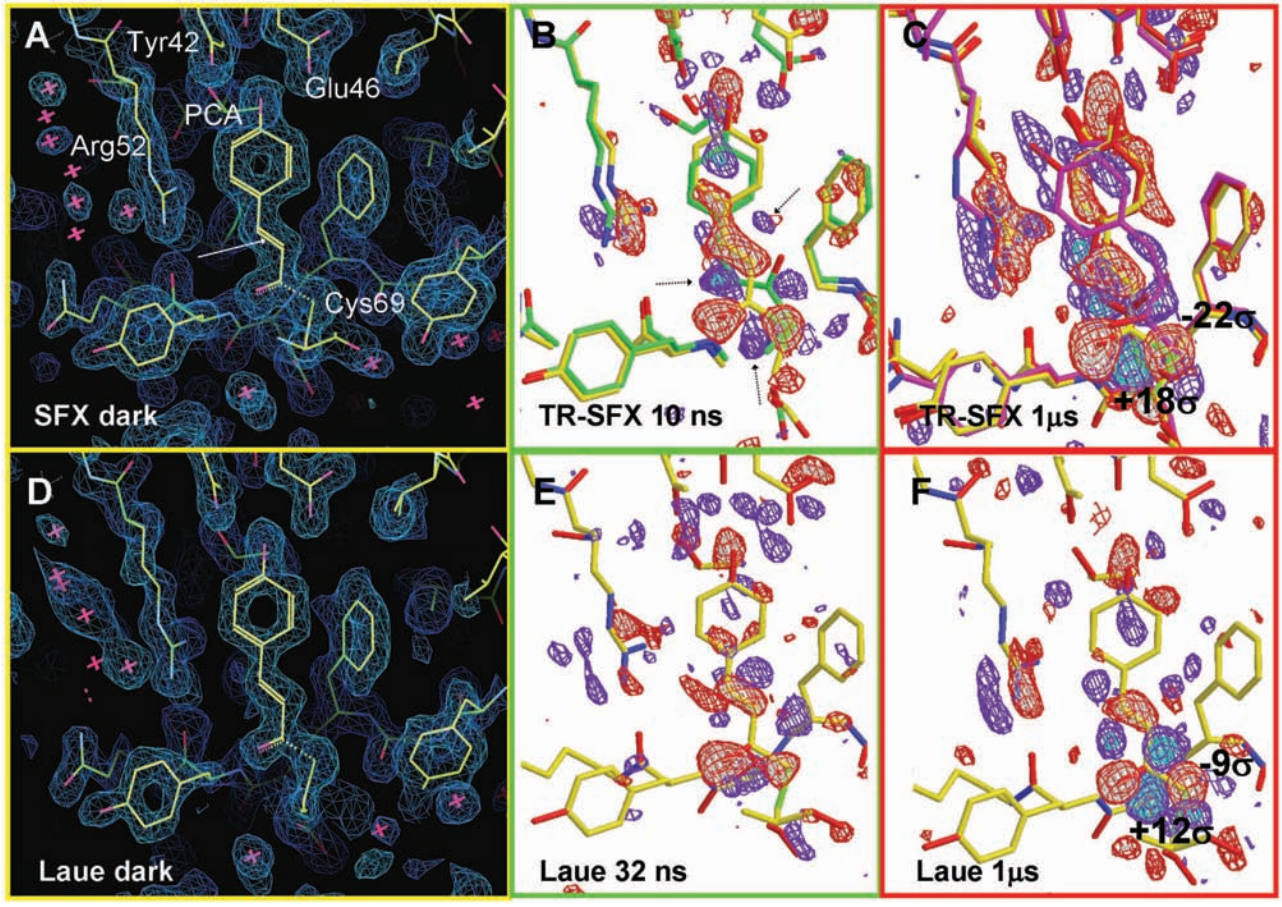


Fig. 3. Comparison of electron density and DED maps in the chromophore pocket obtained by TR-SFX and the Laue method. The dark state is shown in yellow in all maps. (**A** and **D**) Electron density maps for the PYP dark state obtained with TR-SFX and Laue, respectively (contour level 1.1σ, 1.6 Å resolution). The PCA chromophore and nearby residues are marked in (A). Arrow: Double bond in the chromophore about which isomerization occurs. (**B**) TR-SFX DED map at 10 ns. Light green structure: I_{CT} intermediate. Features marked by dotted arrows belong to additional intermediates not shown. (**C**) TR-SFX DED map at 1 µs. Pink and red structures: structures of pR_1 and pR_2 intermediates, respectively. (**E**) Laue 32-ns DED map correlates best to the TR-SFX 10-ns map. (**F**) Laue 1-µs DED map. Contour levels of the DED maps: red/white −3σ/−4σ, blue/cyan +3σ/+5σ, except for (C) where cyan is +7σ. See fig. S8 for stereo versions of (B) and (C).

(*3*, *4*, *26*). Negative DED features in both panels are accounted for by the yellow reference (dark) structure. Each DED map arises from a mixture of intermediates. For the 10-ns map, we show here only the I_{CT} intermediate (*4*) in green as a guide to the eye. Figure 3, D to F, shows corresponding maps collected by Laue diffraction at 0°C. The Laue 32-ns DED map correlates well with the 10-ns TR-SFX map. Many features are present in both the TR-SFX and Laue maps, and it is evident that they show the same mixture of intermediates. Particularly intriguing is the displacement of Glu^{46} caused by the initial isomerization of the chromophore, shown in both maps. Note that the mixture of intermediates, whose concentrations change rapidly around 10 ns, prevents the refinement of individual intermediate structures until a complete time series of DED maps (*3*–*5*, *26*) becomes available. In the 1-µs map (Fig. 3C), two intermediates, pR_1 and pR_2, are present with substantial occupancy (orange and pink structures, respectively). Because the concentration of these intermediates does not change over several decades in time (fig. S5A), structural characterization of this mixture is possible. The refinement of this mixture with an appropriate pair of conformations reveals hitherto unidentified structural changes (compare fig. S8A with fig. S9). In the TR-SFX maps, the DED features are much more pronounced, with stronger positive and negative features that are also much better connected spatially, and thus are more readily interpretable than the Laue maps.

The fraction of molecules that entered the photocycle can be determined by fitting calculated DED maps of the two intermediates populated at the 1-µs time delay to the observed DED map (see supplementary materials). About 22% of the molecules populate the pR_2 intermediate and 18% the pR_1. The extent of reaction initiation by the nanosecond laser pulse is therefore 40%, versus the 10 to 15% typically achieved in synchrotron experiments (*3*). The higher extent of reaction initiation with the smaller crystals used in TR-SFX demonstrates one of its key advantages for time-resolved studies and provides an explanation for the higher-quality DED maps.

In a time-resolved Laue experiment on a large single crystal of PYP, 3 to 10 complete pump-probe sequences, with waiting times of a few seconds between each sequence to allow completion of the photocycle, are necessary to accumulate a sufficiently exposed diffraction pattern before detector readout. When the nanosecond laser is used for reaction initiation, the laser beam is usually smaller than the crystal size and does not penetrate fully and uniformly through the large, optically dense crystals. This localized application of the repeated, intense laser pulses induces transient strain in the crystals, which results in radially streaked Laue spots. Strain imposes an upper limit on the useful laser energy, which for PYP crystals is around 4 to 5 mJ/mm^2 at 485 nm. This sets a practical limit on the extent of reaction initiation. Further, the repeated laser pulses have a damaging effect on the crystals, which imposes a limit on the total number of laser pulses that a crystal can tolerate (*31*).

Neither limit applies to TR-SFX. Because the crystals are so small, the laser pulse can easily penetrate through them. For example, the absorption length at 450 nm, where the crystal is most optically dense, is ~3 μm (*3*). Most crystals used in this study are smaller and can be near-uniformly illuminated with little local strain. The quasi-monochromatic collimated x-ray beam results in a sharp intersection of the Ewald sphere with each reciprocal lattice point. Even if the crystal mosaicity were to increase transiently, it would only increase the extent of partiality of each spot. Indeed, radially streaked diffraction spots do not appear in our data. In TR-SFX, each microcrystal is illuminated only once by the laser pulse, which allows the laser pulse energy to be increased to otherwise unacceptable levels. For example, the 0.8 mJ/mm^2 laser energy density at 450 nm used here would produce irreversible bleaching if applied in a few repetitive pulses to macroscopic crystals (*32*). Once excited, more than 80% of the PYP molecules return to their dark state on the picosecond time scale without entering the photocycle (*24*, *33*). At the laser pulse power we used, each molecule in the microcrystals is matched by an average of about 24 photons. Thus, each PYP molecule has the potential to be repeatedly activated within the nanosecond pulse. Because the excited-state lifetime is ~500 fs (*24*), the effective photolysis yield with our nanosecond laser may in principle reach levels several times the primary quantum yield (fig. S6). The intermediates earlier in the photocycle with lifetimes up to 10 ns have red-shifted absorption maxima around 500 nm (*25*). Because we excite at 450 nm, the probability that one of these intermediates absorbs a second laser photon is negligible. Despite the very high nanosecond laser flux, no sign of photo-induced damage is evident in our TR-SFX diffraction patterns. As a result, excellent DED maps are obtained of the quality needed for structural interpretation.

The way is now open to study reactions with ultrafast time resolution (*24*). For example, using femtosecond laser pump pulses to initiate the reaction in PYP may allow time resolution in the subpicosecond regime, as recently demonstrated by wide-angle x-ray scattering experiments on a bacterial photosynthetic reaction center at LCLS (*17*). Reaching this time resolution would take structural biology into uncharted territory (*24*). PYP displays rich femtosecond chemistry, but little is known experimentally about the corresponding atomic structures and the way the elementary chemical process of isomerization proceeds. Moreover, on the femtosecond time scale, coherent phenomena may become evident that bear on how the PYP chromophore undergoes its primary photoabsorption. On the ultrafast time scale, the penetration depth under intense femtosecond optical excitation may be dominated by nonlinear cross sections while the photolysis yield becomes fundamentally limited by the primary quantum yield of the PYP chromophore. Intense optical pulses with very short duration (e.g., 10 fs) will create only small population levels, which might be substantially increased by stretching and shaping the laser pulse (*24*). To capture this small population, every x-ray pulse must probe a crystal—such as a microcrystal—that has been excited as completely as possible. These experiments may elucidate the elementary mechanism of light absorption in chromophores, with implications for photosynthesis, light sensing, and the process of vision.

Our results establish that high-resolution TR-SFX is readily possible. Reaction initiation by light to explore fast and ultrafast isomerization might be extended in the future to chemically triggered reactions, which would open the door to the application of high-resolution TR-SFX at x-ray laser sources to a wide range of biologically and pharmaceutically important proteins.

REFERENCES AND NOTES

1. K. Moffat, *Annu. Rev. Biophys. Biophys. Chem.* **18**, 309–332 (1989).
2. M. Schmidt, in *Ultrashort Laser Pulses in Medicine and Biology*, W. Zinth, M. Braun, P. Gilch, Eds. (Springer, Berlin, 2008), pp. 201–241.
3. M. Schmidt *et al.*, *Acta Crystallogr. D* **69**, 2534–2542 (2013).
4. Y. O. Jung *et al.*, *Nat. Chem.* **5**, 212–220 (2013).
5. F. Schotte *et al.*, *Proc. Natl. Acad. Sci. U.S.A.* **109**, 19256–19261 (2012).
6. F. Schotte *et al.*, *Science* **300**, 1944–1947 (2003).
7. D. Bourgeois *et al.*, *Proc. Natl. Acad. Sci. U.S.A.* **103**, 4924–4929 (2006).
8. H. N. Chapman *et al.*, *Nature* **470**, 73–77 (2011).
9. J. C. H. Spence, U. Weierstall, H. N. Chapman, *Rep. Prog. Phys.* **75**, 102601 (2012).
10. R. Neutze, K. Moffat, *Curr. Opin. Struct. Biol.* **22**, 651–659 (2012).
11. U. Weierstall, J. C. Spence, R. B. Doak, *Rev. Sci. Instrum.* **83**, 035108 (2012).
12. L. Lomb *et al.*, *Phys. Rev. B* **84**, 214111 (2011).
13. A. Barty *et al.*, *Nat. Photonics* **6**, 35–40 (2012).
14. R. Neutze, R. Wouts, D. van der Spoel, E. Weckert, J. Hajdu, *Nature* **406**, 752–757 (2000).
15. S. Boutet *et al.*, *Science* **337**, 362–364 (2012).
16. L. Redecke *et al.*, *Science* **339**, 227–230 (2013).
17. D. Arnlund *et al.*, *Nat. Methods* **11**, 923–926 (2014).
18. R. A. Kirian *et al.*, *Acta Crystallogr. A* **67**, 131–140 (2011).
19. T. R. Barends *et al.*, *Nature* **505**, 244–247 (2014).
20. A. Aquila *et al.*, *Opt. Express* **20**, 2706–2716 (2012).
21. J. Kern *et al.*, *Science* **340**, 491–495 (2013).
22. C. Kupitz *et al.*, *Nature* **513**, 261–265 (2014).
23. L. J. van Wilderen *et al.*, *Proc. Natl. Acad. Sci. U.S.A.* **103**, 15050–15055 (2006).
24. C. N. Lincoln, A. E. Fitzpatrick, J. J. van Thor, *PCCP* **14**, 15752–15764 (2012).
25. L. Ujj *et al.*, *Biophys. J.* **75**, 406–412 (1998).
26. H. Ihee *et al.*, *Proc. Natl. Acad. Sci. U.S.A.* **102**, 7145–7150 (2005).
27. H. M. Berman *et al.*, *Acta Crystallogr. D* **58**, 899–907 (2002).
28. J. C. Spence *et al.*, *Opt. Express* **19**, 2866–2873 (2011).
29. J. van Thor *et al.*, *Faraday Discuss.* 10.1039/C4FD00011K (2014).
30. M. Schmidt, S. Rajagopal, Z. Ren, K. Moffat, *Biophys. J.* **84**, 2112–2129 (2003).
31. M. Schmidt, V. Šrajer, N. Purwar, S. Tripathi, *J. Synchrotron Radiat.* **19**, 264–273 (2012).
32. N. Purwar, J. Tenboer, S. Tripathi, M. Schmidt, *Int. J. Mol. Sci.* **14**, 18881–18898 (2013).
33. G. Groenhof *et al.*, *J. Am. Chem. Soc.* **126**, 4228–4233 (2004).
34. T. W. Kim *et al.*, *J. Am. Chem. Soc.* **134**, 3145–3153 (2012).

ACKNOWLEDGMENTS

Supported by NSF career grant 0952643 (M.S.), NIH grant R01GM095583 (P.F.), NIH grant R24GM111072 (V.S., R.H., and K.M.), and NSF Science and Technology Centers grant NSF-1231306 ("Biology with X-ray Lasers"). The work of M.F. and his team was performed in part under the auspices of the U.S. Department of Energy by Lawrence Livermore National Laboratory under contract DE-AC52-07NA27344 and supported by LLNL Lab-Directed Research and Development Project 012-ERD-031. We thank T. White for making the newest version of CrystFEL available to us, R. G. Sierra and H. DeMirci for help setting up crystal preparation in their labs, S. Lisova for making injector nozzles, and D. Deponte for help with the injector setup. M.S. thanks R. Hovey and S. Tripathi for help on early attempts to produce microcrystals. The TR-SFX measurements were carried out at the Linac Coherent Light Source (LCLS) at SLAC National Accelerator Laboratory. LCLS is an Office of Science User Facility operated for the U.S. Department of Energy Office of Science by Stanford University. J.S. is an inventor on a patent applied for by Arizona State University that covers the gas dynamic virtual nozzle. Coordinates and (difference) structure factors are deposited in the Protein Data Bank under accession numbers 4WL9 and 4WLA.

SUPPLEMENTARY MATERIALS

www.sciencemag.org/content/346/6214/1242/suppl/DC1
Materials and Methods
Supplementary Text
Figs. S1 to S10
Tables S1 to S4
References (*35*–*55*)

29 July 2014; accepted 7 November 2014
10.1126/science.1259357

SOLVING THE WORLD'S TOUGHEST HEALTH CHALLENGES TAKES ALL OF US.

It takes the will to find a new way forward. And no one gets there alone.

That's why AbbVie teams with peers, academics, clinical experts and others to take on the most complex health challenges.

Uniting the best of pharma with the boldness of biotech, together we're going beyond conventional thinking to innovate end-to-end approaches that make a real difference.

Starting with science, we arrive at solutions that help millions of patients around the world live better.

abbvie.com/allofus



PEOPLE. PASSION.
POSSIBILITIES.

CM-0140-01-0814





www.cellsignal.com/science125

CST Guide: Pathways and Protocols. From the inception of the antibody as a research tool in the 1890s, to the most up-to-date research, applications, and tools, this is your complete resource for cellular research.

14PADCORPNONE0235END_00

For Research Use Only. Not For Use In Diagnostic Procedures.

© 2014 Cell Signaling Technology, Inc. Cell Signaling Technology® and CST™ are trademarks of Cell Signaling Technology, Inc.

Cell Signaling TECHNOLOGY®



We're celebrating 20 years of our Translational Research Program because this is what we have to show for it.

Ellie
leukemia survivor

The Leukemia & Lymphoma Society (LLS) is proud to announce this year's TRP grantees. They join the ranks of all the grantees we've funded over the 20 years of this program. Thanks to their research, many promising discoveries have moved from bench to bedside quicker than ever before, saving lives and improving outcomes for blood cancer patients. We look forward to the same contributions from our new TRP researchers; healthy men, women and children. And that's certainly a reason to celebrate!

Learn more about LLS's grant programs and see what your research can do, not someday, but today.

someday is today

LEUKEMIA & LYMPHOMA SOCIETY®
fighting blood cancers

www.LLS.org/research



Join the Conversation!

Twitter is a great way to connect with AAAS members and staff about the issues that matter to you most. Be a part of the discussion while staying up-to-date on the latest news and information about your personal member benefits.

Follow us @AAASmember

and join the conversation

with #AAAS

AAAS MemberCentral

MemberCentral.aaas.org

LLS honors this year's TRP grantees

- **Gheath Al-Atrash, D.O., Ph.D.**
  The University of Texas
  MD Anderson Cancer Center
- **Bruce Blazar, M.D.**
  University of Minnesota
- **Katherine Borden, Ph.D.**
  University of Montreal
- **John Byrd, M.D.**
  The Ohio State University
- **Lucio Castilla, Ph.D.**
  University of Massachusetts
  Medical School
- **James Coghill, M.D.**
  University of North Carolina at Chapel Hill
- **John Crispino, Ph.D.**
  Northwestern University
- **Adolfo Ferrando, M.D., Ph.D.**
  Columbia University Medical Center
- **Mark Frattini, M.D., Ph.D.**
  Columbia University Medical Center
- **Paul Frenette, M.D.**
  Albert Einstein College of Medicine
- **Steven Grant, M.D.**
  Virginia Commonwealth University
- **Richard Jones, M.D.**
  Johns Hopkins University School
  of Medicine
- **Andrew Kung, M.D., Ph.D.**
  Columbia University Medical Center
- **Mignon Loh, M.D.**
  University of California, San Francisco
- **Ivan Maillard, M.D.**
  University of Michigan
- **Ari Melnick, M.D.**
  Weill Medical College of Cornell University
- **Tarik Moroy, Ph.D.**
  Institut de Recherches Cliniques
  de Montreal
- **Javier Pinilla, M.D., Ph.D.**
  Lee Moffitt Cancer Center
  and Research Institute
- **Anjana Rao, Ph.D.**
  La Jolla Institute for Allergy and Immunology
- **Katy Rezvani, M.D., Ph.D.**
  The University of Texas
  MD Anderson Cancer Center
- **Aaron Schimmer, MD, PhD.**
  University Health Network
- **Steven Treon, M.D., Ph.D.**
  Dana-Farber Cancer Institute
- **Catherine Wu, M.D.**
  Dana-Farber Cancer Institute
- **B. Hilda Ye, Ph.D.**
  Albert Einstein College of Medicine
- **Qing Yi, M.D., Ph.D.**
  Cleveland Clinic Foundation
- **Johannes Zakrzewski, M.D.**
  Memorial Sloan Kettering Cancer Center

Learn more about our research program

www.LLS.org/research

Online Career Fairs

December 10, 2014



For careers in science, there's only one Science

Meet recruiters without leaving your lab or desk!

Science Careers is excited to bring you an easy, efficient and powerful way to connect with employers from all over... all in one place. This virtual event allows you to queue up to visit with representatives from any companies you are interested in during the event hours.

Features and Benefits of Attending this Event

- No travel required—you can login from anywhere
- Queues tell you how many people are in line ahead of you and how long you will be waiting so you can better manage your time
- Login before the event to learn more about participating employers
- Employers can see your resume while you are talking to them



ScienceCareers
FROM THE JOURNAL SCIENCE AAAS

For more information, visit:
ScienceCareers.org/onlinecareerfair

Odor-Free Evaporator

The "odor reduction" function for the EZ-2 evaporator enables it to be placed on an open bench rather than taking up valuable fume hood space. Many solvent evaporators are routinely sited inside fume extraction hoods because residual solvent vapor, remaining in the chamber at the end of a run, can expose the operator to potentially harmful odors when the system is opened. The EZ-2's Reduce Odor function automatically adds a repeated vent and vacuum cycle to the end of a method, which purges the evaporation chamber of residual solvent vapors. Three settings are available to optimize vapor removal without releasing trapped solvent from the cold trap. Using advanced evaporation science, it has been designed specifically for productive, sample-safe solvent removal, be that concentration of samples, or complete drying. Smart evaporator software with auto-stop provides true walkaway automation—so simple and sample safe that anyone can use it with confidence.

Genevac
For info: +44-(0)-1473-240000
www.genevac.com

Fraction Collection Storage

A complete storage solution for high-performance liquid chromatography (HPLC) fractions comprising 2 mL round deep- well microplates and high-integrity cap mat seals. The revolutionary design of the 2 mL deep-well plate provides scientists with a genuine 2 mL working volume in a 45 mm height plate, coupled with a choice of specially designed cap mats. These flexible, reusable cap mats prevent evaporation and allow transport and storage of samples in the 2 mL plate without the need for expensive heat seals or leaky adhesive-based seals. To ensure complete confidence in the integrity of your sealed HPLC autosampler or fraction collector samples, Porvair has included its popular, flexible pre-scored silicone cap mats with double O-ring in the package. For a limited period, Porvair Sciences is offering a free pack of 50 cap mats with each order for two or more cases of 50 x 2 mL round well plates, creating a valuable saving for your lab.

Porvair Sciences
For info: +44-(0)-1978-666239
www.microplates.com



FISH Slide Incubator

The CytoBrite Duo Slide Incubation System is a dual temperature slide heating instrument for performing FISH hybridization protocols. It consists of two independently controlled heating blocks that each hold a six-slide removable tray. After assay assembly, a slide tray is simply moved from one lower temperature heating position to a higher temperature position to perform the brief probe co-denaturation step then returned to the lower temperature position for hybridization. The snap heating and cooling of slides eliminates heat damage to cells for more reliable results. Slides are sealed with CytoBond Removable Coverslip Sealant eliminating the need for humidification.

SciGene
For info: 408-733-7337
www.scigene.com

ImmPACT Vector Red

The ImmPACT Vector Red AP substrate kit has a new chromogenic enzyme formulation that produces a sharp bright red reaction product that is significantly more sensitive than traditional red alkaline phosphatase substrates. ImmPACT Vector Red precipitate is stable through standard dehydration and clearing methods that enable permanent archiving of stained tissue sections. This substrate is ideally suited as a single label or in combination with other enzyme substrates for multiple label immunohistochemistry applications. The red precipitate generated by this kit is also highly fluorescent and visible under rhodamine or similar microscope filter systems. This bright red fluorescence does not fade or photobleach like fluorescent haptens, and intensity is enhanced when permanently coverslipped. The reagents are presented in convenient dropper bottles and one kit will generate 120 mL of working solution.

Vector Laboratories
For info: 650-697-3600
www.vectorlabs.com

Microsampling Device

The new Mitra (RUO) Microsampling Device is designed for the collection, transport, storage, and analysis of biological fluids. In seconds, the research-use-only Mitra microsampler consistently collects 10 µL of fluid while eliminating the volumetric blood hematocrit bias typically associated with the dried blood spotting technique. Mitra is used for a wide range of biological sampling applications and is offered in two formats including an automation-friendly option for high throughput environments. Based on proprietary Volumetric Absorptive Microsampling (VAMS) technology, the patent-pending Mitra (RUO) Microsampling Device is attuned to biological fluid collection needs. The design features facilitate high throughput and serial sampling, fluid draws from live hosts or tubes, and the ability to collect precise microsamples with limited training and no specialized lab equipment. Once samples are collected, the Mitra microsampler is dried, stored, and transported under ambient conditions eliminating the need for laborious and expensive processing steps and transportation needs.

Phenomenex
For info: 310-212-0555
www.phenomenex.com/mitra

Electronically submit your new product description or product literature information! Go to www.sciencemag.org/products/newproducts.dtl for more information.

Newly offered instrumentation, apparatus, and laboratory materials of interest to researchers in all disciplines in academic, industrial, and governmental organizations are featured in this space. Emphasis is given to purpose, chief characteristics, and availability of products and materials. Endorsement by *Science* or AAAS of any products or materials mentioned is not implied. Additional information may be obtained from the manufacturer or supplier.



This is the start of something big.

Science Advances | AAAS

SIGNIFICANT RESEARCH, GLOBAL IMPACT

Introducing *Science Advances* – the new, online-only, open-access journal from *Science* and AAAS. Find out how you can be among the first authors published at **scienceadvances.org.**



BOUNDARY-BREAKING
ACOUSTIC FOCUSING CYTOMETRY

Introducing the Attune® NxT Acoustic Focusing Cytometer—a high-performance package that's flexible enough for any lab

The Attune® NxT Acoustic Focusing Cytometer combines unmatched precision, speed, and sensitivity, in a modular design that can grow with you. With up to 4 lasers and 14 colors, the Attune® NxT cytometer is designed to accommodate most experimental design needs and lab budgets. Boundaries, beware.

See the next big thing in flow cytometry at
lifetechnologies.com/attune

life technologies

A **Thermo Fisher Scientific** Brand

For Research Use Only. Not for use in diagnostic procedures. ©2014 Thermo Fisher Scientific Inc. All rights reserved.
All trademarks are the property of Thermo Fisher Scientific and its subsidiaries unless otherwise specified. **CO012644 0814**



Science Careers Advertising

For full advertising details, go to ScienceCareers.org and click For Employers, or call one of our representatives.

Tracy Holmes
Worldwide Associate Director
Science Careers
Phone: +44 (0) 1223 326525

THE AMERICAS

E-mail: advertise@sciencecareers.org
Fax: 202 289 6742

Tina Burks
Phone: 202 326 6577

Nancy Toema
Phone: 202 326 6578

Marci Gallun
Sales Administrator
Phone: 202 326 6582

Online Job Posting Questions
Phone: 202 312 6375

EUROPE / INDIA / AUSTRALIA / NEW ZEALAND / REST OF WORLD

E-mail: ads@science-int.co.uk
Fax: +44 (0) 1223 326532

Axel Gesatzki
Phone: +44 (0) 1223 326529

Sarah Lelarge
Phone: +44 (0) 1223 326527

Kelly Grace
Phone: +44 (0) 1223 326528

JAPAN

Katsuyoshi Fukamizu (Tokyo)
E-mail: kfukamizu@aaas.org
Phone: +81 3 3219 5777

Hiroyuki Mashiki (Kyoto)
E-mail: hmashiki@aaas.org
Phone: +81 75 823 1109

CHINA / KOREA / SINGAPORE / TAIWAN / THAILAND

Ruolei Wu
Phone: +86 186 0082 9345
E-mail: rwu@aaas.org

All ads submitted for publication must comply with applicable U.S. and non-U.S. laws. *Science* reserves the right to refuse any advertisement at its sole discretion for any reason, including without limitation for offensive language or inappropriate content, and all advertising is subject to publisher approval. *Science* encourages our readers to alert us to any ads that they feel may be discriminatory or offensive.

ScienceCareers
FROM THE JOURNAL SCIENCE AAAS

ScienceCareers.org

Director of the National Center for Electron Microscopy at the Molecular Foundry



The Molecular Foundry at Lawrence Berkeley National Laboratory (Berkeley Lab) invites outstanding applications and nominations for the position of Director of the National Center of Electron Microscopy (NCEM).

The Molecular Foundry is a U.S. Department of Energy "User Facility" engaged in a broad range of nanoscale science research programs. Scientific staff pursue projects of their own design, and also collaborate with scientists (users) from around the world whose own research efforts benefit from the Foundry's unique equipment, techniques, and staff expertise.

Responsibilities & Challenges:
- Implement a vision for scientific direction, structure, organization, management, and operation.
- Lead development and integration of new electron microscopy and scattering techniques.
- Recruit and retain staff; provide leadership for staff career development.

Applicants should have:
- Distinguished record of excellence in electron microscopy research
- Breadth of expertise and vision in nanoscience and materials science
- Leadership ability to manage a complex and internationally recognized scientific enterprise

This is a career appointment as either a Staff Scientist or Senior Scientist. **Please apply at go.lbl.gov/80259**.

Foundry.lbl.gov **www.lbl.gov**

MOLECULAR FOUNDRY

BERKELEY LAB
Lawrence Berkeley National Laboratory

Discover potential at the nanoscale. The Molecular Foundry is a DOE-funded nanoscience research facility that provides users from around the world with access to cutting-edge expertise and instrumentation in a collaborative, multidisciplinary environment.

AA/EEO

Memorial Sloan Kettering Cancer Center
1884

Postdoctoral Researcher Computational Biology

Sarcoma Disease Management Program
Departments of Surgery, Medical Oncology and Pathology

New York, NY

The Sarcoma Disease Management Program and the Computational Biology Center at MSK is searching for an outstanding scientist with a strong interest in developing and applying computational methods to cancer biology. Specifically we are seeking a candidate with experience in both bioinformatics - in particular, the bioinformatics of next-generation sequencing and high throughput genomic analysis - and systems biology to lead the effort to analyze high throughput and genomic data from an extensive dataset of patients treated at MSK for soft tissue sarcoma.

The candidate will have the opportunity to interact with expert investigators in computational biology, sarcoma biology, translational therapeutics, and molecular pathology. The candidate will also analyze high throughput genomic data and work with computational and laboratory-based investigators to identify the mutational programs and pathways involved in sarcomagenesis and to identify novel therapeutic targets.

Position requires a PhD or equivalent in biological science, mathematics, physics, bioinformatics, or a related field with a strong quantitative background. Proficiency with scientific computing software (Matlab, R) and scripting languages are also required. The ideal candidate will have solid programming skills and extensive research experience in the biological sciences. For consideration, please send CV, bibliography, brief statement of research interests, and names of 3 references to **bic-recruit@cbio.mskcc.org**. Please put "#sarcoma" in the subject line of your reply.

FIND YOUR LIFE'S CALLING AT THE NATION'S #1 CANCER CENTER*
cbio.mskcc.org
*U.S. News & World Report, 2014-2015

MSK is an equal opportunity and affirmative action employer committed to diversity and inclusion in all aspects of recruiting and employment.

RUTGERS

The **Rutgers School of Environmental and Biological Sciences** at Rutgers University - New Brunswick announces faculty searches for three endowed chairs. We seek scholars whose records in teaching, research and service to society are consistent with anticipated appointment as full Professor with tenure. Please visit the websites provided for further information and instructions for applications and nominations.

The Johnson Family Chair in Water Resources and Watershed Ecology

Funded by the Johnson Family and an anonymous donor, the successful candidate will advance understanding of large-scale aquatic systems in complex landscapes spanning urban to rural gradients, such as the Raritan River watershed of central New Jersey. Areas of potential research expertise could include ecology, evolutionary biology, natural resource management, environmental science and engineering, estuarine processes, and environmental policy.
See: http://ohr.rutgers.edu/endowed-chairs/johnson-family-chair.html

The Eveleigh-Fenton Chair in Applied Microbiology

Named in honor of Distinguished Professor Emeritus Douglas Eveleigh, and funded by Linda and Dennis Fenton, the successful candidate will provide leadership in microbial systems biology (microbiomes, metabolic engineering, synthetic biology, host associated microbial communities, ecology and evolution of microbial communities).
See: http://ohr.rutgers.edu/endowed-chairs/eveleigh-fenton-chair.html

The C. Reed Funk Chair in Plant Genetics and Genomics

Named in memory of the distinguished late professor and plant breeder who founded and led Rutgers University's internationally acclaimed turfgrass research program (now the Center for Turfgrass Science; turf.rutgers.edu), this chair will be filled by an individual with expertise in bioinformatics and comparative plant genomics. The successful candidate will focus research on fundamental questions (e.g., reproductive biology, heterosis, apomixis, development, photosynthesis, evolutionary theory and modeling, structural biology, genome structure) that might be addressed, for example, in studies of the graminoid family genomes.
See: http://ohr.rutgers.edu/endowed-chairs/funk-chair.html

Rutgers University is an Affirmative Action/Equal Opportunity Employer.
Women, members of minority groups, and persons with disabilities are encouraged to apply.

THE UNIVERSITY OF ARIZONA. CANCER CENTER

Research Assistant Professor
University of Arizona, Tucson

These funded project(s) in the laboratory of Dr. Andrew Kraft, Director of the Cancer Center focus on the role of the Pim protein kinase in regulating malignant transformation. Emphasis will be given to understanding how Pim regulates protein synthesis to stimulate prostate cancer growth by modulating mTOR and eiF4B (*MCB* **34:**2517, 2014; *Can. Res.* **73:**3402, 2013) and modulates the hypoxic response of this tissue. Animal models, knockout and transgenic mice and targeted small molecules will be used in these studies. Experience in molecular and cellular biology is required. In a separate project, Pim as a driver protein in acute lymphocytic leukemia (T-ALL) will examine how this kinase controls the Jak/STAT pathway (*Blood* **115:**824, 2010) and modulates tumor growth. These experiments will require the transfer of manipulated bone marrow to congenic mice and the study of hematopoiesis.

Please submit a letter of interest, curriculum vitae, and the names of three references to **lfrazier@uacc.arizona.edu**.

Applicants can apply on-line at:
www.uacareers.com/56712

The University of Arizona is an EEO/AA - M/W/D/V Employer.

ACCEPT THE NAVY CHALLENGE

Become a member of an elite research and development community involved in basic and applied scientific research and advanced technological development for tomorrow's Navy.

NAVAL RESEARCH LABORATORY

Senior Scientist for Soft Matter Physics
ST-1310 or 1320, $120,749 to 181,500* per annum
*Rate limited to the rate for level III of the Executive Schedule (5U.S.C. 5304(g)(2))

Serves as the technical expert in the physics of polymers, glasses, molecular liquids, and liquid crystals. Provides vision and technical direction to a multidisciplinary research program pushing the frontiers of soft matter physics, with particular emphasis in the areas of molecular dynamics, shock physics, phase transitions of soft matter emphasizing liquid crystals, and polymer and glassy materials for armor and infrastructure protection applications. This position is located in the Chemistry Division and has major implications for the areas of warfighter and infrastructure protection, fuel economy, environmental impact, life-cycle costs of military vehicles, and defense against terrorism - areas that are of great interest to both the Navy and DoD.

He/she will play a key role in developing advanced programs in elastomer/glass armor, the shock physics of soft matter, the physics of the glass transition, ultrahigh pressure dielectric relaxation, the properties of liquid crystals and their application, and the multiscale dynamics of nanocomposite materials.

As a distinguished scientist and recognized leader in his/her field, the incumbent will be called upon to brief DoD senior officials regarding Laboratory research efforts in the above areas, to serve as an NRL liaison to the Navy and other national and international organizations, and to consult on important scientific and programmatic issues.

Applicants should be recognized as national/international authorities in the above areas of research, and should have demonstrated the scientific vision and organizational skills necessary to bring long term, multi-faceted research programs to successful completion.

For information regarding this vacancy and specific instructions on how to apply, go to **www.usajobs.gov**, log in and enter the following announcement number **NW413XX-00-1237706K9962074S**. Please carefully read the announcement and follow instructions when applying. Please contact Lauren Bowie at **lauren.bowie@nrl.navy.mil** for more information. Vacancy announcement closes on **December 31, 2014**.

Navy is an Equal Opportunity Employer.

ScienceCareers online @sciencecareers.org

UAB COLLEGE OF ARTS AND SCIENCES
Knowledge that will change your world
The University of Alabama at Birmingham

CHAIR
Department of Physics

The College of Arts and Sciences (CAS) at the University of Alabama at Birmingham (UAB) invites applications for the position of Chair of the Department of Physics. UAB is a comprehensive Carnegie Research Intensive University (RU-VH) and medical center with over 2,400 full-time faculty and over 18,500 students.

The Department of Physics at UAB (see: http://www.uab.edu/cas/physics/) offers BS, MS, and Ph.D. degrees in physics. Degree concentrations, which include the biophysics track (BS degree) and the applied physics track (PhD degree), are also available. Research funding is growing and supports diverse programs in computational physics, theoretical physics, condensed matter physics, materials physics, biophysics, laser physics, and photonics. The Department is entering a period of significant growth over the next five years with opportunities to develop new research programs and infrastructure while fostering new innovations in physics education. Interdisciplinary research collaborations are expanding with the UAB School of Medicine and School of Engineering through the Center for Nanoscale Materials and Biointegration and the Center for Optical Sensors and Spectroscopies, both of which are headquartered in the Department of Physics.

The successful candidate will have achieved significant recognition in research and administrative leadership with a fundamental understanding of the operation and advancement of a research-focused Physics department. The Chair, as chief academic, financial, and strategic officer for the Department, is responsible for its overall administration, reporting directly to the Dean of the College of Arts and Sciences. He or she will recruit and retain outstanding faculty and students at all levels, contribute to the intellectual life of the department as an active member of the faculty, and promote the department within the University and outside the University to secure support. The chair will be expected to provide strategic direction, vision, and leadership to the department while serving as an articulate and vigorous spokesperson for the department's scientific and educational missions. The chair will require excellent interpersonal, verbal, and written communication skills.

A Ph.D. in Physics or a closely related field is required. Candidates must possess a distinguished record of publications and achievements in their research specialty, a record of funding, teaching, professional service and promoting diversity consistent with appointment at the rank of Full Professor with tenure.

Applicants should submit (1) a cover letter summarizing qualifications and explaining interest in the position, (2) a complete curriculum vitae, and (3) contact information for three professional references. References will not be contacted without prior permission of the candidate. Screening will begin on 10/01/2014, and will continue until the position is filled. Please go to the following website to apply and upload application materials.

www.uab.edu/cas/application

For more information or to make inquiries about this position, contact

David Graves, Professor, Chair, Department of Chemistry
Chair Search Committee
201C Chemistry Building
901 14th Street South
Birmingham, AL 35294-1152
E-mail: dgraves@uab.edu
(205) 934-5381

UAB is an Equal Opportunity/Affirmative Action Employer committed to fostering a diverse, equitable and family-friendly environment in which all faculty and staff can excel and achieve work/life balance irrespective of, race, national origin, age, genetic or family medical history, gender, faith, gender identity and expression as well as sexual orientation. UAB also encourages applications from individuals with disabilities and veterans.

A pre-employment background investigation is performed on candidates selected for employment.

THE OHIO STATE UNIVERSITY
COLLEGE OF DENTISTRY

COLUMBUS, OHIO

Associate Dean for Research

George C. Paffenbarger Alumni-Endowed Chair in Dental Research

The Ohio State University College of Dentistry seeks a dynamic, experienced candidate for the position of Associate Dean for Research.

This full-time, tenured position will provide leadership and vision for the research mission of the college, while building its extramural funding base and expanding its reputation for world-class research.

The National Science Foundation ranks Ohio State 10th in total research expenditures among public and private universities; seventh among public universities; and second in industry-sponsored research. The College of Dentistry is well funded with a diverse and dynamic research portfolio that includes basic, clinical, and translational science programs that are supported by seven institutes at the NIH and by industry and various foundations. Research foci include cancer, oral and gut microbiome, taste and feeding behavior, psychoneuroimmunology, hard tissue and muscle biology, and dental biomaterials.

The successful candidate will be an established and funded investigator who can develop a compelling research focus for the college, lead and manage existing programs, and foster a collegial work environment. Required qualifications include an earned D.D.S., D.M.D., Ph.D., or equivalent degree in a related field with experience in academic health sciences.

The Associate Dean for Research also will be eligible for the George C. Paffenbarger Alumni-Endowed Chair in Dental Research, which provides additional compensation for the position and resources to support scholarship and office operations.

For more information about the college and this position, visit **dent.osu.edu**

Initial screening of applications will begin immediately and will continue until an appointment is made. Application materials should include: a letter addressing how the candidate's experiences match the position requirements; curriculum vitae; and contact information for five references. Confidential inquiries, nominations, and application materials should be directed to:

Betty Turner Asher or Jan Greenwood
Greenwood/Asher & Associates, Inc.
42 Business Center Drive, Suite 206
Miramar Beach, FL 32550
Phone: 850.650.2277 | Fax: 850.650.2272
bettyasher@greenwoodsearch.com
Jangreenwood@greenwoodsearch.com

The Ohio State University is an equal opportunity employer. All qualified applicants will receive consideration for employment without regard to race, color, religion, gender, sexual orientation or identity, national origin, disability status, and protected veteran status.

南京工業大學
NANJING TECH UNIVERSITY

海外领军人才招聘

Overseas Talents Recruitment

Nanjing Tech University, with a history of more than one hundred years, is a multidisciplinary university with a particular strength in engineering.

Aiming at excellence and innovation, Nanjing Tech University is set to become a first-class research university with a global vision. We are now seeking outstanding academic and research leaders in the following and related fields: Basic disciplines from within the Physical Sciences; Cutting edge disciplines from within the Life Sciences; Applied disciplines from within the Information Sciences; Humanities represented by Management Science.

Applicants should have a Ph.D. with at least 3-years research experience from leading universities or institutes. Candidates should demonstrate an internationally recognized research record and outstanding achievements. Successful candidates are expected to develop vigorous research programs and lead an independent research team. Successful candidates will be provided with a competitive relocation fee and salary package, generous start-up funds and spacious laboratories.

Interested candidates should visit **http://rczyb.njtech.edu.cn** for application details.
Phone: **Ms. Wang +86-25-58139148.**
E-mail: **job@njtech.edu.cn**

西南交通大学 Southwest Jiaotong University

Southwest Jiaotong University, P.R.China Anticipates Your Working Application

Southwest Jiaotong University (SWJTU), founded in 1896, situates itself in Chengdu, the provincial capital of Sichuan. It is a national key multidisciplinary "211" and "985 Feature" Projects university directly under the jurisdiction of the Ministry of Education, featuring engineering and a comprehensive range of study programs and research disciplines spreading across more than 20 faculties and institutes/centers. Boasting a complete Bachelor-Master-Doctor education system with more than 2,500 members of academic staff, our school also owns 2 first-level national key disciplines, 2 supplementary first-level national key disciplines (in their establishment), 15 first-level doctoral programs, 43 first-level master programs, 75 key undergraduate programs, 10 post-doctoral stations and more than 40 key laboratories at national and provincial levels.

Our university is currently implementing the strategy of "developing and strengthening the university by introducing and cultivating talents". Therefore, we sincerely look forward to your working application.

More information available at http://www.swjtu.edu.cn/

I. Positions and Requirements

A.High-level Leading Talents

It is required that candidates be listed in national top talents programs such as ***Program of Global Experts, Top Talents of National Special Support Program, "Chang Jiang Scholars", China National Funds for Distinguished Young Scientists and National Award for Distinguished Teacher.***

Candidates are supposed to be no more than 50 years old. The limitation could be extended in the most-needed areas of disciplinary development.

Candidates who work in high-level universities/institutes and reach the above requirements are supposed to be no more than 45 years old.

B. Young Leading Scholars

Candidates are supposed to be listed in or qualified to apply for the following programs:

•National Thousand Young Talents Program

•The Top Young Talents of National Special Support Program(Program for Supporting Top Young Talents)

•Science Foundation for the Excellent Youth Scholars

Candidates should have good team spirit and leadership, outstanding academic achievements, broad academic vision and international cooperation experience and have the potential of being a leading academic researcher.

C. Excellent Young Academic Backbones

Candidates under 40 years old are expected to graduate from high-level universities/institutes either in China or other countries. Those who are professors, associate professors and other equal talents from high-level universities/institutes overseas could be employed as professors and associate professors as well.

D. Excellent Doctors and Post Doctoral Fellows

Candidates under 35 years old are supposed to be excellent academic researchers from high-level universities either in China or other countries.

II. Treatments

The candidates will be provided with competitive salaries and welfares that include settling-in allowance, subsidy of rental residence, start-up funds of scientific research, assistance in establishing scientific platform and research group as well as international-level training and promotion . As for outstanding returnees, we can offer further or specific treatments that can be discussed personally.

III . Contact us:

Contacts: Ye ZENG & Yinchuan LI Telephone number: 86-28-66366202 Email: *talent@swjtu.edu.cn*

Address: Human Resources Department of SWJTU, the western park of high-tech zone, Chengdu, Sichuan, P.R.China, 611756

http://www.swjtu.edu.cn/

上海交通大學 SHANGHAI JIAO TONG UNIVERSITY

Multiple Faculty Positions in Ultrafast Sciences / Electron Microscopy

Shanghai Jiao Tong University, Shanghai, China

Shanghai Jiao Tong University is establishing a world-class research Center for Ultrafast Sciences in physics, chemistry, materials and biology with integration of both experimental and theoretical efforts. The Center will provide state-of-the-art ultrafast laser spectroscopy, electron diffraction and microscopy, and excellent multi-disciplinary environment for cutting-edge research.

The Center invites applications for a number of open-rank faculty positions to begin in the fall of 2015 (or earlier). Applicants should have a Ph.D. degree, preferably with postdoctoral experience in a closely related field, and a strong record of research accomplishments. Previous experience in electron microscopy and ultrafast sciences is favorable. The successful candidates will be expected to develop world-class research programs and teach classes at both undergraduate and graduate levels. The University will provide attractive annual salary, start-up fund, housing allowance and other benefits.

All applicants should send a cover letter, a curriculum vitae with a publication list, a research proposal (3-4 pages) and a statement of teaching interest in a single pdf file by Jan. 31, 2015 to Dr. Jie Chen, Shanghai Jiao Tong University, Shanghai 200240, China through e-mail to: ultrafast@sjtu.edu.cn. Please also arrange three reference letters directly to the above e-mail address. Applications after the deadline could be reviewed until the positions are filled.

http://join.sjtu.edu.cn/

FUDAN UNIVERSITY 1905

Institutes of Biomedical Sciences, Fudan University

The Institutes of Biomedical Sciences (IBS) at Fudan University, established in 2005, pursues cutting-edge biomedical research from an interdisciplinary and inter-institutional perspective. Under the consistent and strong supports from Fudan University and various China government funding agencies, Fudan IBS has now developed into a vibrant research institution consisting of Epigenetics Research Center, Systems Biology of Medicine Research Center, Molecular Cell Biology Research Center, with the intension to initiate innovative research fields that are centered in China and emphasizing translational medicine.

Principle Investigators

Applicants should have a strong research profile to establish and conduct innovative research in the areas of Epigenetics, Molecular Cell Biology, Bioinformatics and Big-data Analysis, Proteomics, Electron Microscopy 3D Reconstruction, Structure Biology, Small Active Molecule for Drug Screening, Translational Medicine for Cancer, Cardiovascular Diseases, Birth Defect and Stem Cell Technology.

As an eligible candidate for professorship, you should have:

- PhD degree from overseas and more than 3 years working experience abroad or doctorate degree obtained in China with 5 years working experience.
- High-profiled publications as corresponding author
- ≤ 40-years old is preferred

Treatment

The university will provide munificent salary, internationally competitive start-up support, laboratory construction and organizing the research team.

More recruitment information at http://www.ibsfudan.org.

Contact person: Mr. Junhui Bie
Email: biejunhui@fudan.edu.cn Tel: +86-21-54237325

ScienceCareers online @sciencecareers.org
OPPORTUNITIES IN CHINA

ScienceCareers online @sciencecareers.org

Director/CEO SAMS Group

Competitive salary plus benefits

The Scottish Association for Marine Science (SAMS) is one of the world's oldest oceanographic institutions, delivering innovative science for sustainable seas. Our activities incorporate research, education, consultancy services and public engagement, tackling diverse interdisciplinary ocean research questions.

We invite applications for the role of Director of SAMS/CEO of the SAMS Group. The ideal candidate will be a marine scientist of distinction: dynamic, with a compelling vision for the future, and with a track record of delivering success and growth in the marine research environment. They will have excellent organisational, communication and people skills. The post holder will be an accomplished strategist who will further develop SAMS as a world class research organisation, a distinctive education provider and a successful business.

General enquiries should be directed to the SAMS President, Professor Geoffrey Boulton OBE g.boulton@ed.ac.uk; +44 131 667 2531 and/or Acting Director, Professor Axel Miller axel.miller@sams.ac.uk; +44 1631 559272.

Further information is available at www.sams.ac.uk, or e-mail recruitment@sams.ac.uk, or write to: Director/CEO SAMS Group, (D10/14.AM), Human Resources, SAMS, Scottish Marine Institute, Oban, Argyll PA37 1QA

The closing date for applications is **MONDAY 2ND FEBRUARY 2014**

SAMS is a registered Scottish charity (SC 009206), has an equal opportunities policy and welcomes applications from all sections of the community.

University of Colorado
Denver | Anschutz Medical Campus

Dean, Graduate School

The University of Colorado Denver | Anschutz Medical Campus invites applications and nominations for the position of dean of the Graduate School. University of Colorado Denver | Anschutz is a comprehensive research university with two locations, the Denver Campus and Anschutz Medical Campus.

As one of the university's 13 major units, the Graduate School administers the graduate programs and offerings across both campuses. The Graduate School serves approximately 2,400 students through nearly 60 Master's and doctoral programs, in addition to a number of post-master's and certificate programs. Several programs are multidisciplinary with faculty drawn from various departments.

The University of Colorado Denver | Anschutz is known for its distinctive and highly productive research programs, its world-class health facilities at the Anschutz Medical Campus and its well-established partnerships in business, industry and government. The university grants more graduate degrees than any other public institution of higher education in the state and continues to enhance graduate education to support outstanding research programs.

This position requires an earned terminal doctorate degree and a record of scholarship, teaching and service sufficient to be appointed to the rank of tenured Professor at the University of Colorado Denver | Anschutz Medical Campus and a strong leadership background in a comprehensive research university. A Ph.D. and scholarship in a science, technology, engineering or mathematics field is preferred.

For more information, visit: **http://www.ucdenver.edu/about/WhoWeAre/Chancellor/ViceChancellors/Provost/Pages/CurrentSearches.aspx**

Criminal Background investigations will be conducted for all prospective employees.

To apply, go to **https://www.jobsatcu.com/postings**, search Jobs for Graduate School Dean. Along with the application, attach a cover letter addressing the position requirements, current CV and the names and contact information for at least three professional references. Preference will be given to applications received by January 5, 2015. Applications will be accepted until finalists are identified. For additional information, contact **Vicky.starbuck@ucdenver.edu**.

The University of Colorado is an Equal Opportunity/Affirmative Action employer committed to diversity and equality in both education and employment.

Faculty Position in Biomaterials at Johns Hopkins University

The Department of Materials Science and Engineering at Johns Hopkins University invites applications for a junior-level, tenure-track faculty position in biomaterials. Specific areas of interest include regenerative medicine, immunology, neuroscience and neuroengineering, and aging. Candidates are expected to have a demonstrated record of innovative research spanning materials science, bioengineering and medicine. Preference will be given to applicants at the assistant professor level.

The successful candidate will be expected to establish an independent, internationally recognized research program and to contribute fully to the undergraduate and graduate educational missions of the department. Applicants should have a Ph.D. or equivalent in materials science and engineering or a related field; post-doctoral experience is desirable. Candidates must have demonstrated ability to undertake independent, interdisciplinary, and collaborative research. Additional information about the department may be found at http://materials.jhu.edu.

All applications should be submitted electronically as a **single PDF document to matsci@jhu.edu**. Applications should include a cover letter describing the principal expertise and accomplishments of the applicant, a complete resume, statements of research and teaching interest, and the names and contact information for at least three references. For full consideration, **applications should be received by January 1, 2015**.

The Department is committed to building a diverse educational environment; women and underrepresented minorities are strongly encouraged to apply. The Johns Hopkins University is an EEO/AA Employer.

ACCEPT THE NAVY CHALLENGE

Become a member of an elite research and development community involved in basic and applied scientific research and advanced technological development for tomorrow's Navy.

NAVAL RESEARCH LABORATORY

Senior Scientist for Electronic Warfare Technologies
ST-1310, $120,749 to $181,500* per annum
*Rate limited to the rate for level III of the Executive Schedule (5U.S.C. 5304(g)(2))

Serves as the technical expert and plays a key role in the Tactical Electronic Warfare Division (TEWD) by researching, planning, and influencing the direction of programs in advanced technology for Electronic Warfare (EW) systems for both the Navy/Marine Corps and Department of Defense (DoD). Applicants should be recognized as national/international authorities and have demonstrated the scientific vision and organizational skills necessary to bring long term, multi-faceted research programs to successful completion.

As a distinguished scientist and recognized leader, the incumbent will provide vision and technical direction for the establishment and execution of coherent research programs within the Naval Research Laboratory's Tactical Electronic Warfare Division to advance science and engineering concepts of EW systems. Specific duties include:

- Influencing and directing the research undertaken by other members of the TEWD research team, advising them on potential solutions, planning experimental procedures, providing advice on the interpretation of findings, and formulating research programs.
- Providing vision and direction for prototype systems for the NRL, the Department of the Navy (DoN), the Department of Defense (DoD) and other activities and organizations that require the technology he/she is developing.
- Performing research, development and application-oriented activities in all areas of electronic warfare and at all levels, including countermeasures techniques, components, devices, subsystems and systems for the protection of Navy/Marine Corps, DoD and Military assets against electronically RF directed threats.
- Designing EW capabilities, including advanced multi-bit, very broad band digital RF memories and supporting auxiliary circuits for target replication and/or advanced complex signal jamming using a comprehensive understanding of modern digital signal processing components, methods and techniques, as well as a comprehensive knowledge of components such as Field Programmable Gate Arrays (FPGA) and analog to digital converters and digital to analog converters (ADC/DACs).
- Briefing DoD senior officials regarding Laboratory research efforts in the above areas; serving as liaison among NRL, the Navy, and other national and international organizations; and consulting on important scientific and programmatic issues.

Because of the sensitivity of some of the research application areas the incumbent must be eligible for TS-SCI security clearance.

For information regarding this vacancy and specific instructions on how to apply, go to **www.usajobs.gov**, log in and enter the following announcement number: **NW41310-00-1237724K9964502S**. Please carefully read the announcement and follow instructions when applying. The announcement closes on **December 31, 2014**. Please contact Tara Jamison at tara.jamison@nrl.navy.mil for more information.

Navy is an Equal Opportunity Employer.

COLUMBIA UNIVERSITY
IN THE CITY OF NEW YORK

Faculty Positions in Neuro-Z: Engineering and Neural Science Innovation

Continued technological innovation is critical to advancing neuroscience. Columbia University is seeking exceptional applicants for two faculty positions at the intersection of neuroscience, engineering, and applied science. Recruits will be made jointly through The Fu Foundation School of Engineering and Applied Science and the newly named Mortimer B. Zuckerman Mind Brain Behavior Institute.

Successful candidates are expected to establish world-class independent research programs that cross the boundaries between neuroscience and applied science and engineering. Areas of expertise include the development of novel optical imaging and photactivation technologies, hybrid ultrasound methods and ultrasound stimulation, electrical recording and stimulation strategies, genetics approaches, and the intersection of neural science and related computational fields such as machine learning, information processing, and computer vision. Applications that explore synergies between the Zuckerman Institute and Columbia's new Data Science Institute are encouraged.

Available positions will be tenure-track or tenured at the Assistant, Associate or Full Professor level. Successful candidates will have laboratories located within the new Jerome L. Greene Science Center and will be full members of the Zuckerman Institute while holding academic appointments in The Fu Foundation School of Engineering and Applied Science. Home department appointments can be in Applied Physics and Applied Mathematics, Biomedical Engineering, Chemical Engineering, Civil Engineering and Engineering Mechanics, Computer Science, Earth and Environmental Engineering, Electrical Engineering, Industrial Engineering and Operations Research, or Mechanical Engineering. Candidates must be committed to outstanding teaching and mentoring at both the undergraduate and graduate levels in their home departments.

Candidates are encouraged to learn more about the Zuckerman Institute, the Data Science Institute, and The Fu Foundation School of Engineering and Applied Science at the links below. While applicants whose work also intersects with the Institute for Data Sciences and Engineering are encouraged to apply, a research interest in data sciences is not required.

http://zuckermaninstitute.columbia.edu
http://idse.columbia.edu
http://engineering.columbia.edu

Candidates should apply online at: **https://academicjobs.columbia.edu/applicants/Central?quickFind=60131.** No applications can be sent directly. Applications should include curriculum vitae with a publications list, a description of research accomplishments, an articulated vision of how their research would contribute to the goals of the Zuckerman Institute and the home department, and a statement related to teaching interests and plans. Contact information for three people who can provide letters of recommendation and up to three pre/reprints of relevant peer-reviewed publications should also be provided. The available positions will close no sooner than February 15, 2015, and will remain open until filled.

Candidates also applying for neuro related faculty positions within specific Engineering departments should cross reference this advertisement and an interest in Zuckerman Institute within their cover letter. For a listing of ongoing recruiting opportunities in Engineering departments, please see

http://engineering.columbia.edu/faculty-job-opportunities

Columbia is an affirmative action/equal opportunity employer, with a strong commitment to the quality of faculty life.

ScienceCareers online @sciencecareers.org

ScienceCareers online @sciencecareers.org

NANYANG TECHNOLOGICAL UNIVERSITY

TWO FACULTY POSITIONS IN ECOLOGY AT NANYANG TECHNOLOGICAL UNIVERSITY, SINGAPORE

Nanyang Technological University (NTU), Singapore new Asian School of the Environment seeks two full professor level positions in ecology as part of a terrestrial and marine initiative in Southeast Asia. The Asian School of the Environment, a new interdisciplinary School, focuses on Asian environmental challenges. The school integrates Earth systems, environmental life sciences, ecology, engineering, humanities, and the social sciences to address key issues of the environment and sustainability.

1. Full Professor in Tropical Forest Ecology/Ecosystem Science
As part of the transformation, NTU will partner with the Smithsonian Institution, particularly the Tropical Research Institute (STRI), to expand science and education related to the Smithsonian Global Earth Observatories, including the Center for Tropical Forest Science (Forest Global Earth Observatory) and the newly established Marine Global Earth Observatory (Tennenbaum Marine Observatories Network). The successful candidate will also be appointed as a Research Associate with the Smithsonian and expect to spend time each year in Washington, DC, and Panama. We seek an individual who has established a world-class research program that deals with current topics of tropical forest science, such as population and community ecology, ecosystem science, forest-atmosphere interactions, forest-soil interactions, global change effects on forest diversity and function. The successful candidate will take a leadership role in the expansion of science related to the Asian network of the Smithsonian's Center for Tropical Forest Science-Forest Global Earth Observatory.

2. Full Professor in Ecology
We seek an internationally prominent ecologist, who works in marine or terrestrial systems interested in ecological interactions at multiple scales. The new position in ecology will complement the Earth Observatory of Singapore's (EOS) core strengths in natural hazards and Earth systems science; the Singapore Centre on Environmental Life Sciences' (SCELSE) expertise in structure and function of complex microbial communities, and the Complexity Institute's research in coupled human and natural systems.

For both positions, NTU seeks scientists with outstanding track records in the field of (tropical) forest or marine ecology. The successful candidates will establish the new Asian School of the Environment as a leader in studies of tropical ecological and ecosystem processes.

The candidates are expected to:

- Establish a world-class research programme,
- Play a leading role in the formation of the new Asian School of the Environment,
- Enhance the new School's visibility as an international leader in education and research in Ecology and Ecosystem Science,
- Teach undergraduate and graduate courses in Ecology and related environmental sciences, and
- Actively collaborate with NTU faculty and researchers with existing strengths in Earth Systems Science and Environmental Life Sciences.
- Work to strengthen interactions between NTU and the Smithsonian Institution in building and enhancing the Forest and Marine Global Earth Observatories Programs.

NTU offers highly competitive salary as well as comprehensive benefits, including subsidized on-campus housing and childcare. A start-up package, state-of-the-art research infrastructure as well as a yearly research allowance for positions and consumables will be available.

For both positions, please address requests for further information to Professor Alexander J.B. Zehnder (AZEHNDER@ntu.edu.sg); and to Dr. Stuart J. Davies (DaviesS@si.edu) for information pertaining to the joint Smithsonian activity. Applications, including the applicant's experience/philosophy of research, teaching, and extension, a résumé, and contact information for three professional references should be sent to the Provost of NTU, Professor Freddy Boey (ntu-provost@ntu.edu.sg). Review of applications will begin on 30 December 2014 and will continue until the positions are filled.

NTU is an equal opportunity employer.

Jefferson Science Fellowship

The National Academies is pleased to announce a call for nominations and applications for the 2015 Jefferson Science Fellows program. Initiated by the Secretary of State in 2003, this fellowship program engages the American academic science, technology, engineering and medical communities in the design and implementation of U.S. foreign policy.

Jefferson Science Fellows (JSF) spend one year at the U.S. Department of State or the U.S. Agency for International Development (USAID) for an on-site assignment in Washington, D.C. that may also involve extended stays at U.S. foreign embassies and/or missions.

The fellowship is open to tenured, or similarly ranked, academic scientists, engineers and physicians from U.S. institutions of higher learning. Nominees/applicants must hold U.S. citizenship and will be required to obtain a security clearance.

The deadline for 2015-2016 program year applications/nominations is **January 12, 2015.** To learn more about the Jefferson Science Fellowship and to apply, visit the website at:

www.national-academies.org/jsf

THE NATIONAL ACADEMIES
Advisers to the Nation on Science, Engineering, and Medicine

MICHIGAN STATE UNIVERSITY

Open Position in
Microbial Ecology: Microbiome/Infectious Disease
Department of Microbiology & Molecular Genetics

The Department of Microbiology & Molecular Genetics at Michigan State University seeks candidates at the Assistant or Associate Professor level for a position in the microbial ecology of infectious disease including interactions between host, microbiome, pathogen and environment. Of special interest within the broad area of the microbial ecology of infectious disease are systems biology and evolution at the molecular level, physiology and metabolic networks of microbial consortia, interactions of pathogens with mammalian hosts, insect vectors, and/or microbiota within them, host innate immunity to microbes, and the application of "omics" technology to study these areas. Significant opportunities exist for collaboration with faculty associated with the NSF BEACON Center (Evolution in Action), the NIH Enterics Research Investigational Network, the NIH International Center of Excellence for Malaria Research, the RDP, and the Center for Water Sciences. A strong record of research accomplishment and/or potential for an independent, externally funded research program with national visibility is expected. Academic rank will be commensurate with experience. Teaching in graduate, professional, and/or undergraduate programs is expected. The offer will include a competitive startup package and laboratory facility.

Applications should be submitted electronically at **https://jobs.msu.edu** (posting **#0519**) with requisite material (letter of interest, curriculum vitae listing past and current funding if appropriate, a statement of future research goals, and names of three potential references (not to be contacted until approval is received from the applicant)) uploaded as a single PDF. Review of applications will begin immediately and remain open until filled.

Additional information could be obtained via email to the Search Committee Executive Assistant at **mmgchair@msu.edu**. **http://www.mmg.msu.edu**

MSU is an Affirmative-Action, Equal-Opportunity Employer and is committed to achieving excellence through diversity. The University actively encourages applications of women, persons of color, veterans, and persons with disabilities, and we endeavor to facilitate employment assistance to spouses or partners of candidates for faculty and academic staff positions.

POSITIONS OPEN

The Department of Biological Sciences (DBS) at the University of North Carolina at Charlotte is seeking applicants for a tenure-track **ASSISTANT/ASSOCIATE PROFESSOR** position. Applicants should possess a Ph.D. in the biological sciences with expertise in Protein functions in a biological context. Candidates are expected to document expertise in their specialty by a record of postdoctoral training, peer-reviewed publications, and plans for supporting an extramurally funded research program. Higher consideration will be given to applicants that bring needed expertise in large glycoprotein function (i.e., Chaperones, Receptor and Adaptor complexes). Previous teaching and mentoring experience is highly desirable. In addition to contributing to graduate programming in the DBS, this position is part of a long-term effort to establish a resident "Protein Function & Biotechnology Research" Group and will be expected to also make contributions to the Nanoscale Science Ph.D. Program (jointly with the Chemistry, Math & Statistics, Physics & Optics Departments, and academic units in the College of Engineering).

The successful candidate is expected to contribute to teaching and mentoring in our undergraduate and graduate curricula with a focus on Protein function in a cell biological context. The Department of Biological Sciences supports B.S., B.A., M.S. (thesis and non-thesis), and Ph.D. programs with a diverse body of faculty and students and prides itself with hands-on training of its students. The Department and College strongly support and value diversity among their students and faculty.

Candidates must apply online at **website: http://jobs.uncc.edu, position number: 6753.** Please provide complete curriculum vitae, philosophy statements for research and teaching in an ethnically diverse environment, contact information for three references, and three representative publications. Screening of applications will begin December 15, 2014, and continue until the position is filled. The expected start date is August 15, 2015.

For more information, please refer to the Department of Biological Sciences **website: http://biologicalsciences.uncc.edu** for contact information.

The University of North Carolina at Charlotte is an Equal Opportunity Employer/Affirmative Action Employer and an ADVANCE Institution that strives to create an academic climate in which the dignity of all individuals is respected and maintained. Therefore, we celebrate diversity that includes, but is not limited to ability/disability, age, culture, ethnicity, gender, language, race, religion, sexual orientation, and socio-economic status.

DIRECTOR
Forensic Science Program

Middle Tennessee State University invites qualified applicants for a tenure-track faculty position serving as Director of the B.S. in Forensic Science program (rank open). The Forensic Science degree program is an interdisciplinary program involving the departments of Biology, Chemistry, and Criminal Justice Administration. Responsibilities for the director will include direction and evaluation of program activities, oversight of internships, and management of initial program accreditation through FEPAC. The director will teach in undergraduate specialty courses. The director will also be expected to direct his/her own research program involving undergraduate and graduate students. For more information about the position requirements and application procedure, visit **website: http://www.mtsu.edu/hrs/.**

Stop searching
for a job;
start your career.

ScienceCareers
FROM THE JOURNAL SCIENCE AAAS

ScienceCareers.org

THE UNIVERSITY OF ALABAMA AT BIRMINGHAM

Chair
Department of Computer and Information Sciences
College of Arts and Sciences

The UAB College of Arts and Sciences (CAS) invites applications for the position of Chair of the Department of Computer and Information Sciences. For additional information on the department, please visit https://cis.uab.edu/.

Computer and Information Sciences at UAB offers BS, MS, and PhD degrees. The Department has a strong research focus, excellence in teaching, and a strong commitment to outreach, innovation, and industrial partnerships. Research grants are growing significantly, and the Department has a leading role in an Interdisciplinary Research Center in Information Assurance and Computer Forensics. Departmental strengths include research programs in diverse areas of Computer Science including programming languages and software engineering, information assurance, natural language processing, machine learning, data mining, computer graphics, visualization, 3D printing, computer forensics, and high performance computing. Collaborations with UAB's school of engineering and the medical enterprise are strong and growing, with opportunities for faculty to participate in interdisciplinary R&D.

The successful candidate will combine excellence in research and management with a fundamental understanding of the operation and advancement of a research-focused Computer Science department at a Carnegie Research Extensive University (RU-VH). The chair is responsible for overall departmental administration and reports to the Dean of the College of Arts and Sciences. The successful candidate will be expected to provide strategic direction, vision, and leadership to the department and to participate actively in development across the UAB campus and in the city of Birmingham. The University is now embarking on the development of a 5 and 10 year plan to develop research computing. There is an opportunity for significant growth of the department over the next five years and the new Chair is expected to play an active role in the development of research computing infrastructure at UAB.

The Chair is the chief academic, financial, and strategic officer for the Department. He or she will work to recruit and retain outstanding faculty and students at all levels, contribute to the intellectual life of the department as an active member of the faculty, and promote the department within the University and, as importantly, outside the University to secure support. A PhD in Computer Science or a closely related field is required. Candidates must possess a distinguished record of scholarship, grant funding, teaching, and professional service consistent with appointment at the rank of Full Professor with tenure. Candidates must exhibit excellent interpersonal, verbal, and written communication skills, and interest in commercialization and entrepreneurship is welcome.

Applicants should submit (1) a cover letter summarizing qualifications and explaining interest in the position, (2) a complete curriculum vitae, (3) a statement of vision and management style, and (4) contact information for at least five references. References will not be contacted without prior permission of the candidate.

Screening will begin on **October 1, 2014**, and will continue until the position is filled. Please go to the following web-site to apply and upload application materials.

http://www.uab.edu/cas/application

For more information or to make inquiries about this position, contact:

Yogesh K. Vohra, PhD
Professor/Associate Dean
Chair, CIS Chair Search Committee
E-mail: ykvohra@uab.edu
Tel: (205) 934-6662

UAB is an Equal Opportunity/Affirmative Action Employer committed to fostering a diverse, equitable and family-friendly environment in which all faculty and staff can excel and achieve work/life balance irrespective of race, national origin, age, genetic or family medical history, gender, faith, gender identity and expression as well as sexual orientation. UAB also encourages applications from individuals with disabilities and veterans.

A pre-employment background investigation is performed on candidates selected for employment.

ScienceCareers online @sciencecareers.org

Institute of Marine and Environmental Technology

UNIVERSITY SYSTEM OF MARYLAND

Assistant Professor: Fish/Shellfish Immunology

The Institute of Marine and Environmental Technology (IMET) of the University System of Maryland seeks applications for the position of Assistant Professor (tenure-track) working on fish/shellfish immunology. The successful candidate will have a track-record of outstanding research using molecular biology/genetics approaches to study fish and comparative immunity in species that are important to aquaculture and fisheries, or in species that are established animal models (i.e. zebrafish) for immunological studies that are relevant to both fish and human health. Candidates with an interest in practical applications of their fundamental research, including interactions with industry, are encouraged to apply. A demonstrated ability to establish a well-funded research program is expected of the successful candidate. The primary focus of the appointee will be on research; teaching at the graduate level is encouraged.

IMET's mission is to study the biology of coastal marine biosystems and ensure their sustainable use, as well as exploit marine-derived systems to improve human health (www.imet.usmd.edu). IMET brings together faculty members from three major USM research institutions - the University of Maryland Baltimore (UMB), the University of Maryland Baltimore County (UMBC), and the University of Maryland Center for Environmental Science (UMCES) - in an integrated state-of-the-art research facility located at Baltimore's Inner Harbor.

A Ph.D. or equivalent terminal degree is required in molecular biology, microbiology, aquatic pathology or related fields and candidates should have postdoctoral experience and a strong publication record. Applicants should send the following in a single PDF file to Russell Hill, Director, IMET; email to imetdirectorsoffice@umces.edu: (1) detailed curriculum vitae, (2) statement of research interests and goals and (3) names and contact details of three to five references. To receive full consideration, application materials should be submitted by **15 January, 2015** (the position will be open until filled).

The USM is an Equal Opportunity, Affirmative Action Employer. The University of Maryland, Baltimore is an Equal Opportunity/Affirmative Action Employer. Minorities, women, individuals with disabilities, and protected veterans are encouraged to apply.

Institute of Marine and Environmental Technology

UNIVERSITY SYSTEM OF MARYLAND

Assistant Professor: Basic biological processes at the interface between human health and the environment

The Institute of Marine and Environmental Technology (IMET), University of Maryland seeks applications for the position of Assistant Professor (tenure-track). The successful candidate will have a track-record of outstanding research on basic biological processes at the interface between human health and the environment. Focus areas of particular interest include but are not limited to marine natural products discovery using (meta)genomic approaches to identify biosynthetic gene clusters and use of zebrafish or other model systems to study disease or development. Candidates with an interest in practical and biomedical applications of their fundamental research, including interactions with industry, are encouraged to apply. A demonstrated ability to establish a well-funded research program is essential, with strong preference for candidates with active K99, RO1 or equivalent funded research programs. Primary appointment is in the School of Pharmacy at the University of Maryland Baltimore, with a secondary appointment at the University of Maryland Center for Environmental Science. The primary focus of the appointee will be on research; teaching at the graduate level is encouraged. Candidates should explicitly outline the links of their research to human health and environmental applications.

IMET's mission is to study the biology of coastal marine biosystems and ensure their sustainable use, as well as exploit marine-derived systems to improve human health (www.imet.usmd.edu). IMET brings together faculty members from three major University of Maryland research institutions - the University of Maryland Baltimore (UMB), the University of Maryland Baltimore County (UMBC), and the University of Maryland Center for Environmental Science (UMCES) - in a dedicated state-of-the-art research facility located in Baltimore's Inner Harbor.

A Ph.D. or equivalent terminal degree is required in molecular biology, microbiology, biochemistry, bioengineering or related fields and candidates should have postdoctoral experience and a strong publication record. Applicants should send the following in a single PDF file to Russell Hill, Director, IMET; email to imetdirectorsoffice@umces.edu: (1) detailed curriculum vitae, (2) statement of research interests and goals and (3) names and contact details of three to five references. The position remains open until filled; to receive full consideration, applications should be submitted by **January 15, 2015**.

The USM is an Equal Opportunity, Affirmative Action Employer. The University of Maryland, Baltimore is an Equal Opportunity/Affirmative Action Employer. Minorities, women, individuals with disabilities, and protected veterans are encouraged to apply.

POSITIONS OPEN

The Illinois Natural History Survey (INHS) is soliciting applications for a two-year **POSTDOCTORAL RESEARCH ASSOCIATE**. Scientists whose research interests fit within those of the Illinois Natural History Survey are encouraged to apply. A salary of $42,000 per year with benefits is provided as well as a $5,000/year research stipend. Applicants should submit curriculum vitae and Research Proposal. The Research Proposal is limited to three pages, not including references, and should address the research plan and budget proposed for the two-year postdoctoral position. In advance of the application deadline, applicants must identify and contact a research sponsor at the INHS (**website: http://wwx.inhs.illinois.edu/opportunities/postdoc-sponsors/list/**) who is willing to sponsor the Postdoctoral Associate. Preference will be given to applicants who can develop a strong research plan that merits additional and continued external funding. Research plans that build on existing INHS research strengths by adding new directions or new analytical techniques are encouraged.

Applicants should have completed a Ph.D. by the start date of the position (expected before December 31, 2015) and within the last five years. In addition to the Research Proposal and curriculum vitae, applicants should arrange for two letters of recommendation to be sent. Applications must be sent electronically to **e-mail: hroffice@inhs.illinois.edu** by January 31, 2015.

Help employers find you.
Post your resume/cv.
www.ScienceCareers.org

Join the Conversation!

Twitter is a great way to connect with AAAS members and staff about the issues that matter to you most. Be a part of the discussion while staying up-to-date on the latest news and information about your personal member benefits.

Follow us @AAASmember and join the conversation with #AAAS

AAAS MemberCentral
MemberCentral.aaas.org

Sheppard Pratt-Lieber (SPL) Research Institute
Executive Director

To advance our mutual vision of creating new treatment options for individuals with serious mental illness, Sheppard Pratt Health System, Inc. and the Lieber Institute for Brain Development (LIBD) have established a joint nonprofit research institution. This institute will focus on translating scientific advances in genetics, neuroimaging, and other aspects of brain research into clinical practice with the goal of improving patient care and outcomes.

The SPL Research Institute will leverage the respective strengths of both of the founding organizations. The Institute's collaborative research activities will encompass the broad areas of human clinical research, including genetics, neuroimaging, clinical trials, novel therapeutics, repurposing of existing therapeutic agents, digital clinical record data mining, and the creation of a biobank.

The SPL Research Institute Board of Directors is seeking a clinician-scientist to serve as a full time Executive Director (ED). This individual will have overall strategic and operational responsibility for the staff, programs, organization, and execution of the mission of this new psychiatric research organization. Working with the Board of Directors and an independent Scientific Advisory Board, along with key partners from the Sheppard Pratt Hospital and the Lieber Institute for Brain Development (LIBD), the successful candidate will develop core research and administrative programs, operations, and business plans as the first Executive Director.

The SPL Research Institute is located in newly renovated space on the campus of Sheppard Pratt Health System in Towson, MD. Candidates for this position must have an M.D. and a strong background in clinical neuropsychiatric research. The SPL Research Institute is an equal opportunity employer, and encourages candidate applications from individuals with diverse backgrounds.

For more information about this opportunity, please contact **Kathleen Hilzendeger**, Director of Professional Services at **410-938-3460** or **khilzendeger@sheppardpratt.org**.

University of Nebraska Lincoln

GROWING IANR
Faculty Positions
Institute of Agriculture and Natural Resources

The Institute of Agriculture and Natural Resources (IANR) at the University of Nebraska-Lincoln (UNL) is committed to world-class excellence in applications of agricultural and life sciences towards a sustained high quality of life for the citizens of Nebraska, and for a quickly growing global population. Early in 2013, reflecting this commitment, IANR launched an initiative to hire new tenure-track faculty members in strategic impact areas of Science Literacy; Stress Biology of Plants, Animals, and Agroecosystems; Healthy Humans; Healthy Systems for Agricultural Production and Natural Resources; and Computational Sciences. This Phase 1 effort was very successful, resulting in the recruitment and hiring of 35 highly skilled tenure-line faculty members (with two searches still active).

We are pleased to announce Phase 2 of this effort with recruitment for an anticipated 30+ additional tenure-line faculty positions. The focus for Phase 2 will be to strengthen the six strategic impact areas in Phase 1, with an additional focus area – Drivers of Economic Vitality for Nebraska.

We invite you to view brief explanations of the positions currently being released and those to be released soon at http://ianr.unl.edu to explore whether your skills and experience make you a good fit for our team.

The positions will be advertised and posted beginning **December 1, 2014**. We invite you to visit the UNL employment web site at **http://employment.unl.edu** to learn which positions are posted.

The University of Nebraska is committed to a pluralistic campus community through affirmative action, equal opportunity, work-life balance, and dual careers.

IANR



AAAS is here –
helping scientists achieve career sucess.

Every month, over 400,000 students and scientists visit ScienceCareers.org in search of the information, advice, and opportunities they need to take the next step in their careers.

A complete career resource, free to the public, *Science* Careers offers hundreds of career development articles, webinars and downloadable booklets filled with practical advice, a community forum providing answers to career questions, and thousands of job listings in academia, government, and industry. As a AAAS member, your dues help AAAS make this service available to the scientific community. If you're not a member, join us. Together we can make a difference.

To learn more, visit
aaas.org/plusyou/sciencecareers

AAAS + U = Δ

Science Careers
Cernet

"《科学》职业" 已经与Cernet/赛尔互联开展合作。中国大陆的高校可以直接联系Cernet/赛尔互联进行国际人才招聘。



请访问 Sciencecareers.org/CER 点得联系信息。

招募学术精英,《科学》是您的不二之选 Science

ScienceCareers online @sciencecareers.org

By **Vincent F. Scalfani**

Finally free

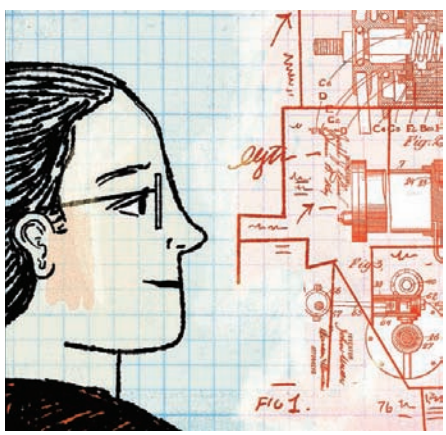
As a child, I found relief from the stress of stuttering by burying myself in numerous hobbies. I built rockets and radio-controlled vehicles. I rebuilt engines. I did these things because when I was building something, I did not have to think about speaking. ¶ My hobbies eventually led me to study chemistry. After finishing a B.S. in chemistry at the State University of New York, Oswego, I studied polymer chemistry and earned a Ph.D. at Colorado State University. I enjoyed chemistry research for the same reasons I enjoyed my hobbies as a child: I could do interesting things, free from the stress of speaking. In the laboratory, I could be alone and build things, although now I was building molecules instead of model cars.

I noticed early on that when I forgot about stuttering, my speech became much more fluent. The first few words of a question or first few minutes of a presentation were rough, but then I forgot about the audience, forgot about stuttering, and forgot about worrying. When that happened, my speaking improved. I felt free.

I wanted to feel free all the time. Unfortunately, there were always new people to meet and presentations to deliver, so there were many awkward beginnings. I was ashamed of my stutter and did everything I could to hide it. Far from forgetting about it, I developed strategies for dealing with it. Whenever I felt I was going to stutter, I would substitute a new word that was easier to say. I obsessed over how to deliver a talk or just hold a conversation. I studied every tiny detail and came up with alternative explanations ahead of time so that I could always change terminology or the direction of the conversation. It was a wonderful irony: My incapacity for spontaneous speech led to a highly developed skill for improvisation. My adaptations were so successful that most of my peers and professors probably did not even know I stuttered.

Later, I would learn that hiding my stutter only perpetuated my anxiety and frustration with my speech. The skills I acquired by hiding it, though, never left me.

After graduate school, my interests shifted away from the laboratory, and I started to investigate alternative career paths. I accepted a position as assistant professor and science and engineering librarian at the University of Alabama, Tuscaloosa. In my new job, I communicate regularly and spontaneously with students, faculty, and staff. I knew that if I wanted to succeed, I needed to change my attitude toward stuttering. I could no longer hide behind a lab bench.



"My incapacity for spontaneous speech led to a highly developed skill for improvisation."

I decided to check out the campus Speech and Hearing Center. There, I met an amazing group of therapists, scientists, and students. They helped me realize that my success was a consequence of my stutter, not in spite of it. When I was a child, stuttering had led me to explore certain hobbies. It forced me to become an independent learner. It made me a very hard worker. My largely successful attempts at hiding my stutter led to a remarkable mental agility. Strangely (but successfully) my therapists challenged me to try to stutter more. With all the useful skills I had developed largely because of my stutter, I felt unstoppable when I no longer had to devote energy to hiding it.

I have flourished in my new job. I created and taught a semester-long graduate chemical information course. I manage a 3D-printing lab, edit the American Chemical Society's *Chemical Information Bulletin*, and have published several research articles. Earlier this year, *Library Journal* named me a "Mover and Shaker," a prestigious early-career award for librarians.

I have accomplished more than I would have thought possible in my first 2 years here because I stopped worrying about my stutter and decided instead to embrace it. Sometimes the things you struggle with the most, I've realized, end up making you who you are. Now that I know that, I am ready for whatever is next in my career, because I am finally free. ■

Vincent F. Scalfani is assistant professor and science and engineering librarian at the University of Alabama.
For more on life and careers, visit www.sciencecareers.org.

ILLUSTRATION: ROBERT NEUBECKER

Downloaded from www.sciencemag.org on December 5, 2014

Published by AAAS